INFORMATION TO USERS

This manuscript has been reproduced from the microfilm master. UMI films the text directly from the original or copy submitted. Thus, some thesis and dissertation copies are in typewriter face, while others may be from any type of computer printer.

The quality of this reproduction is dependent upon the quality of the copy submitted. Broken or indistinct print, colored or poor quality illustrations and photographs, print bleedthrough, substandard margins, and improper alignment can adversely affect reproduction.

In the unlikely event that the author did not send UMI a complete manuscript and there are missing pages, these will be noted. Also, if unauthorized copyright material had to be removed, a note will indicate the deletion.

Oversize materials (e.g., maps, drawings, charts) are reproduced by sectioning the original, beginning at the upper left-hand corner and continuing from left to right in equal sections with small overlaps.

Photographs included in the original manuscript have been reproduced xerographically in this copy. Higher quality 6" x 9" black and white photographic prints are available for any photographs or illustrations appearing in this copy for an additional charge. Contact UMI directly to order.

Bell & Howell Information and Learning
300 North Zeeb Road, Ann Arbor, MI 48106-1346 USA
800-521-0600

UMI®

Hydrocarbons and Condensible Volatiles of Jupiter's Galileo Probe Entry Site

by

Michael H. Wong

A dissertation submitted in partial fulfillment
of the requirements for the degree of
Doctor of Philosophy
(Atmospheric and Space Science)
in the University of Michigan
2001

Doctoral Committee:

Professor Sushil K. Atreya, Chair
Paul R. Mahaffy, Ph.D., NASA Goddard Space Flight Center
Professor Anthony W. England
Professor William R. Kuhn
Assistant Professor Peter E. van Keken

UMI Number: 3001068

UMI®

UMI Microform 3001068
Copyright 2001 by Bell & Howell Information and Learning Company.
All rights reserved. This microform edition is protected against
unauthorized copying under Title 17, United States Code.

Bell & Howell Information and Learning Company
300 North Zeeb Road
P.O. Box 1346
Ann Arbor, MI 48106-1346

From Jove, O Muse, my mother—for all things yield to the sway of Jove—inspire my song! ...now I need the gentler touch, for I would sing of boys beloved by gods, and maidens inflamed by unnatural love and paying the penalty of their lust.

The king of the gods once burned with love for Phrygian Ganymede, and something was found which Jove would rather be than what he was. Still he did not deign to take the form of any bird save only that which could bear his thunderbolts. Without delay he cleft the air on his lying wings and stole away the Trojan boy, who even now, though against the will of Juno, mingles the nectar and attends the cups of Jove.

—Publius Ovidius Naso, 43 B.C. – 17 A.D.

DEDICATION

I dedicate my dissertation for the benefit of all beings.

ACKNOWLEDGEMENTS

There are so many people to thank for my academic development. Of course it started with Ma (a.k.a. Bonnie) who managed to raise the kids largely free of the mind-controlling and thought-suppressing device known as television. Paradoxically, Daddy (a.k.a. Pat) stimulated my interest in planets (and science in general) by exposing me to Carl Sagan's *Cosmos* series and *Nova* on PBS, as well as the breathtaking images from the Voyager encounters with the giant planets on the nightly news. Ma gets credit for subscribing the young proto-scientist to *Odyssey* and *Discover* magazines, and Daddy gets credit for the 6" reflecting telescope, with which we saw lunar craters, the Galilean satellites, and Saturn's rings from our San José backyard, and nebulae and Comet Halley from Grant's Ranch (between San José and Lick Observatory). Both parents are responsible for taking us all the way to Lick Observatory one night, where we saw Saturn and the surface of the moon; Peter filled the family car with vomit and its cloying odor during the winding descent from Mt. Hau-ta-ton, and thus became a linguist and electronic musician instead of a planetary scientist like me. Somehow our parents were able to instill a sense of the importance of education in all three of us, without the pressure that many of the other kids faced (except for those %@#&$! multiplication tables), and they unbegrudgingly paid for some 28 semesters of UC education, which I know was not easy.

The long line of influential teachers started in the gifted/honors programs in the Alum Rock and East Side Unified School Districts. Of all the teachers there, Mr. Nalty deserves proper respect for teaching me most of what I know about English, in only two semesters of high school. He's retired now, but many of his former students are still awe-struck by the effectiveness of his grammar notebooks and plastic orange projectiles. At UC Berkeley I received a thoroughly rigorous education in Astrophysics, but I learned the most from Imke de Pater and her enthusiasm for training me to do research. Imke, Carl Heiles,

and Ron Maddalena provided guidance during one of the most exciting moments of my planetary science career: the observation of Jupiter's 20-cm response to the Shoemaker-Levy 9 impacts at the (now decommissioned) 140' telescope at NRAO Green Bank (de Pater et al., 1995; Wong et al., 1996). Sorry, but that's the only way I could get those references into the Bibliography. Finally, in my graduate career, I should first thank Hasso Niemann, the jovial mass-spectrometer head honcho of NASA, PI on the GPMS, and ultimate source of funding for most of my graduate school expenses. His colleague, Paul Mahaffy, showed me many kindnesses, from allowing me to stay in his basement while I worked at Goddard for about four months, to serving on my thesis committee and making the trek out to Michigan for the defense. In the mean time he helped direct my GPMS data analysis, and did the calibration experiments that are discussed in Chapters 4 and 5. Professor Kuhn was very helpful on the committee as well, but I will mainly remember him for having the best facility, out of all the AOSS faculty members, to share the true excitement of atmospheric physics within the classroom. Sushil Atreya has been a superb advisor. His comprehensive knowledge of planetary atmospheres and solar system formation is much better than any search engines I have used. My grad brothers and I are especially grateful to Sushil for sending us to numerous planetary meetings, including good old DPS, NASA launches and first encounters, and special meetings in Europe. He really lived up to the title of advisor, guiding me safely through several grad student crises.

My survival is due in part to the collective strength of "our generation" as we suffered together in the sometimes windowless confines of the Space Research Building. I give tremendous thanks to Scott Edgington, Eric Wilson, and Maarten Roos-Serote, and Dan Marsh for sharing code. Mike Barlage, Scott, Kandis Lea Jessup, and the custodial staff made me feel like less of a freak for being at work at 2am, and Jan Beltran's stories (and wine) made the office a bit more interesting. The Lovelab's road trip to/from Madison DPS will always be memorable. And thanks to lunar scientist Stefanie Lawson for making the Tucson and Pasadena DPSs much more fun than they would have been otherwise.

Learning is not limited to the university: the Ann Arbor YMCA Judo Club and Jewelheart made sure of that. I've had a great six years on the mat with judo Senseis Kevin

Watkins, Tony Springfield, Neil Simon, Sanjoy Ghosh the hairdresser, Karen DuPage from Jackson, and Phillipe Ezanna, as well as with lower ranks Scott Helmstadter, Ken Hauser, John Judge, and Mickey, and numerous newcomers and short-term Ann Arbor judokas. Here at the Ann Arbor YMCA I learned that what distinguishes judo black belts is not the ability to take an opponent with an 80-lb weight advantage, throw him on his back, break his elbows, and choke him unconscious, but rather a true understanding of Sensei Jigoro Kano's two principles: "Mutual Welfare [and] Benefit," and "Maximum Efficiency Minimum Effort." In my last couple years in Ann Arbor, I found Jewelheart (www.jewelheart.org). At Jewelheart, Kyabje Gelek Rinpoche has been an amazing guide on the spiritual path. In fact, before Rinpoche, I did not even realize I was *on* any kind of spiritual journey. The teachings I received from him, which ultimately come from Buddha, are responsible for my almost complete lack of stress during the four months of all-nighters leading up to my dissertation defense.

I have always kept my social life separate from work, but in order to beat Scott's 3.5 pages of acknowledgements, I would like to first thank several of my pre-Michigan friends for actively keeping me in their lives. The phattest props go to Randall Kuhn, Thomas Phan, Simone Chou, Anne Marks, J.B. from Berkeley judo, Ethan Bodle, Lisa Jantzen, Tara Lee, and Crouton (a.k.a. Mike Reilly), as well as to my brothers Peter and Jonathan, my parents, and Auntie D, for actually visiting me in Michigan. Anti-thanks go to Jenny Eng and Laura Teasley who promised to visit but never did. Exes Diego Pacheco and Quentin Lee were nice enough to keep in touch, and Yao-Fen You even moved to Michigan to be with me. She is responsible for furnishing the quote on the frontispiece.

While in Ann Arbor I have been fortunate enough to make many good friends. At the North Campus Coop I met kinetic sculptor Joan Giroux, hip-hop dancer Dr. Anna Yeakley, and Peace Corps veteran Michelle Jensen. In my second month at UM I met Eric Kessell, just because he was so "active in the community;" later we made it through a semester of coop life together. Outside the coop I lived with workaholic Elysée Matsubara in the %@#&$! Nollars' building, and pixel princess Jen Concepcion in the Yellow Dragon Palace, where we spent many hours watching Iron Chef and Tenchi Muyo. Then there are

MOTHRA members Daniel Tsao, Melissa Chiu, Izumi Sakamoto, Haruna Madono, and Lulu Chou. One of the funnest experiences at UM was WCBN-FM (wcbn.org), where DJs JJ Heldmann (along with her cat Delgado and husband Mac), Jamie Rollins, and Sara Grosky became close friends. The Michigan music scene has been a tremendous inspiration to me, from space rock and indy pop to techno and hip hop. The amount of talent concentrated in southern Michigan is truly amazing, and they do it not to get rich, but for the sake of art.

Thanks go to all those who satisfied primal urges with me. Yao-Fen and Daniel are much more obsessed with food than I am, and the adventures I've shared in the kitchen and restaurants with them are experiences that I could never have approached on my own, ranging from the exorbitant feasts at West End Grill, Yamato, and Seoul Garden, to the simple meals at Dinersty, Coffee Break, and Northside Grill, to homemade tempura, sushi, ravioli, and braised fennel. I enjoyed consuming obscene amounts of clementines with Daniel, Yao-Fen, and Jen. Finally, I could not have maintained interest in school without the distraction of several experiences which are not appropriate to describe in this document. Thus, I simply offer thanks to Daniel, Lulu, Melissa, Michelle, Jen, Eric, Haruna and her sister, Elysée, Charlie, Sara, Jesse, Hak and Michael, Jamie, Brian, Jeff, and Max.

Due to the weak commitment to human rights in the United States, I have no spouse to thank in this paragraph. The distinction between calling Daniel my domestic partner and calling him my spouse is more than a semantic one; since our committed union is not recognized by the United States government, Daniel has no automatic right to remain in the country with the person he loves. Daniel, a Hong Kong citizen, came to UM for two years of architecture grad school. He was curious and went to a MOTHRA meeting in 1995. We did not meet again for a week after the meeting, but we exchanged 8-kb emails daily. Within a year he was asking me to marry him, and on 1999-04-17, we finally signed domestic partnership papers, with the Campus Bike Store lady as the notary. So I thank Daniel for his love and commitment, the years of mutual growth, the future we're planning together, and his help during the final days of defense preparation—especially his help in rushing to the

store on the morning of the defense to get some decent clothes for me to wear in place of my normal t-shirt, sweatshirt, and wide-leg jeans.

This research was supported in part by the NASA Graduate Student Researchers Program [NGT 5-27].

TABLE OF CONTENTS

DEDICATION ii

ACKNOWLEDGEMENTS iii

TABLE OF CONTENTS viii

LIST OF TABLES xi

LIST OF FIGURES xiii

LIST OF APPENDICES xxi

CHAPTER I
Welcome to Jupiter 1
Overview of dissertation 1
Origin of Jupiter 1
Tropospheric structure: Belts, zones, hotspots 7
Composition 10
Non-condensing minor gases 12
Condensible volatiles 14
Photochemical products 24
Disequilibrium species 25
Clouds and Probe site meteorology 26

CHAPTER II
The Galileo Probe Mass Spectrometer 34
Galileo Probe and Orbiter Instrumentation 34
Principles of Mass Spectrometry 36
GPMS Gas Handling System Components 37
Descent Sampling Sequence 45
The Flight Unit (FU) and the Experimental Unit (EU) 48

CHAPTER III
GPMS Data Analysis Procedure 49
Using count ratios 49
The deadtime correction 55
The background correction 57
Choosing the appropriate reference gas 59
Correcting for mass-interference using predetermined splitting patterns 60
The Calibration Constant 62
Estimation of Error 63
Propagation of Error 67

CHAPTER IV
GPMS Calibration:
Experimental Procedures 71
Flight Unit: Calibration Experiments and Protoflight Sequence 71
Experimental Unit:
Sample Gas Mixture Preparation 73
Experimental Unit:
Pressure and Inlet Leak Considerations 77
Calibration Data Processing 79

CHAPTER V
GPMS calibration constants 84
Overview 84
C_2H_6 (Ethane) 85
C_3H_8 (Propane) 88
C_4H_{10} (Butane) 90
C_3H_6 (Propene, Cyclopropane) 93
C_2H_4 (Ethylene) 95
C_2H_2 (Acetylene) 97
N_2 (Nitrogen) 99
CH_4 (Methane) 100
H_2S (Hydrogen sulfide) 105
H_2O (Water) 107
NH_3 (Ammonia) 115
Summary 120

CHAPTER VI
GPMS results: isotopic ratios, mixing ratios, error analysis 123
Hydrocarbons: overview 123
Ethane 127

Propane and butane from C[29] and C[43] 130
Butane from C[58] 134
C_4H_6 from C[54] and C[53] 134
Vinylacetylene (C_4H_4) from C[52] 135
Biacetylene (C_4H_2) from C[50] 135
C_3H_6 from C[41] and C[42] 135
C_3H_4 from C[37], C[38], C[39], C[40] 137
Ethylene (C_2H_4) from C[27] 143
Acetylene (C_2H_2) from C[26] and C[25] 145
Non-hydrocarbon counts at C[28] 146
^{15}N / ^{14}N isotopic ratio 149
Condensible volatiles: overview 153
Hydrogen sulfide (H_2S) 153
Ammonia (NH_3) 155
Water (H_2O) 159
Methane (CH_4) 162

CHAPTER VII
Implications for hydrocarbon photochemistry 164

Physics, chemistry, and code heritage of the photochemical model . 164
Formulation of the photochemical model 168
Photochemical model environmental conditions 172
Eddy diffusion profiles and model results 176

CHAPTER VIII
Model of Jovian Downdraft with Entrainment 190

Review of terrestrial and Jovian downdraft modeling work 190
Downdraft modeling method 202
Effect of DDE model inputs 205

CHAPTER IX
Conclusions 215

GPMS composition measurements 215
Bulk composition of Jupiter 221
Tropospheric structure 222
Vertical transport of hydrocarbons 226

APPENDICES 232

BIBLIOGRAPHY 299

LIST OF TABLES

Table

1.1 Solar and Jovian abundances and isotopic ratios. 3

1.2 Summary of the composition of Jupiter prior to this dissertation. 4

1.3 Observed and ECCM-modeled cloud properties. 15

2.1 Galileo orbiter and probe instrumentation. 34

2.2 Inlet leak conductances. 43

2.3 GPMS valve program. 43

3.1 Reference gas polynomial fit orders. 51

3.2 Deadtime correction coefficients. 57

4.1 FU calibration experiment gas mixtures. 72

4.2 Gas mixture preparation. 74

4.3 EU calibration experiment gas mixtures. 75

4.4 Deadtime correction coefficients for calibration experiments. 81

5.1 Ethane calibration constants. 85

5.2 Propane calibration constants. 88

5.3 Butane calibration constants. 93

5.4 Propene calibration constants. 93

5.5 Effect of varying the deadtime correction for FU sequence 16. 94

5.6 Acetylene calibration constant. 99

5.7 Nitrogen calibration constants. 99

5.8 Comparison of methane calibration experiments. 101

5.9 Methane calibration constants. 105

5.10 Summary of calibration constants. 121

5.11 Summary of calibration constant fit parameters. 122

6.1 Hydrocarbon splitting pattern and calibration constant references. 126

6.2 MS45 search constraints. 129

6.3 GPMS and C_3H_4 count ratios. 142

6.4 Jovian CO + N_2 mixing ratio. 149

6.5 Jovian water mixing ratio. 161

6.6 Jovian methane mixing ratio. 163

7.1 Photochemical model data: lower boundary mole fractions. 174

8.1 DDE parameter sets. 209

9.1 Summary of GPMS mixing ratios derived in this dissertation. 216

B.1 Photochemical model data: reaction rates, reactants, and products. . . . 261

B.2 Photochemical model data: condensation. 271

B.3 Photochemical model data: photolysis products, quantum yields, and cross sections. 273

C.1 Entraining downdraft constants and variables. 282

C.2 Entraining downdraft variable indexes. 283

LIST OF FIGURES

Figure

1.1 Belts and zones of Jupiter. 8

1.2 Views of Jupiter at thermal infrared (L) and visible (R) wavelengths. 9

1.3 Galileo Probe entry site (PES), from Orton et al. (1998). 10

1.4 Helium saturation curves for helium-hydrogen solution, from Stevenson (1982). 14

1.5 Hydrogen sulfide in the PES. 20

1.6 Jupiter's microwave spectrum in the 1.3-cm NH_3 line. 21

1.7 Ammonia in the PES.. 22

1.8 Equilibrium cloud condensation model results. 28

2.1 GPMS gas handling system. 37

2.2 GPMS experimental sequence. (A) shows intervals during which EC1 was exposed to Inlet 1, Getter 2, Getter 1, and the mass spectrometer (MS). Similarly for (B), (E), (F). Shaded region in (F) indicates interval during which NGC and EC1 contents were simultaneously sampled by the MS. (C) and (D) show atmospheric pressure and temperature during the probe descent, and (G) shows GPMS step number. Each GPMS step had a duration of 0.5 s, so (G) is directly proportional to time.. 38

2.3 Mass/charge ratio measured by the GPMS, steps 0-1800. 39

2.4 Mass/charge ratio measured by the GPMS, steps 1800–3600. 40

2.5 Mass/charge ratio measured by the GPMS, steps 3600-5400.. 41

2.6 Mass/charge ratio measured by the GPMS, steps 5400–6900. 42

2.7 GPMS experimental unit (EU).. 48

3.1 Polynomial fit to C[2] reference gas H_2. Dark squares are 75-eV high sensitivity GPMS counts at mass 2. Grey squares indicate points at other ionization energies (15eV or 25 eV) or low sensitivity points. Grey curves are least square polynomial fits to the log of counts, with fit orders given in Table 3.01. DL2b counts are highly uncertain due to detector saturation (see text below Equation. 3.6). 52

3.2 Polynomial fit to C[4] reference gas He. As Figure 3.1 but with counts at mass 4. Triangles are low sensitivity points corrected to match high sensitivity counts; see text for discussion. DL2b counts are highly uncertain due to detector saturation (see text below Equation 3.6). . . . 53

3.3 Polynomial fit to C[12] reference gas product C^+. As Figure 3.1 but with counts at mass 12 C^+ is a fragment of methane, which has a constant mixing ratio in Jupiter's troposphere. 53

3.4 Polynomial fit to C[13] reference gas product CH^+. As Figure 3.3 but with counts at mass 13. CH^+ is a fragment of methane, which has a constant mixing ratio in Jupiter's troposphere. I favor mass 13 as a reference gas because it has a stronger signal than 12, does not suffer from confusion with N^+ as 14 does, and does not approach deadtime count saturation as 2 and 4 do. 54

3.5 Polynomial fit to C[14] reference gas product $CH_2{}^+$. As Figure 3.3 but with counts at mass 14. Mahaffy favors 14 as a reference gas because it has a stronger signal than 13. 54

3.6 Illustration of the loss of detector efficiency at high ion source pressure. 55

3.7 Functional form of detector response to increasing ion source pressure.. 56

3.8 Mass spectrum of water, ammonia, and methane. 60

3.9 Relative error in clusters of repeated FU measurements vs. Poisson-distributed error.. 64

3.10 Contour plot of deadtime-based uncertainty in count ratio CR[x/ref] as a bivariate function of count ratio numerator C[x] and denominator C[ref]. 65

4.1 Three EU calibration scans, illustrating data analysis challenges. 80

5.1 Ethane calibration constant with pressure as the ISP proxy ($\nu = 0.5$). . . . 86

5.2 Ethane calibration constant with C[2] as the ISP proxy ($\nu = 0.5$). 87

5.3 Propane calibration constant ($\nu = 0.5$). 89

5.4 Propane calibration constant ($\nu = 0.5$) 90

5.5 Butane, propane, and ethane splitting patterns 91

5.6 Butane cal4 calibration constant 92

5.7 Partial splitting patterns of propene, benzene, 1–hexene, butane, and propane 95

5.8 Ethylene calibration constant ($\nu = 0.6$) 96

5.9 Ethylene calibration constant ($\nu = 0.6$) 97

5.10 Acetylene cal4 calibration constant 98

5.11 N_2 calibration constant ($\nu = 1.0$) 100

5.12 Data used to estimate methane calibration constant uncertainty, for CR[16/4], leak 1 103

5.13 Data used to estimate methane calibration constant uncertainty, for CR[13/4], leak 1 103

5.14 Data used to estimate methane calibration constant uncertainty, for CR[16/4], leak 2 104

5.15 Data used to estimate methane calibration constant uncertainty, for CR[13/4], leak 2 104

5.16 H_2S calibration constant ($\nu = 0.3$) 106

5.17 H_2S calibration constant ($\nu = 1$) 107

5.18 Water mole fraction bin S: $q_{H2O} = 4 \times 10^{-5}$ 108

5.19 Water mole fraction bin M: $q_{H2O} = 7 \times 10^{-5}$ 108

5.20 Water mole fraction bin L: $q_{H2O} = 1.2 \times 10^{-4}$ 109

5.21 Water mole fraction bin XL: $q_{H2O} = 1 \times 10^{-3}$ 109

5.22 Change in EU deadtime "constant" over time 112

5.23 Water calibration constant 113

5.24 Water calibration constant 114

5.25 Water calibration constant 114

5.26 Ammonia mole fraction bin XS: $q_{NH3} = 1.0 \times 10^{-5}$. 116

5.27 Ammonia mole fraction bin S: $q_{NH3} = 2.2 \times 10^{-4}$. 116

5.28 Ammonia mole fraction bin M: $q_{NH3} = 1.0 \times 10^{-3}$. 117

5.29 Ammonia mole fraction bin L: $q_{NH3} = 2.4 \times 10^{-4}$. 117

5.30 Ammonia calibration constant for mole fraction bin S: $q_{NH3} = 2.2 \times 10^{-4}$. 119

5.31 Ammonia calibration constant for mole fraction bin M: $q_{NH3} = 1.0 \times 10^{-3}$. 119

5.32 Ammonia calibration constant for mole fraction bin L: $q_{NH3} = 2.4 \times 10^{-4}$. 120

6.1 Hydrocarbon contributions to masses 25 through 37. 124

6.2 Hydrocarbon contributions to masses 38 through 44. 124

6.3 Hydrocarbon contributions to masses 49 through 58. 125

6.4 Jovian ethane mixing ratio. 128

6.5 C[29]/C[43] count ratio. 130

6.6 Jovian butane mixing ratio (upper limit). 131

6.7 Jovian propane mixing ratio from CR[43/4] (squares) and CR[29/4] (triangles). 132

6.8 Jovian butane mixing ratio derived from C[58]/C[4]. 134

6.9 Jovian C3H6 mixing ratio (corrected for propane) derived from C[41]/C[4] (squares), and from C[42]/C[4] (triangles). 136

6.10 C[38]/C[36] ratio in the NGC region. 137

6.11 C[40]/C[36] ratio in the NGC region. 138

6.12 C[37]/C[38] count ratio, corrected for argon contribution. 139

6.13 Count ratio C[37]/C[13]. 140

6.14 Count ratio C[38]/C[13], corrected for argon. 140

6.15 Count ratio C[39]/C[13], corrected for C3H6 and early-DL2a propane. 141

6.16 Count ratio C[39]/C[13], corrected for C3H6 and late-DL2a propane. 141

6.17 Count ratio C[40]/C[13], corrected for C3H6 and argon. 142

6.18 Jovian ethylene mixing ratio, corrected for ethane, C_3H_6, and high (squares) / low (triangles) propane. 144

6.19 Jovian acetylene DL2a mixing ratio. 146

6.20 Combined CO + N2 mixing ratio from CR[28/13] without hydrocarbon correction (squares) and from CR[28/13] (triangles) and CR[28/4] (circles) with hydrocarbon correction. 147

6.21 Combined CO + N2 mixing ratio from CR[28/4] without hydrocarbon correction (squares) and from CR[28/13] (triangles) and CR[28/4] (circles) with hydrocarbon correction. 148

6.22 GPMS EC1 C[18] corrected to remove non-H_2O contributions; curves are labeled with corresponding values of the $^{14}N/^{15}N$ correction. 152

6.23 Jovian H_2S mixing ratio from CR[34/13] (squares) and CR[34/4] (triangles). 154

6.24 CR[17/13] with correction for post-EC1 ammonia outgassing. 157

6.25 CR[17/13] before (squares, circles) and after (triangles, diamonds) correction for interference from water, methane, and argon. 158

6.26 DL2 water mixing ratio for three ISP-proxies: pressure (squares), C[13] (triangles), and C[2] (circles). 160

6.27 Jovian methane mixing ratio. 162

7.1 Simplified photochemical reaction scheme (see text). Stable species are shown as ovals. 165

7.2 Longitudinally-averaged eddy mixing profiles derived by Edgington et al. (1999). 167

7.3 Altitude steps used in the photochemical model. 169

7.4 Solar ultraviolet spectra. 173

7.5 Atmospheric structure. Compare with subsequent figures to match pressure and temperature with altitude. 175

7.6 Eddy mixing profiles corresponding to Figures 7.7 and 7.9–7.13. 178

7.7 Model hydrocarbon profiles corresponding to eddy mixing profile K_{x00} in Figure 7.6. See Figure 7.8 for an enlargement of the GPMS-derived hydrocarbon mole fractions. 179

7.8 Mixing ratios of hydrocarbons derived from GPMS data in Chapter 6. 180

7.9 Model hydrocarbon profiles corresponding to eddy mixing profile K_{x05} in Figure 7.6. 181

7.10 Model hydrocarbon profiles corresponding to eddy mixing profile K_{x08} in Figure 7.6. 181

7.11 Model hydrocarbon profiles corresponding to eddy mixing profile K_{x10} in Figure 7.6. 183

7.12 Model hydrocarbon profiles corresponding to eddy mixing profile K_{x15} in Figure 7.6. 183

7.13 Model hydrocarbon profiles corresponding to eddy mixing profile K_{x20} in Figure 7.6. 184

7.14 Eddy mixing profiles corresponding to Figures 7.15–7.19. 185

7.15 Model hydrocarbon profiles corresponding to eddy mixing profile K_{x25} in Figure 7.14. 186

7.16 Model hydrocarbon profiles corresponding to eddy mixing profile K_{x28} in Figure 7.14. 186

7.17 Model hydrocarbon profiles corresponding to eddy mixing profile K_{x30} in Figure 7.14. 187

7.18 Model hydrocarbon profiles corresponding to eddy mixing profile K_{x35} in Figure 7.14. 188

7.19 Model hydrocarbon profiles corresponding to eddy mixing profile K_{x40} in Figure 7.14. 188

8.1 Potential temperature profile in the environment of the South Park thunderstorm described in Cotton (1989). 193

8.2 Comparison of PES CV mixing ratio profiles with column-stretched ECCM CV profiles. 195

8.3 Mole fraction profiles for experiment DDE-303. 210

8.4 Mole fraction profiles for experiment DDE-304. 211

8.5 Mole fraction profiles for experiment DDE-301. 212

8.6 Mole fraction profiles for experiment DDE-306. 213

9.1 Possible (but unlikely) sources of the 9–12 bar hydrocarbons (from Gallant, 1980). 228

A.1 Deadtime-corrected GPMS counts: masses 2–7. 234

A.2 Deadtime-corrected GPMS counts: masses 8–13. 235

A.3 Deadtime-corrected GPMS counts: masses 14–19. 236

A.4 Deadtime-corrected GPMS counts: masses 20–25. 237

A.5 Deadtime-corrected GPMS counts: masses 26–31. 238

A.6 Deadtime-corrected GPMS counts: masses 32–37. 239

A.7 Deadtime-corrected GPMS counts: masses 38–43. 240

A.8 Deadtime-corrected GPMS counts: masses 44–49. 241

A.9 Deadtime-corrected GPMS counts: masses 50–55. 242

A.10 Deadtime-corrected GPMS counts: masses 56–61. 243

A.11 Deadtime-corrected GPMS counts: masses 62–67. 244

A.12 Deadtime-corrected GPMS counts: masses 68–73. 245

A.13 Deadtime-corrected GPMS counts: masses 74–79. 246

A.14 Deadtime-corrected GPMS counts: masses 80–85. 247

A.15 Deadtime-corrected GPMS counts: masses 86–91. 248

A.16 Deadtime-corrected GPMS counts: masses 92–97. 249

A.17 Deadtime-corrected GPMS counts: masses 98–103. 250

A.18 Deadtime-corrected GPMS counts: masses 104–109. 251

A.19 Deadtime-corrected GPMS counts: masses 110–115. 252

A.20 Deadtime-corrected GPMS counts: masses 116–121. 253

A.21 Deadtime-corrected GPMS counts: masses 122–127. 254

A.22 Deadtime-corrected GPMS counts: masses 128–133. 255

A.23 Deadtime-corrected GPMS counts: masses 134–139. 256

A.24 Deadtime-corrected GPMS counts: masses 140–145. 257

A.25 Deadtime-corrected GPMS counts: masses 146–150. 258

LIST OF APPENDICES

Appendix

A Galileo Probe Mass Spectrometer Data 233

B Photochemical model data 259

C Derivation of entraining downdraft model equations 282

CHAPTER I

Welcome to Jupiter

Overview of dissertation

Analysis of Galileo Probe Mass Spectrometer (GPMS) data makes up the core of this work. The first chapter provides relevant scientific background information: current ideas about the origin of Jupiter and its atmosphere, a description of some major atmospheric features, and the state of our knowledge of the composition and cloud structure of Jupiter's troposphere. Chapter 2 describes the GPMS instrument, its function, and the descent sequence program, and Chapter 3 presents the data analysis pipeline, including various count corrections, calibration factors, and error propagation. Chapter 4 describes the calibration experimental process, with the resulting calibration functions presented in Chapter 5. Chapter 6 contains the GPMS mixing ratios derived using the process described in Chapters 3–5. The results shown in Chapter 6 are interpreted using two one-dimensional computational models: a hydrocarbon photochemical code (Chapter 7) and a downdraft with entrainment model (Chapter 8). Finally, conclusions are reached in Chapter 9.

Origin of Jupiter

The origin of Jupiter and its atmosphere is one of the fundamental questions that drives the study of the planet. The focus of this dissertation is on chemical and dynamic processes in Jupiter's atmosphere, and thus does not directly address the issue of planetary formation. However, since atmospheric composition is a major constraint used to distinguish between various planetary formation models as well as between atmospheric origin models, a discussion of the origin of Jupiter is provided here to demonstrate the motivation for some of the work presented later.

The two most recently discussed giant planet formation models are the gas instability model, which features a direct collapse of solar nebula gas to form gaseous protoplanets, and the core instability model, which proposes that a dense core of rock and ice formed first and later acquired a large gaseous envelope. According to the gas instability model, a portion of the solar nebula (the great disk of gas and dust around the early Sun) experienced an instability and contracted to form a gravitationally-bound giant gaseous protoplanet. This model is described by Cameron (1978, 1989) and co-workers, and has the advantage of predicting a rapid formation of giant planets, which easily satisfies the constraint that the giant planets must have reached their current masses before the solar nebula dissipated. However, several problems confront the gas instability model. One problem is that a relatively massive solar nebula is required in order to furnish enough material to form the giant protoplanets. For example, the model of Cameron (1989) requires a solar nebula with at least one solar mass in order to generate the instabilities necessary to trigger the collapse and formation of a giant gaseous protoplanet. However, Strom et al. (1989) state, in their paper on pre-main sequence circumstellar disk lifetimes, that the mass of the IR-radiating dust disks in their sample of observed stars is between 0.01 to 0.001 $M_\odot$, an order of magnitude smaller than the typical disk masses that they quote from other studies of similar objects. The resulting upper limit for pre-main sequence circumstellar disk masses is 0.1 $M_\odot$, considerably less massive than the $> 1\ M_\odot$ required by Cameron (1989) for giant gaseous protoplanet formation. In addition, the gas instability model predicts planets with largely solar elemental abundances, since the planets form by direct collapse of solar nebula gas. Thus, the model fails to explain observations that the giant planets have greater than solar abundances of high-mass (heavier than helium) elements. Solar elemental abundances and Jovian relative abundances are given in Table 1.1, and abundances for gases in Jupiter's atmosphere are given in Table 1.2. The gas instability model's inability to explain the enrichment of heavy elements in Jupiter's atmosphere is magnified on the other giant planets. For example, the carbon abundance, as shown by the atmospheric mixing ratio of methane on these planets, increases from 3 at Jupiter (this work) to 6 at Saturn (Courtin et al. 1984) to 25 at Uranus and 35 at Neptune (Baines et al.

1995). Moreover, the total masses of the giant planets are considerably smaller than the minimum size of 20 M_{Jup} for an object formed by direct collapse of interstellar H-He cloud material, as calculated by Boss (1986). Finally, interior modeling of Jupiter and Saturn based on their gravitational moments is consistent with the presence of a dense core of on the order of 10 $M_{\oplus}$. If the gas instability model is accurate, then these cores must be explained by a mechanism such as settling of grains or accretion of planetesimals after the collapse and formation of the giant protoplanets. But the high temperatures and pressures deep in the envelopes of these protoplanets would have dissolved and mixed any settling solids (Stevenson 1982), making it difficult to form a dense, differentiated core by this method.

Table 1.1 Solar and Jovian abundances and isotopic ratios.

Elements	Sun [a]	Jupiter/Sun
^{4}He/H	0.0975	0.807±0.02 [b]
^{20}Ne/H	1.15×10^{-4}	0.10 ± 0.01 [c]
^{36}Ar/H	3.05×10^{-6}	1.7 ± 0.6 [c]
^{84}Kr/H	9.20×10^{-10}	3.0±1.0 [d]
^{132}Xe/H	4.45×10^{-11}	2.5±0.7 [d]
C/H	3.62×10^{-4}	3.05±0.85 [e]
N/H	1.12×10^{-4}	global: 1.0–3.6 [f] hotspot: 3.6±0.5 [g]
O/H	8.51×10^{-4}	0.032±0.008 (PES, 12 bars) [e] 0.44±0.14 (PES, 19 bars) [e]
P/H	3.7×10^{-7}	0.82 [h,i]
S/H	1.62×10^{-5}	2.16±0.65 [e]

(a) Anders and Grevesse (1989); (b) von Zahn et al. (1998); (c) Niemann et al. (1996; 1998); (d) Mahaffy et al. (1998); (e) results derived in this dissertation; (f) de Pater et al. (2001); (g) Folkner et al. (1998); (h) Kunde et al. (1982); (i) Encrenaz et al. (1978).

Table 1.2 Summary of the composition of Jupiter prior to this dissertation.

Species	Mixing ratios relative to H_2
Major species	
H_2	1.0
He	0.157 ± 0.0036 [a, b]
Principal minor species	
H_2O	global: see text [d], [e] $\leq 10^{-6}$ (≤ 4 bar, hotspot) [b] $\leq 5.6 \pm 2.5 \times 10^{-5}$ (12 bar, hotspot) [b] $\leq 6 \pm 3 \times 10^{-4}$ (19 bar, hotspot) [b] $2–20 \times 10^{-9}$ (upper stratosphere) [g]
CH_4	$2.1 \pm 0.4 \times 10^{-3}$ [b]
C_2H_6	$1–5 \times 10^{-6}$ (stratosphere) [j, k]
C_2H_2	$3–10 \times 10^{-8}$ (stratosphere) [m, n] $<2.5 \times 10^{-6}$ (1–10 μbar) [j]
C_2H_4	$7 \pm 3 \times 10^{-9}$ (north polar region) [o]
C_3H_4	$2.5(+2,-1) \times 10^{-9}$ (north polar region) [o]
C_3H_8	Detection [b]
C_6H_6	$2(+2,-1) \times 10^{-9}$ (stratosphere, north polar region) [o] Detection (global average) [p]
NH_3	global: $2.3–2.9 \times 10^{-4}$ (see text) [q] $\sim 0.2–1 \times 10^{-5}$ (0.5–2 bar, hotspot) [r] $3.3 \pm 1.5 \times 10^{-4}$ (4 bar, hotspot) [s] $8.1 \pm 1.16 \times 10^{-4}$ (≥ 8 bar, hotspot) [s]
H_2S	$<1 \times 10^{-7}$ (≤ 4 bar) [b] 7×10^{-6} (8.7 bar) [b] $7.7 \pm 0.5 \times 10^{-5}$ (≥ 16 bar) [b]
Disequilibrium species	
PH_3	$1–2 \times 10^{-7}$ (0.2–0.6 bar) 6×10^{-7} (>1 bar) [w, x]
CO	1.6×10^{-9} [z]
CO_2	Detection (<10 mb) [l]
GeH_4	$7 \pm 2 \times 10^{-10}$ [w]
AsH_3	$2.2 \pm 1.1 \times 10^{-10}$ [aa]
Other minor constituents	
H	Variable [ab, ac]
$(H_2)_2$	Variable [ad, ae]

Table 1.2 Summary of the composition of Jupiter prior to this dissertation. (Continued)

Species	Mixing ratios relative to H_2
H_3^+	Variable [af]
Cl	Tentative detection [b]

(a) von Zahn et al. (1998), (b) Niemann et al. (1998), (d) Supersolar values were reported by Carlson et al. (1993), (e) However, subsolar values are reported by others who further analyzed the same Voyager IRIS data as Carlson et al. (1993) as well as other data (see text), (f) Drossart (1998), (g) Feuchtgruber et al. (1997), (h) Courtin et al. (1984), (i) Bézard et al. (1998), (j) Festou et al. (1981), (k) Kostiuk et al. (1983), (l) de Graauw et al. (1997), (m) Noll et al. (1986), (n) Hanel et al. (1979), (o) Kim et al. (1985), (p) Bézard (1998), (q) de Pater & Massie (1985), (r) Sromovsky et al. (1998), (s) Folkner et al. (1998), (t) Owen et al. (1977), (u) Caldwell (1977), (v) Noll and Larson (1991), (w) Kunde et al. (1982), (x) Encrenaz et al. (1978), (y) Weisstein & Serabyn (1994), (z) Noll et al. (1988), (aa) Noll and Larson (1990), (ab) Judge & Carlson (1974), (ac) Broadfoot et al. (1979), (ad) Gautier et al. (1983), (ae) Frommhold & Birnbaum (1984), (af) Drossart et al. (1989), Kim et al. (1991), Baron et al. (1991), (ag) Weisstein & Serabyn (1996).

The core instability model, on the other hand, seems to fit many of the compositional and structural constraints imposed by the current state of the giant planets. The core instability model calls for the initial accretion of solid (ice and rock) planetesimals to form a dense core, which eventually grows to a large enough mass such that a gaseous envelope surrounding the core cannot be hydrodynamically stable. In other words, the gas pressure at the surface of the rocky core cannot support the weight of the atmosphere above it, and the atmosphere collapses down onto the protoplanet at a rate balanced by the contraction of the gaseous envelope. A study by Perri and Cameron (1974) found the critical core mass to be $> 70\ M_\oplus$ for the solar nebula region near Jupiter. The envelope modeled by Perri and Cameron (1974) was adiabatic; when Mizuno et al. (1978) included an isothermal layer for the outer optically-thin component of the gaseous envelope, they found considerably smaller critical core masses. However, Mizuno et al. (1978) found the critical core mass to depend on distance from the sun and grain opacity in the envelope, at odds with the approximately equal core masses of the giant planets. Mizuno (1980) improved the model by considering a layer in radiative equilibrium; as a result, the critical core mass was constant with distance from the sun and only depended on grain opacity, a solar nebula parameter. Bodenheimer and Pollack (1986) described the time evolution of giant planet formation in the core instability model, and further improvements to the model are described by Pollack et al. (1990, 1991) and Podolak et al. (1993), who examined the effects of factors such as self-consistent variable core and gas accretion rates, molecular

water opacity in the envelope, and increased planetesimal capture radius due to gravitational focusing and envelope effects.

Comparison of these models with the available constraints favors the core instability model. Where the gas instability model has difficulty explaining the enrichment of heavy elements in the giant planets, the core instability model requires the enrichment. Where the gas instability model has difficulty explaining a differentiated dense core in Jupiter and Saturn, the core instability model requires it. If this model provides an accurate description of the formation of Jupiter, then heavy elements in the Jovian atmosphere should be enriched both from outgassing from the solid core as well as from dissolution of planetesimals in the gaseous envelope of the forming protoplanet. At the distances of the giant planets, the condensed heavy element component of the solar nebula was composed of grains, icy planetesimals, and rocky planetesimals. The increase with distance from the sun in carbon abundance noted previously is expected to also apply to other heavy elements that were also partitioned into the solid component of the solar nebula. This compositional gradient is explained as a race between the accretion of nebular gas and the dissipation of the nebula. The cores of Jupiter, Saturn, Uranus, and Neptune grew simultaneously, but the accretion rate was faster for the innermost giant planets, largely because the planetesimal orbital velocities were greater, and the radial gradient in orbital velocity was also more extreme for the innermost planets. Thus it would seem that Jupiter was first to reach critical mass for runaway gas accretion, whereas Uranus and Neptune came very close to (but did not reach) their respective critical masses at the time of the dissipation of the solar nebula (Pollack and Bodenheimer, 1989). The dissipation of solar nebula gas before Uranus and Neptune experienced significant runaway gas accretion resulted in their greater enrichments of carbon, and presumably their greater enrichments in other elements that were present in the solid phase in the solar nebula.

An additional compositional difference among the giant planets is due to the increase in the ability of some gases to be trapped in ice as temperature decreases. Laboratory studies by Bar Nun et al. (1988) of the trapping efficiencies of CH_4, CO, Ar, and N_2 show that these gases are very inefficiently trapped in ice at deposition temperatures

greater than 30–50 K. Since this is colder than the formation temperature of planetesimals near Jupiter's orbit, the core instability model would predict relatively small enrichments of these gases for Jupiter and Saturn. The enrichments at Uranus and Neptune would be even greater, because their proximity to the Kuiper belt, a reservoir of planetesimals which formed at very low temperatures, would have allowed these planets to accrete greater concentrations of the poorly-trapped gases. The core instability model ties studies of Jovian atmospheric composition to studies of the origin of the solar system, since the composition of Jupiter's atmosphere contains information about both the composition of solar nebula gas and the composition of the planetesimals which contributed to the formation of the planet. The possibility of giant planet migration during or after the formation of the planet further complicates inferences about solar nebula conditions based on the current composition of Jupiter's atmosphere.

Tropospheric structure: Belts, zones, hotspots

Jupiter, with its multiple belts and zones, presents an easily recognized striped face at visible wavelengths. Figure 1.1 shows the conventional belts and zones of the Jovian atmosphere. It is commonly thought that belts, with their warmer infrared (IR) brightness temperatures and reduced cloud opacity, correspond to areas of general downwelling, whereas zones, with their colder IR brightness temperatures and thicker clouds, are identified as areas of upwelling (Smith and Hunt, 1976). The model for this system is the Hadley circulation on the earth, where differential solar heating creates an equator-to-pole temperature gradient, but the coriolis force resulting from the earth's rotation deflects the poleward (equatorward) flows into zonal eastward (westward) flows. Jupiter makes one rotation in 9 hours and 55 minutes, and has a diameter of 143,200 km (Smoluchowski, 1976; Wong, 1982). This much more rapid rotation and greater size result in a substantially greater coriolis force at Jupiter, and the large internal heat source and lack of continents presumably lead to a much more longitudinally symmetric heating pattern on Jupiter. The greater coriolis force and longitudinal symmetry on Jupiter are both factors that lead to the

more extensive dominance of zonal flows on Jupiter (from the equator to ±50°), as compared to the earth, where Hadley circulation only applies to the tropics.

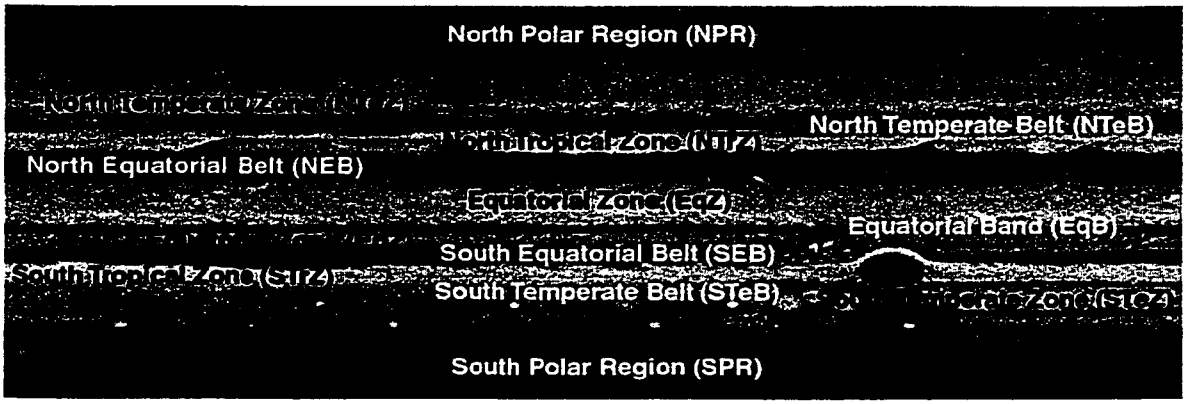

Figure 1.1 Belts and zones of Jupiter.

Peculiar regions of Jupiter known as 5-μm hotspots hold a particular relevance for this work. These areas are mainly restricted to Jupiter's NEB (see Figure 1.1 for the location of the NEB). They are characterized by relatively high brightness temperatures at 5 μm, an effect of their greatly reduced cloud opacity, which allows observation of thermal emission from deeper levels of Jupiter's atmosphere. This is a valuable characteristic because observations at other wavelengths suffer from much smaller depths of penetration. For instance, unit optical depth due to Rayleigh scattering is reached in the ultraviolet at about 50 mbar at 175 nm, and 1 bar at about 310 nm (Edgington, 1997; Atreya, 1986, p.82). Scattering from ammonia cloud particles limits seeing in the visible region to the top cloud deck height (around 700 mbar). On the other hand, 5-μm observations are relatively unaffected by these ammonia clouds (Bjoraker, 1985). However, outside the relatively cloud-free hotspots, 5-μm observations are limited by 2-bar cloud opacity. Within the hotspots, the 2-bar cloud transmittance is higher, allowing infrared measurements to sense to depths of 4–8 bar (Roos-Serote et al. 1998). Microwave measurements have a model-dependent sensitivity to depths of around 3–4 bar, but at wavelengths longer than about 6 cm, the increasing amount of synchrotron radiation from Jupiter's magnetosphere makes it difficult to extract information about Jupiter's atmosphere from the signal (de Pater, 1991). Thus the combination of large depths of penetration in 5-μm hotspots, as well as the

rich variety of molecular signatures in this infrared region, make 5-μm hotspots a natural target for IR remote sensing of Jupiter. Attention to 5-μm hotspots has been given by ground-based telescope facilities, airborne observatories, ISO, the Voyager spacecraft, and the Galileo Orbiter.

The other chief reason for the attention devoted to hotspots is the fact that the entry site of the Galileo Probe was within a hotspot. Figure 1.2 contrasts views of Jupiter at visible and 5 μm wavelengths, and Figure 1.3 shows the entry site of the Galileo Probe at 6.53° N planetocentric latitude and 4.88° W System III longitude (Orton et al., 1998; Young 2000). The image in Figure 1.3 is a reconstruction of the 5-μm hotspot geometry as described in Orton et al. (1998), who estimate that the hotspot extended from about 11°W to 359°E and 5° to 8°N. Figure 1.3 was created by interpolating between 4.78-μm images taken with the NFSCAM at the IRTF on 21 November 1995 and 22 January 1996. Orton et al. (1998) had to interpolate the images to estimate the hotspot configuration on the probe encounter date (7 December 1995) because Jupiter's proximity to the sun (as seen from the earth) prevented the high-resolution NFSCAM from observing the planet on that date. Orton et al. (1998) were able to image the hotspot at the time of the probe encounter with the lower-resolution MIRAC2 instrument.

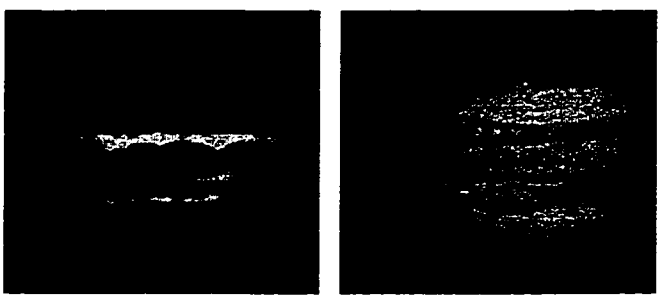

Figure 1.2 Views of Jupiter at thermal infrared (L) and visible (R) wavelengths.

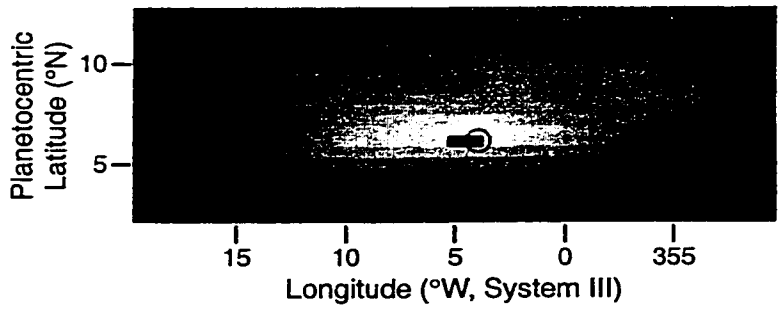

Figure 1.3 Galileo Probe entry site (PES), from Orton et al. (1998).

Figure 1.3 shows the approximate geometry of the hotspot, in relation to the Galileo PES. Orton et al. (1998) did not publish the brightness scale of the image, so the "boundary" of the hotspot is difficult to determine. In order to monitor the hot spot's radiance over some three years of observations, Orton et al. looked at the behavior of a quantity obtained by averaging the intensity over an 8° longitude × 6° latitude region centered on the PES hotspot. Although hotspots change size and shape over time, this 8° × 6° area tracked by Orton et al. (1998) gives a general idea of the average hotspot size. The probe entry site at 4.88° W is about 2.5° west of the apparent center of the hotspot, placing it well within the spot. At the latitude of the PES, 1° of longitude is equivalent to about 1200 km. Note that Figure 1.3, published in Orton et al. (1998), uses correct PES coordinates (6.5° N and 4.88° W), which were incorrectly stated in Young (1998) but later corrected in Young (2000).

Composition

A primary goal of this thesis is to understand the composition of Jupiter's atmosphere. Spectroscopic analysis of Jupiter was rapidly advanced once observations could be made without interference from the Earth's atmosphere. Remote sensing observations with the Voyager infrared and ultraviolet spectrometers between 1979 and 1982 provided comprehensive data on the composition of the atmospheres of the giant planets, and further contributions were made by the Infrared Space Observatory (ISO). The Hubble Space Telescope's (HST) ultraviolet spectrometer has been used to constrain stratospheric

chemistry and composition. Reviews of the composition as it relates to the physics, chemistry, and origin of the Jovian atmosphere have been presented by Gautier and Owen (1989), Atreya (1986), and Atreya et al. (1999). Ground-based observations at infrared, submillimeter, millimeter, and radio wavelengths also take advantage of transparent spectral "windows" in the earth's atmosphere. Of particular importance is the first and only direct in situ measurement of the composition of Jupiter's deep atmosphere, which was carried out by the Galileo Probe, from 0.5 bar to 21 bar.

Jupiter's atmosphere is primarily hydrogen and helium (see Table 1.2), but the trace constituents comprising the remainder of the atmosphere provide an enormous amount of information about the formation of the planet, as well as the processes active in its atmosphere today. As is usually the case in planetary science, the "flood of information" raises at least as many questions as it answers. Abundances in this work will be expressed for the most part in terms of mixing ratios w_X, a standard quantity defined as

$$w_x = \frac{n_x}{n_{H_2}}. \qquad 1.1$$

In Equation 1.1, n_x is simply the number density of atmospheric constituent x, so w_x is also referred to as the number mixing ratio or volume mixing ratio, but is distinct from the mass mixing ratio, which is found by replacing the number densities in Equation 1.1 with the mass densities. Many scientists instead prefer to describe composition in terms of the mole fraction, q_x, where

$$q_x = \frac{n_x}{n_{\text{atm.}}}, \qquad 1.2$$

and the denominator is now the total atmospheric number density. When dealing with an atmospheric component x whose concentration is variable, mixing ratio is a slightly more convenient measure of the component's abundance, since a significant change in the concentration of another component y will cause the value of the mole fraction of x to change, whereas the mixing ratio of x remains constant when the concentration of y changes. Another major advantage to using mixing ratios to quantify atmospheric concentrations is that it facilitates comparison between jovian and solar compositions, since

the solar concentration of a minor constituent x is represented as a ratio of the number of x atoms to the number of H atoms.

The Galileo Probe Helium Abundance Detector determined a mixing ratio for the major component helium of 0.1573 ± 0.0031 (Von Zahn et al., 1998). The comfortingly similar w_{He} derived by the GPMS is 0.157 ± 0.030 (Niemann et al., 1998). The remaining minor atmospheric constituents can be classified into four useful categories: the non-condensible volatile gases, the cloud-forming condensible volatiles, the photochemical products, and the disequilibrium gases. These atmospheric constituents will be described in the following sections.

Non-condensing minor gases

The following sections will discuss gases whose mixing ratios change as a result of various thermodynamic/physical/chemical sources and sinks, but this section deals with the gases whose mixing ratios remain constant in the portion of Jupiter's troposphere sampled by the Galileo probe. The Jovian non-condensibles listed in Table 1.2 include methane, nitrogen, and the noble gases.

Methane is the major reservoir of carbon in Jupiter's current atmosphere. Carbon in the solar nebula was thought to have been partitioned into gas-phase CO, as well as solid-phase organics and water-ice clathrates that could have trapped CO. Subsequently, in the high pressures and temperatures of Jupiter's deep atmosphere, CO should have combined with hydrogen to form methane and water. Thus, a determination of the atmospheric methane mixing ratio is desirable as an indication of the atmospheric carbon component. An analysis of Voyager IRIS 7-μm spectra done by Gautier et al. (1982) gave $w_{CH4} = 1.95 \pm 0.22 \times 10^{-3}$, the best pre-Galileo data constraining the Jovian carbon component. Chapter 6 gives the GPMS methane mixing ratio, which is at least 10% higher than previous estimates.

Abundances of molecular nitrogen and the noble gases (other than helium) were completely unconstrained before the arrival of the Galileo Probe at Jupiter, since these gases have no direct spectroscopic signatures useful for remote sensing. Chapter 6 gives the

GPMS constraints on nitrogen and the noble gases. Supersolar abundances of the noble gases argon, krypton, and xenon are derived in Chapter 6. Especially notable is the highly subsolar abundance of Ne in Jupiter's atmosphere. The missing neon is believed to have been sequestered deep in Jupiter's liquid metallic region along with helium. As pressures increase with depth in Jupiter's atmosphere, the hydrogen becomes more and more dense but never forms a liquid, since the temperatures are much higher than hydrogen's critical temperature of 33 K. But a phase transition does occur near pressures of 300 GPa (3 million bars) in Jupiter's interior (Stevenson 1982), where molecular hydrogen becomes ionized and forms liquid metallic hydrogen. Helium is less soluble in liquid metallic hydrogen than in molecular hydrogen, as shown in Figure 1.4, which shows Stevenson's (1982) saturation curves for helium in hydrogen, on the T-P plane, for a solar helium to hydrogen ratio. Helium saturation occurs for values of T and P lying below the solid line in the molecular regime, and below the dash-dot line in the metallic hydrogen regime. The dashed lines labeled "Saturn adiabats" show modeled T-P curves for Saturn's interior; as the planet cooled over time, the adiabats lowered. As the adiabat lowers over the saturation curve at the lowest-pressure part of the metallic hydrogen region, helium raindrops would have condensed, and diffusion down from the molecular hydrogen region would have driven a continuous rainout of helium. Like the virga seen on earth when rain evaporates high over the desert, the helium raindrops would again dissolve into the hydrogen when they fell to warmer depths. A similar process should operate on Jupiter, but the current Jovian adiabat lies approximately along the line for the 2 billion year Saturn adiabat. Thus the loss of hydrogen through condensation at the molecular/metallic hydrogen interface should not have been as extreme on Jupiter, and may possibly have only just begun. There is considerable uncertainty in the determination of the saturation curve for helium in Figure 1.4 because although the hydrogen is ionized, helium is neutral, and theoretical descriptions of the interactions between neutral helium and metallic hydrogen at the appropriate pressures and temperatures are incomplete. The falling of the helium raindrops would have converted gravitational energy into thermal energy as the raindrops viscously interacted with the liquid metallic hydrogen during their descent. Roulston and Stevenson (1995)

suggest that neon would dissolve into the helium raindrops, possibly explaining the depletion (relative to solar composition) of Ne observed by the GPMS.

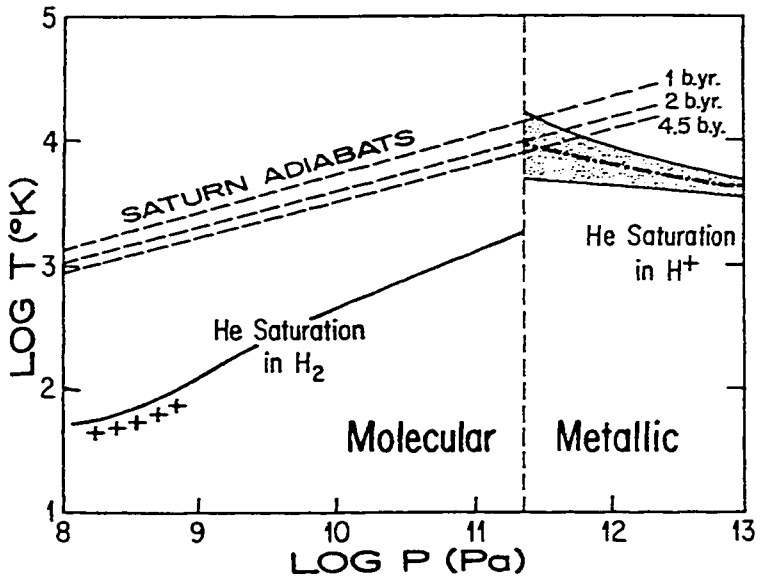

Figure 1.4 Helium saturation curves for helium-hydrogen solution, from Stevenson (1982).

Condensible volatiles

Jovian condensible volatiles, especially in the Galileo probe site, present a complex problem. The best approach is to first understand the behavior of an ideally predictable Jupiter, and then examine the observed differences from that situation. The condensible volatiles (CVs) in the atmosphere of Jupiter are ammonia (NH_3), hydrogen sulfide (H_2S), and water vapor (H_2O). Ammonia condenses into NH_3 ice, and water condenses to water ice or an aqueous ammonia solution. The fate of H_2S is still open to question; it reacts with NH_3 to form either ammonium hydrosulfide, NH_4SH, or ammonium sulfide, $(NH_4)_2S$ (Owen and Mason, 1969; Weidenschilling and Lewis, 1973; Ibragimov and Solodovnik, 1991). In an ideally predictable Jupiter, the CVs would be well-mixed in the deep atmosphere, so that below the cloud levels, the mixing ratios of the CVs should be everywhere constant. As the temperature decreases with height, the relative humidities of the CVs will increase, until they reach the saturation point. For example, water in solar abundance in Jupiter's atmosphere would have a relative humidity of 51% at a temperature

of 290 K (corresponding to a pressure of 6.1 bar in the PES), and a relative humidity of 87% at a temperature of 280 K (5.4 bar). At 277 K (5.2 bar), 100% humidity is reached and the water cloud should form. This cloud base level, or lifting condensation level (LCL), is different for each of the three CVs. Above the LCL, the mixing ratio of the gaseous CV is equal to its saturation mixing ratio (a function of temperature) and decreases with increasing altitude. This simple model is the basis for the equilibrium cloud condensation model, and is described in more detail in the Clouds section below. An early version of this type of equilibrium cloud condensation model (ECCM) is the classic work of Weidenschilling and Lewis (1973), and the current model used in this work is an adaptation of the model of Romani (1986) and Atreya and Romani (1985). The LCLs for solar and for 3 × solar CVs, as calculated by the ECCM, are given in Table 1.3.

Table 1.3 Observed and ECCM-modeled cloud properties.

Case	Water cloud			NH_4SH cloud			Ammonia cloud		
	P (bar)	T (K)	ρ_c (kg m^{-2})	P (bar)	T (K)	ρ_c (kg m^{-2})	P (bar)	T (K)	ρ_c (kg m^{-2})
Observed in PES	2.45–3.58	247	1.1–3.2 × 10^{-4}	1.0–1.34	176	7.6–1300 × 10^{-4}	0.46–0.53	138	0.3–5.7 × 10^{-4}
Solar CVs	5.69	277	< 251	2.21	210	< 6.6	0.72	146	< 3.6
3 × solar CVs	7.22	299	< 958	2.61	221	< 22	0.84	154	< 12

It must be emphasized that the ECCM is an idealized case that is expected to differ substantially from the atmosphere of Jupiter (or any planet). The ECCM calculates CV mixing ratio profiles and cloud densities for a parcel rising adiabatically through the entire atmospheric column. In a real planetary atmosphere, the atmospheric cloud densities would be considerably smaller than those predicted by the ECCM, since some of the condensed material would be lost through precipitation. In addition, both microphysics and dynamics would alter the CV gas profiles in a real atmosphere. Within a cloud, condensation could occur in subsaturated conditions if cloud condensation nuclei (CCN) were very efficient, or supersaturation could occur in the absence of CCN. A realistic treatment of dynamics would

replace the ECCM-predicted CV profiles with more irregular profiles, probably featuring layers of subsaturated air above the cloud tops. These features cannot be replicated in the simple ECCM, and in fact the ECCM has no well-defined cloud tops! The clouds simply taper off according to the saturation vapor pressure. Nonetheless, the ECCM serves a useful purpose as an extreme bounding case for atmospheric cloud and CV distributions.

Qualitative predictions can also be made concerning the abundances of the CVs, assuming the previously-described core instability model of the formation of Jupiter is correct. The major reservoir of oxygen in the solar nebula was in the form of icy planetesimals. Since planetesimals accreted to form the protoplanetary core, and continued to be captured in the gaseous envelope surrounding the core, a prediction of supersolar water would seem to be quite reasonable. The source of Jupiter's sulfur component is also thought to be planetesimals, this time of the rocky variety. Therefore an enrichment of sulfur would also be predicted by the core instability model. The third condensible volatile, nitrogen, is quite different. Most of the nitrogen in the solar nebula should have been in the form of gaseous N_2, so the nitrogen/hydrogen ratio on Jupiter should be very similar to the nitrogen/hydrogen ratio in the solar nebula. In order for enrichment of nitrogen to have occurred, some mechanism for incorporating it into planetesimals must be invoked. Although nitrogen compounds can be trapped in icy planetesimals, N_2 is very inefficiently trapped at temperatures > 35 K (Bar Nun et al. 1988). If the majority of the icy planetesimals involved in the formation of Jupiter were formed at solar distances comparable to that of Jupiter, and thus at temperatures closer to 100 K, then not much of the nebular N_2 should have been incorporated into the planetesimals, and the core instability model would favor a roughly solar abundance of nitrogen on Jupiter. However, GPMS results show supersolar enrichments of nitrogen, argon, and other gases that are poorly trapped at the canonical 100 K planetesimal formation temperature for Jupiter's region of the solar nebula. In order to explain this enrichment, Owen et al. (1999) concluded that the planetesimals which formed Jupiter must have formed at much lower temperatures, and therefore at greater distances from the sun.

Both the abundances and the altitude profiles of the condensible volatiles, as constrained by remote sensing, depart significantly from the simple predictions given above. The Galileo probe encounter only served to intensify the disagreement. In this section I will first describe the problems posed by the observed CV altitude profiles, and conclude with the difficulties in reconciling the predicted bulk abundances with those measured by remote sensing and by the Galileo probe.

Because water forms the deepest cloud layer, it can be sensed only in the 5-μm spectral region, the deepest-reaching spectral window. But near-IR radiation is absorbed by water vapor in the earth's atmosphere, so 5-μm datasets are limited to observatories far enough above the earth's surface to be free from water vapor, such as Voyager-IRIS, Kuiper Airborne Observatory (KAO), ISO, and Galileo-NIMS. As previously described, cloud opacity near 2 bar on Jupiter (well above the water LCL for solar water abundance on Jupiter) limits the depth of penetration of 5-μm observations. Thus, most attempts to measure water concentrate on the relatively cloud-free 5-μm hotspots.

The simplest water abundance profiles derived from 5-μm studies consist of a constant deep water abundance up to a certain level, with zero water vapor above that level. Such a "step profile" was found by Drossart and Encrenaz (1982), who modeled five H_2O lines and compared them with the average of all Voyager 1 IRIS 5-μm spectra for latitudes between $\pm 30°$. The "step" in the Drossart and Encrenaz (1982) water vapor profile occurred at 250 K (about 3.76 bar), and the abundance deeper than the step was $w_{H_2O} = 10^{-5}$, corresponding to a relative humidity of about 4% at that level. Lellouch et al. (1987) described new laboratory measurements of the NH_3 spectrum near 5-μm, prompting a revised analysis of the IRIS spectra in Lellouch et al. (1989). These workers also derived a step water vapor profile, with the step this time at 230 K, and w_{H_2O} = several times 10^{-6} deeper than 230 K. This profile is everywhere subsaturated, with a maximum relative humidity of around 10%. If the step profiles of Drossart and Encrenaz (1982) and Lellouch et al. (1989) persist to deeper levels, a water cloud would never form on Jupiter. But since these thermal infrared spectra are strongly weighted by the anomalously dry 5-μm hotspots, it can be speculated that the water vapor profiles may also be different on other parts of the

planet. An atmospheric multiprobe would be an effective mechanism for investigating the possibility of heterogeneous condensible volatile distributions on Jupiter.

The Kuiper Airborne Observatory (KAO) dataset obtained by Bjoraker et al. (1986) had the advantage of a higher spectral resolution than the IRIS dataset, and the disadvantage of a lower spatial resolution. The KAO observations spanned the $\pm 40°$ latitudes of Jupiter, but since disk averaged 5-μm radiation is dominated by emission from 5-μm hotspots, the conclusions of Bjoraker et al. (1986) apply mainly to hotspots. The greater spectral resolution allowed Bjoraker et al. (1986) to distinguish between strong, medium, and weak water lines in the spectrum, and thus constrain the vertical variation of w_{H_2O}, since strong lines are formed at higher altitudes, and weak lines contain information about deeper regions. Their favored profile featured saturated water higher than the 2 bar level, subsaturated w_{H_2O} at pressures greater than 2 bar, increasing to 3.3×10^{-5} ($0.02 \times$ solar) at 6 bar ($\sim$285 K). Bjoraker et al. (1986) complimented their KAO results with an analysis of Voyager IRIS data in order to look for spatial variation in the w_{H_2O} profile. The spatial variation they retrieved applied only to pressures < 4 bars, where they found the NEB to be more depleted in water than other regions. Deeper than 4 bars, they found no difference in the deepest retrieved abundances of water between spectral ensembles at different latitudes, all of which were fit by the same deep abundance derived from their KAO analysis. Bjoraker et al.'s water vapor gradient between 2 and 6 bar brings their profile a little closer to the behavior predicted by the ECCM, when compared with the step profiles of Drossart and Encrenaz (1982) and Lellouch et al. (1989). However, Bjoraker et al.'s w_{H_2O} subsaturated gradient, like the step profiles, disagrees with the ECCM-predicted gradient, which follows the saturation vapor curve. The depth at which Bjoraker et al.'s deep abundance is reached, however, is in the neighborhood of the LCL for water in solar abundance.

Seemingly at odds with these determinations of subsolar, subsaturated water vapor is the analysis of Carlson et al. (1993), who simultaneously fit IRIS 45-μm and 5-μm spectra using a complex radiative transfer model with many new features, including multiple-scattering, thermally-emitting clouds with spectrally-dependent extinction, and LCLs determined self-consistently by the assumed condensible volatile abundances. Their

surprising conclusion, given the agreement among the previously-mentioned studies, was that the slope of the IRIS spectra required the presence of a water cloud. Although they admitted that their analysis did not allow the unique determination of the deep well-mixed water abundance, the link in their model between the required water LCL and the deep w_{H_2O} led them to derive a deep $w_{H_2O} \approx 1.2 \times$ solar. Although the analysis of Carlson et al. (1993) may seem to give hope to the possibility that the ECCM bears some resemblance to Jupiter's atmosphere, that hope was destroyed by a comparison between IRIS, Galileo NIMS, and ISO/SWS spectra of Jupiter (Roos-Serote et al., 1998b), which revealed an anomalous slope in the IRIS 5-μm spectra, of the right sense to give the impression of a water cloud in the Carlson et al. (1993) model. The previously discussed analyses of Voyager IRIS data are also possibly discounted by the calibration problem identified by Roos-Serote et al. (1999), but since the other analyses lacked spectrally-dependent cloud continuum contributions to the IRIS spectrum, their conclusions would probably be affected to a lesser degree than would those of Carlson et al. (1993). The NIMS spectra themselves are consistent with subsaturated and subsolar w_{H_2O} profiles between 4 and 8 bar (Roos-Serote et al., 1998a).

Galileo probe measurements of water vapor were done directly by the mass spectrometer, and indirectly by the net flux radiometer (NFR). Both experiments agree that water was subsaturated and subsolar in the PES. These results will be discussed in greater detail in Chapter 6.

Consistent with the prediction that H_2S would combine with ammonia and condense near 2 bar, H_2S has never observed by earth-based or space-based observations. Larson et al. (1984) found an upper tropospheric mixing ratio upper limit of 3.3×10^{-8} from observations at 2.7 μm, which agrees with the ECCM-predicted mixing ratio. Thus the GPMS yielded the first and only measurement of the hydrogen sulfide abundance on Jupiter. GPMS measurements of w_{H2S} are shown in Figure 1.5 and described in more detail in Chapter 6. The w_{H2S} profile of Figure 1.5 is quite different from ECCM predictions, which would call for a constant mixing ratio (horizontal line) at pressures greater than the LCL

(vertical dashed line). The depletion of H_2S to pressures of around 12 bar cannot be explained by condensation alone.

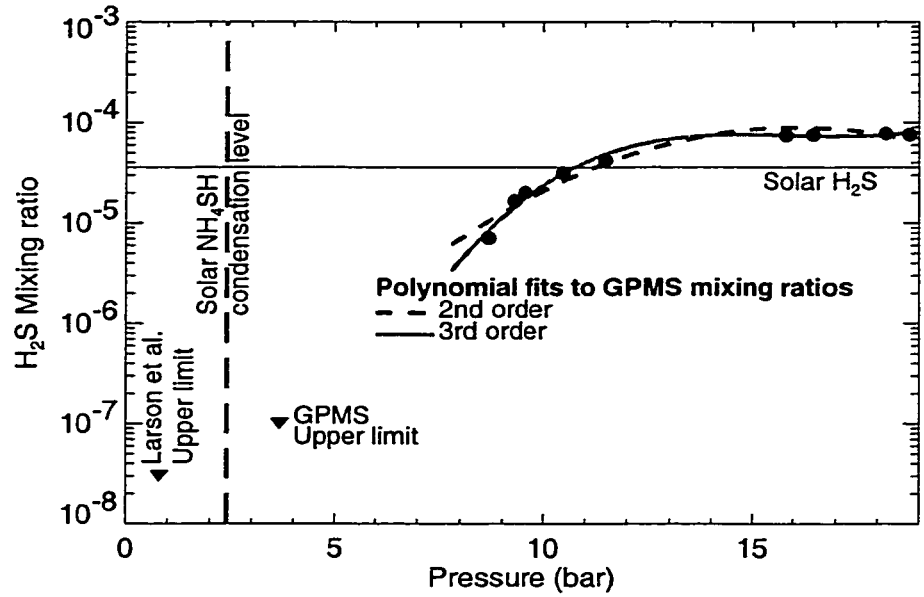

Figure 1.5 Hydrogen sulfide in the PES.

De Pater and Massie (1985) derived an ammonia mixing ratio profile for Jupiter using the 1.3-cm NH_3 absorption feature (Figure 1.6). The globally-averaged microwave data (points with error bars) were compared with spectra generated using different ammonia profiles. The best fit curve (solid line) corresponds to the ammonia profile titled "Global radio" in Figure 1.7. Both the global radio and the PES NFR ammonia profiles share one key detail: they feature increasing ammonia mixing ratios with depth, *even below* the NH_3 LCL. Note that in Figure 1.7, there are two vertical LCLs depicted, since NH_3 is consumed in the NH_4SH cloud as well as in the NH_3 ice cloud. Thus it may appear that the global radio profile and the PES NFR profile can be reconciled with the ECCM, since condensation of NH_4SH could be invoked to explain the depletion of ammonia below the ammonia-ice LCL. However, the depletion of ammonia required by the global radio results is so extreme that some 10 × solar H_2S would need to be present. This H_2S abundance, especially in the altitude region of the ammonia depletion, is ruled out by the Galileo probe measurement of H_2S (Figure 1.5). de Pater et al. (2001) discuss several possible explanations

for the ammonia depletion below the ammonia cloud, most notably that ammonia might be adsorbed onto cloud particles in the NH_4SH cloud. The microwave data in Figure 1.6 are additionally compared to line profiles calculated based on ECCM profiles (constant mixing ratio below the cloud base; saturation-limited above), assuming two values of the deep ammonia abundance. The disagreement between the radio data and the calculated line profiles for these two ammonia distributions can be resolved only with depleted ammonia below the NH_3-ice LCL. Retrieval of the ammonia abundance at 2–15 bar was also done by Folkner et al. (1998) using the attenuation of the Galileo probe-to-orbiter signal, giving the first-ever ammonia mixing ratio measurements at atmospheric pressures greater than about 4 bar. The results of this study show that ammonia continues to increase down to 8 bars in the PES. Once again, the pattern predicted by the ECCM is strongly contradicted by the observed condensible volatile profile.

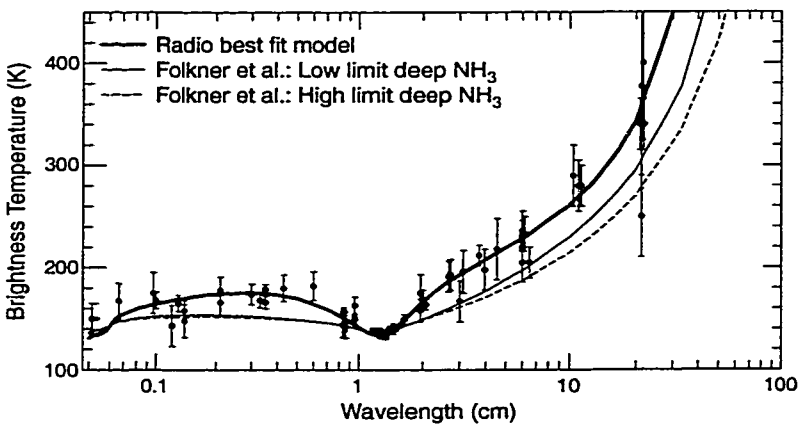

Figure 1.6 Jupiter's microwave spectrum in the 1.3-cm NH_3 line.

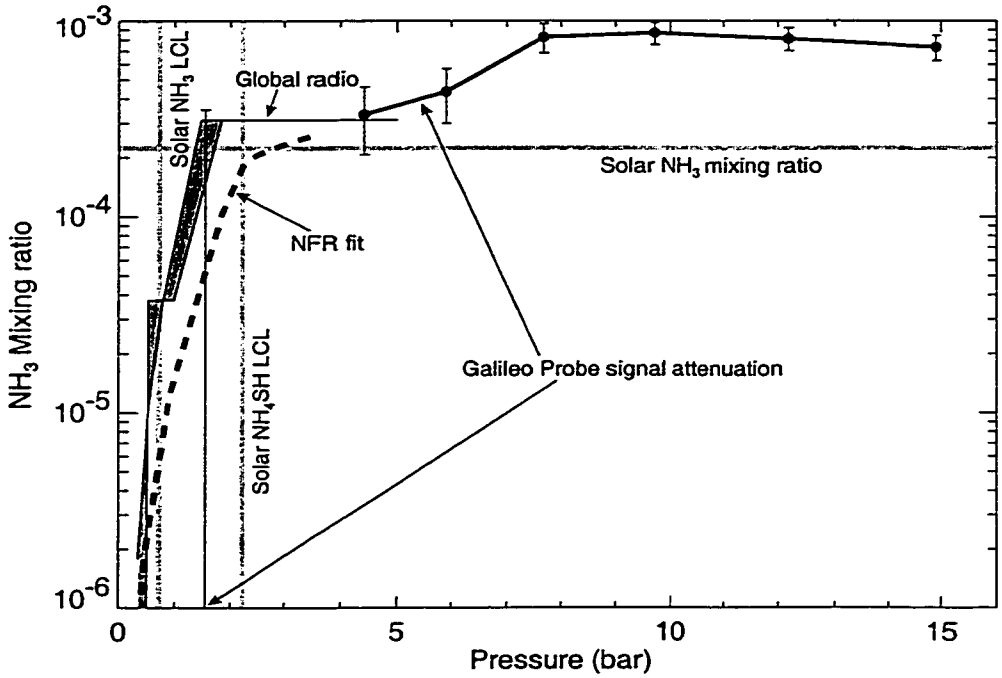

Figure 1.7 Ammonia in the PES.

The CV profiles discussed above have implications for meteorology in the probe entry site, 5-μm hotspots in general, and the planet as a whole (for the globally-averaged measurements). Chapter 8 will provide a full discussion of 5-μm hotspot meteorology. Chapter 8 also introduces a model of a forced downdraft with horizontal entrainment, a controversial idea that attempts to explain the surprising CV mixing ratio profiles of the PES. But the condensible volatile deep abundances, to the extent that they are known, are as much of a puzzle as are the condensible volatile mixing ratio profiles.

The abundance of water on Jupiter is one of the many holy grails of planetary science. As discussed before, the location of the predicted water cloud so deep in Jupiter's atmosphere has made it impossible (so far) to determine the deep well-mixed water mixing ratio. The Galileo probe was intended to reach depths well below the predicted water LCL, but its descent into a 5-μm hotspot interfered with that plan. Chapter 6 contains further discussion of GPMS water measurements.

The deep abundance of H_2S measured by the GPMS was about 2.5 × solar (see Table 1.2). A supersolar abundance of sulfur is entirely consistent with the core instability model

of Jupiter's formation, since sulfur in the solar nebula was in condensed form, carried by the planetesimals that formed Jupiter's core, and later continued to be accreted into the gaseous envelope surrounding the core.

Before the Galileo Probe encounter with Jupiter, the deep abundance of ammonia was thought to be consistent with radio observations yielding an ammonia mixing ratio of 1–1.3 × solar in the Jovian atmosphere (de Pater and Massie, 1985). This ammonia value is consistent with the core instability model, since most nitrogen in the solar nebula was present in the form of gaseous N_2. In addition to the nitrogen accreted as a gas during the runaway gas accretion phase predicted by the core instability model, there could be additional small amounts of nitrogen incorporated in icy planetesimals. This source of nitrogen is thought to be small, since N_2 is captured in ice only at temperatures below 50 K (much colder than the temperatures in Jupiter's region of the solar nebula). Some additional nitrogen may have been provided by NH_3 captured in icy planetesimals, but the capture of NH_3 into ice is also inefficient, and the proportion of solar nebula nitrogen available in the form of NH_3 is not large. Therefore a Jovian abundance of nitrogen that is solar or near-solar supports the core instability model.

The Galileo probe's Net Flux Radiometer was used to constrain ammonia in the 0.5–3 bar region (Sromovsky et al., 1998), finding near-solar ammonia at its limit of sensitivity near 4 bar. However, the NFR profile implies that the ammonia mixing ratio is still increasing with depth at that level. Folkner et al. (1998) extended the PES ammonia mixing ratio profile to around 15 bar using an analysis of the attenuation of the probe to orbiter radio signal. They indeed found that the NH_3 mixing ratio continued to increase with depth, stabilizing at a deep abundance of 3.6 × solar. Clearly such a result threatens the core instability model and assumptions about the distribution of nitrogen in the solar nebula. Alternately, a different interpretation of the probe signal attenuation data could be attempted, perhaps resulting in a lower deep abundance of ammonia. Hoffman et al. (1999) found that current models seriously underestimate the centimeter wavelength opacity of PH_3. Their experiments, done at room temperature and at pressures of ≈ 5 bar, showed that phosphine absorptivity depended strongly on wavelength and pressure. If this variability

persists to higher pressures, such as those appropriate for the analysis of the probe-to-orbiter radio signal, then additional opacity from phosphine may have been mistakenly attributed to ammonia by Folkner et al. (1998). However, this possibility is somewhat remote, given the estimate by Hoffman et al. (1999) that 10 × solar PH_3 is required at $P > 5$ bar on Jupiter in order to reduce Folkner et al.'s deep ammonia abundance to the solar value. However, the observed PH_3 mixing ratio at 1 bar is close to solar (see Tables 1.1 and 1.2), and the core instability model is unable to support heavy element enrichments substantially greater than the enrichments of carbon and sulfur.

Although absorption by phosphine or some other unidentified atmospheric component might potentially explain some of the signal attenuation measured by Folkner et al., and thus reduce their derived ammonia mixing ratios, new problems would arise with the interpretation of the globally-averaged centimeter-wavelength spectrum of Jupiter. The de Pater and Massie (1985) ammonia profile would have to be adjusted, probably resulting in everywhere smaller ammonia mixing ratios. This would bring their derived ammonia profile closer to the NFR profile (see Figure 1.7), accentuating the difference between the observed ammonia profiles and those predicted by the ECCM. The idea of completely dispensing with the ECCM may seem tempting, but if the observed ammonia profiles accurately described the global altitude profiles, no ammonia clouds would form on the planet. This conclusion is refuted by observations of a ubiquitous Jovian ammonia cloud deck with a base at a pressure of ~750 mbar (e.g. Banfield et al., 1998). Clearly, the probe site investigation of ammonia has raised more questions than it has answered: Is Jovian nitrogen really enriched over solar by a factor of 3.6? If so, where did all the nitrogen come from? If not, how can the probe-to-orbiter signal attenuation be explained? Why does the ammonia mixing ratio continually increase with depth down to about 8 bar, when the ammonia LCL is near 0.7 bar?

Photochemical products

The stratosphere of Jupiter is exposed to solar ultraviolet radiation, which drives photochemical reactions involving methane, hydrogen, ammonia, and water. Methane,

hydrogen, and ammonia are supplied from the troposphere to the stratosphere, but water condenses out in the troposphere and is present only in trace amounts (saturation mixing ratio on the order of a part per trillion) at the tropopause. Thus stratospheric water is limited to the flux provided by interplanetary micrometeorites and sources within the Jovian system. Solar UV provides the energy to break apart these simple molecules, and the resulting fragments recombine to form new molecules. Observational constraints on stratospheric composition and structure are provided largely by measurement of the ultraviolet spectrum of sunlight reflected by Jupiter's atmosphere, since transitions between vibrational energy levels of the stratospheric molecules provide a wealth of absorption lines. The observed spectra are interpreted with the aid of complex photochemical models, which seek to calculate the vertical distribution of photochemical products using laboratory-measured chemical reaction rates and ultraviolet absorption cross sections.

Some of the products of the Jovian stratospheric chemistry are thought to be stable enough to diffuse down to the troposphere, where they could possibly be detected by the Galileo Probe Mass Spectrometer. A detailed analysis of hydrocarbon photochemical products detected by the GPMS at pressures of 8–11 bar will be presented in Chapter 6, and in Chapter 7 a photochemical model will be introduced for comparison with the observed hydrocarbon abundances.

Disequilibrium species

Disequilibrium gases are another group of minor constituents of Jupiter's atmosphere. Previously detected disequilibrium gases include CO, PH_3 (phosphine), GeH_4 (germane), and AsH_3 (arsine). These molecules are in thermochemical equilibrium in the 800-3000 K region, and are wafted to the upper atmospheric levels where they can be observed using remote sensing, or by *in situ* GPMS measurements. When combined with models of thermochemical equilibrium at the high pressures and temperatures of Jupiter's deep atmosphere, observations of the disequilibrium gases yield information about deep convective activity and vertical transport, as modeled by eddy diffusion. Chapter 9 discussed thermochemistry in relation to the GPMS results presented in Chapter 6.

Clouds and Probe site meteorology

Clouds are a poorly understood component of even the relatively accessible atmosphere of the Earth. Attempts to fully characterize Jovian clouds using computational models are limited by both computational resources, and more significantly, a wide range of completely unconstrained factors. For example, even when 100% humidity is reached in the earth's atmosphere, a cloud will not form without the presence of tiny particles known as cloud condensation nuclei. On Jupiter, the abundance, composition, and nature of cloud condensation nuclei (if any exist) are completely unknown. Even so, rudimentary computational models still play a vital part in the analysis of giant planet cloud systems. The equilibrium cloud condensation model (ECCM), introduced previously in the discussion of condensible volatile mixing ratio profiles, was first developed by Weidenschilling and Lewis (1973). Atreya and Romani (1985) developed this model further by replacing the lower water cloud with a solution cloud containing dissolved NH_3 and H_2S.

The ECCM takes as its initial conditions the pressure and temperature of a parcel of Jovian air, as well as its composition. The model then steps up through the atmosphere, calculating the condition of the parcel at each step according to the simplifying assumptions that the atmosphere is in hydrostatic equilibrium, that the parcel is adiabatic, and that any condensation formed as the parcel cools remains at the level where it condenses (no precipitation or upward lofting of cloud particles). The change in temperature with height is given by the wet adiabatic lapse rate for Jupiter (Atreya 1986),

$$\frac{dT}{dz} = -\frac{\bar{\mu}g}{\bar{C}_p} \frac{1 + \frac{1}{RT}\left(\frac{2q_{H_2S}q_{NH_3}L_{rxn}}{q_{H_2S} + q_{NH_3}} + \sum_k q_k L_k\right)}{1 + \frac{1}{\bar{C}_p T^2}\left(10{,}834\frac{q_{H_2S}q_{NH_3}L_{rxn}}{q_{H_2S} + q_{NH_3}} + \sum_k \frac{q_k L_k^2}{R}\right)} \qquad 1.3$$

Here, μ is the average atmospheric molecular weight and C_p is the specific heat of the atmosphere. When there is no condensation, the parenthetical terms, which account for the heat of condensation, go to zero and the expression gives the dry adiabatic lapse rate. R is the universal gas constant, q gives the atmospheric mole fractions of the condensible volatiles, and L is the latent heat of condensation for each condensate. After the

temperature for a step in the ECCM is calculated using Equation 1.3, the model calculates the saturated mole fractions for each of the condensing volatiles as a function of the new temperature, and the CV mole fractions of the parcel are adjusted to reflect the vapor lost to condensation. The specific heat of the atmosphere is also recalculated as a function of the new temperature and the para hydrogen fraction, but the latent heats of the CVs are assumed to be constant with temperature.

Cloud densities calculated by the ECCM are shown in Figure 1.8, using 1 × solar and 3 × solar condensible volatile abundances in the left panel, and greatly depleted condensible volatiles on the right. The depleted case is for comparison with clouds inferred by Galileo Probe data, and will be discussed later. The 3 × solar case roughly follows previously-discussed current estimates of CV deep abundances. Although the deep abundance of water is not known, an enrichment factor of three was chosen to match the observed enrichments in sulfur and carbon, since all of these elements were brought to Jupiter by the same mechanism of planetesimal accretion, and thus oxygen should be at least as enriched as carbon. This argument relies on acceptance of the core instability model, which is challenged by the unexpected high probe-site mixing ratio of ammonia. If the core instability model can be supplanted by another model, then the assumed water mixing ratio will need to be adjusted. Table 1.3 summarizes the cloud base pressure, cloud base temperature, and total condensate column density for the modeled solar and supersolar cases, as well as cloud locations and column densities for the nephelometer observations at the Galileo Probe site (Ragent et al. 1998).

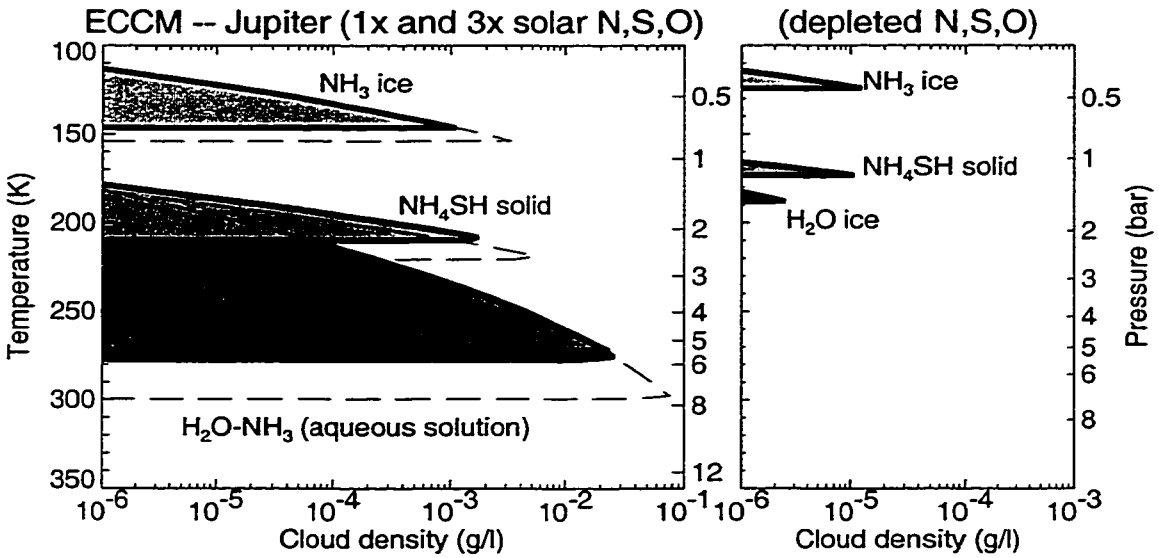

Figure 1.8 Equilibrium cloud condensation model results.

The usefulness of equilibrium cloud condensation models has been attacked on both theoretical and observational grounds. West et al. (1986) is one of many papers to raise the theoretical objection that ECCM cloud densities are much greater than any densities that would actually be expected in the Jovian atmosphere. Even if the model were improved to include microphysical processes describing cloud particle development and loss through precipitation, atmospheric dynamics would not normally support a continuous wet adiabatic ascent that persisted through the entire atmospheric column from the deep well-mixed atmosphere to the tops of the ammonia cloud. Despite the lack of microphysics and atmospheric dynamics in the ECCM, it is nevertheless accurate in predicting lifting condensation levels for the condensible volatiles. The ECCM calculates a cloud base at 0.72 bar for solar N/H, and Banfield et al. (1998) used the Galileo Orbiter Solid State Imaging (SSI) system to find a mean cloud pressure of 750 mbar, based on images in three wavelength bands in the red and near-infrared, corresponding to a strong methane band, a weak methane band, and continuum emission. Their cloud layer varied in pressure between 550 and 950 mbar, and in optical depth between 0 and 20. Optical depth can be compared with the cloud densities given in Table 1.3 if the particle size distribution is assumed. For spherical perfectly absorbing ammonia particles with a radius of 10 μm, the solar abundance

column density upper limit of 3.6 kg m^{-3} given in Table 1.3 corresponds to an optical depth of 35.

Another challenge to the utility of the ECCM is made by the altitude profiles of the condensible volatiles. Even before the Galileo Probe encounter with Jupiter, previously-discussed 5-μm retrievals of the water vapor mixing ratio profiles (Bjoraker et al. 1986, Drossart and Encrenaz 1982, Lellouch et al. 1989) showed substantial subsaturation, even in the region predicted to hold the water cloud. Likewise, the globally-averaged ammonia mixing ratio profile obtained by fitting the 1.3-cm ammonia feature (de Pater and Massie 1985) showed subsaturated ammonia even at the pressure levels predicted to hold the ammonia cloud.

Since the above observations are weighted towards regions of the planet with higher-than average flux at the observed wavelengths, it may be argued that the derived condensible volatile profiles may not be representative of conditions in all regions of the planet. The 5-μm hotspots contribute a disproportionate amount of the planet's radiated flux at 5 μm when compared to their spatial coverage of the Jovian disk. Figure 1.2 demonstrates this effect; the infrared image is mostly dark compared to the bright NEB, EqB, and SEB, which occupy only a few percent of the visible disk. The brightest parts of the infrared image are in the NEB and correspond to 5-μm hotspots. Moreover, since the 5-μm hotspots are identified as regions with reduced cloud opacity, water mixing ratio profiles derived from spatially averaged spectra at 5 μm are likely to feature reduced condensible volatile mixing ratios. Radio observations of Jupiter are also biased towards bright regions of the planet. de Pater and Dickel (1986) found a contrast at 2 cm of some 40% between the bright NEB (~170 K) and the midlatitudes (~120 K). The effect of such a contrast on the derived ammonia profile can be estimated by inspecting Figure 1.6, derived from Atreya et al. (1999). If a point were added at 2 cm with a 120 K brightness temperature, corresponding to the darkest parts of the disk at 2 cm, that datapoint would be more consistent with an ECCM profile than the subsaturated radio best fit model (solid line).

The disagreement between localized probe site CV mixing ratio profiles and ECCM profiles is even more extreme than the disagreement between the abovementioned spatially-

averaged remote sensing results and the ECCM. The NFR-derived ammonia mixing ratio profile describes an even more ammonia-poor atmosphere than the "radio best fit model." In addition, if Folkner et al.'s deep ammonia abundance holds, then the ammonia depletion extends to 7 bar below the LCL, instead of just 1 bar below the LCL according to the global radio profile of de Pater and Massie (1986). The GPMS measurement of H_2S is also in disagreement with the ECCM, since it also is depleted in the predicted cloud region, and recovers to its deep abundance at around 13 bars, over 10 bars deeper than the LCL for NH_4SH. The Bjoraker et al. (1986) water profile featured depleted water down to their limit of sensitivity at around 7 bar, and again the GPMS results exacerbate the problem, since even at the deepest level of the probe descent at around 22 bar, the water mixing ratio has still not even reached solar abundance.

Remote sensing observations of Jovian clouds present a complex picture. Banfield et al. (1998) analyzed Galileo Orbiter SSI data to find optical depths and altitude distributions of stratospheric aerosols, upper tropospheric haze, and an optically-thick 750-mbar cloud. Comparison of the position and thickness of the latter cloud to the ECCM results implies a composition of ammonia ice. SSI observations of different areas of the planet resulted in variations of ± 200 mbar for the cloud height, and optical depths ranging from 0 to 20. Roos-Serote et al. (1998) derived the transmittance for a cloud located between 1 and 2 bar from Galileo NIMS 5-μm spectra, and found it to be strongly correlated with 5-μm brightness temperature. Their cloud transmittances ranged from about 0.15 to 0.7 over the areas analyzed, all of which were in or near 5-μm hotspots. A water cloud on Jupiter has never been definitively measured, but Banfield et al. (1998) claim to have detected a cloud at 4 bar in a single area northeast of the Great Red Spot. Carlson et al. (1993) needed a water cloud to fit the observed slope in the Voyager IRIS spectra, but this conclusion is suspect given the identification by Roos-Serote (1998) of calibration errors in the IRIS instrument that mimic the spectrally-dependent cloud extinction of the Carlson et al. (1993) model. The variation in cloud properties seen in these datasets emphasizes the importance of the effect of atmospheric dynamics on cloud processes.

Given the numerous discrepancies between the ECCM clouds and CV profiles and the 5-μm hotspot characteristics determined from remote sensing and Galileo Probe measurements, it is not surprising that probe site clouds did not resemble the ECCM clouds. Ragent et al. (1998) reported that the Galileo Probe Nephelometer detected particulate matter throughout the probe descent path, with defined cloud structures in the regions 0.46–0.53 bar, 1.0–1.34 bar, and 2.45–3.58 bar. These workers found that the signal from two of the nephelometer's five channels, corresponding to reflection angles of 40° and 70°, was anomalously low. They considered the possibility that the reduced signal in these two channels was a result of a systematic error (such as aerodynamic effects in the circulation around the probe), and with the three remaining reflection angles, they were only able to constrain particle properties to lie within broad solution spaces for each cloud. For each cloud body in the analysis, extreme values of the column mass density reported in Ragent et al. (1998) for the volumes of the particular solution spaces are presented in Table 1.3.

Each of the cloud structures reported by the nephelometer can be compared with other cloud data and with ECCM calculations. The uppermost 0.46–0.53 bar structure could be the lower portion of an ammonia cloud and is consistent with Net Flux Radiometer (NFR) measurements (Sromovsky et al. 1998), which also indicate the presence of a thin cloud at pressures less than 0.5 bar. A glance at Table 1.3 affirms that the PES cloud is drastically thinner than the ECCM ammonia cloud, and occurs at a lower pressure. However, the probe site cloud fits barely within the range of cloud properties inferred by Banfield et al. (1998). The cloud location is very close to 550 mbar, the highest cloud base reported by Banfield et al., and for a cloud column density of 3×10^{-4} kg m^{-2}, within the range reported by Ragent et al., the resulting optical depth is on the order of 0.03 (for 1-μm ammonia particles). The middle cloud detected by the nephelometer was the most substantial, and it extended from 1.0–1.34 bar. An ammonia cloud at that position, given the extremely subsaturated ammonia gas mixing ratio derived from the NFR experiment, would rapidly sublimate, so the 1.0–1.34 bar cloud may be speculated to be an NH_4SH cloud. However, it is important to note that the nephelometer could not measure the composition of cloud particles. Particles sensed by the nephelometer could be a combination

of the condensible volatiles discussed here or the poorly-understood chromophores (the undiscovered colorful component of Jovian clouds). The NH_4SH condensate column density predicted by the ECCM, for 2 × solar NH_3 and H_2S, is roughly 10 kg m^{-2}, but this value is of course a generous upper limit. Even so, it is clear that the clouds of the Galileo Probe region are in considerable disagreement with the solar- or supersolar-abundance ECCM. The ECCM calculations for greatly depleted condensible volatile abundances are displayed in the right part of Figure 1.8. According to Atreya et al. (1999), the reduced abundances relative to solar used for this model (H_2O: 0.01%; NH_3: 1%; H_2S: 0.5%) provide an acceptable match to PES CV mixing ratios, and the resulting clouds are in at least qualitative agreement with those observed in the probe site. Atreya et al. also note that the ECCM calculates a particle column density of 1.8×10^{-2} kg m^{-2} for the main cloud (1.34 bar), in agreement with the upper range of the nephelometer's measured value for the cloud at this level. Although adjusting the CV abundances may make the ECCM seem like a realistic description of the probe site atmosphere, remember that the probe site CV mixing ratios increase with depth, whereas the ECCM's mixing ratios remain constant below the condensation level. In addition, the sense of circulation for the ECCM and for the probe site atmosphere is likely to be considerably different. The ECCM describes the wet adiabatic ascent of a parcel of air from the deep atmosphere to above the cloud tops, while the probe site may be better characterized by downward as well as horizontal motions (see Chapter 8).

In order to simultaneously explain the difference between the modeled vs. the observed cloud and mixing ratio profiles, local meteorology in the form of a downdraft with entrainment has been invoked in numerous discussions (Atreya et al. 1996, 1997; Owen et al. 1996, 1997; Showman and Ingersoll 1998; Wong et al. 1998; Hueso et al. 1999). Downdraft systems had previously been considered to explain depleted water based on 5-μm remote sensing (Lunine and Hunten 1987, West et al. 1986). Column-stretching, as proposed in Showman and Ingersoll (1998), is a different mechanism that may explain the condensible volatile profiles without requiring horizontal mixing. The downdraft scenario, on the other hand, calls for a normal Jovian atmosphere as described by the ECCM, and downward flow of air in the probe region. The downdraft takes air from upper levels of the

ambient atmosphere, which have been depleted of condensible volatiles through condensation and formation of the standard clouds, and forces this dry air downwards. The downward movement of air, dried of its condensible volatiles through condensation, is a logical way to explain the depleted condensible volatile profiles of the probe region, since no tropospheric sources or sinks of these gases, other than cloud formation, have been established. But a useful model must also explain both the increase of the condensible volatiles with depth as well as their staggered recovery levels, which led many of the authors cited above to the straightforward conclusion that an additional process, such as horizontal mixing and entrainment, must operate in the hotspots. The downdraft scenario is further discussed in Chapter 8.

CHAPTER II

The Galileo Probe Mass Spectrometer

Galileo Probe and Orbiter Instrumentation

The Galileo Probe Mass Spectrometer (GPMS) was one of 11 atmospheric investigations using the Galileo Probe (Table 2.1). The quantities simultaneously measured by these complementary investigations can be tied together to obtain a much clearer picture than could be drawn from any single investigation. The probe investigations are listed in Table 2.1.

Table 2.1 Galileo orbiter and probe instrumentation.

Acronym	Instrument or Experiment
Aboard the Galileo Orbiter	
SSI	Solid State Imaging Camera
NIMS	Near Infrared Mapping Spectrometer
PPR	Photopolarimeter/Radiometer
UVS/EUV	Ultraviolet Spectrometer and Extreme Ultraviolet Spectrometer
MAG	Magnetometer
EPD	Energetic Particle Detector
PWS	Plasma Wave Subsystem
PLS	Plasma Instrument (ion characteristics)
DDS	Dust Detector Subsystem
HIC	Heavy Ion Counter
—	various radio science experiments
Aboard the Galileo Probe	
ASI	Atmospheric Structure Instrument
GPMS	Galileo Probe Mass Spectrometer

Table 2.1 Galileo orbiter and probe instrumentation. (Continued)

Acronym	Instrument or Experiment
HAD	Helium Abundance Detector
NEP	Nephelometer
NFR	Net Flux Radiometer
LRD/EPI	Lightning and Radio Emissions Detector/Energetic Particles Instrument
DWE	Doppler Wind Experiment

Probe instruments of particular significance to this work other than the GPMS are the nephelometer (NEP), the net flux radiometer (NFR), the atmospheric structure instrument (ASI), and the studies of the probe radio signal attenuation due to absorption by ammonia (Folkner et al., 1998). Results from these instruments are discussed in Chapter 1 in the context of probe site meteorology, and pertain to the model in Chapter 8. The NEP detected cloud particles using a laser at a wavelength of 904 nm (near IR) which measured light scattered in one backward (178°) and four forward directions (5.8°, 16°, 40°, 70°) by the atmosphere near the probe (Ragent et al., 1998). These multiple scattering angles were intended to allow both an estimate of the cloud particle sizes by sampling the scattering phase function of the particles, as well as a measurement of the total particle density and cloud opacity. The NFR took measurements through a rotating window that sliced between upward and downward measurements at a frequency of 2 Hz (Sromovsky et al., 1996, 1998). Measurements were taken through three infrared and two optical channels, in order to distinguish between thermal and solar flux and thus measure the radiation balance throughout the probe descent region. The function of the ASI was to measure the atmospheric temperature, pressure, and density during the probe descent (Seiff et al., 1996, 1998).

The Galileo Orbiter is an observing platform with 12 *in situ* and remote sensing instruments (see Table 2.1). Of these, the near infrared mapping spectrometer (NIMS) is the most relevant to this work, since measurements in the infrared region are sensitive to ammonia and water distributions and cloud opacity and are thus quite helpful in the understanding of the structure of 5-μm hotspots (like the probe entry site hotspot).

Principles of Mass Spectrometry

Mass spectrometers directly measure the composition of a sampled material by counting ions of different atomic and molecular masses. The GPMS is an example of a neutral mass spectrometer, indicating that neutral gases must first be ionized before measurement. Depending on the ionization energy of the neutral molecules, doubly ionized species can sometimes be created, so it should be noted that the mass spectrometer actually measures the mass-to-charge (m/q) ratios. At the ionization energy chiefly used in the GPMS (75 eV), singly ionized ions are usually formed, so that $q = 1$, and the term "mass" is usually synonymous with m/q. The GPMS is described in more detail by Niemann et al. (1992) than is presented here. Gases flow into an ionization chamber, where a stream of electrons impacts the gaseous molecules and ionizes them by removing one or more electrons from the neutral molecules. Molecules are sometimes broken by the ionization source into smaller fragments in a process graphically described as splitting or cracking. For example, neutral CH_4 cracks into CH_4^+ (at $m/q = 16$), CH_3^+ ($m/q = 15$), CH_2^+($m/q = 14$), CH^+($m/q = 13$), and C^+($m/q = 12$) in the ion source region. Additional complications arise with some gases that feature significant isotopic contributions at different masses. In any case, it is clear that extracting information from the mass spectrometer data involves analyzing not just the counts returned at a single mass, but rather a spectrum of counts returned at a number of important values of m/q. This grows more complicated when the mass spectra of different gases overlap at some values of m/q.

After neutral gas molecules are ionized, an electric field accelerates the ions into the mass spectrometer's detector. The type of field featured in the GPMS is a quadrupole field. Since the acceleration experienced by the ion will depend on its ratio of mass to charge, the configuration of the field allows ions of a specific mass to be selected for measurement. The selection of the value of m/q is accomplished by varying the static and radio frequency (RF) oscillating potentials applied to the diagonal rod pairs that generate the quadrupole field. The RF oscillator has a frequency shift at 19 amu.

Ions of the selected m/q impact the electron multiplier, where each ion produces an electron, and each electron creates a cascade of further electrons. The cascade of electrons

creates a voltage pulse when it reaches the detector. The detector counts the number of pulses; the final data returned from the GPMS are the number of pulses detected in each integration period.

GPMS Gas Handling System Components

The gas inlet system of the GPMS performed the functions of introducing gas to the ion source, enriching gases, pumping ions out of the source region, and controlling the pressure in the ion source. A schematic diagram (Figure 2.1), after Niemann et al. (1982), shows the elements of the gas inlet system.

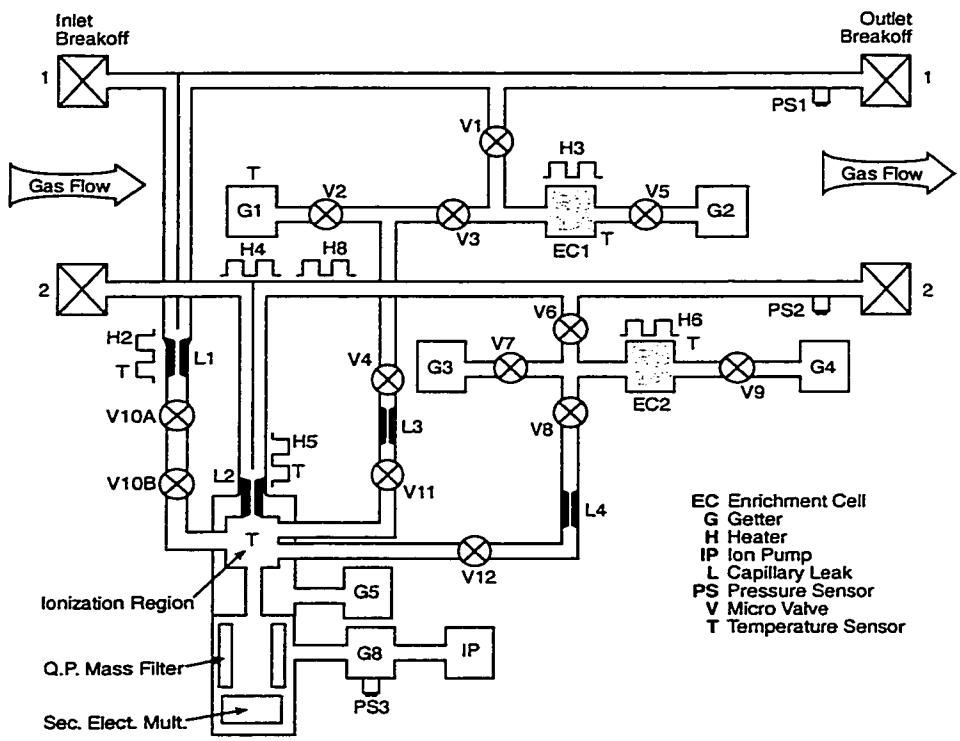

Figure 2.1 GPMS gas handling system.

Atmospheric sampling occurred both through direct leaks to the ambient atmosphere and indirectly through sample enrichment cells. Inlet/outlet system 1 was opened at the beginning of the descent sequence when pyrotechnic actuators broke metal-ceramic seals from the inlet openings. Gas flow from inlet to outlet was driven by a pressure difference between the inlet at the apex of the probe and the outlet at the minimum

pressure point in the probe interior. Atmospheric contact with inlet 1 was ended by valve closure so that the first enrichment cell could be sampled, and then inlet 2 was opened via identical pyrotechnic actuators. Once inlet 2 was opened, there was no further provision to seal the mass spectrometer from the ambient atmosphere. The sampling source program is described in greater detail in the following section and depicted in Figures 2.2 and 2.3 to 2.6. The Noble Gas Cell (NGC) does not appear as a separate element in Figure 2.1, because it is simply the volume between V4 and V2+V3. After reactive species were adsorbed onto EC1 and pumped by getters G1 and G2, valves V2 and V3 were closed, isolating the NGC, until V4 was opened and the contents were exposed to the mass spectrometer.

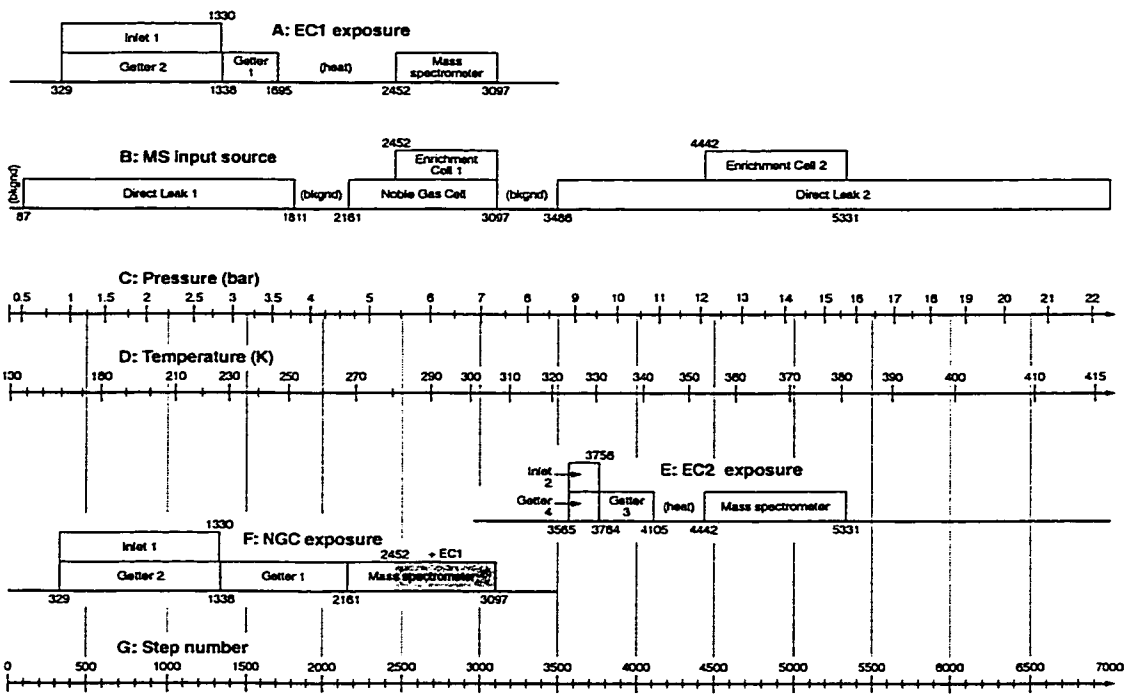

Figure 2.2 GPMS experimental sequence. (A) shows intervals during which EC1 was exposed to Inlet 1, Getter 2, Getter 1, and the mass spectrometer (MS). Similarly for (B), (E), (F). Shaded region in (F) indicates interval during which NGC and EC1 contents were simultaneously sampled by the MS. (C) and (D) show atmospheric pressure and temperature during the probe descent, and (G) shows GPMS step number. Each GPMS step had a duration of 0.5 s, so (G) is directly proportional to time.

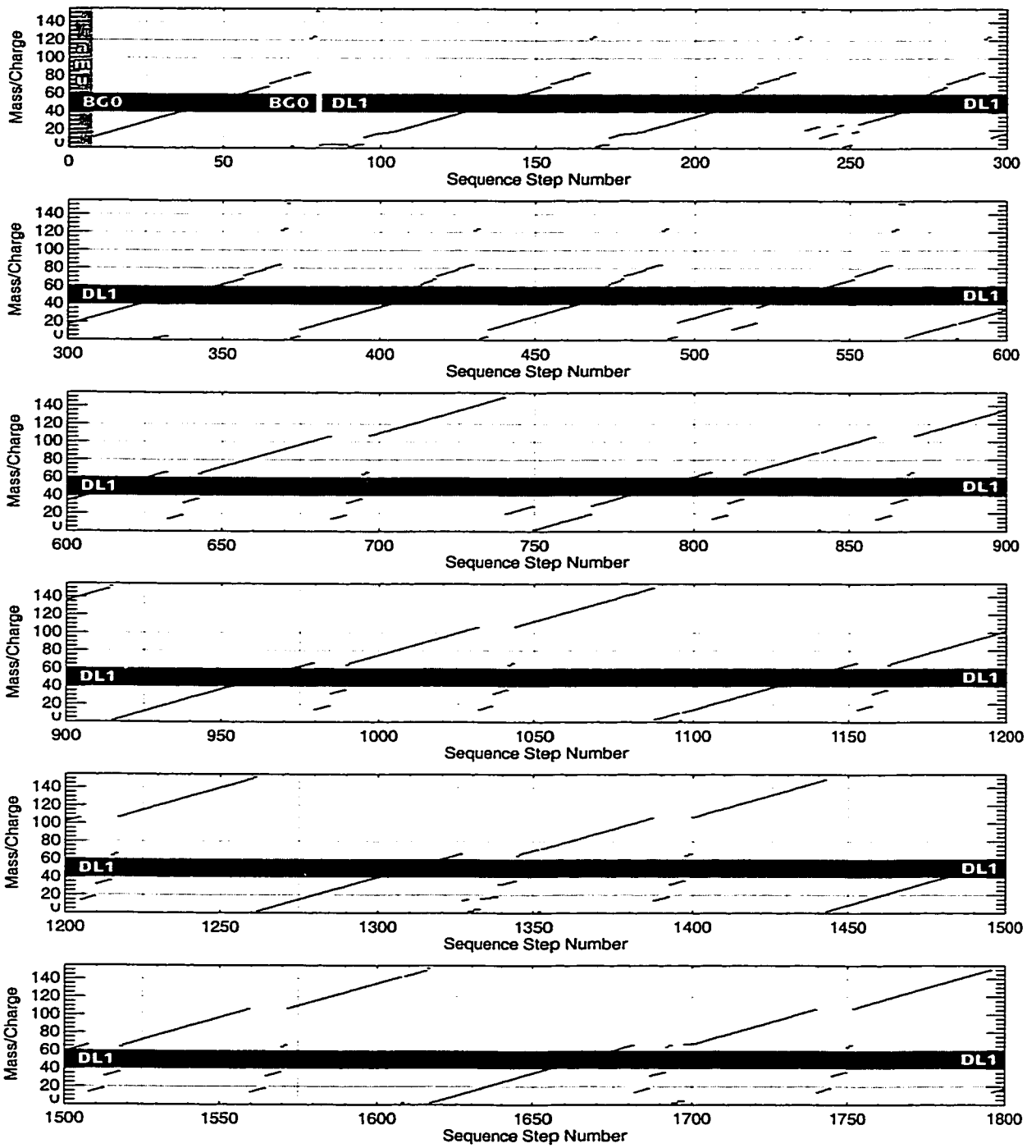

Figure 2.3 Mass/charge ratio measured by the GPMS, steps 0-1800.

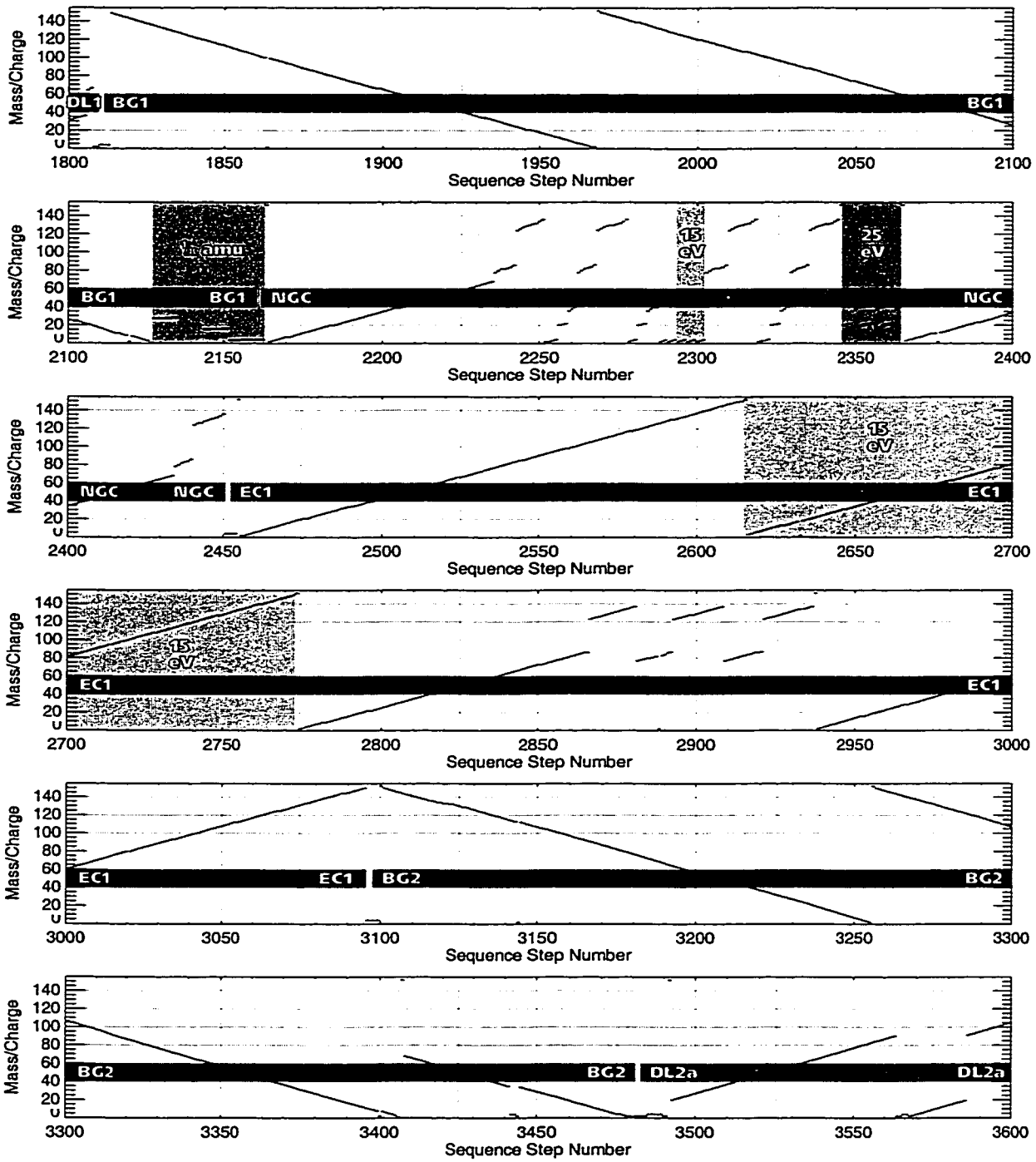

Figure 2.4 Mass/charge ratio measured by the GPMS, steps 1800–3600.

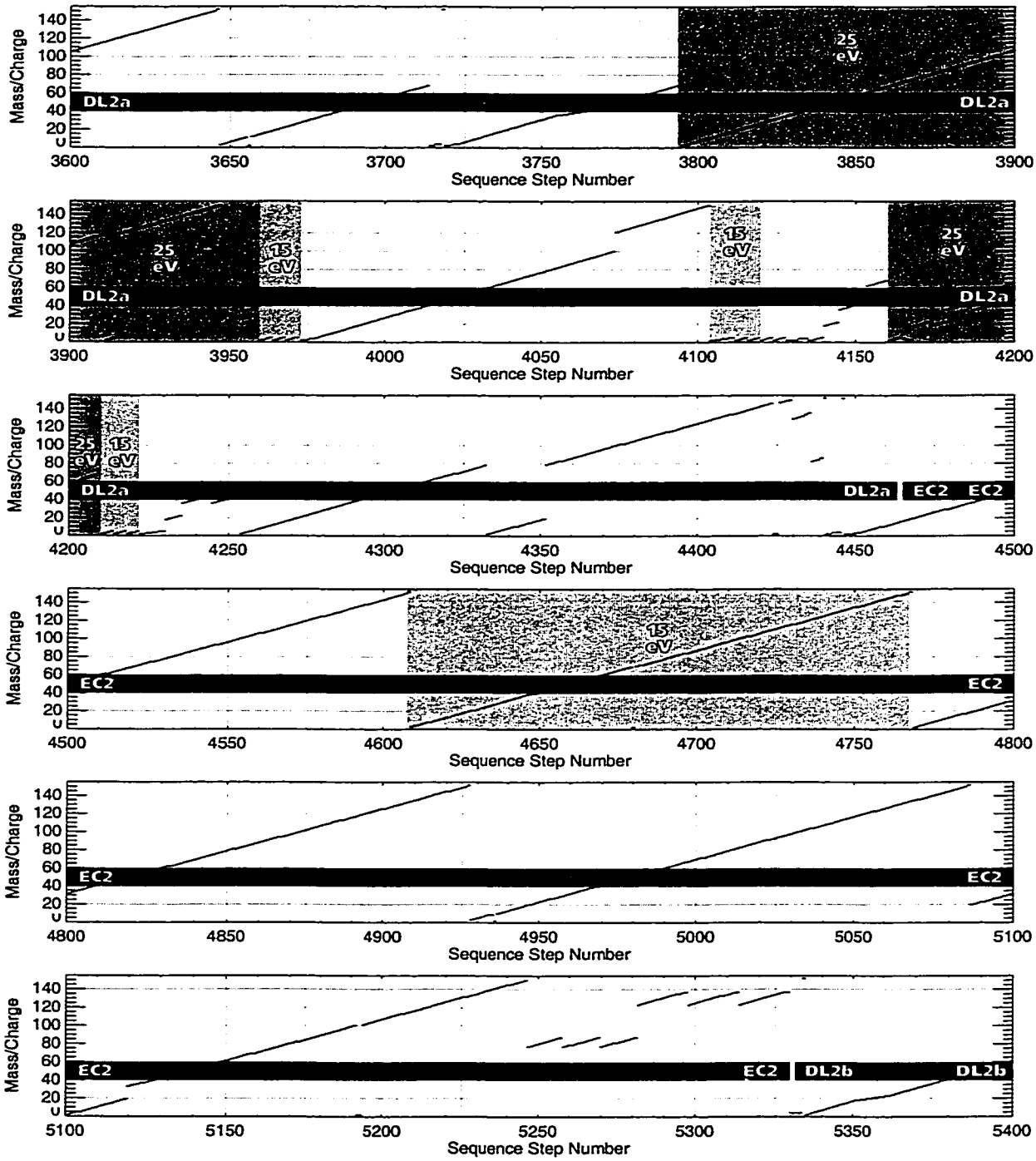

Figure 2.5 Mass/charge ratio measured by the GPMS, steps 3600-5400.

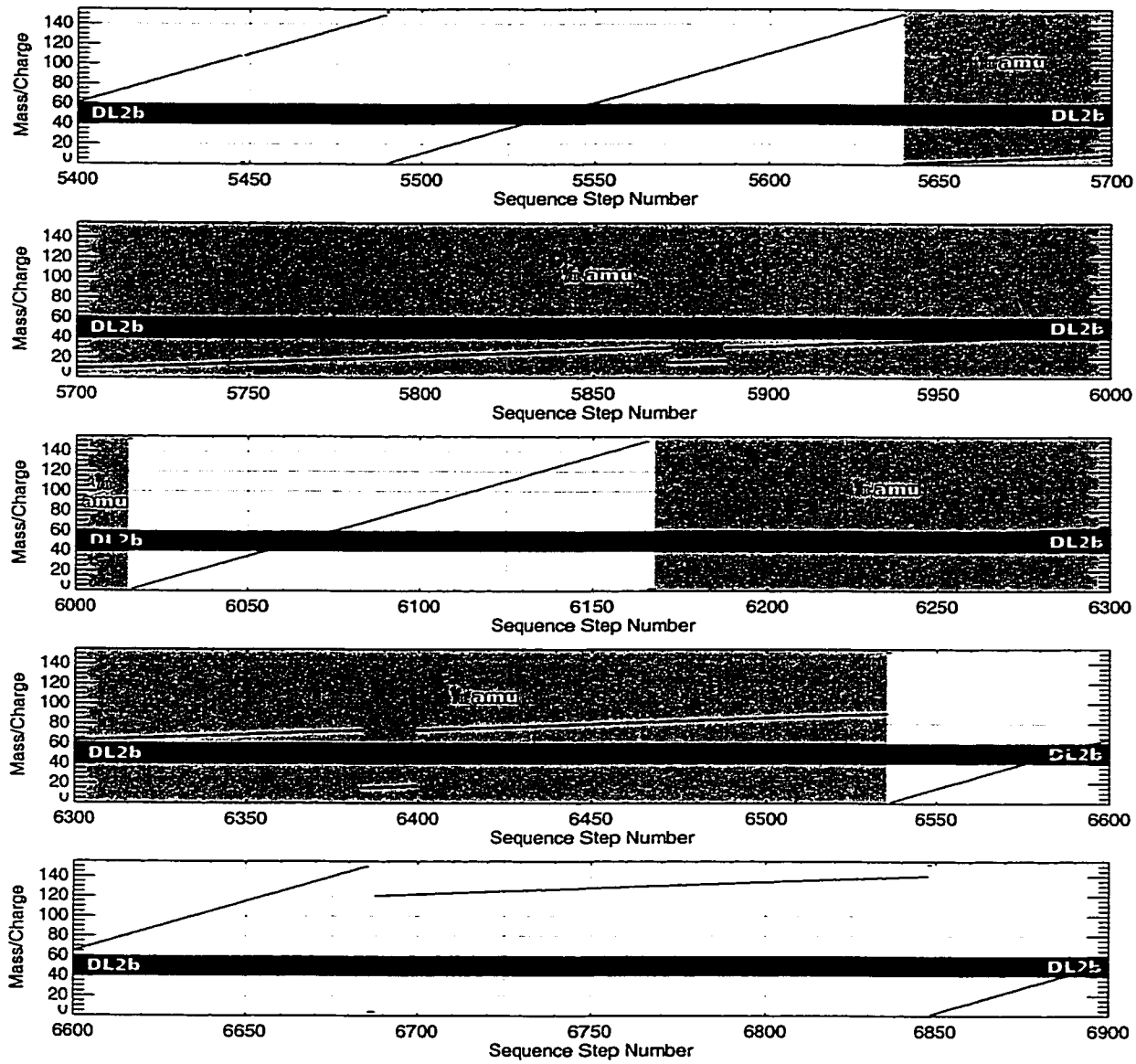

Figure 2.6 Mass/charge ratio measured by the GPMS, steps 5400–6900.

Ambient and enriched gases were brought into the mass spectrometer by way of four glass capillary leaks (L1 to L4 in Figure 2.1). The leak conductances (see Table 2.2) were chosen to prevent the pressure in the ion source region from exceeding 0.1 μbar.

Table 2.2 Inlet leak conductances.

Unit designation	Effective dates	Conductance at 1 bar (mbar l s^{-1}) L1	L2
Flight Unit	1985 to 1994	1.3×10^{-6}	2.7×10^{-7}
Experimental Unit	before 1997-09-27	6.7×10^{-6}	1.6×10^{-7}
Experimental Unit	after 1997-09-27	6.7×10^{-6}	2.9×10^{-7}

Symbols V1–V12 in Figure 2.1 mark the valves used to control the gas flow pathways. A command processor read a sequence of instructions from read-only memory and controlled the opening and closing of the valves and actuators. Part of the telemetry stream returned from the probe contained information confirming successful valve operation. The valve operation program is described in Table 2.3.

Table 2.3 GPMS valve program.

			Inlet System Valve Status (1 = closed)											
Step	MS Input	Inlet System Operations	1	2	3	4	5	6	7	8	9	10	11	12
0	NONE (BG)		1	0	1	1	0	1	1	1	0	0	0	0
87	L1		1	0	1	1	0	1	1	1	0	0	0	0
329	L1	EC1 + G2 exposed to IN1	0	0	1	1	0	1	1	1	0	0	0	0
1330	L1	EC1 isolated from IN1	1	0	1	1	0	1	1	1	0	0	0	0
1334	L1	EC1 isolated from G2	1	0	1	1	1	1	1	1	0	0	0	0
1338	L1	EC1 exposed to G1	1	0	0	1	1	1	1	1	0	0	0	0
1695	L1	RG ("rare gas cell") isolated from EC1	1	0	1	1	1	1	1	1	0	0	0	0
1811	NONE (BG)		1	0	1	1	1	1	1	1	0	1	0	0
2157	NONE (BG)	RG isolated from G1	1	1	1	1	1	1	1	1	0	1	0	0
2161	RG		1	1	1	0	1	1	1	1	0	1	0	0
2452	RG + EC1		1	1	0	0	1	1	1	1	0	1	0	0
3097	NONE (BG)		1	1	0	0	1	1	1	1	0	1	1	0
3116	NONE (BG)		1	1	1	0	1	1	1	1	0	1	1	0

Table 2.3 GPMS valve program.

			Inlet System Valve Status (1 = closed)											
Step	**MS Input**	**Inlet System Operations**	**1**	**2**	**3**	**4**	**5**	**6**	**7**	**8**	**9**	**10**	**11**	**12**
3121	NONE (BG)		1	0	1	0	1	1	1	1	0	1	1	0
3476	NONE (BG)		1	0	1	1	1	1	1	1	0	1	1	0
3486	L2		1	0	1	1	1	1	1	1	0	1	1	0
3565	L2	EC2 + G4 exposed to IN2	1	0	1	1	1	0	1	1	0	1	1	0
3756	L2	EC2 + G4 isolated from IN2	1	0	1	1	1	1	1	1	0	1	1	0
3760	L2	EC2 isolated from G4	1	0	1	1	1	1	1	1	1	1	1	0
3764	L2	EC2 exposed to G3	1	0	1	1	1	1	0	1	1	1	1	0
4105	L2	EC2 isolated from G3, heated	1	0	1	1	1	1	1	1	1	1	1	0
4442	L2 + EC2		1	0	1	1	1	1	1	0	1	1	1	0
5331	L2		1	0	1	1	1	1	1	0	1	1	1	1
5641	L2		1	0	1	1	1	1	1	1	1	1	1	1

The pumping system maintained the flow of gas from the sample source through the ion source. The system consisted of a pair of getters (G5 and G8 in Figure 2.1) and a sputter ion pump (IP), and operated without any moving parts. Although hydrogen was very efficiently absorbed by the getters, helium, other noble gases, and methane were relatively unaffected by them, leaving the sputter pump to remove these species. But helium presents a challenge to the sputter pump as well: it must be implanted in the pump elements in order to be removed, since chemical binding or solution are ineffective for helium, and it has a low ionization cross section. Thus, the sputter pump must use large quantities of cathode material to remove the helium. This vigorous sputtering is problematic, since it synthesizes hydrocarbons through reactions between hydrogen ions and carbon trapped on the surfaces of the pump elements. The effect of the synthesized hydrocarbons on the mass spectrometer is reduced in two ways. First, gases must pass the getter before they reach the sputter pump, so the amount of hydrogen, carbon, and other reactive gases available for reactions inside the sputter pump is reduced. Secondly, the placement of the getter also requires any products of the sputter pump to again pass (and hopefully to be absorbed by) the getter

before reaching the mass spectrometer. Getter and pump specifications can be found in Niemann et al. (1982).

Three enriched gas samples were prepared during the probe descent. The first enriched sample was the noble gas cell (NGC). In this sample, reactive gases (especially hydrogen) were extracted by absorption into chemical getters G1 and G2. Complex hydrocarbons and heavy gases were additionally adsorbed in enrichment cell 1 (EC1), leaving chiefly noble gases in the NGC sample. The second enriched sample (EC1) was composed of the NGC contents plus the gases released upon heating of the enrichment cell. The third sample (EC2) was also enriched by extraction of H_2 by chemical getters (G3 and G4) and by the release of hydrocarbons trapped by the second enrichment cell. However, because there was no way of sealing the ambient atmosphere from the ion source once the second inlet system was opened, the contents of EC2 were added to the directly-sampled atmospheric gases.

In addition to the heaters used to release hydrocarbons from the enrichment cells, heaters H2 and H5 were used to keep the direct leaks heated above ambient atmospheric temperature. This heating was intended to prevent clogging of the inlets by condensed particles that could be introduced from any cloud layers penetrated by the probe. The precaution of heating the inlets was a response to the loss of data experienced by mass spectrometers on atmospheric probes in the atmosphere of Venus, where sulfuric acid cloud droplets had clogged the inlets (Hoffman et al., 1979)

Also depicted in Figure 2.1 are temperature and pressure sensors. These devices returned their results in the telemetry stream at specific intervals, and were intended to monitor the functional environment of the mass spectrometer, to provide data to compare with environmental conditions of the calibration experiments.

Descent Sampling Sequence

The quantity actually being measured by the mass spectrometer at any instant was a function of several variables, including sample source (as controlled by the valve configuration), mass to charge ratio, ionization energy, and detector sensitivity level. I will

describe each of these variables separately. Except for detector sensitivity level, the values of all the sampling sequence variables were determined by a pre-programmed sequence of 8192 steps. Useful data were returned from the GPMS up to step 6886. Each step was a single mass spectrometer integration period of 0.5 seconds and returned a single data point consisting of the counts measured during that integration period. Steps corresponding to programmed valve and heater events are given in Table 2.3. Figure 2.2 shows both the atmospheric temperature and pressure corresponding to the descent sequence steps, as well as the step numbers corresponding to the valve events that determined the gas flow configurations.

The sample source providing input to the ion source at any time during the descent can be read from Figure 2.2.B. Until step 87, the mass spectrometer takes measurements with no input source connected to the ion source, in order to characterize the instrument background count levels. During the DL1 segment, the ambient atmosphere is sampled. Another background sample follows, and at step 2161, the contents of the noble gas cell are sampled. After 2452, the stacking of the enrichment cell box in the Figure 2.2.B on top of the noble gas cell box, and the grey area in Figure 2.2.F, indicate that the contents of EC1 are measured simultaneously with those of the NGC. After the final background measurement, inlet 2 was opened, allowing the direct measurement of the atmosphere once again at step 3486. This direct sampling continued to the end of the mission, combined between steps 4442 and 5331 with the contents of EC2.

Parts A, E, and F of Figure 2.2 show all the sampling events relevant to the enrichment and noble gas cells. The inlet boxes indicate the intervals during which atmospheric gases were admitted into the cells. The getter boxes indicate periods during which the valve configuration allowed contact between the getters and the cells. During the application of heat to the enrichment cells, they were completely sealed from all getters and the mass spectrometer. The last boxes on these sections of the diagram correspond to the times during which the contents of the cells were being sampled by the mass spectrometer. In addition, grey shading in the last box of the NGC exposure timeline indicates the interval during which EC1 contents were simultaneously sampled.

Parts C and D of Figure 2.2, the pressure and temperature at each step in the probe descent, are derived from the ASI experiment (Seiff et al., 1996).

Figures 2.3 to 2.6 gives the sequence of m/q settings as a function of step number throughout the descent. Step number can be related to pressure or temperature using Figure 2.2. Mass spectrometer input sources are shown in Figures 2.3 to 2.6. Most GPMS data were collected with an ionization energy of 75 eV. Measurements taken at ionization energies of 15 and 25 eV are indicated in Figures 2.3 to 2.6. Portions of the descent sequence that used a mass to charge ratio resolution of 0.125 amu are also indicated. The main purpose of these high mass-resolution scans is to verify tuning of the mass spectrometer. However, additional information can be obtained from these scans about doubly-ionized species with odd atomic mass numbers, such as NH_3^{++}, which is detected at $m/q = 17/2 = 8.5$.

Detector counts were returned in either high or low sensitivity mode. High sensitivity mode was the default, and low sensitivity mode was triggered whenever counts exceeded a certain level, and also at preprogrammed points in the descent sequence. The count limit for triggering the low sensitivity mode was designed to be about 5×10^7 counts per second, or 2.5×10^7 counts per period (Niemann et al., 1992). Low-sensitivity mode was triggered 62 times during the experiment, almost exclusively limited to masses 2 and 4. Since there was a large number of available high-sensitivity data for masses 2 and 4 (H_2 and He), and since the primary value of these masses is their usefulness as reference gases, I did not use the low-sensitivity data for quantitative analysis. Despite the stated upper detector limit of 2.5×10^7 counts per period in high sensitivity mode, the data returned from the GPMS contained many measurements of counts above this limit, including some in excess of 1×10^8 in the noble gas cell and the first enrichment cell. These high counting rates are an indication that the threshold value for low sensitivity mode activation must not have been strictly constant. Since only high sensitivity data are examined in this work, the instability of the low sensitivity mode trigger level is not a serious concern.

The Flight Unit (FU) and the Experimental Unit (EU)

Two duplicate versions of the GPMS instrument existed. The flight unit (FU) was used to perform some limited calibration experiments, and integrated into the Galileo Probe. After a dormancy of 10 years, the probe dropped into Jupiter's atmosphere and returned its data. The flight spare experimental unit (EU; see Figure 2.7) has remained permanently at NASA's Goddard Space Flight Center (GSFC), where it has been used to perform a wide array of calibration experiments in order to facilitate interpretation of the data returned by the FU from Jupiter. These experiments will be described in rich detail in Chapters 4 and 5.

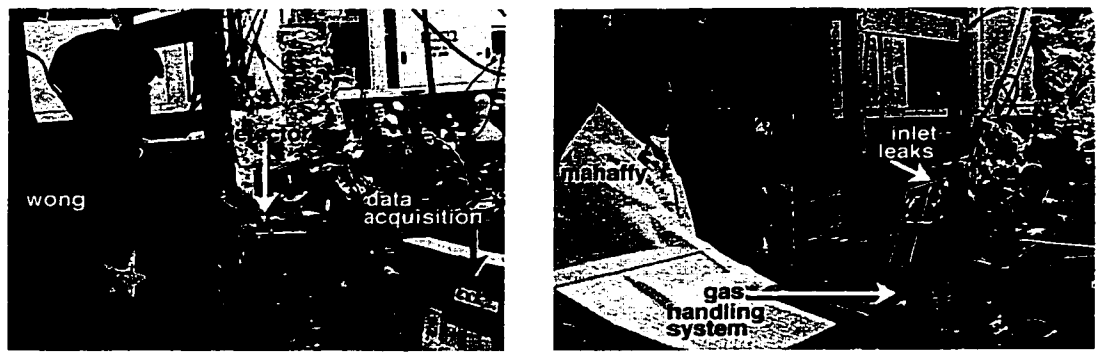

Figure 2.7 GPMS experimental unit (EU).

CHAPTER III

GPMS Data Analysis Procedure

Using count ratios

The physically meaningful result extracted from the GPMS dataset is the mixing ratio (w) of the atmospheric constituents. Mixing ratio, in terms of atmospheric number densities, is expressed in this work as:

$$w_x = \frac{n_x}{n_{H_2}} \qquad 1.1$$

However, the mixing ratio of a particular constituent (w_x) in Jupiter's atmosphere is not simply related to the atmospheric pressure and the counts measured by the GPMS for that constituent ($C[x]$). Instead, a count ratio of $C[x]$ to the counts measured for an atmospheric "reference gas" ($C[ref]$) must be examined to determine the mixing ratio of interest:

$$w_x \sim \frac{C_x}{C_{ref}} \equiv CR[x/\mathrm{ref}] \qquad 3.1$$

But the above relation is not an equality; a "calibration constant" must be introduced in order to finally obtain the mixing ratio:

$$w_x = cc^{sp}_{x/ref} \frac{C[x]}{C[ref]} \qquad 3.2$$

Indexes to the symbol for calibration constant show that it depends on both "*sp*," the chemical species in question, and "*x*," the particular peak of that species being examined in the mass spectrum. For example, at mass 34, both phosphine and hydrogen sulfide could be detected, using (respectively) $cc^{PH3}_{34/4}$ or $cc^{H2S}_{34/4}$. Phosphine could also be analyzed by using its peak at mass 31 and the calibration constant $cc^{PH3}_{31/4}$. The count ratios in Equation 3.2

are obtained from flight unit (FU) data, while the calibration constants are derived from either experimental unit (EU) data or pre-launch calibration information obtained from the FU.

Since the GPMS measured only a single mass-to-charge value (m/q) for each 0.5-second integration period, both $C[x]$ and $C[ref]$ in Equation 3.2 cannot be measured at the same time. Therefore, some approximation must be made in order to determine a count ratio at a given instant during the probe descent, since pressure increased continually with time. The three approximation techniques I have used to obtain $C[ref]$ are nearest measured value, interpolated counts, and polynomial-fitted counts. In all cases, actual measured counts were used for the numerator of the count ratio in Equation 3.2, and an approximation was used to obtain the denominator. IDL software developed by the GSFC group applied polynomial fits to every mass sampled by the GPMS and used the fits for either (or both) the numerator and denominator of the count ratio. I use real counts for count ratio numerators and fitted counts for count ratio denominators in order to simplify error analysis as well as to explicitly reveal problems in the data that might be camouflaged by fitted polynomials. Because calibration experiments measured an entire scan across the mass spectrum at a constant pressure, there is no need to employ any interpolation or polynomial fitting to obtain reference gas counting rates; the measurements of $C[x]$ and $C[ref]$ from the same scan can be used together.

The nearest measured value algorithm simply searches for the closest step at which the reference gas was measured by the mass spectrometer and uses the counts measured at that nearby step as the denominator of the count ratio. I use this method for non-standard reference gases, and for isotopic ratios. This method is well-suited to deriving isotopic ratios, since the isotopic ratios of interest are usually very close in m/q, and thus are usually sampled at nearly the same descent time and pressure. As can be seen in Figures 2.3 to 2.6, the value of m/q sampled often increased or decreased one-to-one with step number. Care must be taken to ensure that the nearest value for the denominator matches the numerator in ionization energy and in sensitivity mode. Also, the denominator must be

chosen from the same source region as the numerator (so that the ratio is not composed, for instance, of one point sampled in DL2 and one in EC2).

The interpolated counts and fitted counts methods of finding values for the count ratios are very similar. For the set of standard reference gases (H_2, He, and CH_4), fitted counting rates were derived for every step of the GPMS descent sequence. Between steps at which the mass spectrometer actually measured these gases, values were derived by either linearly interpolating between the observations, or by fitting polynomial curves to all the measurements within specified source regions. For each of the various reference gases in the different source regions, Table 3.1 presents the number of datapoints in the source region (columns labeled "N") and the order of the polynomial fit (columns labeled "O"). Plots of the fitted/interpolated values are displayed in Figures 3.1–3.5.

Table 3.1 Reference gas polynomial fit orders.

Reference gas		DL1		NGC		EC1		DL2	
Mass	Molecule	N	O	N	O	N	O	N	O
2	H_2	19	3	7	1	5	2	27	5
4	He	16	3	6	1	4	2	20	5
12	CH_4	13	3	2	1	3	2	10	3
13	CH_4	13	3	2	1	3	2	10	3
14	CH_4	28	3	2	1	3	2	10	5

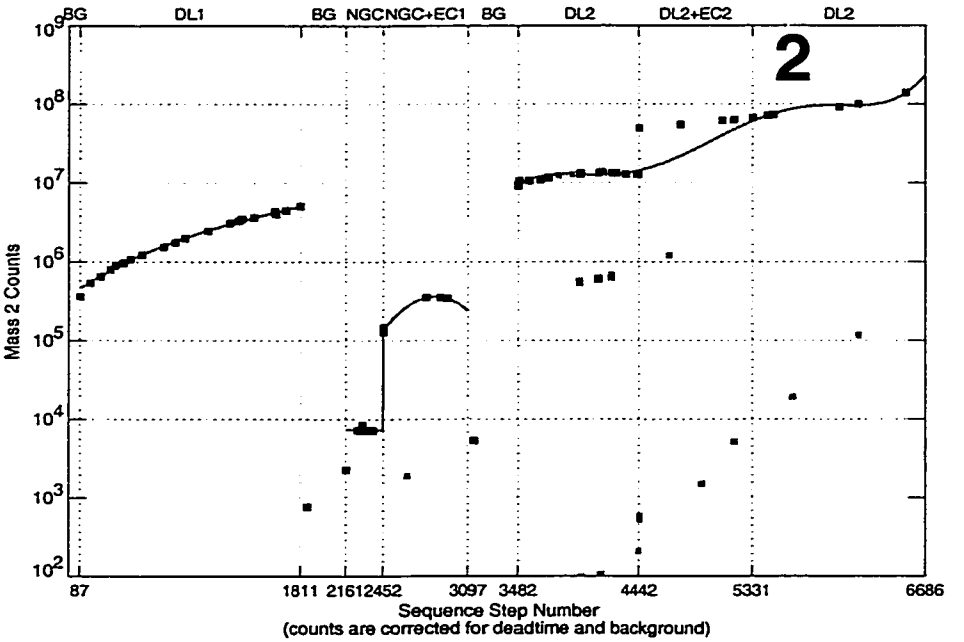

Figure 3.1 Polynomial fit to C[2] reference gas H_2. Dark squares are 75-eV high sensitivity GPMS counts at mass 2. Grey squares indicate points at other ionization energies (15eV or 25 eV) or low sensitivity points. Grey curves are least square polynomial fits to the log of counts, with fit orders given in Table 3.01. DL2b counts are highly uncertain due to detector saturation (see text below Equation. 3.6).

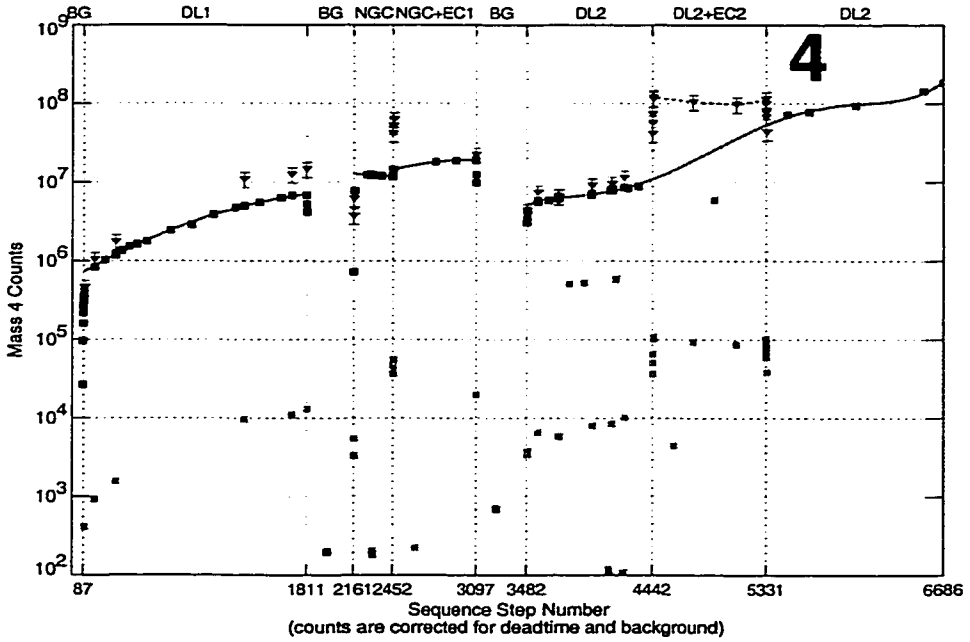

Figure 3.2 Polynomial fit to C[4] reference gas He. As Figure 3.1 but with counts at mass 4. Triangles are low sensitivity points corrected to match high sensitivity counts; see text for discussion. DL2b counts are highly uncertain due to detector saturation (see text below Equation 3.6).

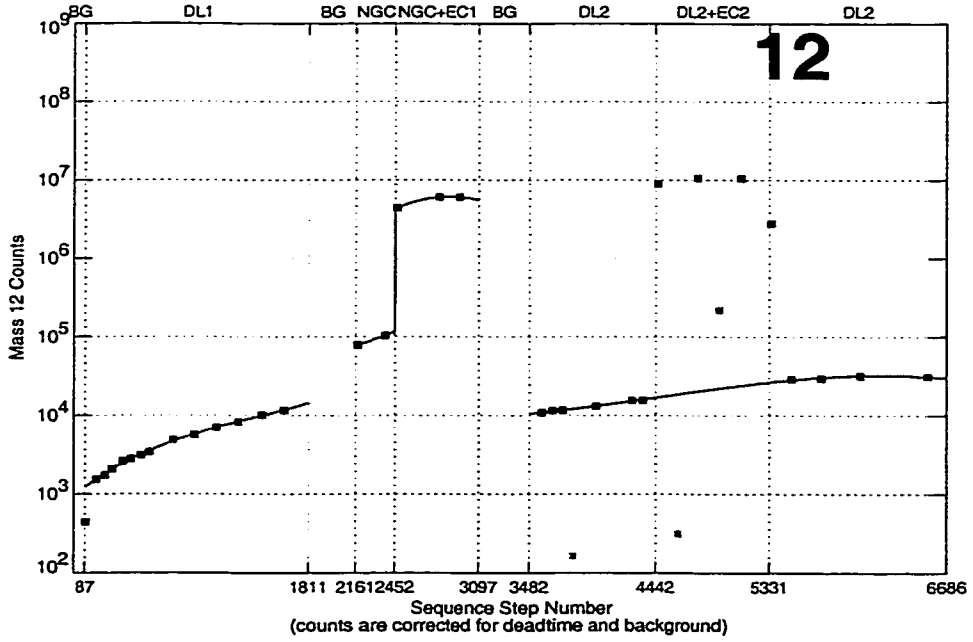

Figure 3.3 Polynomial fit to C[12] reference gas product C^+. As Figure 3.1 but with counts at mass 12 C^+ is a fragment of methane, which has a constant mixing ratio in Jupiter's troposphere.

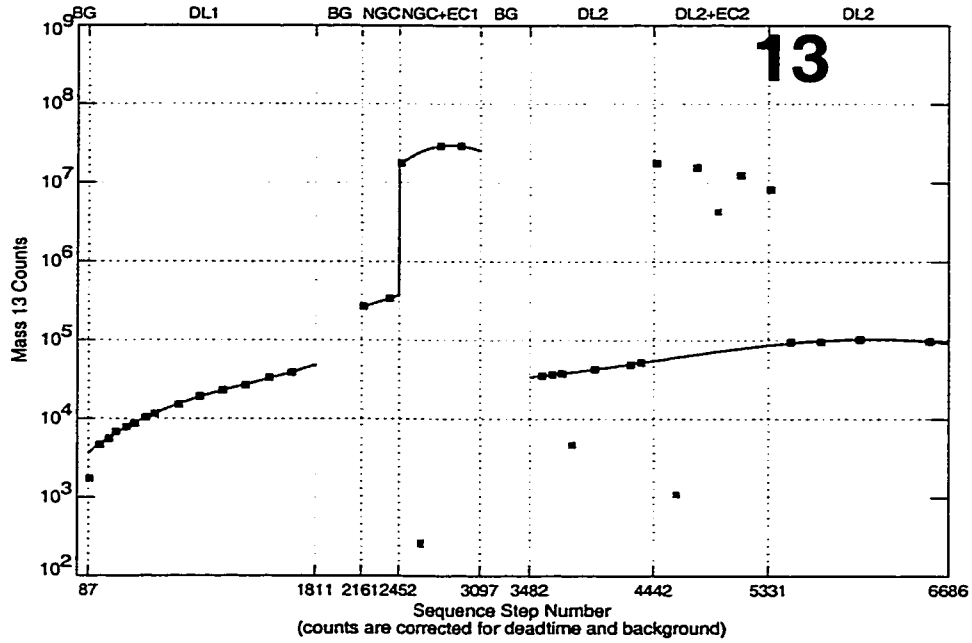

Figure 3.4 Polynomial fit to C[13] reference gas product CH^+. As Figure 3.3 but with counts at mass 13. CH^+ is a fragment of methane, which has a constant mixing ratio in Jupiter's troposphere. I favor mass 13 as a reference gas because it has a stronger signal than 12, does not suffer from confusion with N^+ as 14 does, and does not approach deadtime count saturation as 2 and 4 do.

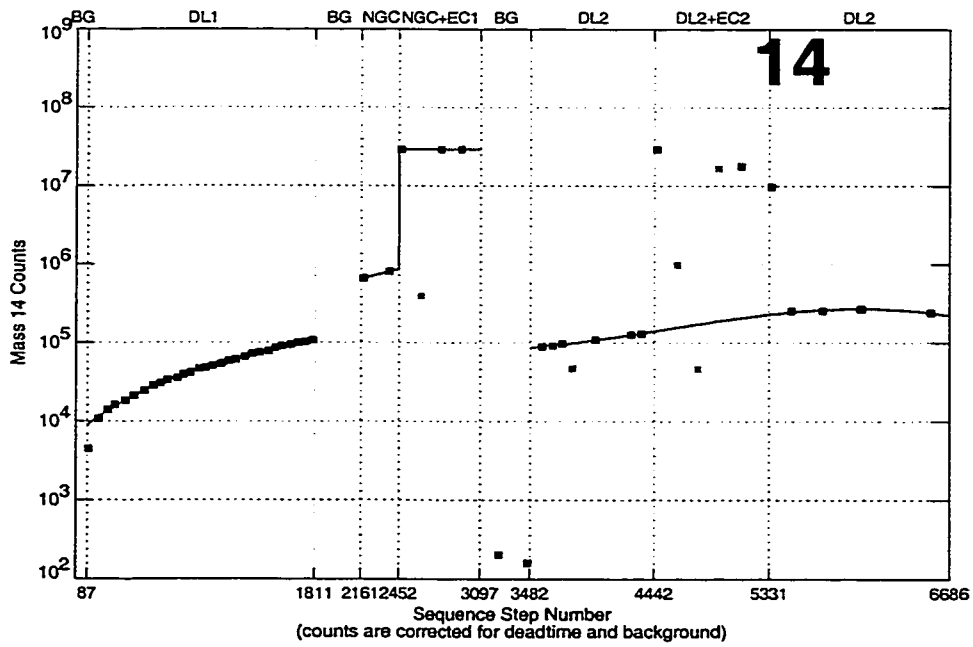

Figure 3.5 Polynomial fit to C[14] reference gas product CH_2^+. As Figure 3.3 but with counts at mass 14. Mahaffy favors 14 as a reference gas because it has a stronger signal than 13.

The deadtime correction

At high count levels, detector saturation effects become important. An ion entering the mass spectrometer's electron multiplier will create a shower of electrons that are then intercepted by the detector. After an electron is counted by the detector, there is a short interval during which the detector will be unable to detect any other electrons. At low pressures in the ion source, this detector deadtime will be small compared to the interval between ion impacts. But at higher pressures, an appreciable fraction of the counts will be lost during the detector deadtime.

Figure 3.6 illustrates detector behavior in deadtime-unsaturated (low-pressure) and deadtime-saturated (high-pressure) conditions. The relation between impacting ions and detected ions is given by

$$C_o = C_i \, e^{-\tau C_i}, \qquad 3.3$$

where C_o are the observed counts, C_i are the ions actually reaching the electron multiplier, and τ is the deadtime correction constant (Mahaffy, 1996). Since τ and C_i are positive, the exponent will grow more and more negative as C_i increases, and the observed counts will reach a maximum and then decline with increasing levels of ions entering the mass spectrometer (see Figure 3.7).

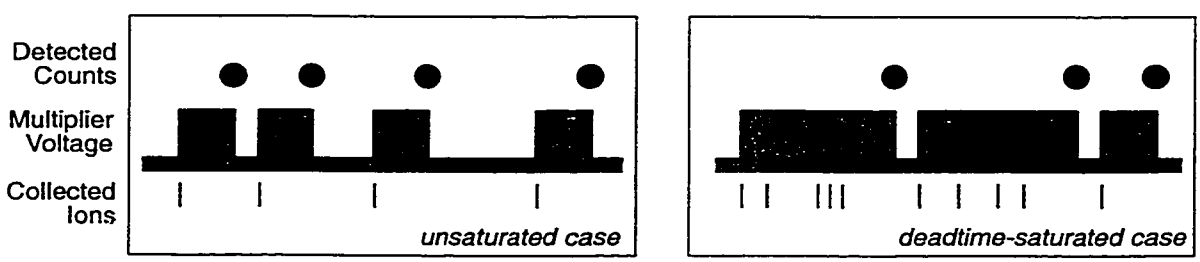

Figure 3.6 Illustration of the loss of detector efficiency at high ion source pressure.

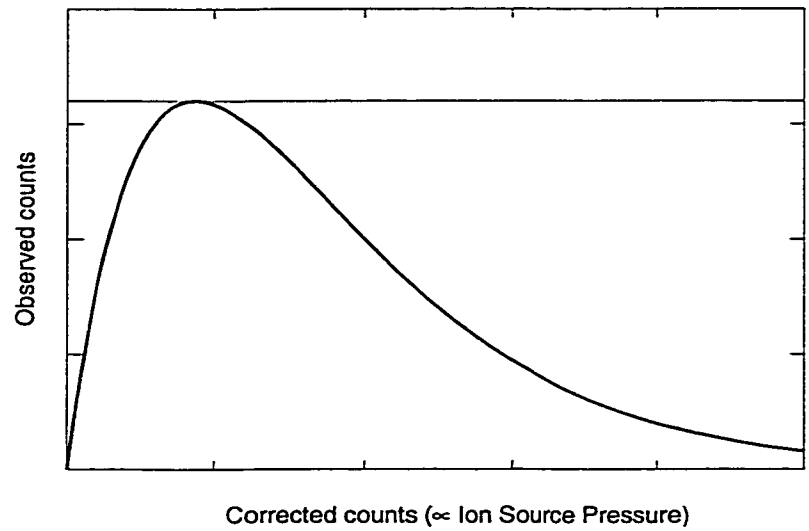

Figure 3.7 Functional form of detector response to increasing ion source pressure.

The location of the maximum in the observed counts function, or the detector saturation point, can be used to find the deadtime correction constant (Mahaffy, 1997):

$$\left.\frac{dC_o}{dC_i}\right|_{\text{sat.}} = 0 = \left.\frac{d}{dC_i}(C_i\, e^{-\tau C_i})\right|_{\text{sat.}} = e^{-\tau C_i^{\text{sat.}}}(1-\tau C_i^{\text{sat.}}) \qquad 3.4$$

$$\tau = \frac{1}{C_i^{\text{sat.}}} \qquad 3.5$$

But the number of ions actually entering the spectrometer is unknown, so I insert Equation 3.5 into Equation 3.3 and evaluate at the detector saturation point to find:

$$\tau = \frac{1}{eC_o^{\max}} \qquad 3.6$$

Equation 3.3 can then be solved numerically for every step in the GPMS descent sequence to yield the deadtime-corrected counts. Since for every C_o, C_i has two solutions, some care must be taken to select the appropriate solution. The solution for unsaturated detector counts ($C_i < C_i^{\text{sat.}}$) was used everywhere except for hydrogen at pressures greater than about 10 bar and helium in DL2b. The saturated detector solution was used for hydrogen and helium in DL2b (see Figures 3.1 and 3.2), but note that the saturated solution results in highly questionable values and is not good for quantitative analysis.

Different observed values of C_o^{max} lead to the derivation of different deadtime constants. The discrepancy between the values gives the only available information to estimate an error in the determination of the deadtime constant. Table 3.2 lists deadtime constants for the FU. Saturation of C[2] during the probe descent, during the DL2a phase, led to τ_2. The PFU experiment, conducted using the flight unit at NASA Goddard during calibration testing of the instrument, attempted to simulate conditions expected to apply during the probe descent; C[2] possibly reached saturation at the end of the experiment and led to the derivation of τ_c. Unfortunately, documentation for the PFU experiment is incomplete, and there is some possibility that detector settings may have changed between the PFU run and the final flight configuration. In this case, the applicable deadtime constant would b affected. Nevertheless, an average of the two values τ_c and τ_2 resulted in the intermediate value of τ_m, while the difference was taken to represent an approximate 2σ error around the central value τ_m. FU calibration runs were also generally corrected using the τ_c deadtime constant, whereas EU calibration runs required a range of deadtime constants and were analyzed with deadtime constants internally derived for each experiment, whenever possible. Deadtime constants used for calibration runs will be presented in a later chapter.

Table 3.2 Deadtime correction coefficients.

	Value	Maximum Uncorrected Counts	Source
τ_2	4.3174×10^{-8}	8,520,851	C[2] saturation in DL2a (Jupiter)
τ_c	3.4098×10^{-8}	10,788,864	C[2] saturation at end of PFU (lab)
τ_m	3.86×10^{-8}	(9,530,556)	average of τ_2 and τ_c

The background correction

At three separate times during the descent sequence (see Chapter 2), the mass spectrometer was completely isolated from its input sources, and measurements were taken.

Since these measurements were above the zero-count level, we assumed that they represent the background level. A separate background level is subtracted from each value of m/q. Figures in Appendix A show counts vs. step for all GPMS values of m/q; these values are not corrected for background, but the background levels are plotted as dark grey lines, with 1-σ uncertainties in the background corrections represented by the surrounding grey bands.

I attempt to use the background measurements for each source region that are most appropriate to that source region. For most masses, background measurements from background region BG1 (see Figure 2.2 or Table 2.3) were used to correct measurements in DL1. Measurements from BG1 were also used to correct all measurements in the noble gas cell and in the first enrichment cell regions. In most cases, data in DL2 were corrected using the background measurements from BG2. Background corrections for EC2 are much higher than those derived from BG2, but the appropriate EC2 background corrections were not derived here because EC2 data is not used in the analysis below.

Even after the closure of the enrichment cell valves, some gases (e.g., water and ammonia) were found to persist at enriched levels, as seen by the higher post-EC counts at $m/q = 17$, 18, etc. Correction of this effect is relatively straightforward for the DL2a region, since the first enrichment cell was followed by a background region before direct leak 2 was opened. For the gases present at enriched levels even after the close of EC1, I used the BG2 data to model an exponential decay in counts in the leak 2 region, and I subtract the extrapolated exponentially-decaying background level from the DL2a data. These exponential corrections can be seen in the plots in Appendix A. An exponentially decaying background correction for ammonia had to be determined without the aid of the BG measurement prior to DL2a, as will be discussed in Chapter 6.

The correction for DL2b is somewhat more complicated for the gases which did not immediately resume their unenriched atmospheric levels after the closure of the EC2 valves. Since the EC2 experiment could not be followed by a background measurement, the mass spectrometer measured contributions both from the decaying residual enriched component as well as from the continual direct atmospheric input. For these problematic gases, I subjectively determined a set of datapoints to use for an exponential fit to the background

contribution. This set typically includes 1–3 points at the beginning of DL2b, as well as either a point in EC2, or a value at the last step of EC2 formed by linearly extrapolating EC2 datapoints. I assume that the points in this set characterize the background level for DL2b, and that the relatively constant contribution from the direct atmospheric component is small within the selected set of points. I subtract from all the DL2b data an exponential fit to the points in the set.

Choosing the appropriate reference gas

Atmospheric mixing ratios are obtained using count ratios, where counts of the gas of interest are divided by counts of an appropriate reference gas (see Equation 3.2). For mixing ratios, the reference gas should be a well-mixed atmospheric constituent with a constant mixing ratio. Reference gases tested in this study are hydrogen, helium, methane, and argon.

Hydrogen is the most obvious choice as a reference gas, and indeed many scientists use the ratio to hydrogen to define mixing ratios, as in Equation 1.1. However, hydrogen is present in such great abundance in Jupiter's atmosphere that its count levels saturate in the GPMS at a pressure of around 10 bar in DL2. Although we can use the deadtime function to correct for this count saturation, the results are much less reliable than are unsaturated counts at another mass, making hydrogen largely useless as a means of obtaining mixing ratios. Helium provides a better reference gas because it is not saturated until DL2b. Thus helium can be used as a reference gas for the DL1 and DL2a regions without a problem.

Methane is another reference gas candidate, since its mixing ratio should be constant throughout the Galileo probe descent region. Methane is orders of magnitude less abundant than hydrogen and helium in Jupiter's atmosphere, so it has the advantage that its counts do not saturate the mass spectrometer. However, methane counts at mass 16, the primary methane peak, are not good to use because mass 16 also contains contributions from ammonia (NH_2^+) and water (O^+) fragments, and because the C[16] approaches saturation during the GPMS experiment. The contributions of ammonia and water to C[16] vary with altitude in the probe descent. However, methane peaks are also present, in

decreasing amounts, at masses 14, 13, and 12 (see Figure 3.8). A small contribution from ammonia is present at mass 14 (1.11% of the counts from ammonia at 17), and 12 and 13 are free of interference from ammonia and water. The advantage of using methane as a reference gas is that counts at 12, 13, or 14 can be used consistently throughout the descent sequence, since they do not saturate at any level. However, analysis of the methane splitting patterns throughout the probe descent reveal further complications in that the count rates of methane fragments inexplicably changed relative to C[16] by 4–8% over the course of the DL1 experiment. There is another advantage to using an unsaturated reference gas such as C[13]; uncertainty in count ratios is reduced when both the denominator (reference gas) and the numerator are in similar deadtime regimes (either both unsaturated or both near saturation). This effect will be discussed below in the error analysis section.

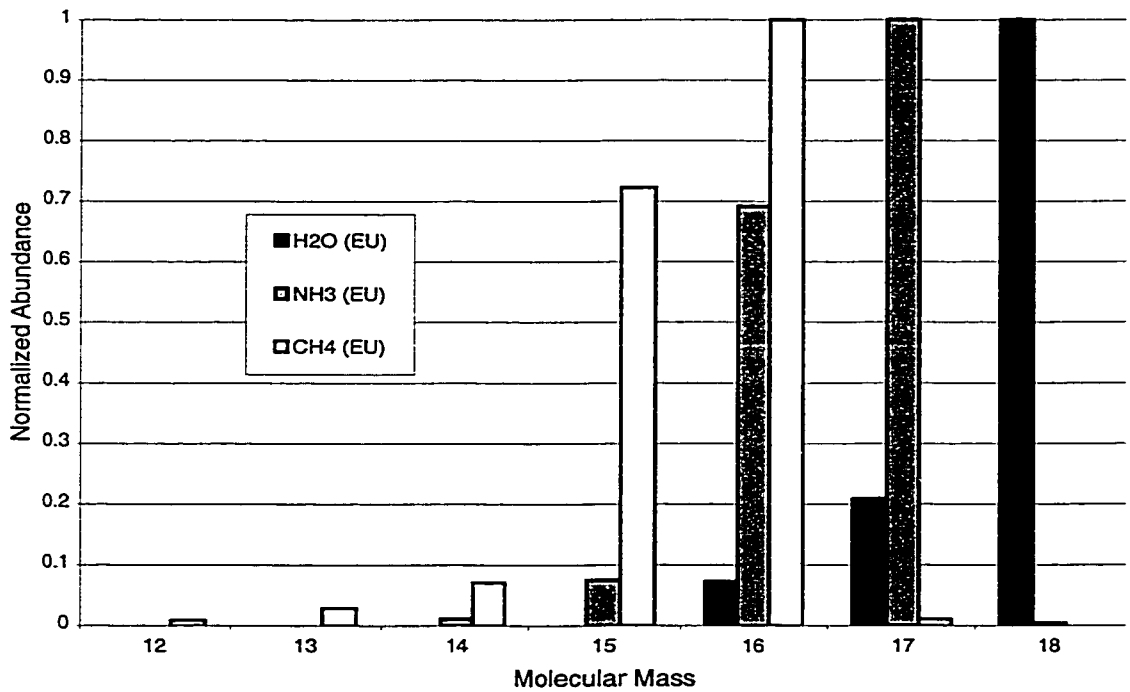

Figure 3.8 Mass spectrum of water, ammonia, and methane.

Correcting for mass-interference using predetermined splitting patterns

One of the most challenging data analysis tasks is to determine the relative counts present at a given value of m/q due to contributions from multiple atmospheric gases. This

task requires knowledge of the splitting patterns of the relevant atmospheric gases. Depending on the complexity of the particular mass-interference problem, either a simple or a complex solution can be chosen.

The simple solution can be applied whenever all interfering gases but one have at least one mass peak that is clear of any interference. An example of this situation is the neon-carbon dioxide interaction at mass 22. The contribution of doubly ionized CO_2 at mass 22 interferes with the determination of the $^{22}Ne/^{20}Ne$ ratio. Mathematically, the interference correction is performed by solving the equation:

$$C'[22] + \alpha C[44] = C[22] \qquad 3.7$$

Since it is known that CO_2 in the flight unit has a 22/44 ratio of $\alpha = 0.01047$, the flight data at mass 22 can be corrected by subtracting 1.047% of the counts at 44, presuming that only CO_2 contributes to mass 44. In this fashion, any number of interfering contributions could be removed from the mass 22 counts, as long as the contributions were due to gases having peaks at other masses, such that all the counts at these other masses are due entirely to the interfering gas in question (just as the counts at 44 are due entirely to CO_2).

The "complex solution" must be employed whenever the interfering gas lacks peaks at other masses that are themselves clear of interfering components. A good example of this condition is the methane-ammonia-water system, which spans the mass peaks from 12–18. The three primary peaks of each of these gases all contain contributions from the other gases (see Figure 3.8).

The system can be represented as a system of simultaneous linear equations:

$$\begin{aligned} C'[16] + \gamma C'[17] + \delta C'[18] &= C[16] \\ \beta C'[16] + C'[17] + \alpha C'[18] &= C[17] \\ C'[18] &= C[18] \end{aligned} \qquad 3.8$$

Here, $C[n]$ are the observed counts at $m/q = n$, and $C'[n]$ are the counts at mass n due only to the gas whose major peak is at n (e.g., $C'[17]$ are the counts at 17 due only to ammonia). The Greek letters are constant ratios determined by the splitting patterns of these three gases as measured in the EU (e.g., α is the 17/18 count ratio for water). With the previously obtained splitting patterns ($\alpha, \beta, \delta, \gamma$), the three observations ($C[n]$), and three unknowns ($C'[n]$), I can now solve the system of Equations 3.8 to correct for the mass

interferences between these three gases. The ratio of the $C'[n]$ to the counts of a reference gas can then be used to obtain mixing ratios. In this specific case water is assumed to be the sole contributor to $C[18]$, neglecting the ammonia 18/17 count ratio of 0.88%. This assumption introduces a minimal error: for the case of a calibration run in leak 2 at 10 bar with solar enrichments of 2.6, 1.0, and 0.5 for methane, ammonia, and water, neglecting the ammonia contribution to mass 18 introduces less than a 0.3% difference in the counts at 18 (see Chapter 5).

An even more extreme version of this technique of using known splitting patterns to extract count ratios simultaneously for many overlapping gases is used by Paul Mahaffy and Willis Wilson. They fit polynomial curves to the GPMS counts of every mass, in order to get the approximate counts for each mass at a single particular step number (e.g., Niemann et al. 1998). Then, at a chosen step, they attempt to fit either the entire mass spectrum or a sizable portion of it with a superposition of spectra of selected molecules. The drawback of this method is that it makes error propagation difficult to characterize.

The Calibration Constant

The calibration constant translates count ratios to mixing ratios (Equation 3.2). Calibration constant data analysis is discussed in great detail in the following two chapters. Calibration constants are obtained from calibration experiment count ratios and mixing ratios via the formula:

$$\mathrm{cc}^{\mathrm{parent}}_{x/\mathrm{ref}} = \underbrace{\left.\frac{C[\mathrm{ref}]}{C[x]}\right|_{\mathrm{lab}} \left.\frac{n_x}{n_{\mathrm{ref}}}\right|_{\mathrm{lab}}}_{\mathrm{cal4}} \left.\frac{n_{\mathrm{ref}}}{n_{\mathrm{H_2}}}\right|_{\mathrm{Jup.}} \qquad 3.9$$

The intermediate quantity cal4 is obtained first from calibration experiments, and later multiplied by the Jovian reference gas mixing ratio in order to obtain the calibration constant. This procedure allows the isolation of error contributions from calibration data uncertainty and from Jovian reference gas mixing ratio uncertainty. Throughout this work, calibration constants are presented (rather than the intermediate cal4 values) wherever

possible, but some older figures generated at early stages of the data analysis pathway may still display cal4 values (check captions).

One of the disturbing early revelations of the calibration experiments was that the calibration constant is not constant! Depending on the gas in question, the calibration constant can be a function of pressure or mixing ratio or both. Nevertheless, the term "calibration constant" was retained for the sake of continuity in the documentation of the calibration research effort, in which numerous calibration experiments were performed in order to determine the behavior of the calibration constants for various gases. The experimental procedures involved are discussed in Chapter 4, and the experimental results for each gas are presented in Chapter 5.

Estimation of Error

Each of the corrections and adjustments mentioned previously in this Chapter contributes to the uncertainty in the final mixing ratio. Individual sources of error will be discussed in this section, and the following section will address the propagation of these individual errors to the uncertainty in atmospheric mixing ratios.

All mass spectrometer data suffer from statistical fluctuation due to the intrinsically random nature of the sampling process. This statistical fluctuation is described by the Poisson distribution (Bevington and Robinson, 1992; p.62), which has the feature that the standard deviation of a group of Poisson-distributed points is equal to the square root of the mean. Thus, the uncertainty in a mass spectrometer counting rate measurement due to statistical fluctuations can be approximated by the square root of the measurement. An opportunity to test this statement is given by the FU calibration dataset, in which two to four consecutive integration periods were devoted to measurements of the same value of m/q. Figure 3.9 shows the standard deviation of these small ensembles of between two and four FU calibration datapoints as a function of counting rate. The solid line is the standard deviation of the poisson distribution, equal to the square root of the counting rate. Standard deviations in Figure 3.9 are represented as percentages of the total counting rate.

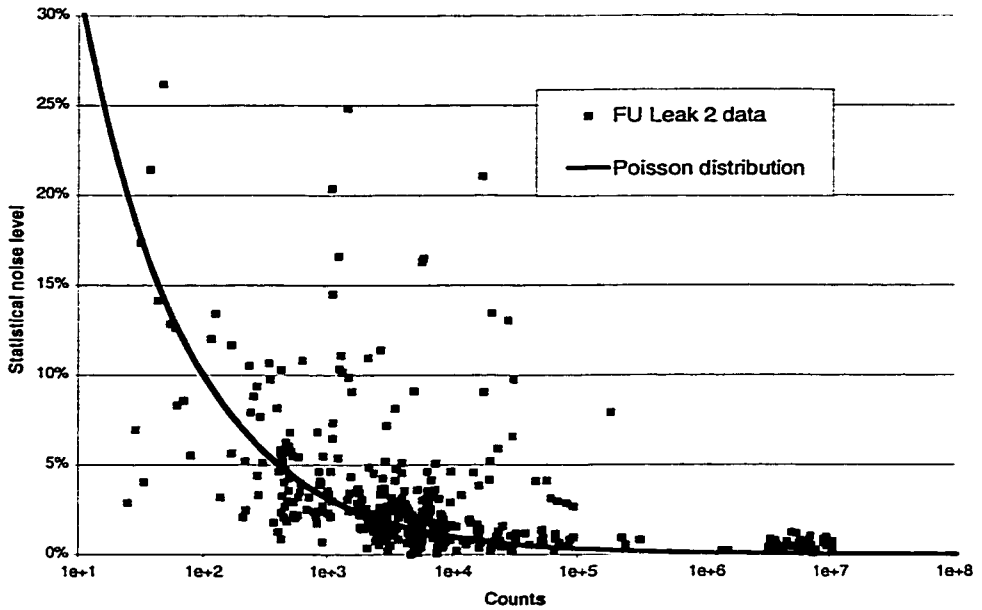

Figure 3.9 Relative error in clusters of repeated FU measurements vs. Poisson-distributed error.

The majority of standard deviations seem to be well-approximated by the Poisson distribution. However, at high counting rates, the ensemble standard deviations did not decay to zero as quickly as predicted by the Poisson distribution. In order to quantify this behavior, the average of the cluster of points in Figure 3.9 near the 1×10^7 count rate was obtained. This average was 0.4874%, and was derived from all available points at counting rates greater than 3×10^6 counts per integration period. Thus, the statistical uncertainty in counting rates for all mass spectrometer measurements is taken to be the greater of either 0.4874% of the counting rate, or the square root of the counting rate.

GPMS and FU calibration data counting rates were recorded in units of counts per half-second integration period, appropriate units for the error estimation described here. However, most EU calibration experiments used integration periods (IP) of 0.125, 0.2, or 0.25 sec, and were recorded in datafiles in normalized units of counts per second. This normalization required the counting rates to be multiplied by 1/IP. However, if the normalized counting rates are used to estimate statistical uncertainty, they will underestimate the uncertainty by a factor of $\sqrt{IP}$. Thus, for EU calibration runs, the statistical uncertainty based on the normalized counting rates was divided by $\sqrt{IP}$.

Since the deadtime function is solved numerically to obtain deadtime-corrected counts, error estimation is challenging. In order to estimate the error σ_{CR} in the deadtime-corrected count ratio $CR'[x/\mathrm{ref}]$ due to an change $\Delta\tau$ in the deadtime coefficient τ, I take the following approach:

$$\sigma_{CR} \equiv \left| \frac{CR'[x/\mathrm{ref}]|_{\tau} - CR'[x/\mathrm{ref}]|_{\tau+\Delta\tau}}{CR'[x/\mathrm{ref}]|_{\tau}} \right| \qquad 3.10$$

For the GPMS data, $\Delta\tau$ was taken to be half the difference between the deadtime coefficients τ_2 and τ_c (see Table 3.2), and is 12% of the average coefficient τ_m. Figure 3.10 shows contour levels in the count ratio uncertainty (expressed as a percentage of the count ratio) as a function of $C[x]$ and $C[\mathrm{ref}]$. The lowest errors in count ratio occur when both $C[x]$ and $C[\mathrm{ref}]$ are in the same deadtime regime (both low or both high). The highest uncertainties occur when $C[x]$ is low and $C[\mathrm{ref}]$ is high (lower right corner), as would be the case for a typical minor species and a reference gas of either hydrogen or helium. This is a major reason for choosing reference gases with smaller counting rates.

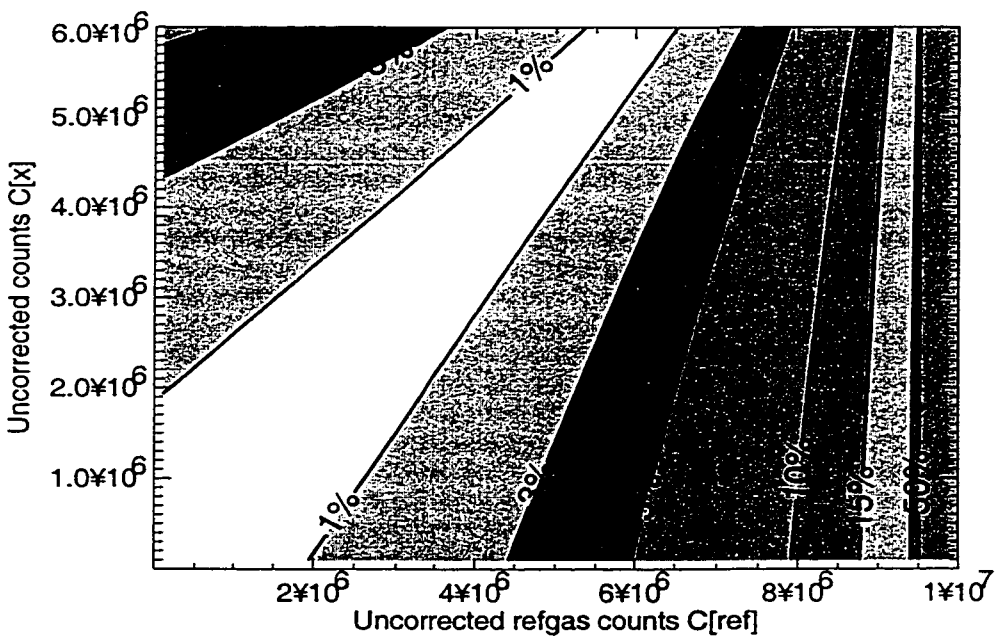

Figure 3.10 Contour plot of deadtime-based uncertainty in count ratio *CR*[x/ref] as a bivariate function of count ratio numerator *C*[x] and denominator *C*[ref].

The "God's rays" shape of the error-contours is due to the fact that the change in $C[x]$ due to a change in τ is of course correlated with the change in $C[\mathrm{ref}]$. In cases where the error in a counting rate, rather than the error in a count ratio, must be estimated, Equation 3.11 is used:

$$\sigma_{C[x]} \equiv \left| \frac{C'[x]|_{\tau} - C'[x]|_{\tau+\Delta\tau}}{C'[x]|_{\tau}} \right| \qquad 3.11$$

However, this error estimate is exaggerated, because when $C[x]$ is used to obtain a mixing ratio, the correlation between count ratio numerator and denominator deadtime uncertainties cannot be accounted for in Equation 3.11.

Uncertainties in the background corrections are shown as grey bands in the GPMS counting rate plots of Appendix A. For background corrections obtained by averaging points in background sampling intervals, the uncertainty is simply taken to be the standard deviation of the points from the average value. For exponentially decaying backgrounds, estimated errors in the fitted coefficients were extremely large due to the scarcity of available datapoints. Therefore the uncertainty of exponential background corrections was taken to be 0 in the mixing ratio calculations, and the caveat is made that background correction uncertainty could be quite high.

There are two basic sources of error associated with corrections for mass interference. Using Equation 3.7 as an example, the uncertainty in the corrected counts due to the mass interference correction is given by:

$$\begin{aligned} C'[22] &= C[22] - \alpha C[44] \\ \sigma^2_{C'[22]} &= \sigma^2_{C[22]} + \sigma^2_{\alpha}(C[44])^2 + \sigma^2_{C[44]}\alpha^2 \end{aligned} \qquad 3.12$$

One source of error is σ_{α}, the uncertainty in the value of the splitting fraction used to determine the correction. Splitting patterns were not measured with the FU in the lab, and EU and NIST splitting patterns often disagree, sometimes by as much as 20%. Whenever possible, EU splitting patterns are used, under the assumption that the FU had much more in common with the EU than with the unknown mass spectrometers used to obtain splitting patterns for NIST. Except in specific cases where better information is available, a default uncertainty in splitting fractions of 5% was assumed.

The mass interference correction also requires tracking of the uncertainty in the parent mass used to perform the correction, or $\sigma_{C[44]}$ in the example of Equation 3.12. This error is an accumulation of all available sources of error: statistical, deadtime, background, and any errors caused by similar mass interference corrections previously performed on the parent mass. Since σ_α and $\sigma_{C[\text{parent}]}$ are assumed to be random and are definitely uncorrelated, they are combined as the sum of squares in Equation 3.12, and no correlation term is included.

All of the previously described sources of error apply to count ratios both in calibration data as well as in probe data. In addition, the intermediate calibration constant "cal4" suffers from another source of error: uncertainty in the mole fractions of gases in the calibration sample gas mixture (see Equation 3.9). A discussion of the techniques for estimating the uncertainty in laboratory sample gas mixture composition must wait until Chapter 4, where the procedure for preparing sample gas mixtures is described in full detail. Finally, for calibration constants that were found to be variable with ion source pressure (ISP), uncertainty is introduced by the choice of ISP proxy (either gas system pressure, $C[2]$, or $C[13]$). This uncertainty is very difficult to characterize, and will be discussed on a strictly case-by-case basis in Chapter 5.

Following Equation 3.9, the total uncertainty in the calibration constant can be expressed as a combination of errors from laboratory count ratios, laboratory mole fractions, and Jovian reference gas mixing ratio. Then the total calibration constant uncertainty becomes a source of error for derived Jovian mixing ratios.

Propagation of Error

Propagation of error from multiple sources for a single datapoint, such as the three terms in Equation 3.9, is straightforward and follows the error propagation equation of Bevington and Robinson (1992; pp. 42–43). For a multivariate function,

$$x_i = f(u_i, v_i, \ldots), \qquad 3.13$$

the variance (in the limit of an infinite number of measurements) goes to:

$$\sigma_x^2 \approx \sigma_u^2\left(\frac{\partial x}{\partial u}\right)^2 + \sigma_v^2\left(\frac{\partial x}{\partial v}\right)^2 + \cdots + \text{covariance terms}. \qquad 3.14$$

In all cases here, the identified sources of error are uncorrelated and covariance terms are ignored.

A more complicated issue is the propagation of error from an ensemble of datapoints (each with their own uncertainties) to a mean, or to a set of fit parameters. This issue pertains to total calibration constant errors, as well as to averaged mixing ratios from GPMS data. The statistical treatment of this situation is well-defined for the case of datapoints with individual random errors which are normally-distributed around "true values." However, systematic effects significant in the calibration datasets are not properly treated with this approach, and are in fact poorly accommodated using statistical analysis. Available statistical literature does not discuss the treatment of unidentified systematic errors. Ideally, systematic effects should be eliminated or at least characterized through good experiment design, but calibration datasets show evidence of mysterious systematic effects that are as yet unidentified, and thus cannot be compensated for by experiment design.

The mean and variance of a group of datapoints with known uncertainties are given by (Bevington and Robinson, 1992; p.64):

$$\mu \approx \frac{\sum_i (x_i/\sigma_i^2)}{\sum_i (1/\sigma_i^2)} \quad \text{and} \quad \sigma_\mu^2 = \frac{1}{\sum_i (1/\sigma_i^2)} \qquad \text{(E1)} \qquad 3.15$$

In the case of identical uncertainties in the datapoints ($\sigma_i = \bar{\sigma}$), the expression for the uncertainty in the mean reduces to:

$$\sigma_\mu^2 = \frac{\bar{\sigma}^2}{N} \qquad \text{(E1)} \qquad 3.16$$

Error reduction scheme E1 is valid when the uncertainties in individual datapoints are attributed to random fluctuations around the "true values," so that repeated measurements act to reduce the error in the result. But what if the uncertainties are due to a systematic effect that affects all the datapoints in the same way? Then repeated measurements should *not* reduce the variance in the final result, and the variance in the mean is just the average of

the individual variances:

$$\sigma_\mu^2 = \frac{\sum_i \sigma_i^2}{N} = \bar{\sigma}^2 \text{ (if errors are sytematic and identical)} \qquad 3.17$$

$$\sigma_\mu^2 \equiv \frac{N}{\sum_i (1/\sigma_i^2)} \text{ (if errors are systematic)} \qquad \text{(E2)} \qquad 3.18$$

Although Equation 3.18 is not mathematically equivalent to Equation 3.17, it is used in the analysis to follow, for cases where the error is systematic. Equation 3.18 was formulated by first noting that the variance in the mean indicated by Equation 3.17 is greater than that in Equation 3.16 by a factor of N: $\sigma_{\mu(3.17)}^2 = N\sigma_{\mu(3.16)}^2$. Then Equation 3.15 for the variance of the mean was substituted for $\sigma_{\mu(3.16)}^2$, resulting in Equation 3.18. A key difference between the variances in the mean as given by Equations 3.17 and 3.18 is that in Equation 3.17, the largest variances in the individual datapoints will dominate the variance in the mean, whereas with Equation 3.18 the variance in the mean will be weighted towards individual datapoints with the smallest uncertainties. For large numbers of datapoints, or identical errors for the individual datapoints, the two formulations converge to the same result. In calibration constant datasets, both systematic and random error components can be identified, necessitating an error treatment scheme intermediate to E1 and E2. Using the parameter ν, scheme E3 bridges the gap between E1 and E2:

$$\sigma_\mu^2 = \frac{1}{\sum_i (1/\sigma_i^2)}[\nu(1-N)+N] = \begin{cases} \dfrac{1}{\sum_i (1/\sigma_i^2)} & \nu = 1 \quad \text{(E1)} \\ & \text{(random error)} \\ \dfrac{[\nu(1-N)+N]}{\sum_i (1/\sigma_i^2)} & 0 < \nu < 1 \quad \text{(E3)} \\ & \text{(mixed error)} \\ \dfrac{N}{\sum_i (1/\sigma_i^2)} & \nu = 0 \quad \text{(E2)} \\ & \text{(systematic error)} \end{cases} \qquad 3.19$$

Error analysis scheme E3 allows a quantitative estimation of error from a combination of systematic and random sources. For example, a calibration constant calculated from an ensemble of datapoints such that 40% of their uncertainty affects the ensemble randomly,

while 60% of the uncertainty affects the entire ensemble systematically, would use scheme E3 with a value of $\nu = 0.6$. For linear or polynomial fits to datasets, errors in the fitted data are generated from the covariance matrix of the fitted parameters. These fitted data uncertainties are then multiplied by the same factor of $[\nu(1-N)+N]$.

One final complication arises in the analysis of a suite of condensible volatile calibration runs done with the EU in 1996. This group of calibration experiments, referred to as CVMIXES, is described fully in Chapters 4 and 5, and in this section I simply provide the framework for the statistical analysis that will be performed in Chapter 5. Multiple calibration runs were done with gas mixtures of water, ammonia, methane, hydrogen, and helium. Looking at the scatter among datapoints (calibration constants for water or ammonia) in a single run provides the impression that error estimated from known sources accurately describes the scatter in the datapoints. However, when multiple runs are examined together, it would appear that an additional source of error randomly effects entire runs. This unidentified source of error acts *randomly* from run to run, but *systematically* on datapoints within individual runs. Bevington and Robinson (1992; p.106) allows the derivation, from the data itself, the standard deviation of this unidentified random systematic effect with the expression,

$$\sigma^2 \approx s^2 \equiv \frac{1}{N-m}\sum_i (y_i - \hat{y})^2, \qquad 3.20$$

where N is the number of datapoints, m is the number of parameters estimated from the data (1 for the mean, or 2 for a linear fit), and $\hat{y}$ is the fitted value corresponding to datapoint i. Using N = number of datapoints would imply that the unknown effect acts randomly on all datapoints, but using instead N = number of separate runs accounts for the fact that the effect seems to be systematic within each run. Thus, as far as the uncertainty in the final result is concerned, each calibration run acts as a single "datapoint."

CHAPTER IV

GPMS Calibration: Experimental Procedures

Flight Unit: Calibration Experiments and Protoflight Sequence

In 1985, prior to the anticipated launch of the Galileo mission, a limited range of calibration data was collected using the GPMS flight unit (FU) in order to quantify the instrument's response to gases of known composition. The datasets were small compared to those taken later using the flight spare experimental unit (EU), because the instrument team did not want to excessively pollute the gas flow system with gases that might leave traces in the gas handling system and produce residual signals during the probe descent at Jupiter. Additionally, an experimental run was performed following the programmed descent sequence (Chapter 2), during which the pressure was varied in order to match Jovian conditions expected to apply throughout the probe descent.

Sample gas compositions for the FU calibration runs are shown in Table 4.1. Mole fractions are given in percent for hydrogen and helium and in parts per million for minor species. Most of the calibration runs used gases from pre-mixed gas cylinders with predetermined compositions, except for sequences 18A and 20, which were augmented by the addition of hydrogen to the mixtures. In the case of 18A, hydrogen was added to a mixture of helium and ammonia, and in sequence 20, hydrogen was added to the mixture of helium and hydrocarbons. The addition of hydrogen introduced an additional uncertainty in the abundances of the sample gases relative to hydrogen, because the three pressure measurements taken to determine the hydrogen fraction added for each sequence yielded slightly different values. However, abundances of the minor constituents relative to helium is not affected by this uncertainty. Hydrogen was added so that the calibration mixtures

would more closely resemble Jovian air. Table 4.1 shows only the best-estimate (based on averages of values derived from different pressure measurements) mole fractions for sequences 18A and 20. In addition, two alternate methods of referring to the calibration runs are listed: the alphanumeric file number, and the more descriptive text name of the data files.

Table 4.1 FU calibration experiment gas mixtures.

File Number	Seq.	Filename	% H_2	% He	ppm Sp	ppm Sp
85-08713.20D	3B	i1-rg{p}.dat	89.8903	10.0500	147 Ne 147 Kr	151 Ar 152 Xe
85-08717.40D	8	i1-ph3.dat	99.9895	0	105 PH3	
85-08810.42D	6	i1-hcn.dat	0	99.9855	145 HCN	
85-08815.25D	10	i1-h2s.dat	99.9861	0	139 H2S	
85-08817.25D	13	i1-hydr.dat	90.0417	9.9000	180 AsH3 214 SiH4	189 PH3
85-08715.42D	4A?	i2-rg.dat	89.8903	10.0500	147 Ne 147 Kr	151 Ar 152 Xe
85-08716.06D	4A?	i2-rgdes.dat	89.8903	10.0500	147 Ne 147 Kr	151 Ar 152 Xe
85-08717.05D	7	i2-ph3.dat	99.9895	0	105 PH3	
85-08809.44D	5	i2-hcn.dat	0	99.9855	145 HCN	
85-08814.39D	9	i2-h2s.dat	99.9861	0	139 H2S	
85-08816.21D	12	i2-hydr.dat	90.0417	9.9000	180 AsH3 214 SiH4	189 PH3
85-08818.31D	14	i2-alkan.dat	90.2259	9.7300	142 CH4 150 Propane	149 Ethane
85-08819.19D	16	i2-unsat.dat	0	99.9551	144 C2H2 149 Propylane	156 Ethylene
85-08913.57D	19	i2-h2o.dat	0	99.9860	140 H2O	
85-08914.42D	18	i2-nh3.dat	0	99.9683	317 NH3	
85-08915.33D	18A	i2-h2nh3	79.1202	20.8732	066 NH3	
85-08916.30D	20	i2-chmix.dat	83.9056	16.0619	024 CH4 031 Butane 028 Propylane 029 Propane 042 Benzene	031 Ethane 029 Ethylene 062 Acetylene 048 1-Hexene

For most of the FU calibration runs, there were three key steps:

1. Prepare and compress the gas mixture, to about 2 bar for leak 1 calibration, and 5–7 bar for leak 2 calibration.

2. Perform a background scan at all masses, before introducing the sample gas to the mass spectrometer. These experimentally-determined background levels are then subtracted from the counts in the calibration runs.

3. Admit the sample gas, and take measurements. Some scans were done with different filaments (1, 2, or 5). The filaments produce the electrons for the ion source. Some scans were done with different ionization energies (15, 25, 75 eV). At this point only data for filament 1 (the same one used during the probe descent) are used, and only the 75 eV data are relevant to the analysis presented in this work.

Sequence 3b, featuring noble gases in its sample mixture, yielded data for a range of inlet pressures. Measurements were taken at 124 mbar, 214 mbar, 524 mbar, 1.034 bar, 2.020 bar, 2.08 bar, and 3.06 bar. Some runs also included data taken under conditions such as desensitized mode counting or no ion pumping, but such data are not used for the analyses in this work.

The protoflight sequence experiment, referred to as PFU, was not used to obtain calibration constants. The PFU was used to study the behavior of the GPMS under conditions similar to flight conditions. Pressure was increased from 99 mbar to 21 bar. The enrichment cells were not used in the PFU; instead direct leak sampling was maintained throughout the sequence. The most useful result of the PFU was measurement of an apparent count saturation for mass 2 at the end of the sequence. This count saturation is the basis for the τ_c deadtime constant.

Experimental Unit: Sample Gas Mixture Preparation

Sample gases for calibration runs done with the experimental unit (EU) required mixing in the laboratory. This mixing process is a source of uncertainty in the final composition of the sample gas, and leads to uncertainty in the calibration constants ultimately obtained from the experiments. Table 4.2 illustrates the process used to produce the mixture of hydrogen, helium, methane, argon, and ethylene for an EU calibration run. A quantitative estimate of the uncertainty in the sample gas mole fractions is then used as an

estimate of the mole fraction uncertainties in all EU calibration experiments, since I do not have access to detailed descriptions of the gas mixing procedures for all the calibration runs.

Table 4.2 Gas mixture preparation.

	Action	P1 (0.000–20.000 bar)	P1 bkgnd (bar)	P2 (0.0–200.0 mbar)	P2 bkgnd (mbar)	Volume
[1]	Add C_2H_4	0.127	0.005	126.6	0.4	V1
[2]	Add Ar	0.262	0.127			V1
[3]	Expand	0.02		14.6		V1 + V2
[4]	Circulate He	0.815				V1 + V2
[5]	Pump all	0.679				V1 + V2
[6]	Pump V2, V3					mix [5]: V1
[7]	Flush with N_2					mix [5]: V1
[8]	Pump V2, V3					mix [5]: V1
[9]	Expand	0.037		36.9		V1 + V2
[10]	CH_4 V1	0.44	0.037			mix [9]: V1 + V2 CH_4 + mix [9]: V1
[11]	Expand V1, V2, V3	0.058		58.5		V1 + V2
[12]	Add He	1.55				V1 + V2
[13]	Add H_2	11.483	1.55			V1 + V2

The uncertainty in the ratio of the volumes $V1/(V1+V2) \equiv \alpha$ leads to an uncertainty in the final derived calibration gas mole fractions. The mixing procedure outlined above offers three opportunities to determine α:

$$
\begin{aligned}
[2] \rightarrow [3]: \quad \alpha &= \frac{14.6 \text{ mbar}}{262 \text{ mbar}} = 0.55725 \\
[8] \rightarrow [9]: \quad \alpha &= \frac{0.037 \text{ bar}}{0.679 \text{ bar}} = 0.054492 \\
[10] \rightarrow [11]: \quad \alpha &= \frac{0.058 \text{ bar} - 0.037 \text{ bar}}{0.44 \text{ bar} - 0.037 \text{ bar}} = 0.052109
\end{aligned}
\tag{4.1}
$$

Based on the above results, mole fractions for this ethylene calibration run were derived based on an average value of $\alpha = 0.54109$ with a standard deviation among the three values of 3.4%. Argon and ethylene undergo expansions at steps [3] and [9] (expansion [11]

only affects methane) and thus have an increased mole fraction uncertainty relative to e.g. hydrogen, which does not undergo any expansions. Instrumental error in the pressure gauges is presumed to be 1 mbar for P1 and 0.1 mbar for P2; steps [1], [3], [9], and [11] can be used to verify the accuracy of gauge P1. It is clear that the measurement uncertainty error at any step in the mixing process is less than 1%, so that the mole fraction uncertainties are dominated by the uncertainty in α. Since ethylene and argon undergo two expansions, their mole fraction uncertainties are 1.034^2, or about 7%. I prefer to slightly overestimate this value in generalizing that minor species in sample gases mixed in the lab suffer from 10% mole fraction uncertainties, while uncertainties in major species (hydrogen and helium) are negligible.

Table 4.3 presents the compositions of the sample gases used in EU calibration runs relevant to this work, which focuses on condensible volatiles and hydrocarbons. Hydrocarbon calibration experiments are presented chronologically in Table 4.3, followed by condensible volatile runs.

Table 4.3 EU calibration experiment gas mixtures.

Date	Name	Scans	Inlet Leak	H_2 (MF)	He (MF)	Species: MF	Species: MF	Species: MF
981116	C2H4	s00–s16, s20–s21	1+2	0.868	0.130	C_2H_4: 2.88e-5	Ar: 3.19e-5	CH_4: 1.83e-3
981116	C2H4_sp	s17–s19	2	0.000	0.000	C_2H_4: 1.00e+0		
960617	C2H6_A	s08–s13	2	0.889	0.110	C_2H_6: 1.20e-3		
960617	C2H6_B	s15–s19	2	0.890	0.110	C_2H_6: 1.34e-4		
960618	C3H8	s18–s23	2	0.889	0.110	C_3H_8: 7.03e-4		
960618	C3H8_sp	s27, s31	2	0.000	0.000	C_3H_8: 1.0e+0		
970630	N2_A	s04–s11	2	0.867	0.131	CH_4: 2.07e-3	N_2: 9.90e-6	
970630	N2_B	s12–s29	1	0.871	0.127	CH_4: 1.96e-3	N_2: 2.11e-4	
981119	CO2_sp	s00–s11	1+2	0.000	0.000	CO_2: 1.00e+0		
960407	CH4_A	s07,s09, 6 more	2	0.888	0.110	CH_4: 2.10e-3		
960407	CH4_B	s21,s22, 6 more	1	0.888	0.110	CH_4: 2.19e-3		
960407	CH4_sp	s10,s14, s16,s18	—	0.000	0.000	CH_4: 1.00e+0		

Table 4.3 EU calibration experiment gas mixtures.

Date	Name	Scans	Inlet Leak	H_2 (MF)	He (MF)	Species: MF	Species: MF	Species: MF
960526	MIX96_A	s01–s15 (odd nums.)	2	0.869	0.129	CH_4: 1.67e-3	NH_3: 1.96e-4	H_2O: 0.00e+0
960527	MIX96_B	s00–s10	2	0.867	0.131	CH_4: 1.90e-3	NH_3: 2.20e-4	H_2O: 0.00e+0
960811	MIX96_C	s08–s20	2	0.796	0.195	CH_4: 1.47e-3	NH_3: 7.27e-4	H_2O: 1.04e-4
960812	MIX96_D	s02–s16	2	0.856	0.140	CH_4: 1.61e-3	NH_3: 1.43e-3	H_2O: 5.01e-5
961123	H2S_A	s00, s04–s09	2	0.862	0.138	H_2S: 2.17e-5		
961129	H2S_B	s01–s09	2	0.861	0.137	H_2S: 2.15e-5	CH_4: 1.59e-3	
970110	MIX97_A	s00–s25	1+2	0.888	0.110	CH_4: 1.91e-3	NH_3: 0.00e+0	H_2O: 0.00e+0
970110	MIX97_B	s26–s45	1+2	0.888	0.110	CH_4: 0.00e+0	NH_3: 9.95e-4	H_2O: 7.05e-5
970113	MIX97_C	s00–s22	1+2	0.800	0.198	CH_4: 1.93e-3	NH_3: 9.98e-4	H_2O: 6.67e-5
970113	MIX97_D	s23–s40	1+2	0.888	0.110	CH_4: 1.90e-3	NH_3: 9.00e-4	H_2O: 6.95e-5
970116	MIX97_E	s21–s41	1+2	0.888	0.110	CH_4: 1.91e-3	NH_3: 1.04e-5	H_2O: 0.00e+0
970116	MIX97_F	s42–s62	1+2	0.888	0.110	CH_4: 1.80e-3	NH_3: 8.89e-4	H_2O: 0.00e+0
970117	MIX97_G	s00–s19	1+2	0.888	0.110	CH_4: 1.87e-3	NH_3: 8.79e-4	H_2O: 6.86e-5
970117	MIX97_H	s20–s38	1+2	0.887	0.110	CH_4: 1.92e-3	NH_3: 9.57e-4	H_2O: 1.33e-4
970117	MIX97_I	s40–s56	1+2	0.887	0.110	CH_4: 2.13e-3	NH_3: 1.09e-3	H_2O: 3.87e-5
970120	MIX97_J	s00–s20	1+2	0.863	0.134	CH_4: 1.81e-3	NH_3: 9.14e-4	H_2O: 9.16e-4
970121	MIX97_K	s00–s19	1+2	0.864	0.134	CH_4: 1.91e-3	NH_3: 2.29e-4	H_2O: 6.82e-5
970121	MIX97_L	s20–s39	1+2	0.864	0.134	CH_4: 1.91e-3	NH_3: 0.00e+0	H_2O: 6.93e-5
970121	MIX97_M (IP+turbo)	s40–s59	1+2	0.850	0.146	CH_4: 1.91e-3	NH_3: 2.37e-3	H_2O: 7.03e-5
970122	MIX97_N	s00–s19	1+2	0.865	0.132	CH_4: 1.89e-3	NH_3: 2.38e-3	H_2O: 6.85e-5
970122	MIX97_O	s20–s38	1+2	0.860	0.137	CH_4: 1.84e-3	NH_3: 2.29e-4	H_2O: 9.27e-4
970122	MIX97_P	s39–57	1+2	0.863	0.134	CH_4: 1.90e-3	NH_3: 0.00e+0	H_2O: 9.27e-4
970122	MIX97_Q	s58–s76	1+2	0.864	0.134	CH_4: 1.90e-3	NH_3: 2.23e-4	H_2O: 0.00e+0
970123	MIX97_R	s00–s18	1+2	0.866	0.132	CH_4: 1.91e-3	NH_3: 0.00e+0	H_2O: 3.30e-5
970123	MIX97_S	s19–s37	1+2	0.864	0.134	CH_4: 1.89e-3	NH_3: 0.00e+0	H_2O: 1.33e-4
970123	MIX97_T	s38–s56	1+2	0.864	0.134	CH_4: 1.89e-3	NH_3: 2.10e-4	H_2O: 3.47e-5
970124	MIX97_U	s00–s18	1+2	0.864	0.134	CH_4: 1.90e-3	NH_3: 2.32e-4	H_2O: 1.32e-4
970124	MIX97_V	s19–s38	1+2	0.862	0.134	CH_4: 1.90e-3	NH_3: 2.34e-3	H_2O: 0.00e+0
970125	MIX97_W	s00–s20	1+2	0.862	0.134	CH_4: 1.89e-3	NH_3: 2.39e-3	H_2O: 3.57e-5
970125	MIX97_X	s21–s38	1+2	0.842	0.152	CH_4: 2.15e-3	NH_3: 2.64e-3	H_2O: 1.09e-3
970127	MIX97_Y	s00–s18	1+2	0.866	0.130	CH_4: 1.89e-3	NH_3: 2.22e-3	H_2O: 1.32e-4

Calibration experiments with names ending in "_sp" were done with single-component gases, and are used for establishing splitting patterns. Dates and scan numbers give the file names for the original data scans; for instance, 012797.s00 is a single mass spectrum for the MIX97_Y experiment. Ambiguous records for experiments CH4_A and CH4_B are the reasons for the lack of names for 6 scans in each run. Experiment MIX97_M was done while the ion pump and turbo pump were both activated, producing unusual conditions in the mass spectrometer, so that MIX97_M was not used to constrain calibration constants for GPMS data analysis.

Experimental Unit: Pressure and Inlet Leak Considerations

The early FU pressure-dependent noble gas calibration runs demonstrated that calibration "constants" might not be constant, and could vary as functions of pressure. EU calibration runs indeed revealed pressure dependences for condensible volatiles as well as for some hydrocarbons. Pressure ranges explored in the different calibration runs varied, but ideally extended up to 11 bar for leak 1 and over 20 bar for leak 2. However, there was a variable correspondence between EU behavior as a function of calibration gas system pressure and FU behavior as a function of Jovian atmospheric pressure. The discrepancy was noted when count rates of hydrogen and helium were compared between the two instruments under similar pressure conditions.

There are two identified reasons for the difference between EU and FU responses under similar pressure conditions. First, the conductances of the capillary leaks in the EU were found to differ from those on the FU. Table 2.2 gives a history of the leak conductances in the EU over time. A higher conductance in the EU results in higher count rates in the EU, when both instruments sample gas at the same pressure. A comparison of Tables 4.3 and 2.2 shows that mismatched leak conductances were used for all of the listed calibration experiments, except for C_2H_4, N_2, and CO_2 experiments. The second reason for discrepancies between EU and FU responses to pressure was the counting efficiency of the detector. The dynamic nature of the counting efficiency became apparent from examination

of the hydrogen and helium counting rates, as functions of pressure, during the MIX97 calibration campaign. Hydrogen and helium count rates, sampled at the highest pressure levels, decreased almost monotonically with time over the MIX97 calibration campaign. Although the exact nature of the detector degradation is unknown, it can be at least partly understood in terms of a change in the deadtime constant over time. The spread in τ of approximately $1.6–2.8 \times 10^{-8}$ can be seen in Table 4.4 at the end of the chapter, and in Figure 5.22 in the water section of Chapter 5. To the extent that the simplification that detector degradation can be represented entirely as a change in τ is true, hydrogen and helium counts will be most strongly affected, while minor species counts will be less affected. Then the calibration constants for C[x]/C[4] will be strongly affected, but since C[13], a fragment of methane, is the preferred reference gas, and since C[13] is in the same relatively deadtime-unaffected regime as ammonia and water, calibration constants using methane as the reference gas are relatively safe from the effect of dynamic detector efficiency.

In the molecular flow regime, the solution to the problem of mismatched conductances is straightforward: multiply experimental pressure by the ratio of conductances to obtain the probe descent pressure relevant to the calibration constant in question:

$$P_{\text{corr.}} = \frac{\text{1-bar cond.}_{\text{FU}}}{\text{1-bar cond.}_{\text{EU}}} P_{\text{obs.}} = \frac{1.6\times10^{-7}\ \text{mbar l sec}^{-1}}{2.7\times10^{-7}\ \text{mbar l sec}^{-1}} P_{\text{obs.}} = 0.5926\ P_{\text{obs.}}\ . \qquad 4.2$$

Then the calibration constants can simply be fit as functions of P_{corr}. The suitability of this method will be discussed in greater detail in Chapters 5 and 6. In slip or viscous flow regimes, the leak conductance will change as a function of pressure, and the relation in Equation 4.2 will not yield the correct independent variable to use to describe the variation in calibration constant.

Different approaches were attempted in order to quantify the pressure dependence of calibration constants. In other words, if calibration constants are plotted on the Y-axis, different variables, called ion source pressure (ISP) proxies, were used for the X-axis. The justification for testing such a multitude of ISP proxies is that theoretically the calibration

constant pressure dependence should be a function of pressure in the mass spectrometer ion source region, which is different from pressure in the ambient atmosphere of Jupiter, or pressure in the sample gas circulation system in the laboratory. Thus the objective was to find a pressure proxy that could best match ion source pressures in both the calibration run and the flight experiment, even though ion source pressure was not directly measured in either case. Early EU calibration runs contained hydrogen and helium as reference gases, so counts at mass 2 or 4 could be used as ISP proxies. Later experimental sample gases contained methane for use as a reference gas, and for these runs methane-derived counts (C[12] or C[13]) could also serve as ISP proxies.

Calibration Data Processing

Several adjustments to the calibration experiment data must be made before calibration constants can be extracted. These adjustments include correction for tuning errors, compensation for detector noise, and the familiar deadtime, background, and mass-interference corrections. Tuning errors can be detected when an expected mass peak at x amu appears in the mass spectrum at a shifted value of $x + \varepsilon$. Since calibration experiments were free from the time limitations imposed by the quick descent of the Galileo probe, mass spectra were taken at higher mass resolutions; typically, the mass resolution in the calibration runs was 0.125 amu. Figure 4.1 shows three typical scans at 0.125-amu resolution, with positive tuning error ε for the 1998 scans and negative ε for the 1996 scan. The procedure for calibration data reduction was to take the highest counting rate within 0.25 amu of the expected integral mass number, rather than to attempt to find the tuning error ε, and then offset all the integral mass numbers by ε to find the appropriate counting rate to analyze. This selection procedure compensates for both tuning errors (peak off-center compared to integral mass number), as well as for peak distortion (mass peak not flat). Figure 4.1 also shows a slightly "irregular" peak; in a few cases (not pictured) noise in the electronics system resulted in a much more severe situation, with very large "spikes" in the data. These spikes had to be individually identified and flagged, and were present only in a few runs with electronics problems.

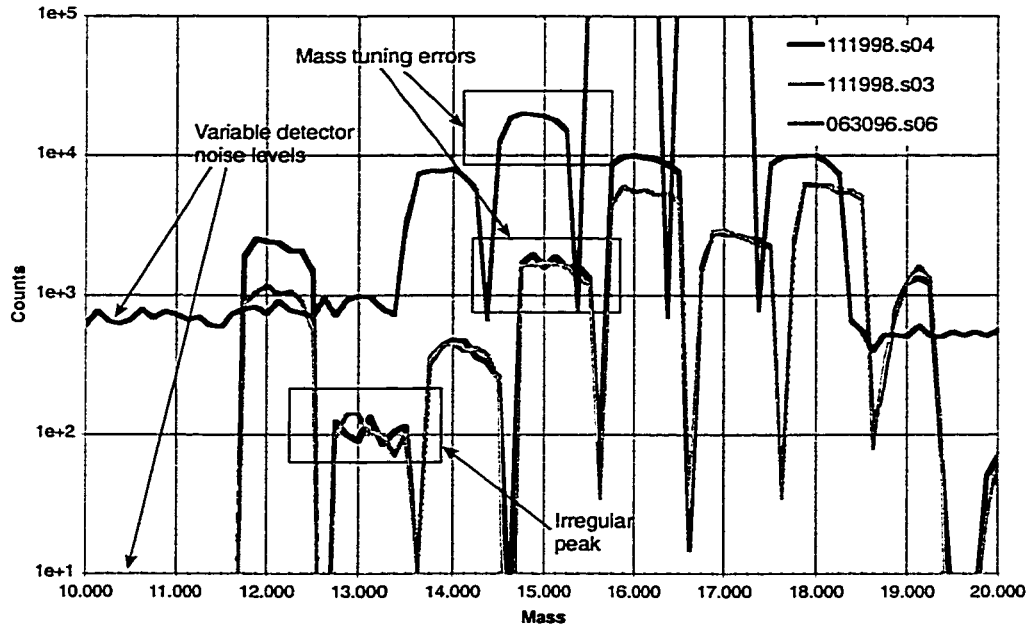

Figure 4.1 Three EU calibration scans, illustrating data analysis challenges.

Imperfect electronics in many of the calibration runs also led to detector noise, which was measured for each distinct scan by taking the average of counting rates at masses which were supposed to be free of signal. Figure 4.1 shows a severe detector noise problem (in the 1996 scan), with noise levels at almost 1000 counts. This detector noise was subtracted from the data in much the same way as the background corrections previously discussed, although the physical mechanisms responsible for the two effects are different. Detector noise is attributed to characteristics of the electronics of the mass spectrometer, while background counting rates, obtained from scans taken under vacuum conditions, are attributed to residual gas signatures in the system, not directly related to abundances in the sample gas in question. Two radio frequency (RF) oscillators were used to tune the mass spectrometer; one for masses less than 19 amu, and one for masses greater than 19 amu. Therefore detector noise levels were determined separately for these two mass ranges. At some point the RF board was replaced in the EU to duplicate the flight electronics.

Many of the problems facing GPMS data analysis described in Chapter 3 are also present in calibration data analysis. For instance, appropriate deadtime corrections must be made to mass spectrometer counts. Whenever possible, deadtime constants were

determined self-consistently for each calibration experiment by searching for count saturations within the experiments. Table 4.4 gives a summary of the deadtime constants employed, and indicates which calibration experiments actually had internally-determined deadtime constants. Other experiments were assumed to have deadtime constants similar to those of calibration experiments conducted immediately before or after them. Background counting rates were also an issue faced by both the GPMS and EU experiments. Correction for background counting rates was a simple matter of taking measurements under vacuum conditions in the mass spectrometer, and then subtracting the resulting background spectrum from all relevant scans taken with the sample gas in the mass spectrometer.

Table 4.4 Deadtime correction coefficients for calibration experiments.

Date	Sequences	Leak	τ	σ_τ
960407	CH4_A, CH4_B	1, 2	*	—
960407	CH4_sp	—	—	—
960526	MIX96_A	2	†	—
960527	MIX96_B	2	†	—
960617	C2H6_A, C2H6_B	2	1.73×10^{-8}	20%
960618	C3H8	2	1.73×10^{-8}	25%
960618	C3H8_sp	2	—	—
960811	MIX96_C	2	—	—
960812	MIX96_D	2	—	—
961123	H2S_A	2	2.09×10^{-8}	6%
961129	H2S_B	2	2.09×10^{-8}	6%
970110	MIX97_A	1, 2	1.600×10^{-8}	7%
970110	MIX97_B	1, 2	1.621×10^{-8}	7%
970113	MIX97_C	1, 2	1.642×10^{-8}	7%
970113	MIX97_D	1, 2	1.663×10^{-8}	7%
970116	MIX97_E	1, 2	1.683×10^{-8}	7%
970116	MIX97_F	1, 2	1.704×10^{-8}	7%
970117	MIX97_G	1, 2	1.725×10^{-8}	7%
970117	MIX97_H	1, 2	1.746×10^{-8}	7%
970117	MIX97_I	1, 2	1.767×10^{-8}	7%

Table 4.4 Deadtime correction coefficients for calibration experiments.

Date	Sequences	Leak	τ	σ_τ
970120	MIX97_J	1, 2	1.788×10^{-8}	7%
970121	MIX97_K	1, 2	1.808×10^{-8}	7%
970121	MIX97_L	1, 2	1.829×10^{-8}	7%
970121	MIX97_M (IP+turbo)	1, 2	1.850×10^{-8}	7%
970122	MIX97_N	1, 2	1.871×10^{-8}	7%
970122	MIX97_O	1, 2	1.892×10^{-8}	7%
970122	MIX97_P	1, 2	1.913×10^{-8}	7%
970122	MIX97_Q	1, 2	1.933×10^{-8}	7%
970123	MIX97_R	1, 2	1.954×10^{-8}	7%
970123	MIX97_S	1, 2	1.975×10^{-8}	7%
970123	MIX97_T	1, 2	1.996×10^{-8}	7%
970124	MIX97_U	1, 2	2.017×10^{-8}	7%
970124	MIX97_V	1, 2	2.038×10^{-8}	7%
970125	MIX97_W	1, 2	2.058×10^{-8}	7%
970125	MIX97_X	1, 2	2.079×10^{-8}	7%
970127	MIX97_Y	1, 2	2.100×10^{-8}	7%
970630	N2_A, N2_B	1, 2	2.89×10^{-8}	10%
981116	C2H4	1	3.32×10^{-8}	10%
981116	C2H4, C2H4_sp	2	3.0×10^{-8}	10%
981119	CO2_sp	1, 2	3.32×10^{-8}	—

* Deadtime correction for this run was approximated with a first-order Taylor approximation instead of a full numerical inversion of the deadtime function.

† Deadtime correction for this run was approximated with a third-order Taylor approximation instead of a full numerical inversion of the deadtime function.

The problem of mass interference is dealt with in fundamentally the same way for both GPMS data and calibration data. Any system of interfering gases can be resolved as long as the splitting patterns of all the gases are known, and the number of gases being analyzed is less than or equal to the number of mass peaks available. In the simplest case, analysis starts at the mass number where only one species contributes to the measured

counts. A system consisting of argon, with peaks at 40 and 20 from $^{40}Ar^{+}$ and $^{40}Ar^{++}$, and neon, with a peak at mass 20, can be described with the equations:

$$
\begin{aligned}
C'[40] &= C[40] \\
C'[20] &= C[20] - \alpha C'[40] \\
\\
\sigma^2_{C'[40]} &= \sigma^2_{C[40]} \\
\sigma^2_{C'[20]} &= \sigma^2_{C[20]} + C'[40]^2\sigma^2_{\alpha} + \alpha^2\sigma^2_{C'[40]}
\end{aligned}
\qquad 4.3
$$

Primes indicate corrected count levels, where all the counts at the mass in question are from a single sample gas. In some cases the equations are more laborious, when systems of up to four sample gases interfere. The error equations here are deceptively simple; each σ_C in the error equations is really a combination of errors from various sources, as described in greater detail in Chapters 3 and 6. On the other hand, σ_α is more subjectively determined. When multiple splitting pattern measurements exist, either from EU splitting pattern experiments such as C2H4_sp (see Table 4.3), from multiple mass spectra in the NIST database (ref.), or from both sources, a somewhat quantitative estimate of the error in the splitting fraction α can be determined. However, the apparent error in α from EU experiments is heavily influenced by the number of available measurements (usually quite small). In the NIST database, multiple spectra are almost always from different measurement teams, and could be influenced by a host of experimental variables. Therefore, for the most part, splitting fraction errors are assumed to be in the neighborhood of 5%, based on typical differences between NIST and EU mass spectra of identical molecules.

CHAPTER V

GPMS calibration constants

Overview

This chapter contains detailed presentations of calibration data for individual gases. Calibration data have been obtained using both the GPMS flight unit (FU) and flight spare experimental unit (EU). The distinctions between these instruments have been explored in Chapter 2. Chapter 4 described the experimental procedures followed in calibration experiments using both devices, so discussion of experimental procedures will be omitted from this chapter except in cases where procedures were altered in individual calibration experiments. Chapter 3 detailed the numerous considerations particular to GPMS data reduction, so data analysis problems discussed here will reference that chapter for background information whenever necessary. The formula for obtaining calibration constants was presented in Chapter 3:

$$\mathrm{cc}_{x/\mathrm{ref}}^{\mathrm{parent}} = \underbrace{\left.\frac{C[\mathrm{ref}]}{C[x]}\right|_{\mathrm{lab}} \left.\frac{n_x}{n_{\mathrm{ref}}}\right|_{\mathrm{lab}}}_{\mathrm{cal4}} \left.\frac{n_{\mathrm{ref}}}{n_{\mathrm{H_2}}}\right|_{\mathrm{Jup.}} \qquad 3.9$$

Another key formula from Chapter 3 gives the approach used to estimate uncertainties in averaged calibration constants, given the estimated uncertainties in the calibration constant datapoints:

$$\sigma_\mu^2 = \frac{1}{\sum_i (1/\sigma_i^2)}[\nu(1-N)+N] = \begin{cases} \dfrac{1}{\sum_i (1/\sigma_i^2)} & \nu = 1 \quad \text{(E1)} \\ & \text{(random error)} \\ \dfrac{[\nu(1-N)+N]}{\sum_i (1/\sigma_i^2)} & 0<\nu<1 \quad \text{(E3)} \\ & \text{(mixed error)} \\ \dfrac{N}{\sum_i (1/\sigma_i^2)} & \nu = 0 \quad \text{(E2)} \\ & \text{(systematic error)} \end{cases} \qquad 3.19$$

C_2H_6 (Ethane)

Ethane calibration experiments were done with both the FU and the EU. Inspection of Table 4.1 reveals two FU calibration runs containing ethane: sequence 14 and sequence 20. Both of these FU experiments provided multiple measurements of the ethane calibration constant for the mass ratio 30/4, or $cc_{30/4}^{ethane}$, so averages of the redundant measurements were taken to reduce the level of uncertainty. In addition, some values were discarded in order to eliminate time-dependent effects; this operation will be explained later in relation to the butane calibration constant. The resulting FU calibration constants were:

Table 5.1 Ethane calibration constants.

Calibration constant	Value, 1-σ uncertainty	Leak	Data source	Error randomness ν*
$cc_{30/4}^{ethane}$	$(6.9 \pm 1.1) \times 10^{-2}$	L2	FU: seq. 14	0.25
$cc_{30/4}^{ethane}$	$(4.29 \pm 0.59) \times 10^{-2}$	L2	FU: seq. 20	0.33

*see Equation 3.19.

Before discussing the disagreement between these values, it is helpful to also examine the results of the EU calibration experiment for ethane. Figure 5.1 shows the variation of $cc_{30/4}^{ethane}$ as a function of pressure in the gas circulation system. Because FU and EU leak conductances were different, the ratio of leak conductances was used to scale the pressures. This approach allows gas system pressure to serve as a better approximation to ion source pressure, but it implies that calibration constants for flight-relevant ISPs was not

measured. Although calibration data was taken at gas flow system pressures of up to 12 bar (the highest pressure relevant to DL2a), scaling by the ratio of FU to EU conductances shifts the data so that 7 bar is the highest scaled pressure.

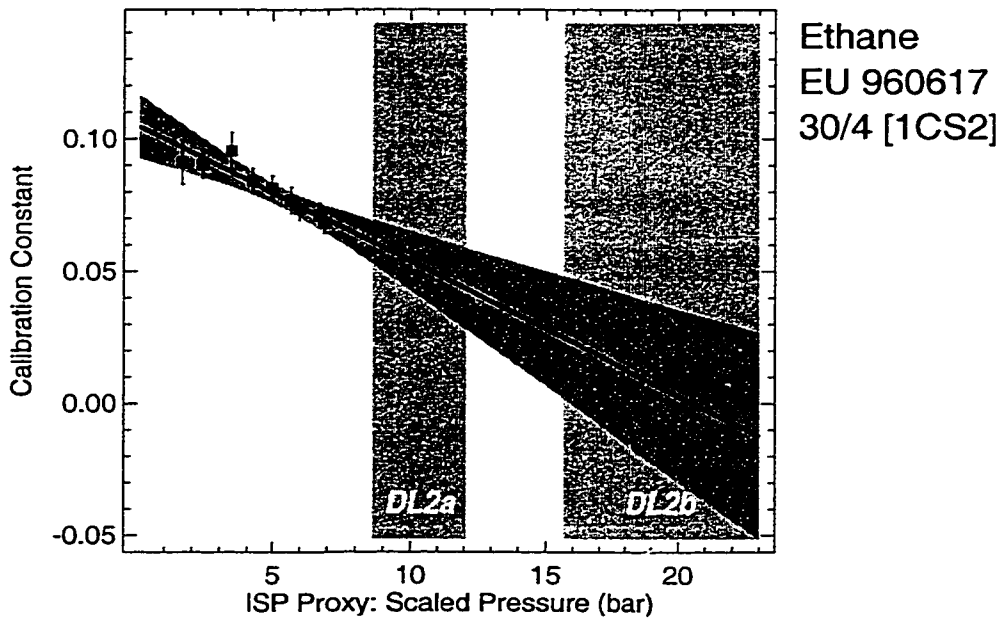

Figure 5.1 Ethane calibration constant with pressure as the ISP proxy (v = 0.5).

Light grey regions of Figure 5.1, extending from 8.4–12 bar and from 15.7–23 bar, indicate atmospheric pressure ranges encountered by the Galileo probe during its descent through Jupiter's atmosphere. The gap results from the EC2 experiment, where atmospheric gases were combined with gases captured by the enrichment cell (see Chapter 2). The plotted data points are from the EU calibration experiment conducted on 17 June 1996, with pressure scaled by the ratio of leak conductances serving as the ISP-proxy as discussed above. The discrepancy between flight-relevant and calibration ISP-proxy ranges is emphasized in Figure 5.2, where C[2] is used as the ISP proxy. Since the EU count rates are represented as counts per second, while GPMS data was recorded as counts per 0.5-second integration period, C[2] in Figure 5.2 has been divided by two. Additionally, in order to account for the difference in hydrogen mole fraction between the EU calibration run and the probe descent, C[2] was scaled for use as an ISP by the ratio of hydrogen mole fractions, $q_{H_2}\big|_{\text{Jup.}} / q_{H_2}\big|_{\text{lab.}}$.

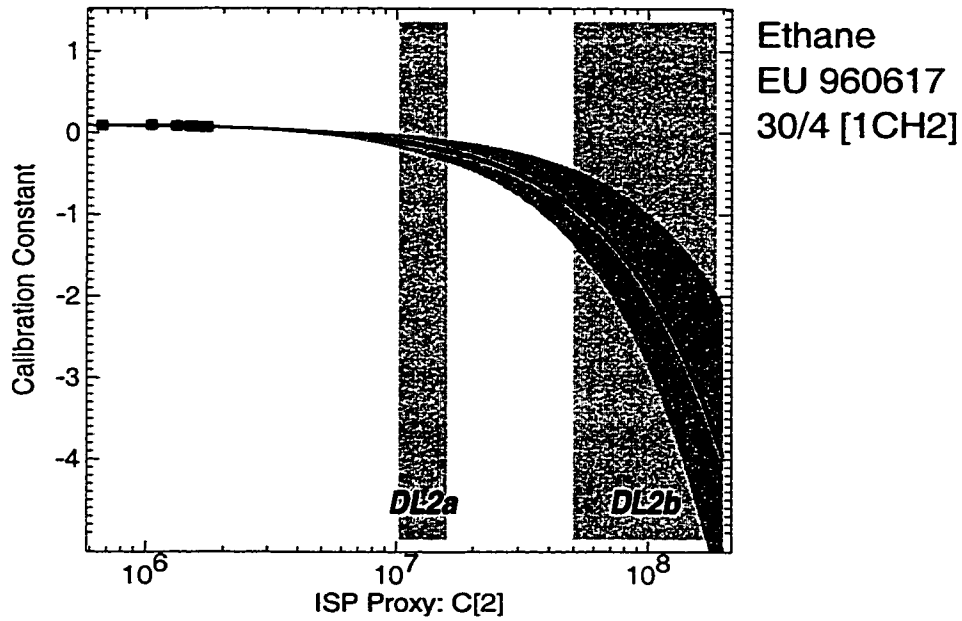

Figure 5.2 Ethane calibration constant with C[2] as the ISP proxy (v = 0.5).

Counts at mass 2, or C[2], were investigated as a possible ISP proxy because the relationship between ISP and C[2] should be independent of any of the leak or wall effects. However, since C[2] is so large, deadtime effects are very significant and may be part of the reason for the order of magnitude difference seen in Figure 5.2 between flight C[2] rates (the light grey areas between 10^7 and 2×10^8), and the C[2] values encountered in the EU ethane calibration run (the x-values for the data points). Because the domains for the observed ccs and the flight relevant ccs are so different, the extrapolated linear fit of cc as a function of C[2] would produce negative calibration constant values for use in the flight data analysis. This is clearly unphysical (since it would produce negative mixing ratios), and in cases such as this we have no choice but to select the ISP proxy which gives physically meaningful values. Thus we use the fitted calibration curve shown in Figure 5.1 for analysis of ethane in the DL2a region.

A final consideration to make when comparing ccs from different calibration experiments is that there is sometimes a dependence of the cc on the mixing ratio of the gas of interest in the calibration run. Ammonia and water ccs have a well-demonstrated dependence on mixing ratio, as will be explored later. Such dependencies are annoying

because calibration constants are needed to obtain mixing ratios from count ratios, but determination of the value of the calibration constant requires that the mixing ratio already be known! To investigate whether ethane shares such a dependence on mixing ratio, note that for the progression in the experiments EU-C2H6_A:EU-C2H6_B:FU-seq14:FU-seq20, the calibration constants fall roughly in the ratios 17:17:15:10, and the mixing ratios scale as 39:4:5:1 (see Tables 4.1 and 4.3). Thus if there is a dependence of ethane cc on sample mixing ratio, it is very weak and possibly significant only at low mixing ratios. Further discussion of this problem will be presented in Chapters 6 and 9, during the discussion of Jovian ethane mixing ratios.

C_3H_8 (Propane)

Like ethane, propane was featured in two FU calibration runs (again, sequences 14 and 20) as well as an EU calibration experiment. As with ethane, final propane ccs from FU data are obtained from averages of repeated measurements, reducing the uncertainty in the final value. Results of the FU experiments are:

Table 5.2 Propane calibration constants.

Calibration constant	Value, 1-σ uncertainty	Leak	Data source	Error randomness ν*
$cc_{29/4}^{propane}$	$(7.1 \pm 2.8) \times 10^{-2}$	L2	FU: seq. 14	0
$cc_{29/4}^{propane}$	$(5.3 \pm 1.2) \times 10^{-2}$	L2	FU: seq. 20	0.875
$cc_{43/4}^{propane}$	$(2.25 \pm 0.21) \times 10^{-2}$	L2	FU: seq. 14	0.33

*see Equation 3.19.

There is no $cc_{43/4}^{propane}$ for sequence 20, because C[43] in that run was used to determine $cc_{43/4}^{butane}$. Data from sequence 14 are more reliable (note the smaller relative uncertainty) because the nine different sample species in sequence 20 (see Table 4.1) necessitated extensive corrections for mass interference. Uncertainties in both the splitting fractions as well as the parent counting rates propagate to create large uncertainties in the final C[43]. The less-complicated sequence 14 contained only methane, ethane, and propane, so that only a correction for ethane was made to C[29], and uncorrected C[43] was attributed

entirely to propane.

The EU calibration experiment for propane (1996-06-18) yielded ISP-dependent ccs at masses 29 and 43. For the DL2a region, using either external pressure or C[2] as ISP proxy resulted in very similar fitted calibration constant values, with C[2] modified to account for integration period and mole fraction differences as described above in the ethane section. However, extrapolation of the linear fit of propane cc to C[2] produced unrealistically large calibration constants for the DL2b region. Displayed below are the ISP-dependent propane cc fits from the EU calibration experiments, using external pressure (scaled for leak conductance differences) as the ISP proxy. In both cases, errors were approximately evenly attributed to random and systematic effects, so the error randomness parameter ν was set to 0.5.

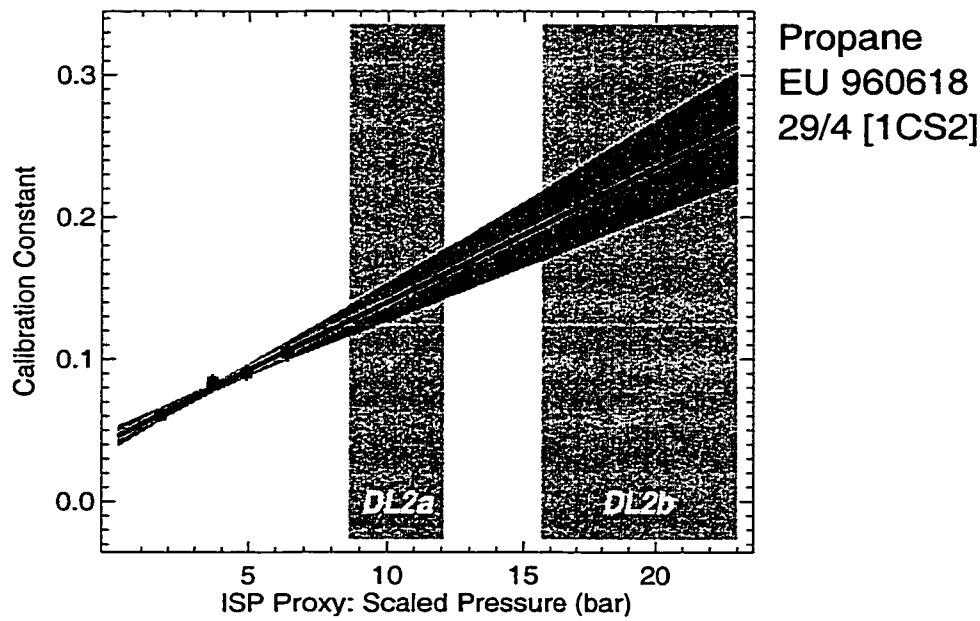

Figure 5.3 Propane calibration constant (ν = 0.5).

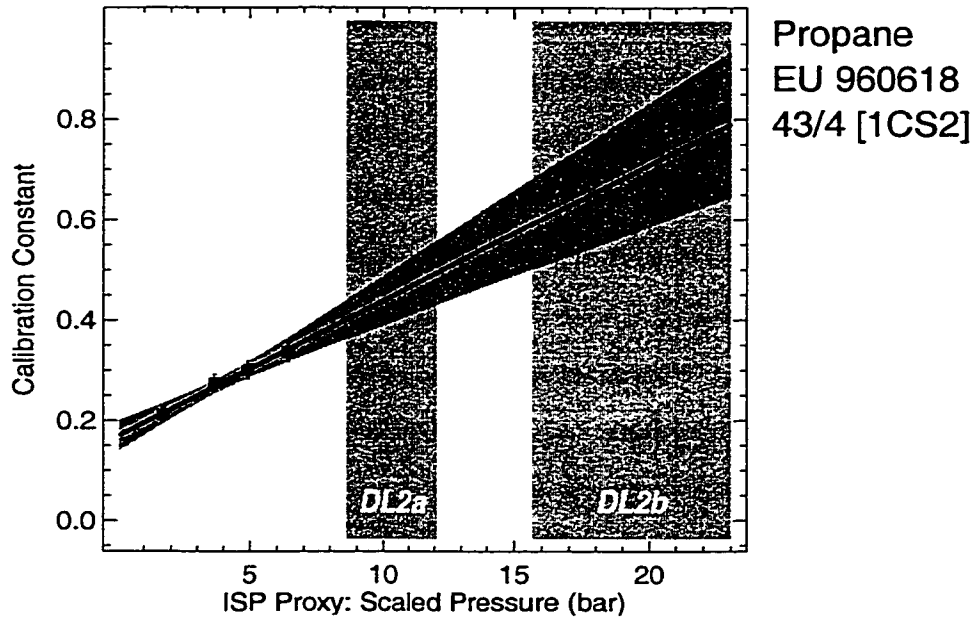

Figure 5.4 Propane calibration constant (v = 0.5).

Comparison of propane mixing ratios and calibration constants, for the 29/4 ratio, show that for the EU:FU-seq14:FU-seq20 series, mixing ratios were in the relationship 23:5:1 and ccs were proportional to about 2.6:1.3:1. These results indicate that dependence of propane ccs on mixing ratio can be neglected, but ISP-dependent effects are significant.

C_4H_{10} (Butane)

No EU calibration experiments were done for butane. Table 4.1 shows that butane was used only in sequence 20, which contained nine hydrocarbons in addition to hydrogen and helium. Figure 5.5 shows the splitting patterns of butane, propane, and ethane, which are needed to isolate mass spectrometer counts that are solely due to butane.

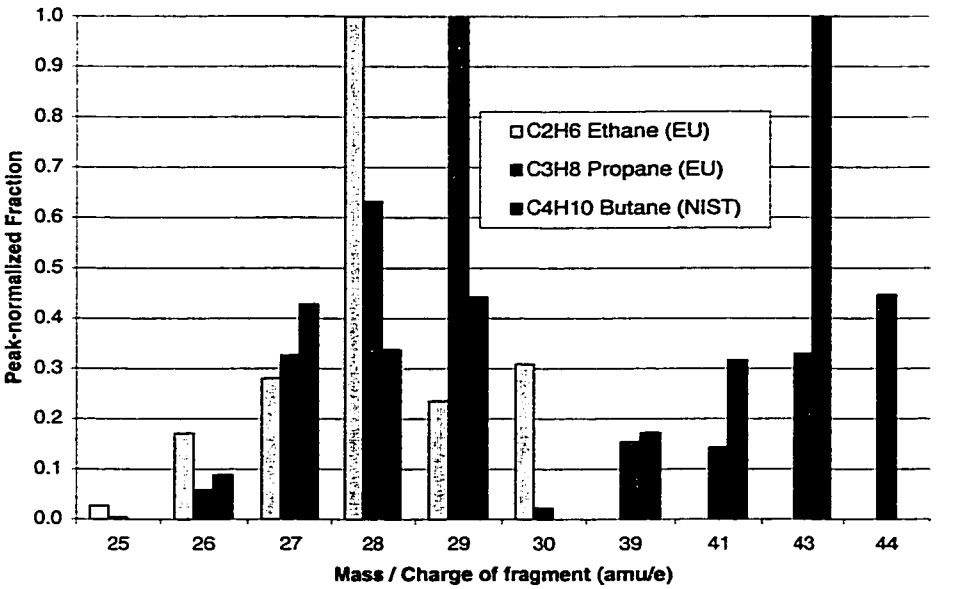

Figure 5.5 Butane, propane, and ethane splitting patterns.

Using the counting rates C[29], C[30], and C[43], and the splitting patterns shown in Figure 5.5, solutions can be found for purified counts C′[29], C′[30], and C′[43], which are the counts only due to ethane, propane, and butane (respectively):

$$\begin{aligned} C'[29] &= \frac{C[29]-\alpha C[30]-\beta C[43]}{1-\beta\gamma} \\ C'[30] &= C[30] \\ C'[43] &= \frac{C[43]-\gamma(C[29]-\alpha C[30])}{1-\beta\gamma} \end{aligned} \qquad 5.1$$

The splitting fractions come from EU runs for ethane and propane (experiments C2H6_sp and C3H8_sp in Table 4.3), and from the NIST mass spectrometry database v4.5 (simply referred to as NIST in this work) for butane, and have the values:

$$\begin{aligned} \alpha &= 0.7614 = \text{ethane}\ \frac{C[29]}{C[30]} \\ \beta &= 0.4424 = \text{butane}\ \frac{C[29]}{C[43]} \\ \gamma &= 0.3298 = \text{propane}\ \frac{C[43]}{C[29]} \end{aligned} \qquad 5.2$$

Butane at C[58] should also have been used, but during this analysis C[58] was somehow

not extracted from original datafiles. A re-analysis including this mass peak would be a good goal for future research.

The sequence 20 calibration run took 14 measurements of C[43] using filament 1 and four measurements of C[43] using filament 2; datapoints with filament 2 were discarded because filament 1 was the impact electron source during the actual probe descent. Additional points were also discarded due to time-dependent effects in the calibration run. Figure 5.6 shows the value of $cc_{43/4}^{butane}$ derived from each measurement in sequence 20; datapoints 1 through 4, corresponding to the beginning of the calibration experiment, were attributed to transient phenomena and discarded for the purpose of calculating the average cc. Similar transient effects were noticed at the beginning of many of the other FU calibration runs.

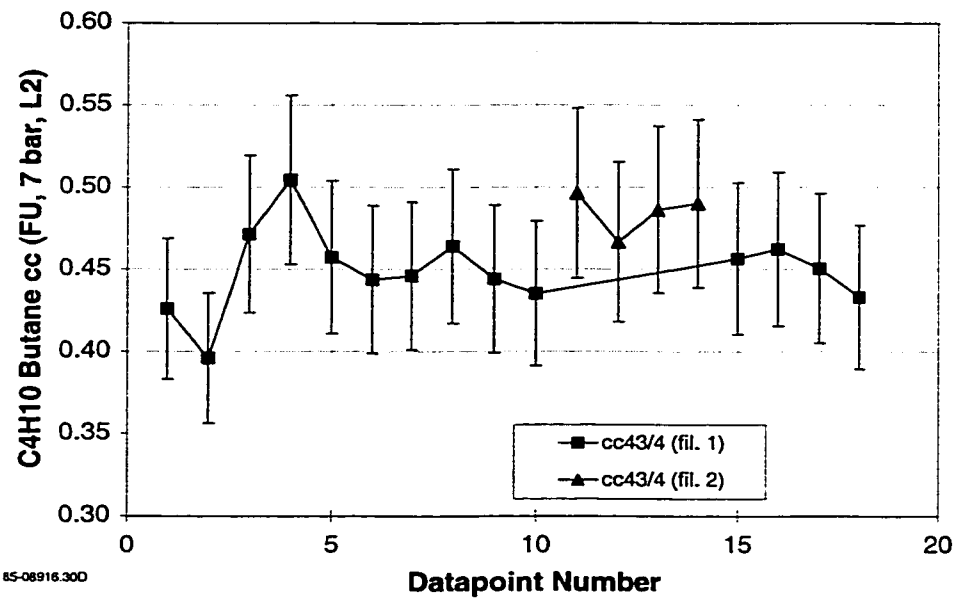

Figure 5.6 Butane cal4 calibration constant.

The value of $cc_{43/4}^{butane}$ was obtained from the average of the last 10 filament 1 datapoints in Figure 5.6, weighted by the standard deviations of each of the points. The quantity plotted in Figure 5.6 is actually cal4 (see Equation 3.9), so values must be

multiplied by the helium mixing ratio of 0.157 to obtain the calibration constant. The value in Table 5.3 includes all known sources of error.

Table 5.3 Butane calibration constants.

Calibration constant	Value, 1-σ uncertainty	Leak	Data source	Error randomness ν
$cc_{43/4}^{butane}$	$(7.04 \pm 0.97) \times 10^{-2}$	L2	FU: seq. 20	0.6

C_3H_6 (Propene, Cyclopropane)

Propene and cyclopropane are two isomers of C_3H_6. Propene was the only isomer to be used in calibration experiments, appearing in the gas mixture descriptions for sequence 16 and sequence 20 FU experiments as "propylane" (sic; propylene is another name for propene). No EU calibration runs were done for C_3H_6, so any variation of its calibration constant with ISP is unknown. Many jovian photochemical models neglect the cyclopropene isomer, so the FU calibration experiments using propene should be sufficient for analysis of jovian C_3H_6. Averaged values for propene calibration constants are:

Table 5.4 Propene calibration constants.

Calibration constant	Value, 1-σ uncertainty	Leak	Data source	Error randomness ν
$cc_{41/4}^{propene}$	$(4.5 \pm 43.2) \times 10^{-2}$	L2	FU: seq. 16	0
$cc_{41/4}^{propene}$	$(1.16 \pm 0.29) \times 10^{-2}$	L2	FU: seq. 20	0.86
$cc_{42/4}^{propene}$	$(8.6 \pm 91.1) \times 10^{-2}$	L2	FU: seq. 16	0
$cc_{42/4}^{propene}$	$(1.15 \pm 0.28) \times 10^{-2}$	L2	FU: seq. 20	0.86

The extraordinarily large errors reported for sequence 16 can be ascribed to strange behavior of C[4] (from helium) in that calibration experiment. Sequence 16 was one of several runs to feature calibration gas mixtures composed mainly of helium (see Table 4.1). In particular, sequences 5, 16, and 18 were done with similar helium mole fractions, at about 7 bar gas system pressure, using inlet leak 2. Table 5.5 compares C[4] among these FU calibration experiments:

Table 5.5 Effect of varying the deadtime correction for FU sequence 16.

FU Seq.	Approx. Raw C[4] ($\times 10^6$)	Deadtime correction	Saturated (Y/N)	Approx. Corrected C[4] ($\times 10^6$)
5	8.9–9.4	$\tau_c = 3.41 \times 10^{-8}$	N	15–17
18	10.4–10.6	τ_c	N	22–24
16	3.2	$\tau_c + 2\sigma = 4.23 \times 10^{-8}$	N	3.9
16	3.2	$\tau_{16} = 1 \times 10^{-7}$	N	5.7
16	3.2	$\tau_c + 2\sigma$	Y	62
16	3.2	τ_{16}	Y	16

Based on the presumption that the difference between C[4] in the sequences in Table 5.5 is primarily due to a change in detector deadtime constant, the final line of the table would be the best choice since it places the corrected sequence 16 C[4] in the range of C[4] in sequences 5 and 18. However, this would require an abrupt and transient change in the deadtime coefficient of more than a factor of two, which is difficult to justify. A further mystery with sequence 16 is that in addition to helium and C_3H_6, there are two other gases (acetylene and ethylene), but based on the known splitting patterns of these gases, approximately 65% of the counts at mass 27 must be produced by an unknown molecule or fragment. I analyzed sequence 16 data by subtracting this unknown contribution, which affects $cc_{25/4}^{acetylene}$ and $cc_{26/4}^{acetylene}$, and by using $\tau_{16} = 1 \times 10^{-7}$ as discussed above, with the difference $\tau_{16} - \tau_c$ serving as the uncertainty in the deadtime coefficient. The factor of 2 uncertainty in τ resulted in a factor of about 4 uncertainty in the calibration constants for sequence 16, but averaging over 10 to 12 datapoints reduced the error back to about a factor of 2. Given the massive uncertainty, it seems reasonable to discard the calibration constants from sequence 16 and focus on sequence 20, even though the large number of test gases in sequence 20 introduces uncertainties of its own, through mass interference.

For the analysis in Chapter 6, propene calibration constants for masses 41 and 42 are needed. Figure 5.7 shows several mass peaks for propene; significant mass peaks are also present at 27, 28, 29, and 40. In order to obtain calibration constants for propene,

contributions from butane, propane, and 1–hexane must be subtracted from C[41] and C[42]; an additional correction for benzene would be made to obtain $cc_{39/4}^{propene}$. Peaks at C[44] and C[56] were used to estimate corrections for propane and 1–hexene respectively, since those masses are free of any other interfering contributions. For butane, C[43] was used, after subtractions for the propane and 1–hexene contributions to C[43], because the magnitude of the butane signal at 43 is so much greater than at 58. Each interference correction increased the error estimates for the corrected counts at C[41] and C[42], so that count interference comprises the main part of the almost 35% relative error reported above for $cc_{41/4}^{propene}$ and $cc_{42/4}^{propene}$.

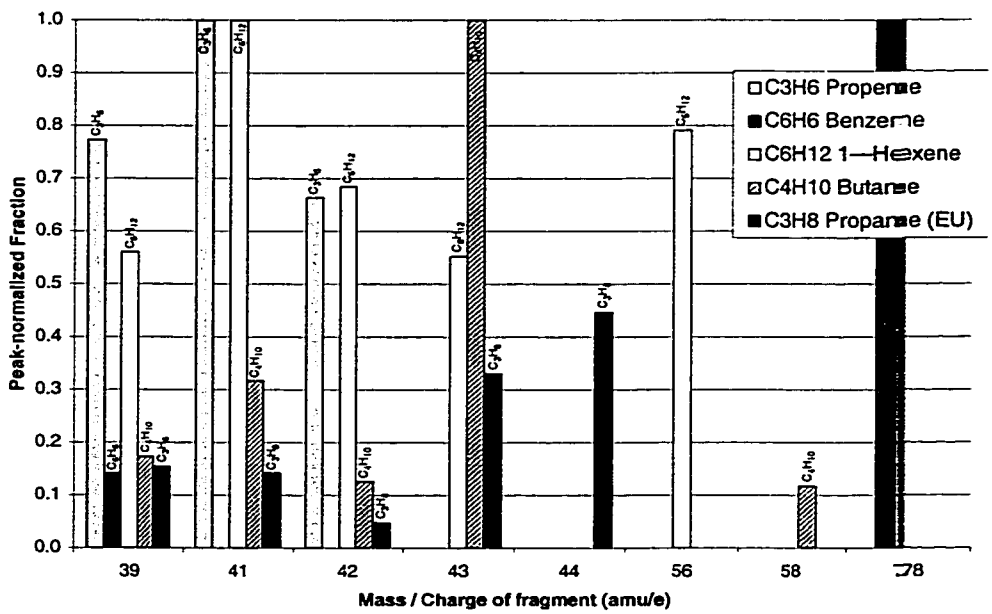

Figure 5.7 Partial splitting patterns of propene, benzene, 1–hexene, butane, and propane.

C_2H_4 (Ethylene)

Ethylene calibration experiments were done in 1998 by Paul Mahaffy using the experimental unit at NASA Goddard. By 1998 it was well known that counts (such as C[13]) derived from methane served as a better count ratio denominator, or reference gas, than counts from helium or hydrogen, since the smaller counting rates of methane were free from deadtime saturation effects. Thus calibration constants for ethylene use C[13] as a reference gas; C[13] is a better choice than C[12] because the larger methane splitting

fraction for C[13] results in slightly better count rate statistics, since poisson-distributed statistical noise is equal to the square root of the counting rate. Although C[14] provides more counts than C[13], interference from other fragments, such as N^+ from jovian NH_3, introduce errors at that mass.

In the EU ethylene calibration experiment, both C[13] and gas system pressure served as ISP-proxies, as shown in Figures 5.8 and 5.9. Since this calibration run was done after the EU leak 2 replacement on 1997-09-29, scaled pressure (Figure 5.8) is effectively the same as the actual pressure in the gas circulation system and spans the DL2a pressure interval. However, C[13] falls short of the relevant flight values after being scaled to units of counts per 0.5-second integration period (Figure 5.9).

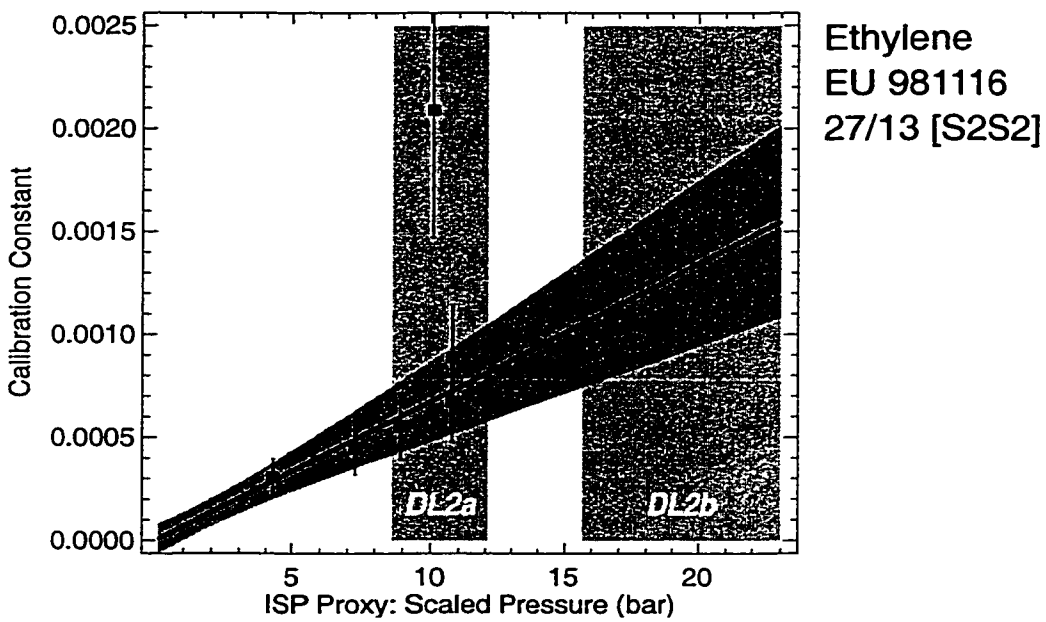

Figure 5.8 Ethylene calibration constant (v = 0.6).

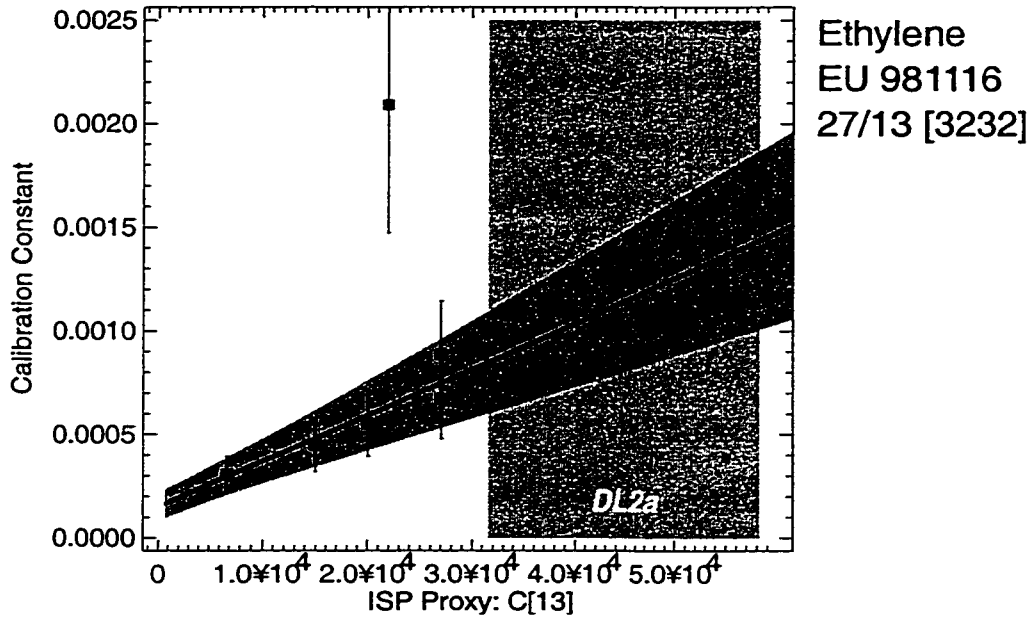

Figure 5.9 Ethylene calibration constant (v = 0.6).

A case could be made for either C[13] or external pressure as the ISP-proxy for the EU C_2H_4 runs, but theoretically both ISP-proxies should span the same flight-relevant domains. The reason for the 50% discrepancy between the fitted calibration constants for DL2a shown in the above two figures is not clear, and Chapter VI will present mixing ratios obtained from both fits, in order to explore the influence of ISP-proxy choice on the final result. Gas system pressure is the preferred choice, since it results in calibration data overlapping the flight-relevant values for DL2a. However, this is a subjective preference, since there is no scientific justification for favoring pressure over C[13] as an ISP proxy.

C_2H_2 (Acetylene)

Availability of C_2H_2 calibration data is the same as availability of C_3H_6 data: no EU experiments exist, and sequences 16 and 20 were the only FU experiments to contain acetylene. Peculiar uncertainties in C[4] in sequence 16, as discussed in the propene calibration constant section, lead to the conclusion that calibration data from sequence 16 should not be used. Again, as with propene, sequence 20 acetylene mass peaks are plagued with substantial contributions from many different gases. The main mass peak for acetylene

is at 26, a very popular mass for hydrocarbon fragments. Corrections for propene and ethane were based on counts at 40and 30 respectively, since these masses were "pure" in the sense that no other molecules had interfering mass peaks at these values. Additional count corrections to C[26] were made to account for ethylene, propane, and butane contributions, this time based on C'[28], C'[29], and C'[43] respectively, where the prime symbols indicate that corrections have been made for mass interference from other gases. Propane and butane corrections to obtain C'[29] and C'[43] were discussed earlier and summarized in Equation 5.1. For C[28], subtractions are made for butane (based on C'[43]), propane (based on C'[29]), and ethane (from C[30]).

A result of such a large number of corrections to C[26] is to increase the uncertainty in the corrected counts. Corrected C'[26] in sequence 20 are in the range of 2000–3000, with 1-σ uncertainties due to the correction for mass interference (from butane, propane, propene, ethane, and ethylene) on the order of 1000 counts. This source of error dominates the uncertainty in the acetylene calibration constants derived from sequence 20 (see Figure 5.10). Although the higher values of $cc_{26/4}^{acetylene}$ in the first half of the experiment may suggest the influence of time-dependent phenomena, any such variation is not significant given the magnitude of the calibration constant uncertainties.

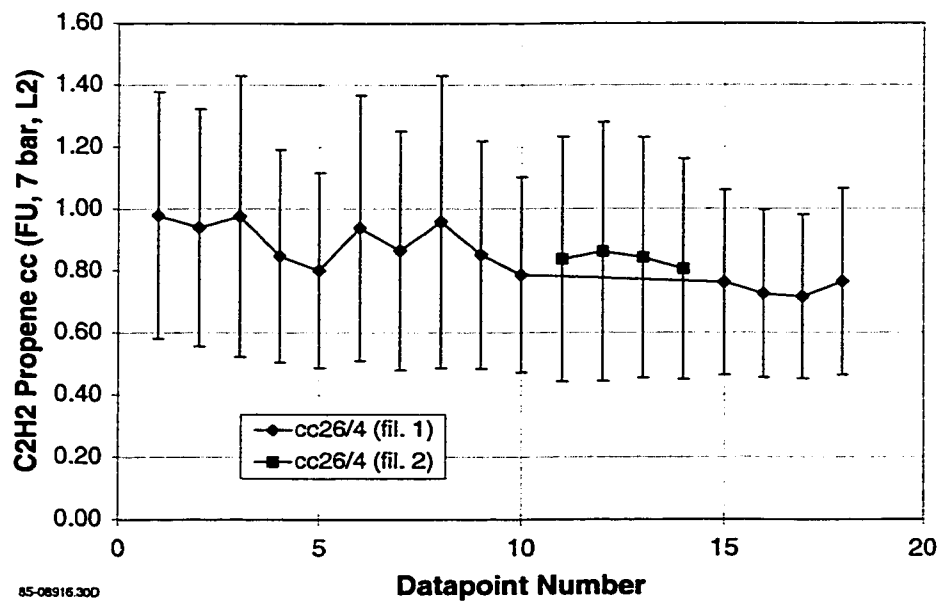

Figure 5.10 Acetylene cal4 calibration constant.

Therefore an average value was obtained from the data shown in Figure 5.10 using all 14 filament 1 datapoints. Note that the intermediate calibration factor cal4 (see Equation 3.9) is shown in Figure 5.10, while Table 5.6 below gives the average value of the corresponding calibration constant:

Table 5.6 Acetylene calibration constant.

Calibration constant	Value, 1-σ uncertainty	Leak	Data source	Error randomness ν
$cc_{26/4}^{acetylene}$	$1.29 \pm 0.33 \times 10^{-1}$	L2	FU: seq. 20	0.9

N_2 (Nitrogen)

Molecular nitrogen calibration experiments were done by Paul Mahaffy using the experimental unit on 1997-06-30; no FU calibration data for this gas exist. Both inlet leak 1 (L1) and leak 2 (L2) data were obtained. Fitted calibration constants for DL2a agreed to within about 10%, using C[2], C[13], or scaled pressure as the ISP. The fit using C[13] as the ISP is shown in Figure 5.11. Since the calibration data did not reach flight relevant ranges for DL2b for any of the ISP proxies, extrapolation led to more drastically varying results in that interval. C[13] as the ISP gives the flattest fit, while using scaled pressure gives values up to 15% higher, and C[2], due to detector deadtime issues, gives unreliable values greater than those for C[13] by up to a factor of 1.8. The DL2 $cc_{28/4}^{N_2}$, although not pictured, ranged from 7.1×10^{-3} to 8.6×10^{-3} in the DL2a region, with pressure as the ISP proxy.

Table 5.7 Nitrogen calibration constants.

Calibration constant	Value, 1-σ uncertainty	Leak	Data source	Error randomness ν
$cc_{28/13}^{N_2}$	$3.8 \pm 1.1 \times 10^{-4}$	L1	EU 1997-06-30	1.0
$cc_{28/4}^{N_2}$	$7.44 \pm 0.16 \times 10^{-2}$	L1	EU 1997-06-30	1.0

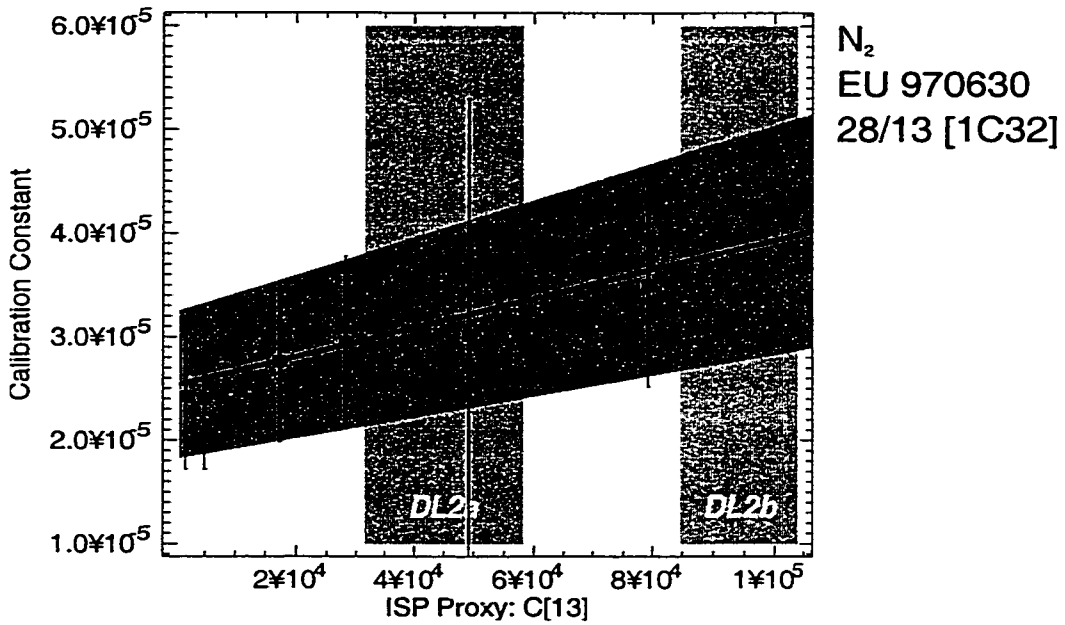

Figure 5.11 N_2 calibration constant (v = 1.0).

CH_4 (Methane)

Several EU calibration experiments included methane along with other species in the sample gas mixture. One reason for doing this was to more closely match Jupiter's atmosphere in the calibration run; a stronger reason was to obtain C[13] from methane to use as a reference gas and ISP-proxy. EU calibration experiments done with leak 1 and methane-containing sample gases are the MIX97 experiments, the C2H4 run, and the N2METH run. The EU H2S experiment also included methane but was limited to leak 2. The $cc_{16/4}^{CH4}$, with full error analysis, was presented in panel 5 of DPS99, but utilized only data from the N2METH run. Unfortunately, the DPS99 error analysis results in final mixing ratio uncertainties on the order of 5%, while the range of values of calibration constants shown in Table 5.8 below is much greater.

Table 5.8 Comparison of methane calibration experiments.

EU Calibration experiment	Date	Approx. cal4 value	Leak	Approx. Jovian CH_4 mixing ratio	Comments
MIX97	1997-01	0.120	L1, L2	3.2×10^{-3}	Plentiful data; old detector; old inlet leak
C2H4	1998-11-16	0.110	L1, L2	2.9×10^{-3}	New inlet leak; heavy L1 count saturation
N2METH	1997-06-30	0.075	L1, L2	2.0×10^{-3}	New inlet leak; analysis published at DPS99
H2S	1996-11-29	0.085	L2	2.2×10^{-3}	Old detector; old inlet leak

Several considerations should be observed when comparing these values:

1. L2 was replaced on 1997-09-29 in order to match its conductance with that of the flight unit. Thus, C2H4 and N2METH runs had the correct conductances for L2.

2. L1 for the EU has the wrong conductance, more than five times larger than the FU L1 conductance.

3. The N2METH L1 run extended to 12 bar. The other two L1 runs reached maximum pressures of around 2 bar. Max pressure in the probe descent DL1 experiment was 4 bar. But due to the difference between FU and EU L1 conductances, this means the maximum pressures reached in the calibration runs would produce ISPs that would correspond to atmospheric pressures seen by the FU of 62 bar (N2METH) and 10 bar (others), based on Equation 402e and Table 2.2.

4. $cc_{16/4}^{CH4}$ is largely flat as a function of ISP, with a sharp increase at the lowest pressures.

5. Substantial count interference compensation was used in MIX97, but not needed for C[16] in the other two runs.

6. Detector electronics were replaced sometime in early 1997 (but after MIX97).

7. Helium counts did not reach saturation in the N2METH run, but did reach detector saturation (as did C[2]) in the C2H4 run.

Clearly the spread in calibration constant values indicates the influence of unaccounted-for factors. The two available choices are to select one of the calibration runs

and discount the others, or to use the scatter in derived ccs to estimate uncertainties based on these unknown variables. Points 1 and 2 can be used to eliminate the MIX97 and H2S calibration runs, since calibration data taken with the correct leak conductances should be used if possible. Points 3 and 4 provide a weak suggestion that the C2H4 run is suspect, since the low pressures sampled in that run are more susceptible to the greater low-pressure calibration constant variability. Point 7 (saturated reference gas in C2H4 run) also argues against using the C2H4 run, since an accurate determination of C[4] is needed to derive the methane calibration constant. This count saturation is the reason for the very large error bars seen in Figures 5.12 through 5.15. However, the above arguments are somewhat subjective. Following the alternate approach and using all available data to characterize the unknown systematic errors in the methane calibration constant, a final uncertainty of more than 30% is indicated in the methane mixing ratio.

The final approach taken in this work is to fit the calibration constant to the data from the "best" run, while estimating the calibration constant uncertainty from the spread in values between the "best" two runs. For the reasons discussed above, the N2METH run was selected as the "best" run for calibration constant determination. Error analysis of the N2METH run was presented in Wong et al. (1999), but the Wong et al. (1999) results featured erroneously small errors because they did not account for the spread in calibration constant values from calibration run to calibration run. The approach taken here is to estimate the calibration constant uncertainty by finding the mean of the combined N2METH and C2H4 data, while setting $N = 2$ for the degrees of freedom in the calculation of the standard deviation, rather than N = number of datapoints as is usually done. This approach to error analysis is discussed in greater detail in the section below on the water calibration constant (in particular see Equation 5.5, but can be qualitatively understood by thinking of each calibration run as a single "datapoint" as far as the error analysis is concerned.

The four Figures 5.12 through 5.15 show calibration constants from the N2METH run (squares) and the C2H4 run (triangles), for both $cc_{16/4}^{CH4}$ and $cc_{13/4}^{CH4}$ in L1 and L2. The estimated calibration constant uncertainties from these fits are taken as the final estimates

and presented in Table 5.9 along with the mean calibration constants derived using only N2METH datapoints.

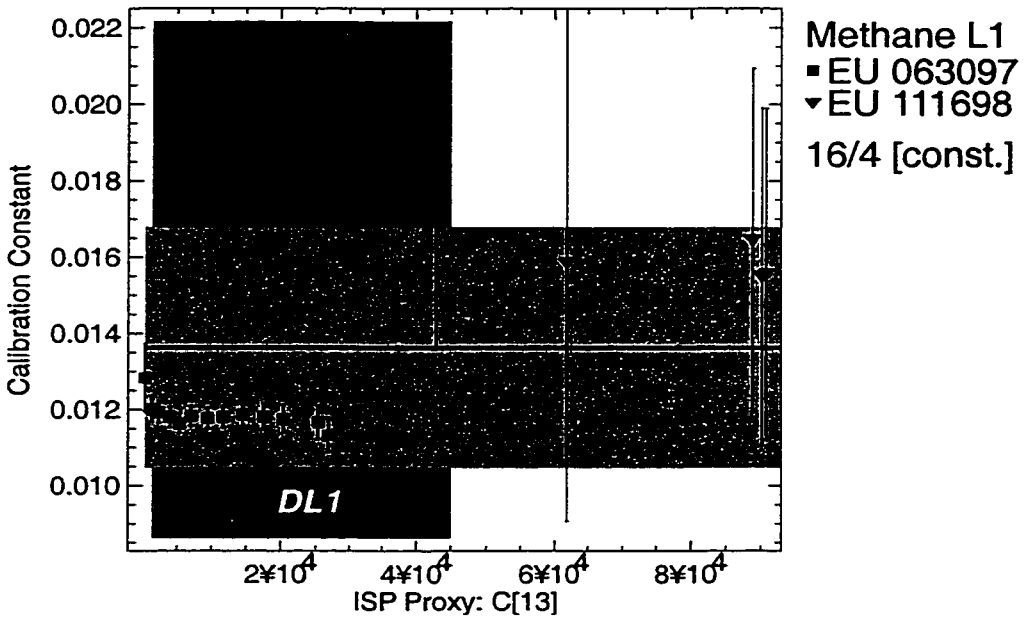

Figure 5.12 Data used to estimate methane calibration constant uncertainty, for *CR*[16/4], leak 1.

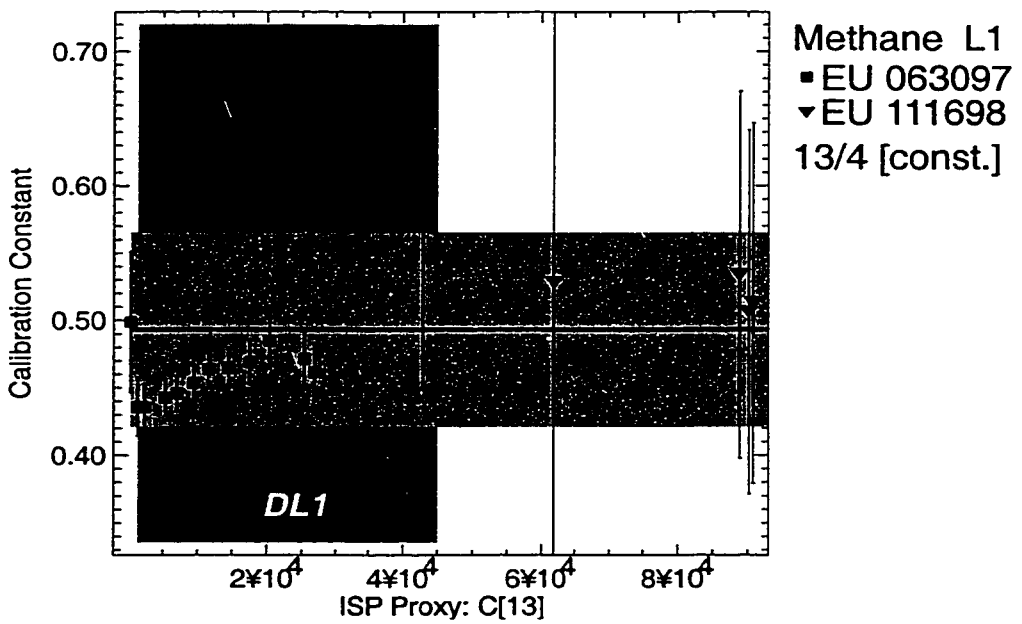

Figure 5.13 Data used to estimate methane calibration constant uncertainty, for *CR*[13/4], leak 1.

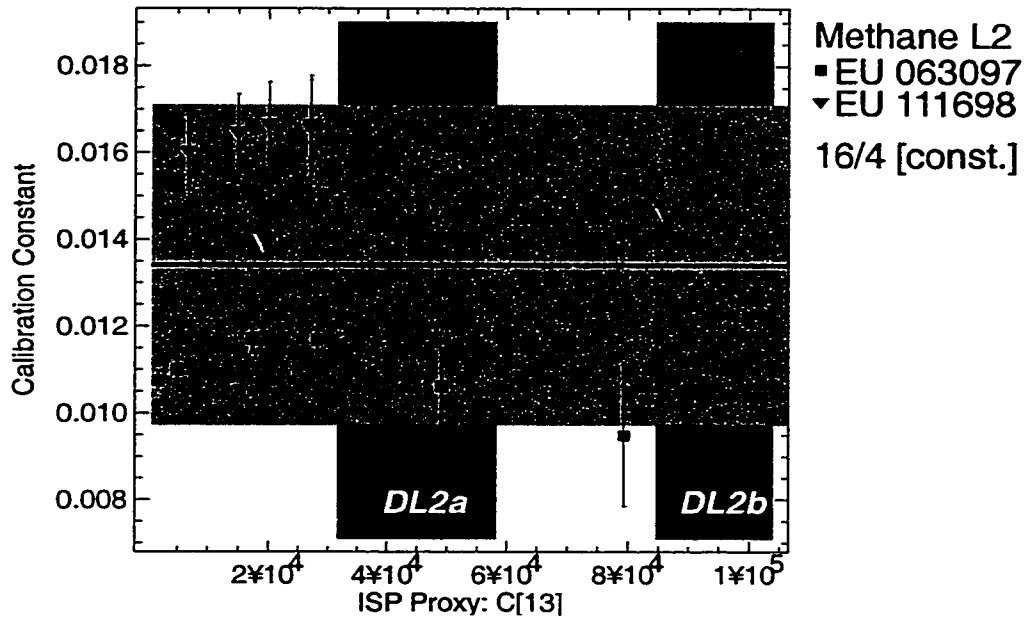

Figure 5.14 Data used to estimate methane calibration constant uncertainty, for *CR*[16/4], leak 2.

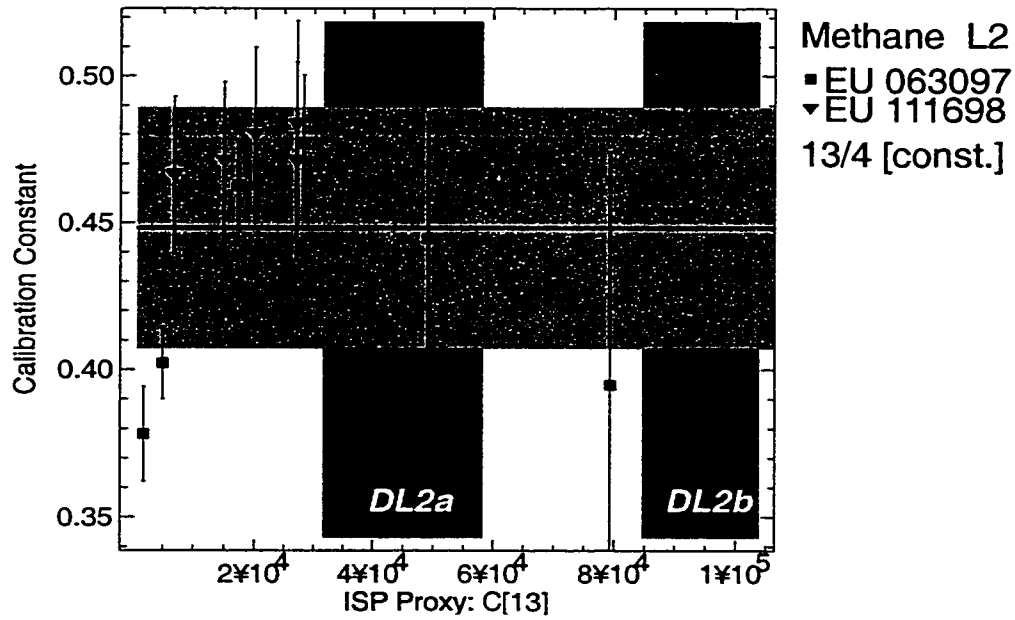

Figure 5.15 Data used to estimate methane calibration constant uncertainty, for *CR*[13/4], leak 2.

Table 5.9 Methane calibration constants.

Calibration constant	Value, 1-σ uncertainty	Leak	Data source
$cc^{CH4}_{16/4}$	$(1.18 \pm 0.32) \times 10^{-2}$	L1	value: EU/N2METH uncertainty: EU/N2METH + EU/C2H4
$cc^{CH4}_{13/4}$	$(4.52 \pm 0.72) \times 10^{-1}$	L1	(same as above)
$cc^{CH4}_{16/4}$	$(1.10 \pm 0.37) \times 10^{-2}$	L2	(same as above)
$cc^{CH4}_{13/4}$	$(4.21 \pm 0.41) \times 10^{-1}$	L2	(same as above)

One final problem influencing the determination of methane calibration constants should be mentioned, although no satisfactory explanation of this effect has yet been advanced. In EU calibration experiments, the splitting pattern of methane showed variation with ISP, a condition that was not observed for other molecules. The change in splitting patterns is consistent with an excess of C[16] (relative to counts due to fragments of methane) at high ISP. As measured by the C[16]/C[13] ratio, the relative C[16] contribution is greater at 20 bar than at 2 bar by 20–30% in both the N2METH and CVMIXES experiments. This behavior is puzzling since other species do not show evidence of splitting pattern variability as a function of ISP. The GPMS data show a similar but less extreme variation of methane splitting fraction.

H_2S (Hydrogen sulfide)

A single EU calibration experiment, consisting of one L1 run and two L2 runs, was performed for H_2S. The L1 run is useful only for obtaining an upper limit on H_2S, since the DL1 counting rates for mass 34 were not statistically significant. Only one of the two L2 runs contained methane. Using *CR*[34/13] to obtain the H_2S mixing ratio reduces the large uncertainty due to deadtime correction associated with using C[4] from helium as a reference gas. Unfortunately, this is compensated for by the fact that the Jovian mixing ratio of helium is more precisely defined (by the Galileo probe HAD) than is the methane mixing

ratio (by the GPMS). Thus, both H_2S calibration constants ($cc_{34/4}^{CH4}$ and $cc_{34/13}^{CH4}$) will be examined in the next chapter.

Figures 5.16 and 5.17 show the H_2S calibration constants with methane as a reference gas. Both the run containing methane (squares in Figure 5.16) and the run with no methane (triangles) give comparable results for $cc_{34/4}^{CH4}$. The larger relative uncertainty in the $cc_{34/13}^{CH4}$ is primarily due to the aforementioned disparity between the uncertainties of the reference gases helium and methane (see Equation 3.9), although the smaller number of datapoints available for the fit contributes as well. Pressure is used as the ISP for all fits, and is scaled by the EU to FU ratio of leak conductances.

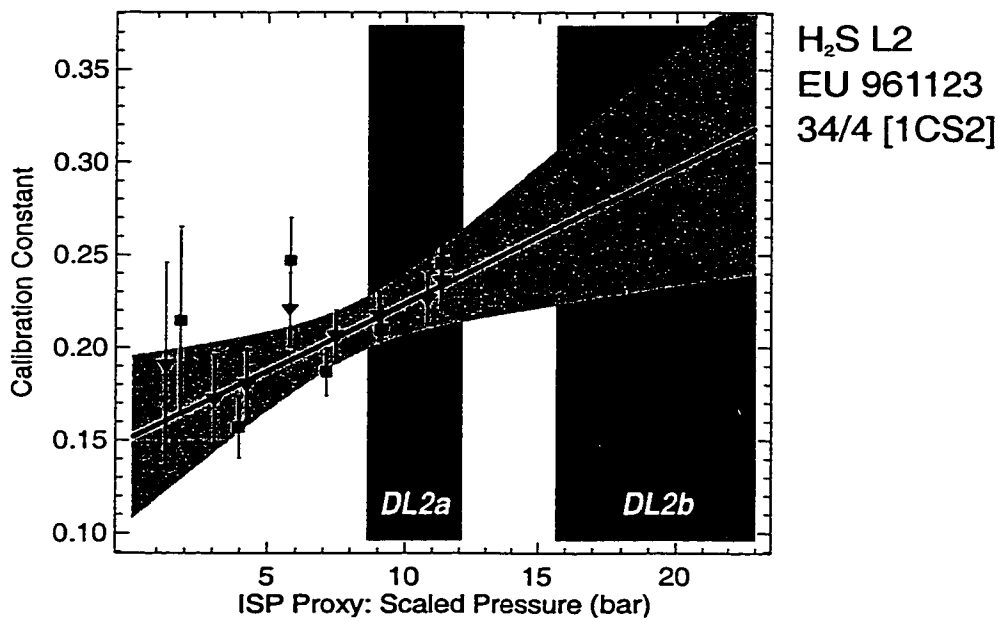

Figure 5.16 H_2S calibration constant ($\nu = 0.3$).

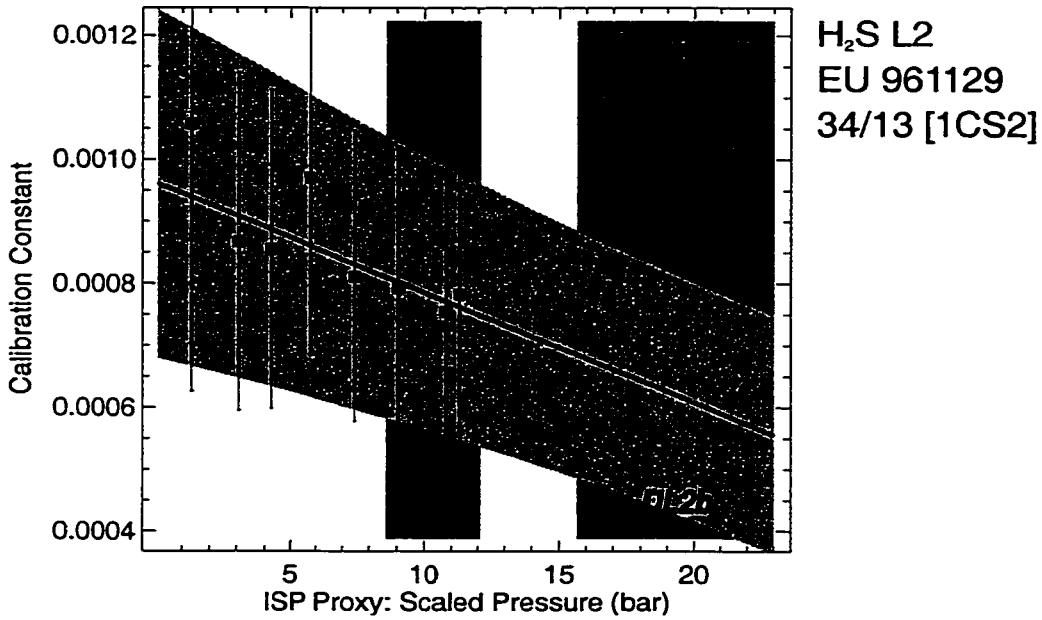

Figure 5.17 H_2S calibration constant (v = 1).

H_2O (Water)

Paul Mahaffy conducted a suite of calibration experiments using varying NH_3 and H_2O abundances in a mix of hydrogen, helium, methane, ammonia, and water. Perhaps he noticed that it was unusual to be able to get the same $cc_{18/*}^{H_2O}$ results from repeated experiments. Indeed a high degree of variability in $cc_{18/*}^{H_2O}$ was found from run to run, but any connection between water or ammonia mole fraction and the variability in $cc_{18/*}^{H_2O}$ is not clear. Figure 5.18 through 5.21 show the water calibration constant data obtained in the MIX97 runs, grouped into four bins based on the water mole fractions used. Values of water mole fraction for each specific run are given in Table 4.3. Note that the values shown in Figures 5.18 through 5.21 are cal4 (intermediate; see 3.9), and thus do not include uncertainties from the Jovian reference gas (methane) mixing ratio.

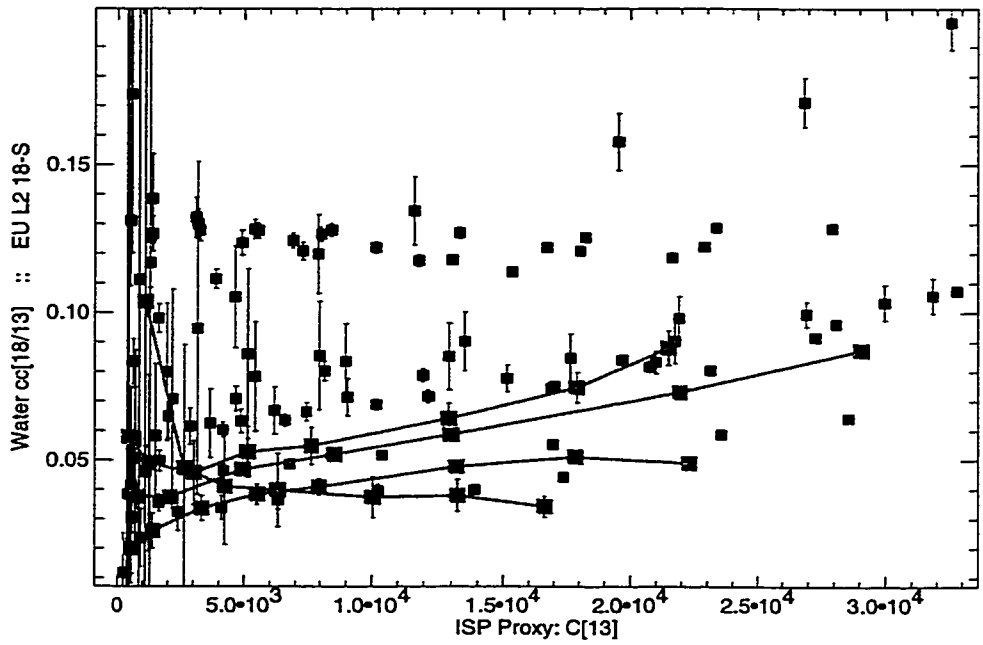

Figure 5.18 Water mole fraction bin S: $q_{H2O} = 4 \times 10^{-5}$.

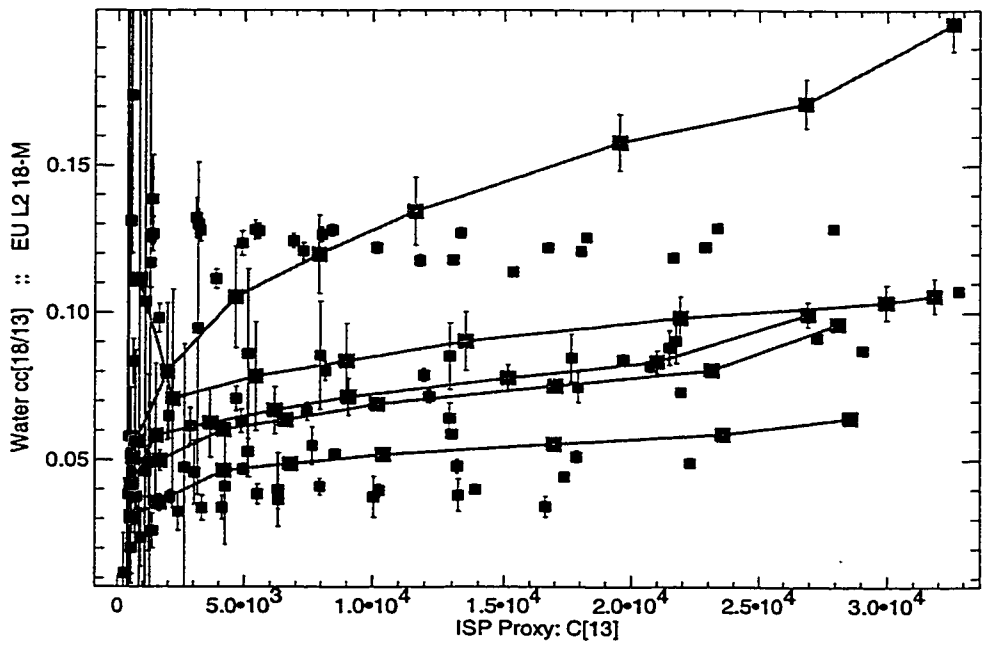

Figure 5.19 Water mole fraction bin M: $q_{H2O} = 7 \times 10^{-5}$.

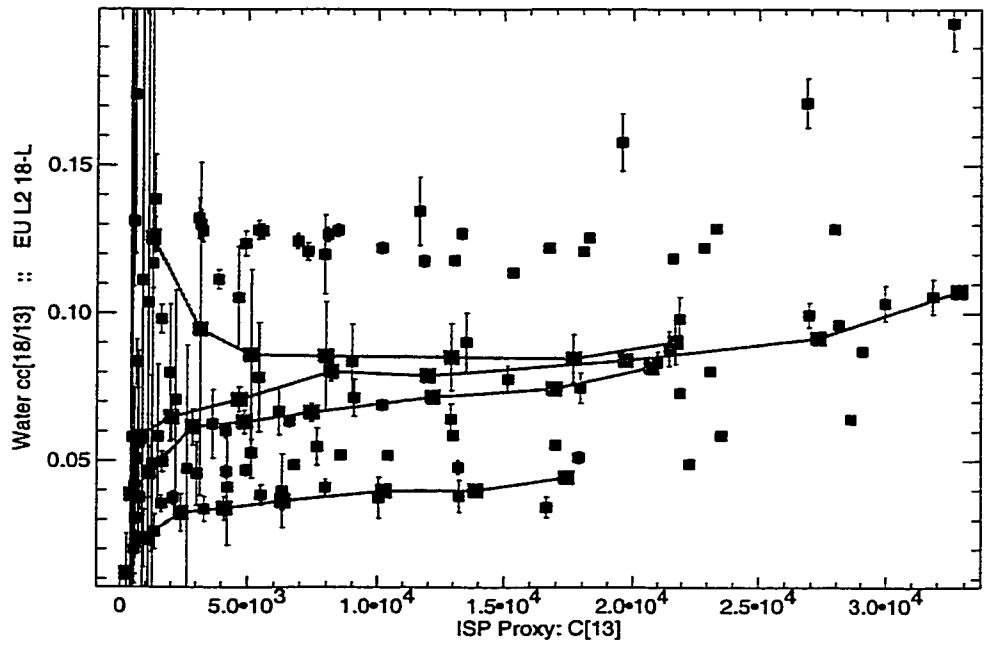

Figure 5.20 Water mole fraction bin L: $q_{H2O} = 1.2 \times 10^{-4}$.

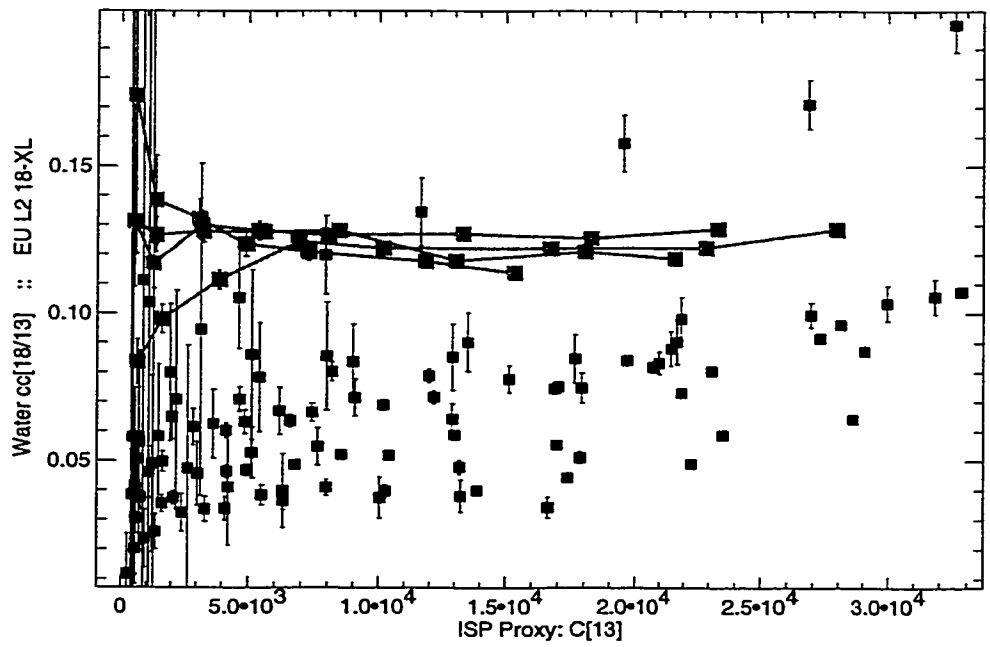

Figure 5.21 Water mole fraction bin XL: $q_{H2O} = 1 \times 10^{-3}$.

The relatively tight clustering of datapoints in figures 5.18 and 5.21 strongly suggest a correlation between water mole fraction and calibration constant value. The calibration

constant for the XL bin is about a factor of 2 larger than that for the S bin. However, bins M and L are closer to the water abundance at the DL2 portion of the probe descent. For bins M and L, the deviation from run to run is so great that only the slightest correlation with mole fraction is seen, and the sense is opposite to that between bins S and XL. The larger scatter within the M and L bins in fact makes the average values statistically identical.

The plotted error bars, calculated as described in Chapter 3 from known or estimated sources of error such as deadtime correction, mass interference, etc., are substantially smaller than the deviations in average cc from run to run, suggesting that as-yet unidentified factors have a large influence on the water calibration constant. This unknown influence is predominantly systematic within each run, since each unique run, connected by shaded lines, shows a similar basic shape or slope. However, from run to run, it is presumed that the unexplained errors act randomly.

To account for this unidentified influence on the water calibration constant, the calculation of uncertainty in the fitted calibration constant parameters is altered, as discussed at the end of Chapter 3. The standard formula for the variance of the mean of a set of datapoints is (Bevington p.71):

$$\sigma_\mu^2 = \frac{1}{\sum_i (1/\sigma_i^2)} \quad \left(= \frac{\bar{\sigma}^2}{N} \text{ when } \sigma_i = \bar{\sigma} \text{ for all } i \right) \qquad 5.3$$

This formula is applied when deriving calibration constants which are independent of ISP. When fitting calibration constants using the form $\mathrm{cc} = a\ \mathrm{ISP} + b$, uncertainties in the parameters a and b are given by the formulas (Bevington and Robinson 1992, pp104, 108-109):

$$\sigma_a^2 = \frac{1}{\Delta}\sum_i \frac{x_i^2}{\sigma_i^2}$$

$$\sigma_b^2 = \frac{1}{\Delta}\sum_i \frac{1}{\sigma_i^2}$$

$$\Delta = \begin{vmatrix} \sum_i \frac{1}{\sigma_i^2} & \sum_i \frac{x_i}{\sigma_i^2} \\ \sum_i \frac{x_i}{\sigma_i^2} & \sum_i \frac{x_i^2}{\sigma_i^2} \end{vmatrix} = \sum_i \frac{1}{\sigma_i^2} \sum_i \frac{x_i^2}{\sigma_i^2} - \left(\sum_i \frac{x_i}{\sigma_i^2}\right)^2 \qquad 5.4$$

These formulations apply to datapoint errors σ_i which are randomly distributed around their true values, so that repeated measurements reduce the uncertainty in the estimated fit parameters. This can be clearly seen in Equation 5.3, where the uncertainty in the mean is inversely proportional to the number of measurements (for the $\sigma_i = \bar{\sigma}$ case). Normally N is the number of datapoints, but for the water calibration constant in MIX97, using N = number of datapoints underestimates the error in the fitted calibration constant because it neglects the consistent deviation from run to run. A more appropriate treatment in this case is to consider each complete run to be a single measurement of the water calibration constant, so that N = number of complete runs.

A final statistical detail must be discussed before obtaining fits to water calibration constant data: the deviation from run to run seen in Figures 5.18 through 5.21 is considerably larger than the painstakingly calculated estimated uncertainties represented by the puny error bars. Thus the estimated errors should not be used to calculate the uncertainty in the fit parameters; instead we use the data itself to estimate a uniform uncertainty (adapted from Bevington p.106):

$$\bar{\sigma}^2 \approx s^2 = \frac{1}{N-m}\sum_i (cc_i - \hat{cc}(x_i))^2 , \qquad 5.5$$

where $\hat{cc}(x_i)$ is the fitted calibration constant, x_i is the ISP proxy, N is the number of degrees of freedom (normally the number of datapoints), and m is the number of parameters estimated from the data (1 for a calibration constant which is constant with ISP proxy, 2 for a calibration constant varying linearly with ISP proxy). In order to find a $\bar{\sigma}$ that characterizes the scatter from run to run, set N equal to number of separate runs.

One known systematic effect plaguing the MIX97 runs is the degradation of the detector, as evinced by the change in deadtime coefficient over time. Each run in the MIX97 suite was deadtime-corrected using a unique deadtime coefficient. Figure 5.22 shows the estimated deadtime coefficient for each run (points) along with the subjectively-determined uncertainty (error bars). Since deadtime coefficients are estimated using count saturation maxima, the reliability of the estimate of the deadtime coefficient is greatly decreased if the run does not near saturation. However, even with these uncertainties, the nearly linear increase in deadtime constant over time is clearly apparent in Figure 5.22. The three grey lines show values actually used to correct the data: the central line is the deadtime constant used, and the outer lines show the subjectively-estimated average uncertainty in the deadtime constant that was used to establish uncertainties in the final count ratios due to deadtime uncertainty. The deadtime correction discussed here applies to all the data in the MIX97 suite of calibration runs, and was thus also used in the derivation of ammonia and methane calibration constants.

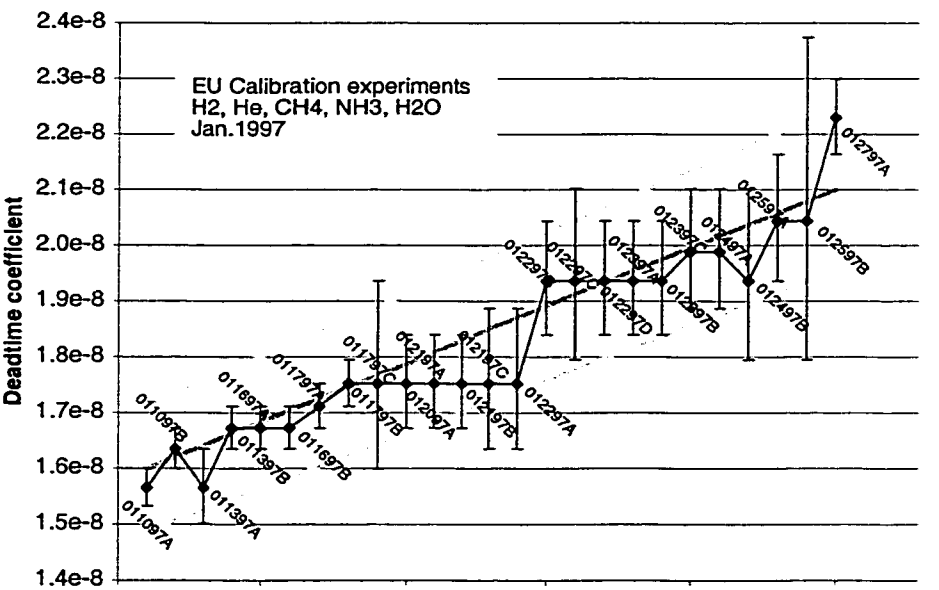

Figure 5.22 Change in EU deadtime "constant" over time.

Since the more moderate water mixing ratios in bins M and L more closely match the Jovian water abundance in the probe entry site at DL2 altitudes, I use data from those

two bins to obtain the water calibration constant. The resulting fit is shown in Figures 5.23 through 5.25, with pressure, C[13], and C[2] as the ISP proxies. Pressure has been scaled by the EU/FU ratio of leak conductances, and C[13] and C[2] have been converted to units of counts/IP, where the IP is set to 0.5 sec to match the probe data. In Chapter 6, reference will be made to all three fits shown below, and the water mixing ratios resulting from all three calibration constant fits will be compared and discussed.

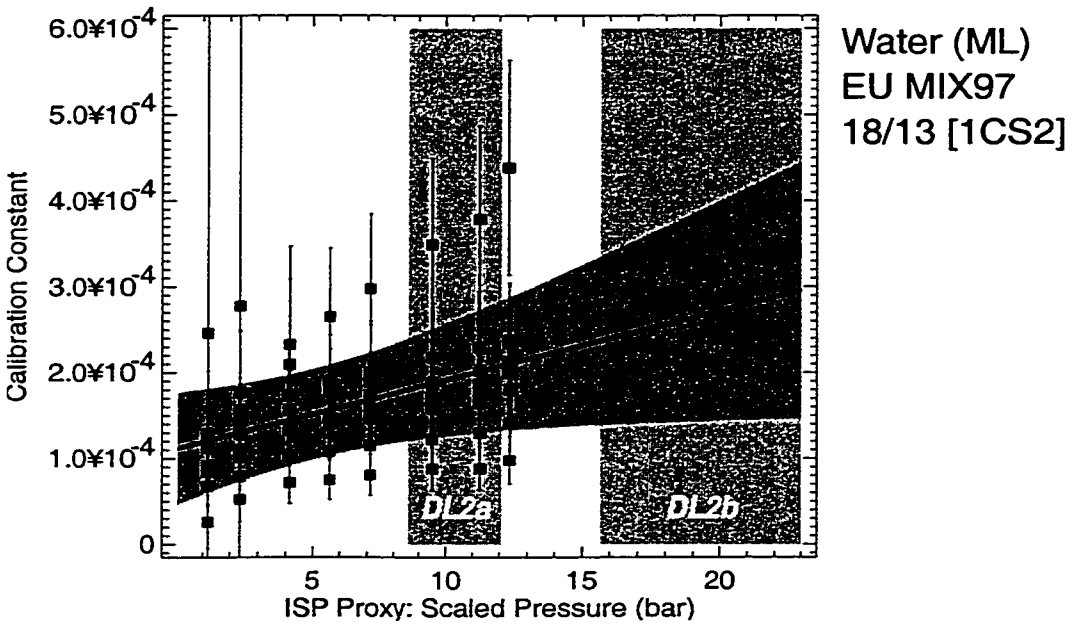

Figure 5.23 Water calibration constant.

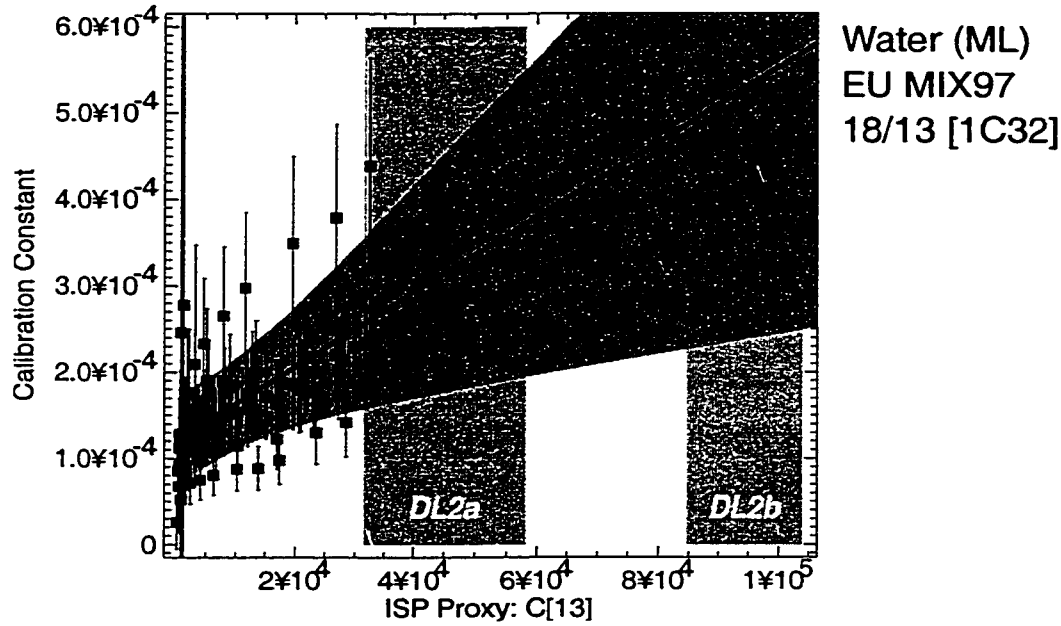

Figure 5.24 Water calibration constant.

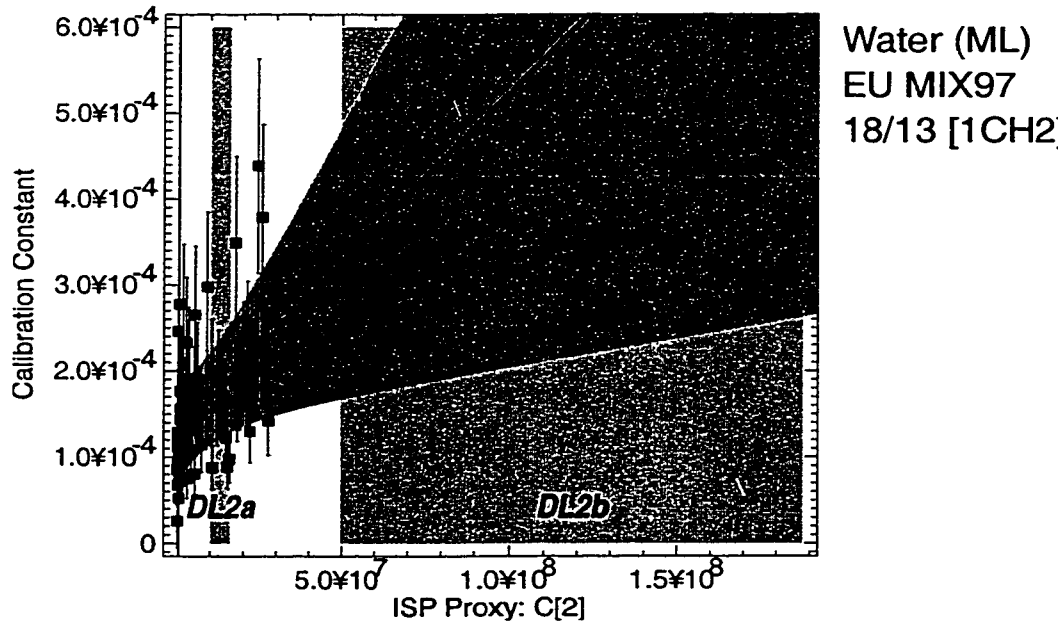

Figure 5.25 Water calibration constant.

NH_3 (Ammonia)

Ammonia calibration constants are available only for leak 2. Wall interactions inhibit the detection of ammonia using leak 1. Ammonia mixing ratio was derived for DL2a and published in Mahaffy et al. (1999). Neither the calibration constant nor the fit parameters used for that result were given in Mahaffy et al. (1999), but the ammonia abundance was quoted as $(3.5 \pm 1.5) \times$ solar, corresponding to a mixing ratio of $(7.7 \pm 3.3) \times 10^{-3}$ (using the Anders and Grevesse (1989) solar nitrogen abundance). The method used in Mahaffy et al. (1999) was to fit C[17] from DL2a ammonia using the model:

$$C[17] = \alpha \exp(-\beta t) + \gamma C[13] \qquad 5.6$$

This approach was justified by two 1999 EU experiments conducted by Mahaffy and Demick, in which the EU was first flooded with ammonia to emulate conditions in EC1, and then pumped back to vacuum conditions, similar to the BG2 portion of the descent sequence. Finally a calibration gas mixture containing either 3.08 or 1.07 $\times$ solar ammonia abundance was introduced to the EU, and NH_3 that had been adsorbed to the walls of the system during the EC1-simulation was desorbed over time through collisions with H_2 molecules, contributing a decaying component to the total C[17]. Using the definition of the calibration constant, for the case with no wall ammonia desorption ($\alpha = 0$ in Equation 5.6), γ can be recognized as:

$$\gamma = \frac{C[17]}{C[13]} = \frac{1}{cc_{17/13}^{NH_3}} \frac{n_{NH_3}}{n_{CH_4}} \qquad 5.7$$

Thus, fits of the form in Equation 5.6 can derive ammonia mixing ratios if the calibration constant is known (for GPMS data), or they can derive ammonia calibration constant if the mole fraction is known (for EU calibration data).

The MIX97 calibration set was previously described. Figures 5.26 through 5.29 show ammonia $cc_{17/13}^{NH3}$ as obtained from the MIX97 EU calibration experiments. The individual runs are grouped into four bins based on the ammonia mole fractions used. Values of ammonia mole fraction for each specific run are given in Table 4.3, and approximate ammonia mole fraction bin values are given in the figure captions. As with

water, the intermediate cal4 values are depicted instead of the actual calibration constants (see Equation 3.9).

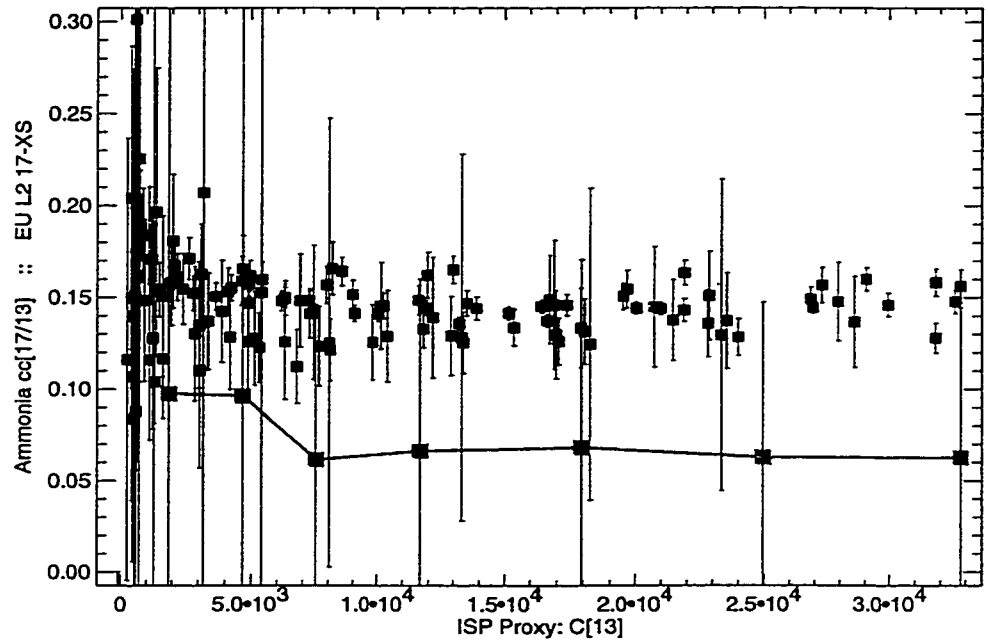

Figure 5.26 Ammonia mole fraction bin XS: $q_{NH3} = 1.0 \times 10^{-5}$.

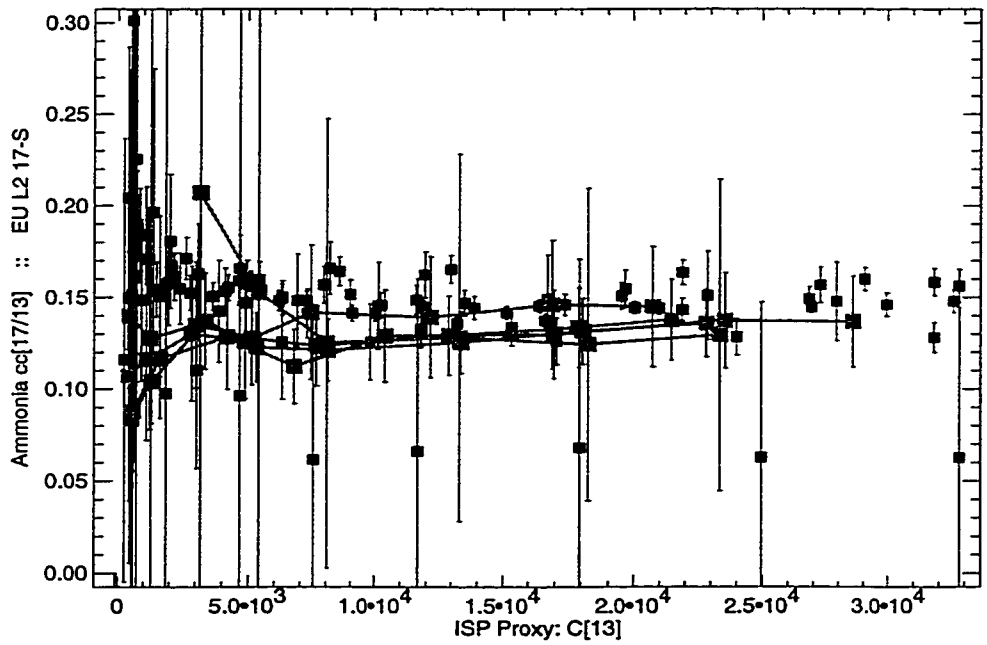

Figure 5.27 Ammonia mole fraction bin S: $q_{NH3} = 2.2 \times 10^{-4}$.

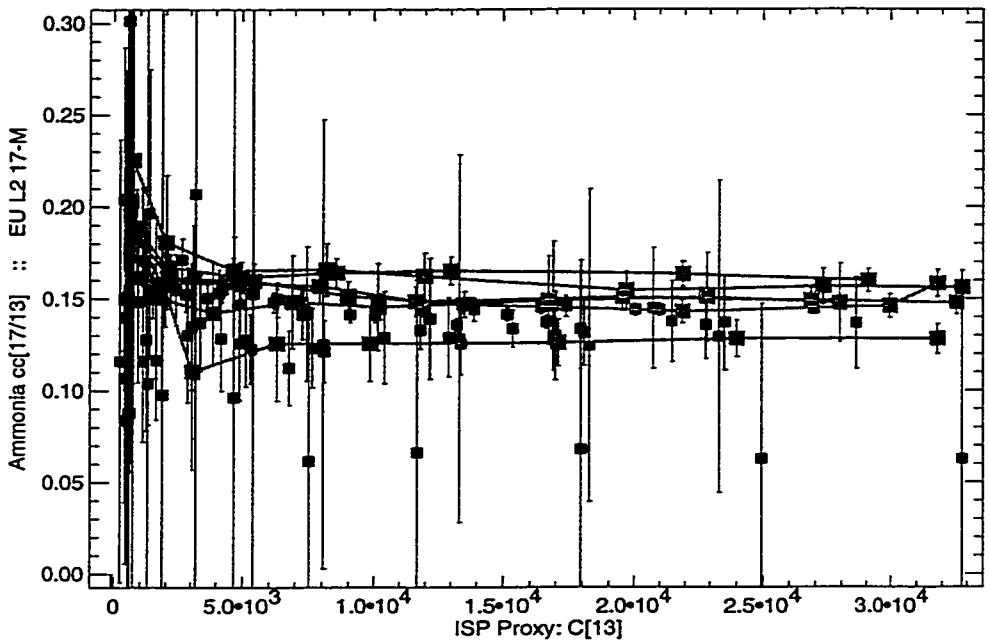

Figure 5.28 Ammonia mole fraction bin M: $q_{NH3} = 1.0 \times 10^{-3}$.

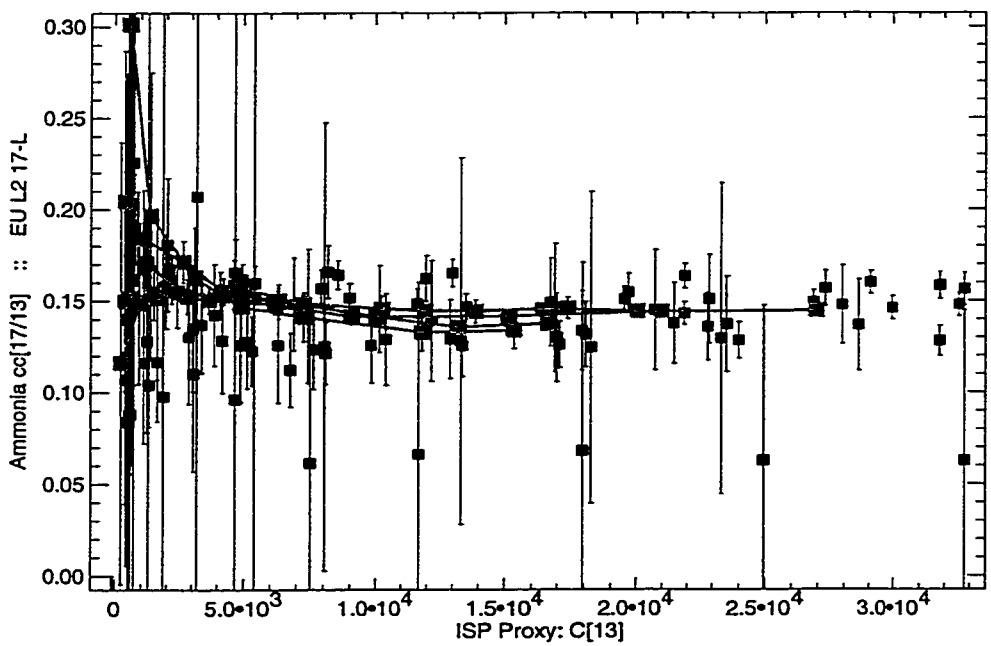

Figure 5.29 Ammonia mole fraction bin L: $q_{NH3} = 2.4 \times 10^{-4}$.

The four figures shown above give some indication that $cc_{17/13}^{NH3}$ has a dependence on ammonia mole fraction. Two of the bins, XS (containing only a single run) and L, used experimental gas mixtures with ammonia abundances considerably different from the conclusions of Folkner et al. (1998) that the NH_3 mole fraction is around 6×10^{-4}. Figures 5.26 through 5.29 show a general trend of increasing ammonia calibration constant with increasing ammonia mole fraction. This increase stops at bin L, since Figure 5.29 shows calibration constants essentially identical to those in bin M. A possible explanation for this behavior is the now familiar phenomenon of adsorption of ammonia onto the gas system walls: at low NH_3 mole fraction, there is a larger contribution from desorbed ammonia. In other words, when w_{NH_3} is small, $C[x]$ in Equation 3.9 is disproportionately larger due to the desorbed NH_3 from the gas system walls, leading to a smaller calibration constant overall. With increasing NH_3 mole fraction, the contribution from ammonia beamed directly into the mass spectrometer increasingly dominates the desorbed ammonia signal. If this explanation is accurate, then when ammonia mixing ratio becomes as large as the bin L mixing ratio, the desorbed contribution is not significant and changes in the ammonia calibration constant with ammonia mole fraction are no longer observed.

Figures 5.30 through 5.32 show fitted ammonia calibration constants; bin XS is neglected. Figures 5.30 and 5.31 show calibration constants used in Chapter 6 to obtain ammonia mixing ratios. Figure 5.32 is shown for comparison with Figure 5.31 to illustrate the lack of any statistically significant difference in calibration constant from bin M to bin L. Unlike the other abundance bins, bin L exhibited a variable calibration function at low ISP, but a simple constant fit is nevertheless shown in order to facilitate comparison with Figure 5.31. For both bin M and bin L, very low ISP points had a heavy influence on the fitted calibration constant, so datapoints taken at pressures less than 5 bar in those two bins were not considered in the fits, since those values of ISP did not pertain to the GPMS dataset.

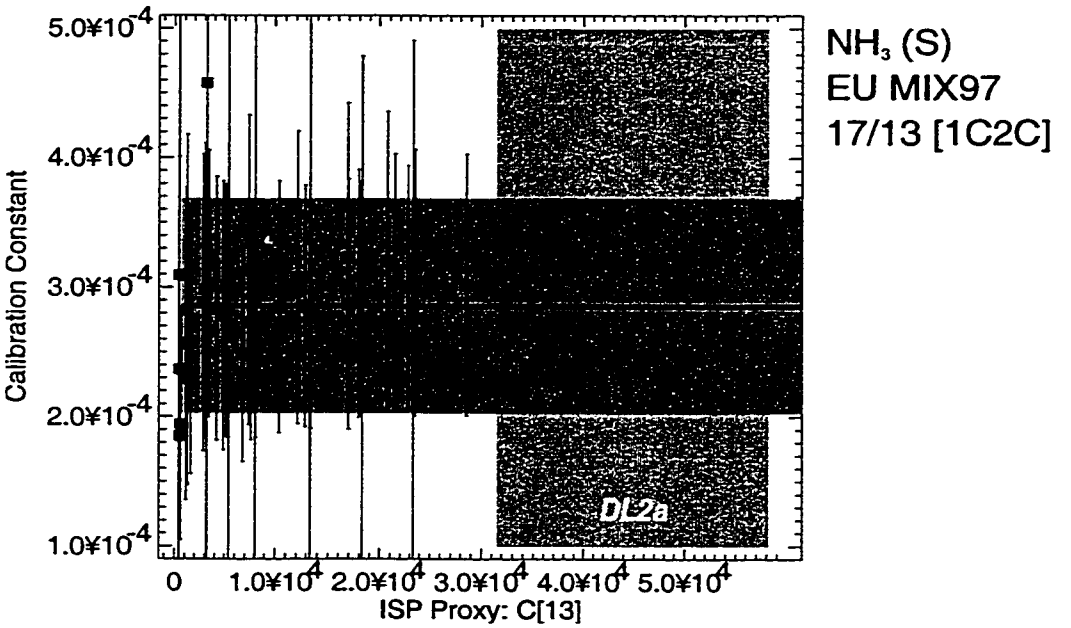

Figure 5.30 Ammonia calibration constant for mole fraction bin S: $q_{NH3} = 2.2 \times 10^{-4}$.

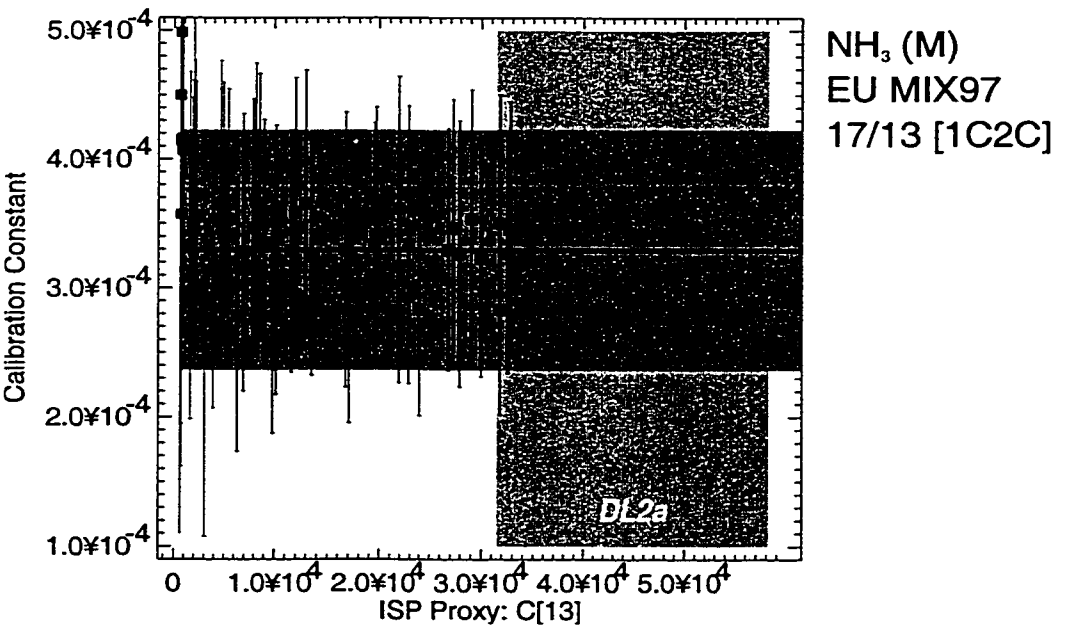

Figure 5.31 Ammonia calibration constant for mole fraction bin M: $q_{NH3} = 1.0 \times 10^{-3}$.

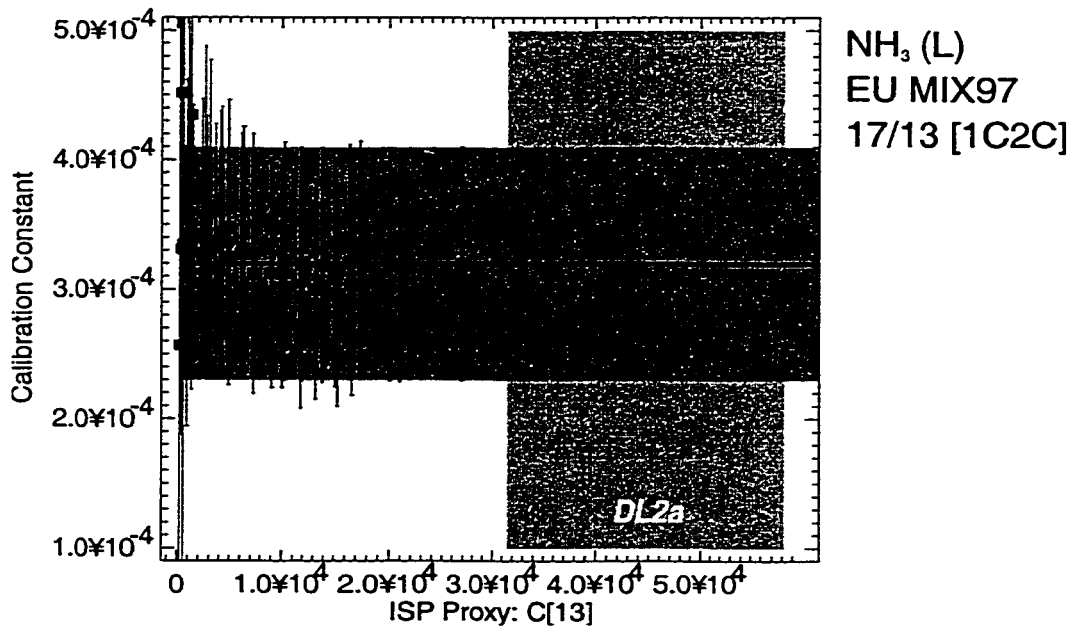

Figure 5.32 Ammonia calibration constant for mole fraction bin L: $q_{NH3} = 2.4 \times 10^{-4}$.

Further discussion of ammonia calibration studies will be given in Chapter 6, especially as concerns the exponential fit to desorbed ammonia from the mass spectrometer walls.

Summary

Calibration constants discussed in this chapter, which are used in the analysis presented in Chapter 6, are summarized in Table 5.10 below. Ranges are given for pressure-varying calibration constants, indicating the full variation of the calibration constants over the specified interval. Functional fit parameters are given in Table 5.11, but please note that evaluation of the parameters results in a quantity, cal4, which must then be multiplied by the mixing ratio of the appropriate reference gas to obtain the actual calibration constant. The covariance matrix for the fitted parameters is needed in order to calculate the uncertainties in the fitted calibration constants, but covariance matrices are omitted for simplicity. Uncertainties in the fitted parameters should be estimated directly from the figures presented in this chapter when the fitted calibration constant varies with ISP. Approximate

levels of calibration constant uncertainty are rounded to the nearest 5% and listed in Table 5.10 as a percentage of the lowest calibration constant in the range.

Table 5.10 Summary of calibration constants.

ID	Parent molecule	Count ratio	Leak	ISP proxy	Calibration constant	1-σ error	ν	Calibration data
1	C_2H_6	30/4	L2	–	0.069	15%	0.25	FU sequence 14
2	C_2H_6	30/4	L2	–	0.043	15%	0.33	FU sequence 20
3	C_2H_6	30/4	L2a	P	0.06–0.04	20%	0.50	EU 1996-06-17 C2H6
4	C_3H_8	29/4	L2	–	0.071	40%	0.00	FU sequence 14
5	C_3H_8	29/4	L2	–	0.053	25%	0.88	FU sequence 20
6	C_3H_8	29/4	L2a	P	0.13–0.16	15%	0.50	EU 1996-06-18 C3H8
7	C_3H_8	43/4	L2	–	0.23	10%	0.33	FU sequence 14
8	C_3H_8	43/4	L2a	P	0.4–0.5	20%	0.50	EU 1996-06-18 C3H8
9	C_4H_{10}	43/4	L2	–	0.07	15%	0.60	FU sequence 20
10	C_3H_6	41/4	L2	–	0.045	960%	0.00	FU sequence 16
11	C_3H_6	41/4	L2	–	0.116	25%	0.86	FU sequence 20
12	C_3H_6	42/4	L2	–	0.086	1060%	0.00	FU sequence 16
13	C_3H_6	42/4	L2	–	0.115	25%	0.86	FU sequence 20
14	C_2H_4	27/13	L2a	P	$6–7 \times 10^{-4}$	30%	0.60	EU 1998-11-16 C2H4
15	C_2H_4	27/13	L2a	C[13]	$9–14 \times 10^{-4}$	30%	0.60	EU 1998-11-16 C2H4
16	C_2H_2	26/4	L2	–	0.129	25%	0.90	FU sequence 20
17	N_2	28/13	L2	C[13]	$3–4 \times 10^{-5}$	30%	1.00	EU 1997-06-30 N2CH4
18	CH_4	16/4	L1	–	0.16–0.11*	–	–	EU 1997-01 MIX97
19	CH_4	16/4	L2	–	0.09–0.12*	–	–	EU 1997-01 MIX97
20	CH_4	16/4	L1	–	0.12–0.10*	–	–	EU 1998-11-16 C2H4
21	CH_4	16/4	L2	–	0.10*	–	–	EU 1998-11-16 C2H4
22	CH_4	16/4	L1	–	0.075*	–	–	EU 1997-06-30 N2CH4
23	CH_4	16/4	L2	–	0.075*	–	–	EU 1997-06-30 N2CH4
24	CH_4	16/4	L2	–	0.10–0.08*	–	–	EU 1996-11-29 H2S
25	CH_4	16/4	L1	–	0.0118	25%	†	(see Table 5.9)
26	CH_4	13/4	L1	–	0.452	15%	†	(see Table 5.9)
27	CH_4	16/4	L2	–	0.0110	30%	†	(see Table 5.9)
28	CH_4	13/4	L2	–	0.421	10%	†	(see Table 5.9)

Table 5.10 Summary of calibration constants.

ID	Parent molecule	Count ratio	Leak	ISP proxy	Calibration constant	1-σ error	ν	Calibration data
29	H_2S	34/4	L2	P	0.22–0.32	~15%	1.00	EU 1996-11-29 H2S
30	H_2S	34/13	L2	P	$8–6 \times 10^{-4}$	35%	1.00	EU 1996-11-29 H2S
31	H_2O	18/13	L2	P	$18–29 \times 10^{-5}$	30%	†	EU MIX97 (H_2O-ML)
32	H_2O	18/13	L2a	C[13]	$25–37 \times 10^{-5}$	60%	†	EU MIX97 (H_2O-ML)
33	H_2O	18/13	L2a	C[2]	$15-18 \times 10^{-5}$	45%	†	EU MIX97 (H_2O-ML)
34	NH_3	17/13	L2	–	2.9×10^{-4}	30%	†	EU MIX97 (NH_3-S)
35	NH_3	17/13	L2	–	3.3×10^{-4}	25%	†	EU MIX97 (NH_3-M)
36	NH_3	17/13	L2	–	3.2×10^{-4}	25%	†	EU MIX97 (NH_3-L)

ID number can be used to match entries in Tables 5.10 and 5.11.

* These methane values are approximate cal4 values (see Equation 3.9) and are included here solely to facilitate comparison of relative methane calibration constant values obtained from different calibration runs.

† Errors for these calibration constants have been attributed to unknown systematic effects, and estimated using the scatter between calibration values from run to run.

Table 5.11 Summary of calibration constant fit parameters.

ID	Parent molecule	Count ratio	Leak	ISP proxy	Fit order	Calibration constant expression
3	C_2H_6	30/4	L2a	P	2	$0.669 - 0.033\ P$
6	C_3H_8	29/4	L2a	P	2	$0.288 - 0.060\ P$
8	C_3H_8	43/4	L2a	P	2	$1.07 + 0.17\ P$
14	C_2H_4	27/13	L2a	P	2	$1.46 \times 10^{-3} + 3.03 \times 10^{-2}\ P$
15	C_2H_4	27/13	L2a	C[13]	2	$6.74 \times 10^{-2} + 1.00 \times 10^{-5}\ C[13]$
17	N_2	28/13	L2	C[13]	2	$1.14 \times 10^{-2} + 6.34 \times 10^{-8}\ C[13]$
29	H_2S	34/4	L2	P	2	$9.62 \times 10^{-1} + 4.63 \times 10^{-2}\ P$
30	H_2S	34/13	L2	P	2	$4.35 \times 10^{-1} - 8.01 \times 10^{-3}\ P$
31	H_2O	18/13	L2	P	2	$5.03 \times 10^{-2} + 3.63 \times 10^{-3}\ P$
32	H_2O	18/13	L2a	C[13]	2	$5.41 \times 10^{-2} + 1.96 \times 10^{-6}\ C[13]$
33	H_2O	18/13	L2a	C[2]	2	$5.82 \times 10^{-2} + 1.78 \times 10^{-9}\ C[2]$

ID number can be used to match entries in Tables 5.10 and 5.11.

Pressure is in bars, counts are in counts/IP, with 0.5-second integration period.

CHAPTER VI

GPMS results: isotopic ratios, mixing ratios, error analysis

Hydrocarbons: overview

Splitting patterns of the hydrocarbons are necessary to plan the sequence of analysis, so graphs of the relevant splitting patterns are presented in Figures 6.1 to 6.3. Unfortunately, splitting pattern graphs are best viewed in color. For readers of the black and white printed version of this work, note that the order of species in the legend is the same as the order of the splitting fraction bars for each mass. Bars have also been labeled whenever possible. Numerical values used to generate the graphs are available upon request. A few notes about the splitting pattern data are given after Figure 3, followed by an outline of the analysis sequence.

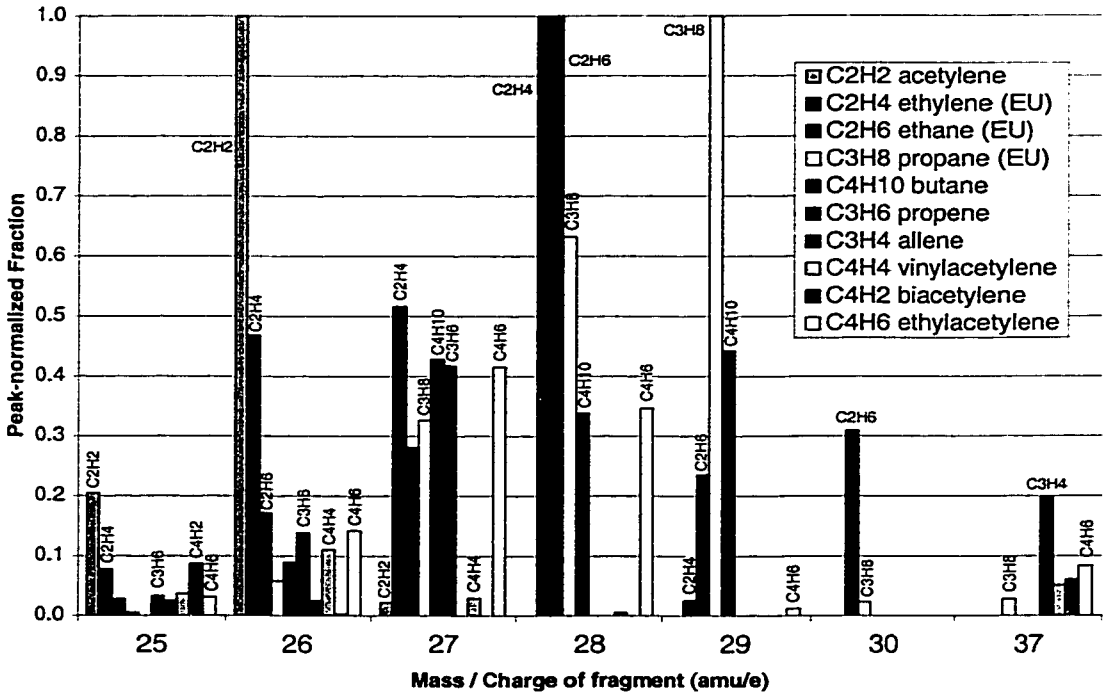

Figure 6.1 Hydrocarbon contributions to masses 25 through 37.

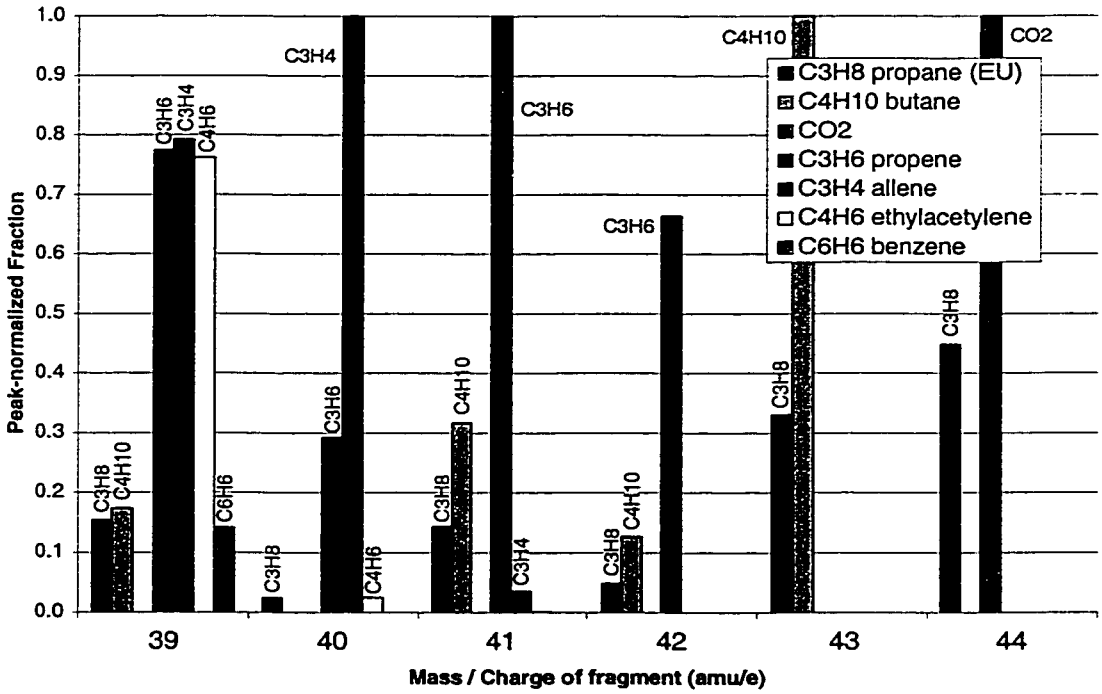

Figure 6.2 Hydrocarbon contributions to masses 38 through 44.

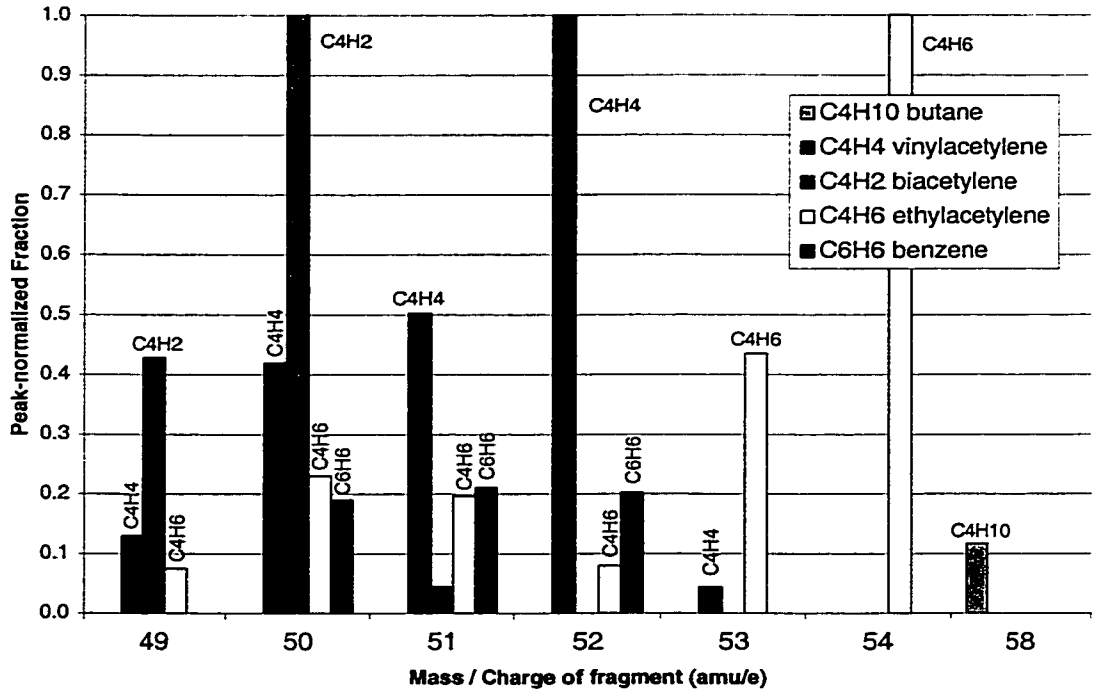

Figure 6.3 Hydrocarbon contributions to masses 49 through 58.

Splitting fractions shown in the three previous figures are taken from either the *NIST/EPA/NIH Mass Spectral Database* (1994; hereafter MS45) or from mass spectra taken with the experimental unit (EU), containing a pure sample of the gas in question. In some cases the values were the same from both sources, but in other cases discrepancies are observed between these sources, with differences up to 15%. In order to simplify error analysis, a constant uncertainty of 5% was assumed in all splitting fractions. This splitting fraction uncertainty is included in the error estimates both for the calibration constants presented in Chapter 5, whenever corrections to calibration data for mass interference were required, and for the mixing ratios obtained throughout this chapter, whenever subtractions are made based on known splitting fractions. Table 6.1 shows the source of the splitting fractions and calibration constants used in the hydrocarbon analysis.

Table 6.1 Hydrocarbon splitting pattern and calibration constant references.

Hydrocarbon	Name(s)	Split source	Calibration constant
C_2H_2	acetylene	NIST	FU sequence 20
C_2H_4	ethylene, ethene	EU C2H4_sp 981116	EU C2H4 981116
C_2H_6	ethane	EU C2H6 960617	EU C2H6 960617
C_3H_4	(multiple isomers)	NIST	(none)
C_3H_6	(multiple isomers)	NIST	FU sequence 20 (and 16)
C_3H_8	propane	EU C3H8_sp 960618	EU C3H8 960618
C_4H_{10}	butane	NIST	FU sequence 20
C_4H_2	biacetylene	NIST	(none)
C_4H_4	vinylacetylene	NIST	(none)
C_4H_6	(multiple isomers)	NIST	(none)
CO_2	carbon dioxide	EU CO2_sp 981119	(none)

Molecules with multiple isomers have distinct splitting patterns for each isomer. For C_3H_6, the splitting pattern for the propene isomer is shown in the bar charts, and the cyclopropane isomer is ignored, as will be discussed below. The bar charts show the splitting patterns of the allene isomer of C_3H_4, and the splitting values for key peaks of the other isomer, methylacetylene, will be discussed below. C_4H_6 has four isomers, with very similar splitting patterns. The analysis below will concentrate on C_4H_6 contributions to C[53] and C[54], where the largest deviations in splitting fractions for the four isomers are on the order of 10%. Thus only the ethylacetylene isomer is shown in the bar charts. Three isomers (including ethylacetylene) have their main peak at mass 54, while the fourth (divinyl) is at 82% of its peak value at mass 54. At mass 53, splitting fractions for the other isomers are all within 5–10% of the splitting fraction for ethylacetylene.

Based on the splitting patterns, I developed a gas-by-gas analysis strategy that avoided the need to simultaneously fit more than one mixing ratio to the data at any one time. Simultaneously deriving multiple mixing ratios requires solving systems of linear equations (a reasonable task), but the propagation of error rapidly becomes extremely tedious. A second advantage of this simpler gas-by-gas strategy is that it also simplifies

tracing the effects of making specific assumptions about individual gases. The GPMS data for the hydrocarbon analysis comes from the DL2a region, since that is the only part of the direct atmospheric data that gives a large enough signal at the masses in question (unlike DL1), yet is free of enrichment cell products (unlike DL2b). Some of the steps in the analysis strategy below may seem reasonable based on the splitting patterns, but will result in non-detections. The hydrocarbon analysis strategy is:

1. C[30] is easy to analyze. Just assume that all counts are due to ethane.
2. Using the results from C[30], subtract the ethane contribution to C[29]. Propane and butane mixing ratios can be obtained from C[29] and C[43], since there are two knowns (C[29] and C[43]) and two unknowns (the mixing ratios).
3. Derive butane separately, using C[58].
4. Derive C_4H_6 (all isomers) from C[54] and C[53].
5. Derive vinylacetylene from C[52].
6. Using results from steps 4 and 5, make vinylacetylene and C_4H_6 corrections to C[50]. Remainder is biacetylene.
7. Use C[41] and C[42] to determine C_3H_6. Subtract propane/butane contributions based on step 2 if necessary.
8. Now that C_3H_6, C_4H_6, propane, and butane are known, the only unknown hydrocarbon remaining at C[37], C[38], C[39], C[40] is C_3H_4. Substantial argon contributions are present at C[38] and C[40].
9. Use C[27] to derive the ethylene mixing ratio. Make corrections for contributions from ethane, propane/butane, C_3H_6, C_4H_6 as necessary.
10. Obtain acetylene from C[26]. Make corrections for contributions from ethane, propane/butane, C_3H_4, C_3H_6, C_4H_6 as necessary.
11. Subtract ethylene, ethane, propane, butane, C_4H_6 contributions from C[28] as necessary. Use remaining counts to obtain CO + N_2 mixing ratio.

Ethane

Ethane mixing ratio, derived from C[30]/C[4] count ratio, is shown in Figure 6.4. The pressure-dependent calibration constant used is shown in Figure 5.1, and ranged from 0.06–0.04 through the pressures seen in DL2a (about 8 to 12 bar). The average and standard deviation of the five mixing ratio datapoints in DL2a are $(9.2 \pm 4.8) \times 10^{-8}$,

assuming that all C[30] were ethane. Significant counts appear to be present in DL1 as well, but the values in Figure 6.4 were calculated without a calibration constant for DL1. Thus, ethane may be detected in 4–8 bar, but the corresponding mixing ratio is unknown. Given the uncertainties in the count ratios, the apparent change with pressure in DL1 may not be statistically significant.

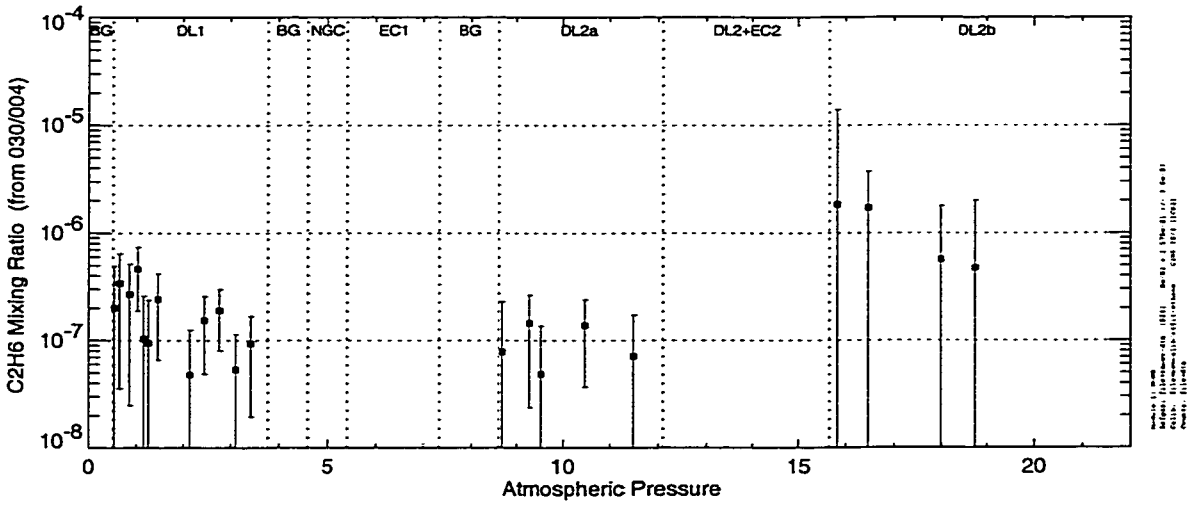

Figure 6.4 Jovian ethane mixing ratio.

Using the NIST Mass Spectrometry Database version 4.5 (MS45), searches were made to identify possible unexpected molecules that could be contributing to the GPMS signal at C[30]. The search method is described in detail here, using mass 30 as the search mass example, and applies to similar searches conducted in subsequent sections. The first search constraint is that the candidate molecule must have a splitting fraction at the search mass (in this case 30) with an abundance of at least 65% of the peak mass in its mass spectrum. For example, $C_4H_7NO_2$ has counts at mass 30 that are 71% of its peak mass of 29, so it would pass the first criteria. The second criteria is that the molecules be composed only of the elements H, C, O, N, S, P, Cl, and Br, since these are the only molecule-forming elements thought to be abundant enough to be detected by the mass spectrometer. Another constraint, that no more than three different heavy elements be present, was meant to eliminate unreasonably complex molecules present in MS45. Again, $C_4H_7NO_2$ passes the test since it contains three heavy elements. In addition, the number of atoms of each

element was restricted to be below the following maximum values: C < 7, O < 3, N < 3, S < 3, P < 5, Cl < 4 Br < 4. The final constraint is that no peaks be present at masses where the GPMS data show no significant counts. Table 6.2 shows the list of masses in the GPMS data used to constrain MS45 searches.

Table 6.2 MS45 search constraints.

Forbidden Mass/Charge Ratio				
21	48–49	83	97–127	138–150
23	51–65	85–93	133	
45–46	67–81	95	135	

Although the search would be greatly simplified by the condition that all forbidden masses be completely absent from the candidate spectra, such a requirement is overly strict. Therefore, two sensitivity levels (5% and 20%) were tested for the constraint that none of the forbidden masses in Table 6.2 be present in the spectra of candidate molecules. If the main peak of a candidate molecule's spectra is barely detectable by the GPMS, then smaller peaks will certainly be undetectable. For instance, assume that the peak of $C_4H_7NO_2$ at mass 30 is barely detectable by the GPMS. Then the 11% peak of $C_4H_7NO_2$ present at 71 would be below the level of detectability. Even though 71 is one of the "forbidden masses" because no significant counts are present at that mass in the GPMS data, in this case using it to rule out the candidate molecule $C_4H_7NO_2$ would be premature. In order to quantify this dilemma I test two splitting fraction sensitivity levels, 5% and 20%. Thus at the 5% sensitivity level, the 11% peak of $C_4H_7NO_2$ present at mass 71 would eliminate the molecule from consideration, but at the 20% sensitivity level the molecule would still qualify.

Many candidate molecules were identified with contributions to mass 30. At the 20% sensitivity level, 32 candidate molecules were identified, with glycine ($C_2H_5NO_2$) and 19 others surviving at the 5% splitting fraction sensitivity level. Of these, the simplest are methylamine (CH_5N) and nitric oxide (NO). The other candidate molecules (with the

exception of ClNO) were more complex hydrocarbons with attached N, N_2, NO, or NO_2. The following analysis of the GPMS dataset will presume that all counts at C[30] can be attributed to ethane, since it has already been observed in Jupiter's atmosphere. However, on purely scientific grounds, the more complex candidate molecules (however unlikely) cannot be discounted based on the mass spectrometer data alone.

Propane and butane from C[29] and C[43]

From the splitting patterns in Figures 6.1 and 6.2 it can be seen that butane and propane have strong peaks at C[29] and C[43], with hydrocarbon interference from only ethane at C[29], so I attempt an analysis of GPMS C[29]/C[43] ratio in DL2a. The predicted C[29]/C[43] is 0.442 for pure butane, or 3.032 for pure propane. The observed CR[29/43] (see Figure 6.5), corrected for the ethane mixing ratio found in step 1 ($9.2 \pm 4.8 \times 10^{-8}$), is higher than either of these predicted ratios. The C[29]/C[43] ratio in DL2a after ethane correction is 4.4 ± 1.7. Considering the uncertainty, this ratio is consistent with the value expected for pure propane, but cannot be reconciled with pure butane. If the correction to C[29] from ethane is ignored, the DL2a C[29]/C[43] ratio is even more extreme: 6.3 ± 2.1.

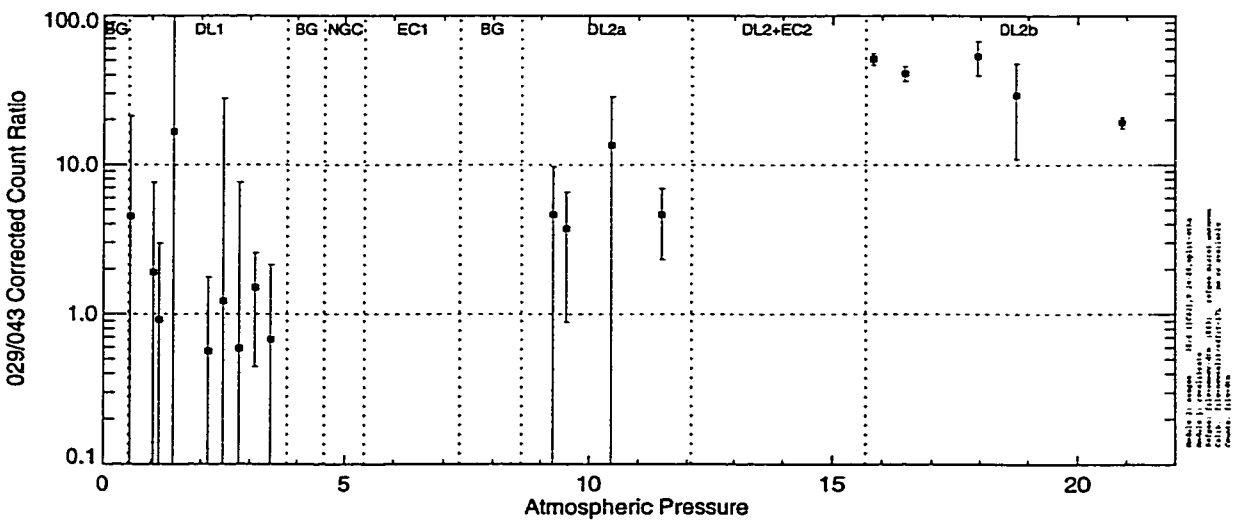

Figure 6.5 C[29]/C[43] count ratio.

Although the C[29]/C[43] ratio would imply that butane is absent from the GPMS data, I look at a limiting case where I assume that all C[43] is butane (Figure 6.6). This is then a generous upper limit for butane. The average of the seven DL2a butane mixing ratio datapoints is $(4.4 \pm 1.7) \times 10^{-8}$, and the average of the last 4 points is $(6.4 \pm 2.9) \times 10^{-8}$. So it should be safe to say that the upper limit on butane is 6×10^{-8}. Butane mixing ratios were obtained using a calibration constant derived from FU calibration runs with a mixture of nine hydrocarbons (sequence 20; see Table 4.1). Butane counts in the calibration run were corrected for the effects of ethane and propane, and the calibration constant used was 0.0704 ± 0.0097 (see Table 5.10 and the discussion in Chapter 5).

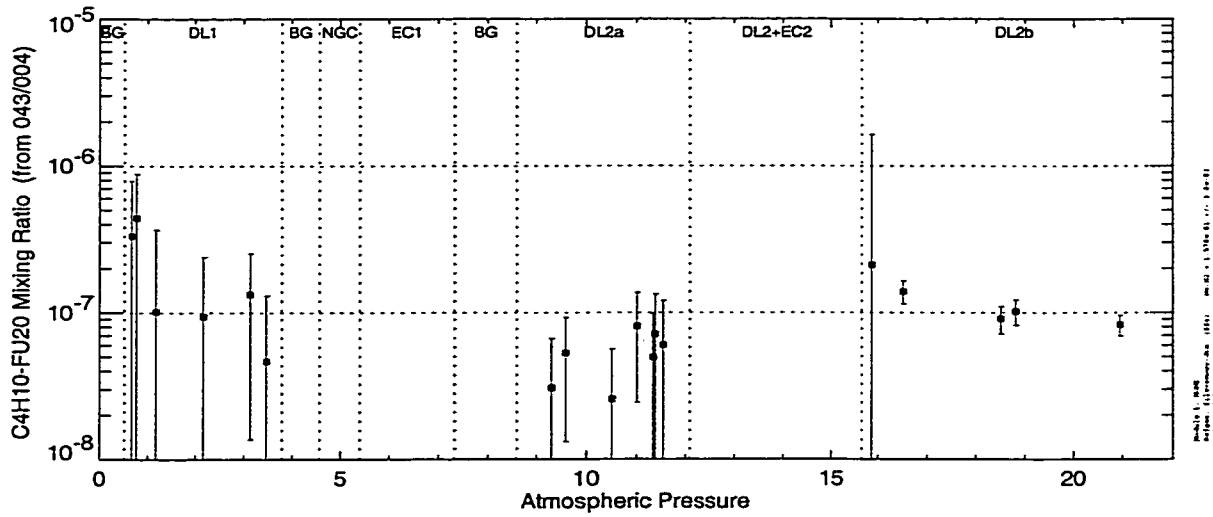

Figure 6.6 Jovian butane mixing ratio (upper limit).

Now making the opposite assumption, that all the counts at 43 are propane, I obtain the propane mixing ratio, plotted as squares in Figure 6.7. The calibration constant is fully described in Chapter 5, and also appears on line 8 of Table 5.10. The propane mixing ratio seems to increase with depth in DL2a, with central values ranging from 2 to 6×10^{-7}. Technically these mixing ratios should be considered an upper limit, since they ignore the possibility of butane contribution to C[43]. However, in light of the difference between the observed C[43]/C[29] ratio and the expected ratios based on propane and butane splitting patterns, any contribution from butane to C[43] is at most 10% of the amount of C[43] due to propane, which is well within the uncertainty in the mixing ratio itself. Propane mixing

ratio obtained from CR[29/4] is also shown in Figure 6.7 (triangles), using the calibration constant described in Chapter 5 and summarized in line 6 of Table 5.10. Counts at mass 29 have been corrected for ethane, assuming an ethane abundance of $(9.2 \pm 4.8) \times 10^{-8}$ as described above. The actual correction for mass interference is done by solving Equation 3.2 for C[x],

$$C[x] = C[ref]\,\frac{w_x}{cc_{x/ref}} \qquad 6.1$$

where in this case x refers to the parent molecule ethane at the parent mass 30. Then the parent mass counts can be generated for any step where the reference gas counts are known, based on the calibration constant and the assumed mixing ratio. Knowledge of the mass splitting fraction of the parent molecule then allows calculation of the child fragment interference contribution (at mass 29 in this case). A specific subroutine then "kidnaps" the counts which can be attributed to the interfering parent mass. Specifically, the ethane contribution to C[29] would be calculated by:

$$C[29] = C[4]\,\frac{w_{\text{ethane}}}{cc^{\text{ethane}}_{30/4}}\left(\frac{C[29]}{C[30]}\right)\Bigg|_{\text{lab. ethane}} \qquad 6.2$$

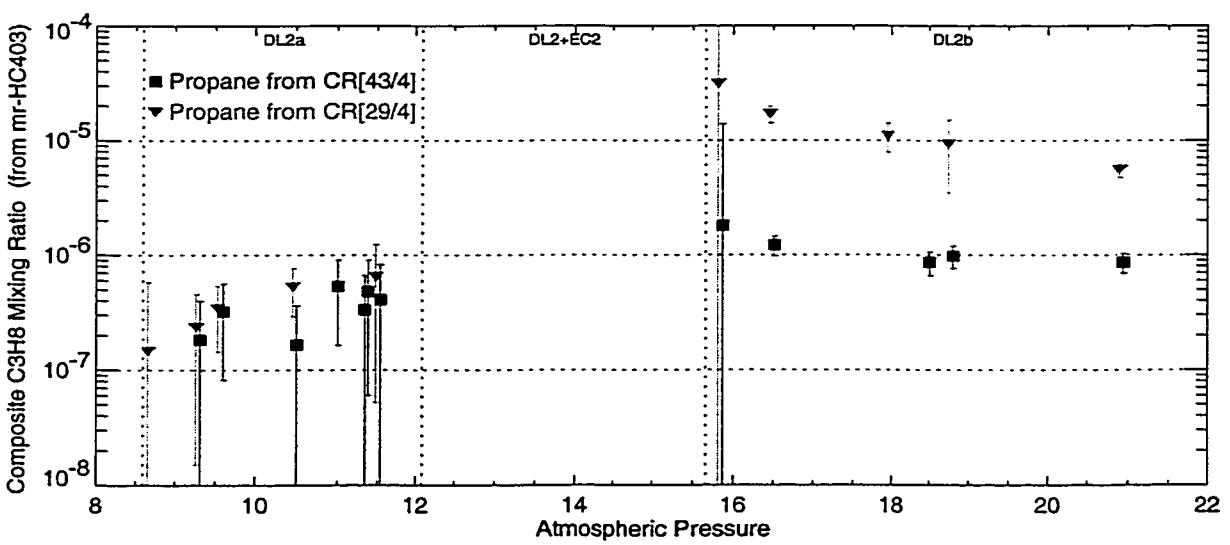

Figure 6.7 Jovian propane mixing ratio from CR[43/4] (squares) and CR[29/4] (triangles).

Both CR[43/4] and CR[29/4] suggest that propane increases with depth; the average of the first five DL2a points in Figure 6.7 is $(2.6 \pm 1.1) \times 10^{-7}$, and the average of the last five DL2a points is $(4.5 \pm 1.8) \times 10^{-7}$. The result based on C[29] is in very good agreement with the mixing ratios obtained by assuming that all the C[43] are due to propane, providing more evidence that no butane is present. Although the data suggest that propane increases over DL2a, the large uncertainty in the late DL2a mixing ratio render any such conclusions statistically suspect. The 1-σ lower bound of the late DL2a propane mixing ratio is $(4.5 - 1.8 = 2.7) \times 10^{-7}$, quite close to the central value of the early DL2a result of $(2.6 \pm 1.1) \times 10^{-7}$. Therefore the most statistically justified approach would be to simply report the averaged value of $(3.13 \pm 0.78) \times 10^{-7}$ for the DL2a propane mixing ratio. However, the effect of assuming minimum and maximum propane values for DL2a propane corrections to other masses will still be examined for the mixing ratios obtained in subsequent sections.

Many candidate molecules were identified with contributions to masses 29 and 43, using the search strategy outlined above in the ethane section. At mass 43, 73 candidate molecules were identified at the 20% sensitivity level. MS45 contains entries for many species which feature a main peak at mass 43, followed by secondary peaks with much smaller abundances. Frequently the second peak was less than 20% of the main peak, and all such molecules were considered matches in the search. When restrictions were increased for the 5% sensitivity level search, only one molecule passed: $CH_4N_2O_2$ (hydroxyurea). For mass 29, 16 candidate molecules were identified at the 20% sensitivity level, dropping to 10 molecules at the 5% sensitivity level. Of these, the simplest are CH_2O (formaldehyde), CH_4O (methyl alcohol), C_2H_4O (two isomers), and C_2H_3NO. However, as previously discussed, the observed C[29]/C[43] ratio is too large, based on the assumption that propane is the major contributor to C[29] and C[43] in the GPMS data. Therefore the presence of any of the mass 29 candidate molecules would help to explain the anomalous C[29]/C[43] ratio, while mass 43 candidate molecules would increase the discrepancy between the observed and predicted (based on the propane splitting fraction) C[29]/C[43] ratio.

Butane from C[58]

Not enough counts are present at C[58] to perform a statistically meaningful analysis. This can be seen from the plot of C[58] in Appendix A, where the shaded areas indicate the 1-σ bounds on the background correction. An upper limit can be obtained if we assume that C[58] at step 3703 is an accurate measurement of butane counts. The point at step 3703 (at 9.37 bar) is the first of the two mixing ratio datapoints in Figure 6.8, and is the only instance of C[58] being significantly above the noise level (not including enrichment cell data). The mixing ratio upper limit from step 3703 is $(5.1 \pm 4.3) \times 10^{-7}$. However, from previous discussion butane derived from C[43], it is clear this value is unrealistically high; if a butane mixing ratio of 5.1×10^{-7} holds, then the butane C[58]/ C[43] splitting fraction of 12% would require counts at C[43] to be an order of magnitude higher than observed.

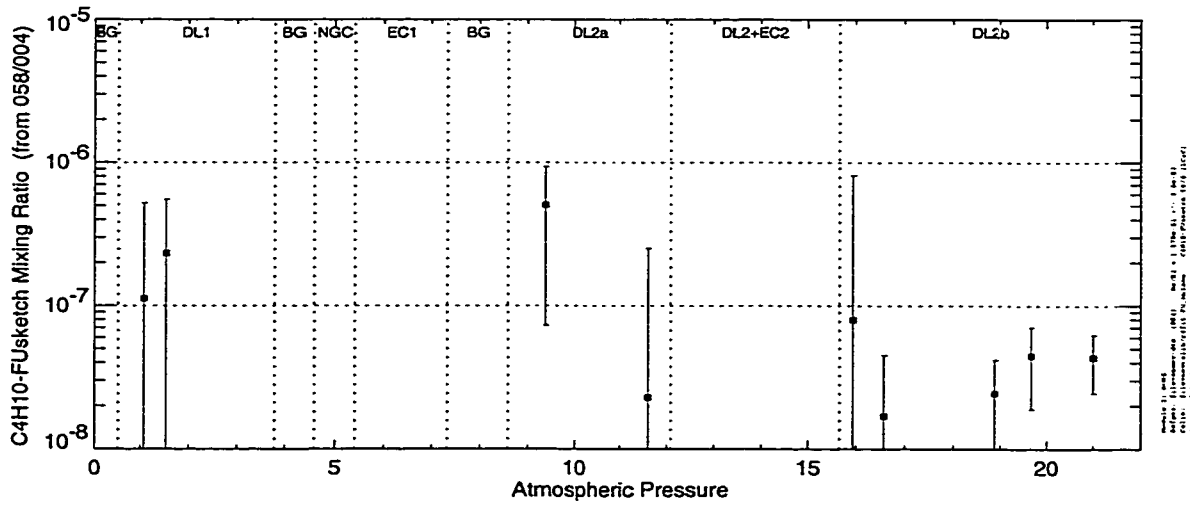

Figure 6.8 Jovian butane mixing ratio derived from C[58]/C[4].

C_4H_6 from C[54] and C[53]

From Appendix A, it is clear that there are no useful counts at mass 54, which is the main peak of three isomers of C_4H_6 (methylallene, crotonolene, ethylacetylene), and 83% of the main peak of the other isomer (divinyl). If no counts are present at the main peak,

then we can safely expect zero contribution to C_4H_6 peaks at other masses. No calibration constant for C_4H_6 is available, so even the calculation of an upper limit is not possible.

Vinylacetylene (C_4H_4) from C[52]

Again, no significant counts are present at this mass. No calibration constant is available to establish an upper limit.

Biacetylene (C_4H_2) from C[50]

There is evidence of a trace signature at C[50] (see the plot of C[50] in Appendix A). The background correction used for the DL2 region is based on C[50] measurements in the BG2 region, and has the value of 0.67 ± 0.58 counts. For DL1, the BG1-based background correction is 1.50 ± 0.71 counts. From the plot it appears that three points, at steps 3523, 3775, and 4023, are above the 1-σ background level, with count rates of 2, 2, and 4 respectively. However, the choice of background corrections is somewhat subjective, and for a mass such as 50 with very low counting rates, the difference between derived background corrections is largely due to statistical fluctuation. If the DL2a data are compared to the BG1 background correction, only the datapoint at step 4023 is greater than the BG1 + 1σ correction of 2.21 counts. The conclusion of this analysis is that there is only one C[50] measurement that is clearly above noise levels, with a background-corrected value of between 1 and 3 counts, providing extremely tenuous evidence of biacetylene on Jupiter at the 10.5 bar level. Using the butane calibration constant based on the assumption that C_4H_2 ionization and pumping characteristics are identical to those of butane would result in a C_4H_2 upper limit of on the order of 10 ppb.

C_3H_6 from C[41] and C[42]

Figure 6.9 shows the C_3H_6 mixing ratio derived from C[41] (squares) and from C[42] (triangles). In both cases, propane subtractions were made by assuming that all counts at mass 43 were due to propane, using the propane splitting fractions determined from EU

experiment C3H8_sp: C[41]/C[43] = 0.433 and C[42]/C[43] = 0.146 (see Figure 6.2). The calibration constant for C_3H_6 was derived from FU calibration sequence 20, and is extensively discussed in Chapter 5 and summarized in Table 5.10 (lines 11 and 13). The C_3H_6 in the calibration experiment was the isomer propene (a.k.a. propylene); cyclopropane was not measured.

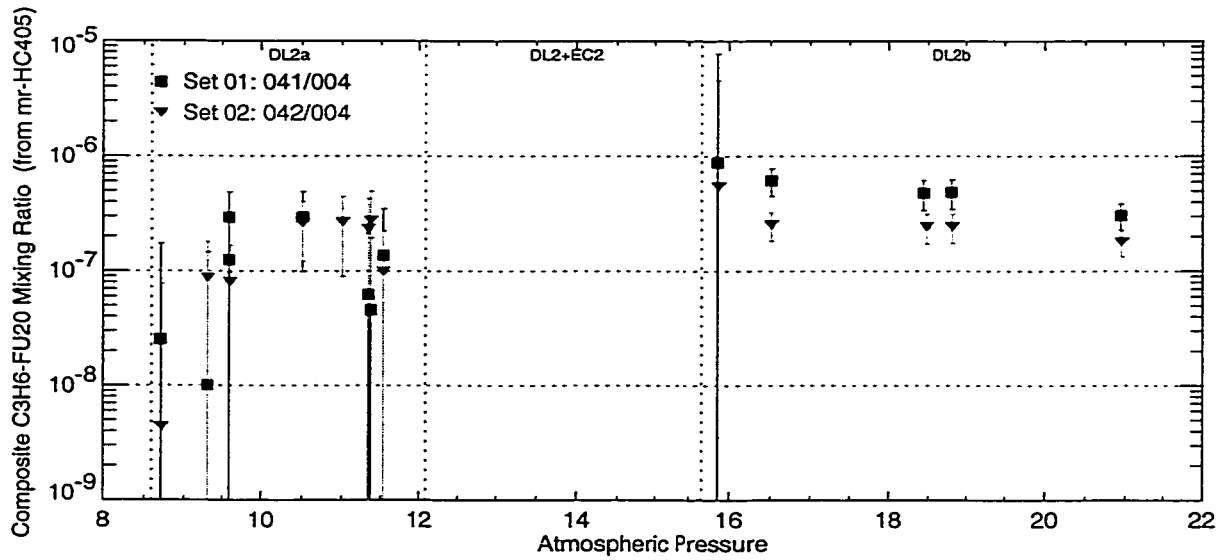

Figure 6.9 Jovian C_3H_6 mixing ratio (corrected for propane) derived from C[41]/C[4] (squares), and from C[42]/C[4] (triangles).

Given the large uncertainties of the C_3H_6 mixing ratio datapoints, there is no statistically sound evidence of variation with pressure in DL2a, so average values are obtained using all available points. The resulting mixing ratios are $(9.8 \pm 5.7) \times 10^{-8}$ from C[41]/C[4] and $(9.8 \pm 4.0) \times 10^{-8}$ from C[42]/C[4]. The two results are in excellent agreement with each other, so future steps needing corrections to remove C_3H_6 will use the mixing ratio obtained from the combined CR[41/4] + CR[42/4] average of $(9.8 \pm 3.3) \times 10^{-8}$. Other candidates are C_2H_3N, $C_3H_7NO_2$, and C_4H_7N at C[41], and C_2H_2O, C_2H_5N, $C_3H_4O_2$, and $C_4H_8O_2$ at C[42], based on the criteria described in the ethane section at the 5% sensitivity level.

C_3H_4 from C[37], C[38], C[39], C[40]

Calibration constants for this gas are unknown, but a look at the counts at the mass numbers in question reveals significant count levels. In order to determine if these counts are from Jovian C_3H_4, I calculate the C[37,38,39,40]/C[13] ratios to see if they are consistent with the splitting pattern of C_3H_4 as given in MS45.

Argon has substantial peaks at mass 38 and 40 from the isotopes ^{38}Ar and ^{40}Ar. Compensation for the argon contribution must be made before C[38] and C[40] are compared to counting rates expected for C_3H_4. The argon mass spectrum, unlike molecular splitting patterns, must be determined from the GPMS dataset instead of laboratory experiments, since there is no guarantee that argon isotopic ratios are identical on Jupiter and the Earth. In order to determine the argon mass spectrum, the ratios C[38]/C[36] and C[40]/C[36] are examined in the NGC experiment, where all other contributions to C[38] and C[40] other than those from argon should be zero. Figures 6.10 and 6.11 show the argon count ratios, and the average NGC values are 0.1113 ± 0.0017 for C[38]/C[36] and 0.01130 ± 0.00064 for C[40]/C[36]. For the CR[40/36] average, the anomalously low first NGC point was dropped.

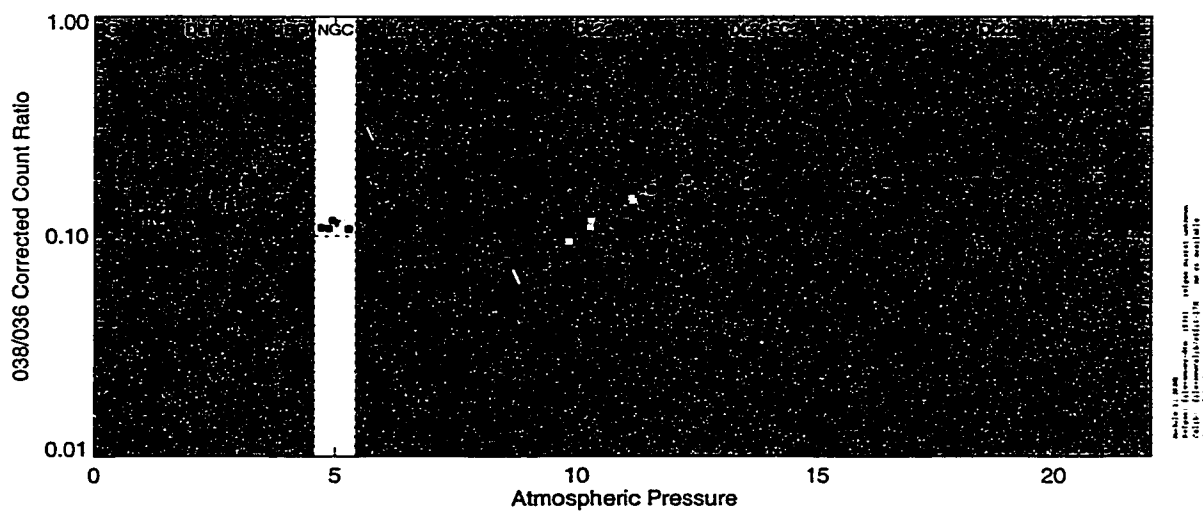

Figure 6.10 C[38]/C[36] ratio in the NGC region.

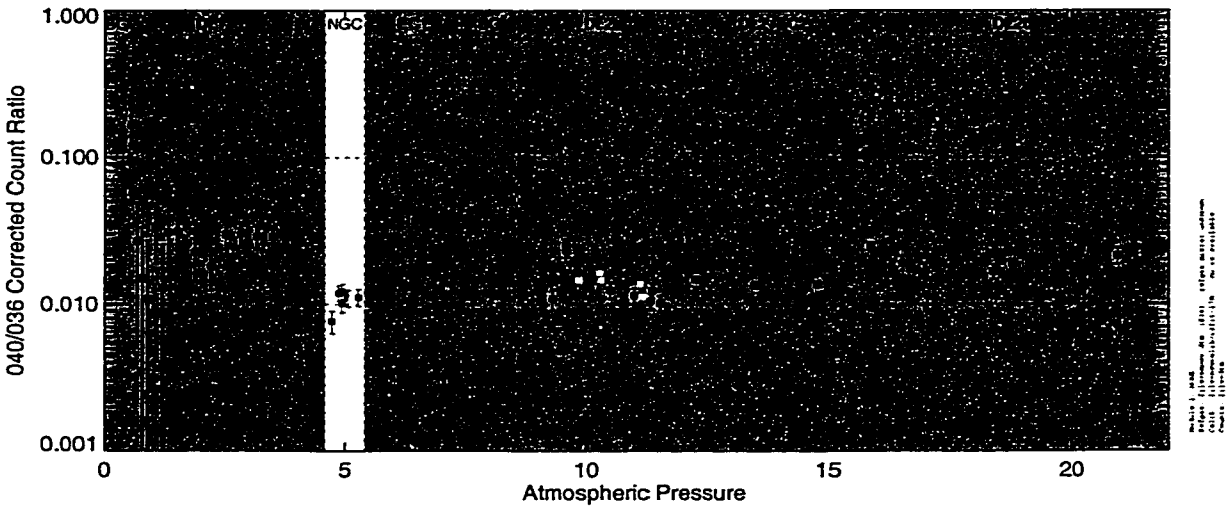

Figure 6.11 C[40]/C[36] ratio in the NGC region.

From Figures 6.1 and 6.1, it would seem that the best chance to distinguish between isomers of C_3H_4 based on their splitting patterns would be at C[37] and C[38]. For methylacetylene, the C[37]/C[38] ratio should be 0.69, whereas for allene it should be 0.80. Unfortunately, even after an argon correction (using C[38]/C[36] = 11.1%), the C[37]/C[38] ratio is 0.0187 ± 0.0050 based on all DL2a points, or 0.0280 ± 0.0069 based on the cluster of three points at the end of DL2a (see Figure 6.12). These numbers are far too low to be consistent with either isomer of C_3H_4, suggesting either that the argon contribution to C[38] is greater than the 11.1% derived above, or C_3H_4 is not detectable in the GPMS data.

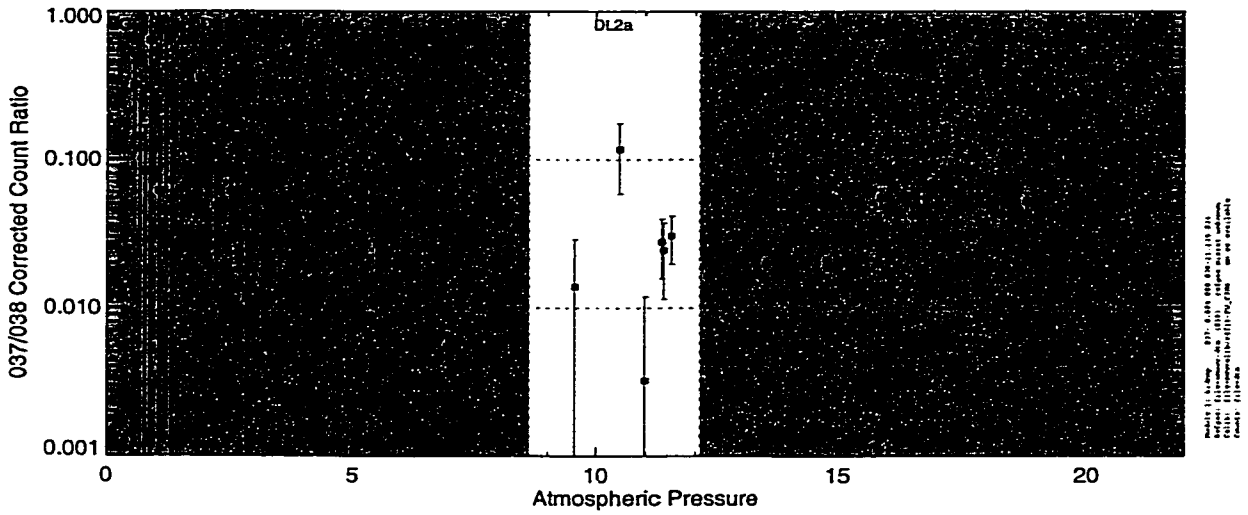

Figure 6.12 C[37]/C[38] count ratio, corrected for argon contribution.

Despite the evidence against the presence of C_3H_4 provided by the C[37]/C[38] in Figure 6.12, I continue with the analysis of the four remaining major peaks of C_3H_4. Both C[38] and C[40] require argon contributions (11.1% and 1.13% respectively of the counts at mass 36; see Figures 6.10 and 6.11). Both C[39] and C[40] require corrections for C_3H_6, with C[39] additionally requiring a correction for propane. Figure 6.13 shows the C[37]/C[13] ratio, which requires no corrections. Figure 6.14 shows C[38]/C[13] with argon correction. Figure 6.15 shows C[39]/C[13] with the standard correction for C_3H_6 of $(9.3 \pm 3.3) \times 10^{-8}$, and a correction for a propane mixing ratio of $(2.6 \pm 1.3) \times 10^{-7}$, which corresponds to the propane in the early part of DL2a. Figure 6.16 shows C[39]/C[13] with correction for C_3H_6, and a correction for a propane mixing ratio of $(4.5 \pm 1.8) \times 10^{-7}$, which corresponds to the propane in the later part of DL2a. Finally, Figure 6.17 shows C[40]/C[13], with C_3H_6 and argon corrections.

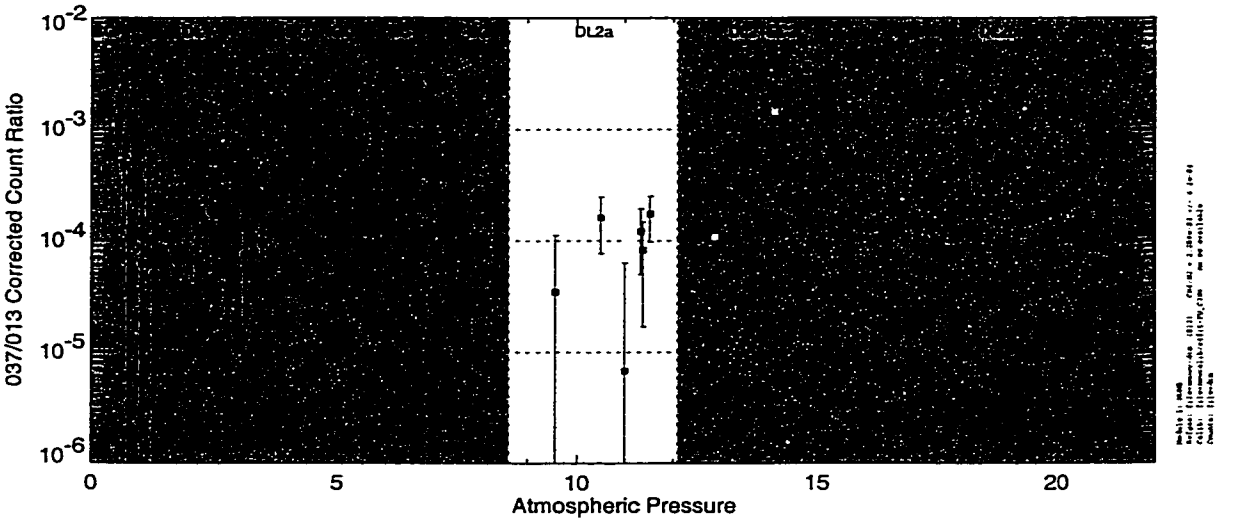

Figure 6.13 Count ratio C[37]/C[13].

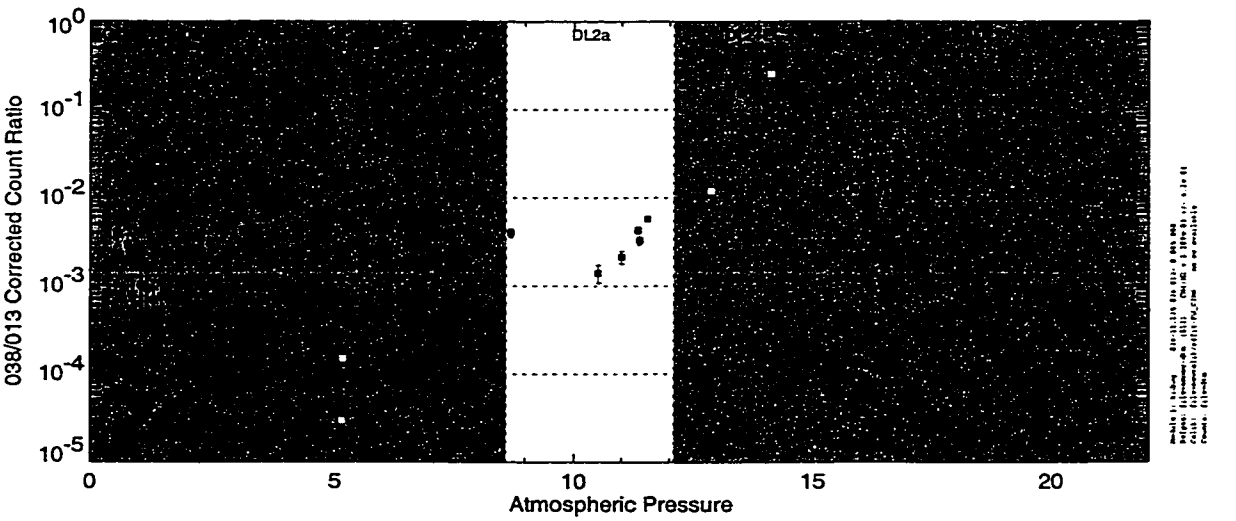

Figure 6.14 Count ratio C[38]/C[13], corrected for argon.

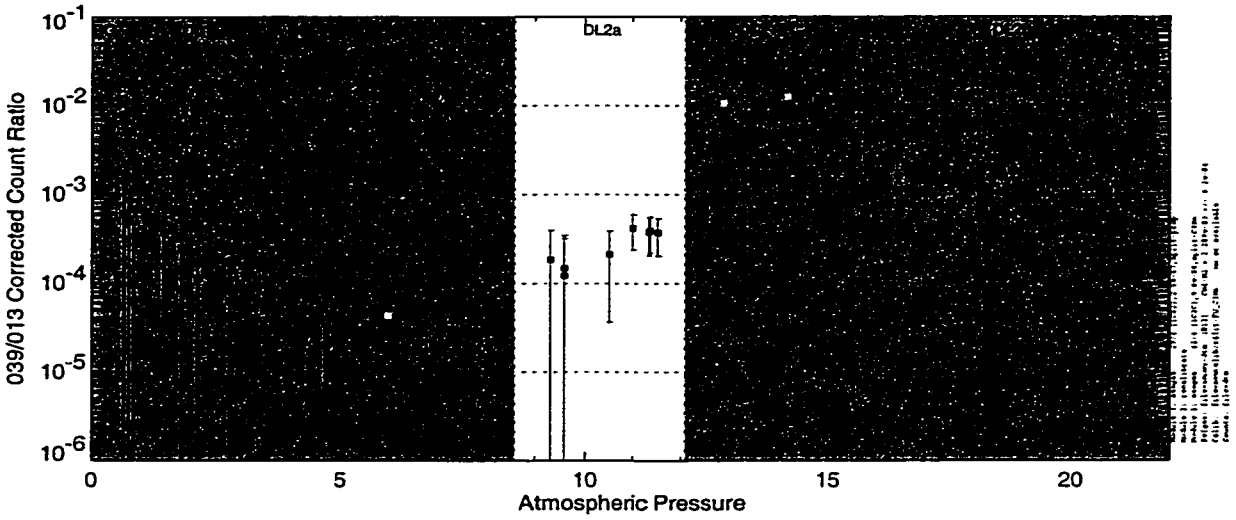

Figure 6.15 Count ratio C[39]/C[13], corrected for C_3H_6 and early-DL2a propane.

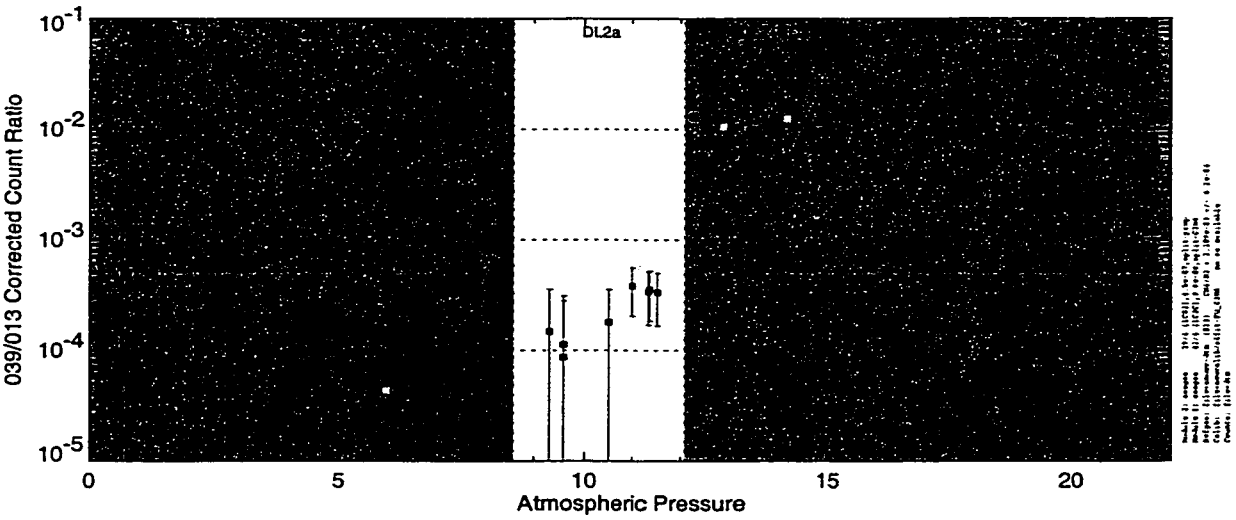

Figure 6.16 Count ratio C[39]/C[13], corrected for C_3H_6 and late-DL2a propane.

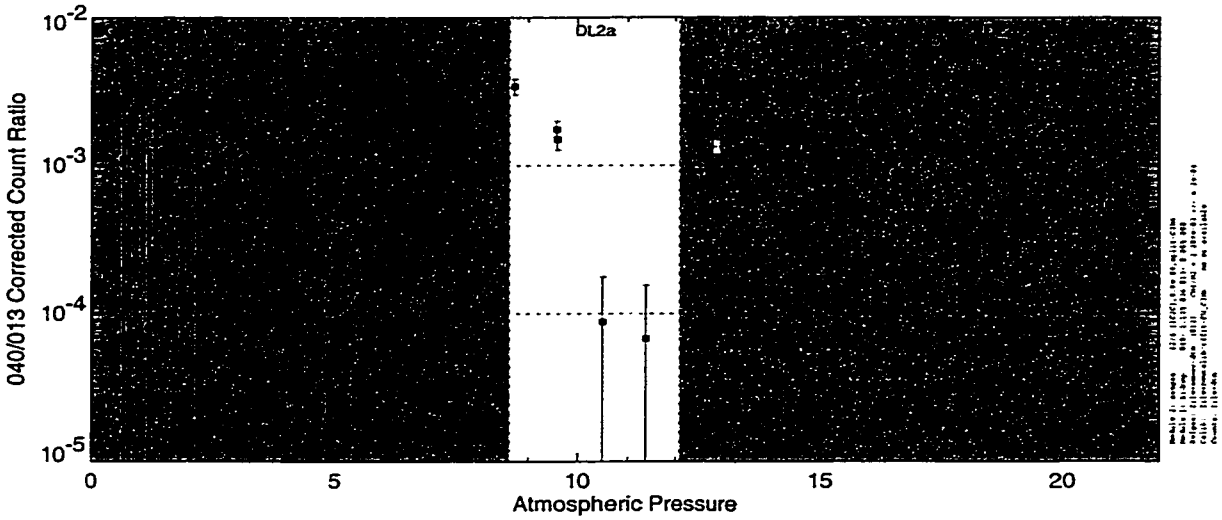

Figure 6.17 Count ratio C[40]/C[13], corrected for C_3H_6 and argon.

The DL2a count ratio averages from Figures 6.13–6.17 are summarized in Table 6.3:

Table 6.3 GPMS and C_3H_4 count ratios.

	C[37]	C[38]	C[39]	C[40]
Corrected average ratio to C[13] in DL2a	$8.5 \pm 2.9 \times 10^{-5}$	$3.17 \pm 0.37 \times 10^{-3}$	$2.91 \pm 0.64 \times 10^{-4}$ (low propane) $2.56 \pm 0.64 \times 10^{-4}$ (high propane)	$3.4 \pm 1.3 \times 10^{-4}$
Ratio to C[13], normalized to C[40]/C[13]	0.25 ± 0.09	9.3 ± 1.1	0.86 ± 0.19 (low propane)	1.0
Number of DL2a points considered	6	6	8	5
Expected ratio to [40] for C_3H_4	~0.25	~0.35	~0.85	1.0

There is shockingly good agreement between the normalized GPMS count ratios in the third line of Table 6.3 and the expected count ratios in the first line, from the NIST MS45 database. For better results, count ratios were constructed relative to C[13] and then normalized to C[40] because C[13] was easily fitted to a smooth polynomial curve, whereas

C[40] varied somewhat irregularly over DL2a. Although the DL2a GPMS count ratios for masses 37, 39, and 40 support the detection of C_3H_4, C[38] is some 30 times too large to be consistent with C_3H_4 using the previously discussed argon correction based on a 11.1% value for $^{38}Ar/^{36}Ar$. Inspection of the count rates of masses 36 and 38 in DL2a (see Appendix A) reveals that C[38] increases *faster* than C[36] in DL2a, even though most of the counts at C[38] should be due to argon. This means that any constant ratio for $^{38}Ar/^{36}Ar$ used to remove the C[38] argon contribution will result in too extreme of a correction for early DL2a, and too small of a correction for late DL2a. The difference in rates of increase for C[36] and C[38] explains the absence of early-DL2a values of CR[38/13] in Figure 6.14. Although it could be argued that the relatively faster increase in C[38] is due to some species other than argon, the increasing signal would need to be something other than C_3H_4, based on the count ratios examined in this section.

A search was made for other candidate molecules at C[37], C[39], and C[40], according to the procedure described above in the ethane section. So such search was made for C[38] due to the poorly understood argon contribution at that mass. At the 20% sensitivity level, the only possibilities found were C_3H_3Cl, C_3H_5Cl, C_4H_6O, and $C_5H_6N_2O$ at mass 39, and C_4H_6O at mass 40. No additional candidates were found for C[37]. At the 5% sensitivity level, all these molecules were eliminated, except for C_3H_3Cl at mass 39.

Ethylene (C_2H_4) from C[27]

From Figure 6.1 it can be seen that any ethylene on Jupiter should show up primarily at C[26], C[27], and C[28]. However, C[26] is problematic because the contribution from acetylene is large, and C[28] is not good because CO and N_2 are also present at that mass. So the best approach is to look at C[27] first, since the interfering contributions there are due only to ethane, propane, and C_3H_6, gases whose DL2a abundances have been conveniently estimated in previous steps of this analysis.

Figure 6.18 shows the ethylene mixing ratio calculated with low ($2.6 \pm 1.1 \times 10^{-7}$) and high ($4.5 \pm 1.8 \times 10^{-7}$) propane corrections, as discussed above and appropriate for

early and late DL2a. Both cases assume the same ethane mixing ratio, $(9.2 \pm 4.8) \times 10^{-8}$, and the same C_3H_6 mixing ratio, $(9.8 \pm 3.3) \times 10^{-8}$.

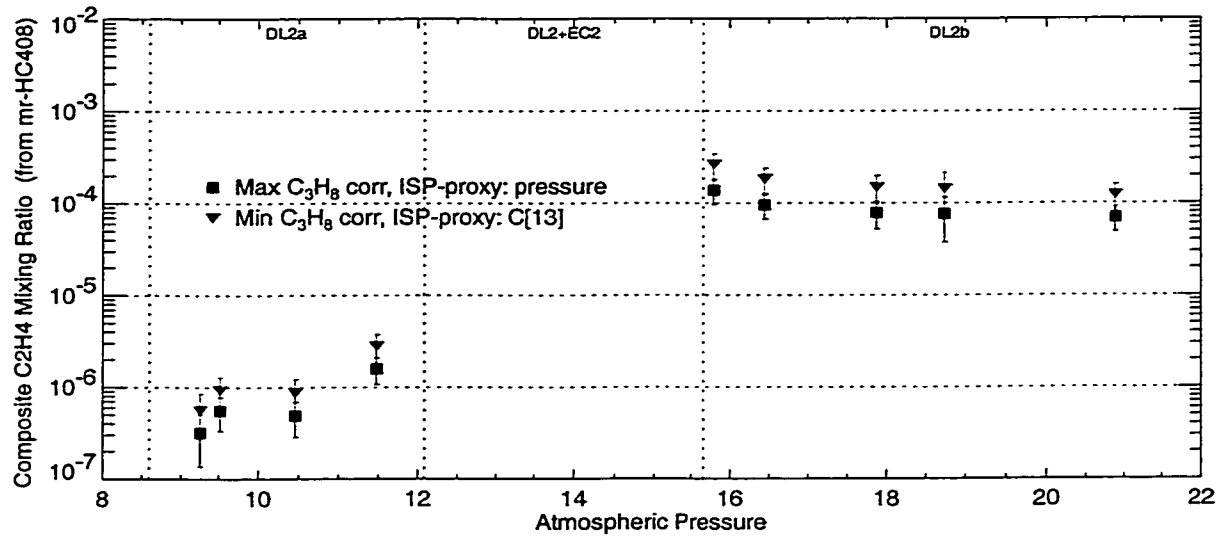

Figure 6.18 Jovian ethylene mixing ratio, corrected for ethane, C_3H_6, and high (squares) / low (triangles) propane.

Figure 6.18 implies that ethylene, like propane, increases in DL2a. Most of the difference between the two plotted cases is due to the value of the calibration constant; the magnitude of the propane correction is relatively minor, causing an approximately 10% difference versus about 30% for the calibration constant difference. For mass interference correction in the subsequent steps of this data analysis, a low ethylene value will be derived from the first three datapoints, and a high ethylene value will be taken from the last point. Although the choice of ISP-proxies to use for the calibration constant affects the magnitude of the C_2H_4 increase over DL2a, it cannot eliminate the increase. For this analysis, the more moderate low and high values of ethylene will be assumed: the first three points in the C[13]-ISP/minimal correction case (triangles in Figure 6.18) provide the low ethylene value of $(7.5 \pm 3.3) \times 10^{-7}$, and the final point of the pressure-ISP/maximal correction case (squares) provides the high value of $(1.58 \pm 0.51) \times 10^{-6}$. These results seem to present reasonably robust evidence that ethylene increases with depth in the DL2a region, although the uncertainties of the low and high ethylene results overlap slightly. The DL2a average of the three low points and the single high point is $(8.6 \pm 3.5) \times 10^{-7}$.

HCN also has a mass peak at C[27]. Chapter 9 discusses the possibility of HCN contamination leading to an overestimation of C_2H_4, as suggested by the photochemical model results of Chapter 7.

Acetylene (C_2H_2) from C[26] and C[25]

Now that we can estimate ethylene, the only remaining unknown contributor to C[25] and C[26] is acetylene. For each mass, corrections were made for both low ethylene abundance (for early DL2a) and high ethylene abundance (for late DL2a). Ethane and propene corrections were taken to be the same for each case. Mixing ratios used to determine these corrections are given in the previous sections. Propane also makes a small contribution of about 1 count at C[26] and 0.1 count at C[25]. For C[25] the propane contribution was ignored. For the late-DL2a, higher-hydrocarbon case for C[26], propane was approximated by doubling the C_3H_6 contribution. Since the C_3H_6 correction to C[26] is on the order of 2 counts, this technique overestimates the propane contribution, but the final result was insensitive to the propane contribution in any case; the corrected C[26] was on the order of –60 counts!

For the case with minimum ethylene correction, corrected C[26] was on the order of –10 counts, except at step 4278 (the circle in DL2a in Figure 6.19), which gives a mixing ratio of $(2.3 \pm 6.3) \times 10^{-7}$. Three possibilities (or any combination of them) could explain the acetylene situation presented by the CR[26/4] data. The first possibility is that acetylene is not present in the DL2a data. Alternately, the ethylene splitting pattern, used to determine the ethylene correction at C[26], could have been incorrectly determined by the EU. A final possibility is that significant contributions to C[27] by other molecules caused the ethylene mixing ratio to be overestimated, so that the correction applied to C[26] was too large.

Acetylene mixing ratios derived from C[25]/C[4] are shown as squares (low ethylene abundance correction) and triangles (high ethylene abundance correction) in Figure 6.19. Both cases are also corrected for standard ethane and C_3H_6. An average value obtained from the first two squares and the triangle is $(6.6 \pm 9.7) \times 10^{-7}$, assuming that the total mixing ratio errors are systematic. Note that given the uncertainties in the mixing ratios, the results

are entirely consistent with zero acetylene mixing ratio, as indicated by the error bars which extend off the lower boundary of the plot. Assuming that the errors are completely random reduces the average uncertainty to 5.6×10^{-7}, but this is not justified since some sources of error are certainly systematic (e.g., acetylene calibration constant uncertainty, deadtime correction to C[4]). The acetylene mixing ratio detection threshold using C[25]/C[4] is on the order of 10^{-7}. Given the results from C[25]/C[4] and C[26]/C[4], the simplest conclusion is that acetylene was not detected. However, the previously mentioned possibilities that the ethylene contribution could be overestimated should be kept in mind.

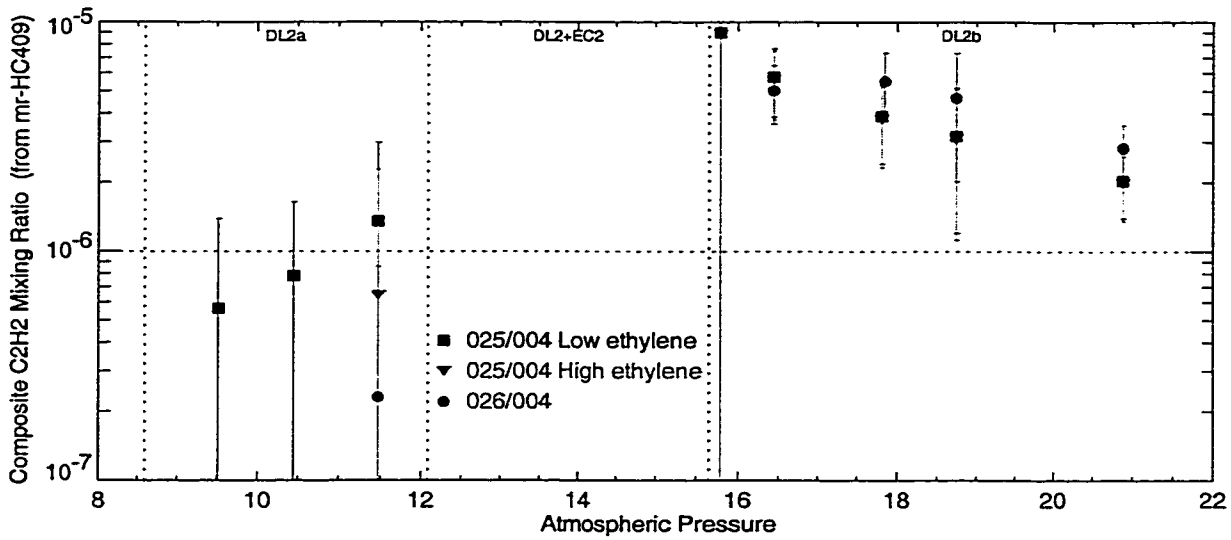

Figure 6.19 Jovian acetylene DL2a mixing ratio.

Non-hydrocarbon counts at C[28]

Finally, estimates can be made for all the hydrocarbon contributors to C[28], allowing a determination of the CO + N_2 signature at this mass. Figures 6.20 and 6.21 show the combined CO + N_2 mixing ratio, derived using the EU calibration constants for the count ratios CR[28/13] and CR[28/04]. Nitrogen calibration constants were discussed in Chapter 5, and DL2 $cc^{N_2}_{28/13}$ was summarized in line 17 of Table 5.10. For comparison, squares in Figures 6.20 and 6.21 show N_2 mixing ratios before correction for hydrocarbon contributions using CR[28/13] (Figure 6.20) and CR[28/4] (Figure 6.21). In both figures, triangles represent the N_2 + CO mixing ratios derived from hydrocarbon-corrected CR[28/

13], and circles depict N_2 + CO mixing ratios derived from hydrocarbon-corrected CR[28/4]. The DL2b data seems to show heavy contamination from the second enrichment cell, and after the hydrocarbon correction, no C[28] are left in DL1 except for a single point at 2.15 bar. Propane and ethane calibration constants are unknown for DL1, so the hydrocarbon correction for DL1 consisted only of ethylene. The hydrocarbon corrections for the N_2 + CO mixing ratio assumed the standard ethane contribution ($9.2 \pm 4.8 \times 10^{-8}$) and moderate propane ($3.13 \pm 0.78 \times 10^{-8}$) and ethylene ($8.6 \pm 3.5 \times 10^{-8}$) corrections.

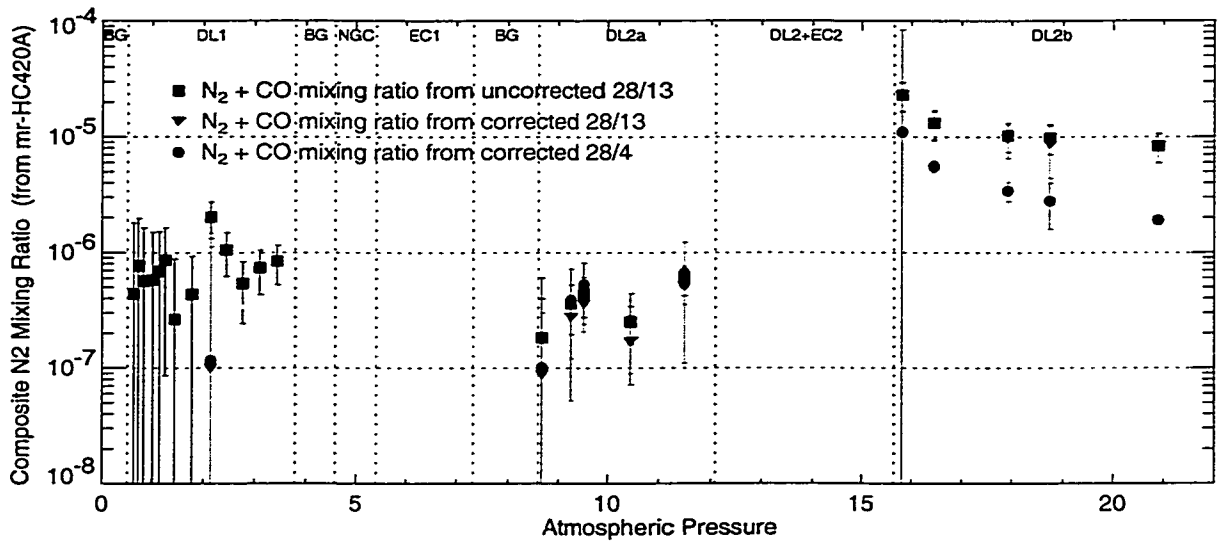

Figure 6.20 Combined CO + N2 mixing ratio from CR[28/13] without hydrocarbon correction (squares) and from CR[28/13] (triangles) and CR[28/4] (circles) with hydrocarbon correction.

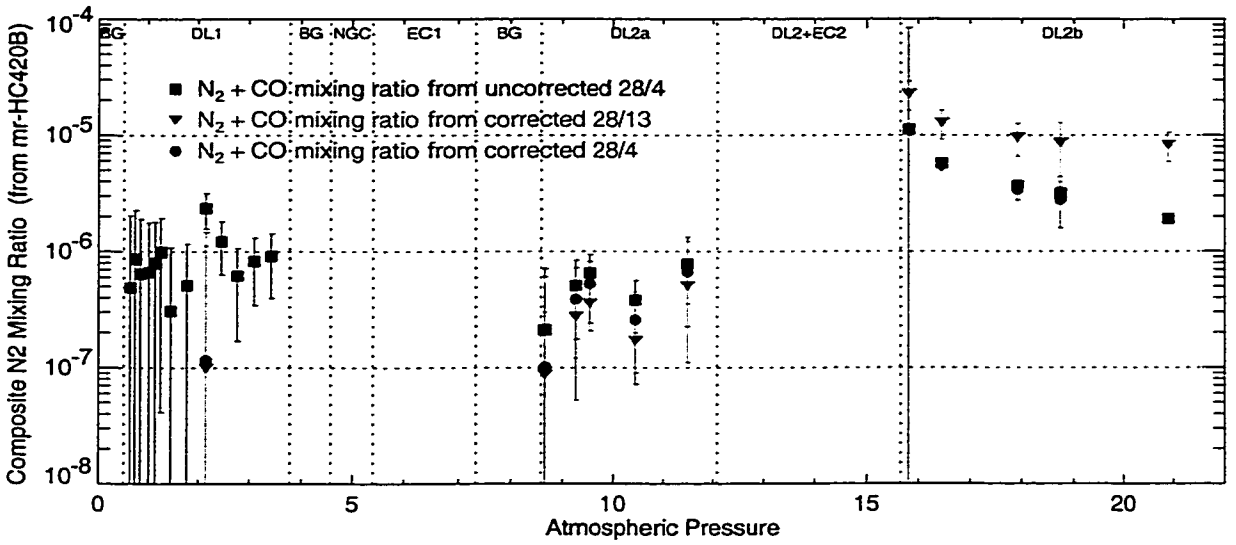

Figure 6.21 Combined CO + N2 mixing ratio from CR[28/4] without hydrocarbon correction (squares) and from CR[28/13] (triangles) and CR[28/4] (circles) with hydrocarbon correction

According to Paul Mahaffy, CO and N_2 should have roughly the same calibration constant, so if the amount of CO present can be independently determined, then the N_2 mixing ratio is just equal to the combined mixing ratio minus the independently-determined CO mixing ratio. CO cannot be measured by the GPMS, since all of its mass peaks (12, 16, and 28) are dominated by other gases (respectively: methane, water, and the combination of N_2 and hydrocarbons discussed above). The 1 ppb concentration of tropospheric CO reported by Noll et al. (1988) would mean that most of the signal at C[28] was due to N_2.

If the hydrocarbon corrections are correct, this is a very robust result in view of the high counting rate available at C[28] in DL2a, in the hundreds of counts. In other words, the limiting sensitivity to CO + N_2 mixing ratio is in the 10 ppb range, well below the values shown in Figures 6.20 and 6.21. The above discussion in the acetylene section pointed out the possibility that the C_2H_4 abundance is overestimated, leading to overcompensation for the C_2H_4 contribution in the N_2 + CO results shown here. Indeed, in DL1, where the lack of calibration constants means that no corrections were made for ethane and propane, the high ethylene abundance case has only one datapoint left with positive C[28], another independent hint that either the derived ethylene abundance is too high, or that the late DL2a ethylene result indicates an actual increase in ethylene

abundance with depth. The results of the C[28] studies are summarized in Table 6.4, with errors calculated using $\nu = 0$ (see Equation 3.19):

Table 6.4 Jovian $CO + N_2$ mixing ratio.

Data used	$CO + N_2$ mixing ratio: DL1	$CO + N_2$ mixing ratio: DL2a	$CO + N_2$ mixing ratio: DL2a last point
Count ratio: 28/04 NO hydrocarbon correction	$8.7 \pm 7.1 \times 10^{-7}$	$4.7 \pm 2.9 \times 10^{-7}$	$7.8 \pm 5.5 \times 10^{-7}$
Count ratio: 28/13 NO hydrocarbon correction	$7.4 \pm 5.0 \times 10^{-7}$	$3.4 \pm 1.4 \times 10^{-7}$	$5.9 \pm 1.7 \times 10^{-7}$
Count ratio: 28/04 WITH hydrocarbon correction	$1 \pm 14 \times 10^{-7}$	$3.5 \pm 3.0 \times 10^{-7}$	$6.7 \pm 5.5 \times 10^{-7}$
Count ratio: 28/13 WITH hydrocarbon correction	$1 \pm 10 \times 10^{-7}$	$2.5 \pm 1.3 \times 10^{-7}$	$5.0 \pm 1.5 \times 10^{-7}$
Average of 28/04 + 28/13 WITH hydrocarbon correction	$1 \pm 12 \times 10^{-7}$	$2.7 \pm 1.7 \times 10^{-7}$	$5.1 \pm 2.0 \times 10^{-7}$

^{15}N / ^{14}N isotopic ratio

Determination of the $^{14}N/^{15}N$ ratio (ϕ) on Jupiter has been most recently done by Fouchet et al. (2000). Their analysis of ISO-SWS measurements of the 10.88 μm and 11.07 μm $^{14}NH_3$ and $^{15}NH_3$ lines found a value of $\phi = 530^{+590}_{-170}$. This value is considerably higher than the terrestrial value of 272 (Anders and Grevesse, 1989). The solar ϕ is not well constrained, but the terrestrial value is included in the range of solar values determined from analysis of N trapped from the solar wind in lunar soils. Such a large ϕ for Jupiter relative to the earth is consistent with the pre-Galileo prediction by Owen and Bar-Nun (1995) that the Jovian ϕ would be different from that of the Earth, which they explained in terms of solar nebula chemistry; the earth's nitrogen component is derived from planetesimal outgassing, whereas Jupiter's nitrogen component is chiefly derived from N_2 captured directly from the solar nebula. However, the fact that solar wind and terrestrial nitrogen isotopic ratios are so close, while Jupiter's nitrogen isotopic ratio is much higher, invalidates this explanation, since solar and Jovian nitrogen should have come from the same reservoir.

GPMS data shed some additional light on the nitrogen isotopic ratio problem. However, the atmospheric quantity $\phi = {}^{14}N/{}^{15}N$ is very difficult to obtain from the GPMS dataset. Nitrogen in Jupiter's troposphere is present in two forms: molecular nitrogen (N_2) and ammonia (NH_3). Most of the primordial solar nebula N_2 captured during Jupiter's formation has been thermochemically converted to ammonia in Jupiter's interior. Direct measurement of ϕ from Jovian N_2 is impossible because N_2, at mass 28, is in a very rich part of the mass spectrum, and is confused by signals from many hydrocarbons, as well as CO, while ${}^{15}N{}^{14}N$ at mass 29 would be hidden by ethane and propane counts. This hydrocarbon/nitrogen/carbon monoxide issue was discussed in the previous section.

The mechanics of the GPMS gas handling system are described in Chapter II, as well as in Naming et al. (1989) and other papers. For several reasons, most of the GPMS data cannot be used to obtain ϕ from the ammonia signal. During the first direct sampling period, DL1, wall interactions between ammonia molecules and the GPMS gas inlet leak interfered with sensing of ammonia. Throughout the second direct sampling period, DL2, mass spectral interference from water (main peak at mass 18) swamped the signal of heavy ammonia (${}^{15}NH_3$ also at mass 18). This leaves us with only data from the noble gas cell (NGC) sequence, and data from the first enrichment cell (EC1).

The method of analysis described here was developed by Paul Mahaffy to obtain a lower limit for ϕ from the EC1 data. The EC1 experiment directly follows the NGC experiment. In the NGC, only noble gases are present, so the signal from both water and ammonia should be zero. As we enter EC1, ammonia counts are first to increase, followed quickly by water. This order is crucial to the analysis and is based on the fact that ammonia is more volatile than water, and thus its more rapid desorption from the enrichment cell causes its source density to rise faster during the enrichment cell experiment. As of this report, Paul Mahaffy is conducting and analyzing results from a detailed experiment (using the flight spare mass spectrometer) designed to measure the relative rates of increase of water and ammonia in EC1, since the GPMS data at the particular masses of interest are sparse and are not sufficient fully characterize the behavior of the gases with time.

Figure 6.22 shows C[18] in the NGC and EC1 experiments. Several corrections have been made to the counts, with the objective of removing any counts that can be attributed to any gas other than water. The first correction accounts for doubly-ionized argon. Argon, at mass 36, becomes doubly ionized in the mass spectrometer and thus produces counts at mass 18. To correct for this, 10.5% of the counts at mass 36 were subtracted from the counts at mass 18. Since this analysis focuses on ammonia, we also need to remove counts from mass 17 that are not due to ammonia. A contribution from methane, due to $^{13}CH_4^+$, was removed by subtracting 101.5% of the counts present at mass 12 (C^+). This ratio was determined from DL1 data, where counts at mass 17 are free from ammonia due to the aforementioned wall interactions. After the methane and argon corrections, we are left with counts at 17 due only to ammonia, and counts at 18 due only to water and heavy ammonia. Different assumptions for ϕ will yield different values for corrected counts at 18 due only to water, as shown in Figure 6.22. The data point at mass 18 at the end of NGC shows little change with different values of ϕ; this is because there is no ammonia present in the NGC to produce counts at mass 18. The first datapoint in EC1 is shown with four different corrections for heavy ammonia; the value of ϕ for each corrected datapoint is printed next to the point. The strict lower limit of ϕ is 220, because any lower value would produce negative counts at mass 18 in the EC1 data. However, values of ϕ as low as 220 produce a decrease in counts at mass 18 going from the NGC into EC1. This is unreasonable, leading to a more reasonable estimate of the lower limit for ϕ of around 230 or 240. Thus the best value for the lower limit of $^{14}N/^{15}N$ is 230 $\pm$ 10, since it encompasses both the strict lower limit and the more reasonable lower limit values.

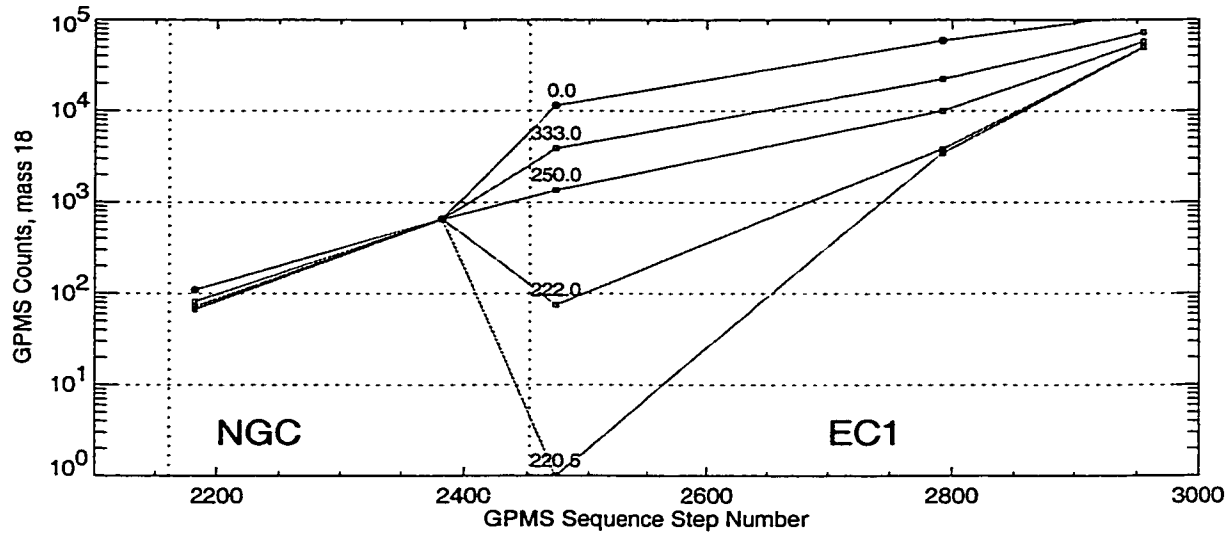

Figure 6.22 GPMS EC1 C[18] corrected to remove non-H_2O contributions; curves are labeled with corresponding values of the $^{14}N/^{15}N$ correction.

A ratio of 230 or above is not a useful result, because it is consistent with both the terrestrial value of 272, as well as the very large value of 530^{+590}_{-170} for Jupiter obtained by Fouchet et al. (2000). The Fouchet et al. (2000) result is sensitive to atmospheric levels at about 0.4 bar, which is above the ammonia cloud base, raising the possibility that the nitrogen isotopic ratio could be affected by fractionation processes in the ammonia cloud. Thus the nitrogen isotopic ratio retrieved by Fouchet et al. (2000) could truly be different from the ratio measured by the GPMS. However, there is some question about the GPMS analysis above. Should the mass 18 datapoint at GPMS step 2473 be used, as in Figure 6.22, or should the data be interpolated to a step number closer to the beginning of the EC1 experiment? Paul Mahaffy chose to interpolate to a step number closer to the beginning of the EC1 experiment, but realized that the GPMS data do not provide enough information to confidently characterize the rate of increase in the 18 and 17 counts in EC1.

The uncertainties in interpreting the rate of increase in the 18 and 17 counts in EC1 inspired Mahaffy to conduct new enrichment cell experiments with the EU. Eventually this method of analysis was replaced by the new approach of Mahaffy et al. (2000), using the doubly-ionized heavy ammonia ($^{15}NH_3^{++}$) signal at C[9] in the EC1 experiment, and taking the ratio to C[8.5] from $^{14}NH_3^{++}$. The C[8.5] signal was synthesized from corrected C[17].

The result of this investigation was a more tightly constrained value of $^{15}N/^{14}N = 2.23 \pm 0.3 \times 10^{-3}$ or $^{14}N/^{15}N = 448^{+70}_{-53}$.

Condensible volatiles: overview

Probe site condensible volatile (CV) profiles were introduced in Chapter 1. Here I describe the particular problems and concerns relating to the derivation of the CV mixing ratios. Methane is discussed in this section, not because it condenses in Jupiter's atmosphere, but because its main peak at C[16] suffers from mass interference from water and ammonia.

Hydrogen sulfide (H_2S)

Hydrogen sulfide is detected at its main peak at mass 34. This is also the main peak in the splitting pattern of phosphine (PH_3). Both gases also share peaks at 33 and 32, but only phosphine shows up at mass 31 with its P^+ fragment. The MS45 gives a C[31]/C[34] ratio for phosphine of 32%. C[31] is at the background noise level in DL1, less than 10 counts in DL2a, and less than 200 counts in DL2b. Assuming that all C[31] is due to phosphine, these levels would predict PH_3 contributions to C[34] of 0 in DL1, about 30 in DL2a, and around 600 in DL2b. These contributions are quite small compared to the total C[34] of up to 3000 in DL2a, and around 10,000 in DL2b, so it is acceptable to analyze C[34] as if it were all H_2S, and as a final step estimate the effect of phosphine.

The H_2S calibration constants were found to vary with ion source pressure (ISP) in the EU calibration run (see Figures 5.16 and 5.17). When working with a count rate such as C[34] which is far below the deadtime saturation region, it is best to also use a reference gas that is far from saturation to reduce uncertainties introduced by the deadtime correction. However, since the Jovian helium mixing ratio is better constrained than the methane mixing ratio, the total mixing ratio uncertainties for mixing ratios derived using CR[34/13] (squares in Figure 6.23) are about the same as those for C[34/4] results (triangles in Figure 6.23). Figure 6.23 shows error bars considerably larger than those previously presented in

Wong et al. (1999), because that analysis underestimated the methane mixing ratio uncertainty (see the following section on methane).

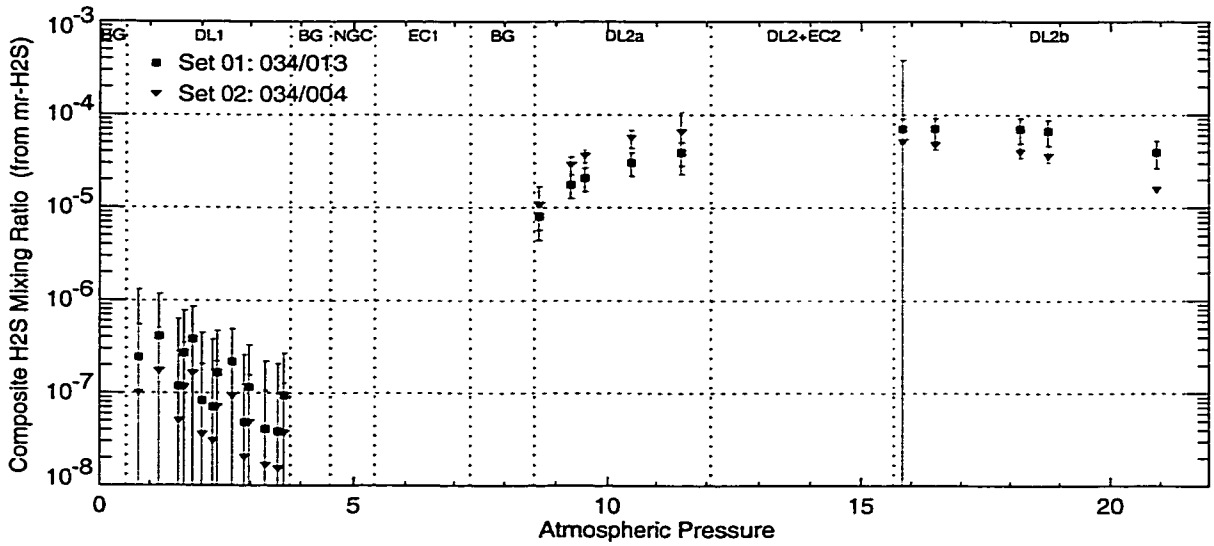

Figure 6.23 Jovian H_2S mixing ratio from CR[34/13] (squares) and CR[34/4] (triangles).

In DL1, C[34] were statistically meaningless (see Appendix A), corresponding to a non-detection of H_2S in the DL1 pressure range of 0.4–3.8 bar.

The difference between mixing ratios calculated using *CR*[34/13] or *CR*[34/4] in DL2a is probably an effect of familiar but unexplained systematic variation of the calibration constants. Thus, the most reasonable approach would be to assume that the actual H_2S mixing ratio is an average of the two calculated mixing ratio profiles, and use the deviation between them to estimate the uncertainty in the result based on the unexplained systematic calibration constant variation. Following this approach, H_2S in DL2a increases from $(2.85 \pm 0.58) \times 10^{-5}$ at 9.55 bar to $(4.1 \pm 1.5) \times 10^{-5}$ at 11.50 bar. This increase is real, even though error bars for the 9.55 bar and 11.50 bar averages overlap, because the stated uncertainty includes the uncertainty based on the difference between using *CR*[34/13] or *CR*[34/4]. This uncertainty is systematic and shifts the 9.55 bar and 11.50 bar averages in the same direction. However, examining the triangles and squares in Figure 6.23 shows that this correlation reverses in DL2b; this is precisely the expected behavior based on the pressure-variation of the respective calibration constants shown in Figures 5.16 and 5.17.

In DL2b, the average of the 15.8 bar to 18.8 bar points, assuming that the uncertainty can be characterized by the deviation between the CR[34/13] and CR[34/4] values, is $(4.36 \pm 0.53) \times 10^{-5}$, or $1.35 \times$ the solar mixing ratio of 3.24×10^{-5} (Anders and Grevesse 1989). Although averaging the CR[34/13] and CR[34/4] results in DL2a is justified, the large (and underrepresented in Figure 6.23) uncertainty in the DL2b CR[34/4] due to the saturated C[4] means that the CR[34/13] should be favored. Then the H_2S mixing ratio estimated from the first four DL2b points, focusing only on CR[34/13] results, is $(7.0 \pm 2.1) \times 10^{-5}$, or $(2.16 \pm 0.65) \times$ solar. This estimate is consistent with previously stated GPMS deep H_2S mixing ratios (Wong et al. 1999, Atreya et al. 1999, Niemann et al. 1998), but has a larger uncertainty to reflect the more thorough error analysis in this work. For H_2S and other molecules determined using the methane fragment C[13] as the reference gas, this larger uncertainty is mainly due to the uncertainty in the methane mixing ratio on Jupiter, which in turn is primarily due to the variation in methane calibration constant from run to run (see the methane section in this chapter).

Ammonia (NH_3)

Ammonia is one of the most difficult gases to analyze with the GPMS, as discussed in Niemann et al. (1996) and Niemann et al. (1998). This section outlines the numerous complications plaguing ammonia data reduction, and the approaches taken to minimize the problems, which involve calibration constant ambiguities, mass interference, and interactions between ammonia molecules and the walls of the mass spectrometer gas handling system.

Ammonia molecules readily react with the mass spectrometer gas flow system by "sticking" to the walls. A detailed discussion of this phenomenon was given in Mahaffy et al. (1999), and is summarized here. In DL1, the indirect beaming (see Figure 2.1) combined with the smaller leak conductance to prevent ammonia from reaching the ionization region. The gas system was subsequently flooded with ammonia (and other gases) during the EC1 experiment. During this phase, ammonia was adsorbed onto microscopic sites on the gas flow system walls, notably between valve 11 and the ion source (see Figure 2.1), and when

inlet 2 was opened for the DL2 experiment, the sudden flux of hydrogen facilitated the desorption of ammonia from the walls. This desorbed ammonia was measured along with directly-sampled atmospheric ammonia during DL2a, leading to an erroneously large signal at C[17].

The solution to this problem, presented in Mahaffy et al. (1999), is to simultaneously fit a decaying exponential component and a "constant abundance" component, which is conveniently proportional to C[13] reference gas counts, since $cc_{17/13}^{NH3}$ is constant with ISP:

$$C'[17] = \alpha \exp(\beta t) + \gamma C[13] \qquad 6.3$$

Paul Mahaffy measure the desorption time constant β in Equation 6.3 in two different experiments on 1999-04-28 and 1999-05-13 using the EU. The values obtained from these experiments were -3.58×10^{-3} sec^{-1} and -3.03×10^{-3} sec^{-1} respectively. For analysis of the GPMS data, I use an averaged value of $\beta = -3.31 \times 10^{-3}$ sec^{-1}, with an uncertainty of $\pm 0.55 \times 10^{-3}$ sec^{-1} based on the assumption that the full deviation between the two measured time constants characterizes the uncertainty in their value.

Exponentially decaying background corrections were discussed in Chapter 3. However, those corrections consisted of exponentials fit to counts due to species remaining in the system in gaseous form, a situation that differs from the ammonia case in that background ammonia was present in the system, but adsorbed on the walls, where it was not detectable during the background cycles of the GPMS. Thus the previously-discussed exponential background contributions for other species could be fit to counts in e.g. the BG2 cycle, whereas ammonia requires that the background exponential be fit to the actual DL2a data. Figure 6.24 shows that the raw count ratio CR[17/13] (squares) is very well fit with the combination of one component that is proportional to C[13] (diamonds) and another component decaying exponentially with a laboratory-determined time constant β discussed above (circles). Triangles depict the fitted points, composed of the sum of the exponentially decaying and the constant abundance components. The observed CR[17/13] is so well fit by this approach that the fitted and observed points are difficult to distinguish in Figure 6.24.

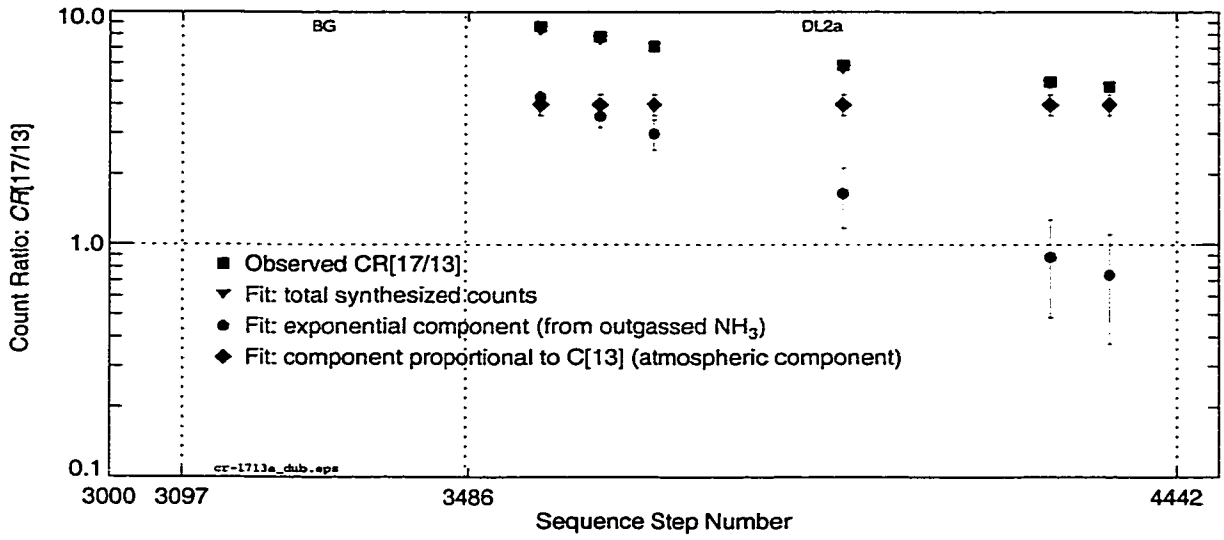

Figure 6.24 CR[17/13] with correction for post-EC1 ammonia outgassing.

In the DL2a region, both methane and water contaminate ammonia's main peak at C[17]. The water splitting pattern is used to determine the correction to C[17] based on C[18], but first the contribution to C[18] from $^{36}Ar^{++}$ must first be eliminated. This method neglects the contribution of ammonia to C[18] via $^{14}NH_2D^+$ and $^{15}NH_3^+$, but these contributors are quite insignificant in comparison to the uncertainties introduced by other corrections. The correction to C[17] for methane contribution (via $^{13}CH_4^+$) is applied based on either methane's main peak at C[16], requiring simultaneous calculation of the water and ammonia contributions to C[16]. A system of three equations is solved for the three unknowns: the corrected C'[16], C'[17], and C'[18]. The interference corrections add to the cumulative uncertainty in C[17], due to both uncertainty in the parent mass counting rates as well as uncertainties in the splitting fractions themselves. Figure 6.25 shows the effect of interference correction (triangles) on the raw 17/13 count ratio (squares). The interference correction is largest at the end of DL2a, because the water abundance is increasing in the atmosphere throughout DL2a, and also because the relative contribution from ammonia (outgassed + atmospheric) is smaller at the end of DL2a. Circles and diamonds in Figure 6.25 show the constant-abundance component γ (see Equation 6.3) before (circles) and after

(diamonds) the interference correction. Correction for mass interference reduces γ by almost a factor of 2.

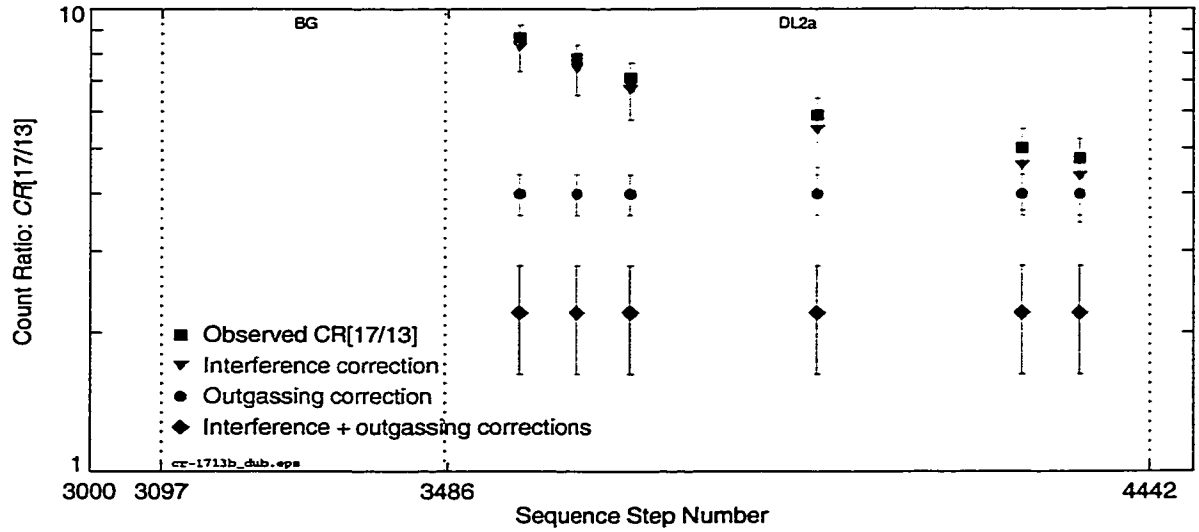

Figure 6.25 CR[17/13] before (squares, circles) and after (triangles, diamonds) correction for interference from water, methane, and argon.

Problems with the ammonia calibration constant were discussed previously in Chapter 5. One feature of the ammonia calibration constant is that it shows a dependence on the ammonia mixing ratio itself. The ammonia mole fraction at the 8–12 bar portion of the probe descent was estimated to be about 3.6 × solar by Folkner et al.'s analysis of probe radio signal attenuation (see Chapter 1). Folkner et al.'s abundance $(8 \pm 1) \times 10^{-4}$ is between bins S (2.2×10^{-4} NH_3 mole fraction) and M (10^{-3} NH_3 mole fraction) in the MIX97 experiment suite (see Chapter 5), so those subsets are used to obtain the best calibration constants for ammonia in DL2a (see Figures 5.30 and 5.31). Since the post-EC1 outgassing correction results in a constant value of corrected CR[17/13] in DL2a, there is no need for a figure to depict the ammonia abundance; the ammonia mixing ratio was $7.3 \pm 2.8 \times 10^{-4}$ for bin M and $6.3 \pm 2.5 \times 10^{-4}$ for bin S.

The data analysis method for ammonia is summarized as follows:

1. Make all corrections to C[17] for mass interference from water, argon, and methane. Combine uncertainties from all corrections. See Figure 6.25.

2. Fit a decaying exponential component plus constant abundance (proportional to C[13]) component to the DL2a C[17] datapoints, using estimated uncertainties as weights for the nonlinear fit. See Figure 6.24.

3. Multiply the constant abundance component by the calibration constant for ammonia, combining estimated fit parameter uncertainty with calibration constant uncertainty, in order to obtain the final mixing ratio with its own estimated uncertainty.

Following these steps, and averaging the two values obtained using results from the two calibration constant bins gives a constant DL2a ammonia mixing ratio of $(6.7 \pm 2.6) \times 10^{-4}$, or $(3.0 \pm 1.2) \times$ solar ammonia abundance in the 9–12 bar region. This value overlaps with the estimate of Folkner et al. (1998), and is close to the independently calculated value in Mahaffy et al. (1999) of $(3.5 \pm 1.5) \times$ solar.

Water (H_2O)

The only significant mass interference at C[18] comes from doubly ionized argon-36, or $^{36}Ar^{++}$. The correction for this is straightforward: subtract a proportion of C[36] from C[18]. The splitting fraction in MS45 is 14.6%, but tests using the EU and FU yield consistently smaller splitting fractions, in the neighborhood of 11%, but always above 10%. The correction applied here is the best value of 10.5%, with an estimated uncertainty of ±2%.

The largest uncertainty in water mixing ratio comes from the calibration constant. This issue was discussed in Chapter 5. In addition to the easily quantified errors from background corrections, deadtime constant uncertainty, interference corrections, and statistical uncertainties, the value of the calibration constant is affected strongly by the choice of ISP-proxy (see Figures 5.23 to 5.25). An additional large systematic uncertainty in water calibration constant remains unexplained. As noted in Chapter 5, intercept values differ markedly from run to run, while the slope of the calibration constant line as a function of pressure is relatively constant. This unexplained effect is the cause of the large uncertainty in the water calibration constant fitted values. Figure 6.26 displays the mixing ratio for water (corrected for argon contribution) calculated using three different ISP-

proxies for the calibration constant. Water mixing ratio results for the DL1 region are not pictured because more work needs to be done with the L1 water calibration constant.

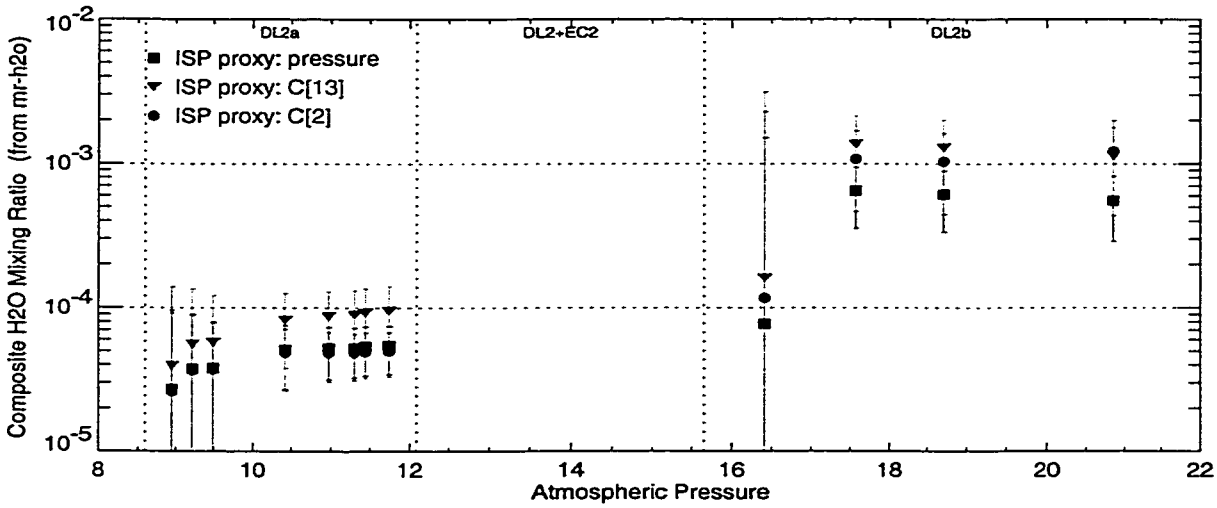

Figure 6.26 DL2 water mixing ratio for three ISP-proxies: pressure (squares), C[13] (triangles), and C[2] (circles).

The datapoints in DL2a seem to suggest an increase in water abundance with depth, but due to the large mixing ratio uncertainty, this increase is not a statistically justifiable phenomenon. Appendix A shows the background corrections made for C[18]; in DL2a an exponential background was subtracted based on the decrease in C[18] in the BG2 experiment (ending at about 8.6 bar), and in DL2b the exponentially decaying signal was fit to first two actual C[18] measurements in DL2b (the point at about 16.4 bar and one before it that was eliminated by the exponential background correction). Uncertainties in these exponential background corrections were not estimated and do not contribute to the error bars of the mixing ratio points in Figure 6.26, so the earliest DL2a and DL2b points should be ignored, since they were the most strongly affected by the exponential background correction. DL2b data are more severely affected by the uncertainty in the choice of ISP-proxies for the calibration constant (see Figures 5.23 to 5.25). Since the variation with depth is poorly constrained, I present just two values for the water mixing ratio in Table 6.5: an 11–12 bar value from the average of the last four DL2a datapoints, and a 17–21 bar average of the last three DL2b datapoints. Values are provided for each of the three ISP-

proxies, as well as an average value whose error estimate includes the variation in mixing ratio with choice of ISP-proxy.

Table 6.5 Jovian water mixing ratio.

Calibration constant ISP proxy	Water mixing ratio DL2a/11–12 bar	Water mixing ratio DL2b/17–21 bar
pressure	$(5.3 \pm 2.0) \times 10^{-5}$	$(6.0 \pm 2.8) \times 10^{-4}$
C[13]	$(9.1 \pm 4.4) \times 10^{-5}$	$(1.25 \pm 0.70) \times 10^{-3}$
C[2]	$(5.0 \pm 2.0) \times 10^{-5}$	$(1.09 \pm 0.65) \times 10^{-3}$
Average:	**$(5.4 \pm 1.3) \times 10^{-5}$ or $(0.0317 \pm 0.0076) \times$ solar**	**$(7.5 \pm 2.4) \times 10^{-4}$ or $(0.44 \pm 0.14) \times$ solar**

The DL2a water mixing ratio in Table 6.5 is relatively unchanged from the Niemann et al. (1998) result of $(5.6 \pm 2.5) \times 10^{-5}$, although Niemann et al.'s result was reported as an upper limit. Niemann et al.'s DL2b upper limit was $(5.2 \pm 2.6) \times 10^{-4}$, presumably derived using pressure as the calibration constant ISP-proxy, and thus agreeing quite well with Table 6.5. However, the average value derived here includes the effects of alternative calibration constant ISP proxies, and results in a slightly higher value. Figures 5.23 through 5.25 show that C[13] and C[2] as ISP proxies in DL2b result in calibration constants extrapolated to ISP proxy values far from those measured in the laboratory calibration experiments, so an argument may be made in favor of discarding those calibration constants for DL2b and using only the mixing ratio value calculated using pressure as the ISP proxy. Future calibration experiments may resolve the dilemma, but any significant future reduction in the uncertainty of the mixing ratios will require an understanding of the systematic run-to-run variation of calibration constants exhibited by most gases tested. The unexplained systematic variation of calibration constant seems most troublesome for water, ammonia, and methane, but this observation could result from the selection effect that these gases have the highest number of separate calibration runs available for analysis.

Methane (CH_4)

Methane mixing ratio can be obtained from the primary peak at C[16] corresponding to CH_4^+, or at a secondary peak such as C[13], from CH^+. Both options should be examined. Using C[16] reduces deadtime error but introduces uncertainty via the interference corrections for water, argon, and ammonia, whereas using C[13] eliminates error from mass interference but leads to greater deadtime uncertainty (see Figure 3.10). Several calibration runs contained methane and helium, but the derived $cc_{16/4}^{CH4}$ and $cc_{13/4}^{CH4}$ showed substantial variation from experiment to experiment, leading to large uncertainties in the final calibration constants, as discussed in Chapter 5.

Figure 6.27 shows methane mixing ratios calculated from CR[16/4] (triangles) and from CR[13/4] (circles). Methane mixing ratio from CR[16/4] is also shown before correction for mass interference (squares); the only area noticeably affected by this correction is the early DL2a data, where the signal from desorbed post-EC1 ammonia is large (see the ammonia section). Table 6.6 summarizes the methane mixing ratio values; the best value derived from averaging all available data is $(2.21 \pm 0.62) \times 10^{-3}$.

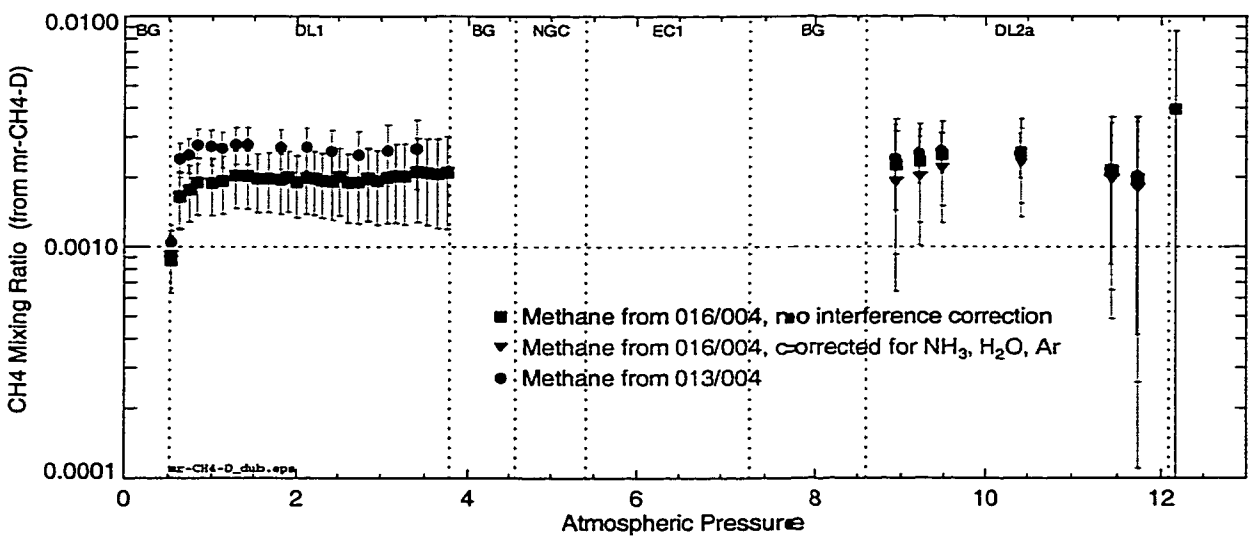

Figure 6.27 Jovian methane mixing ratio.

Table 6.6 Jovian methane mixing ratio.

Count ratio used	CH_4 mixing ratio DL1	CH_4 mixing ratio DL2a	CH_4 mixing ratio DL1 + DL2a
CR[16/4]	$(1.98 \pm 0.64) \times 10^{-3}$	$(2.1 \pm 1.1) \times 10^{-3}$	$(1.98 \pm 0.69) \times 10^{-3}$
CR[13/4]	$(2.64 \pm 0.52) \times 10^{-3}$	$(2.52 \pm 0.74) \times 10^{-3}$	$(2.62 \pm 0.57) \times 10^{-3}$
Combined CR[16/4]+CR[13/4]	$(2.19 \pm 0.58) \times 10^{-3}$ or $(3.02 \pm 0.80) \times$solar	$(2.39 \pm 0.87) \times 10^{-3}$ or $(3.3 \pm 1.2) \times$solar	**$(2.21 \pm 0.62) \times 10^{-3}$ or $(3.05 \pm 0.85) \times$solar**

CHAPTER VII

Implications for hydrocarbon photochemistry

Physics, chemistry, and code heritage of the photochemical model

The complex hydrocarbons detected by the GPMS in the DL2a (8.5–12 bar) region are created far overhead in Jupiter's stratosphere, when methane is broken apart by solar ultraviolet radiation. The resulting fragments combine with each other and with methane and hydrogen to form more complex molecules, which are themselves subject to ultraviolet photolysis. Vertical transport distributes the molecules in the stratosphere and also brings them down into the troposphere, where they were sampled by the Galileo probe. In order to quantitatively analyze the GPMS results, we use an idealized photochemical model to simulate the photochemical reactions and generate mixing ratio profiles for a zonally-averaged steady-state solution in a vertical column at the latitude of the Galileo Probe descent. The solar radiation is averaged over a complete rotation of Jupiter by choosing an average solar zenith angle. Although this temporal averaging scheme introduces some error into the calculated hydrocarbon mole fractions, the photochemical lifetimes of the species of interest are longer than the Jovian day, so the diurnal averaging gives good results. Edgington is currently beginning to investigate the effect of horizontal inhomogeneities and transport on stratospheric photochemistry by adapting the model to three dimensions. Spatial inhomogeneities are already known to exist in the stratosphere, particularly at high latitudes where energy is available from charged particles trapped in Jupiter's magnetic field.

Chemical species with known absorption cross sections absorb solar UV radiation, both direct and scattered. The model includes both Rayleigh scattering and Raman

scattering. Rayleigh scattering is directional, but the scattered photons do not experience an energy change. In Raman scattering, a photon is absorbed by a hydrogen molecule, which then undergoes a transition to a different energy state before re-emitting the photon nearly isotropically. If the molecule moves to a higher rotational or vibrational state as a result of the Raman scattering of an UV photon, the scattered photon will have a lower energy.

The model currently includes 49 species. Figure 7.1 presents a simplified view of some of the key reactions leading to the formation of heavier hydrocarbons through the photolysis of methane. Most molecules can be formed via different pathways, and the dominant pathway can change at various altitude levels. The formation of butane, for example, is dominated by the C_3H_7 + CH_3 pathway at pressures less than about 1 mbar, whereas the C_2H_5 + C_2H_5 pathway dominates lower in the atmosphere. Propane formation is dominated by the C_3H_7 + H pathway above about 10 mbar, while the deeper levels see an equal contribution from the C_3H_7 + H and C_2H_5 + CH_3 pathways. The relative contributions from different production pathways are a result of many factors, including temperature-dependent reaction rate coefficients, reactant mole fraction gradients, and variation in the available ultraviolet radiation.

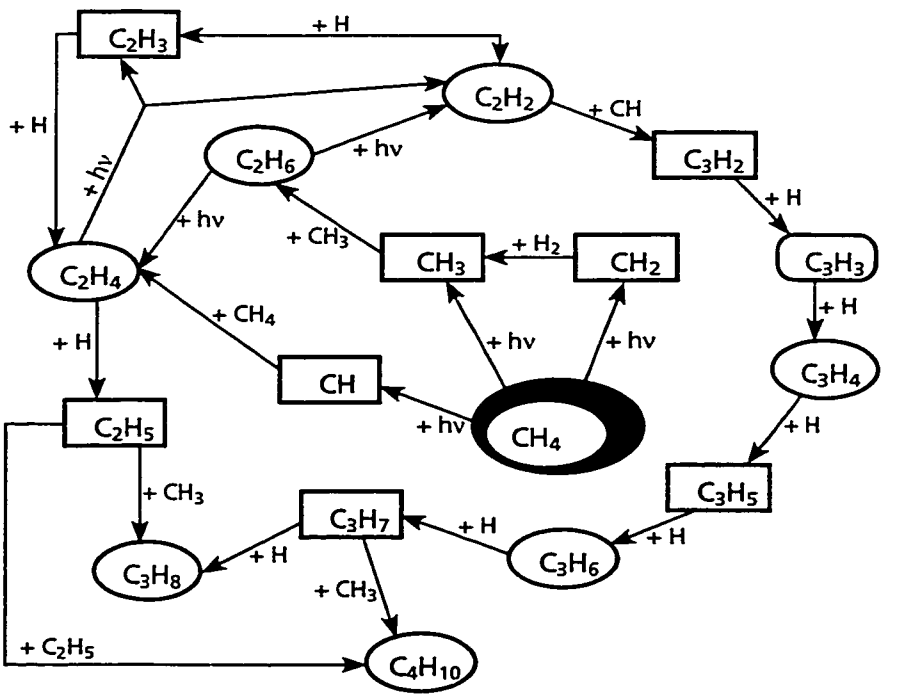

Figure 7.1 Simplified photochemical reaction scheme (see text). Stable species are shown as ovals.

Vertical transport in the stratosphere is governed by two processes: molecular diffusion and turbulence/bulk motion. Molecular diffusion results in a compositional layering of the atmosphere, such that mixing ratios of heavy molecules decrease with height, while molecules lighter than the average atmospheric molecular weight have mixing ratios that tend to increase with height. Above the level known as the homopause, molecular diffusion dominates, while below the homopause, turbulence and bulk motion control the vertical transport of gases and tend to homogenize the atmosphere. For ease of modeling, the strength of this type of mixing is parametrized by a single number, the eddy diffusion coefficient K. Formally, the molecular diffusion coefficient D_i and eddy diffusion coefficient K are related to the vertical flux ϕ_i of constituent i by the equation:

$$\phi_i = -n_i D_i\left(\frac{1}{n_i}\frac{\partial n_i}{\partial z} + \frac{1}{H_i} + \frac{(1-\alpha_i)}{T}\frac{\partial T}{\partial z}\right) - n_{\text{atm.}} K \frac{\partial}{\partial z}\left(\frac{n_i}{n_{\text{atm.}}}\right), \qquad 7.1$$

where α_i is the thermal diffusivity of the species, n_i is the number density of the species (related to the mole fraction via Equation 1.2), and H_i is the scale height of species i, given by

$$H_i = \frac{R^* T}{\mu_i g}, \qquad 7.2$$

where R^* is the universal gas constant, all quantities are in cgs units, and μ is in units of g mol^{-1}. The molecular diffusion term includes vertical mixing driven by chemical gradients, gravity, and thermal gradients, respectively. Although the molecular diffusion constant can be analytically derived, the eddy diffusion constant is a parametrization of convenience and is not simply derived from physical principles. Instead, it is iteratively obtained by matching model output to observations. For example, Edgington et al. (1999) derive K in the 50–400 mbar range of Jupiter by requiring the resulting ammonia distributions to produce synthetic spectra whose ammonia spectral signatures match those in the Hubble Space Telescope observations. Their derived K-profiles are shown in Figure 7.2:

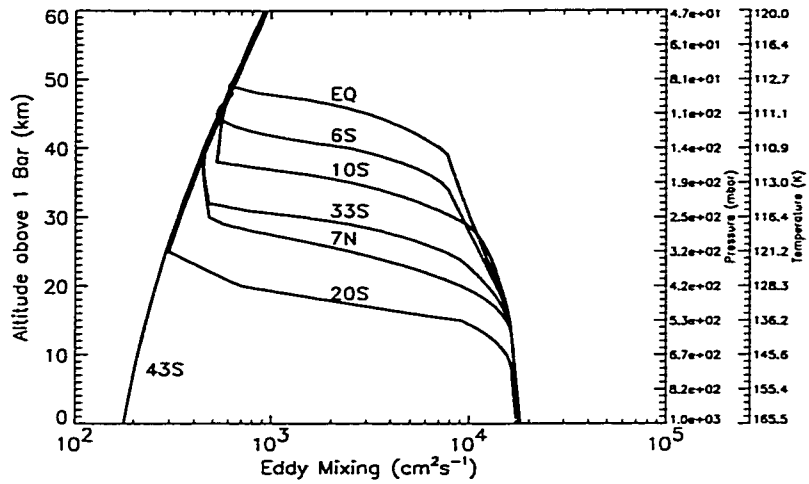

Figure 7.2 Longitudinally-averaged eddy mixing profiles derived by Edgington *et al.* (1999).

The eddy mixing parameter largely controls the mixing ratios of hydrocarbons deep below their source region. Since this work is focused on hydrocarbon mixing ratios in the 8.5–11 bar DL2a region, much attention will be given in a later section to the choice of eddy mixing profile used by the photochemical model.

The FORTRAN code for the model used in this work was adapted from that used in Edgington (1997), Edgington et al. (1998), and Edgington et al. (1999). These three works, hereafter collectively referenced as ESET, used code version pc-v7.2.4, containing 29 species, whereas the current version pc-v8.3 includes more three- and four-carbon hydrocarbons for a total of 49 model species. Except for minor bug fixes, the radiative transfer portion of pc-v8.3 is unchanged from pc-v7.2.4. The propagation of radiation in the atmosphere is calculated using a two-stream discrete ordinates approximation to the radiative transfer equation for computational model iterations. Radiative transfer details are concisely discussed in Edgington et al. (1998), and an exhaustively comprehensive presentation of the formulae employed is given in Appendix C of Edgington (1997).

As in the ESET papers, the present model includes chemistry of the families of ammonia as modeled by Atreya et al. (1977), phosphine as modeled by Strobel (1977) and Kaye and Strobel (1984), and the hydrocarbons as modeled by Atreya and Romani (1985) and Bishop et al. (1998). All of these chemical systems were included in a single model for pc-v7.2.4 and described in ESET. For the current version, new species and reactions from

Gladstone et al. (1996) were included in order to calculate abundances of C_3 and C_4 hydrocarbons. Many reaction rates and pathways, as well as photolysis cross sections and quantum yields, were also updated to include information not available to the ESET or Gladstone et al. (1996) models. The final set of chemical data, including photolysis, condensation, and chemical kinetics, is covered in Appendix B.

Formulation of the photochemical model

The core of the photochemical model is a numerical engine that solves the continuity equation in spherical coordinates:

$$\frac{1}{r^2}\frac{\partial(r^2\phi_i)}{\partial r} = P_i - L_i \qquad 7.3$$

P_i and L_i represent the production and loss processes for species i, while ϕ_i is the vertical flux as given by Equation 7.1. Production comprises the sum of all relevant chemical reactions as well as photolysis of all relevant parent molecules, while loss includes photolysis, reaction with other molecules, and condensation. In order to solve the continuity equation for the mole fractions of each of the model species, both sides of the equation are integrated over an altitude interval centered around predetermined gridpoints:

$$\int_{R_j}^{R_{j+1}} \frac{1}{r^2}\frac{\partial(r^2\phi_i)}{\partial r} r^2 dr = \int_{R_j}^{R_{j+1}} (P_i - L_i) r^2 dr \qquad 7.4$$

At each grid level r_j, the array of all the model species mole fractions can be represented as

$$\Theta_j = [q_1, q_2, \ldots, q_{n_{sp}}]\Big|_{r_j} \qquad 7.5$$

Figure 7.3 demonstrates the grid structure implemented, and Edgington (1997) shows that this method of finite differencing numerically ensures flux conservation, which could be violated if careless finite differencing introduced false source/sink terms in the integrated continuity equation. Making the assumption that production and loss remain constant over the interval, Equation 7.4 reduces to:

$$r_{j+1}^2 \phi_i\Big|_{R_{j+1}} - r_j^2 \phi_i\Big|_{R_j} \approx \frac{1}{3}(P_i - L_i)\Big|_{r_j} (R_{j+1}^3 - R_j^3) \qquad 7.6$$

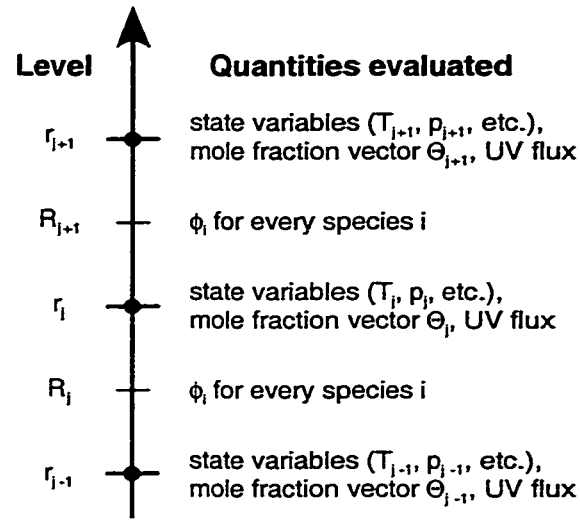

Figure 7.3 Altitude steps used in the photochemical model.

The flux terms at R_j and R_{j+1} in Equation 7.6 are calculated using Equation 7.1, which requires the temperature and mole fraction differentials to be evaluated at the levels R_j and R_{j+1}. Each differential function f is evaluated using

$$\left.\frac{df}{dr}\right|_{R_j} = \frac{f(r_j) - f(r_{j-1})}{r_j - r_{j-1}} \qquad 7.7$$

Other quantities such as temperature and density are taken to be the average of values at the adjacent gridpoints. Through the production and loss terms, mole fraction q_i at level r_j is linked to every other mole fraction at r_j, and through the vertical flux terms it is linked to mole fraction q_i at every other model altitude level. Therefore, for a model with n_{sp} species and n_z altitude steps, each step has n_{sp} equations, each of which is a function of the mole fractions of all the species at all the levels ($n_z \times n_{sp}$ mole fractions). The equation for a particular species i at an altitude level j can be represented as a function of the mole fraction vectors Θ and can be arranged as

$$f_{ij}(\Theta_1, \Theta_2, \ldots, \Theta_{n_z}) = 0\,, \qquad 7.8$$

which can then be expanded in the Taylor series,

$$f_{ij}(\Theta_1 + \Delta\Theta_1, \ldots, \Theta_{n_z} + \Delta\Theta_{n_z}) = f_{ij}(\Theta_1, \ldots, \Theta_{n_z}) + \sum_{m=1}^{n_z} \sum_{k=1}^{n_{sp}} \frac{\partial f_{ij}(\Theta_1, \ldots, \Theta_{n_z})}{\partial q_{km}} \Delta q_{km} + \cdots \tag{7.9}$$

Terms higher than first order are neglected. For a given set of ϕ_i at R_j and R_{j+1}, the expression $f_{ij}(\Theta_1, \Theta_2, \ldots, \Theta_{n_z})$ in Equation 7.8 will usually evaluate to a non-zero residual. The iterative technique is to then find a $\Delta\Theta_j$ for each altitude step such that

$$f_{ij}(\Theta_1 + \Delta\Theta_1, \ldots, \Theta_{n_z} + \Delta\Theta_{n_z}) = 0 . \tag{7.10}$$

Then the $\Delta\Theta_j$ can be found from Equation 7.9, which becomes

$$\sum_{m=1}^{n_z} \sum_{k=1}^{n_{sp}} \frac{\partial f_{ij}(\Theta_1, \ldots, \Theta_{n_z})}{\partial q_{km}} \Delta q_{km} = -f_{ij}(\Theta_1, \ldots, \Theta_{n_z}) . \tag{7.11}$$

The entire system of $n_{sp} \times n_z$ equations can be represented by the matrix equation

$$\bar{\bar{\mathrm{J}}}(\bar{\Theta})\Delta\bar{\Theta} = -\bar{\mathrm{f}}(\bar{\Theta}) , \tag{7.12}$$

where $\bar{\bar{\mathrm{J}}}(\bar{\Theta})$ is the Jacobian matrix as a function of the mole fractions of all species at all levels. Then the values for iteration k yield the values for the subsequent iteration $k + 1$ via

$$\bar{\Theta}^{\langle k+1 \rangle} = \bar{\Theta}^{\langle k \rangle} - (\bar{\bar{\mathrm{J}}}^{\langle k \rangle})^{-1} \bar{\mathrm{f}}^{\langle k \rangle} . \tag{7.13}$$

The inversion of the Jacobian uses Crout LU decomposition. In equations 7.12 and 7.13, $\bar{\Theta}$ and $\bar{\mathrm{f}}$ are generally 1-dimensional vectors each with $n_{sp} \times n_z$ elements, and the Jacobian is generally a 2-dimensional matrix having $n_{sp} \times n_z$ elements in each dimension. For more efficient computation, the actual matrix inverted is smaller than the $n_{sp}^2 \times n_z^2$ elements of the formal Jacobian, because the mole fraction of species i at level j is not really a function of the mole fractions of every other species at every other level. The transport terms depend only on the mole fractions at the levels $j+1$, j, and $j-1$, reducing the mole fraction variables used in e.g. Equation 7.8 from $n_{sp} \times n_z$ to $n_{sp} \times 3$. A further reduction comes from the fact that for species i at level j, the only dependence on levels $j+1$ and $j-1$ is through the two mole fractions $q_{i,j-1}$ and $q_{i,j+1}$; the mole fractions of the other species do not affect species i at level j. Due to the way the matrices are represented in the code, this further

reduces the size of the mole fraction arrays in e.g. Equation 7.8 from $n_{sp} \times 3$ to $(n_{sp} \times 2) + 1$. Thus the size of the matrix to be inverted in Equation 7.13 is reduced from $n_{sp}^2 \times n_z^2$ elements to $(2n_{sp} + 1) \times n_{sp} \times n_z$ elements.

Since the goal is to compare photochemical model results with GPMS hydrocarbon mixing ratios in the deep troposphere, boundary conditions of the photochemical model are particularly critical. The model solves Equation 7.3, which requires either that the mole fraction or the flux be specified at both the upper and lower boundaries, for each model species. For species with long lifetimes relative to the Jovian day, the top boundary condition is diffusive equilibrium ($\phi = 0$). For the short-lived species, whose chemical lifetime is shorter than the diffusion timescale, local chemical equilibrium holds at the top boundary, and the left side of Equation 7.3 is set to zero. At the lower boundary, constant mole fraction boundary conditions were used for radicals (which were set to zero) and for well-constrained tropospheric species such as NH_3, CH_4, and PH_3; lower boundary conditions will be discussed in the following section in greater detail. In previous implementations of the code, mixing ratios of the long-lived stratospherically-generated species, such as C_2H_2 and C_2H_6, were also set to zero at the lower boundary. For the current study a zero-abundance lower boundary condition is not appropriate, since it causes the mole fraction profiles of the long-lived stratospheric hydrocarbons to be artificially defined by the position of the model's lower boundary level. Instead, a constant velocity profile was adopted for these species, following the scheme of Gladstone et al. (1996), where species were set to diffuse downwards across the lower boundary with the velocity K/H, with K and H equal to the eddy diffusion coefficient and the scale height at the lower boundary. The actual diffusive velocity for a well-mixed species would be zero, so a velocity of K/H is an upper limit to the real diffusive velocity, and would only be correct for a species that changes rapidly with height. In any case, this lower boundary condition allows the deep tropospheric mole fraction profiles for the long-lived stratospheric species to be constrained by the chosen eddy mixing profile, rather than by the altitude level of the chosen lower boundary.

Photochemical model environmental conditions

The photochemical model responds to a full description of the Jovian environment, including the solar radiation field, the pressure-temperature structure of the atmosphere, the assumed deep tropospheric gas composition, and the magnitude of vertical mixing and transport, as parametrized by the eddy mixing coefficient. The eddy mixing parameter is subject to great uncertainty, and is treated as a free parameter. The final section of this chapter is devoted to a discussion of eddy mixing in the troposphere.

Solar ultraviolet radiation is the dynamic energy source that drives the photochemical reactions in Jupiter's stratosphere. The photochemical model includes solar UV from 100 nm to 246 nm, in 147 bins each spanning 1 nm in wavelength. Solar flux at wavelengths below 100 nm is primarily absorbed in the ionosphere, and very little photolysis occurs as a result of wavelengths longer than 246 nm. Seven additional bins span the 121.6-nm Lyman-α line, from 121.45 nm to 121.75, at 0.05-nm resolution. Several sources were combined to create the "gal_comp" spectrum used for the model, shown in Figure 7.4 as the thick black line. The thin black line shows an example spectrum for 1992-05-19, as used in Edgington (1997) and Edgington et al. (1999), and the thick light grey (or yellow) line is the spectrum obtained by Solar Ultraviolet Spectral Irradiance Monitor aboard the Upper Atmosphere Research Satellite (SUSIM UARS), obtained on the same day that the Galileo Probe encountered Jupiter (1995-12-07). SUSIM UARS data was also gridded into 1-nm bins, but with centers offset by 0.5 nm. SUSIM UARS data was used to generate fluxes for the gal_comp spectrum at wavelengths of 115–119 nm and 122–246 nm. An example of the effect of interpolating the SUSIM UARS data from the 0.5-nm offset grid to the integral-wavelength grid used by the photochemical model can be seen in Figure 7.4 at the emission line near 133.5 nm, which gets partitioned into the 133-nm and 134-nm bins for the gal_comp spectrum.

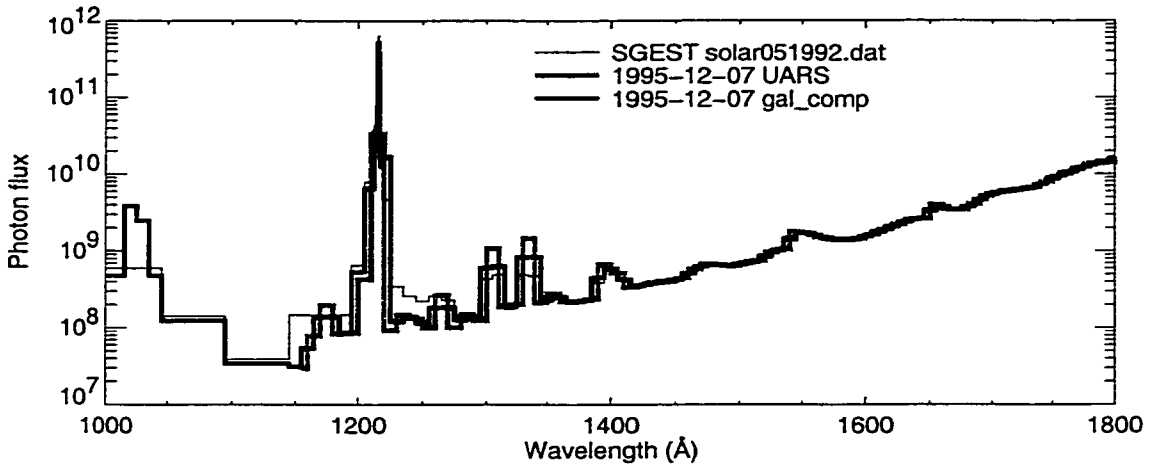

Figure 7.4 Solar ultraviolet spectra.

For the extreme ultraviolet (EUV) up to 105 nm, the EUVAC model as described in Richards et al. (1994) was used to generate the flux. This model calculates EUV flux based on the 10.7-cm radio flux, a quantity that has been monitored daily since approximately 1947 (the observed 10.7-cm radio flux for 1995-12-07 was used as the input to EUVAC). EUVAC generates the flux, in photons cm^{-2} s^{-1}, for the 100–105 nm interval, as well as the flux for the hydrogen Lyman β line at 102.572 nm and for the oxygen VI line at 103.191 nm. For the gal_comp spectrum, the flux from the 100–105 nm EUVAC bin was distributed equally between the 100-nm to 104-nm bins, and the Lyman β and O VI fluxes were added to the 102-nm and 103-nm gal_comp bins.

For the 105–114 nm range, no data were available from either the EUVAC model or the SUSIM UARS dataset, so the 1992-05-19 spectrum used in Edgington et al. (1999; black line in Figure 7.4) was used, after being reduced by a factor of 0.87, to compensate for the drop in solar activity between 1992-05-19 and 1995-12-07. The spectral resolution of the Lyman α profile in the 1992-05-19 spectrum is higher than the resolution of the SUSIM UARS data, so the high-resolution Lyman α profile from 1992-05-19 was used to generate gal_comp, after being scaled by a factor of 0.81 to compensate for the reduced solar activity. The Lyman α scaling factor was obtained from the relation in Tobiska and Eparvier (1998), which models Lyman α intensity as a function of the 10.7-cm solar flux index. Figure 3b

from Hinteregger (1981) demonstrates that the magnitude of the variability of solar flux at 110 nm over one solar cycle is 2/3 as great as the variation at 120 nm over one solar cycle; this factor of 2/3 was then used to scale the 0.81 Lyman α ratio to obtain the value of 0.87 for the 105–114 nm range.

Lower boundary conditions were discussed briefly in the previous section. Krasnopolsky (1995), in discussing a similar photochemical model of the Martian atmosphere, derived the following two requirements necessary to ensure a unique solution:

K1. "The number of boundary conditions given by densities and/or nonzero velocities should not be less than the number of chemical elements in the system, and the species, for which the boundary conditions are densities or velocities, should include all the elements in the system."

K2. "Any species that is produced by photochemical processes, but for which no chemical loss process is assumed, should be given by its density or velocity at one boundary."

As discussed previously, the chosen lower boundary conditions are zero mole fraction for radical (short-lived) species, and diffusive velocity for all other species. In addition, the lower boundary conditions specified in Table 7.1 satisfy Kransnopolsky's requirements. K1 is satisfied because He, CH_4, NH_3, and PH_3 contain all the chemical elements used in the model. An additional specification of a molecule containing the element hydrogen would satisfy the second part of K1, but the H_2 density is specified at every level of the model by the model atmosphere input file, so a specific boundary condition is not required. Although N_2 is a product of ammonia photochemistry, molecular nitrogen is inert and transparent to UV and FUV, there are no loss processes for it in the model, so by K2 a lower boundary density or velocity must be specified. The GPMS-derived value (see Chapter 6) is used for N_2, and is considerably smaller than the 10^{-5} molecular nitrogen mixing ratio predicted by Fegley and Lodders (1994) for "the visible atmosphere." This discrepancy will be examined in the conclusion.

Table 7.1 Photochemical model data: lower boundary mole fractions.

Model species	Lower boundary mole fraction	Reference
He	0.1359	HAD (Von Zahn et al. 1998)

Table 7.1 Photochemical model data: lower boundary mole fractions.

Model species	Lower boundary mole fraction	Reference
CH_4	1.91×10^{-3}	GPMS (Chapter 6)
NH_3	7.01×10^{-4}	Folkner et al. (1998)
N_2	2.33×10^{-7}	GPMS (Chapter 6)
PH_3	5.184×10^{-7}	Voyager IRIS (Kunde et al. 1982)

The model atmosphere uses a smoothed version of the temperature-pressure structure derived by Seiff et al. (1998) from the ASI data, for the Galileo Probe entry trajectory. For use in this simulation, the pressure-temperature profile was extended below the 23.3-bar deepest ASI datapoint following a dry adiabat down to –160 km (about 30 bar). The portion of the temperature profile colder than 500 K is shown in Figure 7.5. Higher than about 1000 km / 1 nbar, the model temperature becomes isothermal at 980 K.

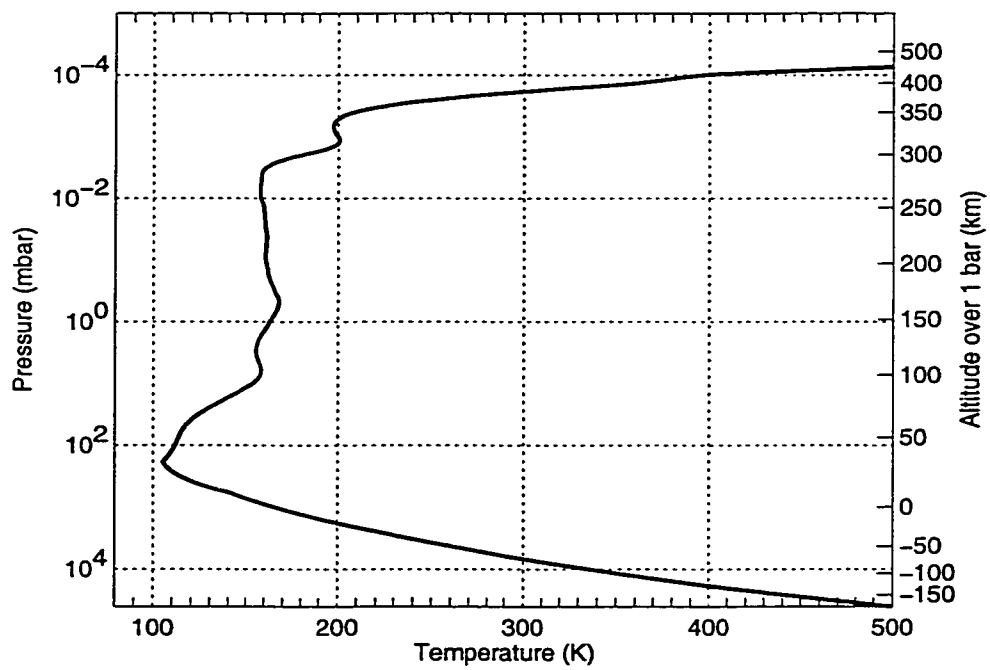

Figure 7.5 Atmospheric structure. Compare with subsequent figures to match pressure and temperature with altitude.

The chemistry of the model encompasses both photolysis and kinetics (chemical reactions between two or more gases), as well as condensation. Appendix B contains a

complete list of data used to model the chemistry, from saturated vapor functions to UV cross-sections and reaction rate constants.

Eddy diffusion profiles and model results

Since the DL2a (8.5–12 bar) hydrocarbon mixing ratios from Chapter 6 are obtained at such a great distance from their stratospheric source region, vertical transport is the most important aspect of the photochemical model in terms of explaining the observed hydrocarbons. Below the homopause, the vertical transport of gases is dominated by turbulence, winds, convection, and waves. As described at the beginning of this chapter, all of these effects are collectively represented by the eddy diffusion coefficient in one-dimensional photochemical models. The canonical formulation for the stratospheric eddy diffusion coefficient is

$$K(n) = K_H\left(\frac{n}{n_H}\right)^{-\gamma}, \qquad 7.14$$

where the subscript H indicates the homopause value. Atreya et al. (1981) constrained K_H to be 1.4×10^6 cm^2 s^{-1} from Voyager UVS stellar occultation, with the homopause number density $n_H = 1.4 \times 10^{13}$ cm^{-3}. The same homopause values were used in ESET and Gladstone et al. (1996), although ESET use the power law exponent $\gamma = 0.6$, while Gladstone et al. (1996) favor $\gamma = 0.45$. According to Lindzen (1971), the power-law eddy diffusion formulation of Equation 7.14 is appropriate in the upper stratosphere as a parametrization of transport via diurnal tides and gravity wave breaking. The value of γ chosen for this study is 0.6 (after ESET), but the exact value of the exponent is not a major influence on the tropospheric hydrocarbon mole fractions, as will be discussed below.

The appropriate magnitude of the eddy diffusion coefficient in much of Jupiter's troposphere is essentially unknown, and is treated as a free parameter in the model. In order to establish a limiting value for K, Hunten (1975) invokes the Prandtl mixing-length hypothesis that

$$K \sim vL. \qquad 7.15$$

Hunten suggests that a typical velocity for this argument would be on the order of 1 cm/s,

ranging up to an extreme value of 100 m/s. A good choice for the mixing length is the atmospheric scale height H, which varies (for a hydrostatic atmosphere) as a function of temperature according to Equation 7.2, but with the average atmospheric molecular weight in the denominator. Jupiter's atmospheric scale height varies from about 20 km near the tropopause to almost 70 km at 30 bar. The above estimates of mixing length and velocity result in typical K values of $2\text{–}7 \times 10^6$ cm^2 s^{-1}, with maximum values reaching $2\text{–}7 \times 10^{10}$ cm^2 s^{-1}.

Eleven different profiles of the eddy diffusion coefficient were used in order to compare photochemical model results with the large tropospheric hydrocarbon mixing ratios presented in Chapter 6. Figure 7.6 shows the first six K-profiles used, which are arbitrarily indexed by numbers x00 through x40. K_{x00} is the nominal profile, based on the Edgington *et al.* (1999) profile for 7° N (see Figure 7.2), with Equation 7.14 giving the eddy mixing constant in the upper stratosphere and with a linear extrapolation of the Edgington *et al.* (1999) profile into the troposphere. Profile K_{x05} is constant below the 40-km level at 450 cm^2 s^{-1}. This value implies a tropospheric mixing timescale on the order of $T \sim L^2/K =$ 780 years. Although such a long mixing timescale is probably not physically realistic, it was nonetheless adopted for profile K_{x05} in order to explore the effect of removing the rapid increase in K with depth below the tropopause on the tracer hydrocarbon concentrations (THCs). Profile K_{x08} follows the functional form of Gladstone *et al.* (1996), which is described by Equation 7.14 above the tropopause, and has a constant K in the troposphere. However, K_{x08} uses a tropospheric value four times that of Gladstone *et al.* (1996), and the transition occurs at 100 km, or about 50 km *above* the tropopause. K_{x08} was intended to test THC sensitivity to the value of K near the tropopause. Finally, profiles K_{x10}, K_{x15}, and K_{x20} return to the Edgington *et al.* (1999) tropopause K, but increase to much larger values in the troposphere. These three profiles examine the effect of parametrizing tropospheric K using Equation 7.15, with the (temperature-dependent) scale height as the mixing length, and respective mixing velocities of 1 cm s^{-1}, 10 cm s^{-1}, and 100 m s^{-1}.

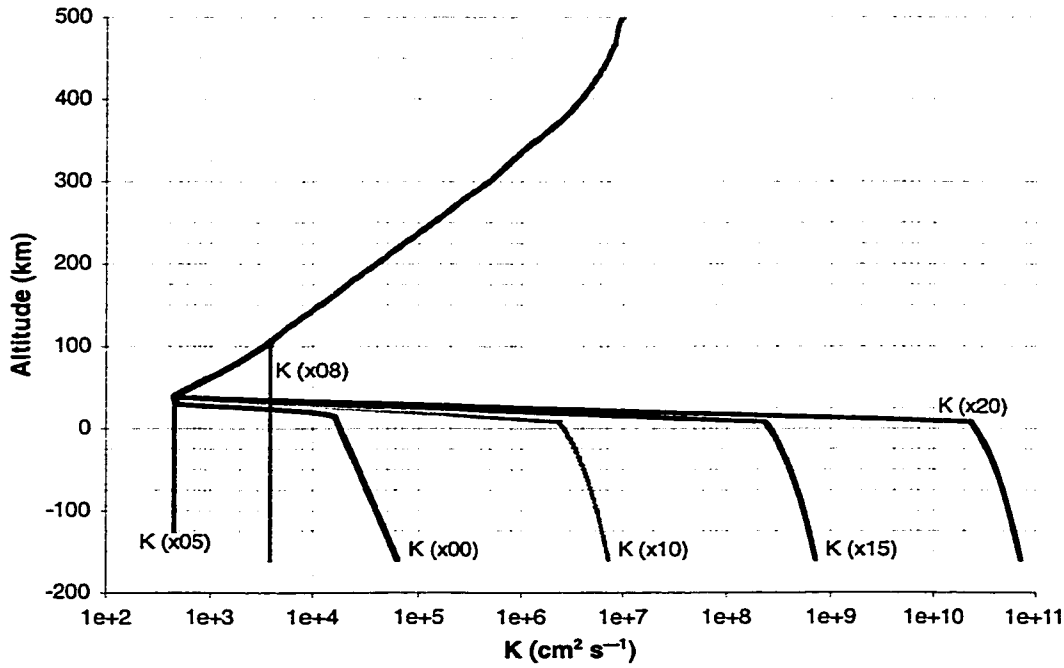

Figure 7.6 Eddy mixing profiles corresponding to Figures 7.7 and 7.9–7.13.

Figure 7.7 presents the vertical distributions of the tracer hydrocarbons (those hydrocarbons constrained by GPMS measurements), following the nominal eddy diffusion profile K_{x00}. Square datapoints in the lower right corner represent the GPMS measurements of Chapter 6; for clarity that region of the plot is enlarged and shown in Figure 7.8. One notable characteristic of the plot is that several species, primarily butane (C_4H_{10}), ethylene (C_2H_4), and propylene (C_3H_6), exhibit "kinks" at around the 40-km altitude, which corresponds to the minimum of K in the tropopause region (see Figure 7.6). Other species exhibit "shelf" behavior instead. The explanation for this difference is not obvious, but comparison of output from all the cases shows that "kinks" are exhibited only in those K-profiles with very low eddy diffusion in the area of the tropopause temperature minimum. Perhaps the very low eddy diffusion coefficient results in a long diffusion timescale, so that the system is closer to local chemical equilibrium, and temperature-dependent chemistry leads to the kinks. In any case, the photochemical model fails to predict the THC mole fractions detected by the GPMS, the rank of the abundances of the hydrocarbons relative to each other, and the spread in the range of values encountered by the GPMS. According to

the analysis in Chapter 6, the rank from most to least abundant is C_2H_4, C_2H_2, C_3H_8, C_3H_6 and C_2H_6, and C_4H_{10} (upper limit). On the other hand, the model output ranking from most to least abundant is C_2H_6, C_2H_2, C_2H_4, C_3H_8, C_4H_{10}, and C_3H_6. The C_2-hydrocarbon abundance ranking is exactly reversed. On the other hand, the model successfully duplicates the GPMS observation that C_3H_8 outranks C_3H_6, and C_3H_8 is more abundant than C_4H_{10}. Compared to the model output for this *K*-profile, the GPMS THCs are overabundant at the 10-bar level by a factor ranging from about 10^4 for ethane to about 10^{10} for C_3H_6. Whereas the GPMS data span about two orders of magnitude (although admittedly some of the GPMS values are upper limits), the model abundances span seven orders of magnitude.

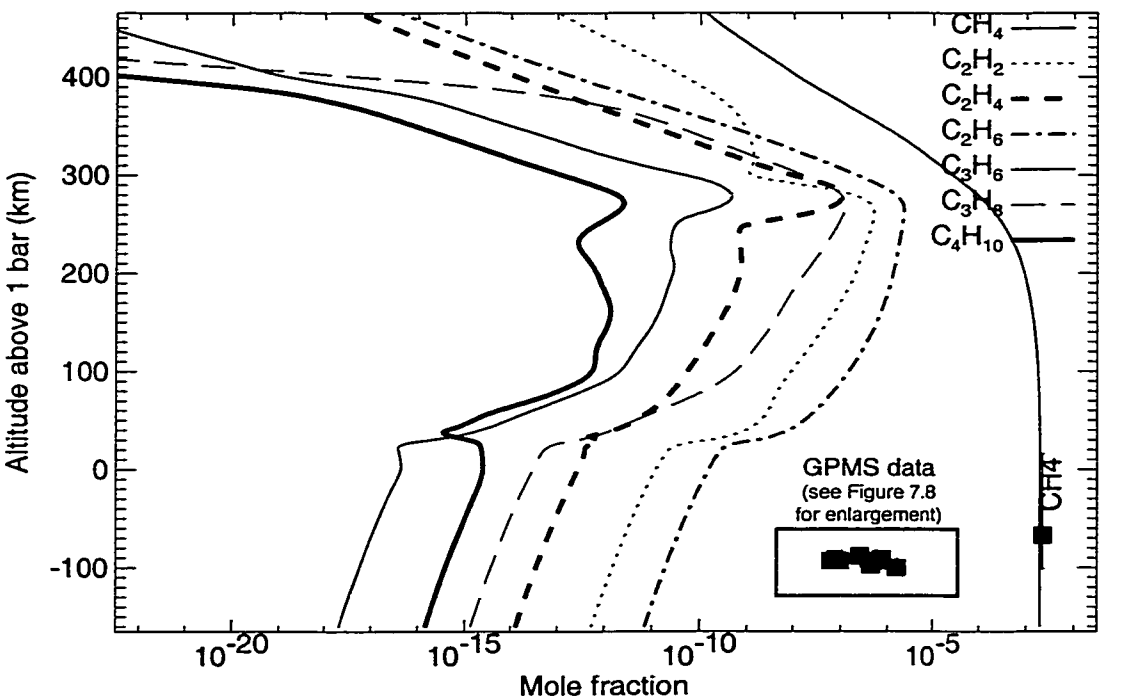

Figure 7.7 Model hydrocarbon profiles corresponding to eddy mixing profile K_{x00} in Figure 7.6. See Figure 7.8 for an enlargement of the GPMS-derived hydrocarbon mole fractions.

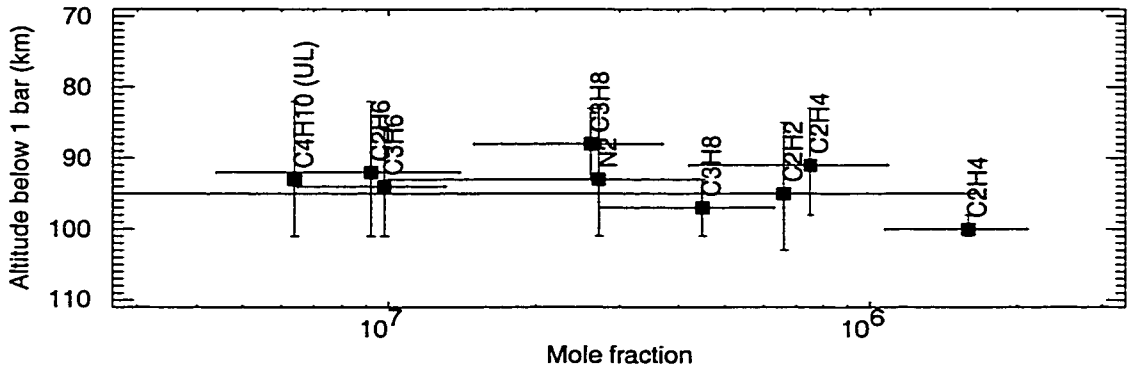

Figure 7.8 Mixing ratios of hydrocarbons derived from GPMS data in Chapter 6.

The dramatic decrease in hydrocarbon mole fractions (at the "shelves" and "kinks" in the mole fraction profiles) from the previous K_{x00} experiment was noted to correspond with the minimum of K in the tropopause. Could the tropospheric hydrocarbon abundances be increased if K did not increase drastically with depth below its minimum value? To investigate this possibility, profiles K_{x05} and K_{x08} were created (see Figure 7.6). Going from profile K_{x00} to K_{x05} leaves much more of the atmosphere in the quiescent state (780-year diffusion timescale) previously confined to the tropopause; if indeed the effect of the reduced diffusion is to allow the system to reach a different local chemical equilibrium as was previously mentioned, then the more severe "kinks" in Figure 7.9 and the even more disturbed THC abundance ranking (compared to the GPMS ranking) is not surprising. All of the discrepancies previously noted between the K_{x00} profile mole fractions and the GPMS mole fractions are even more extreme for the K_{x05} profile: the THC mole fractions are more depleted, their rankings at 10 bar show the same differences, and the overall spread in model mole fractions has increased from about 10^8 to about 10^{10}. However, there is a better match to the GPMS results in that the ethane abundance increased to a mere factor of 30 depletion relative to GPMS (for the K_{x00} simulation it was depleted by about 10^4). Profile K_{x08} is similar to K_{x05} in that it lacks the tropospheric increase in K, but in the K_{x08}-profile, the minimum K is a somewhat greater 4000 cm^{-2} s^{-1}. The tropospheric THC mole fractions (see Figure 7.10) are very similar to those in the K_{x00} experiment, with a larger ethane abundance and more vertically-extended kinks and shelves.

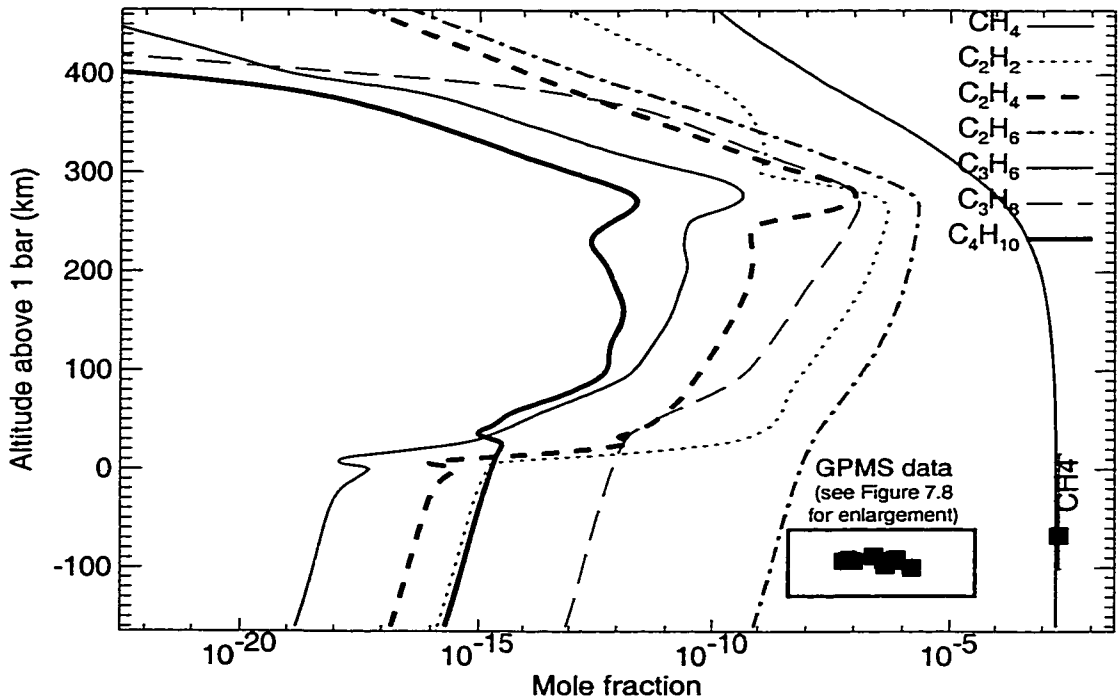

Figure 7.9 Model hydrocarbon profiles corresponding to eddy mixing profile K_{x05} in Figure 7.6.

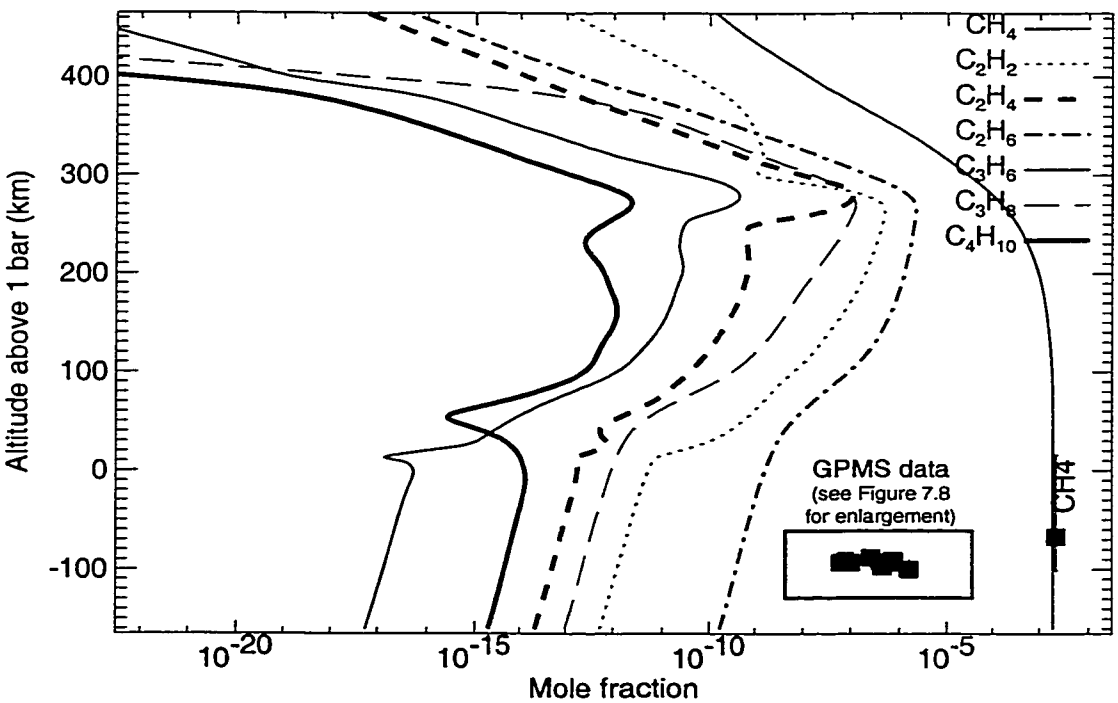

Figure 7.10 Model hydrocarbon profiles corresponding to eddy mixing profile K_{x08} in Figure 7.6.

All of the K-profiles so far have specified mixing in the troposphere that is much weaker than the typical value obtained by Hunten (1975). The following three profiles, K_{x10}, K_{x15}, and K_{x20}, remedy the situation with tropospheric eddy mixing formulated using Equation 7.15, with respective eddy mixing velocities of 1 cm s^{-1}, 10 cm s^{-1}, and 100 m s^{-1}. The model output from these three K-profiles is shown in Figures 7.11 to 7.13. The "kinks" from the previous plots are gone, presumably because eddy diffusion is now too rapid to allow chemistry to control the THC-profiles near the tropopause. Instead, "shelves" are apparent as effects of the strong gradient in eddy diffusion strength moving into the troposphere. With each incremental increase in tropospheric K from run to run, the mole fraction gradients grow increasingly larger. In the troposphere, the model mole fractions maintain the same relative abundances, shifting together as a group to lower values with increasing tropospheric eddy mixing strength. This response makes sense because the weak mixing at the tropopause acts as a bottleneck in the supply of stratospheric hydrocarbons, and stronger mixing below this bottleneck means that the stratospheric source is less effective at contaminating the troposphere. Again, the GPMS THCs are poorly matched; their two order of magnitude spread is much tighter than the eight orders of magnitude spanned by the model THCs, and the actual mole fractions can be seen to be lower in the model by huge factors. The previous comments concerning the THC relative rankings for the K_{x00} case are the same for these runs; a reasonable similarity since the rankings are controlled largely by stratospheric chemistry and transport, while only the tropospheric K-profiles are changing between K_{x00}, K_{x10}, K_{x15}, and K_{x20}.

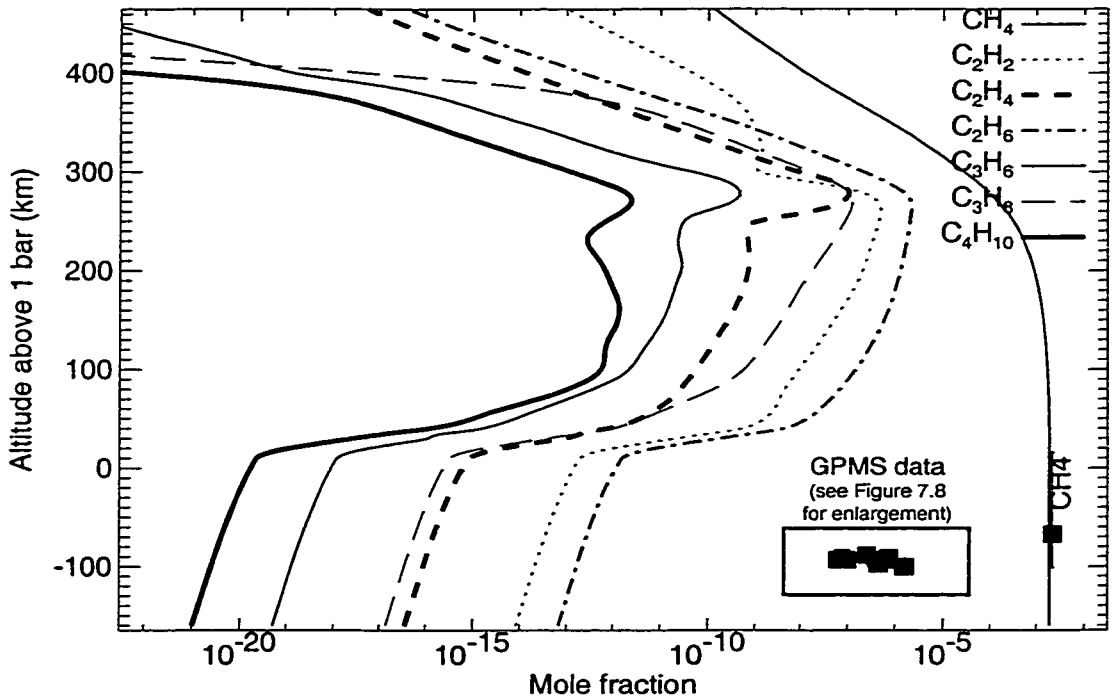

Figure 7.11 Model hydrocarbon profiles corresponding to eddy mixing profile K_{x10} in Figure 7.6.

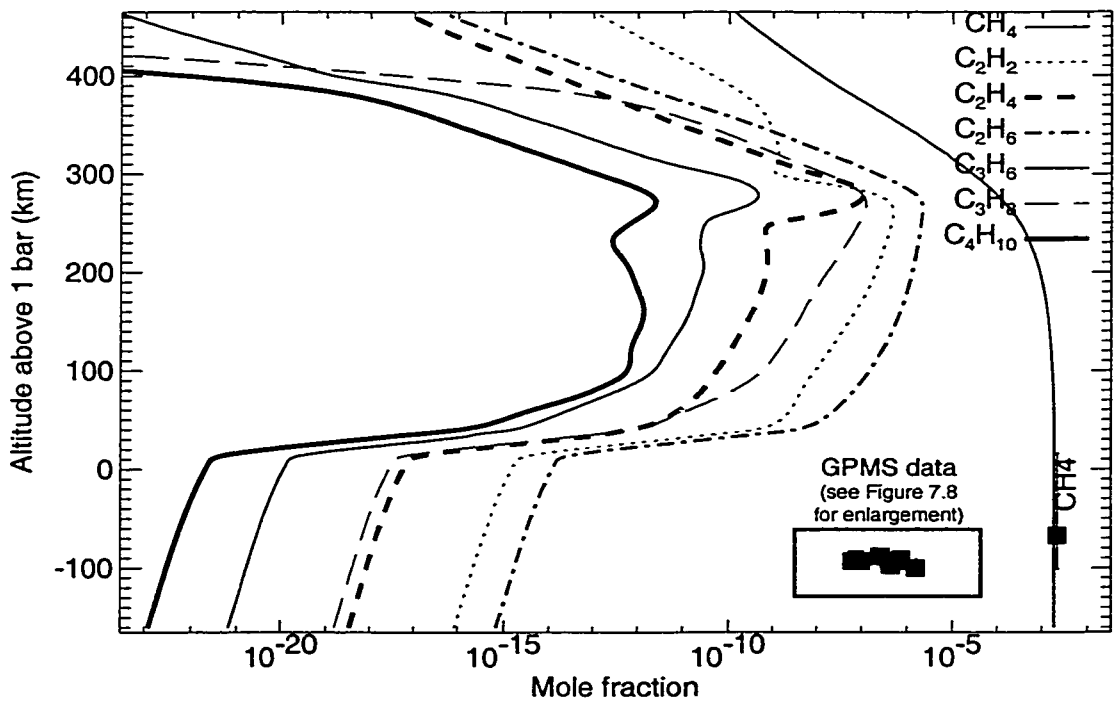

Figure 7.12 Model hydrocarbon profiles corresponding to eddy mixing profile K_{x15} in Figure 7.6.

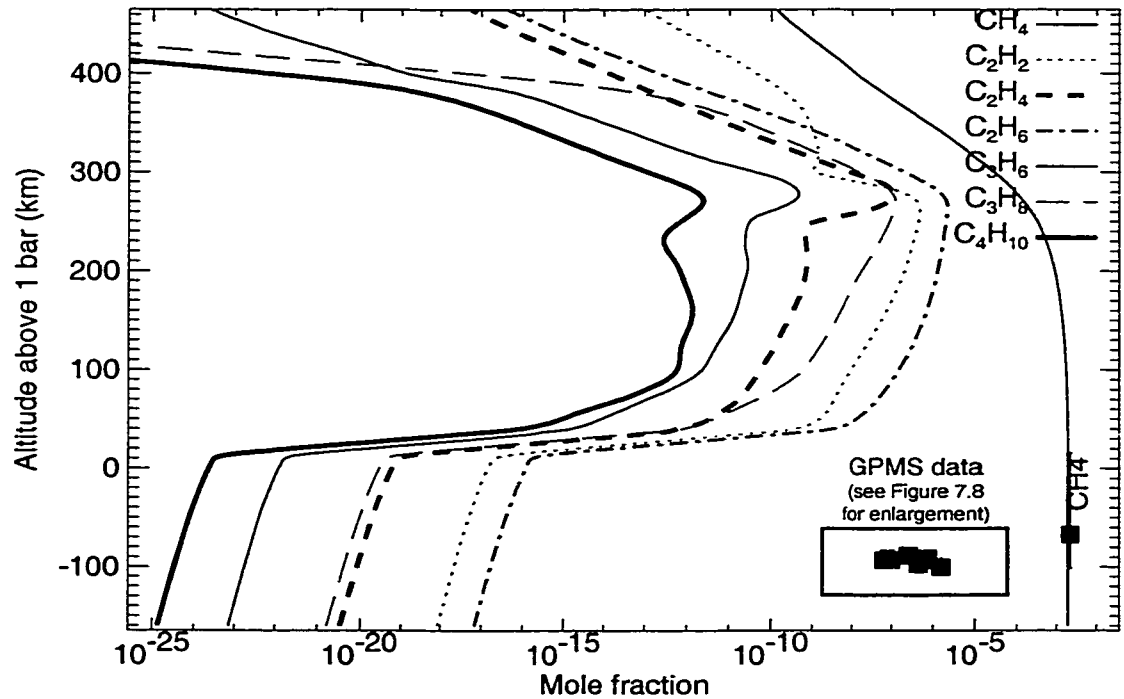

Figure 7.13 Model hydrocarbon profiles corresponding to eddy mixing profile K_{x20} in Figure 7.6.

Figure 7.14 shows several eddy diffusion profiles with forms that are radically different from the profiles considered so far. K_{x25} examines a profile qualitatively based on the Galileo probe entry site zonal winds, and the assumption that high wind shear leads to increased mixing. Deeper than 4 bar, where wind shear was minimal in the probe site, K_{x25} is calculated using Equation 7.15, using a mixing velocity of 1 m s^{-1}. K_{x28} has the same form as K_{x25}, but has strong mixing extending through the tropopause to about 150 km. K_{x30} and K_{x35} are cases with strong mixing across the tropopause, and the same deep tropospheric mixing as K_{x10} and K_{x15}, respectively. Finally, the uniform eddy mixing case K_{x40} is examined, even though it fails to match the observed homopause eddy mixing coefficient of 1.4×10^6 cm^6 s^{-1} at 1 μbar (Atreya *et al.*, 1981).

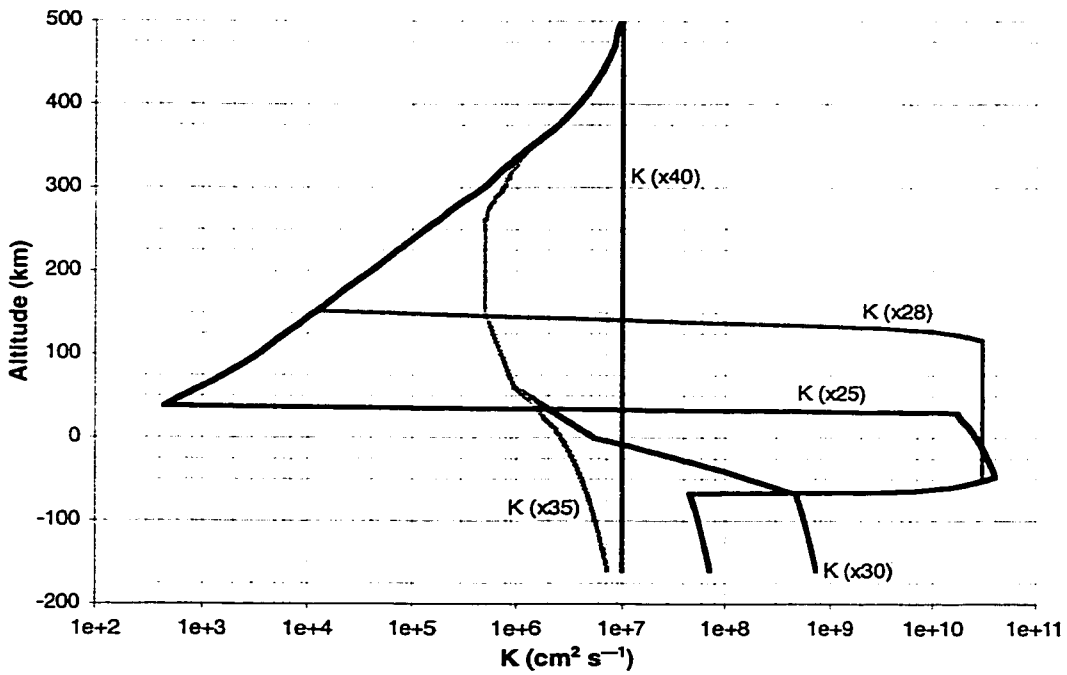

Figure 7.14 Eddy mixing profiles corresponding to Figures 7.15–7.19.

Figure 7.15 shows model THC profiles based on the probe site wind shear inspired profile K_{x25}. The K_{x25} output is similar to the output from the K_{x10}–K_{x20} series; there is a sharp gradient in K_{x25} mole fraction profiles where there is a sharp gradient in eddy mixing coefficient at around 40 km, and the deep THC rankings and mole fractions are similar. In the high wind shear region, where K is set to its largest values, the THC mole fractions are constant with altitude. Profile K_{x28} was developed to test the idea that raising the high-K zone to higher altitudes might bring more stratospheric hydrocarbons into the region of height-independent mole fractions. But Figure 7.16 shows that other than making deep propane more abundant than deep ethylene, raising the high-K zone does very little to change the tropospheric THC profiles. The presence of the steep gradient in K, from the regime of Equation 7.14 to the high-K zone, results in the same familiar "shelf" in the mole fraction profiles of the THCs, but at a higher altitude.

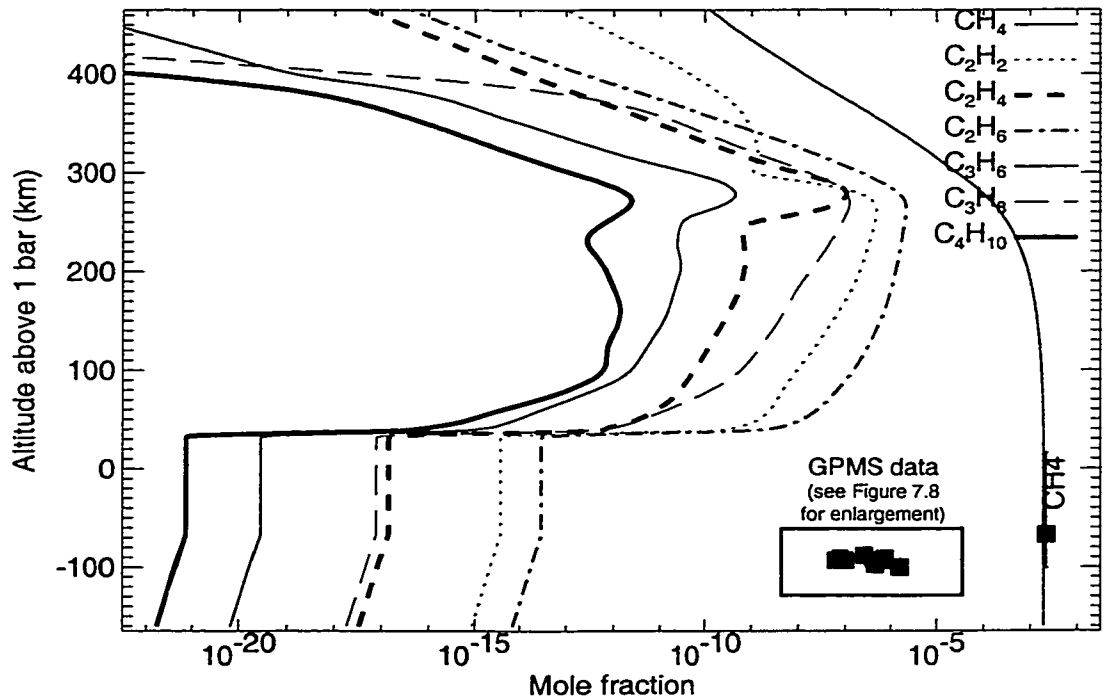

Figure 7.15 Model hydrocarbon profiles corresponding to eddy mixing profile K_{x25} in Figure 7.14.

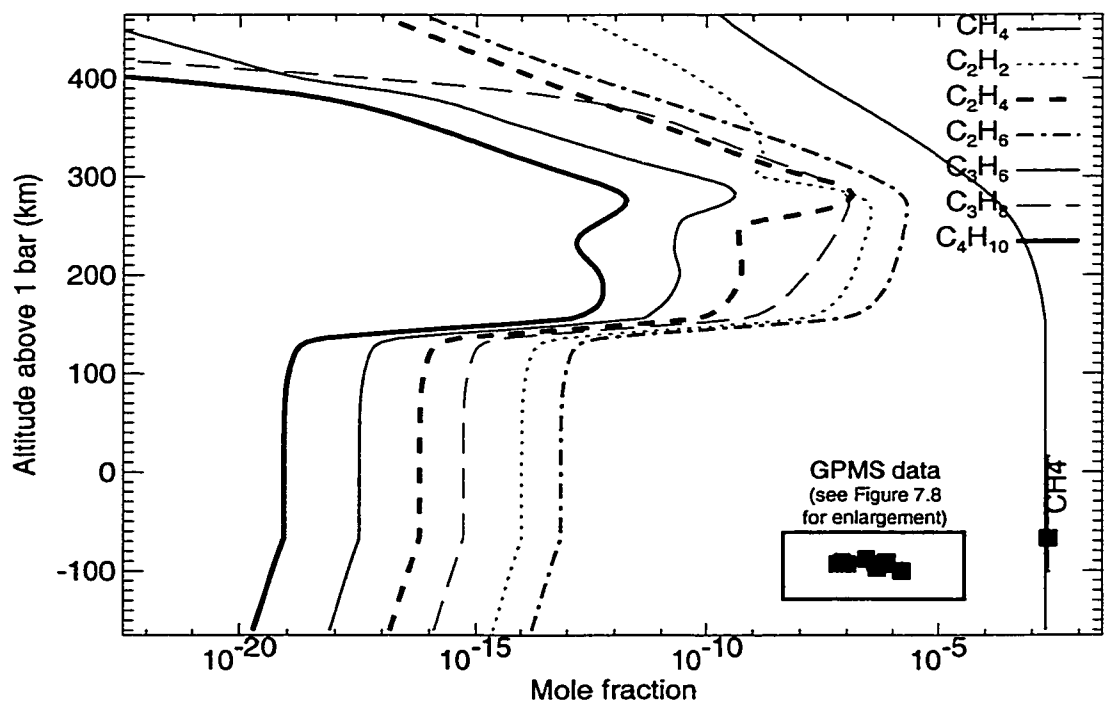

Figure 7.16 Model hydrocarbon profiles corresponding to eddy mixing profile K_{x28} in Figure 7.14.

Since the previous studies had shown that the rapid increase in K with depth corresponds to a rapid decrease in mole fraction with depth, profiles K_{x30} and K_{x35} were created, featuring K that increases with depth but at a slow rate. The resulting model output is shown in Figure 7.17 for K_{x30} and Figure 7.18 for K_{x35}. As expected, the mole fraction gradient shelves are gone, but the problem still remains that the tropospheric mole fractions are at least five orders of magnitude too small. Switching from profile K_{x35} to K_{x40} (see Figure 7.19) results in an increase of tropospheric mole fractions by one order of magnitude, but the upper stratosphere composition is strongly affected, an unlikely scenario.

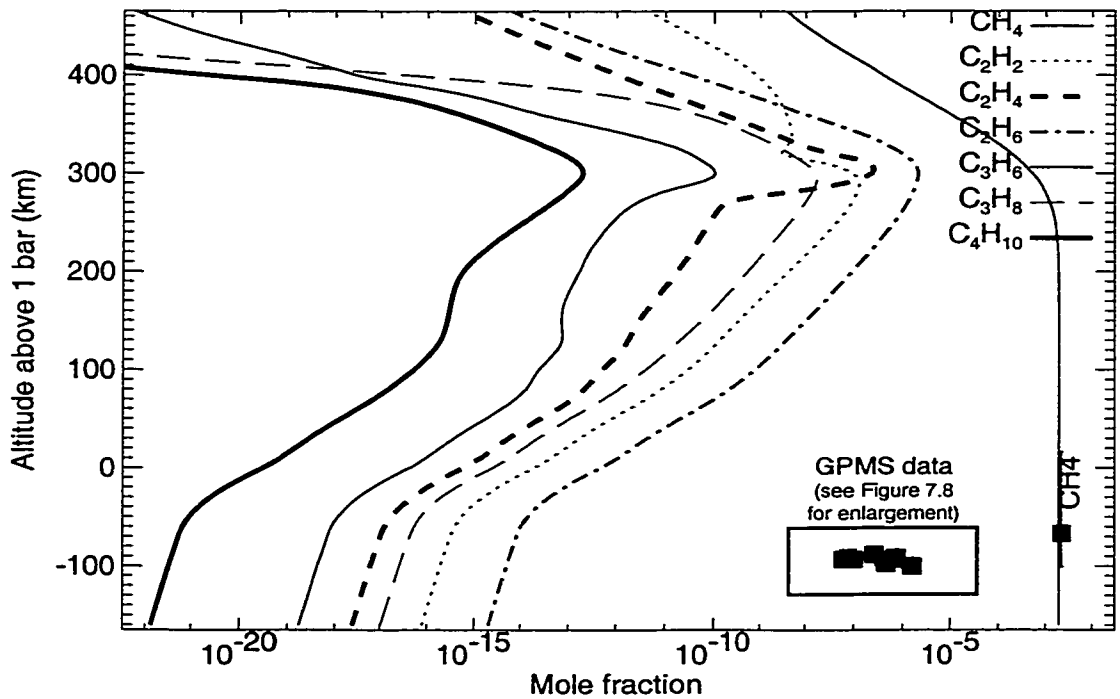

Figure 7.17 Model hydrocarbon profiles corresponding to eddy mixing profile K_{x30} in Figure 7.14.

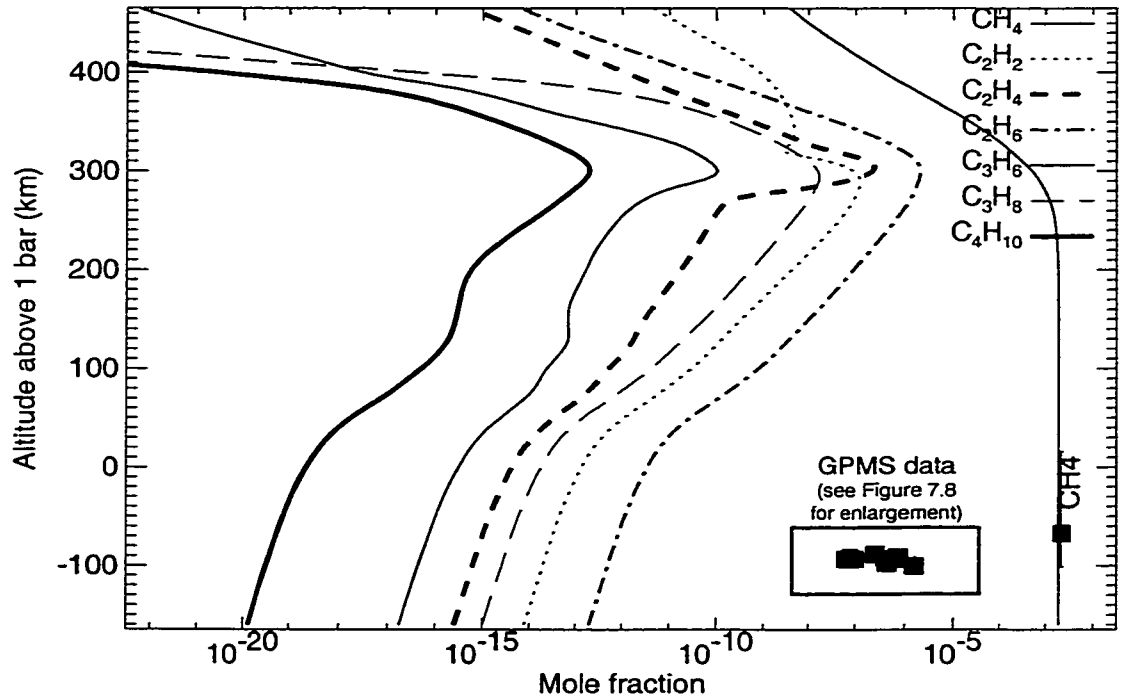

Figure 7.18 Model hydrocarbon profiles corresponding to eddy mixing profile K_{x35} in Figure 7.14.

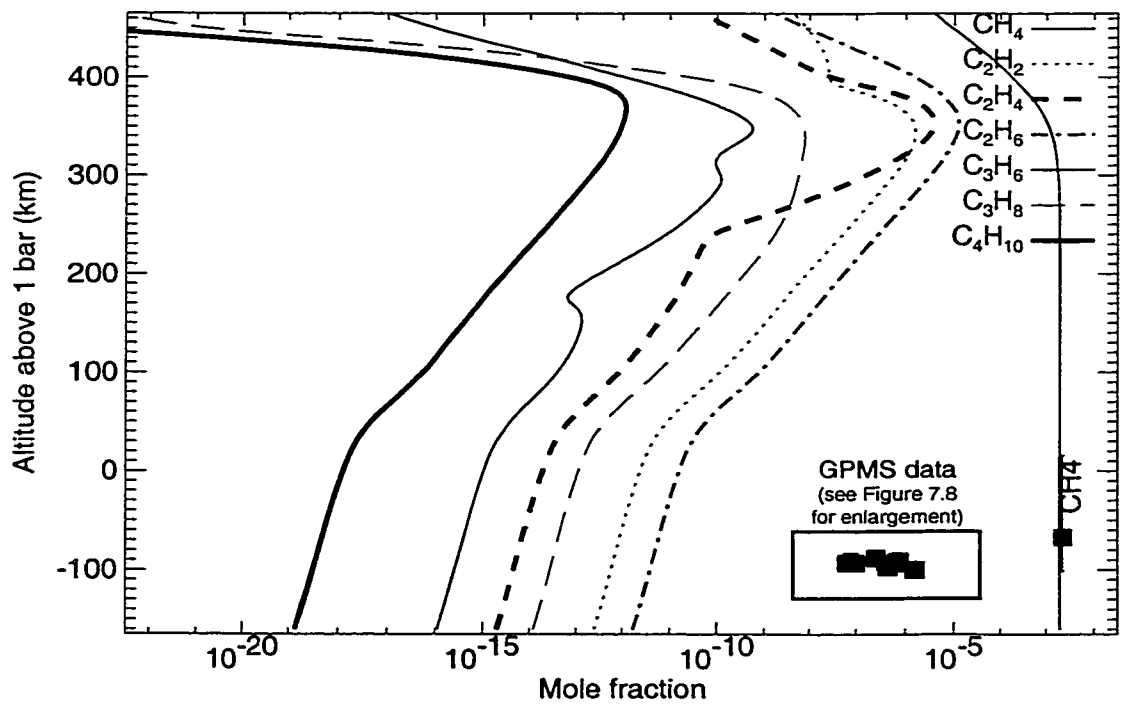

Figure 7.19 Model hydrocarbon profiles corresponding to eddy mixing profile K_{x40} in Figure 7.14.

Although the previous discussion inevitably leads to the realization that the photochemical model is unable to match the 10-bar GMPS hydrocarbon mole fractions, the years of research that lead to this realization were not completely wasted. The disagreement between model and observations is useful for highlighting the limitations and directions of growth for each. The Conclusion (Chapter 9) will explore these aspects of the hydrocarbon data analysis and modeling.

CHAPTER VIII

Model of Jovian Downdraft with Entrainment

Chapter 1 described observations of the distribution of condensible volatile (CV) gases and their associated clouds, and concluded with an introduction to the downdraft scenario. The downdraft scenario is one possibility raised to explain two general conclusions drawn by the Galileo Probe: that the probe site air was "dried out" of its CVs to depths well below the locations of expected clouds, and that the expected clouds themselves were largely missing. Both of these characteristics are thought to be characteristic of Jovian 5-μm hotspots, and not unique to the Galileo PES. All modeling efforts to date ultimately achieved the necessary drying via vertical displacement of Jovian air. In addition to the one-dimensional downdraft approach taken here, vertical displacement has also been accomplished in multidimensional fluid models of either thunderstorm-type circulation, fluid convection, or large-scale wave-type motion.

Review of terrestrial and Jovian downdraft modeling work

The Downdraft with Entrainment (DDE) model presented here has its heritage in models airflow in terrestrial thunderstorms. Equations for the lapse rate $\Gamma = \frac{dT}{dz}$, including the effect of entraining moisture and sensible heat from the surrounding air, are given in atmospheric science textbooks such as Hess (1959) and Pruppacher and Klett (1978).

Pruppacher and Klett (1978; hereafter PK78) describe the rate of mixing using the entrainment rate μ, defined as

$$\mu \equiv \frac{1}{m}\frac{dm}{dz} = \frac{1}{l}, \qquad 8.1$$

where m is the mass of the air parcel and l is a characteristic mixing length. PK78 mention both the steady-state plume or jet as well as the thermal or warm bubble type of one-dimensional entrainment models, which both were intended to describe the upwards motion of entraining parcels in the earth's atmosphere. Depending on the type of model, estimates for the entrainment rate in PK78 are:

$$\begin{aligned} l &= 5R; \quad \mu = \frac{0.2}{R} \qquad \text{plume/jet model} \\ l &= \frac{5R}{3}; \quad \mu = \frac{0.6}{R} \qquad \text{thermal/bubble model} \end{aligned} \tag{8.2}$$

PK78 cite laboratory experiments for justification for both models but do not describe the experiments; the reader is referred to references within PK78 for more information.

Haman (1973) presented a 1-D model with formulations similar to those in PK78 and others, but with several notable differences. Because his goal was to simulate a long-lived downdraft in a terrestrial thunderstorm, Haman (1973) tracked quantities in the ambient atmosphere, the thunderstorm updraft, and the downdraft. He added momentum and condensed water to the list of quantities entrained into and out of the parcel. His formulation for the entrainment rate differed from the definition of μ in Equation 8.1 by replacing the parcel mass m with the parcel vertical mass flux.

Niewiadomski (1979; hereafter N79) used the analytic model of Haman (1973) to build his computational 1-D model of a thunderstorm downdraft. The full derivation of the model equations given in N79 provided the mathematical inspiration for the current DDE model for Jovian small-scale downdrafts. An important consideration regarding simplistic 1-D models is that even though they provide a detailed analysis of physical properties such as moisture content and momentum in an idealized parcel, they are not intended to provide complete descriptions of complex atmospheric systems such as terrestrial thunderstorms or Jovian 5-μm hotspots. N79 addresses this consideration with the statement,

> The aim of this model is not necessary [sic] to give a realistic simulation of a steady cumulonimbus cloud, it is rather a tool for quantitative analysis of various physical processes taking place in such a cloud, especially for investigation of the role and importance of entrainment, cloud and precipitation water evaporation, and environmental conditions in the steady-state downdraft maintenance.

Two more papers from Haman and Niewiadomski's University of Warsaw team further developed the model. In Haman and Niewiadomski (1980; hereafter HN80), several parametrization schemes for the entrainment rate were considered, and condensed water was allowed to entrain into the downdraft at a different rate from cloud air. Whereas Equation 8.2 described an entrainment rate proportional to the jet/thermal radius, HN80 examined parameterizations with constant μ, as well as with μ proportional to the difference in vertical velocity (w) between the jet and environment:

$$\mu \propto \frac{w_{\text{downdraft}} - w_{\text{updraft}}}{R w_{\text{downdraft}}} \qquad 8.3$$

Finally, Pawlowska-Mankiewicz (1987; hereafter PM87) used the same computational model as HN80, but modified the model inputs. HN80 used an ambient atmosphere with an almost constant profile of equivalent potential temperature θ_e,[1] while

---

1. The following quick review of thermodynamic quantities is based on definitions from Iribarne and Godson (1981). Potential temperature θ is often used as a measure of the relative density of unsaturated airmasses, and is defined as the temperature that the airmass would acquire if it were brought to a reference pressure level p_{ref}:

$$\theta = T\left(\frac{p_{\text{ref}}}{p}\right)^{R/c_p} \qquad 8.4$$

Usually the computation is done with the gas constant and specific heat for dry air, which can lead to inaccuracies in the adiabatic transformation to p_{ref}. To correct for this effect, T is replaced by the virtual temperature T_v to define the virtual potential temperature θ_v. For a moist parcel of air, the virtual temperature T_v is defined as the temperature of dry air having the same values of pressure and volume, and is obtained from the relation:

$$pv = R_{\text{moist}}T = R_{\text{dry}}T_v, \qquad 8.5$$

where the Rs are the appropriate moist and dry specific gas constants. Virtual temperature is typically quite close to the actual temperature.

Potential temperature fails as a measure of relative airmass density under saturated conditions, since condensation of vapor releases latent heat and lowers the density of the airmass. The effect of latent heat release can be estimated using one of two equivalent potential temperatures. For a saturated airmass at temperature T_0, the isobaric equivalent potential temperature θ_{ie} is obtained by condensing all the water from the air at constant pressure, with the latent heat release heating the resulting dry air mass, and the water being removed from the system as it condenses. The resulting dry airmass has a temperature T_{ie}, and is then brought to the reference level according to Equation. 8.4. Alternatively, the adiabatic equivalent (or pseudo-equivalent) potential temperature θ_{ae} is obtained by adiabatically expanding the air (to "zero pressure") until all the water condenses out, with the water being removed from the system as it condenses, and then compressing the resulting dry airmass dry adiabatically until it reaches p_{ref}. Neither method is truly adiabatic because the condensed water leaves the system; in the transformation leading to θ_{ie} the water leaves the system at temperatures T such that $T_0 < T < T_{ie}$, whereas in the transformation leading to θ_{ae} the water leaves the system at temperatures T such that $T < T_0$. Thus, $\theta_{ie} < \theta_{ae}$. The migraines induced by attempting to distinguish between

PM87 examined a case with environmental profile of equivalent potential temperature that decreased with height toward a broad minimum and then again increased above the minimum in θ_e (see Figure 8.1). Whereas HN80 adopted a consistent parametrization of μ with height (preferring in fact μ = constant), the PM87 results were based on a case with constant μ around the level of the θ_e minimum, and $\mu = 0$ outside of the layer.

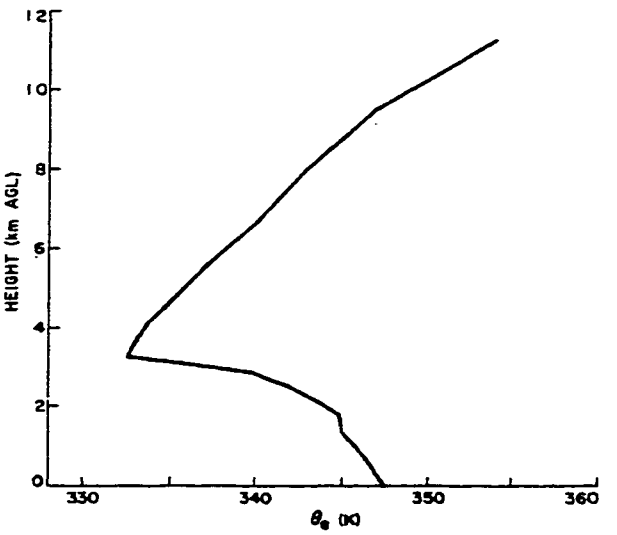

Figure 8.1 Potential temperature profile in the environment of the South Park thunderstorm described in Cotton (1989).

---

1. (continued)

these quantities are presumably the reason that the unspecified quantity "θ_e" is used in works such as PM87 and Cotton (1989).

Rigorous definitions of θ_{ie} and θ_{ae} are beyond the scope of this work, since the variation of the latent heat, specific heat, and water mixing ratio with respect to temperature would require path-dependent integrals. Instead, I quote approximations to the equivalent potential temperatures of saturated airmasses assembled from equations in Iribarne and Godson (1981):

$$\theta_{ie} = \left(T_0 + \frac{L_v}{c_{p(\mathrm{dry})}} r\right)\left(\frac{p_{\mathrm{ref}}}{p}\right)^{R/c_p} \qquad 8.6$$

$$\theta_{ae} = T_0 \exp\left(\frac{L_v r}{T_0 c_{p(\mathrm{dry})}}\right)\left(\frac{p_{\mathrm{ref}}}{p}\right)^{R/c_p}, \qquad 8.7$$

where r is the mass mixing ratio of water with respect to dry air, and L_v is the latent heat of condensation or freezing. If the moist airmass were initially subsaturated, equivalent potential temperatures could be calculated by first expanding it adiabatically until it was saturated at temperature T_s, and then using T_s in Equations 8.6 and 8.7.

The limited entrainment region coupled with the potential temperature profile resembling that of Figure 8.1 allowed the downdrafts of PM87 to reach the ground, a result not satisfactorily achieved by the other Warsaw models. PM87 claims that her stratified θ_e profile is characteristic of terrestrial thunderstorms, and indeed Cotton (1989) shows a profile of θ_e for the environment surrounding a 1977 quasisteady thunderstorm in South Park featuring a minimum in θ_e with a contrast of about 15 K. The propriety of PM87's assumption of an atmospheric profile with a minimum in θ_e is supported by Cotton's (1989) observation that the most significant downdrafts in the South Park system were associated with inflow of the low-θ_e air.

Although the need to explain the dryness of 5-μm hotspots accelerated with the findings of the Galileo probe, pre-Galileo papers such as West et al. (1986) included discussions of downdrafts as drying mechanisms for 5-μm hotspots. Atreya et al. (1996) attempted to simultaneously explain the dryness as well as the gradual, staggered increase of condensible volatile mixing ratios (see Chapter 1) by qualitatively invoking the idea of a downdraft with lateral entrainment. The work of Showman and Ingersoll (1998; hereafter SI98) included a discussion of the atmospheric stability and energy budget of a deep Jovian downdraft. In a separate section they discussed the probe site condensible volatiles. One of the mechanisms invoked by SI98 to explain the CV mixing ratio profiles was "column-stretching," an idea that initially seems plausible. A column of normal Jovian air is stretched so that, for example, air from the base of the water cloud is moved from the ~6 bar level down to some deeper level not seen by the Galileo probe. This idea fits the observation that the three CVs increase in mixing ratio with depth, reaching their deep abundances at staggered levels in the same order as their equilibrium condensation levels (i.e., in the order ammonia, H_2S, and water). However, Figure 8.2 shows the difficulties in reconciling this idea with the observations.

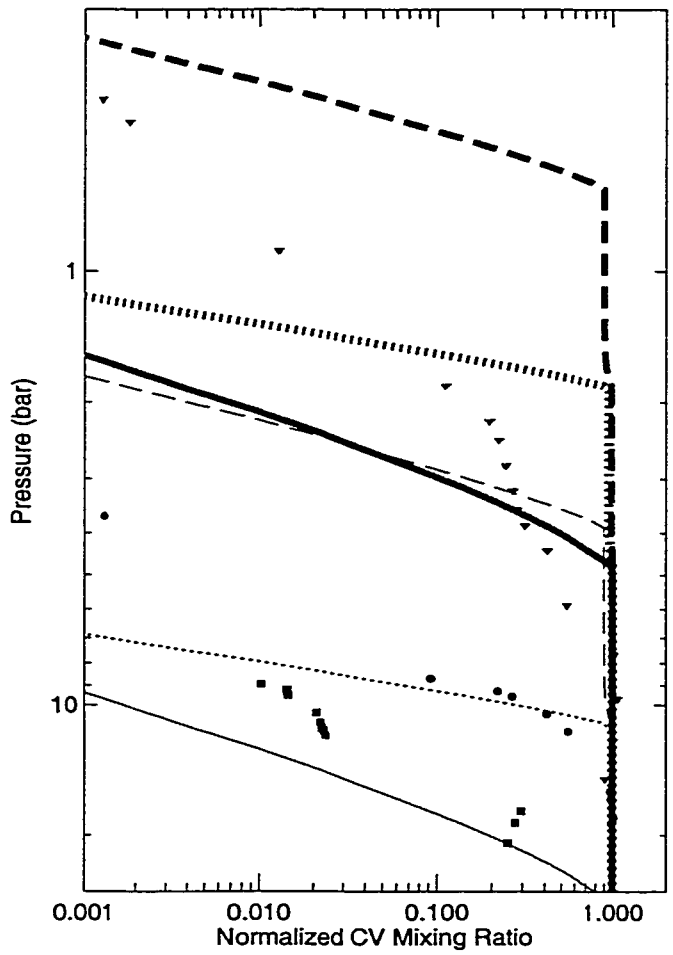

Figure 8.2 Comparison of PES CV mixing ratio profiles with column-stretched ECCM CV profiles.

Figure 8.2 shows the effect of stretching the atmospheric column in pressure coordinates by a factor of 6. The heavier lines (green/long dash for NH_3, black/dots for H_2S, and blue/continuous for water) show the mixing ratio profiles for the ECCM, whereas the corresponding thinner lines are profiles for the stretched column. GPMS mixing ratio results are shown for water (blue squares) and H_2S (black circles), and NFR (Sromovsky et al. 1998) and probe signal attenuation inversion (Folkner et al. 1998) were used for the NH_3 datapoints (green triangles). Ammonia is particularly poorly matched in this scenario; the lowest-pressure points require much less stretching, whereas the deeper ammonia near 6 bar requires greater stretching (needing a factor of 15 instead of 6). The 8–12 bar H_2S and water data preclude column stretching entirely—the H_2S at about 10 bar is well matched

but the water requires a smaller stretching factor. Column stretching cannot resolve this difficulty because there is no level of the atmosphere in the equilibrium cloud case that has the right mixing ratios of both water and H_2S. The pictured case is for 2 × solar water; if 0.5 × solar water is instead assumed for the deep water abundance, the problem persists because both the water datapoints and the stretched water mixing ratio profile move to the right by a factor of 4. Although the column-stretching hypothesis cannot in itself explain the observed condensible volatile profiles, it may fit into the larger picture of 5-μm hotspot structure, and it serves as the drying mechanism in Showman and Dowling's (2000) later 3-dimensional hotspot model, which will be described below. The conclusion that column stretching cannot match PES CV profiles relies on the assumption that the environmental CV profiles are well described by the ECCM. Implications that this assumption may be false are discussed in Chapter 9.

Showman and Ingersoll (1998) also provided a qualitative analysis of lateral mixing as a 5-μm hotspot phenomenon. They make the statement, "The obvious mechanism is that the mixed air follows isopycnals, or surfaces of constant virtual potential temperature." Although this obvious mechanism may be appropriate for large-scale systems like the hydrostatic fluid hotspot model of Showman and Dowling (2000), the possibility is very strong that smaller-scale downdrafts on Jupiter include mixing *across* isopycnals. In fact, the mixing of air from regions of different virtual potential temperature is the mechanism used by PM87 to produce sustained terrestrial thunderstorm downdrafts using the HN80 model (see above). In the cartoon presented in SI98 featuring isopycnals that "bow down" in the hotspot to deeper pressure levels, mixing is actually a poor description of the interaction. Since density in their scenario is due only to compositional gradient, "mixing" along isopycnals involves two air masses with identical compositions combining; but as mentioned above, portions of the CV profiles sampled by the probe cannot be taken directly from ambient air because the relative proportion of water and H_2S is not found in an environment with saturation-defined mixing ratio profiles. Another problem with the idea of mixing only along isopycnals is that the mixing is overly sensitive to the potential temperature profile. Consider for example the environmental θ_e profile shown in Figure

8.1. (However, Figure 8.1 shows equivalent potential temperature, which includes potential for latent heat release. The virtual potential temperature, which does not include this effect, would be "cooler" at altitudes less than 3 km in Figure 8.1.) An adiabatic downdraft with no mixing will have a virtually constant with altitude profile of θ_v or θ_e. If the downdraft started at a height of 11 km with $\theta_e = 353$ K, it would be mixing with 11-km air throughout its descent. If it started at 11 km with $\theta_e = 345$ K, it would mix exclusively with air from the 9 and 1.8 km levels, never seeing air from the level of the θ_e minimum, completely opposite to the PM87 model. For some initial values of θ_e in the downdraft, no mixing would be possible whatsoever, because the downdraft would possess θ_e values not seen in the environment. Another problem with mixing only along isopycnals is that virtual potential temperature is a useful quantity only for dry air with no condensation or change in composition. When air is changing in composition, the average molecular weight and thus the density will change, while the potential temperature will remain constant. If moist air undergoes an adiabatic transformation including condensation, its temperature will change as a result of latent heat release, and therefore the potential temperature will change. But if potential temperature were an accurate measure of density of air with respect to adiabatic transformations, it would not change. *Equivalent* potential temperature θ_e (see the footnote about 5 pages back) could be used instead to include a parcel's potential for condensation or evaporation, but the calculation of θ_e is difficult to accurately perform due to Jupiter's somewhat complex system of three condensing gases, and due to the increasingly rapid change in specific heat of hydrogen at temperatures below around 230 K.

Showman and Ingersoll (1998) examined the energetics of Jovian downdrafts using a kinetic energy equation and assumptions about the density difference between downdraft and environment. First they used a gradient wind equation (balancing pressure gradient, coriolis, and centripetal forces) to establish profiles of this density difference, with the PES wind profile as the input, and assuming different radii of curvature of the airflow. For this investigation they assumed a convective cell with the PES as a downdraft and the equatorial zone to the south as the associated updraft. Their preferred radius of 4000 km resulted in a PES denser than the equatorial belt above about 5 bar, and a PES density less than that of

the environment at pressures of 5–12 bar. This means that the PES downdraft would be thermally direct during the first 5 bar of descent and then become thermally indirect. During the thermally indirect phase, the descending air is less dense than the environment and sinks because of the kinetic energy imparted to it in the thermally direct phase. Using the relatively small PES/environment density difference calculated assuming gradient wind balance, SI98 obtained a depth of penetration of 1000 bar. The same calculation, done with a density difference calculated using the observed PES atmospheric structure and a moist adiabatic environmental profile, resulted in a 9–30 bar depth of penetration, corresponding to a 1–3 × solar abundance of water, respectively. Their final case involves a downdraft that is everywhere less dense than the surroundings, from 0.5–20 bar. In this case the downdraft must be externally forced, and SI98 calculate the power required to drive the downdraft as a function of the downdraft velocity. For a downdraft velocity of 6×10^{-5} Pa s^{-1}, the required power per unit area is 0.1 W m^{-2}. Note that 1 Pa s^{-1} = 315 bar yr^{-1}, so this velocity would require about 1000 years for the downdraft to reach 20 bar. For a 32-year descent time they calculate a power/area of 3 W m^{-2}. On the other hand, Gierasch et al. (2000) estimated the power generated by a single Jovian thunderstorm observed by the Galileo Orbiter to be 5×10^{15} W; if all of this power were channeled into a downdraft or system of smaller downdrafts collectively covering 1000 km^2, then the relation used by SI98 would predict a descent time from 0.5 to 20 bar of about 3 days. Although this timescale is an order of magnitude slower than typical descent rates calculated by DDE, using a smaller filling factor (downdraft/updraft area ratio; see Lunine and Hunten, 1987) over the hotspot area would compensate, an effect justifying the hypothesis that downdrafts are isolated to features smaller in scale than overall 5-μm hotspots.

The one-dimensional model of Hueso et al. (1999) is fundamentally similar to DDE, the model introduced in Wong et al. (1998) and described in more detail below. Thus, rather than concentrating on the mechanics of their model, the focus here is on the relevant conclusions drawn by Hueso et al. (1999; hereafter HSD99). HSD99 investigate different profiles of the para hydrogen fraction (f_p) in the environment, finding that a normal para fraction ($f_p = 0.25$) in the environment leads to slightly stronger downdrafts. The ortho and

para states are two magnetic spin states of the hydrogen molecule. When hydrogen is in equilibrium, the lower-energy para state dominates over the ortho state at low temperatures ($f_p = 1$), while f_p drops to about 0.4 at 100 K and asymptotically approaches 0.25 (the "normal" fraction) at higher temperatures. The transition from the ortho to para states is quantum-mechanically forbidden, so equilibration of deep hydrogen, once brought to the coldest reaches of the upper troposphere, occurs over long timescales and is not well understood in Jupiter's atmosphere (Conrath and Gierasch, 1984). Whenever equilibrium and normal values of f_p are distinct, the normal fraction has a smaller specific heat, resulting in a faster lapse rate. This means that a descending parcel with f_p in equilibrium at the top of the descent will maintain a slightly greater density difference with respect to its surroundings when the surroundings have a normal f_p, consistent with the simulations of HSD99. Since the difference between equilibrium and normal f_p in Jupiter's atmosphere is negligible at pressures greater than about 700 mbar, the ortho/para effect on a downdraft is isolated to the upper portion of the downdraft, and is difficult to distinguish from a greater initial density difference, as if from a slightly colder parcel. Thus the DDE model neglects f_p as a significant parameter.

Another step taken by HSD99 was to adopt unsaturated, cloud-free environmental profiles, with CV mixing ratios following the saturation curves at 99% saturation above the levels where clouds would form. The 99% saturation means that there is little difference in molecular weight between the HSD99 profile and an equilibrium cloud profile, but the latent heat released by cloud formation would be absent. The lack of heating would result in a profile in HSD99 that is denser (colder) than the equivalent level in an equilibrium cloud profile. In other words, HSD99 used an environmental profile qualitatively similar to the observed environment in a terrestrial thunderstorm (recall Figure 8.1), consistent with the findings of fellow downdraft-modeler Pawlowska-Mankiewicz (1987).

Baker and Schubert (1998; hereafter BS98) adapted a two-dimensional hydrostatic model developed for Venus and applied it to Jovian downdraft simulation. Despite several key flaws, the model does provide some insight into the understanding of 5-μm hotspots. A major shortcoming is that molecular weight differences are ignored, since there is no

condensation in the model. Thus, although density can be tracked, the mixing of CVs is not modeled, and BS98 attempt to generate a less-dense downdraft as a proxy for a dry downdraft. Some of the physical parameters in BS98 are unlike those of the probe entry site: wind shear is an obvious omission that would have a strong effect over the 24-hour model time duration of the BS98 simulation. The model domain is 520 km wide, considerably smaller than the 5,000 to 15,000 km extent of Jovian 5-μm hotspots, and the resulting low-density portion of the downdraft is more of a pocket or bubble than any sort of sustained jet. However, the value of BS98 is not in its ability to completely simulate a 5-μm hotspot. Rather, it provides numerical support of the kinetically-driven downdraft idea of Showman and Ingersoll (1998; see above). In the final timestep of BS98, the downdraft/ updraft filling factor is 5–15%, opposite to the 98% downdraft / 2% updraft scenario Lunine and Hunten (1987) based on the weighting of infrared emissions from wet and dry regions of Jupiter to explain 5-μm observations (although it would seem that Lunine and Hunten did not account for the increased IR brightness of the dryer downdrafts). Within the limitations of the crudities of BS98, the model succeeds in demonstrating the effectiveness of mechanical forcing of less-dense downdrafts.

A more complete system was demonstrated in Hueso and Sánchez-Lavega (2001; hereafter HS01), who use a full-featured three-dimensional model with condensation of volatiles and parametrized microphysics, including precipitation. Two cases were examined, each with an initial perturbation at the base of the water cloud level. In the first case, a single coherent "thunderstorm" developed, with a simple mushroom-cloud-like structure quite unlike the relatively chaotic flows of BS98. In the second case, which included PES-like wind shear, some subsidence was encountered on the upwind side of the storm after about 3 hours, and an anvil-like feature developed on the downwind side. The significant model differences between HS01 and BS98 are the inclusion of condensation and microphysics in HS01, and the use of a continuous heat flux as the driving force in BS98 and an initial low density perturbation as the driving force in HS01. Although HS01 may effectively model a Jovian thunderstorm plume, it does not attempt to model the extensive dryness characteristic of 5–μm hotspots. An earlier model by Yair et al. (1995) incorporates

the same microphysics (but only for the water cloud), but is two-dimensional and axisymmetric, whereas HS01 is fully 3-D. As with HS01, the Yair et al. (1995) model produced a mushroom-cloud-like eruption in response to the initial density perturbation used to initiate convection.

A very different 3D model is presented in Showman and Dowling (2000), who solve the nonlinear hydrostatic primitive equations for a matrix of 128 × 90 gridpoints (0.9° / gridpoint) and six vertical levels. They start the simulation by generating initial high-pressure perturbations, which then evolve into periodic structures bearing some similarities to Jovian 5-μm hotspots. The structures, like hotspots, persist for 100–200 days, and the cloud-top wind patterns show some similarities to the flow near Jovian hotspots. However, the SD2000 spots are twice as large as Jovian hotspots, and the SD2000 spots cannot duplicate the profiles of the probe site winds or condensible volatiles. Whereas the SD2000 model lacks condensation, its east-west extent is much greater area than that of the HS01 model (129,000 km versus 160–290 km). Thus, although SD2000 fail to model particular characteristics of the Galileo Probe entry site, they demonstrates how nonlinear wave effects could act to perpetuate and focus hotspot analogues in an initially perturbed atmosphere.

The collection of hypotheses and models described above contain fatal weaknesses when individually examined, but together they illuminate the life cycle of a Jovian hotspot. Moist convective storms provide the energy to drive the circulation. One effect of these storms would be downdrafts, which act to dry the atmosphere. Downdrafts would probably be small-scale structures, like the sinking bubble of Baker and Schubert (1998) or the upwind downdraft in the moist convective storm of Hueso and Sánchez-Lavega (2001). Lateral mixing would transport condensible volatiles into the downdrafts, and also spread the small-scale drying effect of the downdrafts over a larger area. Another result of the moist convective storms would be the large pressure perturbations which carry the kinetic energy lost by the thunderstorm as either Rossby waves or the nonlinear hotspot structures of Showman and Dowling (2000). The DDE model described below is intended to focus on a specific aspect of the process, i.e. condensible volatile profiles in the PES, and not the entire cycle of 5-μm hotspots.

Downdraft modeling method

The downdraft with entrainment (DDE) model presented here performs a one-dimensional simulation of a descending parcel of air, starting from a given initial state, and continuing until the downdraft velocity goes to zero. In addition to the parameters required to describe the initial state of the descending parcel, a complete description of the ambient atmosphere is needed for both entrainment (mixing into the descending parcel) and for calculation of the buoyancy force that accelerates a dense downdraft and slows a lighter downdraft. The ambient atmosphere was modeled by the ECCM, which was described in Chapter 1.

The DDE steps downward through the atmosphere in steps of Δz (250 m was used as the step size), calculating changes in parcel state using a set of eight differential equations. The differential equations are numerically integrated using a customized four-step Runge-Kutta approximation, as described in Press et al. (1989). The differential equations solved by the model describe the change with height of vertical velocity (one variable), gaseous and condensed CV mixing ratios (six variables), and temperature (one variable). The derivations of the model differential equations, along with a full list of all symbols used (Table C.1), are provided in Appendix C, and the key equations will be briefly discussed here. The simplest equation is the equation of motion, which calculates the change with height of the vertical velocity in the downdraft:

$$\frac{dw^d}{dz} = \left(\frac{\rho^e - \rho^{*d}}{\rho^{*d}}\right)\frac{g}{w^d} - \frac{a}{w^d} - \mu_e w^d \qquad \text{C.6}$$

The first term accounts for buoyancy effects, the second term allows the introduction of external forcing via the arbitrary acceleration term a, and the third term reduces the downdraft velocity by entraining momentum from the stationary environment. The arbitrary acceleration term was not present in the model of N79 and coworkers, but is needed to incorporate the thermodynamically indirect (externally forced) circulations discussed by Showman and Ingersoll (1998).

The differential equations describing the variation of gaseous and condensed water with height are given by Equations C.12 and C.13:

$$\begin{aligned}\frac{dq^d_{wc}}{dz} &= (\mathbf{F}_W)\mu_e\left(q^e_{wg}+q^e_{wc}-q^d_{wg}-q^d_{wc}\right)\\ &\quad -(\mathbf{F}_W)\left(\frac{\partial Q_W}{\partial p}\frac{dp}{dz}+\frac{\partial Q_W}{\partial T}\frac{dT}{dz}\right)\end{aligned} \qquad \text{C.12}$$

$$\begin{aligned}\frac{dq^d_{wg}}{dz} &= (!\mathbf{F}_W)\mu_e\left(q^e_{wg}+q^e_{wc}-q^d_{wg}-q^d_{wc}\right)\\ &\quad +(\mathbf{F}_W)\left(\frac{\partial Q_W}{\partial p}\frac{dp}{dz}+\frac{\partial Q_W}{\partial T}\frac{dT}{dz}\right)\end{aligned} \qquad \text{C.13}$$

The symbols used are fully explained in Appendix C. $\mathbf{F}_W$ is unique to this work; it is a delta function having a value of 1 when water is saturated in the parcel, and 0 when it is subsaturated. $!\mathbf{F}_W$ has the inverse values. Specific humidity q_i is a standard quantity (see, for instance, Iribarne and Godson, 1981) equal to the mass of the constituent (water vapor for $i = wg$ or condensed water for $i = wc$) in a unit volume divided by the total mass of the volume. Finally, Q_W is the saturated specific humidity of water at the given values of temperature and pressure. Equations C.12 and C.13 are simple to understand; the first term in each equation dictates that all entrained water (vapor and condensed) is partitioned into either the vapor phase in an unsaturated downdraft, or the condensed phase for a saturated downdraft. The second term in each equation is the change due to condensation/ evaporation for a saturated downdraft. Similar equations exist to describe gaseous (Equation C.29) and condensed (Equation C.14) ammonia, gaseous H_2S (Equation C.31), and condensed NH_4SH (Equation C.30). The formulations describing the ammonia-sulfur CV system are complicated by the considerations that both gases combine to form a single condensate, and that two different condensates (NH_3 ice and NH_4SH) could compete for ammonia gas. Despite the arithmetic complexity of the equations describing the ammonia-sulfur CV system, the physics controlling the changes in the specific humidities of these CVs are the same as for water in Equations C.12 and C.13: entrainment and condensation/ evaporation.

The variation of temperature is given by the lapse rate equation, Equation C.91. The derivation of C.91 roughly follows the lapse rate equation derivation in Niewiadomski (1979; N79), but N79 models a situation which is different from the Jovian downdraft situation. In N79, downdraft, updraft, and environment are modeled, whereas in DDE, there is no modeled updraft. In N79, the environment is assumed to be subsaturated (although the updraft can be saturated), whereas in DDE, the environment is allowed to contain condensed species. Taking these two changes into account, N79's lapse rate equations for the downdraft become:

$$\frac{dT}{dz} = \frac{1}{c_{atm}}\left[\frac{1}{\rho^d}\frac{dp}{dz} + \mu_e c_{atm}(T^e - T^d) - L\mu_e V_e\right] \quad \text{(unsaturated)} \qquad 8.8$$

$$\frac{dT}{dz} = \frac{1}{c_{atm} + Vc_w + L\frac{\partial Q}{\partial T}} \times \left[\left(\frac{1}{\rho^d} - L\frac{\partial Q}{\partial p}\right)\frac{dp}{dz} + \mu_e(c_{atm} + V_e c_w)(T^e - T^d) + L\mu_e(q_e - q_d)\right] \quad \text{(saturated)} \qquad 8.9$$

The symbol V in N79 is the mass fraction of condensed water, and corresponds to q_{wc} in the notation used here. For the unsaturated case, Equation 8.8, the change in temperature is controlled by three effects, corresponding to the three terms within the bracketed expression: adiabatic temperature change due to change in pressure, entrainment of environmental air, and evaporation/sublimation of entrained condensed material. Corresponding terms can be identified in the lapse rate equation for the wet downdraft (Equation 8.9), with some modifications. Energy must heat condensed water as well as the air in the parcel (the Vc_w term in the denominator), sensible heat is entrained through condensed water as well as through entrained air (the $V_e c_w$ term), and the sign of the latent heat term corresponding to entrained water changes to reflect that heat is produced by the condensation of entrained vapor, rather than absorbed by the evaporation/sublimation of entrained condensate as in Equation 8.9. Also, new terms appear in Equation 8.9 to represent the release of latent heat as vapor condenses, as determined by the saturated specific humidity terms $\frac{\partial Q}{\partial p}$ and $\frac{\partial Q}{\partial T}$. Despite their simplicity with respect to Equation C.91, equations 8.8 and 8.9 demonstrate all the physics that go into the lapse rate equation used

in DDE. The much greater complexity of Equation C.91 is due to several factors. Because DDE includes three condensible volatiles, instead of just water as in N79, the two lapse rates of N79 would turn into $2 \times 2 \times 2 = 8$ lapse rate equations. As discussed in Appendix C however, only five distinct cases really exist for Jupiter, and the strategy taken here is to use the F_i delta functions to represent all the possible saturation situations in a single equation. The derivation of Equation C.91 involved the reduction of enthalpy equations into equations containing only physically measurable quantities, and the difficulty in working with the ammonia-sulfur CV system resulted in the last term in Equation C.91, which has no equivalent in the water-only system of N79.

Effect of DDE model inputs

Many free parameters must be set in order to run DDE. The most fundamental of these is the environmental profile of pressure, temperature, and condensible volatile (CV) abundance. The temperature at $P < 1$ bar for two distinct areas of Jupiter is constrained by the Voyager radio occultations (Lindal et al. 1981), but the temperature profile at higher pressures (outside of the Galileo probe entry site) has not been measured. CV abundances are similarly unconstrained (see Chapter 1). Initially, the atmospheric structure calculated by the ECCM, as described in Chapter 1, was used. The release of latent heat at the cloud bases produces layers of atmospheric stability, with the water cloud forming the strongest such layer. A parcel that rises dry adiabatically (no condensation) into such a stable layer will acquire a colder temperature than the environment, and thus sink back down. Likewise, a dry parcel descending through the stable layer will find itself warming more rapidly than the environment, thus becoming more and more buoyant compared to the environment. Thus, in order for downdrafts to penetrate the water cloud level, relatively high values of the external forcing parameter (1–5% of the gravitational acceleration) had to be invoked. However, if the atmospheric profile follows the ECCM cloud structure in terms of cloud mass and CV variation with height, but the temperature is *not* altered by the release of latent heat, then the stability is due only to molecular weight stratification, a much weaker

effect. With this wet/dry hybrid environmental profile, little or no external forcing is required in order to send the downdraft deeper than the water cloud level.

The rate of environmental mixing along the path of the downdraft is governed by the entrainment rate μ, which is conceptually defined as the relative change in the descending parcel over a unit of vertical displacement. However, different authors use different quantitative definitions of the entrainment rate. Equation 8.1 (from PK78) is one standard representation, whereas Hueso et al. (1999) follow Stoker (1986) and use the same form, but express the differential with respect to pressure instead of height. The derivation in Appendix C follows the form of N79, where mass flux is used in the entrainment rate instead of mass (see Equation C.1). In all cases, the models solve differential equations with μ determined outside of the model. Hueso et al. (1999) quote the parametrization of Simpson (1971), which is the same as the PK78 parametrization of Equation 8.2. As the downdraft entrains mass from the environment, its radius should increase and μ should change, but Hueso et al. (1999) simply assume a constant size parameter for the downdraft. Although the choice of a constant μ and the parametrization of Equation 8.2 cannot both hold (because that would violate conservation of mass), it is far from certain that Equation 8.2 is the only appropriate parametrization choice. Constant μ was used in both N79 and HN80. HN80 also investigated three other parameterizations, two of which involved interaction with thunderstorm rainfall (an effect not included in DDE), and one other, which featured a μ that was proportional to the downdraft velocity difference from the environment, which they referred to as the Taylor hypothesis (see Equation 8.3). After examining these parameterizations, HN80 concluded that since they all resulted in approximately constant μ over some range of the downdraft, the "convenient" constant μ parametrization should be used. Finally, PM87 used both a constant μ and a step-function μ, with the latter producing entrainment only in a limited region of the atmosphere corresponding to the minimum in θ_e, an assumption which she claimed "corresponds well to observational evidence known for a long time."

Entrainment rate parameterizations used in DDE included constant μ, μ proportional to downdraft velocity w as in HN80, and also μ proportional to w^{-1} or w^{-2}.

These last two parameterizations model the hypothesis that entrainment is controlled by an external process such as lateral advection or diffusion, and occurs at a more or less constant rate, so that a fast downdraft experiences less mixing than a slow downdraft. As will be seen below, the inverse velocity parametrization leads to very good fits to some aspects of the probe site condensible volatile mixing ratio profiles.

The model requires a complete specification of the initial state of the downdraft airmass, including temperature, pressure, and initial velocity. The initial condensible volatile content of the downdraft airmass is taken to be the same as that of the environment, at the environmental pressure level equal to the initial downdraft pressure level. Thus, it is the initial temperature of the downdraft that specifies its density relative to the environment, and lowered temperatures are used in all model runs to achieve a downdraft that is initially denser than the surroundings. The model results are not greatly sensitive to initial downdraft velocities, so modest starting velocities (in the neighborhood of 5–25 m s^{-1}) are specified. Excessively large downdraft velocities were presumed to be unrealistic, so a speed limit criterion was imposed to abort model runs resulting in velocities greater than the 100 m s^{-1} speed limit. Velocity profiles were not published by Hueso et al. (1999), the model which is most comparable to DDE. DDE velocities typically reached 40–80 m s^{-1}, considerably greater than the 4–8 m s^{-1} downdrafts in PM87 and HN80. The greater speeds may possibly be justified by the larger gravitational acceleration on Jupiter and the difference in downdraft scale (5 km on the Earth compared to 150 km for some DDE runs). From Galileo Probe accelerometer data and parachute drag modeling, Seiff et al. (2001?) derive vertical flow velocities of less than 1 m s^{-1} in the PES at pressures greater than 2 bar, clearly precluding the rapid downdrafts of the DDE. However, the possibility exists that rapid downdrafts may occur as transient phenomena, leaving dried-out and vertically stationary atmospheric columns behind.

Initial experiments with DDE relied on the standard ECCM output to create the environmental profile. Due to the strong stable layer created by the water cloud, model downdrafts could not penetrate below the water cloud. Since the GPMS mixing ratio data imply a drying of the atmosphere to depths of 20 bar or more, the DDE model was designed

to include PES physics that would allow the downdraft to penetrate deeper. Showman (2000) suggested that the buoyancy term in Equation C.6 be reduced, to reflect the reduced influence of buoyancy on relatively large Jovian downdrafts, as compared to the smaller terrestrial thermals and thunderstorm downdrafts which provided the motivation for the earlier formulations of terrestrial researchers such as Hess (1959) and N79. Buoyancy factors between 0.2 (as suggested by Showman, 2000) and 0.6 were used. The mechanical forcing term a_f in Equation C.6 also helps the downdraft overcome the buoyancy force induced by passing through stable layers associated with cloud formation. Values on the order of $a_f/g = 5\%$ were typically required, although actual values used depended on values chosen for other key parameters such as initial temperature and entrainment rate. Using environmental profiles calculated *without* the release of latent heat, i.e. with the drying effect of cloud condensation but with a dry adiabatic temperature profile, resulted in a considerably less stable environment, such that the external forcing a_f/g could be set to 1% or less and still permit a deep downdraft. This type of environmental profile may seem somewhat physically unrealistic, but it leads to provocative implications regarding the evolution of 5-μm hotspots, as will be discussed below.

A final adjustable model parameter, the ice factor, was introduced to allow condensed cloud material to mix from the environment into the downdraft. One motivation for including the ice factor was to help maintain the downdraft by increasing its density. Entraining condensed material into a subsaturated airmass increases the density of the mixed airmass by (1) increasing its average molecular weight, since CVs are heavier than the dry H_2-He atmosphere, and by (2) lowering the temperature of the airmass, since heat is used to evaporate/sublimate the cloud matter. The other motivation for using the ice factor was to provide another adjustable parameter in order to help match the PES CV profiles. In all model runs, it was found that agreement between the predicted CV profiles and the observed PES profiles grew worse when ice factor was increased, leading to the conclusion that advection of cloud particles is unlikely to contribute to the increase in CV mixing ratios with depth in the PES. This finding may seem trivial given the large length scales that are likely to apply to the mixing, since one can easily envision the sublimation of cloud ice

particles along the journey from the environmental source region to the dry downdraft. However, if this were the case, the sublimated cloud ice matter would still be mixed into the downdraft. Thus, the statement that best results are obtained with ice factor = 0 leads to the conclusion that the source region of the environmental air is a cloud-free region itself.

Figure 8.3 shows mole fraction profiles (solid lines) calculated using a constant entrainment parameter (see parameter set DDE-303 in Table 8.1). Dotted lines indicate the environmental mixing ration profiles; the environmental lapse rate did not include the latent heat of cloud condensation, so a very small external forcing (~0.001 *g*) term was used. Although the NH_3 mole fraction at pressures less than 6 bar is well-modeled by this run, agreement vanishes deeper than 6 bar. The only way to increase ammonia at that depth would be to have greater entrainment, so the constant entrainment parameter fails to explain the PES ammonia profile. Neither the water nor the H_2S profiles are well-matched by this set of model parameters. The downdraft velocity is around 50–60 m s^{-1} above the water cloud base (~4.7 bar) but then decreases to a nearly constant 30 m s^{-1} from about 7 bar to the bottom of the model, due to the decrease in the parcel buoyancy from molecular weight stratification in the cloud region of the surrounding environment.

Table 8.1 DDE parameter sets.

	DDE model run name			
Parameter	**DDE-303**	**DDE-304**	**DDE-301**	**DDE-306**
Environment lapse rate	dry adiabatic	dry adiabatic	dry adiabatic	DDE-304
Environment water abundance	dry	dry	wet	DDE-304
μ (entrainment rate)	1×10^{-5}	6×10^{-5}	8×10^{-5}	1.7×10^{-4}
a_f [cm s^{-2}] (external forcing)	2.5×10^{-2}	2.0×10^{-2}	8.0×10^{-2}	0.0
T_{top} [K]	180	180	118	122.3
P_{top} [bar]	0.4	0.4	0.4	0.45
w_{top} [cm s^{-1}]	–3.0	–22.0	–22.0	–5.0

Table 8.1 DDE parameter sets.

Parameter	DDE model run name			
	DDE-303	DDE-304	DDE-301	DDE-306
entrainment parametrization	μ = const.	$\mu \propto w^{-2}$	$\mu \propto w^{-2}$	$\mu \propto w^{-1}$
buoyancy factor	0.5	0.6	0.4	0.6
ice factor	0.0	0.0	0.0	0.0

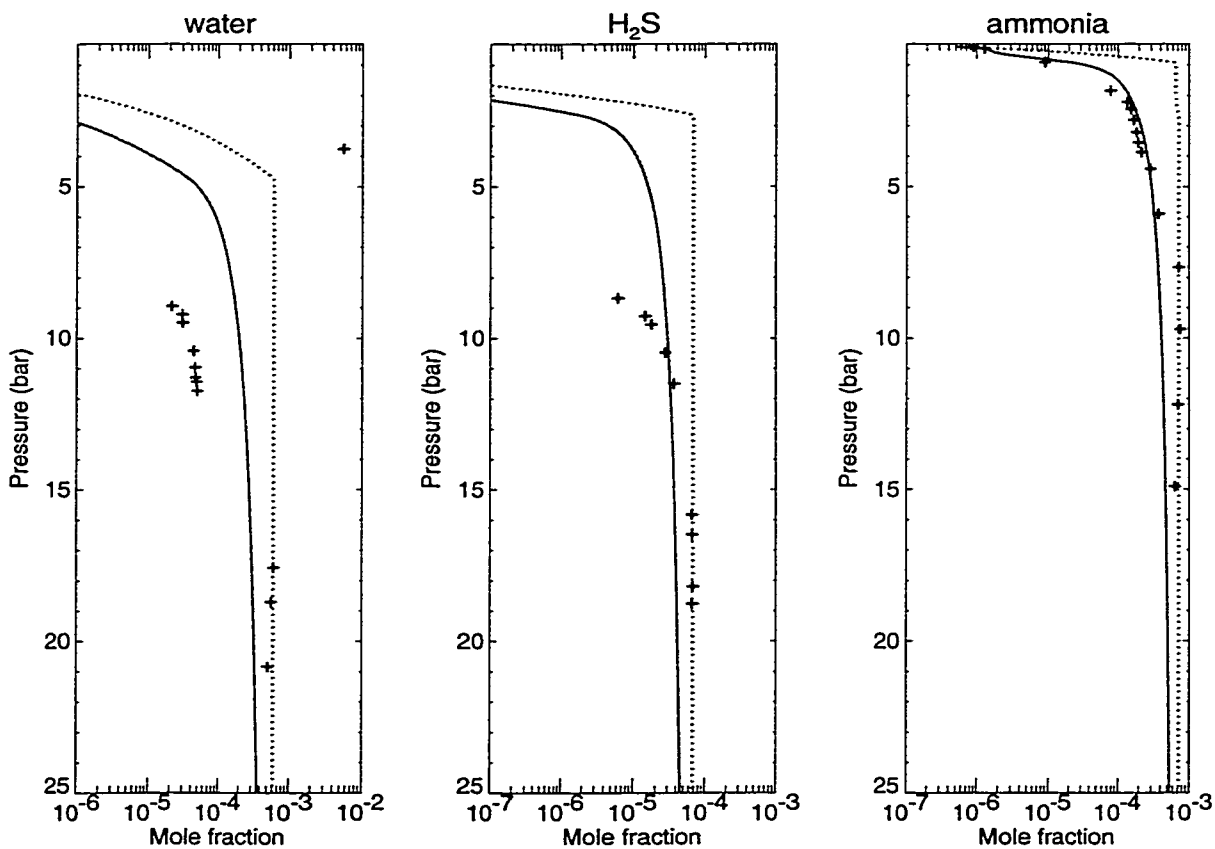

Figure 8.3 Mole fraction profiles for experiment DDE-303.

In order to increase the entrainment below 6 bar, in an attempt to match the entire ammonia profile, the entrainment parametrization $\mu \propto 1/w^2$ was adopted. This scheme makes use of the decrease in downdraft velocity below the water cloud region, resulting in the exceptionally good match to the ammonia profile shown in Figure 8.4 below for parameter set DDE-304. Of course, entraining more ammonia below 6 bar means

entraining more of the other condensible volatiles, so discrepancy between model and PES water and H_2S is considerably worse going from Figure 8.3 to Figure 8.4. The increase in entrainment rate leads to more entrained neutral momentum and therefore lower velocity, so for this parametrization of μ, the velocity is rapidly damped and downdraft termination occurs slightly deeper than 10 bar.

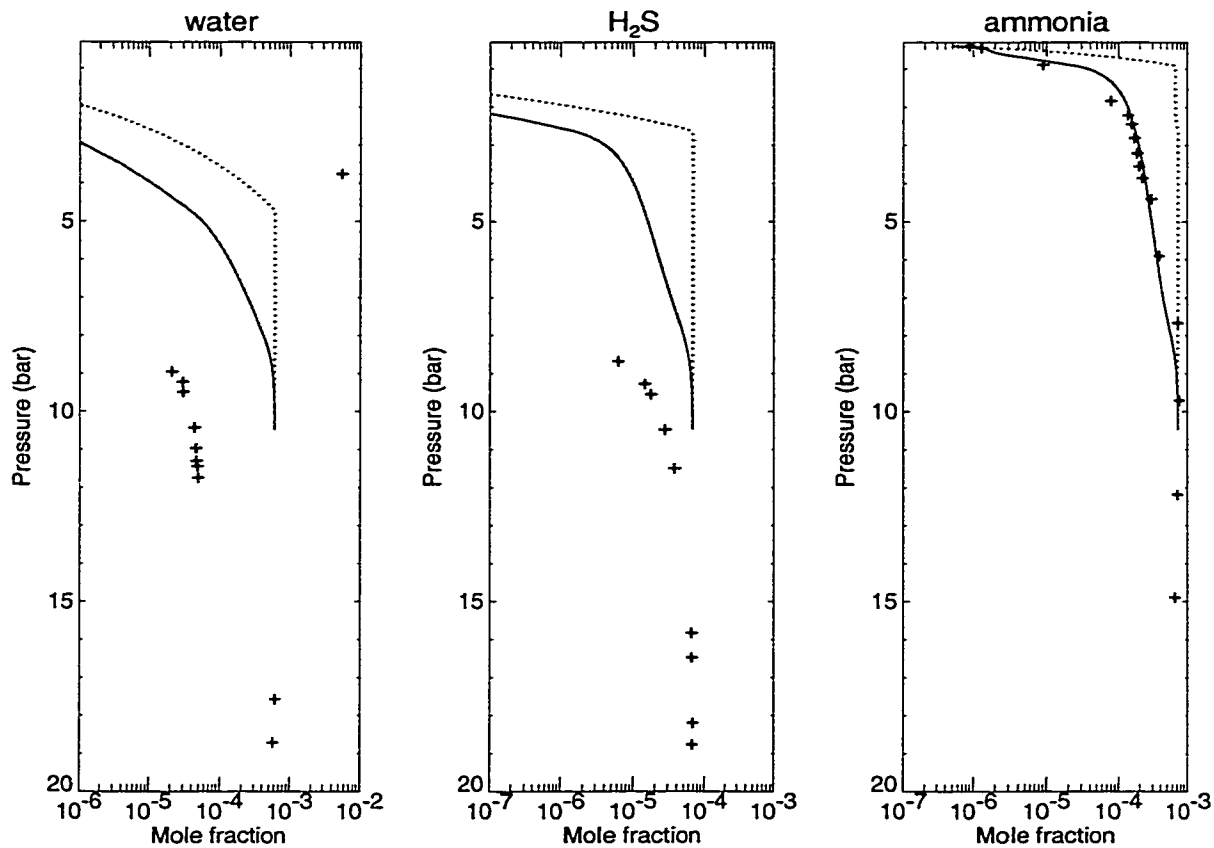

Figure 8.4 Mole fraction profiles for experiment DDE-304.

Figure 8.5 shows mixing ratio profiles that generally match probe site conditions for ammonia above 4 bar, and for H_2S below about 9 bar. This is case DDE-301, with parameters (see Table 8.1) very similar to case DDE-304 pictured above. Again $\mu \propto 1/w^2$, but for DDE-301, the buoyancy factor was reduced, from 0.6 in DDE-304, to 0.4. External forcing remained small relative to gravity (0.08 m s^{-1}) but was greater than the external forcing in DDE-304. As with DDE-304, the stable layer due to the molecular weight stratification in the water cloud region slowed the downdraft, but the smaller buoyancy

factor and the greater mechanical forcing allowed it to carry on to deeper levels. As the downdraft approached 12 bar, its decreasing velocity led to increasing entrainment, but in this model run, the entrained environmental air reduced the density difference between the downdraft and the environment. With the reduced density contrast, the downdraft experienced less resistance due to its buoyancy and was able to continue on to the model base at 25 bar. Entrainment in this run was less than that in the previous example (DDE-304) in the 5–10 bar range, causing the model output to disagree with PES

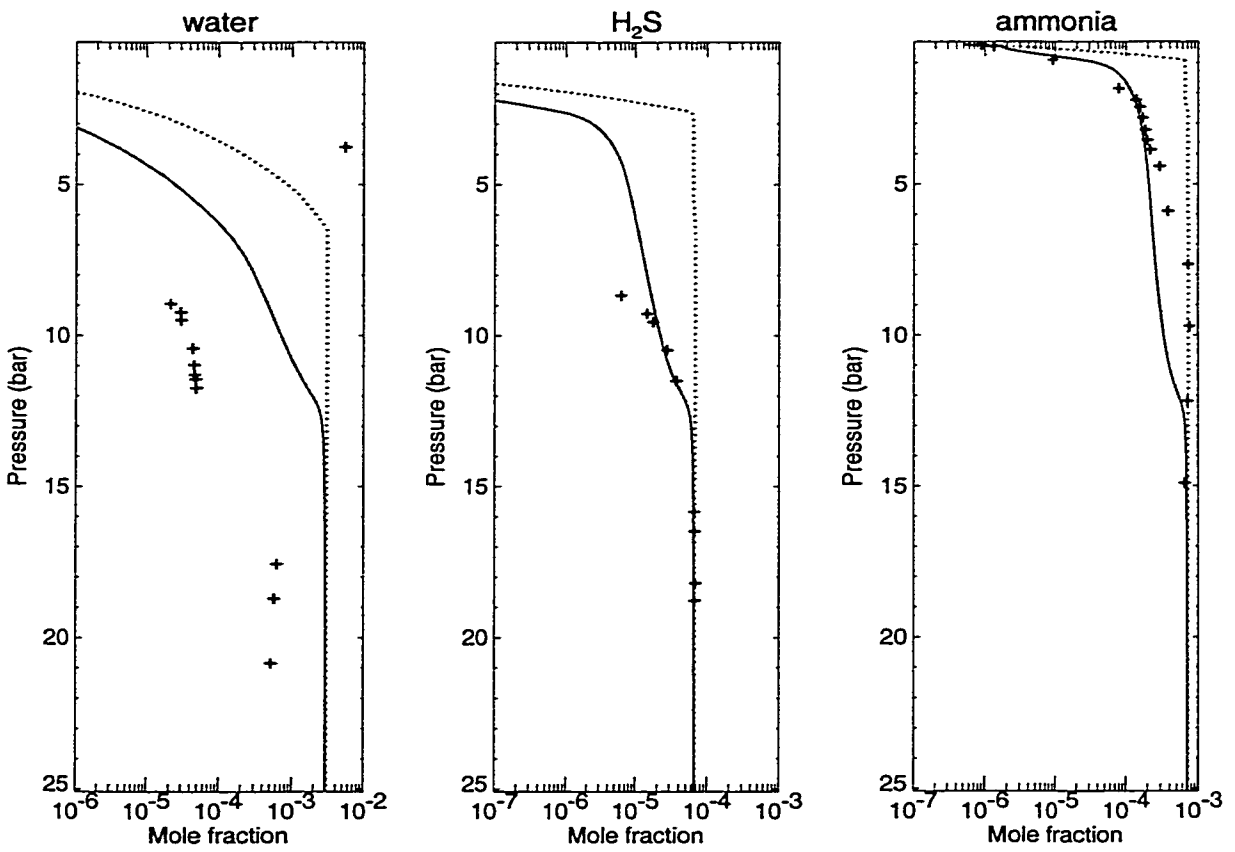

Figure 8.5 Mole fraction profiles for experiment DDE-301.

ammonia. However, the reduced entrainment gave a much better fit to the 9–12 bar GPMS-derived H_2S mixing ratios, and the entrainment peak around 12 bar allowed the CVs to increase to their deep abundances, thus also fitting the deeper H_2S mixing ratios at 16–18 bar. The water mixing ratio profile is poorly matched. Note that in this case the environmental water profile (dotted line) below the cloud is greater than the GPMS water

data points between 17 and 21 bar, whereas the environmental mole fraction profile passed through these points in the previous two examples. The difference is due to the deep water abundance assumed for the environmental profile in each case: 1 × solar for this case, and 0.4 × solar for the previous two examples. In addition to changing the mole fraction profile, the choice of deep water abundance affects the strength of the stable layer in the water cloud region. None of the examples discussed to this point are able to duplicate the water mole fraction profile. For this purpose, a "compound downdraft" was modeled, with results shown in Figure 8.6.

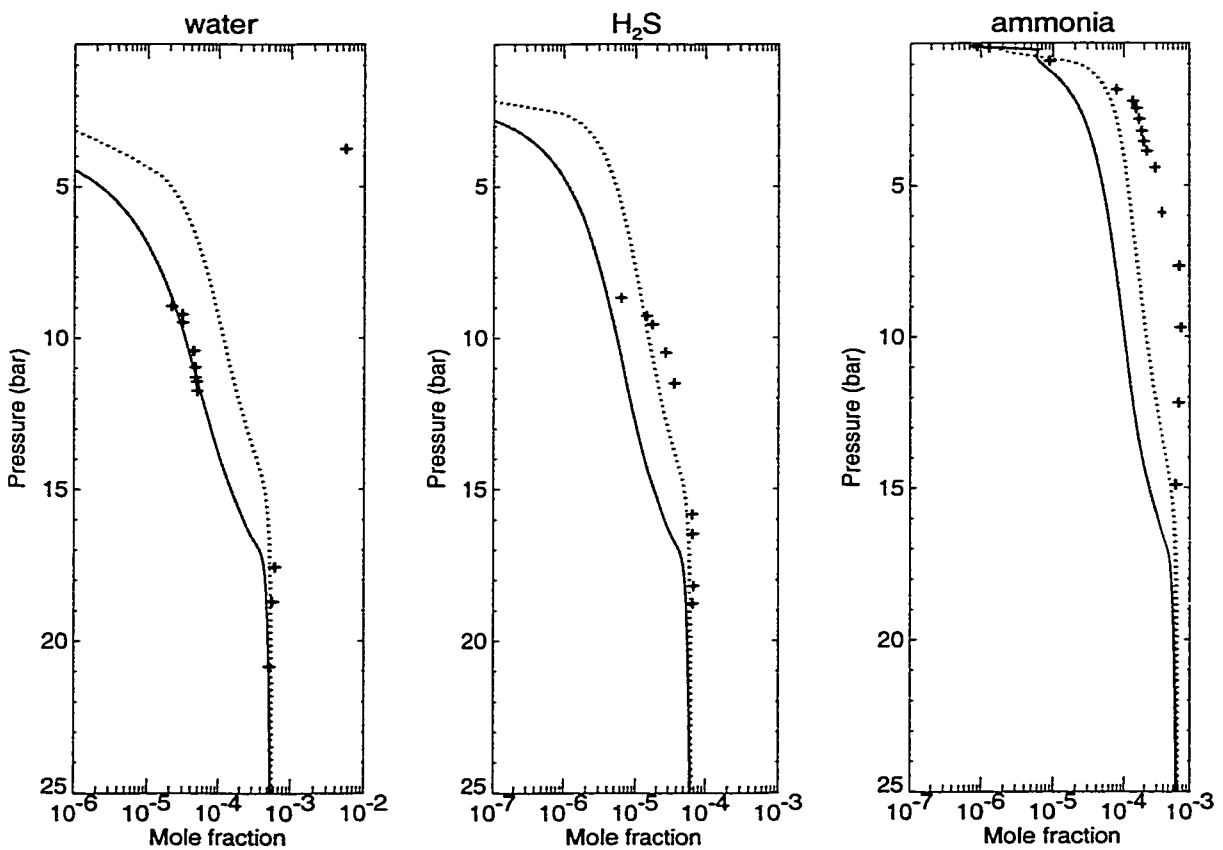

Figure 8.6 Mole fraction profiles for experiment DDE-306.

The compound downdraft (case DDE-306) was modeled by using the output from a previous DDE experiment to describe the environment. This technique allowed the water profile to be matched, but the other condensible volatiles are overly depleted in the simulation, as compared to their probe site profiles.

Despite the encouraging matches to individual CV profiles, these four examples illustrate the inability of the entraining downdraft model to simultaneously match condensible volatile abundance profiles for all three CVs. This problem was also encountered by Hueso et al. (1999), and as shown previously in Figure 8.2, the column stretching hypothesis has the same shortcoming. Although these failures are nonetheless useful results, for they give a strong indication of the complexity of the CV distribution in the PES as well as in whatever Jovian environments participated in the dynamic history of the PES prior to the probe descent. One conclusion of this modeling work is that the staggered recovery levels of the three CVs in the PES are particularly difficult to match using entrainment, since the entrainment of environmental air in the well-mixed part of the atmosphere tends to make all CVs recover to their well-mixed abundances within about 1 bar of each other. This effect is easily understood in terms of the two environmental mixing regimes experienced by a parcel in the downdraft. First, the parcel entrains air from the cloud region, where environmental CV mixing ratios are increasing extremely rapidly with depth, due to the steep vapor pressure curves. In this region, even a small amount of entrained air will bring more of the CV than already is present in the downdraft parcel, so the amount of CV in the downdraft follows the saturation curve. As the downdraft moves into the second regime, where the CV is constant with height, its rate of increase generally slows, since the entrained component is no longer bringing higher and higher concentrations of the CV into the column. In this well-mixed environment entrainment regime, the downdraft essentially "forgets" the cloud regime, and the profiles of all CVs increase together. Since all three CVs were found to approach their well-mixed abundances well below the deepest cloud, they were all in the second entrainment regime, where it is impossible to achieve greatly separated recovery levels. This argument seems to support column stretching as a more likely explanation for the PES CV profiles, but as mentioned previously, the column stretching argument is still unable to explain both the observed water and H_2S abundances in the 9–12 bar region.

CHAPTER IX

Conclusions

This work is done at an exciting time. Year by year, the accumulation of the wealth of observational data on Jupiter's atmosphere has been accelerating, but the vast quantities of fresh data unveil ever more numerous and deeper holes in our understanding of basic processes in Jupiter's atmosphere. The GPMS data, exacerbated the confusion with several intriguing puzzles. Following a summary of the GPMS composition measurements, this chapter examines the implications of the data for the bulk composition of Jupiter, tropospheric structure, and the vertical transport of stratospheric hydrocarbons into the troposphere.

GPMS composition measurements

Details of the Galileo Probe Mass Spectrometer data analysis were presented in Chapters 2 through 6. The mixing ratio w_x of a particular chemical species x was obtained along the probe descent path in terms of mass spectrometer count rates $C[x]$ and $C[ref]$ at two distinct masses, and a calibration constant that compensates for the counting efficiency of species x and the reference gas:

$$w_x = \mathrm{cc}^{\mathrm{sp}}_{x/ref} \frac{C[x]}{C[ref]} \equiv \mathrm{cc}^{\mathrm{sp}}_{x/ref} CR[x/ref] \,. \qquad 3.1$$

Table 9.1 summarizes the hydrocarbon and condensible volatile mixing ratios derived in Chapter 6. Mixing ratios are defined by Equation 1.1, and the solar enrichments listed are with respect to the values of Anders and Grevesse (1989). The calibration constant references are ID numbers of the calibration constants in Table 5.10. See Chapter 5 for a full discussion of the calibration constants, and Chapter 6 for discussion of the assumptions that

led to the listed mixing ratios, errors, and relevant pressure ranges. Additional crucial notes and caveats follow the table

Table 9.1 Summary of GPMS mixing ratios derived in this dissertation.

Species	GPMS counts used	Atmospheric mixing ratio	Pressure range (bar)	Calibration constant reference*	Comments (see text for more info)
CH_4 Methane	CR[16/4], CR[13/4]	$2.21\pm0.62 \times 10^{-3}$ ($3.05\pm0.85 \times$ solar)	0.5–12	Table 5.9	Value slightly changed since Niemann et al. (1998)
H_2O Water	CR[18/13]	$5.4\pm1.3 \times 10^{-5}$ ($0.032\pm0.008 \times$ solar)	9–12	31, 32, 33	
		$7.5\pm2.4 \times 10^{-4}$ ($0.44\pm0.14 \times$ solar)	17–21		
NH_3 Ammonia	CR[17/13]	$6.7\pm2.6 \times 10^{-4}$ ($3.0\pm1.2 \times$ solar)	9–12	34, 35	Slightly less than Mahaffy et al. (1999)
H_2S Hydrogen sulfide	CR[34/13], CR[34/4]	$2.85\pm0.58 \times 10^{-5}$ (0.88 ± 0.18 solar)	9.55	29, 30	Neglects PH_3 contribution, which should be insignificant. Error > in Wong et al. (1999)
		$4.1\pm1.5 \times 10^{-5}$ (1.27 ± 0.46 solar)	11.5		
		$7.0\pm2.1 \times 10^{-5}$ (2.16 ± 0.65 solar)	15.8–18.8		
C_2H_6 Ethane	CR[30/4]	$9.2\pm4.8 \times 10^{-8}$	8.5–12	3	All C[30] assumed to be ethane.
C_2H_4 Ethylene	CR[27/13]	$8.6\pm3.5 \times 10^{-7}$	8.5–12	14 + 15 (see Ch.6)	Corrected for ethane, propane, propene. Maybe confused with HCN, may increase in DL2a.
C_2H_2 Acetylene	CR[25/4], CR[26/4]	$6.6\pm9.7 \times 10^{-7}$	8.5–12	16	Close to detection limit, could be higher if HCN present in C[27].

Table 9.1 Summary of GPMS mixing ratios derived in this dissertation. (Continued)

Species	GPMS counts used	Atmospheric mixing ratio	Pressure range (bar)	Calibration constant reference*	Comments (see text for more info)
C_3H_4	C[37], C[39], C[40]	(detection)	8.5–12	none	Detection based on count ratios and splitting patterns; no calibration constant; C[38] inconsistent with C_3H_4.
C_3H_6 Propene	CR[41/4], CR[42/4]	$9.8 \pm 3.3 \times 10^{-8}$	8.5–12	11, 13	C[41] and C[42] corrected for propane
C_3H_8 Propane	CR[29/4], CR[43/4]	$2.6 \pm 1.1 \times 10^{-7}$ $4.5 \pm 1.8 \times 10^{-7}$	8.5–10 10–12	6, 8	Corrected for ethane. Assumes no butane.
C_4H_{10} Butane	C[29], C[43], C[58]	$< 6.0 \times 10^{-8}$	8.5–12	9	Upper limit
$N_2 + CO$	CR[28/4], CR[28/13]	$2.7 \pm 1.7 \times 10^{-7}$	8.5–12	17	Correction for ethane, propane, ethylene has a minor effect

*Unless otherwise noted, calibration constant references correspond to ID numbers in Table 5.10.

The information in Table 9.1 above requires several points of clarification. Methane is listed first because it is a fundamental result; all the subsequent mixing ratios that use C[13] as a reference gas are derived using the methane mixing ratio (see Equation 3.9) and its corresponding uncertainty. The methane mixing ratio in Table 9.1 differs from the published result of Niemann *et al.* (1998; hereafter N98), which was $2.10 \pm 0.4 \times 10^{-3}$, due to the more exhaustive analysis of the methane calibration constants given in Chapter 5. The current analysis tends to include more calibration runs, and use the scatter in calibration constants to derive a greater uncertainty in the result, whereas the GPMS team had a tendency to disregard some of the outlying calibration runs. In either case, the pre-Galileo methane mixing ratio of $1.95 \pm 0.22 \times 10^{-3}$ (Gautier *et al.* 1982) is within the error bars of the GPMS measurement.

The condensible volatile mixing ratios given in Table 9.1 represent the best values possible at this time, but future calibration work may refine the results significantly,

especially with water, whose calibration constant has a particularly large uncertainty. Although the water mixing ratios presented here differ from those of N98, all values agree within their quoted errors. The most significant difference is that the results given here are central values with 1-σ uncertainties, while the N98 results were given as upper limits (with 1-σ uncertainties). The deepest water mixing ratio, derived from the 17–21 bar DL2b results, is 25% larger than the N98 value of $\leq 6 \pm 3 \times 10^{-3}$. Since the DL1 calibration constants were not analyzed for this study, no 3.6-bar result is available for comparison with N98. The analysis of DL2a ammonia was complicated by the desorption from the mass spectrometer walls of ammonia molecules when atmospheric hydrogen entered the system. Chapter 6 describes the analysis technique used to compensate for this effect, which results in a single ammonia value for the 9–12 bar DL2a region. The same analysis technique was implemented by Mahaffy *et al.* (1999), but the current analysis is 14% lower than the Mahaffy *et al.* (1999) result of $3.5 \pm 1.5 \times$ solar, well within the quoted uncertainties of approximately 40%. The difference is probably due to the estimation of the ammonia decay parameters α and β (see Equation 6.3); future calibration experiments would be very helpful in reducing the uncertainty in the result, since only two experimental studies went into the result in Table 9.1. The GPMS ammonia result is consistent with the probe site deep ammonia abundance derived by Folkner et al. (1998), and represents a significant increase over the 1–1.5 $\times$ solar ammonia previously reported in de Pater (1986), Romani et al. (1995), and references within those papers, based on ground-based microwave observations. The two DL2a H_2S mixing ratios listed are averages over pressure intervals; Figure 6.23 depicts the variation of H_2S with pressure in DL2a. The H_2S results listed here have significantly greater uncertainties than the results presented by Wong *et al.* (1999), with the difference primarily owing to the underestimated uncertainty in the CH_4 mixing ratio used in Wong *et al.* (1999). Mass interference from PH_3 has not been included in the H_2S analysis, largely because the unofficial back-of-the-envelope phosphine mixing ratio derived from C[31] in DL2a is about 6×10^{-7}. This phosphine abundance would result in a contribution of less than 1% of the total count rate at the main H_2S mass of 34, an

insignificant contribution compared to the uncertainty in H_2S. The GPMS result for H_2S is the only measurement of deep sulfur on Jupiter.

Because the hydrocarbon mass spectra overlap significantly, the mixing ratios presented in Table 9.1 are the result of a complicated web of assumptions. One technique is to simultaneously derive mixing ratios of the hydrocarbons by using a matrix inversion technique to solve the set of linear equations describing the superposition of the mass spectra, but the technique used in this work is more akin to species-by-species Gaussian elimination. This approach was adopted in order to simplify error propagation and to clarify the effect of the corrections made based on the assumed hydrocarbon abundances. The hydrocarbon analysis approach was described fully in Chapter 6, so only a brief precis is included here.

The ethane abundance is a very robust result, since it is free of mass interference from other hydrocarbons, as can be seen in Figures 6.1 through 6.3. The ethylene result, on the other hand, includes corrections for the contributions of three interfering hydrocarbons (ethane, propane, and propene). Chapter 6 only briefly mentioned the possibility of C[27] being due to HCN; this important possibility will have to be left to future work. If HCN is present at the 1×10^{-7} level as claimed by Atreya (1986) in his reference of the oral presentation of Larson et al. (1976), then a preliminary back-of-the-envelope estimate based on FU calibration data for HCN would predict about 4 counts at C[27] due to HCN in the DL2a region, a significant amount compared to the approximately 30 counts present after the various hydrocarbon corrections. Although C[27] increases throughout DL2a, at least a portion of the increase is due to the increase in C_3H_8 over that range, and only an averaged value is reported in Table 9.1. The acetylene mixing ratio has a large uncertainty due to propagated uncertainty from the corrections for interfering hydrocarbons, and is statistically consistent with zero acetylene abundance. The value quoted is very close to the GPMS detection limit for acetylene. If indeed some of the counts at C[27] are due to HCN instead of to ethylene, then the acetylene abundance would be correspondingly larger and have a smaller uncertainty, since the HCN C[26]/C[27] ratio is 0.17, compared to about 0.9 for ethylene. As discussed previously in Chapter 7 as well as below, the observed ranking

(most to least abundant) of the C_2 hydrocarbons is nominally C_2H_4, C_2H_2, C_2H_6, in disagreement with the results of the photochemical modeling efforT of Chapter 7, which predicts the ranking C_2H_6, C_2H_2, C_2H_4. Although the possibility of HCN contribution to C[27] might improve the situation between C_2H_2 and C_2H_4, ethane would still remain underabundant, compared to the model predictions, unless the large uncertainty in the C_2H_2 mixing ratio is interpreted as a non-detection of acetylene.

The C_3 hydrocarbons propene and propane, on the other hand, follow the model in that propane is the more abundant, although the difference is about a factor of two in the GPMS data, and a factor of around 100 in many of the photochemical model runs (see Chapter 7). The quoted propane mixing ratio includes a correction for the ethane contribution to C[29], and assumes that no butane is present. The propene mixing ratio has been corrected for the propane contribution to C[41] and C[42].

No conclusive detections of C_4 hydrocarbons were made by the GPMS. Butane was searched for at masses 29, 43, and 58. The counting rate at mass 58 was at the noise level, while the observed C[29]/C[43] ratio was more consistent with pure propane than with a combination of propane and butane. The value in Table 9.1 in an unreasonably high upper limit to the butane mixing ratio made by assuming that C[43] are entirely due to butane; a more likely upper limit would be at least an order of magnitude less.

Molecular nitrogen is discussed below in relation to deep thermochemistry.

The mixing ratio uncertainties given in Table 9.1 are generally on the order of 20–30%, and sometimes greater. The possibility of reducing these uncertainties, primarily through new calibration experiments, is inherently attractive. However, variation of the composition data within the current level of uncertainty would not lead to any drastically different interpretation of the data with respect to planetary origin, PES condensible volatile distribution, or deep hydrocarbons. Thus, the measurement accuracy could be considered "good enough," with the major exception of the hydrocarbons, since the possibility that their calibration response could vary with abundance is not included in the uncertainty estimates quoted in Table 9.1.

Bulk composition of Jupiter

The abundance of the volatile heavy elements carbon, oxygen, nitrogen, and sulfur on Jupiter provide valuable insight into both the formation of planet as well as conditions of the early solar nebula. Chapter 1 introduced the core instability model of gas giant formation, which explains the enrichment of heavy elements on Jupiter via accretion of planetesimals. The carbon and sulfur enrichments given in Table 9.1 fit this scenario nicely, with the approximately solar C/S ratio indicating that the planetesimals responsible for the enrichment were icy rather than rocky (Owen et al. 1997, Anders and Grevesse 1989).

The C/N ratio, however, is problematic. Although N_2 is invisible to radio-wavelength observations of interstellar molecular clouds, it is theorized to be the primary reservoir of nitrogen (Irvine and Knacke, 1989), a condition that is also expected to apply to the solar nebula during the formation of the planets (Prinn and Fegley, 1989). The microwave observations of Jupiter discussed earlier were in agreement with this view of the partitioning of nitrogen in the solar nebula, since the retrieved deep ammonia abundance of 1–1.5 × solar resulted in a C/N ratio of 2–3 × solar. But the 7–15 bar NH_3 retrieval of Folkner *et al.* (1998) based on probe signal attenuation, corroborated by the 9–12 bar GPMS ammonia result of Mahaffy *et al.* (1999) and this work, result in a C/N ratio of approximately solar. The probe signal attenuation and GPMS results are more indicative of the bulk complement of nitrogen in Jupiter's atmosphere, since the microwave retrievals are most sensitive to ammonia abundance at pressures less than 4 bar. In fact, a recent study by de Pater *et al.* (2001) shows that a global ammonia enrichment of 3.5 × solar is entirely consistent with the same microwave data that had previously yielded the deep ammonia abundance of 1–1.5 × solar, although the larger deep abundance of ammonia required substantial subsaturation of ammonia (relative to NH_3-ice) at pressures less than 4 bar. Since planetesimal accretion is still the best explanation for the enrichment of Jovian heavy elements, the solar C/N and C/S ratios combine to indicate that a large fraction of the nitrogen in the solar nebula was incorporated into planetesimals. In addition to challenging the prevailing view that gaseous N_2 was the main form of solar nebula nitrogen, this finding also presents the formidable challenge of how to actually incorporate nitrogen into the icy

planetesimals, since nitrogen is poorly trapped in ice at the temperatures thought to apply to the orbit of Jupiter in the solar nebula (Bar Nun et al., 1988). Inspired by numerous recent observations of large extrasolar planets at very small orbital radii, papers such as Trilling et al. (1998) present numerical simulations of the orbital evolution of giant planets in which planets are able to migrate inwards as a result of gravitational interaction with the protostellar disk. At this point it is not clear whether a revision of nitrogen chemistry or of orbital dynamics is more suitable as an explanation of the solar C/N ratio.

Since condensation limits the amount of water present in Jupiter's atmosphere at pressures less than about 5 bar, no remote sensing method is able to retrieve the deep water abundance. Infrared spectra at 5 μm can sense deeper than 5 bar, but only in 5-μm hotspots, where water is anomalously low. Radio observations are weakly sensitive to ammonia down to 8 bar, but are not sensitive to water. The hope that the Galileo Probe could provide an unequivocal deep water measurement was lost when it descended into a 5-μm hotspot. The deepest measurement of water by the GPMS corresponds to 0.44 $\times$ solar, and is considered to be a local value, depleted by dynamics. There is no conceivable explanation of a global abundance corresponding to this low value.

Tropospheric structure

The deceptively simple distribution of condensible volatiles along the Galileo Probe descent has proved difficult to explain through any single dynamic process. In fact, in addition to demonstrating the complexity of the dynamic history of the PES, it would seem that the CV-profiles provide some additional insight into the state of the air *outside* the descent path. Chapter 1 provided a review of measurements of the Galileo Probe entry site, and Chapter 8 described efforts to model probe entry site condensible volatile profiles. Models ranged from the one-dimensional entraining downdraft developed for this dissertation (DDE) to two- and three-dimensional models of Jovian convection, thunderstorms, and zonal flow. The merits and flaws of these models are also given in Chapter 8, and although some of the models are able to qualitatively explain some of the characteristics of the PES and 5-μm hotspots, none of them are able to provide a full

description of the formation, structure, and evolution of 5-μm hotspots. Such a full description will probably not be achieved for many years, and in the meantime we look to comparisons between PES/5-μm hotspot data and the atmospheric models of Chapter 8 to illuminate specific elements of the problem.

The GPMS revealed one of the most striking features of the PES—that the already well-known dryness typical of 5-μm hotspots persists to at least 22 bar, and probably quite deeper. This fact is most insightful when compared with the results of DDE (see Chapter 8), which indicate that the full latent heat release associated with the condensation of a solar abundance (or more) water cloud creates a strong stable layer in the atmosphere, making it difficult for a downdraft to penetrate below the cloud base at the 5–7 bar level. Thus, driving the downdraft to 22 bar (or deeper) requires either external forcing, or an environment without a substantial water cloud. As discussed in Chapter 8, external forcing is indeed energetically possible. The energy requirements estimated by Showman and Ingersoll (1998) for forcing the downdraft below the 20-bar level are comparable to the Gierasch et al. (2000) estimate of the energy release of a single Jovian thunderstorm. One major consideration in this type of energy estimate is the areal extent of the downdraft coverage; the Gierasch et al. (2000) thunderstorm's estimated energy output would not be sufficient to drive a single downdraft or system of downdrafts large enough to cover an entire 5-μm hotspot.

There is no unidentifiable mechanism capable of explaining how a thunderstorm could drive downdrafts over a large enough area to cover a 5-μm hotspot, but that is not the point. I am simply making the dimensional argument that the thunderstorm energy release and the downdraft energy consumption are on roughly the same scale. Thus, thunderstorms and downdraft systems may play complementary roles, at the 5×10^{15} W level (see Chapter 8 and Gierasch et al., 2000), in the release of Jupiter's internal heat flux through the troposphere. Although Jupiter's internal heat flux is known to be 5.4 W m^{-2} s^{-1} (Atreya, 1986), the detailed nature of the convective transport of this heat flux through the troposphere is not known. Guillot (1995) presented a well-reasoned claim that convection is inhibited due to molecular weight stratification: after a convective event that results in

condensation, molecular weight in the atmosphere decreases with height. Any subsequent ascending parcels would find that their molecular weight is greater than that of the environment into which they have risen, and sink back towards their level of origin. In this type of atmosphere water clouds would be rare, perhaps in agreement with the 7×10^{-10} thunderstorms km^{-2} detected by the Galileo spacecraft based on lightning observations (Little et al., 1999). If indeed convective heat release is limited to very small areas of the planet, then focusing enough energy to drive deep downdrafts becomes more believable.

Alternatively, if the hypothesized downdraft descended into an area of Jupiter's atmosphere lacking a substantial water cloud, then the lack of the stable layer associated with latent heat release in the cloud would permit the downdraft to descend to the 20-bar level or deeper, without requiring significant external forcing. The actual situation on Jupiter is likely to be somewhere between the cloud-free case and the super-stable ECCM-derived massive water cloud case. Future work with DDE simulations should involve such intermediate cases, perhaps using results from the work of Del Genio and McGrattan (1990), who used a 1-D cumulus parameterization adapted from a terrestrial global circulation model to simulate the effects of unresolved moist convective plumes, subsidence, and precipitation on the large-scale environment. They examined several cases, but typically arrived at stabilities (in terms of change in approximate equivalent potential temperature across the water cloud region) of less than 10% of the theoretical maximum stability of $\Delta\theta_e = 4.9$ K for $1 \times$ solar water.

Since the staggered recovery levels of the PES condensible volatiles was discovered, it has been associated with the staggered lifting condensation levels of the condensible volatiles (e.g., Atreya et al., 1996). This association has led to explanations in terms of column stretching (Showman and Ingersoll, 1998) and lateral mixing (Atreya et al., 1996), but Chapter 8 demonstrated that neither hypothesis quantitatively matches the PES CV profiles. As seen in Figure 8.2, the column stretching hypothesis fails because (1) the shapes of the CV profiles are not well represented unless the stretching factor varies from ~1 at the ammonia cloud tops to about 15 at 7 bar, back to 6 at 8 bar, and then increasing again below 8 bar, and because (2) there is no altitude in the ECCM-predicted CV distribution

with the correct relative proportions of water and H_2S that could be stretched to match the PES relative proportions of water and H_2S in DL2a. Also, none of the DDE experiments are able to simultaneously duplicate the PES profiles of all three condensible volatiles. However, Guillot's (1995) suggestion regarding inhibition of convection due to molecular weight layering, along with the sparsity of convective events implied by the lightning storm coverage found by Little et al. (1999), seem to imply that the full cloud development predicted by the ECCM is a poor description for most of the Jovian troposphere. The staggered CV recovery levels in the PES are probably yet another sign that the environment surrounding the hotspot, and/or the atmospheric conditions that applied to the environment into which the downdraft descended, departed drastically from the ECCM situation. However, this conclusion is difficult to explain, since it requires large-scale Jovian depletion of condensible volatiles deeper than the condensation levels predicted by the ECCM, for all three condensible volatiles. Remote sensing of ammonia (de Pater et al., 2001) seems to agree with this pattern of depletion on a global basis, but measurements of typical H_2S and water profiles will probably need to wait until atmospheric multiprobes or other inventive space missions can be launched to Jupiter.

The issue of scale is of primary importance in the understanding of Jupiter's condensible volatile and cloud distributions and method of convective energy release. The validity of generalizing Galileo Probe results to represent conditions throughout the 5-μm hotspot is questionable. Although it seems likely that a downdraft plays some role in the depletion of CVs detected by the probe, it is unknown whether such a downdraft is a small-scale phenomena, as modeled by the DDE, Hueso et al. (1999), or Baker and Schubert (1998). The nonlinear 3-D model of Showman and Dowling (2000) is able to simulate many of the large-scale features of hotspots, but the imposed limitation in its vertical extent of 5 bar is not useful for comparison with the condensible volatile profiles encountered by the Galileo Probe. Both Lunine and Hunten (1987) and Del Genio and McGratten (1990) sought to describe large-scale atmospheric humidity distributions in terms of parameterized small-scale convective elements. A full picture of 5-μm hotspots and their place in Jovian

convective energy transport will require a synthesis of the many spatial scales of these approaches.

Vertical transport of hydrocarbons

Before venturing into comparison between the photochemical model results and GPMS hydrocarbon mixing ratios, two disturbing possibilities must be considered:

1. Hydrocarbon calibration constants may change at low abundances, such that the derived mixing ratios are too high.
2. Hydrocarbons could be produced somewhere in the Galileo Probe, so that the observations are not truly characteristic of Jupiter's atmosphere.

Tables 4.1 and 4.3 show that the hydrocarbon abundances used in the calibration experiments ranged from as low as 2.8×10^{-5} (C_3H_6) to as high as 1.2×10^{-3} (C_2H_6). Fortunately, the EU calibration experiments with ethane mixing ratios of 1.2×10^{-3} and 1.34×10^{-4} agree to within about 0.1%. However, no runs were done with calibration mixing ratios closer to the values derived in Chapter 6, which do not exceed 1 ppm. Thus the possibility is untested that hydrocarbons in very low abundance might produce more counts in the mass spectrometer than would be expected based on the calibration runs done with mixing ratios that were greater than PES mixing ratios by factors of 10 to 1000. Future calibration experiments using very low hydrocarbon mixing ratios in the calibration gases would be very useful in establishing true GPMS detection limits for these species.

The second possibility, that the DL2a hydrocarbons might have been produced somewhere in the probe or the GPMS is troubling because if it can be justified, then no conclusions based on the GPMS-derived hydrocarbon distribution could be made. As discussed in Chapter 2, the mass spectrometer is pumped by an ion sputter pump, which can synthesize hydrocarbons within the mass spectrometer. Getter 8 (see Figure 2.1) is responsible for keeping any synthesized hydrocarbons out of the mass spectrometer. Although it is possible that partial or complete saturation of this getter may be partly responsible for the high count rates in DL2b, it is unlikely that this explanation could be invoked for the counts identified as hydrocarbons in DL2a, because the low count rates in

BG2 would have been affected as well. The rest of the discussion will presume that the possibility of hydrocarbon production on the probe can be discounted.

Two additional hydrocarbon source candidates must be briefly mentioned before discussing the implications of a stratospheric origin of the hydrocarbons detected by the GPMS: biogenic origin, and thermochemical origin in the deep atmosphere. Biogenic hydrocarbon generation is beyond the scope of this work to investigate, but it is of note that the idea that Jupiter's troposphere might be inhabited is not new. Figure 9.1 shows postulated jelly-blimps and swordtails, denizens of a fantastic Jupiter (Gallant, 1980). Given the composition of Jupiter, these beings would have to be carbon-based, so the PES hydrocarbons could be their metabolic byproducts, or could possibly have been desorbed from a chunk of jelly-blimp that had somehow become attached to the probe at some point of its descent prior to the DL2a experiment.

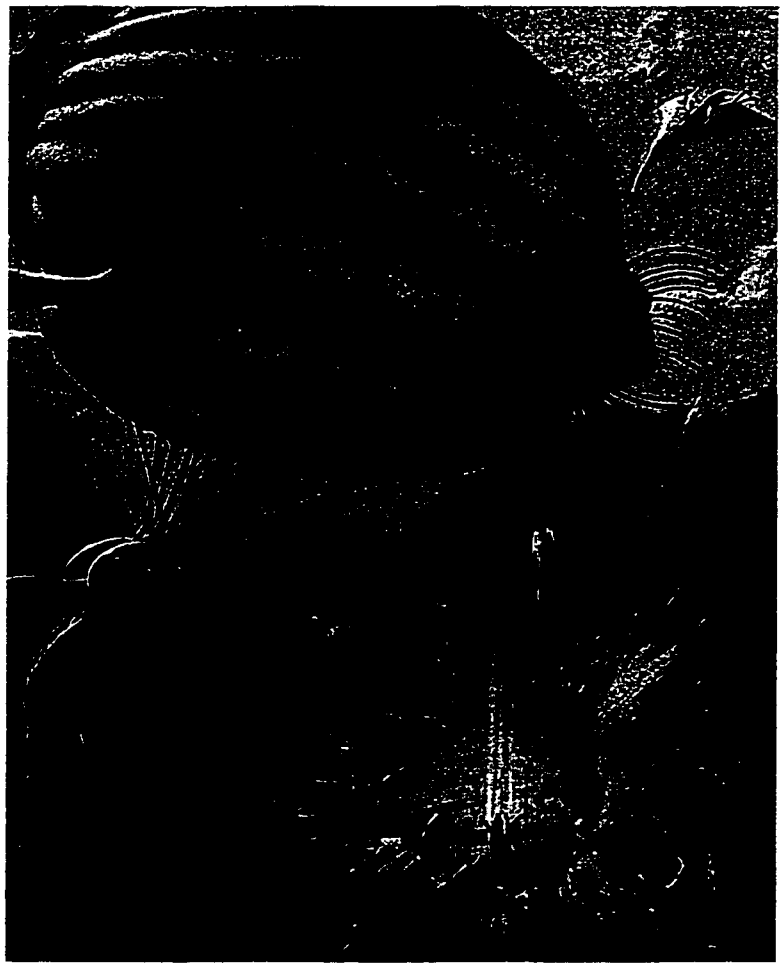

Figure 9.1 Possible (but unlikely) sources of the 9–12 bar hydrocarbons (from Gallant, 1980).

Fegley and Lodders (1994; hereafter FL94) modeled the deep thermochemistry by calculating the equilibrium composition of the atmosphere as a function of temperature. Reactions between molecules proceed throughout the atmosphere, with the equilibrium composition changing with altitude, until the temperature sinks below the quench temperature for particular species. At that point, even though the species may no longer be in equilibrium, it will still be present in concentrations controlled by the eddy diffusion rate. In the troposphere, ammonia is the equilibrium form of nitrogen, and the disequilibrium species molecular nitrogen is brought up from below by eddy diffusion. Tropospheric N_2 is a very weak function of K in FL94, and is in the neighborhood of 2×10^{-4} for values of K between 1 and 10^{18} cm^2 s^{-1}. This value is much larger than the $2.7 \pm 1.7 \times 10^{-7}$ measured by

the Galileo Probe, indicating some problem with the model assumptions of FL94. A deep thermochemical source would also appear to be a poor explanation for the $9.2 \pm 4.8 \times 10^{-8}$ ethane mixing ratio measured by the GPMS. Additional problems with the thermochemical explanation are the rankings of predicted mole fractions: CH_3NH_2 > HCN, and CO > C_2H_6 > C_2H_4. These rankings are directly contradicted by the GPMS data. The CO mixing ratio could not be measured, but is on the order of 1×10^{-9} (Noll et al., 1988), almost 100 times less than GPMS ethane, which is in turn about 10 times less than GPMS ethylene. The ethylene abundance could be reduced by attributing some of the *C*[27] to HCN as discussed above, but that alternative creates problems with the thermochemical prediction that CH_3NH_2 (undetected by GPMS) be more abundant than HCN in the levels visited by the probe.

Chapter 7 presented the results of the stratospheric photochemistry model for comparison with the PES hydrocarbons. Three main problems based on the comparison will be discussed in order:

1. For most eddy diffusion profiles, the ranking of the model hydrocarbon mole fractions was very different from the ranking of the relative abundances deduced from GPMS measurements.

2. Model hydrocarbon mole fractions were smaller than observed mole fractions by at least five orders of magnitude.

3. The influence of the lower boundary condition formulation on tropospheric mixing ratios may be too large in comparison to the influence of the eddy diffusion profile.

The model hydrocarbon mole fraction ranking is somewhat sensitive to the vertical profile of the eddy diffusion parameter *K*. The choice of *K* has the most influence on the relative abundances of the heavier hydrocarbons vs. the C_2 hydrocarbons, but in all cases the model ranking (most to least abundant) for the C_2 hydrocarbons was C_2H_6, C_2H_2, and C_2H_4, whereas in the GPMS data it the hydrocarbons were ranked C_2H_4, C_2H_2, and C_2H_6. The model hydrocarbon ranking is the same as that predicted by the models of Edgington (1997) and Gladstone et al. (1996). The possibility of inaccuracies in the C_2 hydrocarbon reaction scheme is a topic for future research, but there is also room for doubt in the GPMS results. As discussed above, the prospect that HCN could be contributing to *C*[27] could

lower the ranking of ethylene in the GPMS data. Since the uncertainty in the acetylene mixing ratio is large enough that it is consistent with zero acetylene, ethane could then become the most abundant GPMS hydrocarbon. Some of these uncertainties could be reduced if calibration experiments could be done with much lower hydrocarbon abundances in the calibration gas mixtures, especially since some gases (water, some hydrocarbons, and ammonia) did indeed demonstrate calibration constant dependences on species abundance (Chapter 5). Calibration constants showing dependences on abundance were smaller when their mixing ratios were smaller in the calibration mixtures. This variation is in the right sense to produce smaller hydrocarbon mixing ratios, if indeed the hydrocarbons exhibit a similar dependence of calibration constant on species mixing ratio.

Eleven different eddy diffusion profiles were examined in Chapter 7, many differing greatly from the profiles derived by Edgington et al. (1999) and depicted in Figure 7.1. Their *K*-profiles were derived by matching model ammonia distributions to spectra obtained from Hubble Space Telescope Faint Object Spectrograph at the indicated latitude bands. The spatial variation of *K*-profile is likely to be underestimated, since the observations are based on integrated spectra over latitude bands, a supposition that justifies the variation in eddy diffusion profiles explored in Chapter 7. Deeper than about 200 mbar, however, no constraints on eddy diffusion exist other than the limits imposed by the mixing length arguments of Hunten (1975), based on maximum mixing velocities of around 100 m s^{-1}.

Eddy diffusion is a simple parametrization of turbulence, but the dynamic history of the PES before the probe descent may be too complex to be described by a single parameter. The photochemical model describes a steady-state solution, but the PES hydrocarbon distribution could be an indication of a transient large-scale vertical mixing event. A precise description of any such mixing event implied by the PES hydrocarbons cannot be determined from the available data, but it would have to extend about 400 km, from the 1-μbar peak in the hydrocarbon mole fractions, down to the 10-bar region where the GPMS measurements apply. The possibility of a tropopause-crossing transient mixing event is extremely far-fetched, given the strong atmospheric stability of the stratosphere.

The slopes of the mole fraction profiles of all the tracer hydrocarbons (those hydrocarbons measured by the GPMS) at the model base are identical, as seen in the mole fraction profiles of Figures 7.6 through 7.18. This common slope results from the lower boundary condition that the velocity be K/H, following Gladstone et al. (1996) as explained in Chapter 7. With this choice of lower boundary velocity, the K mathematically gets eliminated from the numerical boundary condition, and the mole fractions decay with depth according to the atmospheric scale height. As explained in Gladstone et al. (1996), this lower boundary condition corresponds to the theoretical maximum diffusion velocity; a smaller diffusion velocity at the lower boundary would be more physically realistic and would produce tracer hydrocarbon profiles that decay more slowly with depth. Comparison of the mole fraction profiles of the eleven different eddy diffusion cases in Chapter 7 shows that this lower boundary vertical distribution according to the atmospheric scale height persists, in every case, from the lower boundary up to the first significant gradient in K. Removing the undue influence of this maximum diffusion velocity boundary condition on the mole fraction profiles should be a goal for future research, perhaps through the investigation of lower boundary conditions of zero flux or full diffusive or chemical equilibrium.

APPENDICES

APPENDIX A

Galileo Probe Mass Spectrometer data

This appendix displays graphically all the GPMS data. Black points are high (normal) sensitivity points at 75 eV ionization potential. Grey points are either at 15 or 25 eV, or are low-sensitivity measurements. Plotted points have been corrected for deadtime using τ_m, as described in Chapter 3. Background corrections are represented as grey lines, but have not been subtracted from the plotted points. Constant background corrections are plotted with their uncertainties (shaded bars), and exponential background corrections are shown without error estimates. The large number in the upper left corner of each plot gives the mass/charge ratio plotted. The y-axis is in units of counts per integration period, where the integration period in the GPMS was 0.5 seconds.

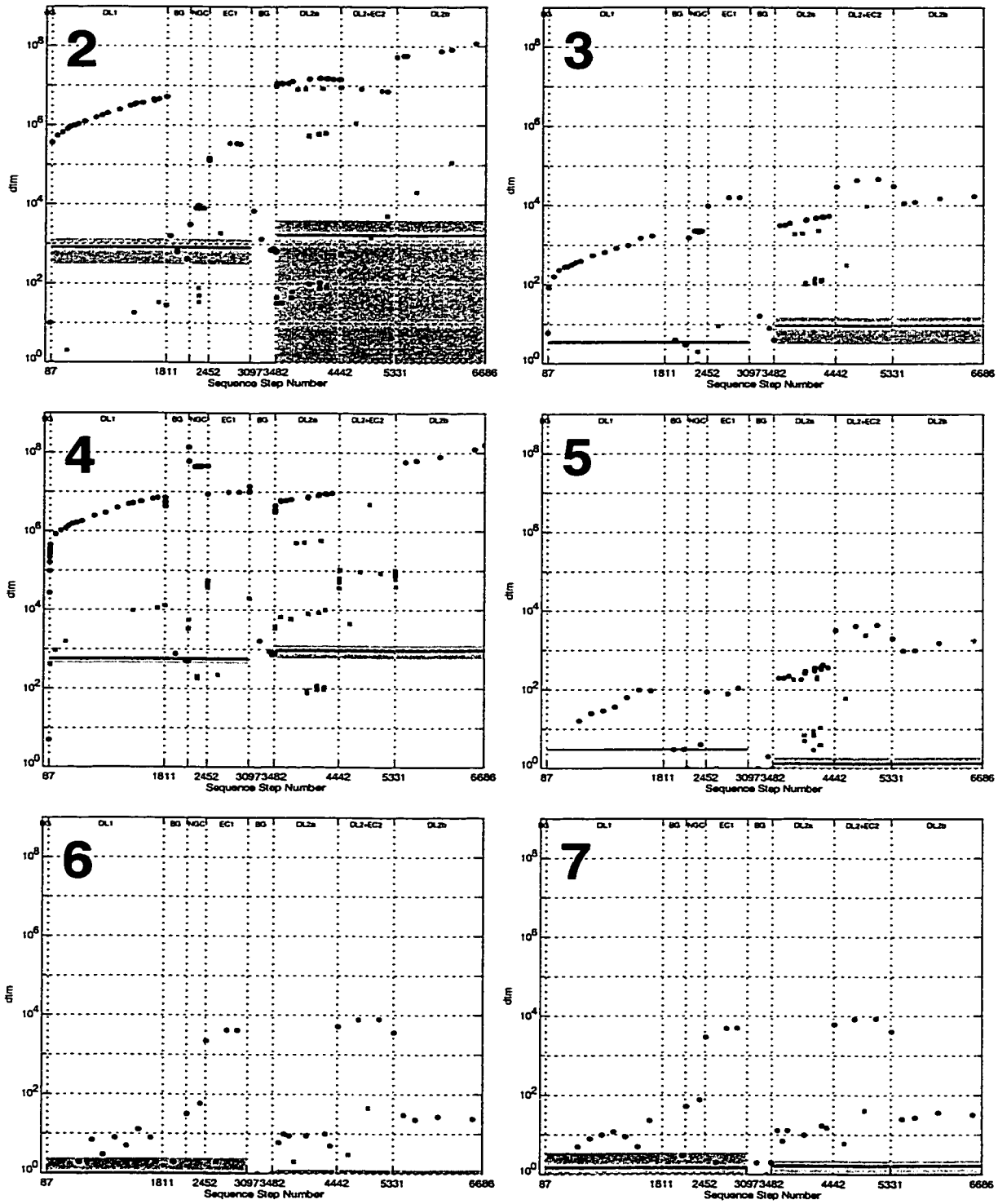

Figure A.1 Deadtime-corrected GPMS counts: masses 2–7.

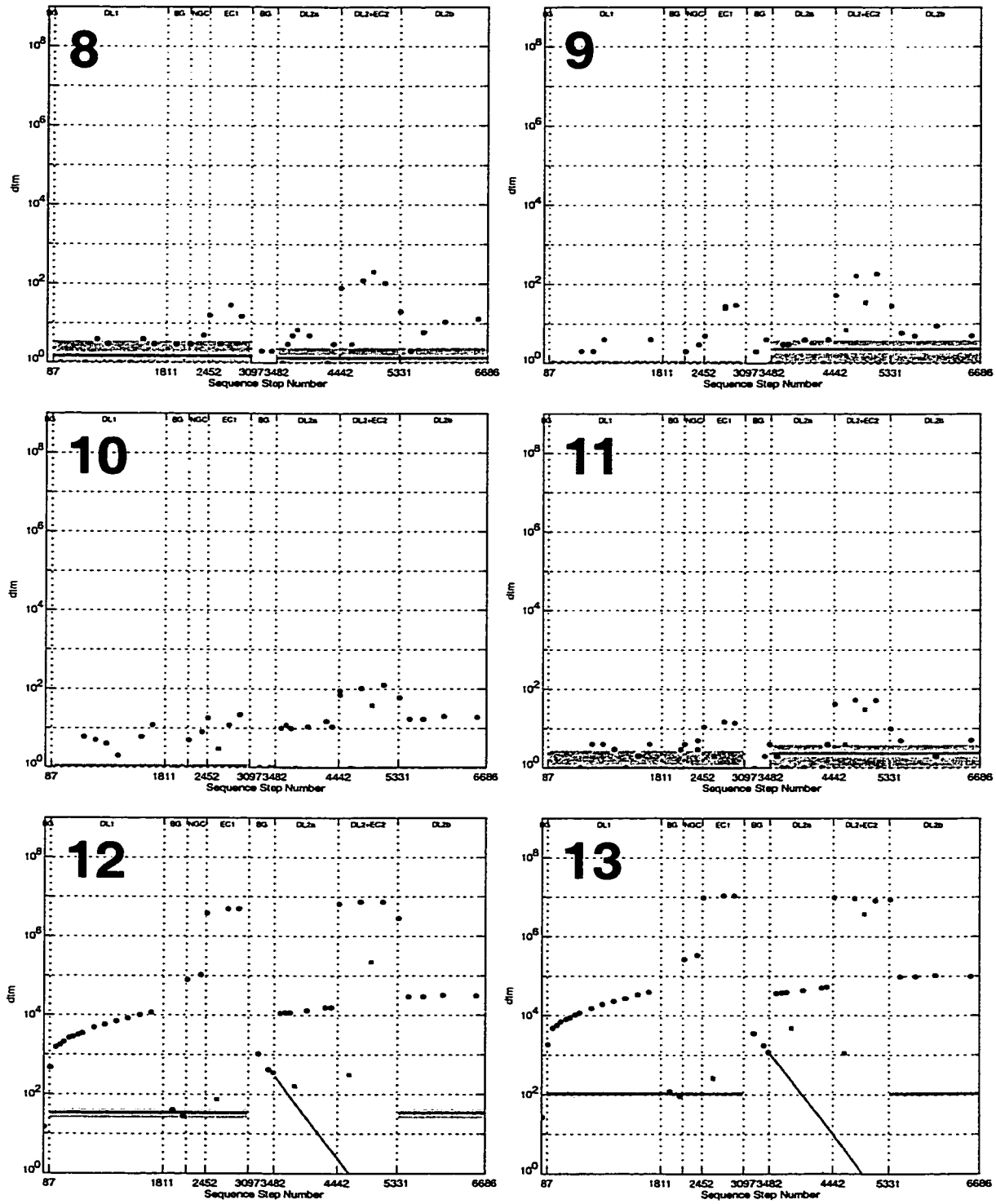

Figure A.2 Deadtime-corrected GPMS counts: masses 8–13.

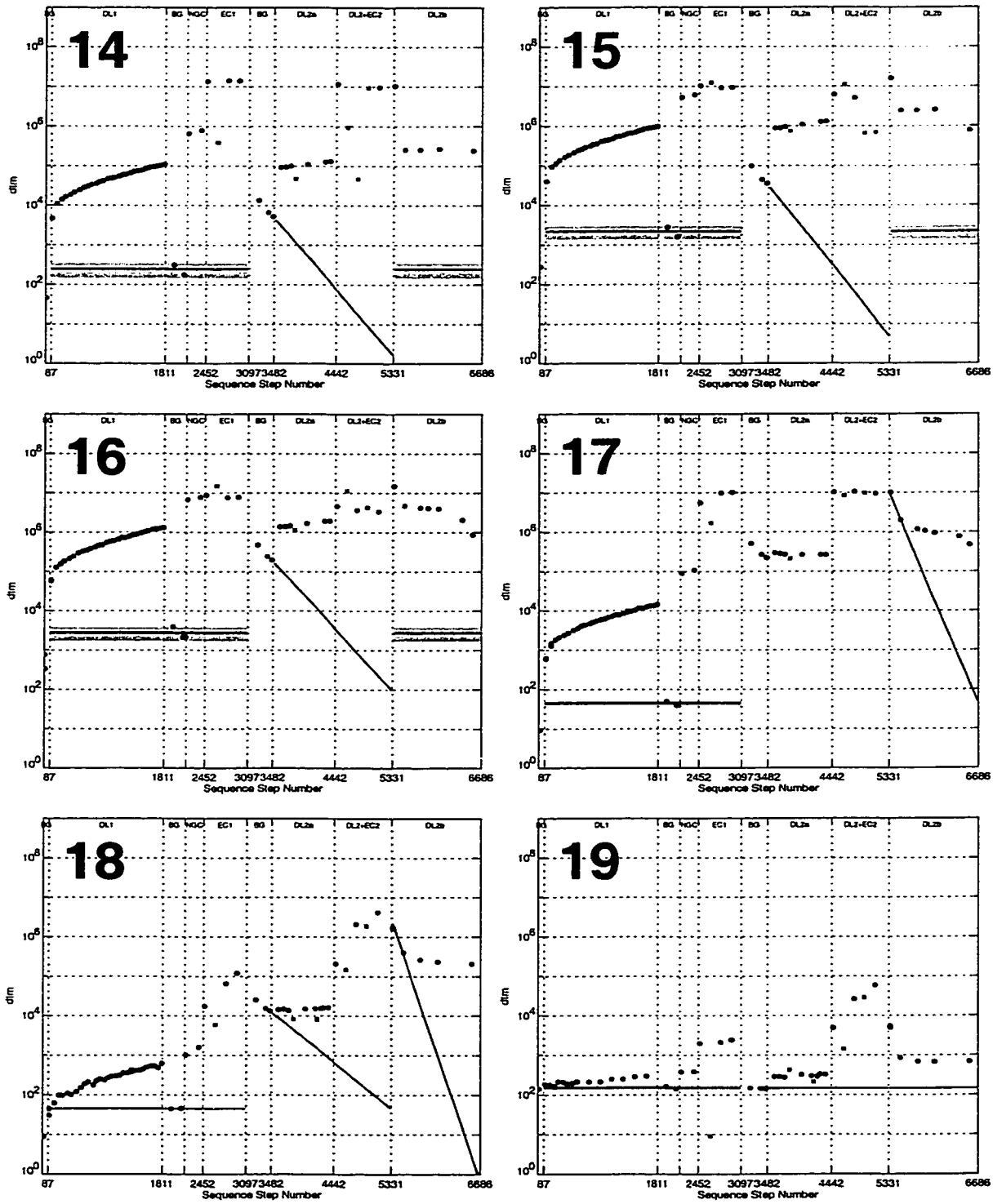

Figure A.3 Deadtime-corrected GPMS counts: masses 14–19.

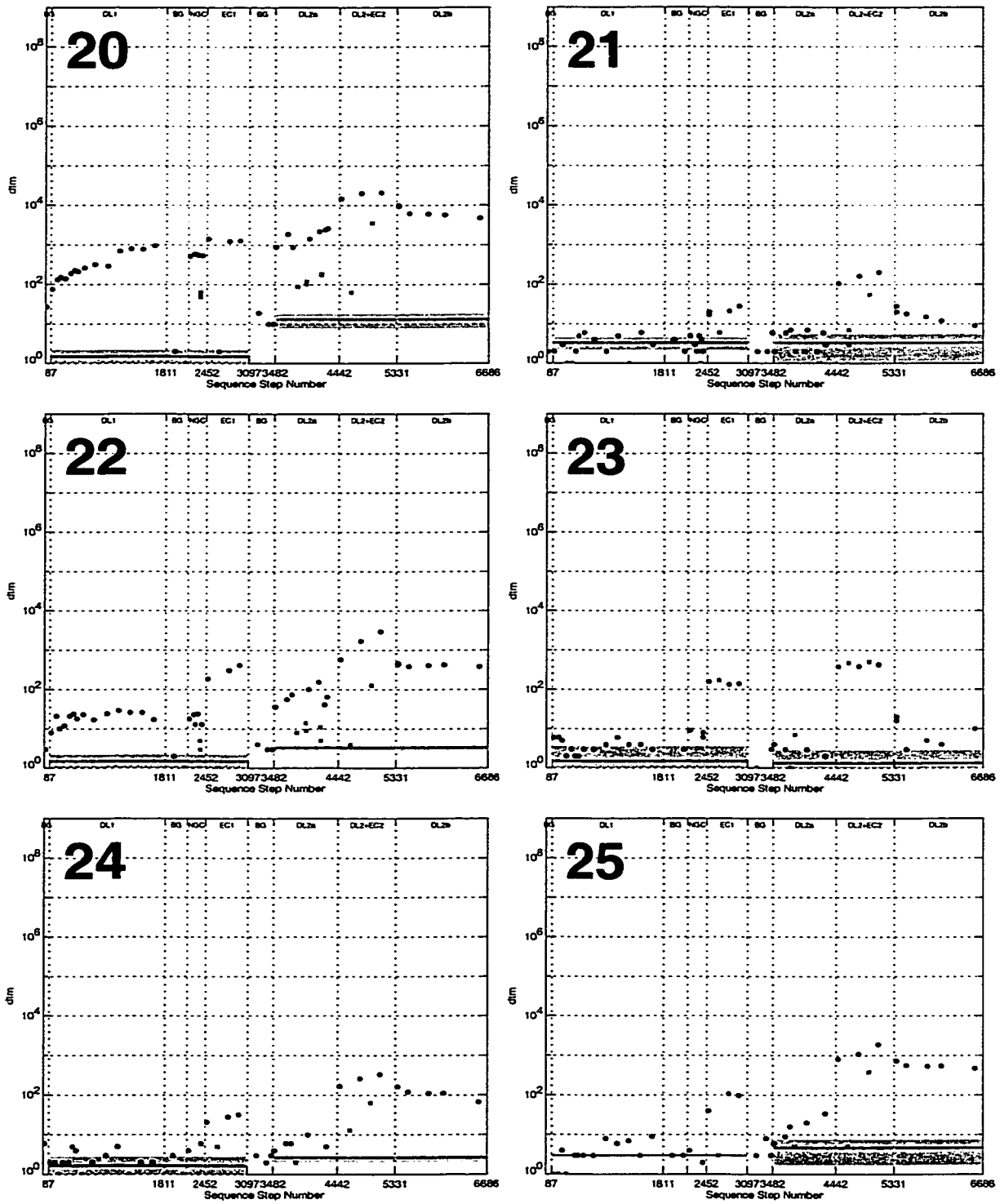

Figure A.4 Deadtime-corrected GPMS counts: masses 20–25.

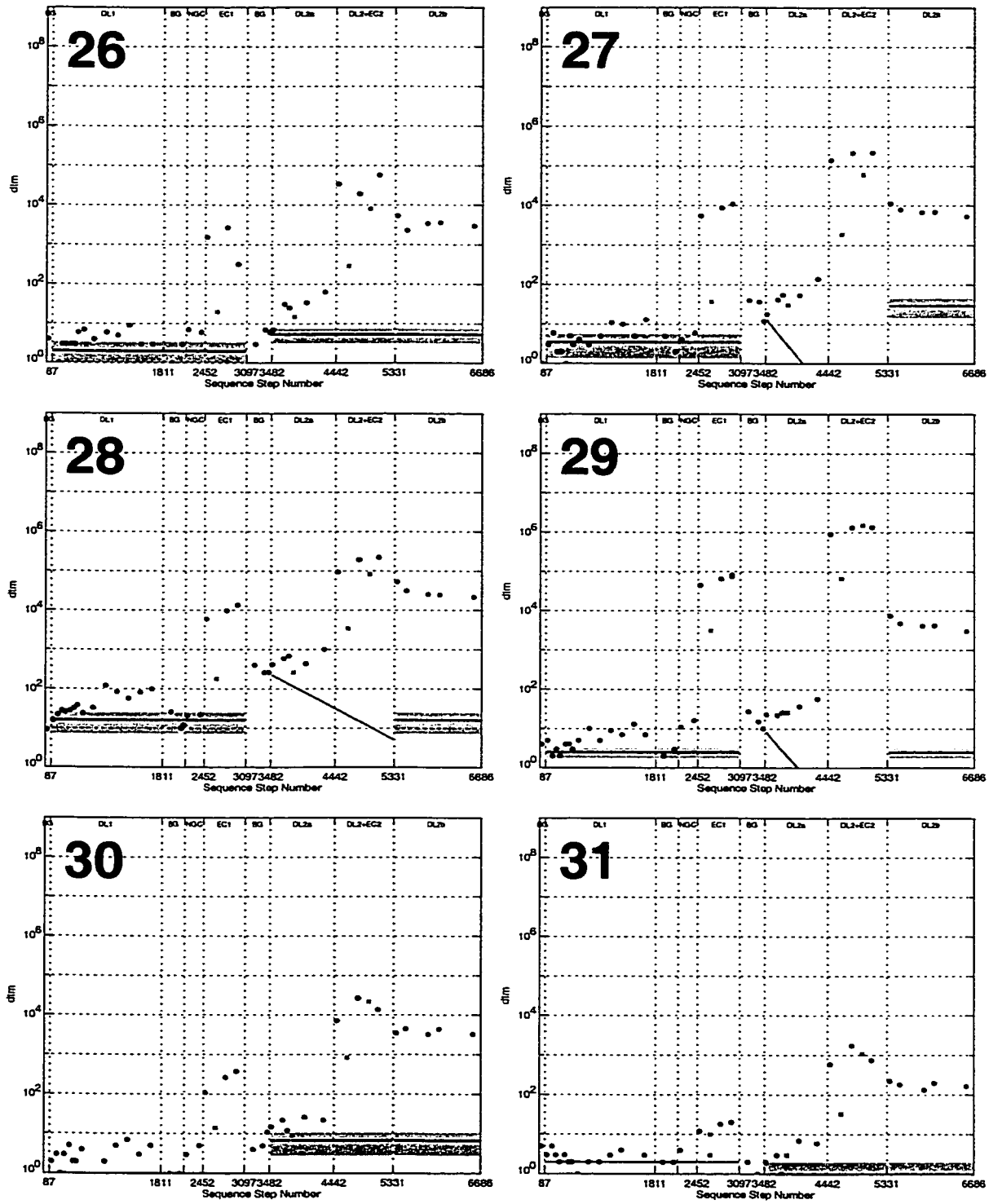

Figure A.5 Deadtime-corrected GPMS counts: masses 26–31.

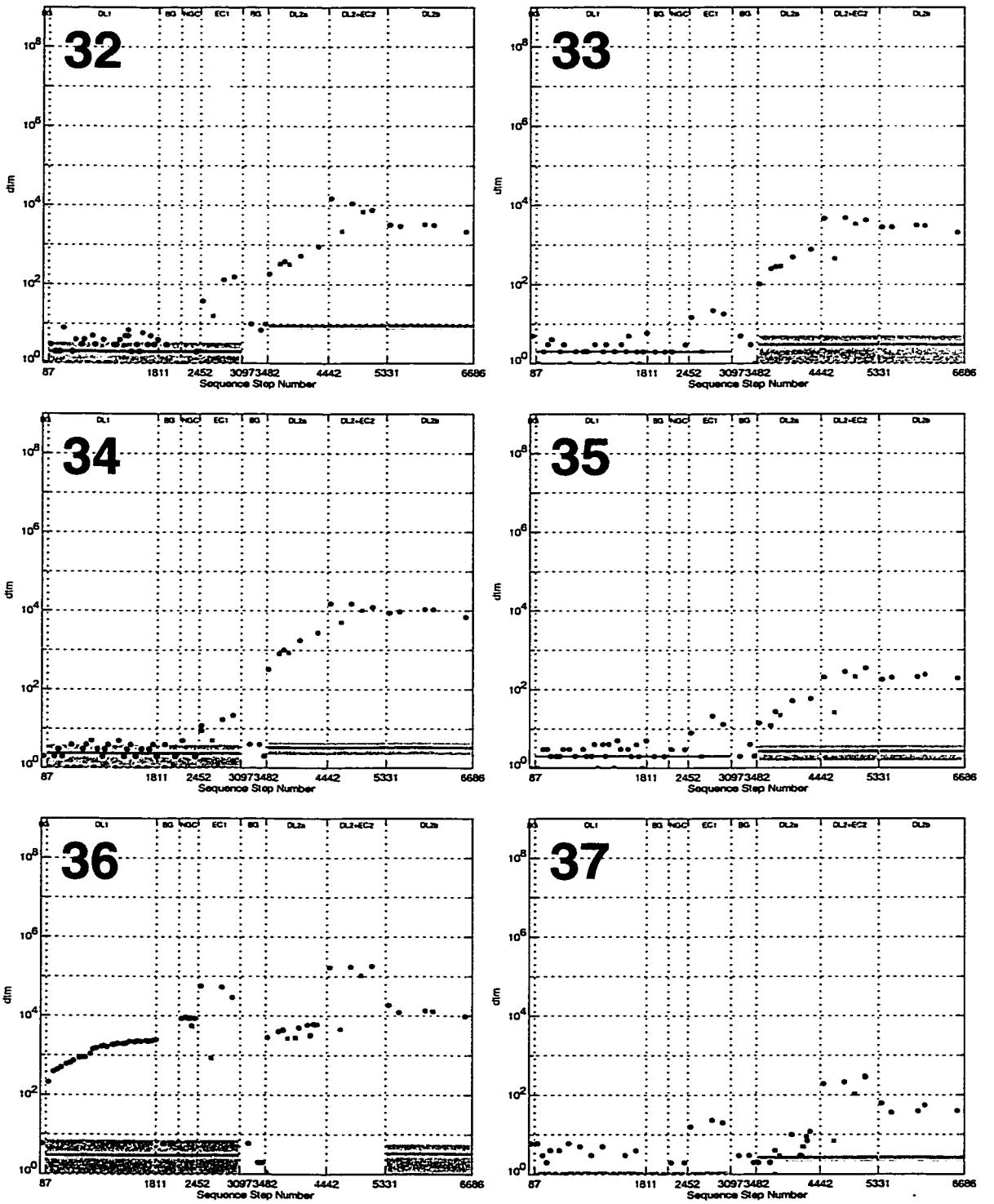

Figure A.6 Deadtime-corrected GPMS counts: masses 32–37.

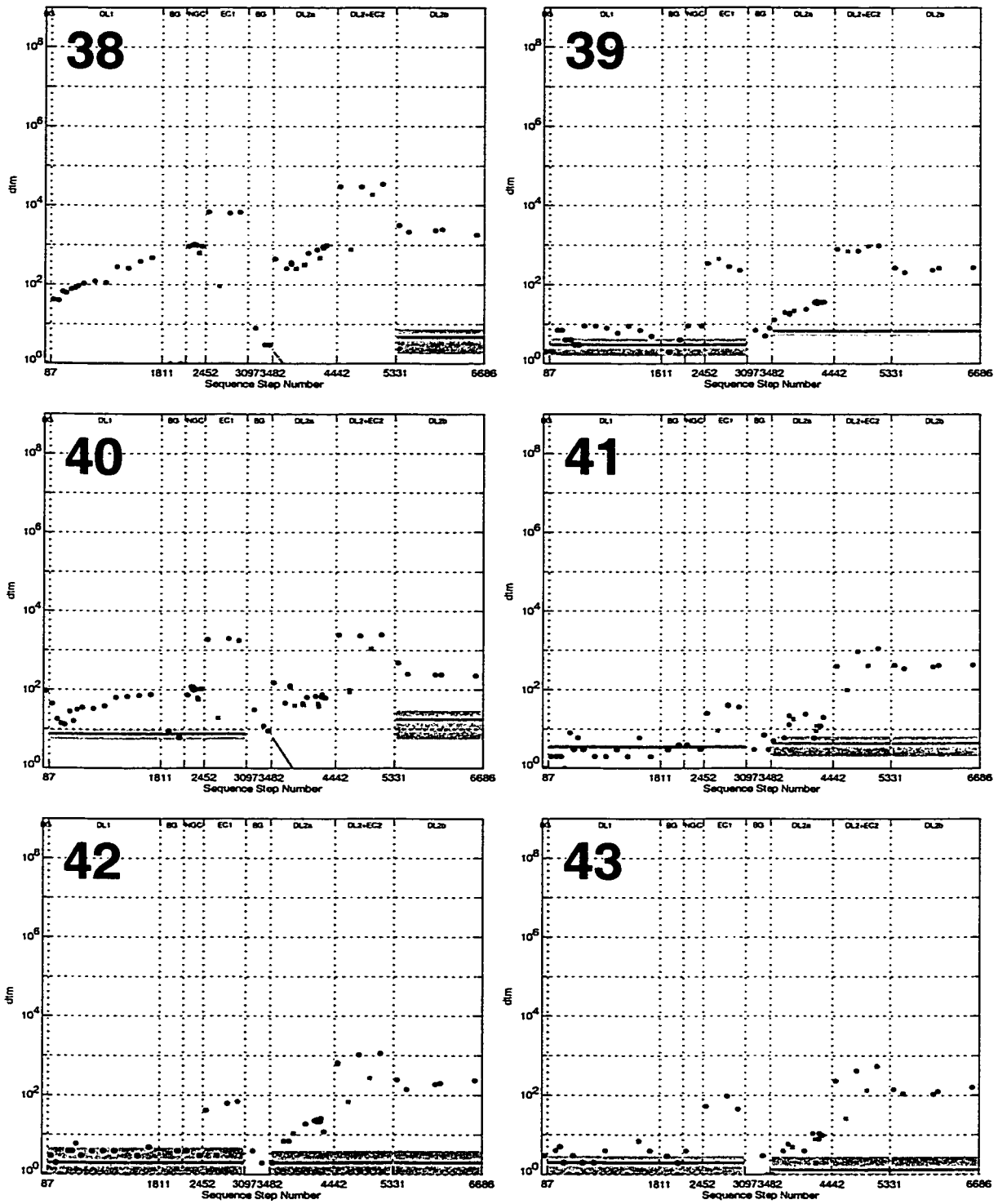

Figure A.7 Deadtime-corrected GPMS counts: masses 38–43.

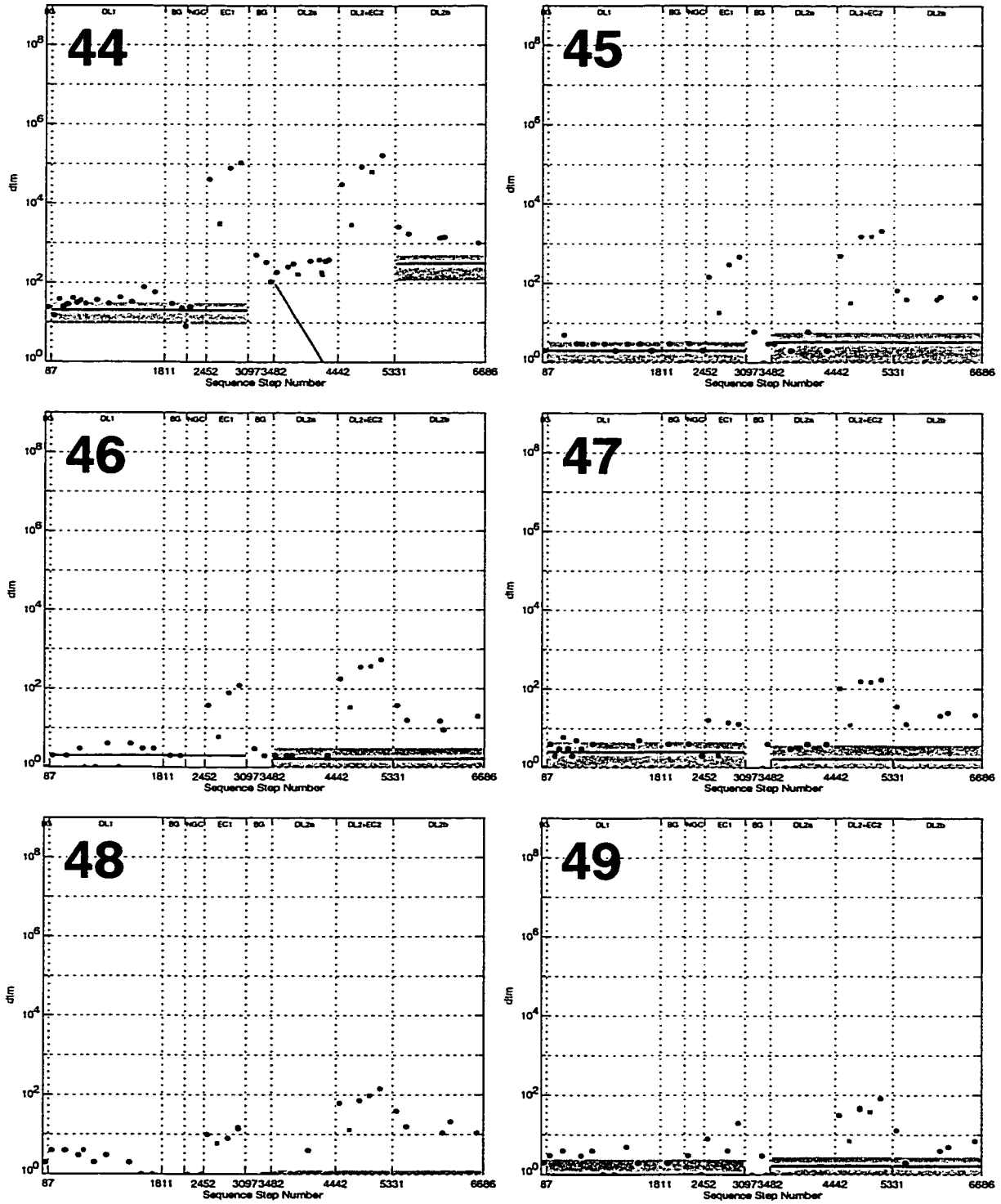

Figure A.8 Deadtime-corrected GPMS counts: masses 44–49.

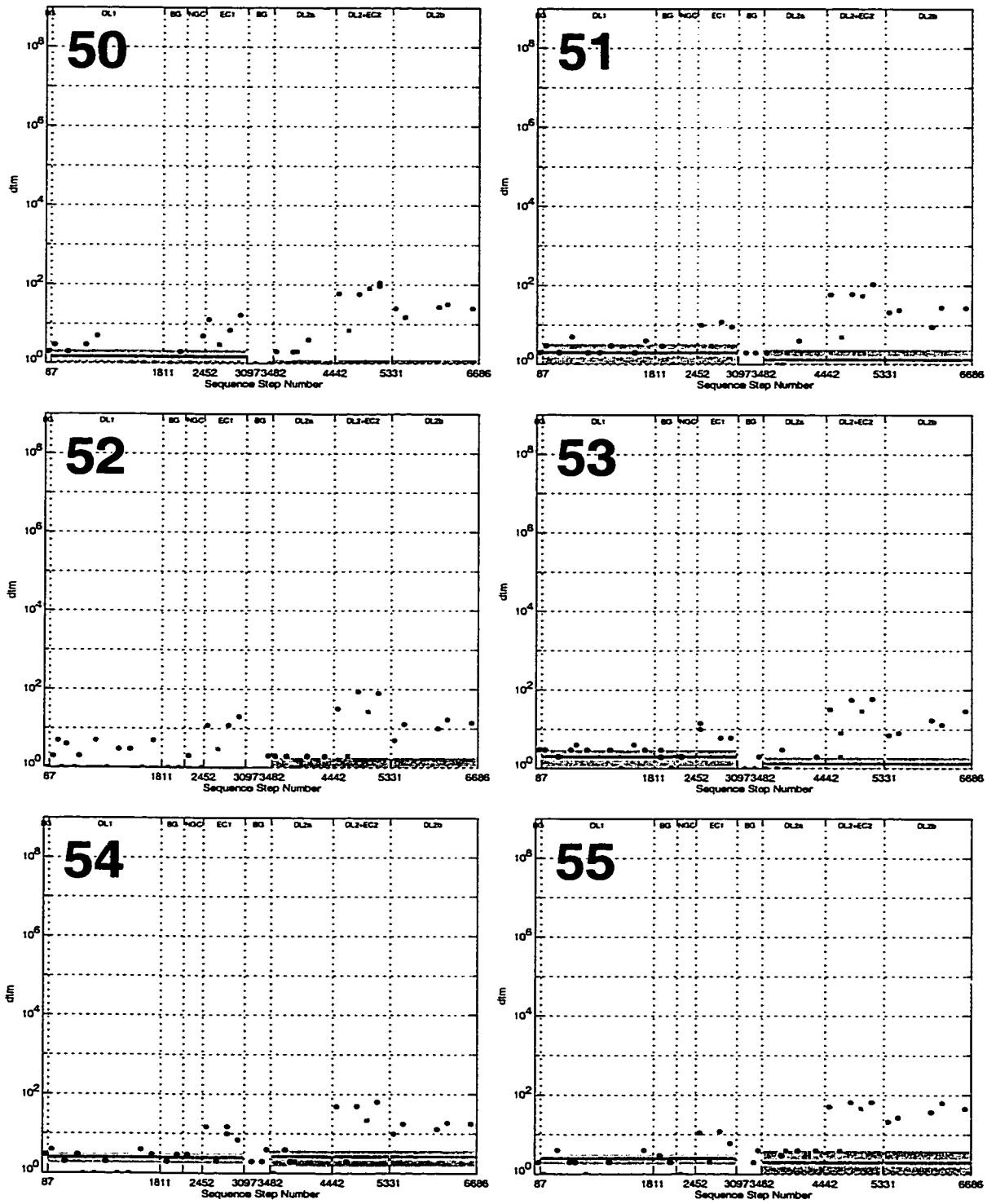

Figure A.9 Deadtime-corrected GPMS counts: masses 50–55.

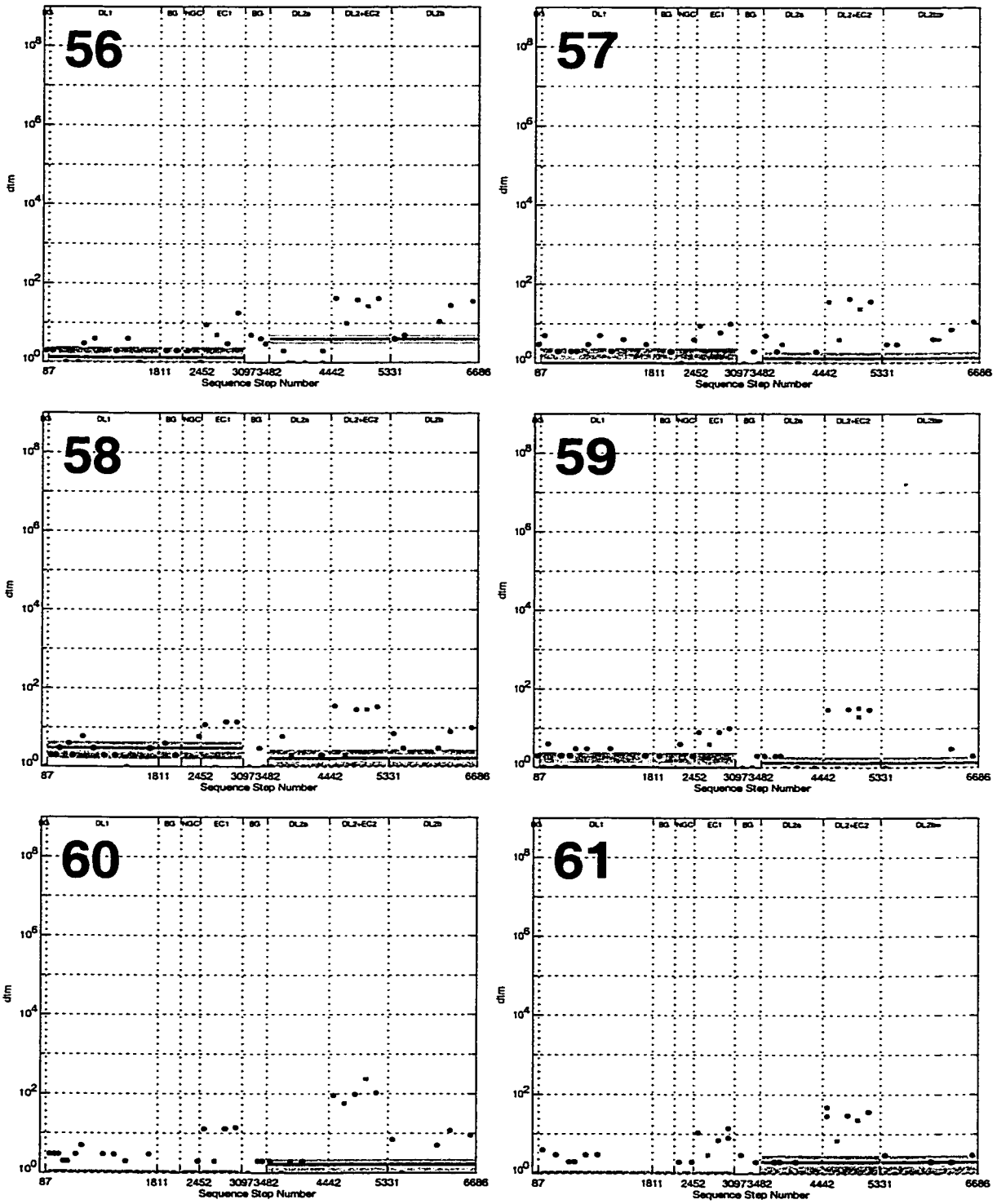

Figure A.10 Deadtime-corrected GPMS counts: masses 56–61.

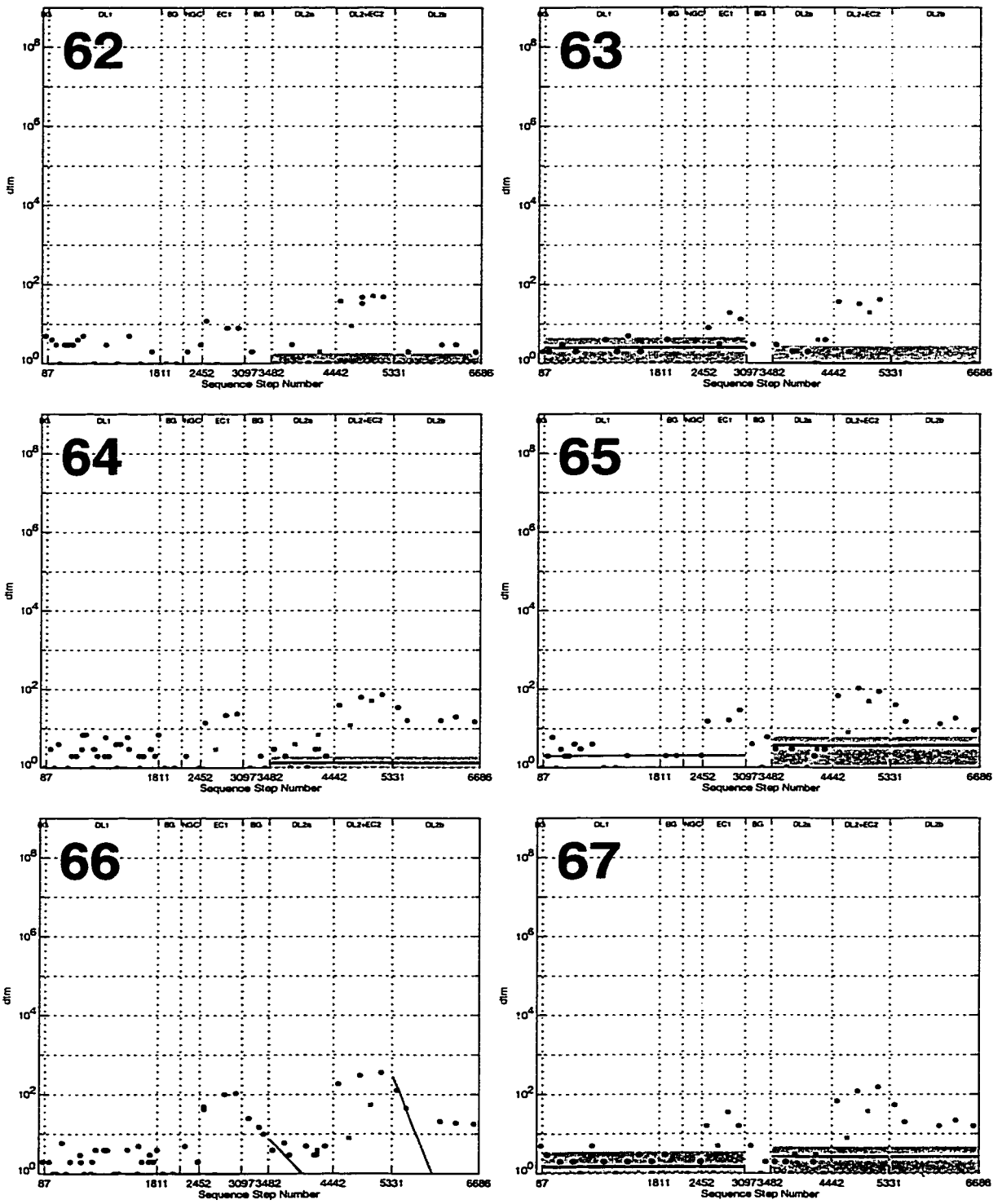

Figure A.11 Deadtime-corrected GPMS counts: masses 62–67.

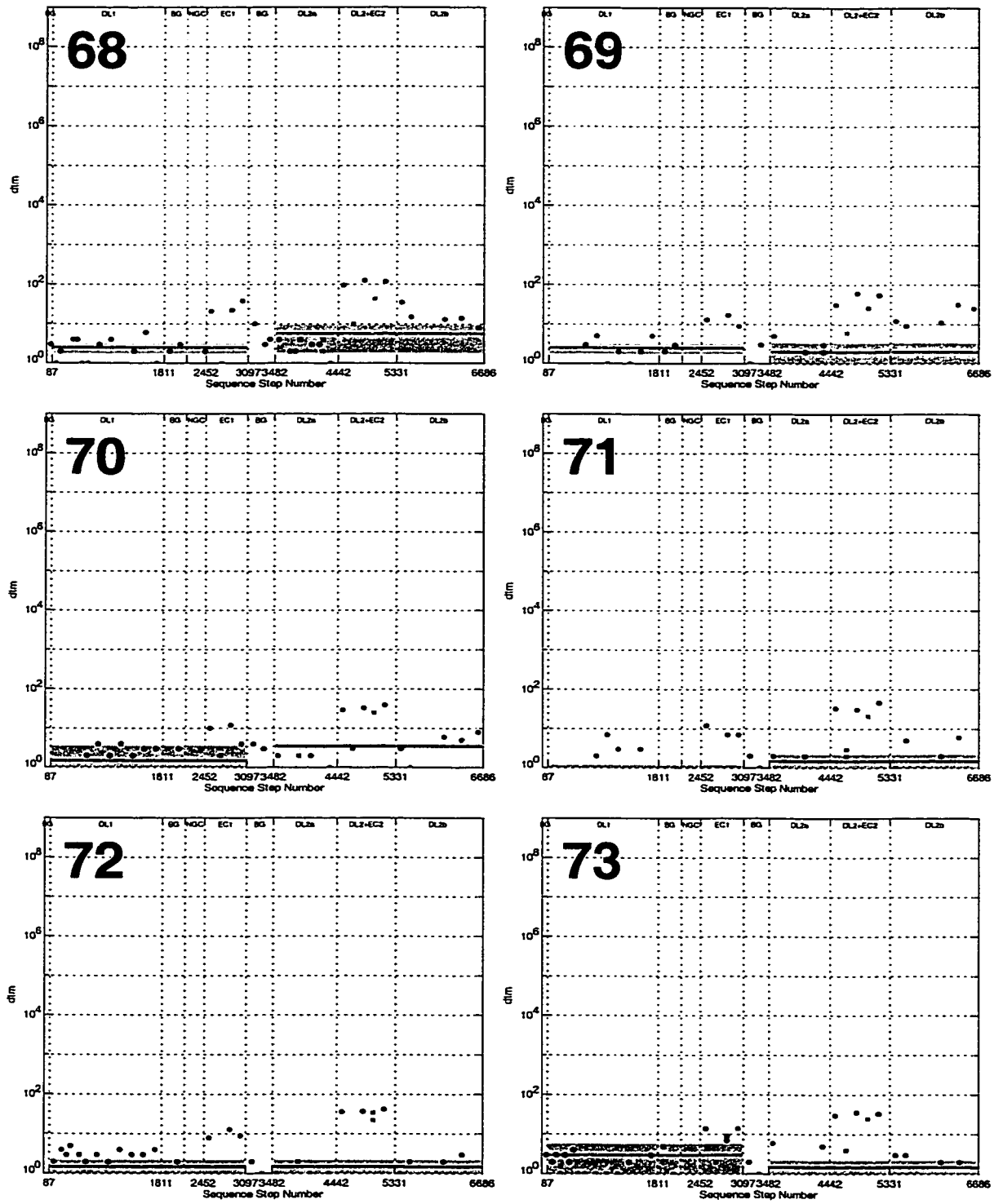

Figure A.12 Deadtime-corrected GPMS counts: masses 68–73.

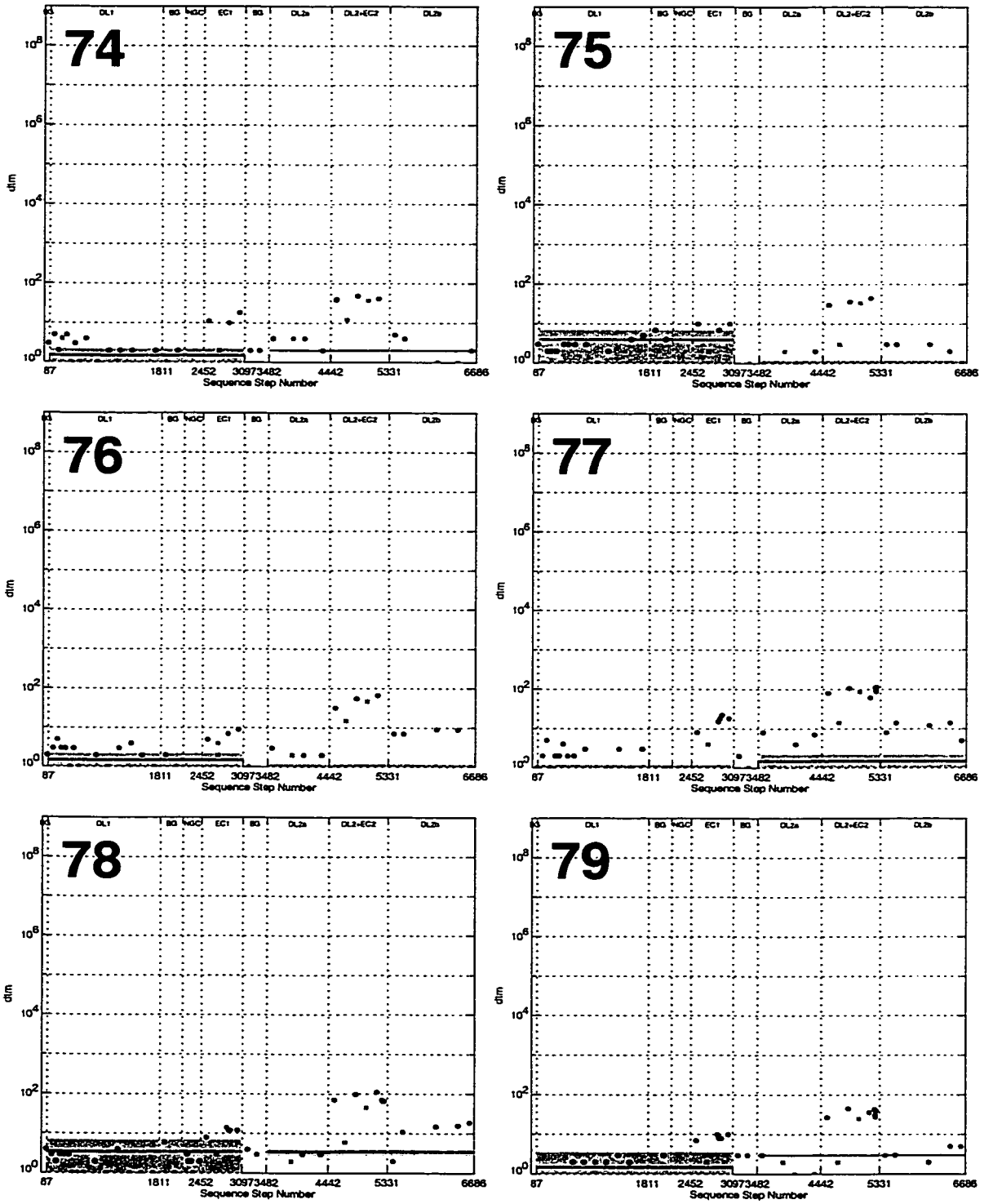

Figure A.13 Deadtime-corrected GPMS counts: masses 74–79.

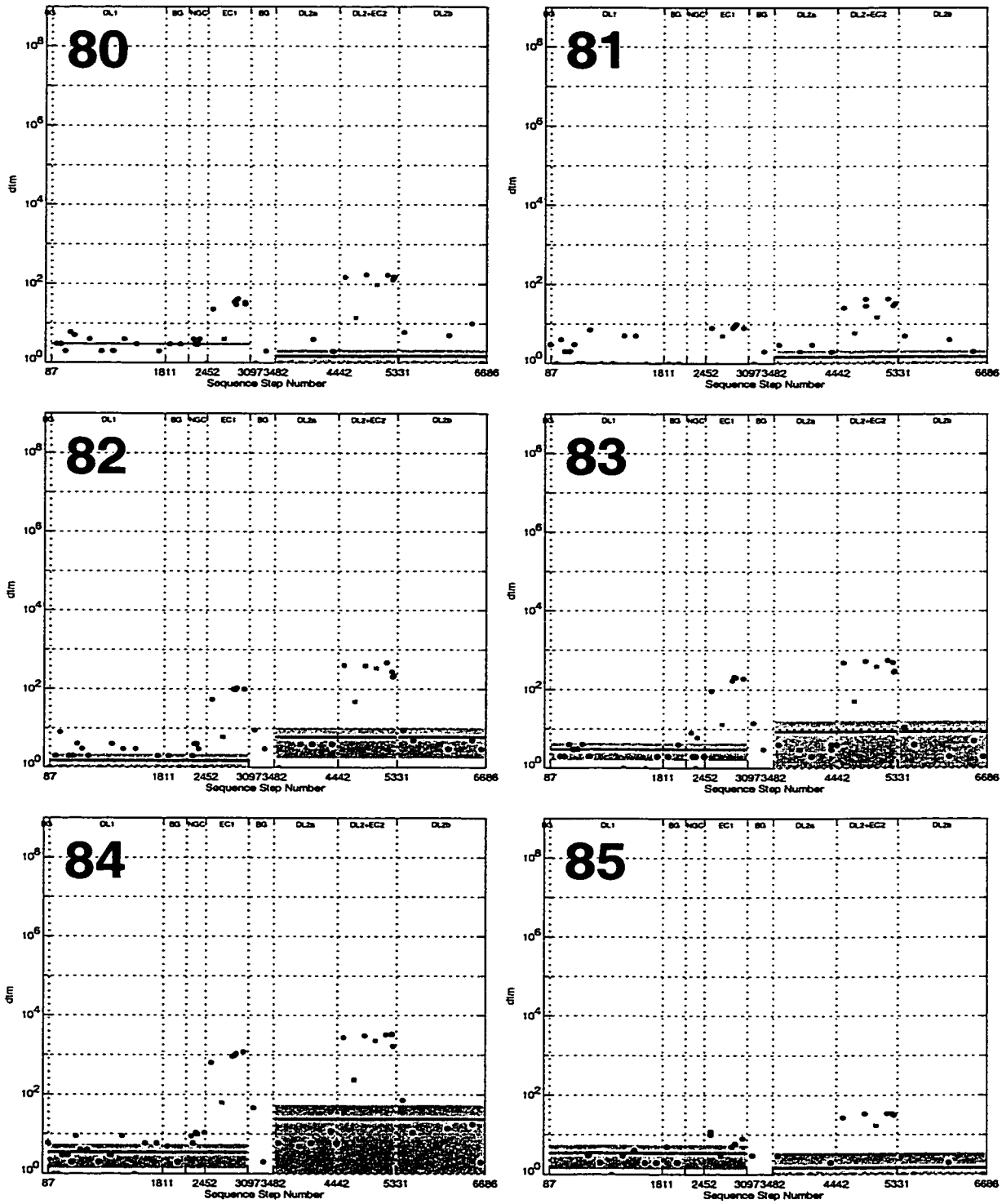

Figure A.14 Deadtime-corrected GPMS counts: masses 80–85.

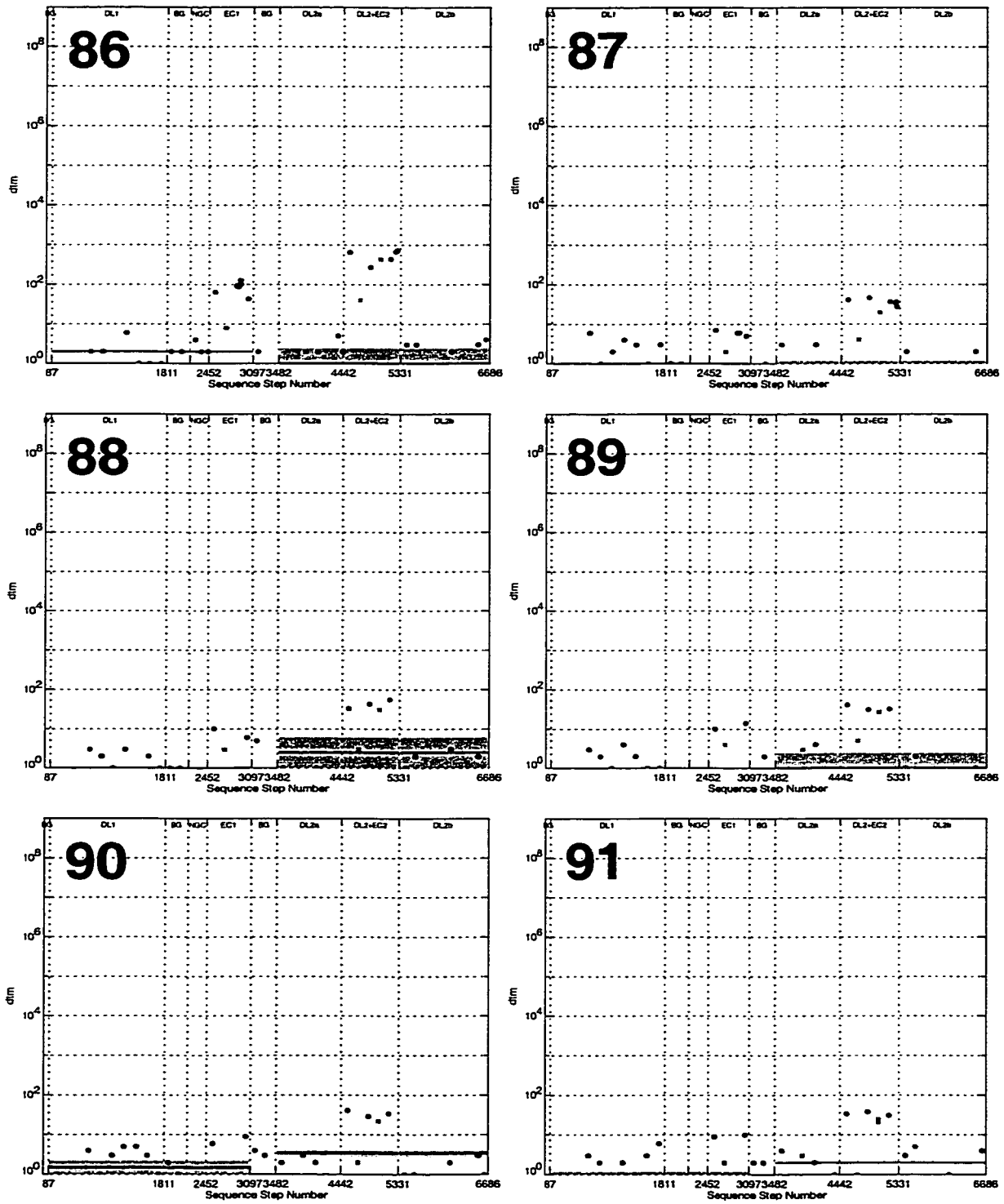

Figure A.15 Deadtime-corrected GPMS counts: masses 86–91.

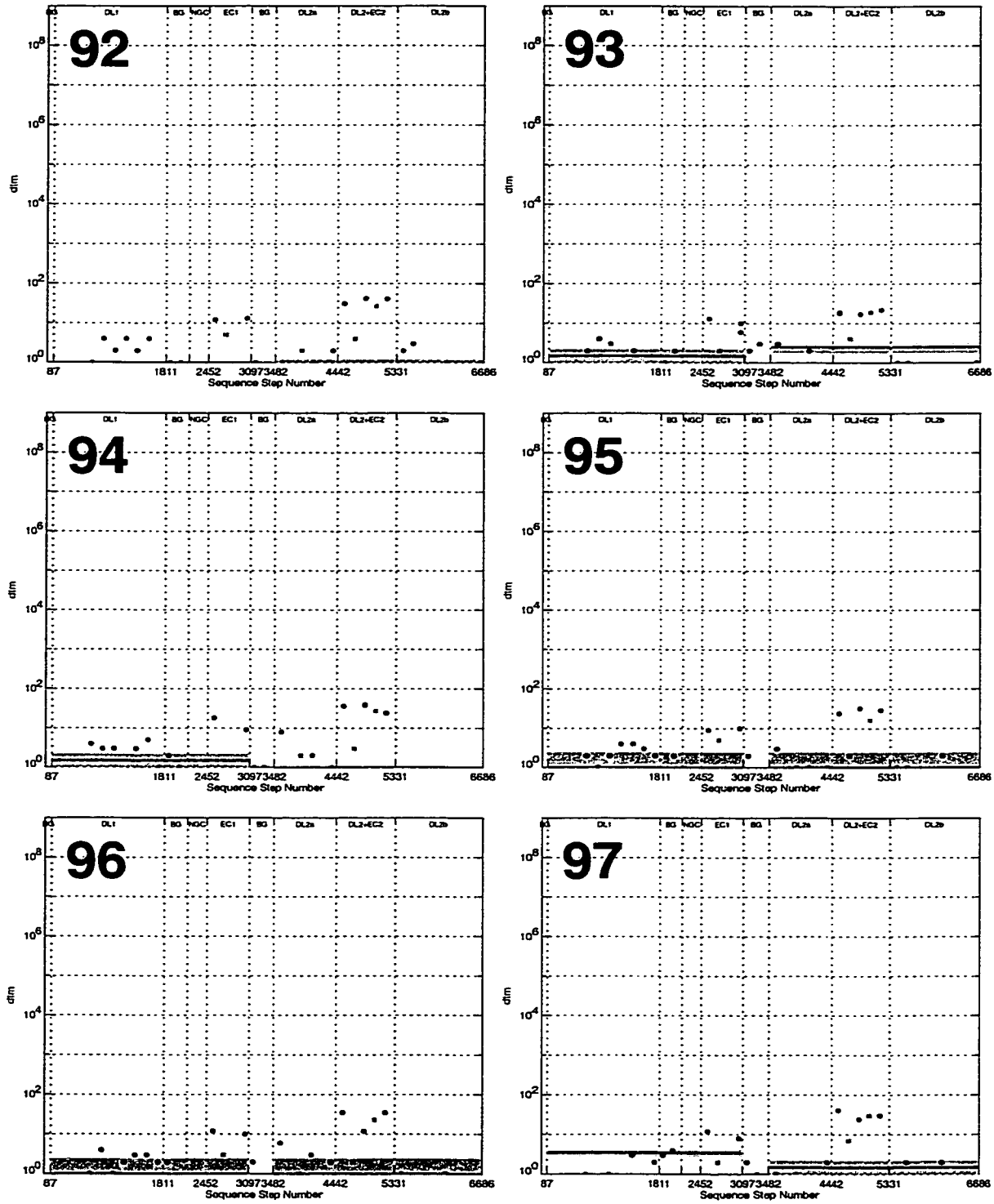

Figure A.16 Deadtime-corrected GPMS counts: masses 92–97.

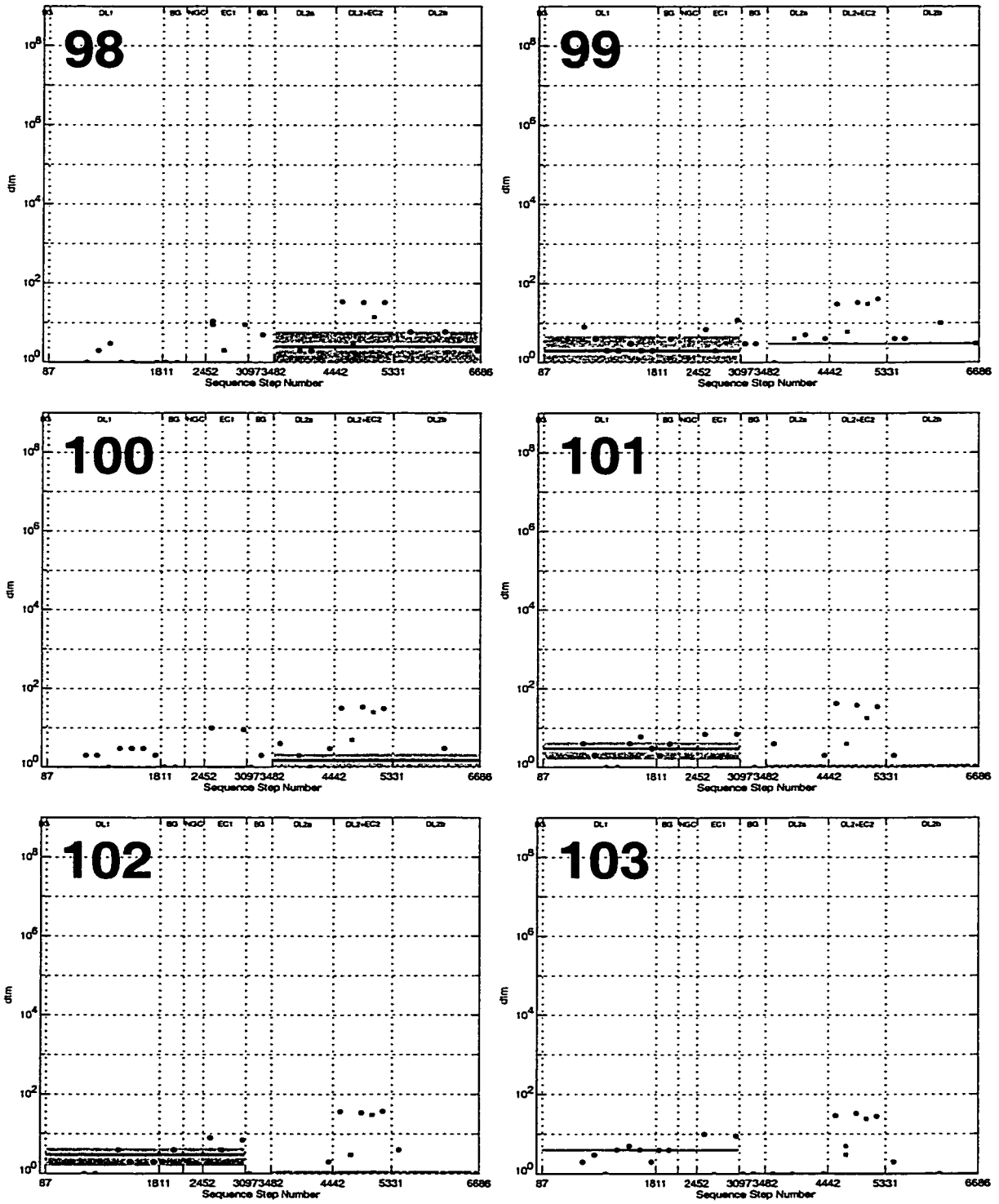

Figure A.17 Deadtime-corrected GPMS counts: masses 98–103.

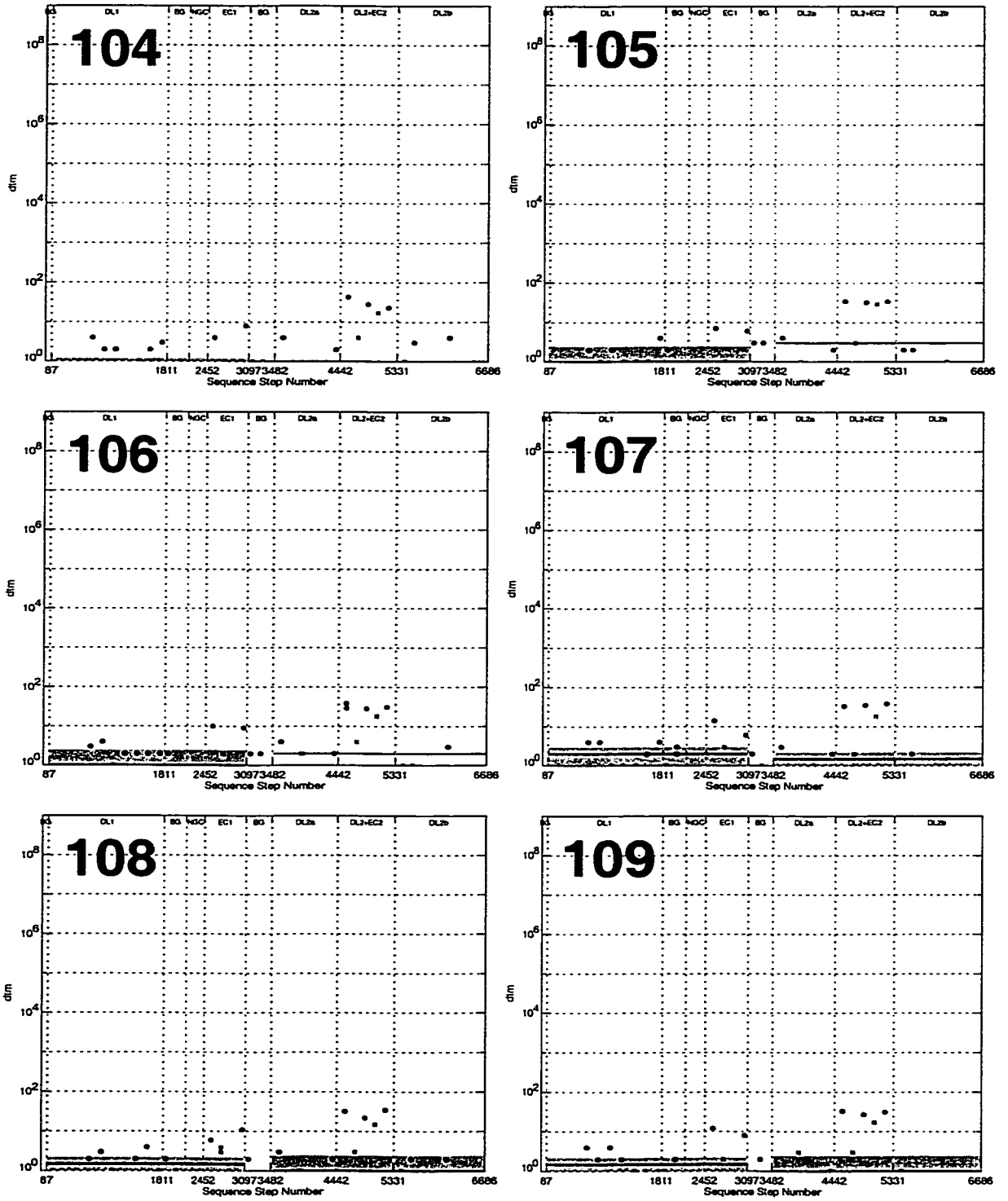

Figure A.18 Deadtime-corrected GPMS counts: masses 104–109.

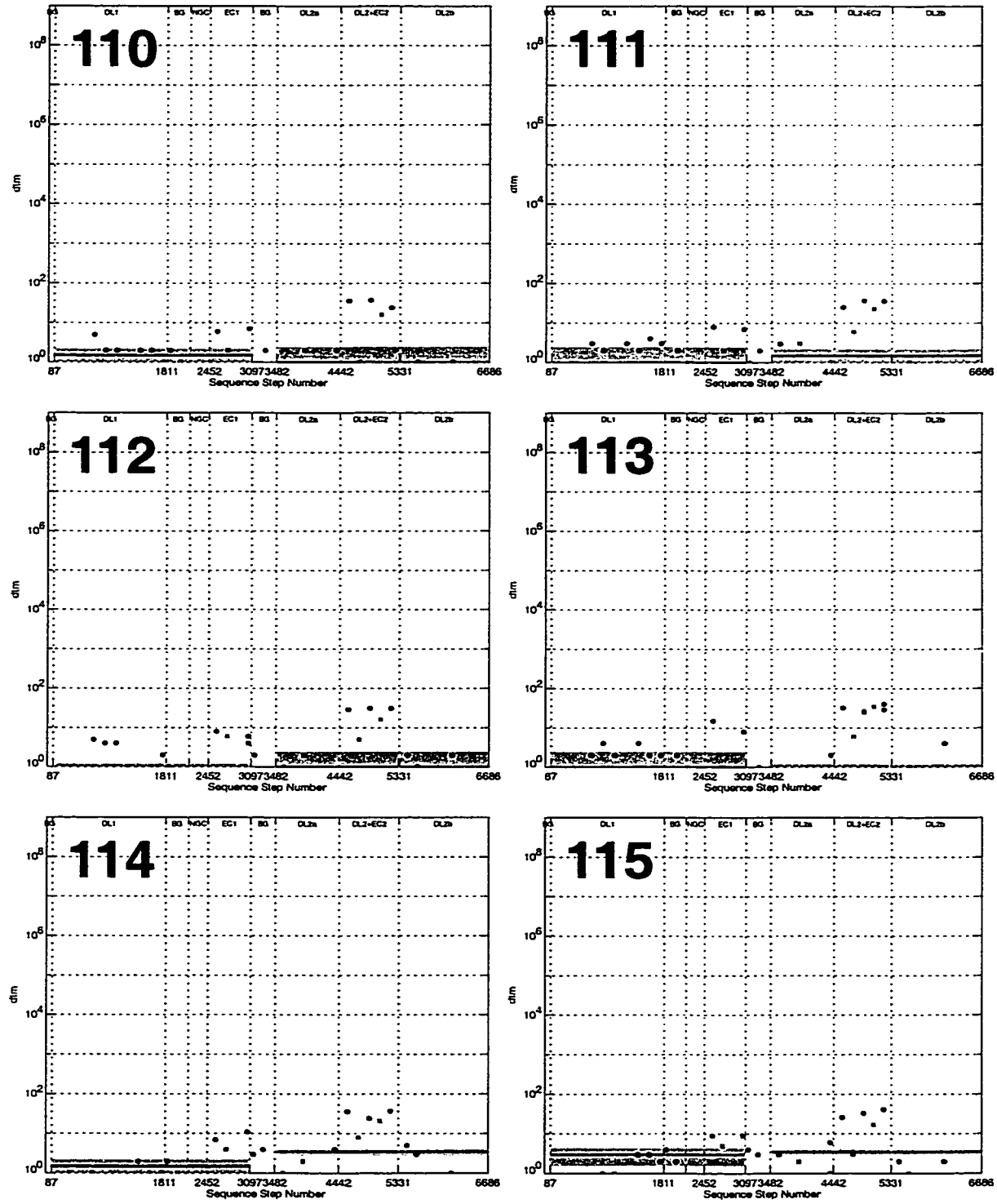

Figure A.19 Deadtime-corrected GPMS counts: masses 110–115.

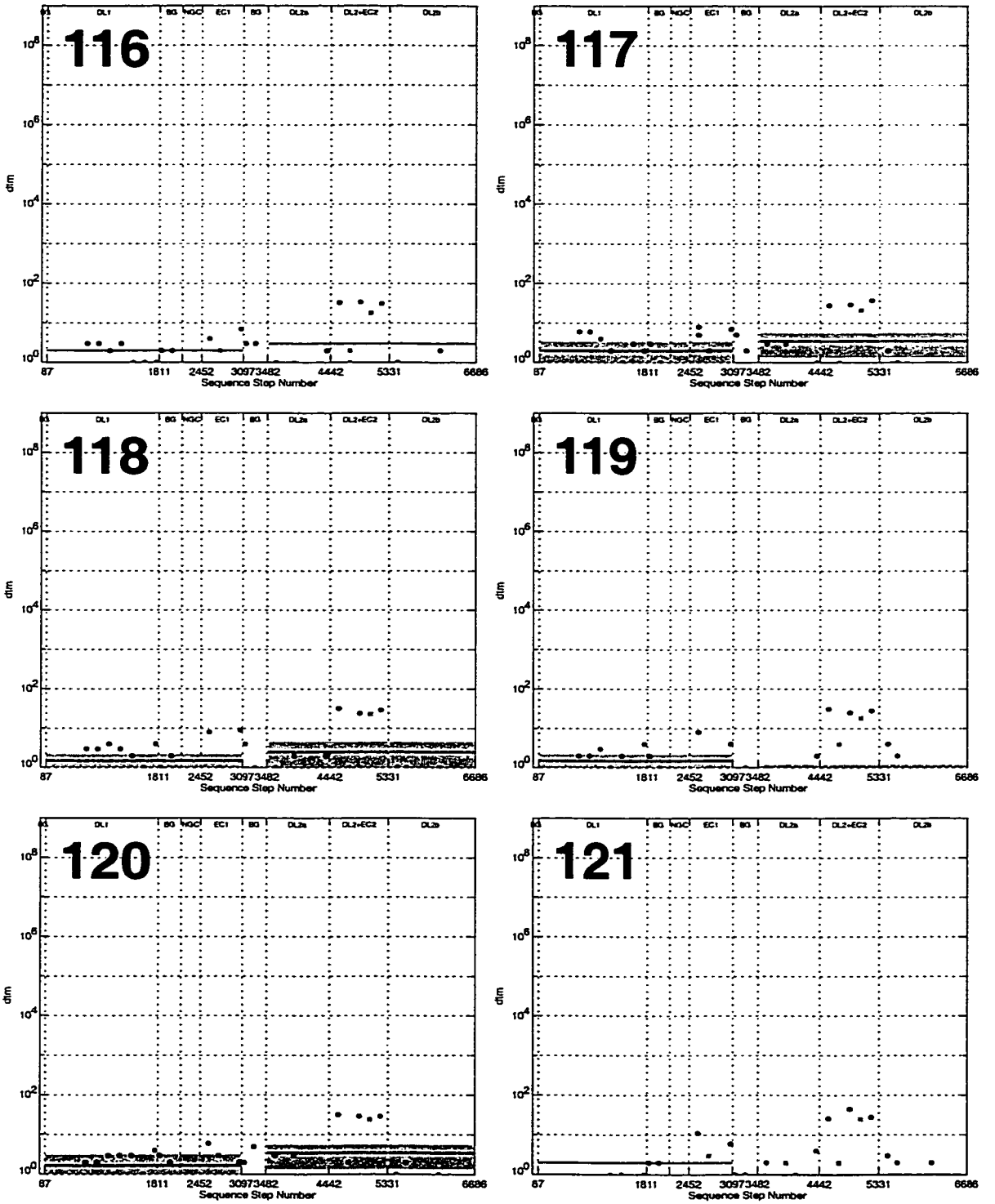

Figure A.20 Deadtime-corrected GPMS counts: masses 116–121.

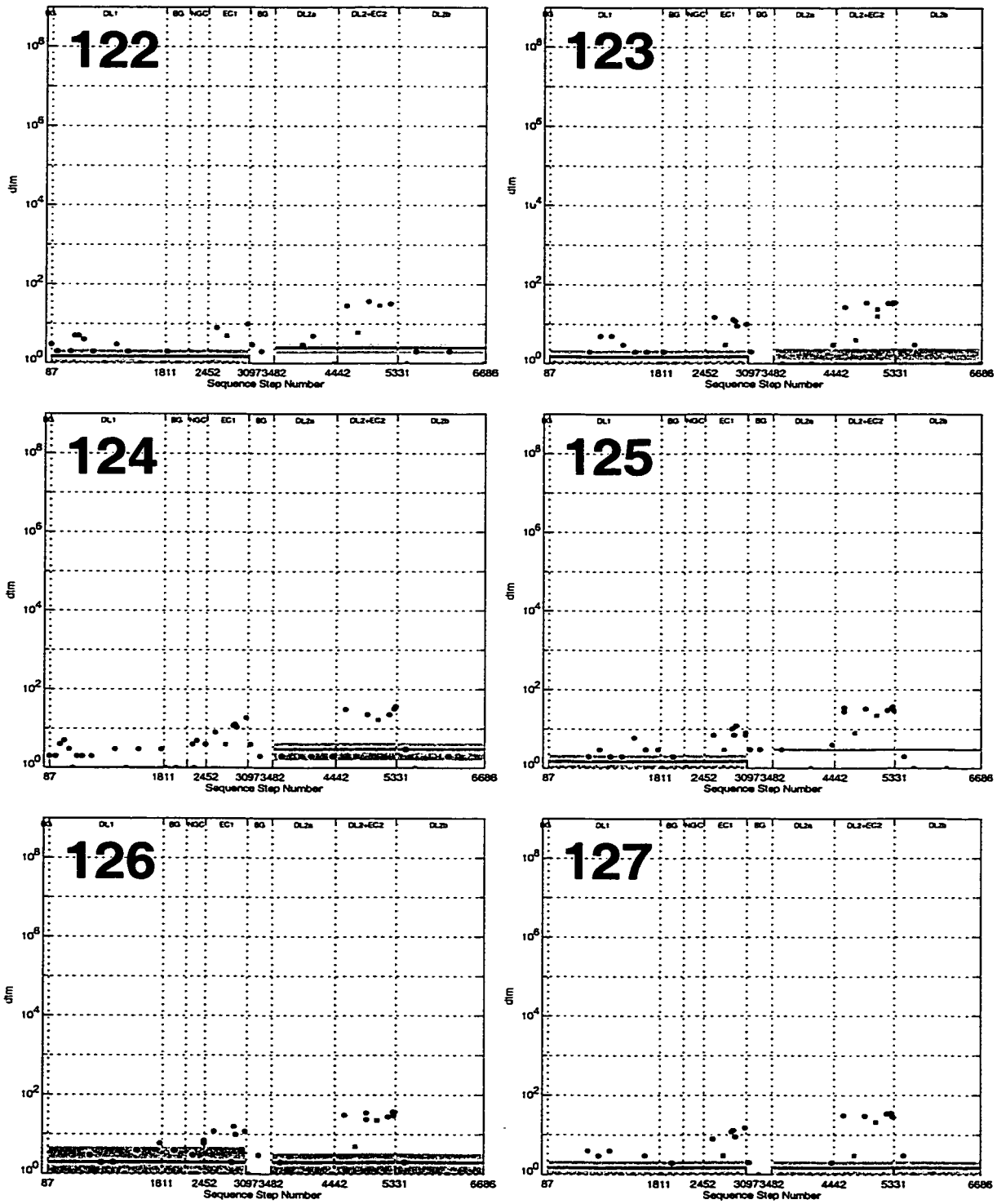

Figure A.21 Deadtime-corrected GPMS counts: masses 122–127.

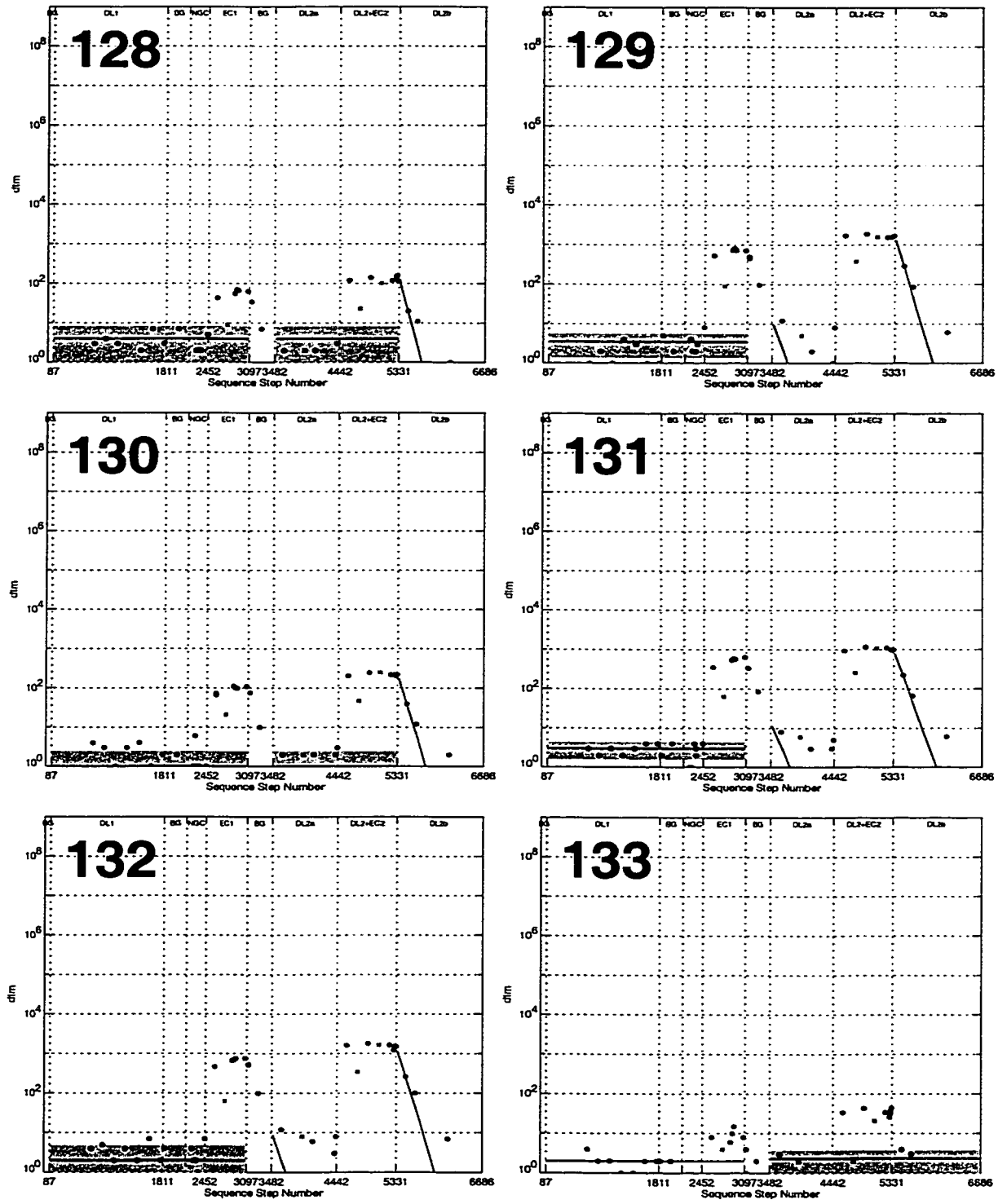

Figure A.22 Deadtime-corrected GPMS counts: masses 128–133.

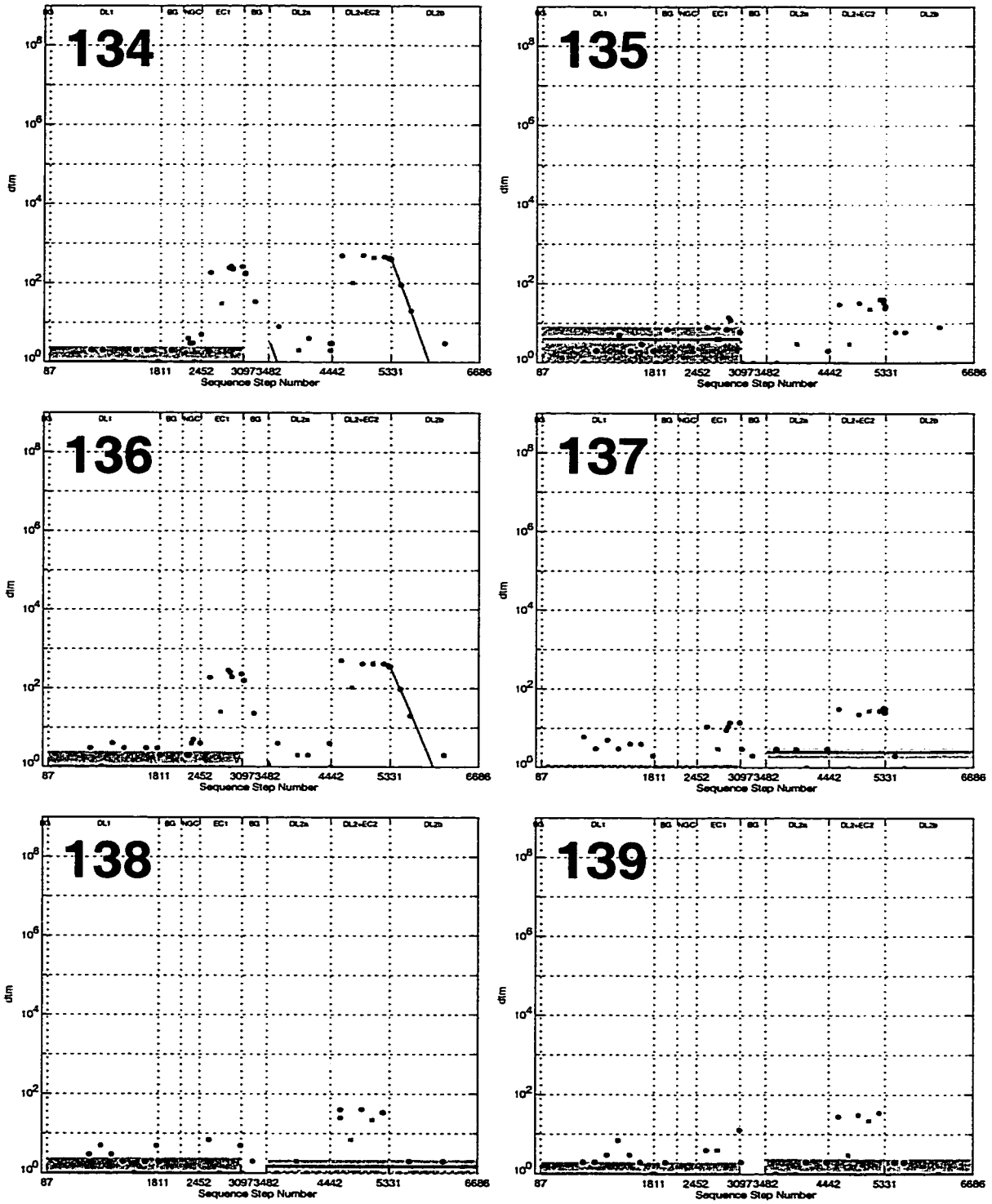

Figure A.23 Deadtime-corrected GPMS counts: masses 134–139.

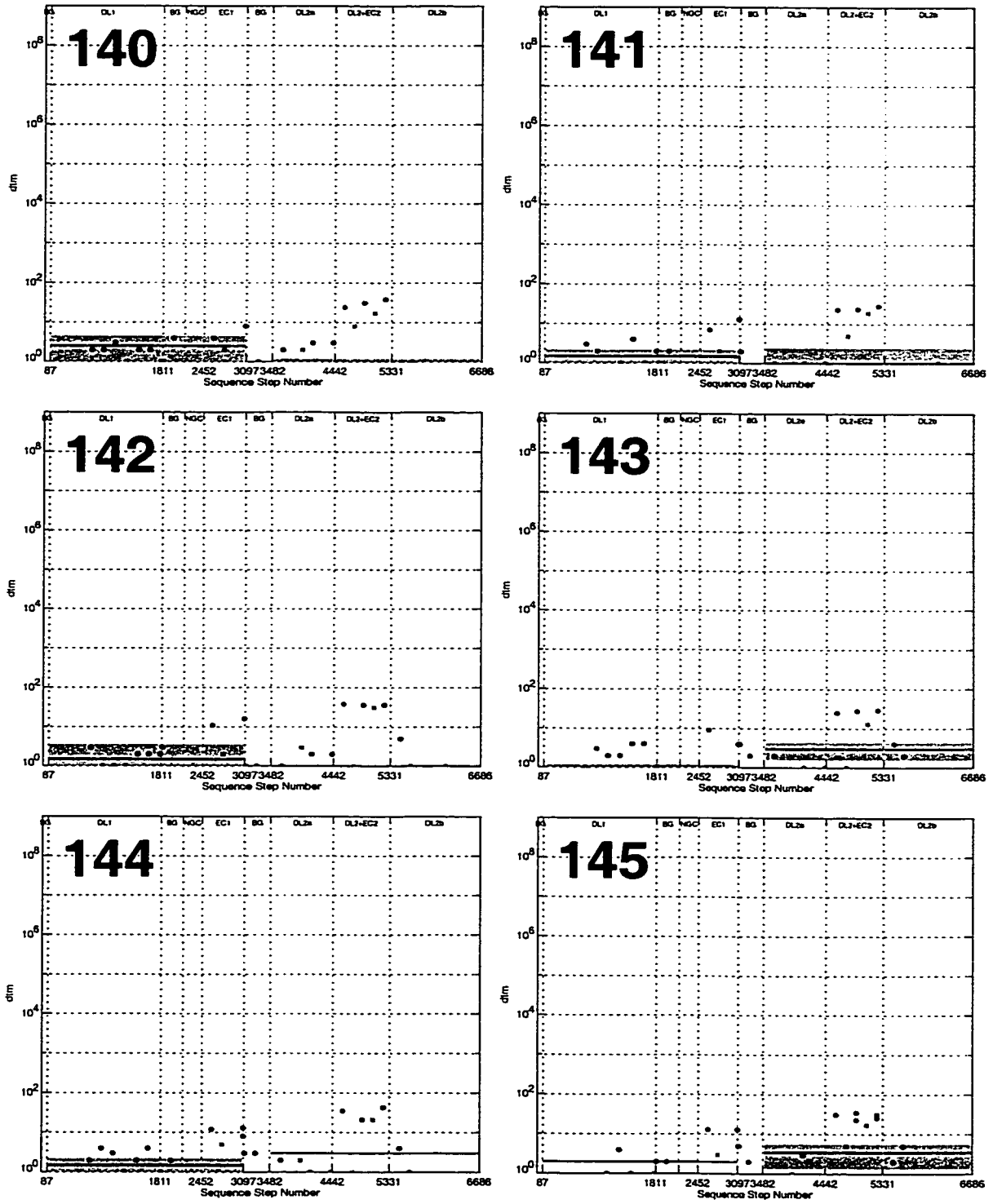

Figure A.24 Deadtime-corrected GPMS counts: masses 140–145.

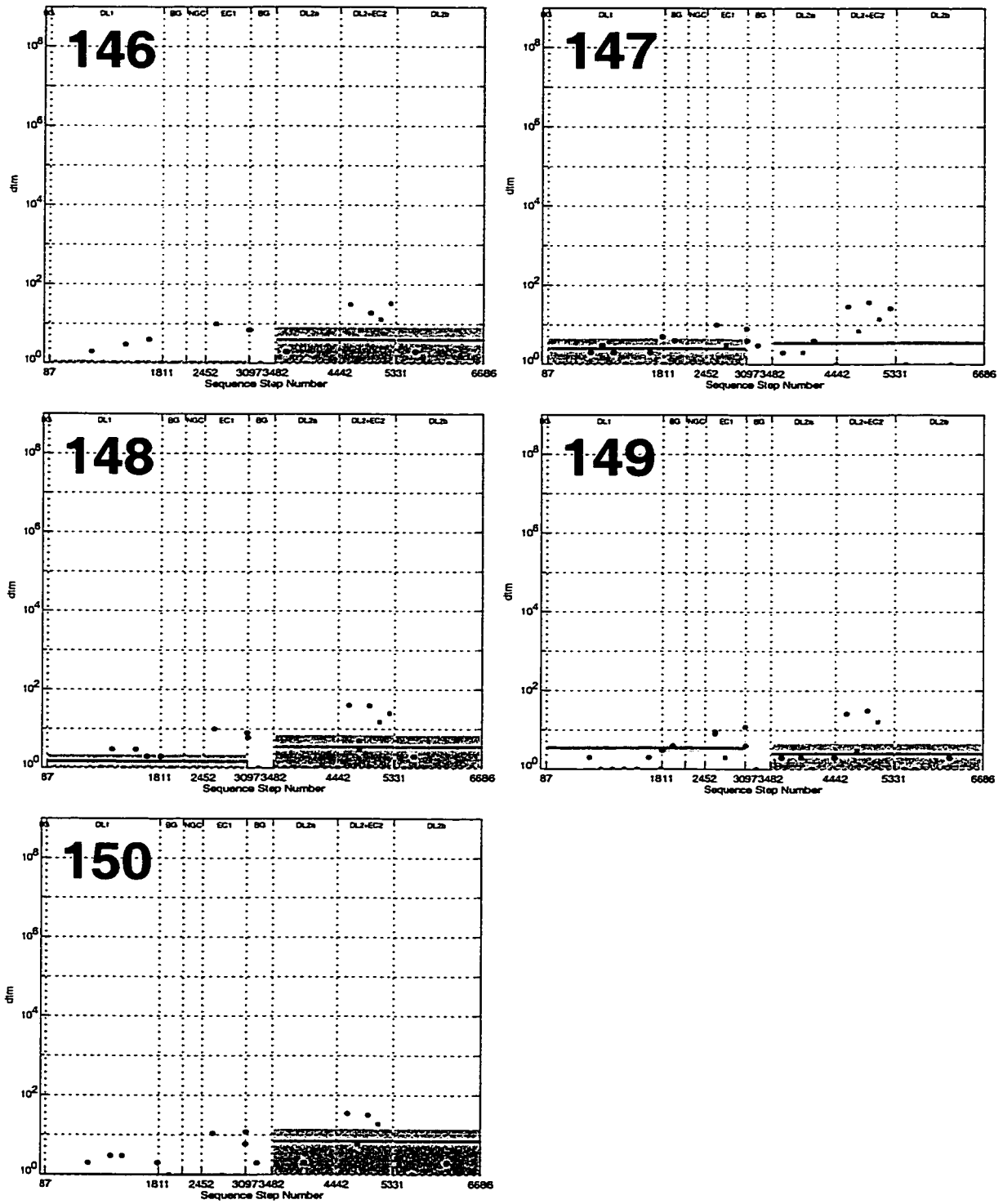

Figure A.25 Deadtime-corrected GPMS counts: masses 146–150.

APPENDIX B

Photochemical model data

The photochemical model presented in this work represents a step forward for the University of Michigan Planetary Science Laboratory photochemical model. Many of the chemical data presented in this appendix are newly included since the Jupiter photochemical model of Edgington et al. (1999) and predecessors. A large number of the new data are adapted from the Titan photochemical model of Wilson and Atreya (2000), as well as from the Jupiter photochemical model of Gladstone et al. (1996).

Table B.1 is a summary of the hydrocarbon chemical reactions included in this model. The first three columns are reaction ID numbers. The R*nnn* series are reaction IDs from Gladstone et al. (1996), the S*nn* series are reaction IDs from Edgington (1997), and the 322-*nnn* series are IDs for reactions that have been added or modified for this model. In the Reactants and Products columns, "M" represents a third molecule (usually hydrogen) in a three-body reaction; the molecule M is chemically unchanged by the reaction. An "hν" in the products column is an emitted photon. p-C_3H_4 indicates propyne, also known as methylacetylene or CH_3C_2H, while a-C_3H_4 is allene, or CH_2CCH_2. For the reaction rates, T is in kelvins and the rates have the units of $cm^3\ s^{-1}$ for 2-body reactions and $cm^6\ s^{-1}$ for 3-body reactions. Three-body reaction rates are calculated from the given parameters and the atmospheric number density n using:

$$\log_{10}k = \log_{10}\left(\frac{k_0 k_\infty n}{k_\infty + k_0 n}\right) + \frac{\log_{10}F_c}{1+\left(\log_{10}\left(\frac{k_0 n}{k_\infty}\right)/F_n\right)^2} . \qquad \text{B.1}$$

For reactions where F_c or F_n are not specified, the unspecified coefficients should be set to 1 in Equation B.1. Some temperature-dependent reaction rates have limiting minimum or maximum rates; these are indicated by k_{min} or k_{max} respectively. PH_3 and NH_3 chemistries are included in the model, but because the reactions are unchanged from Edgington (1997), the NH_3 and PH_3 photochemical complexes are not listed in Table B.1, and the reader is urged to consult Edgington (1997) for those reactions.

Table B.1 Photochemical model data: reaction rates, reactants, and products.

Rxn IDs			Reactants	Products	Reaction Rate	References and comments
R79	S06		$H + H + M$	$H_2 + M$	$2.7\times10^{-31}\ T^{-0.6}$	Baulch *et al.* (1992; H_2 bath gas)
R119	S07	322-072	$CH + H_2 + M$	$CH_3 + M$	$k_0 = 4.7\times10^{-26}\ T^{-1.6}$ $k_\infty = 2.5\times10^{-10}\ T^{-0.08}$	Brownsword *et al.* (1997)
R118	S08	322-073	$CH + H_2$	$^3CH_2 + H$	$3.1\times10^{-10}\ \exp(-1650/T)$	Brownsword *et al.* (1997)
	S09		$CH + H$	$C + H_2$	1.4×10^{-11}	Becker *et al.* (1989)
R120	S10	322-074	$CH + CH_4$	$C_2H_4 + H$	$3.96\times10^{-8}\ T^{-1.04}\ \exp(-36.1/T)$ $k_{max} = 1.7\times10^{-10}$	Canosa *et al.* (1997), upper limit from Berman and Lin (1983)
R121	S11	322-019	$CH + C_2H_2$	$C_3H_2 + H$	$1.59\times10^{-9}\ T^{-0.233}\ \exp(-16/T)$	Canosa *et al.* (1997)
	S12	322-075	$CH + C_2H_4$	$p\text{-}C_3H_4 + H$	$3.87\times10^{-9}\ T^{-0.546}\ \exp(-29.6/T)$	Canosa *et al.* (1997)
R122	S13	322-000		$a\text{-}C_3H_4 + H$	$3.87\times10^{-9}\ T^{-0.546}\ \exp(-29.6/T)$	
		322-076	$CH + C_2H_6$	$C_2H_4 + CH_3$	$1.9\times10^{-8}\ T^{-0.859}\ \exp(-53.2/T)$	Canosa *et al.* (1997)
R123	S14	322-029		$C_3H_6 + H$	$1.9\times10^{-8}\ T^{-0.859}\ \exp(-53.2/T)$	
R125	S15		$^1CH_2 + H_2$	$CH_3 + H$	9.24×10^{-11}	Allen *et al.* (1992), Langford *et al.* (1983), Ashfold *et al.* (1981), Braun *et al.* (1970)
R124	S16			$^3CH_2 + H_2$	1.26×10^{-11}	
R127	S17		$^1CH_2 + CH_4$	$^2CH_3$	6.0×10^{-11}	Bohland *et al.* (1985)
R126	S18			$^3CH_2 + CH_4$	1.2×10^{-11}	
R81	S19		$^3CH_2 + H$	CH_3	$k_0 = 3.1\times10^{-30}\ \exp(457/T)$ $k_\infty = 1.5\times10^{-10}$	Gladstone (1983)
R80	S20			$CH + H_2$	$4.7\times10^{-10}\ \exp(-370/T)$	Zabarnick *et al.* (1986)
R128	S21		$^3CH_2 + {}^3CH_2$	$C_2H_2 + 2H$	3.1×10^{-10}	Darwin (1899)

Table B.1 Photochemical model data: reaction rates, reactants, and products. (Continued)

Rxn IDs			Reactants	Products	Reaction Rate	References and comments
R129	S22		$^3CH_2 + CH_3$	$C_2H_4 + H$	7.0×10^{-11}	Tsang and Hampson (1986)
R132		322-011	$^3CH_2 + C_2H_2$	$C_3H_3 + H$	$1.5\times10^{-11}\exp(-3332/T)$	Bohland *et al.* (1986)
	S24		$^3CH_2 + C_2H_3$	$CH_3 + C_2H_2$	3.0×10^{-11}	Tsang and Hampson (1986)
R133	S25		$^3CH_2 + C_2H_5$	$C_2H_4 + CH_3$	3.0×10^{-11}	Tsang and Hampson (1986)
R82	S26		$CH_3 + H + M$	$CH_4 + M$	$F_c = 0.902 - 1.03\times10^{-3}\,T$ $k_0 = 4.0\times10^{-29}$ $k_\infty = 4.7\times10^{-10}$	Brouard *et al.* (1989)
R135	S27		$CH_3 + CH_3 + M$	$C_2H_6 + M$	$F_c = 0.381\exp(-T/73.2) + 0.619\exp(-T/1180)$ $F_n = 0.75 - 1.27\log_{10}(F_c)$ $k_0 = 3.5\times10^{-7}\,T^{-7.03}\exp(-1390/T)$ $k_\infty = 6.0\times10^{-11}$	Baulch *et al.* (1992)
R138	S28	322-012	$CH_3 + C_2H_3 + M$	$C_3H_6 + M$	$k_0 = 1.3\times10^{-22}$ $k_\infty = 1.2\times10^{-10}$	Laufer *et al.* (1983), Fahr *et al.* (1991)
R136	S29		$CH_3 + C_2H_3$	$CH_4 + C_2H_2$	3.4×10^{-11}	Fahr *et al.* (1991), Tsang and Hampson (1986)
R137	S30	322-013		$C_3H_5 + H$	2.4×10^{-13}	
R140	S31	322-020	$CH_3 + C_2H_5 + M$	$C_3H_8 + M$	$k_0 = 8.0\times10^{19}\,T^{-16.1}\exp(-1897/T)$ $k_\infty = 8.12\times10^{-10}\,T^{-0.5}$	Laufer *et al.* (1983); Tsang *et al.* (1986)
R139	S32	322-077	$CH_3 + C_2H_5$	$CH_4 + C_2H_4$	$3.25\times10^{-11}\,T^{-0.5}$	Tsang *et al.* (1986)
R152	S33		$C_2 + H_2$	$C_2H + H$	$1.77\times10^{-10}\exp(-1469/T)$	Pitts *et al.* (1982)
R153	S34		$C_2 + CH_4$	$C_2H + CH_3$	$5.05\times10^{-11}\exp(-297/T)$	Pitts *et al.* (1982)
R154	S35	322-078	$C_2H + H_2$	$C_2H_2 + H$	$9.2\times10^{-18}\,T^{2.17}\exp(-478/T)$	Opansky *et al.* (1996)
	S36		$C_2H + H + M$	$C_2H_2 + M$	$k_0 = 1.26\times10^{-18}\,T^{-3.1}\exp(-721/T)$ $k_\infty = 3.0\times10^{-10}$	Tsang and Hampson (1986)
R155	S37	322-079	$C_2H + CH_4$	$C_2H_2 + CH_3$	$1.2\times10^{-11}\exp(-491/T)$	Opansky and Leone (1996)

Table B.1 Photochemical model data: reaction rates, reactants, and products. (Continued)

Rxn IDs			Reactants	Products	Reaction Rate	References and comments
R156	S38	322-080	$C_2H + C_2H_2$	$C_4H_2 + H$	$9.53\times10^{-11}\ \exp(30.8/T)$	Chastaing *et al.* (1998)
R157	S39	322-081	$C_2H + C_2H_4$	$C_4H_4 + H$	$4.6\times10^{-11}\ \exp(24.6/T)$	Opansky *et al.* (1996)
		322-082		$C_2H_2 + C_2H_3$	$4.6\times10^{-11}\ \exp(24.6/T)$	Chastaing *et al.* (1998)
R158	S40	322-083	$C_2H + C_2H_6$	$C_2H_2 + C_2H_5$	$3.5\times10^{-11}\ \exp(2.9/T)$	Opansky *et al.* (1996)
R160	S41	322-058	$C_2H + C_4H_2$	$C_6H_2 + H$	$k_{(322\text{-}080)}$	Rate equivalence estimate from Edgington (1997), Kiefer *et al.* (1990), Tanzawa and Gardiner (1980), Frank and Just (1990)
		322-084	$C_2H + C_3H_8$	$C_2H_2 + C_3H_7$	$7.8\times10^{-11}\ \exp(3/T)$	Hoobler *et al.* (1997)
R164	S42		$C_2H_3 + H_2$	$C_2H_4 + H$	$5.0\times10^{-20}\ T^{2.63}\ \exp(-4298/T)$ $k_{min} = 1.0\times10^{-23}$	Fahr *et al.* (1995), Tsang and Hampson (1986)
R85	S43	322-085	$C_2H_3 + H$	$C_2H_2 + H_2$	7.6×10^{-11}	Monks *et al.* (1995)
		322-086	$C_2H_3 + H + M$	$C_2H_4 + M$	$k_0 = 5.76\times10^{-24}\ T^{-1.3}$ $k_\infty = 8.0\times10^{-11}$	Monks *et al.* (1995)
	S44		$C_2H_3 + CH_4$	$CH_3 + C_2H_4$	$2.4\times10^{-24}\ T^{4.02}\ \exp(-2754/T)$	Tsang and Hampson (1986)
R167	S45	322-051	$C_2H_3 + C_2H_3 + M$	$1,3\text{-}C_4H_6 + M$	$k_0 = 8.76\times10^{-6}\ T^{-7.03}\ \exp(-1390/T)$ $k_\infty = 8.2\times10^{-11}$	Laufer *et al.* (1983)
R166	S46		$C_2H_3 + C_2H_3$	$C_2H_4 + C_2H_2$	2.4×10^{-11}	Fahr *et al.* (1991)
R171	S47	322-049	$C_2H_3 + C_2H_5 + M$	$1\text{-}C_4H_8 + M$	$k_0 = 1.9\times10^{-27}$ $k_\infty = 2.5\times10^{-11}$	Fahr *et al.* (1991), Tsang and Hampson (1986)
R168	S48		$C_2H_3 + C_2H_5$	$C_2H_4 + C_2H_4$	2.81×10^{-12}	Estimated rates from Gladstone *et al.* (1996), Tsang and Hampson (1986)
R169	S49			$C_2H_2 + C_2H_6$	2.81×10^{-12}	
R170	S50	322-016		$CH_3 + C_3H_5$	$k_{\infty(S47)} - k_{(S47)}$	

Table B.1 Photochemical model data: reaction rates, reactants, and products. (Continued)

Rxn IDs			Reactants	Products	Reaction Rate	References and comments
R89	S51		$C_2H_5 + H + M$	$C_2H_6 + M$	$k_0 = 5.5\times10^{-23}\ T^{-2}\ \exp(-1040/T)$ $k_\infty = 1.5\times10^{-13}\ \exp(-440/T)$	Gladstone (1983)
R87	S52		$C_2H_5 + H$	$CH_3 + CH_3$	$7.95\times10^{-11}\ \exp(-127/T)$	Pratt and Wood (1984)
R88	S53			$C_2H_4 + H_2$	3.0×10^{-12}	Tsang and Hampson (1986)
R174	S54	322-050	$C_2H_5 + C_2H_5 + M$	$C_4H_{10} + M$	$k_0 = 6.59\times10^{-6}\ T^{-6.39}\ \exp(-301/T)$ $k_\infty = 1.9\times10^{-11}$	Laufer *et al.* (1983), Baulch *et al.* (1992)
R173	S55	322-050.1	$C_2H_5 + C_2H_5$	$C_2H_6 + C_2H_4$	2.4×10^{-12}	Baulch *et al.* (1992)
R95	S56	322-009	$p\text{-}C_3H_4 + H + M$	$C_3H_5 + M$	$k_0 = 8.0\times10^{-24}\ T^{-2}\ \exp(-1225/T)$ $k_\infty = 6.0\times10^{-11}\ \exp(-1233.0/T)$	Whytock *et al.* (1976)
R94	S57	322-087		$CH_3 + C_2H_2 + M$	$k_0 = 8.0\times10^{-24}\ T^{-2}\ \exp(-1225/T)$ $k_\infty = 9.62\times10^{-11}\ \exp(-1560.0/T)$	Wagner and Zellnar (1972)
R179	S58	322-104	$C_4H + H_2$	$C_4H_2 + H$	$k_{(322\text{-}078)}$	Following Edgington (1997), Kiefer *et al.* (1990), Tanzawa and Gardiner (1980), and Frank and Just (1990), C_4H reaction rates are assumed to be the same as for analogous C_2H reactions
	S59	322-105	$C_4H + H + M$	$C_4H_2 + M$	$k_{(S36)}$	
R180	S60	322-106	$C_4H + CH_4$	$C_4H_2 + CH_3$	$k_{(322\text{-}079)}$	
R181	S61	322-056	$C_4H + C_2H_2$	$C_6H_2 + H$	$k_{(322\text{-}080)}$	
R182	S62	322-107	$C_4H + C_2H_6$	$C_4H_2 + C_2H_5$	$k_{(322\text{-}083)}$	
R183	S65	322-057	$C_4H + C_4H_2$	$C_8H_2 + H$	$2.5\%\ k_{(322\text{-}080)}$	
R111	S63	322-901	$C_4H_3 + H$	$C_4H_2 + H_2$	1.2×10^{-11}	Yung *et al.* (1984)
R110	S64	322-902		$C_2H_2 + C_2H_2$	3.3×10^{-12}	Yung *et al.* (1984)
	S66	322-071	$C_4H_2^* + C_4H_2$	$C_8H_2 + H_2$	$4.25\times10^{-12}\ T^{0.5}$	Estimated maximum collision rate, Toublanc *et al.* (1995)
		322-088		$C_6H_2 + C_2H_2$	$4.25\times10^{-12}\ T^{0.5}$	

Table B.1 Photochemical model data: reaction rates, reactants, and products. (Continued)

Rxn IDs		Reactants	Products	Reaction Rate	References and comments
	322-089	$C_4H_2^* + C_3H_6$	products + C_2H_3	4.2% $k_{(322\text{-}071)}$	Frost *et al.* (1996)
	322-090		products + C_2H_2	19.6% $k_{(322\text{-}071)}$	
	322-091		products + CH_3 + H or CH_4	31.5% $k_{(322\text{-}071)}$	
	322-092		products + 2H or H_2	14.7% $k_{(322\text{-}071)}$	
	322-093	$C_4H_2^* + CH_3C_2H$	products + C_2H_3	6.2% $k_{(322\text{-}071)}$	Frost *et al.* (1996)
	322-094		products + C_2H_2	22.3% $k_{(322\text{-}071)}$	
	322-095		products + CH_3 + H or CH_4	17.4% $k_{(322\text{-}071)}$	
	322-096		products + 2H or H_2	16.1% $k_{(322\text{-}071)}$	
R84	S67	$H + C_2H_2 + M$	$C_2H_3 + M$	$F_c = 0.44$ $F_n = 0.75 - 1.27 \log_{10}(F_c)$ $k_0 = 3.3\times10^{-30} \exp(-740/T)$ $k_\infty = 1.4\times10^{-11} \exp(-1300/T)$	Baulch *et al.* (1992), He bath gas
R86	S68	$H + C_2H_4 + M$	$C_2H_5 + M$	$k_0 = 2.15\times10^{-29} \exp(-349/T)$ $k_\infty = 4.95\times10^{-11} \exp(-1051/T)$	Following Edgington (1997), use $\mu + 1\sigma$ value from Lightfoot and Pilling (1987)
R109	S69	$H + C_4H_2 + M$	$C_4H_3 + M$	$k_0 = 1.0\times10^{-28}$ $k_\infty = 1.39\times10^{-10} \exp(-1184/T)$	Nava *et al.* (1986; k_0 is estimate and lower limit)
R97	322-001	a-C_3H_4 + H + M	C_3H_5	$k_0 = 8\times10^{-24}\, T^{-2} \exp(-1225/T)$ $k_\infty = 6.6\times10^{-12} \exp(-1359/T)$	Yung *et al.* (1984), Wagner and zellnar (1972b)
R96	322-002		$CH_3 + C_2H_2$	$k_0 = 8\times10^{-24}\, T^{-2} \exp(-1225/T)$ $k_\infty = 1.4\times10^{-11} \exp(-1006/T)$	Yung *et al.* (1984), Wagner and zellnar (1972b)
R98	322-003	a-C_3H_4 + H	p-C_3H_4 + H	$1\times10^{-11} \exp(-1000/T)$	Yung *et al.* (1984)

Table B.1 Photochemical model data: reaction rates, reactants, and products. (Continued)

Rxn IDs		Reactants	Products	Reaction Rate	References and comments
S—	322-059	$C_4H_2^* + C_2H_2$	$C_6H_2 + 2H$ or H_2	30% $k_{(322\text{-}071)}$	Estimate from Edgington (1997)
SJ8		$C_4H_2^*$	$C_4H_2 + h\nu$	1000	Glicker and Okabe (1987)
R92	322-004	$C_3H_3 + H + M$	p-C_3H_4 + M	$k_0 = 1.7\times10^{-26}$ $k_\infty = 2.5\times10^{-10}$	k_0 from Laufer *et al.* (1983), k_∞ from Atkinson and Hudgins (1999)
R93	322-005		a-C_3H_4 + M	$k_0 = 1.7\times10^{-26}$ $k_\infty = 2.5\times10^{-10}$	
R99	322-006	$C_3H_5 + H$	p-$C_3H_4 + H_2$	1.4×10^{-11}	Hanning-Lee and Pilling (1992)
R100	322-007		a-$C_3H_4 + H_2$	1.4×10^{-11}	
	322-022	$C_3H_5 + H + M$	C_3H_6 + M	$k_0 = 1.0\times10^{-24}$ $k_\infty = 2.52\times10^{-10}$ $F_c = 0.6$	Hanning-Lee and Pilling (1992)
R176	322-017	$C_3H_3 + C_2H_2$	products	2×10^{-13}	Homann and Schweinfurth (1981)
R177	322-018	$C_3H_5 + H_2$	$C_3H_6 + H$	$5.25\times10^{-11}\exp(-9913/T)$	Allara and Shaw (1980)
R91	322-021	$C_3H_2 + H + M$	C_3H_3 + M	$k_0 = 1.7\times10^{-26}$ $k_\infty = 1.0\times10^{-11}$	Laufer *et al.* (1983); Homann and Schweinfurth (1981)
R102	322-022	$C_3H_5 + H + M$	C_3H_6 + M	$k_{0(S56)}$ $k_\infty = 1.66\times10^{-10}$	Estimate from Gladstone *et al.* (1996), Allara and Shaw (1980)
R103	322-023	$C_3H_6 + H$	$C_3H_5 + H_2$	$1.66\times10^{-10}\exp(-1761/T)$	Allara and Shaw (1980)
R104	322-024	$C_3H_6 + H + M$	C_3H_7 + M	$k_0 = 1.5\times10^{-29}$ $k_\infty = 3.7\times10^{-11}\exp(-1040/T)$	Laufer et al (1983)

Table B.1 Photochemical model data: reaction rates, reactants, and products. (Continued)

Rxn IDs		Reactants	Products	Reaction Rate	References and comments
R105	322-025	$C_3H_7 + H$	$C_3H_6 + H_2$	5×10^{-11}	Estimate from Gladstone *et al.* (1996), Allara and Shaw (1980)
R106	322-026		$C_2H_5 + CH_3$	$6\times10^{-11} \exp(-1.32 + 1.533\times10^{-3}\,T - 4.29\times10^{-4}\,T^2)$	Tsang (1988)
R107	322-027	$C_3H_7 + H + M$	$C_3H_8 + M$	$k_0 = k_{(322\text{-}020)}$ $k_\infty = 1.66\times10^{-10}$	Estimate from Gladstone *et al.* (1996), Allara and Shaw (1980)
R108	322-028	$C_3H_8 + H$	$C_3H_7 + H_2$	$2.16\times10^{-18}\,T^{2.4} \exp(2250/T)$	Tsang (1988)
R143	322-014	$C_3H_5 + CH_3$	$CH_4 + p\text{-}C_3H_4$	$k_{(R136/S29)} = 3.4\times10^{-11}$	Estimate from Gladstone *et al.* (1996)
R144	322-015		$CH_4 + a\text{-}C_3H_4$	$k_{(R136/S29)} = 3.4\times10^{-11}$	
R145	322-030	$C_3H_5 + CH_3 + M$	C_4H_8	$k_0\ (T>200) = 5.8\times10^{-30} \exp(355/T)$ $k_0\ (T<200) = 3.8\times10^{-29} \exp(-20/T)$ $k_\infty = 3.3\times10^{-11}$	Estimate from Gladstone *et al.* (1996), Allara and Shaw (1980)
R146	322-031	$C_3H_6 + CH_3$	C_4H_9	$10 \times k_{0(R86)}$ $k_\infty = 5.3\times10^{-13} \exp(-3724/T)$	Estimate from Gladstone *et al.* (1996), Allara and Shaw (1980)
	322-097	$C_3H_6 + C_2H$	products	$1.47\times10^{-10} \exp(65.3/T)$	Chastaing *et al.* (1998)
	322-098	$C_3H_6 + {}^1CH_2$	$C_3H_5 + CH_3$	8.7×10^{-11}	Tsang (1991)
	322-099		C_4H_8	8.1×10^{-11}	
	322-100	$C_3H_6 + {}^3CH_2$	$C_3H_5 + CH_3$	$1.2\times10^{-12} \exp(-3116/T)$	Tsang (1991)
	322-101		C_4H_8	$2.7\times10^{-12} \exp(-2660/T)$	
	322-102	$C_4H_{10} + H$	H_2 + products	$5.14\times10^{-10} \exp(-4318/T)$	Warnatz (1984)
	322-103	$C_4H_{10} + CH$	products	$4.4\times10^{-10} \exp(28/T)$	Baulch *et al.* (1992)
R149	322-034	$C_3H_8 + CH_3$	$CH_4 + C_3H_7$	$1.3\times10^{-24}\,T^4 \exp(-4175/T)$	Hautman *et al.* (1981)
R159	322-035	$C_3H_8 + C_2H$	$C_3H_7 + C_2H_2$	1.4×10^{-11}	Okabe (1983a, 1983b)

Table B.1 Photochemical model data: reaction rates, reactants, and products. (Continued)

Rxn IDs		Reactants	Products	Reaction Rate	References and comments
R175	322-036	$C_3H_2 + C_2H_2$	products	5×10^{-13}	Homann and Schweinfurth (1981)
R178	322-037	$C_3H_7 + H_2$	$C_3H_8 + H$	$3\times10^{-21}\ T^{2.84}\ \exp(-4600/T)$	Tsang (1988)
R112	322-038	$C_4H_5 + H$	$C_4H_4 + H_2$	$k_{(322\text{-}085)}$	Estimate from Gladstone *et al.* (1996)
R113	322-039	$C_4H_5 + H + M$	$1\text{–}C_4H_6 + M$	$k_{0(322\text{-}086)}$ $k_\infty = 1\times10^{-10}$	
R114	322-040	$C_4H_9 + H$	$C_4H_8 + H_2$	1×10^{-10}	
R147	322-032	$C_3H_7 + CH_3$	$C_3H_6 + CH_4$	$1.85\times10^{-12}\ \exp(339/T)$	Allara and Shaw (1980), Anastasi and Arthur (1987)
R148	322-033	$C_3H_7 + CH_3 + M$	$C_4H_{10} + M$	$k_0\ (T<200) = 7.12\times10^{-22}\ \exp(715/T)$ $k_0\ (T>200) = 4.57\times10^{-24}\ \exp(2184/T)$ $k_\infty = 3.47\times10^{-11}$	Laufer *et al.* (1983), Anastasi and Arthur (1987)
R150	322-041	$C_4H_5 + CH_3$	$C_4H_4 + CH_4$	$k_{(R136/S39)}$	Estimate from Gladstone *et al.* (1996)
R151	322-042	$C_4H_5 + CH_3 + M$	products	$k_{(R148)}$	
R165	322-043	$C_2H_3 + C_2H_2 + M$	$C_4H_5 + M$	$10\times k_{0(S67)}$ $k_\infty = 3.1\times10^{-12}\ \exp(-1200/T)$	Estimate from Gladstone *et al.* (1996), Callear and Smith (1986)
R186	322-044	$C_4H_5 + H_2$	$1\text{–}CH_6 + H$	$1.8\times10^{-11}\ \exp(-1699/T)$	Callear and Smith (1986)
R187	322-045	$C_4H_5 + C_2H_2$	$C_6H_6 + H$	$3.0\times10^{-12}\ \exp(-1861/T)$	Cole *et al.* (1984), Gladstone *et al.* (1996)
R141	322-046	$C_3H_3 + CH_3 + M$	$1,2\text{–}C_4H_6 + M$	$10\times k_{0(S27)}$ $k_\infty = 5\times10^{-11}$	Laufer *et al.* (1983), Yung *et al.* (1984)
R142	322-047		$1\text{–}C_4H_6 + M$	$10\times k_{0(S27)}$ $k_\infty = 5\times10^{-11}$	

Table B.1 Photochemical model data: reaction rates, reactants, and products. (Continued)

Rxn IDs		Reactants	Products	Reaction Rate	References and comments
R161	322-048	$C_4H_{10} + C_2H$	$C_4H_9 + C_2H_2$	8.3×10^{-11} exp(112/T)	rate: Hoobler et al (1997), products: Gladstone *et al.* (1996)
	322-102	$C_4H_{10} + H$	H_2 + products	5.14×10^{-10} exp(–4318/T)	Warnatz (1984)
	322-103	$C_4H_{10} + CH$	products	4.4×10^{-10} exp(28/T)	Baulch *et al.* (1992)
R115	322-052	$C_6H_2 + H + M$	$C_6H_3 + M$	$k_{(R109)}$	Estimate from Gladstone *et al.* (1996)
R116	322-053	$C_6H_3 + H$	$C_2H_2 + C_4H_2$	$k_{(R110)}$	
R117	322-070		$C_6H_2 + H_2$	$k_{(R111)}$	
R162	322-054	$C_6H_2 + C_2H$	$C_8H_2 + H$	2.5% $k_{(R156/S38)}$	Tanzawa and Gardiner (1980)
R163	322-055	$C_8H_2 + C_2H$	products	2.5% $k_{(R156/S38)}$	Estimate from Gladstone *et al.* (1996)
R184	322-061	$C_6H_2 + C_4H$	products	2.5% $k_{(R156/S38)}$	
R185	322-062	$C_8H_2 + C_4H$	products	2.5% $k_{(R156/S38)}$	
R188	322-063	$C_6H + H_2$	$C_6H_2 + H$	$k_{(R179/S58)}$	
R189	322-064	$C_6H + CH_4$	$C_6H_2 + CH_3$	$k_{(322\text{-}079)}$	Opansky et al (1996)
R190	322-065	$C_6H + C_2H_2$	$C_8H_2 + H$	2.5% $k_{(R156/S38)}$	Estimate from Gladstone *et al.* (1996)
R191	322-066	$C_6H + C_2H_6$	$C_6H_2 + C_2H_5$	$k_{(R158/S40)}$	Opansky et al (1996)
R192	322-067	$C_6H + C_4H_2$	products	2.5% $k_{(R156/S38)}$	Estimate from Gladstone *et al.* (1996)
R193	322-068	$C_6H + C_6H_2$	products	2.5% $k_{(R156/S38)}$	
R194	322-069	$C_6H + C_8H_2$	products	2.5% $k_{(R156/S38)}$	

Table B.2 below lists saturation vapor curves used to constrain photochemical model abundances. If at any model altitude, the vapor pressure e of a condensible species exceeds the saturated vapor pressure e_{sat}, the model vapor pressure is reduced to the saturated value and the condensed material is removed from the model. Due to the age of the condensation experiments, most of the vapor pressure functions listed compute e_{sat} in units of mm Hg, which can be converted using the relation 760 mm Hg =
1 atm = 1.013 bar.

Table B.3 describes the photolysis reactions included in the model. R*nn*-series reaction IDs refer to Gladstone *et al.* (1996), and J*n*-series reactions are from Edgington (1997). The total absorption cross section is given in units of cm^2. When more than one pathway is given for the photolysis of a particular parent molecule, each pathway is labeled with a letter. The quantum yield for a given pathway is defined to be the fraction of the total number of photons absorbed by the parent molecule that result in a photochemical reaction along the pathway of interest. The sum of the quantum yields of all pathways at any particular wavelength should always be ≤ 1. When experiments give quantum yields at several discrete wavelengths, the wavelength range where the parent molecule has non-zero absorption is broken into a number of bins equal to the number of quantum yield measurements, with the measured quantum yields being as close as possible to the center of each model bin. Photolysis of PH_3 and NH_3 (and their photochemical products) is included in the model in order to properly model the radiation field at levels where nitrogen and phosphorous compounds absorb. As with the chemical reactions presented previously, these nitrogen and phosphorous photolysis reactions are omitted from Table B.3, again because they remain unchanged from the reactions described in Edgington (1997).

Table B.2 Photochemical model data: condensation.

Gas molecule	Condensate	Saturated vapor pressure function	Pressure units	Temperature range (K)	Reference
NH_3	NH_3 ice	$\log_{10}(e_{sat}) = 14.97593 - \frac{1790}{T} - 1.81630\log_{10}T$	mm Hg	< 195	Karwat (1924)
		$\log_{10}(e_{sat}) = 27.376004 - \frac{1914.9569}{T} - 8.4598324\log_{10}T + 2.39309\times10^{-3}T + 2.955214\times10^{-6}T^2$	bar	195–343	International Critical Tables (1928)
N_2H_4	solid N_2H_4	$e_{sat} = 2.6\exp\left(25.8\left(\frac{T-273}{T}\right)\right)$	mm Hg	< 273	Atreya *et al.* (1977), Scott *et al.* (1949)
PH_3	PH_3 ice	$\log_{10}(e_{sat})$ is the minimum of the values: $7.48235 - \frac{794.496}{T-7.94998}$ or $6.71559 - \frac{645.512}{T-8.08398}$	mm Hg	?	Dean (1992)
CH_4	CH_4 ice	$\log_{10}(e_{sat}) = 7.69540 - \frac{532.20}{T+1.842}$	mm Hg	< 90	Ziegler (1959)
C_2H_2	C_2H_2 ice	$\log_{10}(e_{sat}) = 8.29398 - \frac{1.339821\times10^3}{T} - 0.776656\log_{10}T$	mm Hg	?	Romani and Atreya (1988)
C_2H_4	liquid C_2H_4	$\log_{10}(e_{sat}) = 6.74756 - \frac{585}{T-18.16}$	mm Hg	120–155	Ziegler (1959)
		$\log_{10}(e_{sat}) = 50.79 - \frac{1703.0}{T} - 17.14\log_{10}T$	mm Hg	104–120	

Table B.2 Photochemical model data: condensation. (Continued)

Gas molecule	Condensate	Saturated vapor pressure function	Pressure units	Temperature range (K)	Reference
C_2H_4	solid C_2H_4	$\log_{10}(e_{sat}) = 8.724 - \frac{901.6}{T-2.555}$	mm Hg	89–104	Ziegler (1959)
		$\log_{10}(e_{sat}) = 1.5477 - 1038.1\left(\frac{1}{T} - 0.0110\right) + 16537\left(\frac{1}{T} - 0.0110\right)^2$	mm Hg	< 89	
C_2H_6	solid C_2H_6	$\log_{10}(e_{sat}) = 16.67 - \frac{1071.2075}{T} - 3.5247\log_{10}T$	mm Hg	> 90	Ziegler *et al.* (1964)
		$\log_{10}(e_{sat}) = 2.04543 - \frac{1057.5223}{T} - 4.8003\log_{10}T - 0.019973T$	mm Hg	< 90	
C_4H_2	?	$\log_{10}(e_{sat}) = 120.933 - \frac{5181.865}{T} - 41.118\log_{10}T$	mm Hg	?	Romani and Atreya (1988), possibly after Ziegler (1959)

Table B.3 Photochemical model data: photolysis products, quantum yields, and cross sections.

Rxn IDs		Parent	Products	Quantum yields	Cross section (cm^2)	References, comments
J9	R4	CH_3	$^1CH_2 + H$	1.0	1.0×10^{-16} at 150.3 nm 2.0×10^{-17} at 149.7 nm 3.5×10^{-17} at 216.0 nm	Okabe (1978), Ye *et al.* (1988)
J3b				at Ly-α / otherwise	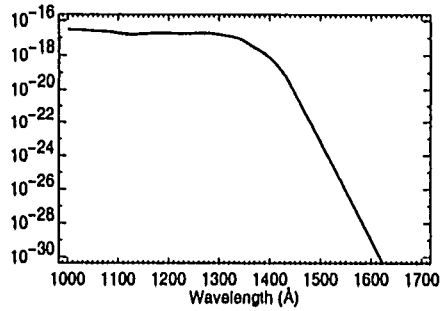	Lee and Chiang (1983), Mount *et al.* (1977), McNesby and Okabe (1964), Calvert and Pitts (1966), Rebbert and Ausloos (1972), Gorden and Ausloos (1967), Slanger and Black (1982), Laufer and McNesby (1968), Mordaunt *et al.* (1993), Wilson and Atreya (2000)
	R5		(A) $^1CH_2 + H_2$	(A) 0.28 / 0.0		
J3a	R6		(B) $^3CH_2 + 2H$	(B) 0.21 / 0.0		
J3c	R7	CH_4	(C) $CH + H + H_2$	(C) 0.10 / 0.0		
J3d			(D) $CH_3 + H$	(D) 0.41 / 1.0		
			(E) $^1CH_2 + 2H$	(E) 0.00 / 0.0		
J3e						
J4a					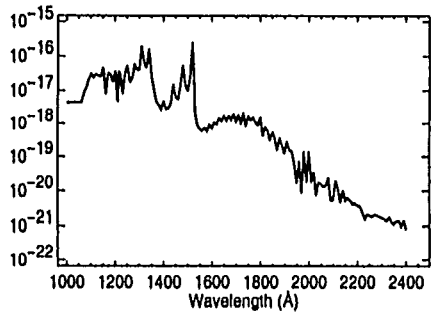	Okabe (1981), Shin and Michael (1991), McDonald *et al.* (1978), Suto and Lee (1984), Wu *et al.* (1989), Nakayama and Watanabe (1964), Chen *et al.* (1997), Seki *et al.* (1993)
	R8		(A) $C_2H + H$			
J4b	R9	C_2H_2	(B) $C_2 + H_2$			
			(C) $H_2C{=}C$			

λ (nm)	(A)	(B)	(C)
100–152	0.30	0.10	0.60
153–185	0.12	0.10	0.78
186–198	0.21	0.10	0.69
199–230	0.21	0.00	0.79

Table B.3 Photochemical model data: photolysis products, quantum yields, and cross sections. (Continued)

Rxn IDs	Parent	Products	Quantum yields	Cross section (cm^2)	References, comments
R10	C_2H_3	$C_2H_2 + H$	1.0	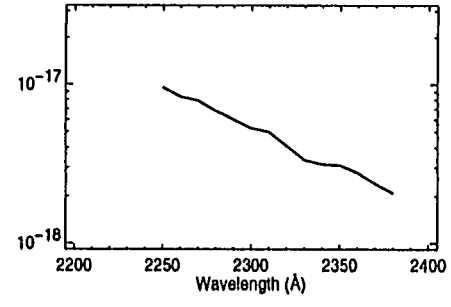	Fahr *et al.* (1998), Hunziker *et al.* (1983)
J5a R11 J5b R12 R13	C_2H_4	(A) $C_2H_2 + H_2$ (B) $C_2H_2 + 2H$ (C) $C_2H_3 + H$	λ (nm) (A)(B) (C) 157 0.560 0.406 0.035 193 0.705 0.261 0.035	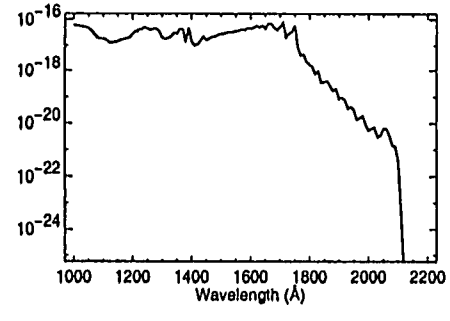	Schmitt and Brehm, (1966), LISA (PSL???), Holland *et al.* (1997), Zelikoff and Watanabe (1953), Chang *et al.* (1998)
R14	C_2H_5	$CH_3 + {}^1CH_2$	1.0	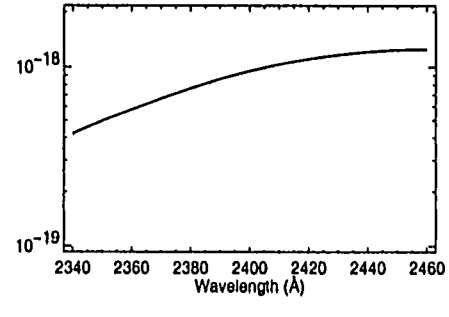	Adachi *et al.* (1979)

Table B.3 Photochemical model data: photolysis products, quantum yields, and cross sections. (Continued)

Rxn IDs		Parent	Products	Quantum yields			Cross section (cm^2)	References, comments
					100 nm	101–169 nm		
J6d							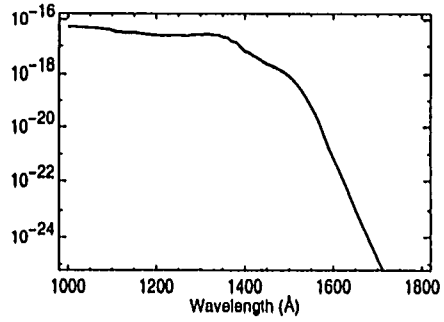	Mount and Moos (1978), Calvert and Pitts (1966), Akimoto *et al.* (1965), Lias *et al.* (1970), Hampson and McNesby (1965), Au *et al.* (1993)
	R15		(A) $C_2H_4 + H_2$	(A)	0.56	0.13		
J6b	R16		(B) $C_2H_4 + 2H$	(B)	0.14	0.30		
J6a	R17	C_2H_6	(C) $C_2H_2 + 2H_2$	(C)	0.27	0.25		
J6c	R18		(D) $CH_4 + {}^1CH_2$	(D)	0.02	0.25		
J6e	R19		(E) $2CH_3$	(E)	0.01	0.08		
	R20	C_3H_3	$C_3H_2 + H$	1.0			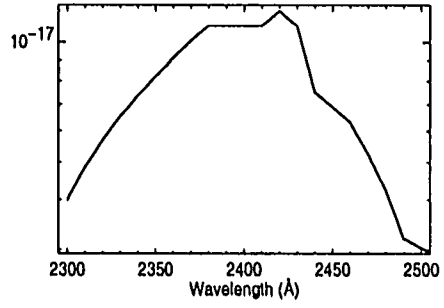	Fahr *et al.* (1998)
	R21	CH_3C_2H	(A) $C_3H_3 + H$	0.56			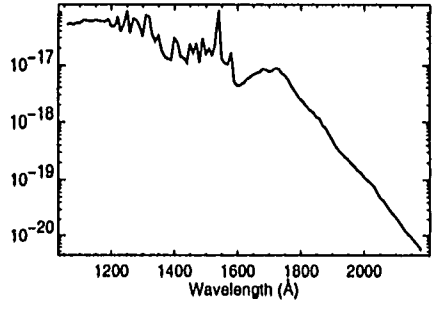	Nakayama and Watanabe (1964), Chen *et al.* (1999)
	R22		(B) $C_3H_2 + H_2$	0.44				

Table B.3 Photochemical model data: photolysis products, quantum yields, and cross sections. (Continued)

Rxn IDs	Parent	Products	Quantum yields	Cross section (cm^2)	References, comments
R23	CH_2CCH_2	(A) $C_3H_3 + H$	0.64	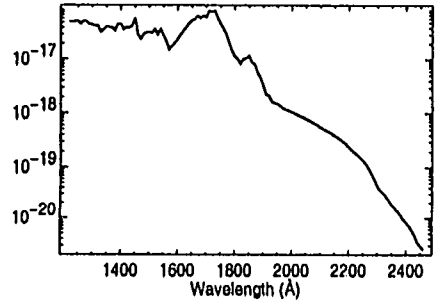	Rabalais *et al.* (1971)
R24		(B) $C_3H_2 + H_2$	0.36		
R25	C_3H_5	(A) $CH_3C_2H + H$	0.16	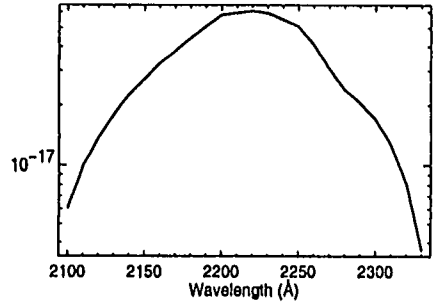	Jenkin *et al.* (1993)
R26		(B) $CH_2CCH_2 + H$	0.01		
R27		(C) $C_2H_2 + CH_3$	0.79		

Table B.3 Photochemical model data: photolysis products, quantum yields, and cross sections. (Continued)

Rxn IDs	Parent	Products		Quantum yields				Cross section (cm^2)	References, comments
				central wavelength (nm)					
				123.6	147	163	185		
R28	C_3H_6	(A) $C_3H_5 + H$	(A)	0.00	0.00	0.565	0.41	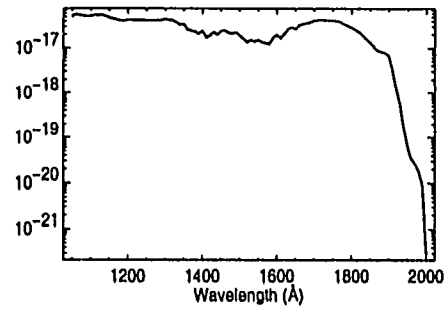	Collin (1988; Q.Y.), Samson et al. (1962; 1049–1923 Å), Fahr and Nayak (1996; 1601–2000 Å @ 223 K). Comparable to Calvert and Pitts (1966) propene, different from Basch et al. (1969) cyclopropane.
R29		(B) $CH_3C_2H + H_2$	(B)	0.11	0.11	0.010	0.01		
R30		(C) $CH_2CCH_2 + H_2$	(C)	0.17	0.22	0.010	0.01		
R31		(D) $C_2H_4 + {}^1CH_2$	(D)	0.06	0.04	0.020	0.03		
R32		(E) $C_2H_3 + CH_3$	(E)	0.21	0.27	0.335	0.40		
R33		(F) $C_2H_2 + CH_4$	(F)	0.05	0.03	0.050	0.04		
				central wavelength (nm)					
				~105	123.6	147	159		
R34	C_3H_8	(A) $C_3H_6 + H_2$	(A)	0.19	0.34	0.66	0.94	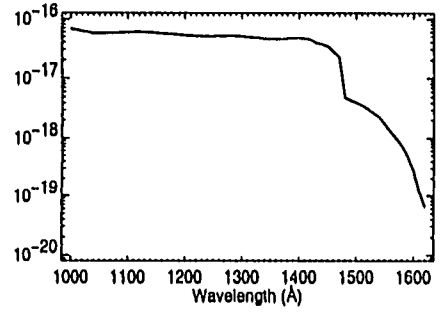	Okabe and Becker (1963; 1202–1629 Å), Koch and Skibowski (1971; 440–1467 Å), Johnston *et al.* (1978; 1000–3000 Å)
R35		(B) $C_2H_6 + {}^1CH_2$	(B)	0.09	0.09	0.04	0.00		
R36		(C) $C_2H_5 + CH_3$	(C)	0.40	0.35	0.19	0.00		
R37		(D) $C_2H_4 + CH_4$	(D)	0.32	0.22	0.11	0.06		

Table B.3 Photochemical model data: photolysis products, quantum yields, and cross sections. (Continued)

Rxn IDs		Parent	Products	Quantum yields	Cross section (cm^2)	References, comments
J7a				100–165 nm166–207 nm	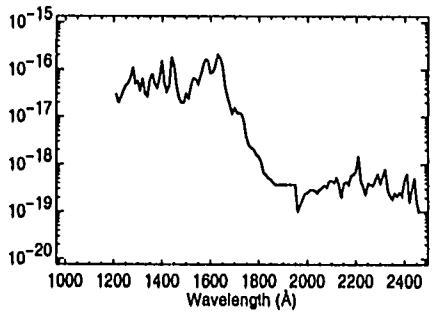	Okabe (1981), Glicker and Okabe (1987), Allan (1984), Smith *et al.* (1998)
	R38		(A) $C_4H + H$	(A) 0.200.00		
J7b	R39	C_4H_2	(B) $C_2H_2 + C_2$	(B) 0.100.06		
J7c	R40		(C) $2C_2H$	(C) 0.030.01		
J7d			(D) C_4H_2*	(D) 0.670.93		
	R41	C_4H_4	$C_4H_2 + H_2$	1.0	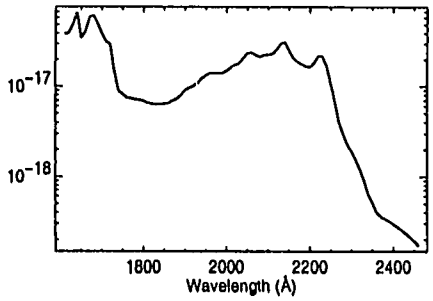	Fahr and Nayak (1996), Yung *et al.* (1984), Braude (1945), Heller and Milne (1978)
	R43		(A) $C_4H_4 + 2H$	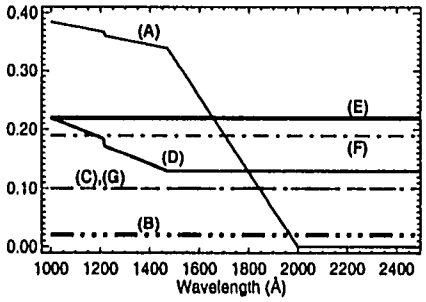	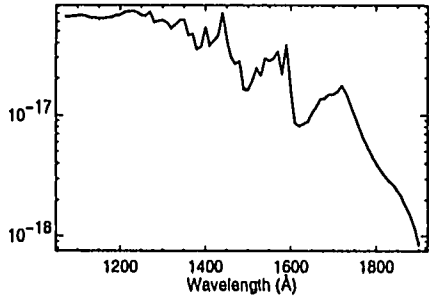	Nakayama and Watanabe (1964; 1050–1650 Å), Jones and Taylor (1955), Hill and Doepker (1972)
	R44		(B) $^1CH_2 + C_3H_4$			
	R45		(C) $C_2H_4 + C_2H + H$			
	R46	$1\text{–}C_4H_6$	(D) $2C_2H_2 + H_2$			
	R47		(E) $C_2H_3 + C_2H + H_2$			
	R48		(F) $C_2H_5 + C_2H$			
			(G) $C_3H_3 + CH_3$			

Table B.3 Photochemical model data: photolysis products, quantum yields, and cross sections. (Continued)

Rxn IDs	Parent	Products	Quantum yields	Cross section (cm^2)	References, comments
R50		(A) $C_4H_4 + 2H$	0.38		
		(B) $C_3H_4 + CH_2$	0.02		
R52		(C) $C_2H_4 + C_2H_2$	0.02		
R55		(D) $2C_2H_2 + H_2$	0.05		
	$1,2-C_4H_6$	(E) $C_2H_4 + C_2H + H$	0.02		
R53		(F) $C_2H_3 + C_2H_2 + H$	0.03		
R51		(G) $C_3H_3 + CH_3$	0.36		
R49		(H) $C_4H_5 + H$	0.09		
R58		(A) $C_3H_3 + CH_3$	0.40		
R56		(B) $C_4H_5 + H$	0.28		
R59	$1,3-C_4H_6$	(C) $C_2H_4 + C_2H_2$	0.17		
R60		(D) $2C_2H_3$	0.10		
R57		(E) $C_4H_4 + H_2$	0.05		

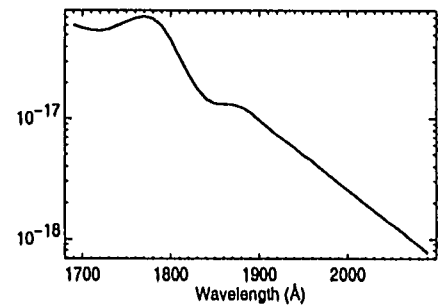

Calvert and Pitts (1966), Diaz and Doepker (1977)

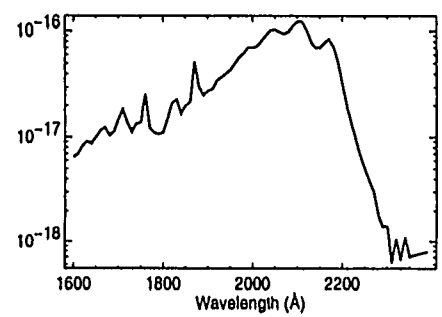

Calvert and Pitts (1966), Bergmann and Demtröder (1968), Fahr and Nayak (1994)

Table B.3 Photochemical model data: photolysis products, quantum yields, and cross sections. (Continued)

Rxn IDs	Parent	Products	Quantum yields			Cross section (cm^2)	References, comments
			wavelength range (nm)				
			≤ 135	136–160	≥ 161		
R61		(A) 1,3–C_4H_6 + 2H	(A)	0.23	0.140.06		
R62		(B) C_3H_5 + CH_3	(B)	0.12	0.390.66		
R63		(C) CH_3C_2H + CH_4	(C)	0.03	0.020.00		
R64		(D) CH_2CCH_2 + CH_4	(D)	0.14	0.100.00		
R65	C_4H_8	(E) C_2H_5 + C_2H_3	(E)	0.25	0.140.04		
R66		(F) $2C_2H_4$	(F)	0.02	0.040.05		
R67		(G) C_2H_2 + $2CH_3$	(G)	0.02	0.000.04		
		(H) C_3H_6 + CH_2	(H)	0.02	0.020.00		
		(I) C_4H_7 + H → C_4H_8	(I)	0.00	0.120.15		
			100–135 nm	136–166 nm			
R68		(A) C_4H_8 + H_2	(A)	0.530.59			
R72	C_4H_{10}	(B) C_2H_6 + C_2H_4	(B)	0.200.17			
R73		(C) $2C_2H_5$	(C)	0.130.12			
		(D) C_3H_7 + CH_3	(D)	0.130.12			

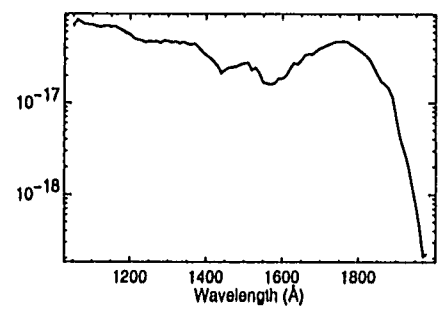

Samson *et al.* (1962), Collin and Wieckowski (1978), Niedzielski *et al.* (1978, 1979)

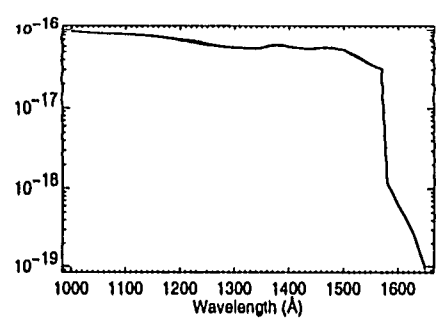

Koch and Skibowski (1971; 397–1573 Å), Okabe and Becker (1963), Obi et al. (1971), Jackson and Lias (1974)

Table B.3 Photochemical model data: photolysis products, quantum yields, and cross sections. (Continued)

Rxn IDs	Parent	Products	Quantum yields	Cross section (cm^2)	References, comments
R75 R76	C_6H_2	(A) $C_6H + H$ (B) $C_4H + C_2H$	0.3 0.3	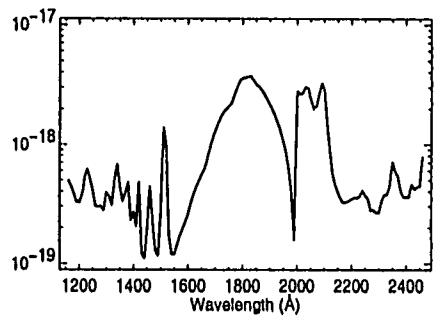	Kloster-Jensen (1974; 1160–1880 Å), PSL (LISA???), Kloster *et al.* (1974)
			100–165 nm166–207 nm		
R77 R78	C_8H_2	(A) $C_6H + C_2H$ (B) $2C_4H$	(A) 0.030.01 (B) 0.030.01	(assumed equal to C_4H_2)	Gladstone *et al.* (1996)

APPENDIX C

Derivation of entraining downdraft model equations

Introduction

This appendix contains the derivation of the governing equations of the downdraft with entrainment (DDE) model. The model and its results were discussed in Chapter 8. Table C.1 presents a list of symbols used in the derivation, and Table C.2 shows the indexes (subscripts and superscripts) used with some of the symbols.

Table C.1: Entraining downdraft constants and variables

Symbol		Definition
a	=	downdraft acceleration due to external forcing
c	=	specific heat at constant pressure
c^*	=	c for mixture of dry air, gaseous CVs, and condensed CVs
$C, C_\star$	=	arbitrary constants of integration (Equations C.50 and C.80)
$\mathbf{F}$	=	condensation delta function: 1 if saturated, 0 if subsaturated
$!\mathbf{F}$	=	inverse $\mathbf{F}$: 0 if saturated, 1 if subsaturated
g	=	gravitational acceleration
h	=	specific enthalpy of air and cloud particles
J_m	=	mass flux of air and cloud particles
J_p	=	momentum flux of air and cloud particles
K	=	equilibrium constant for reaction in Equation C.18

Table C.1: *continued*

Symbol		Definition
L	=	Latent heat of condensation/formation
p	=	pressure
q_i	=	specific humidity of species i, or m_i/m_{air}
q^*	=	like q, but relative to air + condensate mass
	=	$q/(1+\sum_i q_{ic})$
Q	=	saturated specific humidity
R_d	=	gas constant for dry air
S	=	horizontal downdraft cross sectional area
T	=	temperature
w^d	=	downdraft velocity ($w^d > 0$)
z	=	height
α	=	H_2S molecular mass / NH_4SH molecular mass
β	=	NH_3 molecular mass / NH_4SH molecular mass
μ_e	=	environmental entrainment coefficient
ρ	=	density of air
ρ^*	=	density of air/cloud particle mixture

Table C.2: Entraining downdraft varible indexes

Index		Definition
Superscript		
d	=	downdraft
e	=	surrounding environment
Subscript		
W	=	the water system (e.g., Q_W is the saturated specific humidity of water)

continued on next page

Table C.2: *continued*

Index		Definition
A	=	the ammonia system (e.g., $\mathbf{F}_A$ is true if ammonia is condensing)
S	=	sulfur in the NH_3-H_2S-NH_4SH system
$A(S)$	=	ammonia in the NH_3-H_2S-NH_4SH system
d	=	dry air
wg	=	water, gaseous
wc	=	water, condensed
ag	=	ammonia, gaseous
ac	=	ammonia, condensed
sg	=	hydrogen sulfide, gaseous
sc	=	NH_4SH, condensed
i	=	index over all CV gases and cloud particles

Model equation derivations

Entrainment coefficient

This equation is actually a definition, so is not derived.

$$\mu_e \equiv \frac{1}{J_m^d}\frac{d_e J_m^d}{dz} = \frac{1}{\rho^{*d} S w^d}\frac{d(\rho^{*d} S w^d)}{dz} \tag{C.1}$$

Equation of motion

$$d J_p^d = (\rho^e - \rho^{*d}) g\, S\, dz - \rho^{*d} a\, S\, dz + d_e J_p^d, \tag{C.2}$$

where:

$$d J_p^d = J_m^d w^d = \rho^{*d} S w^{d2} \tag{C.3}$$

$$d_e J_p^d = w^e d_e J_m^d = 0 \tag{C.4}$$

then apply $\frac{d}{dz}$ to get:

$$\frac{d}{dz}(\rho^{*d} S w^{d2}) = (\rho^e - \rho^{*d}) g S - \rho^{*d} a S \tag{C.5}$$

then use the definition of μ_e and divide by $\rho^{*d} S w^d$ to get the differential equation of motion:

$$\frac{dw^d}{dz} = \left(\frac{\rho^e - \rho^{*d}}{\rho^{*d}}\right) \frac{g}{w^d} - \frac{a}{w^d} - \mu_e w^d \tag{C.6}$$

Conservation of CV mass

Total flux of CVs, gaseous and condensed, can be changed only by the entrainment process:

$$d\left(J_m^d \sum_i q_i^{d*}\right) = \left(\sum_i q_i^{e*}\right) d_e J_m^d \tag{C.7}$$

then use the definition of μ_e and divide by dz:

$$\frac{d}{dz}\left(J_m^d \sum_i q_i^{d*}\right) = \mu_e J_m^d \sum_i q_i^{e*} \tag{C.8}$$

use the product rule on the left side, use the definition of μ_e again, and divide by J_m^d to get the CV flux equation:

$$\frac{d}{dz}\left(\sum_i q_i^{d*}\right) = \mu_e \sum_i (q_i^{e*} - q_i^{d*}) \tag{C.9}$$

In the following equations, q_i^{e*} will approximated by the simpler q_i^e.

I need separate equations for each phase of each condensible volatile. I assume instant evaporation and condensation, which leads to the relations for saturated and unsaturated conditions of a generic condensible volatile i:

$$\text{saturated:} \quad q_{ig} + q_{ic} \geq Q_i \longrightarrow q_{ig} = Q_i, q_{ic} = q_{ig} + q_{ic} - Q_i \tag{C.10}$$

$$\text{subsaturated:} \quad q_{ig} + q_{ic} < Q_i \longrightarrow q_{ig} = q_{ig} + q_{ic}, q_{ic} = 0 \tag{C.11}$$

Several complications need to be considered in breaking the CV flux equation into separate equations for each CV. One complication is that although Q_A and Q_W are purely functions of temperature and pressure, $Q_{A(S)}$ and Q_S are functions of each other as well as T and p. Similarly, a gram of ammonia gas condenses to a gram of ammonia ice, but α g of H_2S and β g of NH_3 condense to 1 g of NH_4SH.

Finally, some CVs may be saturated while others are not. H_2S and NH_3 do not care whether water is saturated or not. In order to simplify calculations, I assume that whenever ammonia is saturated (the case of $\mathbf{F}_A$), NH_4SH does not actually condense, regardless of whether H_2S and NH_3 are saturated with respect to NH_4SH ($\mathbf{F}_S$) or not ($!\mathbf{F}_S$). Thus, NH_4SH condenses only in the case $!\mathbf{F}_A\mathbf{F}_S$.

Then the change in CV specific humidities with height in the downdraft is given by the following set of equations:

$$\begin{aligned}\frac{dq^d_{wc}}{dz} &= (\mathbf{F}_W)\mu_e\left(q^e_{wg} + q^e_{wc} - q^d_{wg} - q^d_{wc}\right) \\ &\quad -(\mathbf{F}_W)\left(\frac{\partial Q_W}{\partial p}\frac{dp}{dz} + \frac{\partial Q_W}{\partial T}\frac{dT}{dz}\right)\end{aligned} \tag{C.12}$$

$$\begin{aligned}\frac{dq^d_{wg}}{dz} &= (!\mathbf{F}_W)\mu_e\left(q^e_{wg} + q^e_{wc} - q^d_{wg} - q^d_{wc}\right) \\ &\quad +(\mathbf{F}_W)\left(\frac{\partial Q_W}{\partial p}\frac{dp}{dz} + \frac{\partial Q_W}{\partial T}\frac{dT}{dz}\right)\end{aligned} \tag{C.13}$$

$$\begin{aligned}\frac{dq^d_{uc}}{dz} &= (\mathbf{F}_A)\mu_e\left(q^e_{ag} + q^e_{ac} - q^d_{ag} - q^d_{ac}\right) \\ &\quad -(\mathbf{F}_A)\left(\frac{\partial Q_A}{\partial p}\frac{dp}{dz} + \frac{\partial Q_A}{\partial T}\frac{dT}{dz}\right)\end{aligned} \tag{C.14}$$

$$\frac{dq^d_{ag}}{dz} = (!\mathbf{F}_A!\mathbf{F}_S)\mu_e\left(q^e_{ag} - q^d_{ag}\right) + (!\mathbf{F}_A)\mu_e\left(q^e_{ac} - q^d_{ac}\right)$$

$$
\begin{aligned}
&+(!\mathbf{F}_A!\mathbf{F}_S)\beta\mu_e\left(q^e_{sc}-q^d_{sc}\right)+(\mathbf{F}_A)\left(\frac{\partial Q_A}{\partial p}\frac{dp}{dz}+\frac{\partial Q_A}{\partial T}\frac{dT}{dz}\right)\\
&+(!\mathbf{F}_A\mathbf{F}_S)\left(\frac{\partial Q_{A(S)}}{\partial p}\frac{dp}{dz}+\frac{\partial Q_{A(S)}}{\partial T}\frac{dT}{dz}+\frac{\partial Q_{A(S)}}{\partial Q_S}\right) \qquad \text{(C.15)}
\end{aligned}
$$

$$
\begin{aligned}
\frac{dq^d_{sc}}{dz} &= (!\mathbf{F}_A\mathbf{F}_S)\mu_e\left(q^e_{sg}-q^d_{sg}\right)+(\mathbf{F}_A|\mathbf{F}_S)\mu_e\left(q^e_{sc}-q^d_{sc}\right)\\
&+(!\mathbf{F}_A\mathbf{F}_S)\mu_e\left(q^e_{ag}-q^d_{ag}\right)\\
&-(!\mathbf{F}_A\mathbf{F}_S)\left(\frac{\partial Q_{A(S)}}{\partial p}\frac{dp}{dz}+\frac{\partial Q_{A(S)}}{\partial T}\frac{dT}{dz}+\frac{\partial Q_{A(S)}}{\partial Q_S}\right)\\
&-(!\mathbf{F}_A\mathbf{F}_S)\left(\frac{\partial Q_S}{\partial p}\frac{dp}{dz}+\frac{\partial Q_S}{\partial T}\frac{dT}{dz}+\frac{\partial Q_S}{\partial Q_{A(S)}}\right) \qquad \text{(C.16)}
\end{aligned}
$$

$$
\begin{aligned}
\frac{dq^d_{sg}}{dz} &= (\mathbf{F}_A|!\mathbf{F}_S)\mu_e\left(q^e_{sg}-q^d_{sg}\right)+(!\mathbf{F}_A!\mathbf{F}_S)\alpha\mu_e\left(q^e_{sc}-q^d_{sc}\right)\\
&+(!\mathbf{F}_A\mathbf{F}_S)\left(\frac{\partial Q_S}{\partial p}\frac{dp}{dz}+\frac{\partial Q_S}{\partial T}\frac{dT}{dz}+\frac{\partial Q_S}{\partial Q_{A(S)}}\right) \qquad \text{(C.17)}
\end{aligned}
$$

The problematic terms $\frac{\partial Q_{A(S)}}{\partial Q_S}$ and $\frac{\partial Q_A}{\partial Q_{A(S)}}$ can be eliminated as follows, beginning with the reaction constant K for the reaction,

$$
\mathrm{NH_3} + \mathrm{H_2S} \longrightarrow \mathrm{NH_4SH}: \qquad \text{(C.18)}
$$

$$
K = Q_{A(S)}Q_S = \left(\frac{\mu_{\mathrm{NH_3}}\mu_{\mathrm{H_2S}}}{\overline{\mu}^2}\right)\frac{1}{P^2}\exp\left[\left(14.82-\frac{4705}{T}\right)\cdot\ln 10\right] \qquad \text{(C.19)}
$$

So then,

$$
\begin{aligned}
Q_{A(S)} &= \frac{K}{Q_S} \qquad \text{(C.20)}\\
Q_S &= \frac{K}{Q_{A(S)}} \qquad \text{(C.21)}
\end{aligned}
$$

and therefore,

$$
\begin{aligned}
\frac{dQ_{A(S)}}{dz} &= \frac{d}{dz}\left(\frac{K}{Q_S}\right)=\frac{1}{Q_S}\frac{dK}{dz}-\frac{K}{Q_S^2}\frac{dQ_S}{dz} \qquad \text{(C.22)}\\
\frac{dQ_S}{dz} &= \frac{d}{dz}\left(\frac{K}{Q_{A(S)}}\right)=\frac{1}{Q_{A(S)}}\frac{dK}{dz}-\frac{K}{Q^2_{A(S)}}\frac{dQ_{A(S)}}{dz} \qquad \text{(C.23)}
\end{aligned}
$$

In addition, since α g of H_2S and β g of NH_3 condense to 1 g of NH_4SH, I can use the relation:

$$
\frac{dQ_{A(S)}}{dz} = \frac{\beta}{\alpha}\frac{dQ_S}{dz}. \qquad \text{(C.24)}
$$

Then the saturated humidity differentials can be eliminated from the previous two equations:

$$\begin{aligned}\frac{dQ_{A(S)}}{dz} &= \frac{1}{Q_S}\frac{dK}{dz} - \frac{K}{Q_S^2}\left(\frac{\alpha}{\beta}\frac{dQ_{A(S)}}{dz}\right) \\ &= \frac{1}{Q_S}\frac{dK}{dz}\left(\frac{1}{1+\frac{\alpha}{\beta}\frac{Q_{A(S)}}{Q_S}}\right) = \frac{\beta}{\left(\beta Q_S + \alpha Q_{A(S)}\right)}\frac{dK}{dz} \qquad \text{(C.25)}\end{aligned}$$

$$\frac{dQ_S}{dz} = \frac{\alpha}{\beta}\frac{dQ_{A(S)}}{dz} = \frac{\alpha}{\left(\beta Q_S + \alpha Q_{A(S)}\right)}\frac{dK}{dz} \qquad \text{(C.26)}$$

Next I convert the K-differential into the more useful T- and p-differentials:

$$\begin{aligned}\frac{dK}{dz} &= \frac{\partial K}{\partial T}\frac{dT}{dz} + \frac{\partial K}{\partial p}\frac{dp}{dz} \\ &\quad \frac{4705\ln(10)K}{T^2}\frac{dT}{dz} - \frac{2K}{p}\frac{dp}{dz} \qquad \text{(C.27)}\end{aligned}$$

$$\text{(C.28)}$$

This allows me to express Equations C.15-C.17 in their final form:

$$\begin{aligned}\frac{dq_{ag}^d}{dz} &= (!\mathbf{F}_A!\mathbf{F}_S)\mu_e\left(q_{ag}^e - q_{ag}^d\right) + (!\mathbf{F}_A)\mu_e\left(q_{ac}^e - q_{ac}^d\right) \\ &\quad +(!\mathbf{F}_A!\mathbf{F}_S)\beta\mu_e\left(q_{sc}^e - q_{sc}^d\right) + (\mathbf{F}_A)\left(\frac{\partial Q_A}{\partial p}\frac{dp}{dz} + \frac{\partial Q_A}{\partial T}\frac{dT}{dz}\right) \\ &\quad +(!\mathbf{F}_A\mathbf{F}_S)\left[\frac{4705\beta\ln(10)K}{T^2\left(\beta Q_S + \alpha Q_{A(S)}\right)}\frac{dT}{dz} - \frac{2\beta K}{p\left(\beta Q_S + \alpha Q_{A(S)}\right)}\frac{dp}{dz}\right] \qquad \text{(C.29)}\end{aligned}$$

$$\begin{aligned}\frac{dq_{sc}^d}{dz} &= (!\mathbf{F}_A\mathbf{F}_S)\mu_e\left(q_{sg}^e - q_{sg}^d\right) + (\mathbf{F}_A|!\mathbf{F}_S)\mu_e\left(q_{sc}^e - q_{sc}^d\right) \\ &\quad +(!\mathbf{F}_A\mathbf{F}_S)\mu_e\left(q_{ag}^e - q_{ag}^d\right) \\ &\quad -(!\mathbf{F}_A\mathbf{F}_S)\left[\frac{4705\ln(10)K}{T^2\left(\beta Q_S + \alpha Q_{A(S)}\right)}\frac{dT}{dz} - \frac{2K}{p\left(\beta Q_S + \alpha Q_{A(S)}\right)}\frac{dp}{dz}\right] \qquad \text{(C.30)}\end{aligned}$$

$$\begin{aligned}\frac{dq_{sg}^d}{dz} &= (\mathbf{F}_A|!\mathbf{F}_S)\mu_e\left(q_{sg}^e - q_{sg}^d\right) + (!\mathbf{F}_A!\mathbf{F}_S)\alpha\mu_e\left(q_{sc}^e - q_{sc}^d\right) \\ &\quad +(!\mathbf{F}_A\mathbf{F}_S)\left[\frac{4705\alpha\ln(10)K}{T^2\left(\beta Q_S + \alpha Q_{A(S)}\right)}\frac{dT}{dz} - \frac{2\alpha K}{p\left(\beta Q_S + \alpha Q_{A(S)}\right)}\frac{dp}{dz}\right] \qquad \text{(C.31)}\end{aligned}$$

A further numerical complication is introduced into the calculation of the three equations above by the quantities $Q_{A(S)}$ and Q_S. These values depend not only on T and p, but also on each other through Equation C.24. I use an approximation to

the integrated Equation C.24, obtained by multiplying by Δz, cancelling $\Delta z/dz$, and approximating $\partial Q_{A(S)}$ and ∂Q_S:

$$\left(q_{ag}^d + \mu_e \Delta z(q_{ag}^e - q_{ag}^d) - Q_{A(S)}\right) = \frac{\beta}{\alpha}\left(q_{sg}^d + \mu_e \Delta z(q_{sg}^e - q_{sg}^d) - Q_S\right) \tag{C.32}$$

For ease of reading, let us temporarily define the abbreviations:

$$q_{ag}^{\Delta} = q_{ag}^d + \mu_e \Delta z(q_{ag}^e - q_{ag}^d) \tag{C.33}$$

$$q_{sg}^{\Delta} = q_{sg}^d + \mu_e \Delta z(q_{sg}^e - q_{sg}^d) \tag{C.34}$$

Then we can solve Equation C.32 for Q_S, using the definition of K and the quadratic equation:

$$Q_{A(S)} = \frac{\beta}{\alpha} Q_S + \left(q_{ag}^{\Delta} - \frac{\beta}{\alpha} q_{sg}^{\Delta}\right) \tag{C.35}$$

$$K = Q_S Q_{A(S)} = Q_S\left[\frac{\beta}{\alpha} Q_S + \left(q_{ag}^{\Delta} - \frac{\beta}{\alpha} q_{sg}^{\Delta}\right)\right] \tag{C.36}$$

$$0 = Q_S^2 + \left(\frac{\alpha}{\beta} q_{ag}^{\Delta} - q_{sg}^{\Delta}\right) Q_S - \frac{\alpha}{\beta} K \tag{C.37}$$

$$Q_S = \frac{-\left(\frac{\alpha}{\beta} q_{ag}^{\Delta} - q_{sg}^{\Delta}\right) \pm \sqrt{\left(\frac{\alpha}{\beta} q_{ag}^{\Delta} - q_{sg}^{\Delta}\right)^2 + 4\frac{\alpha}{\beta} K}}{2} \tag{C.38}$$

So now Q_S (and therefore $Q_{A(S)}$) can be numerically approximated as a function of T, p, and q_{sg}^d, q_{ag}^d, q_{sg}^e, q_{ag}^e from the previous computation step.

For the other condensible volatiles, I use the following relations. For water liquid above 273 K (from Magnus' formula, Iribarne and Godson 1981, p.68),

$$Q_W = \frac{\mu_w}{\overline{\mu} p} \exp\left[\ln(10)\left(-\frac{2937.4}{T} - \frac{4.9283 \ln T}{\ln(10)} + 23.5470\right)\right] \tag{C.39}$$

$$\frac{\partial Q_W}{\partial T} = \left(\frac{2937.4}{T^2} - \frac{4.9283}{T \ln(10)}\right) \ln(10) Q_W \tag{C.40}$$

$$\frac{\partial Q_W}{\partial p} = -\frac{1}{p} Q_W \tag{C.41}$$

For water ice between 173 K and 273 K (from Washburn, 1924),

$$Q_W = \frac{\mu_w}{\overline{\mu} p} \exp\left[\ln(10)\left(-\frac{2445.5646}{T} + \frac{8.2312 \ln T}{\ln(10)} - 0.01677006T +\right.\right.$$

$$1.20514 \times 10^{-5}T^2 - 6.757169\Big)\Big] \tag{C.42}$$

$$\begin{aligned}
\frac{\partial Q_W}{\partial T} &= \left(\frac{2445.5646}{T^2} + \frac{8.2312}{T\ln(10)} - 0.01677006 + \right. \\
&\quad \left. 2.41028 \times 10^{-5}T\right) \ln(10) Q_W \qquad \text{(C.43)} \\
\frac{\partial Q_W}{\partial p} &= -\frac{1}{p} Q_W \qquad \text{(C.44)}
\end{aligned}$$

For ammonia ice between 100 K and 195 K (from Karwat, 1924),

$$\begin{aligned}
Q_A &= \frac{\mu_{NH_3}}{\overline{\mu} p} \exp\left[\ln(10)\left(-\frac{1790}{T} - \frac{1.81630 \ln T}{\ln(10)} + 14.97593\right)\right] \qquad \text{(C.45)} \\
\frac{\partial Q_A}{\partial T} &= \left(\frac{1790}{T^2} - \frac{1.81630}{T\ln(10)}\right) \ln(10) Q_A \qquad \text{(C.46)} \\
\frac{\partial Q_A}{\partial p} &= -\frac{1}{p} Q_A \qquad \text{(C.47)}
\end{aligned}$$

Lapse rate equation

The change in enthalpy with height is a sum of the enthalpy change due to the work done by the change in pressure, and the change due to entrainment of enthalpy:

$$\frac{d(J_m^d h^d)}{dz} = J_m^d \left(\frac{1}{\rho^{d*}} \frac{dp}{dz} + \mu_e h^e\right) \tag{C.48}$$

Then, according to the definition of μ_e, I can write:

$$\frac{dh^d}{dz} = \frac{1}{\rho^{d*}} \frac{dp}{dz} + \mu_e \left(h^e - h^d\right) \tag{C.49}$$

To reduce this enthalpy equation into the lapse rate equation, I will need several pages of supporting equations. The first step is to break the enthalpies into the partial enthalpies of dry air and of the various condensible volatiles:

$$\begin{aligned}
h_i &= c_i (T + C_i) \qquad \text{(C.50)} \\
h &= \left(1 - \sum_i q_i^*\right) h_d + \sum_i q_i^* h_i \qquad \text{(C.51)} \\
c^* &= c_d \left(1 - \sum_i q_i^*\right) + \sum_i c_i q_i^* \qquad \text{(C.52)}
\end{aligned}$$

Then the enthalpy equation becomes:

$$\begin{aligned}\frac{dh^d}{dz} &= c^*\frac{dT}{dz} - h_d^d\frac{d\left(\sum_i q_i^{d*}\right)}{dz} + \sum_i h_i^d\frac{dq_i^{d*}}{dz} \\ &= \frac{1}{\rho^{d*}}\frac{dp}{dz} + \mu_e\left(h^e - h^d\right)\end{aligned} \tag{C.53}$$

The next step is to expand all the enthalpy and humidity terms in the equation above. I have already taken care of the first term with Equation C.9. For the next term, I use Equations C.12-C.14 and C.29-C.31:

$$\begin{aligned}\sum_i h_i^d\frac{dq_i^{d*}}{dz} &= (\mathbf{F}_W)h_{wc}^d\left[\mu_e\left(q_{wg}^e + q_{wc}^e - q_{wg}^d - q_{wc}^d\right) - \frac{\partial Q_W}{\partial p}\frac{dp}{dz} + \frac{\partial Q_W}{\partial T}\frac{dT}{dz}\right] \\ &+(!\mathbf{F}_W)h_{wg}^d\mu_e\left(q_{wg}^e + q_{wc}^e - q_{wg}^d - q_{wc}^d\right) + (\mathbf{F}_W)h_{wg}^d\left(\frac{\partial Q_W}{\partial p}\frac{dp}{dz} + \frac{\partial Q_W}{\partial T}\frac{dT}{dz}\right) \\ &+(\mathbf{F}_A)h_{ac}^d\left[\mu_e\left(q_{ag}^e + q_{ac}^e - q_{ag}^d - q_{ac}^d\right) - \frac{\partial Q_A}{\partial p}\frac{dp}{dz} + \frac{\partial Q_A}{\partial T}\frac{dT}{dz}\right] \\ &+(!\mathbf{F}_A!\mathbf{F}_S)h_{ag}^d\mu_e\left[q_{ag}^e - q_{ag}^d\right] + (!\mathbf{F}_A)h_{ag}^d\mu_e\left[q_{ac}^e - q_{ac}^d\right] \\ &+(!\mathbf{F}_A!\mathbf{F}_S)h_{ag}^d\beta\mu_e\left[q_{sc}^e - q_{sc}^d\right] + (\mathbf{F}_A)h_{ag}^d\left[\frac{\partial Q_A}{\partial p}\frac{dp}{dz} + \frac{\partial Q_A}{\partial T}\frac{dT}{dz}\right] \\ &+(!\mathbf{F}_A\mathbf{F}_S)h_{ag}^d\left[\frac{\beta 4705\ln(10)K}{T^2\left(\beta Q_S + \alpha Q_{A(S)}\right)}\frac{dT}{dz} - \frac{\beta 2K}{p\left(\beta Q_S + \alpha Q_{A(S)}\right)}\frac{dp}{dz}\right] \\ &+(!\mathbf{F}_A\mathbf{F}_S)h_{sc}^d\mu_e\left[q_{ag}^e - q_{ag}^d\right] + (\mathbf{F}_A\|\mathbf{F}_S)h_{sc}^d\mu_e\left[q_{sc}^e - q_{sc}^d\right] \\ &+(!\mathbf{F}_A\mathbf{F}_S)h_{sc}^d\mu_e\left[q_{sg}^e - q_{sg}^d\right] \\ &-(!\mathbf{F}_A\mathbf{F}_S)h_{sc}^d\left[\frac{4705\ln(10)K}{T^2\left(\beta Q_S + \alpha Q_{A(S)}\right)}\frac{dT}{dz} - \frac{2K}{p\left(\beta Q_S + \alpha Q_{A(S)}\right)}\frac{dp}{dz}\right] \\ &+(\mathbf{F}_A\|\mathbf{F}_S)h_{sg}^d\mu_e\left[q_{sg}^e - q_{sg}^d\right] + (!\mathbf{F}_A!\mathbf{F}_S)h_{sg}^d\alpha\mu_e\left[q_{sc}^e - q_{sc}^d\right] \\ &+(!\mathbf{F}_A\mathbf{F}_S)h_{sg}^d\left[\frac{\alpha 4705\ln(10)K}{T^2\left(\beta Q_S + \alpha Q_{A(S)}\right)}\frac{dT}{dz} - \frac{\alpha 2K}{p\left(\beta Q_S + \alpha Q_{A(S)}\right)}\frac{dp}{dz}\right]\end{aligned} \tag{C.54}$$

A number of identities will be used to convert terms involving enthalpies into terms involving the measureable quantities of specific heats, latent heats, and temperature. These identities employ Equation C.50 and the definition of latent heats. The useful identities are:

$$h_{wg} - h_{wc} = L_W \tag{C.55}$$

$$h_{ag} - h_{ac} = L_A \tag{C.56}$$

$$\alpha h_{sg} + \beta h_{ag} - h_{sc} = L_S \tag{C.57}$$

$$h_i - h_i' = c_i (T - T') \tag{C.58}$$

$$h_{ig} - h_{ic}' = L_i' + c_{ig} (T - T') \tag{C.59}$$

$$= L_i + c_{ic} (T - T') \tag{C.60}$$

In the identities above, prime and unprime may interchangeably refer to downdraft and environment, or vice versa. A similar pair of equations to C.59 and C.60 can be derived for NH_4SH:

$$\alpha h_{sg}' + \beta h_{ag}' - h_{sc} = L_{sc}' - c_{sc} (T - T') \tag{C.61}$$

$$= L_{sc} - (\alpha c_{sg} + \beta c_{ag}) (T - T') \tag{C.62}$$

I will use some simple relations between atomic mass ratios of the condensible volatiles:

$$\alpha = \frac{\mu_{H_2S}}{\mu_{NH_4SH}} = \frac{34}{51} = 2\beta \tag{C.63}$$

$$\beta = \frac{\mu_{NH_3}}{\mu_{NH_4SH}} = \frac{17}{51} = (1 - \alpha) \tag{C.64}$$

$$= \alpha - \beta \tag{C.65}$$

And finally, I will use the algebraic relation:

$$AB - CD = \frac{1}{2} [(A + C)(B - D) + (A - C)(B + D)] \tag{C.66}$$

I can expand the last term in Equation C.53, corresponding to the entrainment of enthalpy, using Equations C.51, C.52, and C.66. Then I expand Equation C.53 and prepare to reduce the enthalpy terms to physically measureable terms:

$$0 = -c^* \frac{dT}{dz} + \mu_e h_d^d \sum_i \left(q_i^e - q_i^d\right)$$

$$
\begin{aligned}
&-(\mathbf{F}_W)h^d_{wc}\left[\mu_e\left(q^e_{wg}+q^e_{wc}-q^d_{wg}-q^d_{wc}\right)-\frac{\partial Q_W}{\partial p}\frac{dp}{dz}+\frac{\partial Q_W}{\partial T}\frac{dT}{dz}\right]\\
&-(!\mathbf{F}_W)h^d_{wg}\mu_e\left(q^e_{wg}+q^e_{wc}-q^d_{wg}-q^d_{wc}\right)-(\mathbf{F}_W)h^d_{wg}\left(\frac{\partial Q_W}{\partial p}\frac{dp}{dz}+\frac{\partial Q_W}{\partial T}\frac{dT}{dz}\right)\\
&-(\mathbf{F}_A)h^d_{ac}\left[\mu_e\left(q^e_{ag}+q^e_{ac}-q^d_{ag}-q^d_{ac}\right)-\frac{\partial Q_A}{\partial p}\frac{dp}{dz}+\frac{\partial Q_A}{\partial T}\frac{dT}{dz}\right]\\
&-(!\mathbf{F}_A!\mathbf{F}_S)h^d_{ag}\mu_e\left[q^e_{ag}-q^d_{ag}\right]-(!\mathbf{F}_A)h^d_{ag}\mu_e\left[q^e_{ac}-q^d_{ac}\right]\\
&-(!\mathbf{F}_A!\mathbf{F}_S)h^d_{ag}\beta\mu_e\left[q^e_{sc}-q^d_{sc}\right]-(\mathbf{F}_A)h^d_{ag}\left[\frac{\partial Q_A}{\partial p}\frac{dp}{dz}+\frac{\partial Q_A}{\partial T}\frac{dT}{dz}\right]\\
&-(!\mathbf{F}_A\mathbf{F}_S)h^d_{ag}\left[\frac{\beta 4705\ln(10)K}{T^2\left(\beta Q_S+\alpha Q_{A(S)}\right)}\frac{dT}{dz}-\frac{\beta 2K}{p\left(\beta Q_S+\alpha Q_{A(S)}\right)}\frac{dp}{dz}\right]\\
&-(!\mathbf{F}_A\mathbf{F}_S)h^d_{sc}\mu_e\left[q^e_{ag}-q^d_{ag}\right]-(\mathbf{F}_A||\mathbf{F}_S)h^d_{sc}\mu_e\left[q^e_{sc}-q^d_{sc}\right]-(!\mathbf{F}_A\mathbf{F}_S)h^d_{sc}\mu_e\left[q^e_{sg}-q^d_{sg}\right]\\
&+(!\mathbf{F}_A\mathbf{F}_S)h^d_{sc}\left[\frac{4705\ln(10)K}{T^2\left(\beta Q_S+\alpha Q_{A(S)}\right)}\frac{dT}{dz}-\frac{2K}{p\left(\beta Q_S+\alpha Q_{A(S)}\right)}\frac{dp}{dz}\right]\\
&-(\mathbf{F}_A||\mathbf{F}_S)h^d_{sg}\mu_e\left[q^e_{sg}-q^d_{sg}\right]-(!\mathbf{F}_A!\mathbf{F}_S)h^d_{sg}\alpha\mu_e\left[q^e_{sc}-q^d_{sc}\right]\\
&-(!\mathbf{F}_A\mathbf{F}_S)h^d_{sg}\left[\frac{\alpha 4705\ln(10)K}{T^2\left(\beta Q_S+\alpha Q_{A(S)}\right)}\frac{dT}{dz}-\frac{\alpha 2K}{p\left(\beta Q_S+\alpha Q_{A(S)}\right)}\frac{dp}{dz}\right]+\frac{1}{\rho}\frac{dp}{dz}\\
&+\mu_e h^d_d\sum_i\left(q^e_i-q^d_i\right)+\mu_e\left(h^e_d-h^d_d\right)+\mu_e\left(h^d_d\sum_i q^d_i-h^e_d\sum_i q^e_i\right)\\
&+\frac{1}{2}\mu_e\left[\left(q^e_{wc}+q^d_{wc}\right)\left(h^e_{wc}-h^d_{wc}\right)+\left(q^e_{wc}-q^d_{wc}\right)\left(h^e_{wc}+h^d_{wc}\right)\right.\\
&+\left(q^e_{wg}+q^d_{wg}\right)\left(h^e_{wg}-h^d_{wg}\right)+\left(q^e_{wg}-q^d_{wg}\right)\left(h^e_{wg}+h^d_{wg}\right)\\
&+\left(q^e_{ac}+q^d_{ac}\right)\left(h^e_{ac}-h^d_{ac}\right)+\left(q^e_{ac}-q^d_{ac}\right)\left(h^e_{ac}+h^d_{ac}\right)\\
&+\left(q^e_{ag}+q^d_{ag}\right)\left(h^e_{ag}-h^d_{ag}\right)+\left(q^e_{ag}-q^d_{ag}\right)\left(h^e_{ag}+h^d_{ag}\right)\\
&+\left(q^e_{sc}+q^d_{sc}\right)\left(h^e_{sc}-h^d_{sc}\right)+\left(q^e_{sc}-q^d_{sc}\right)\left(h^e_{sc}+h^d_{sc}\right)\\
&+\left.\left(q^e_{sg}+q^d_{sg}\right)\left(h^e_{sg}-h^d_{sg}\right)+\left(q^e_{sg}-q^d_{sg}\right)\left(h^e_{sg}+h^d_{sg}\right)\right]
\end{aligned}
\tag{C.67}
$$

Now I begin reducing the equation, bit by bit, like a koala bear consuming a eucalyptus tree leaf by leaf. First, the dry air enthalpy entrainment terms:

$$
\mu_e h^d_d\sum_i\left(q^e_i-q^d_i\right)+\mu_e\left(h^e_d-h^d_d\right)+\mu_e\left(h^d_d\sum_i q^d_i-h^e_d\sum_i q^e_i\right)=\mu_e c_d\left(1-\sum_i q^d_i\right)\left(T^e-T^d\right)
\tag{C.68}
$$

Then, the water vapor and water cloud particle terms:

$$
\begin{aligned}
&\frac{1}{2}\mu_e\left[\left(q^e_{wc}+q^d_{wc}\right)\left(h^e_{wc}-h^d_{wc}\right)+\left(q^e_{wc}-q^d_{wc}\right)\left(h^e_{wc}+h^d_{wc}\right)\right.\\
&+\left(q^e_{wg}+q^d_{wg}\right)\left(h^e_{wg}-h^d_{wg}\right)+\left(q^e_{wg}-q^d_{wg}\right)\left(h^e_{wg}+h^d_{wg}\right)\Big]
\end{aligned}
$$

$$
\begin{aligned}
&= \frac{1}{2}\mu_e(\mathbf{F}_W)\left[\left(q^e_{wg}+q^d_{wg}\right)\left(h^e_{wg}-h^d_{wg}\right)+\left(q^e_{wg}-q^d_{wg}\right)\left(h^e_{wg}-h^d_{wc}+h^d_{wg}-h^d_{wc}\right)\right.\\
&\quad \left.+2q^e_{wc}\left(h^e_{wc}-h^d_{wc}\right)\right]\\
&+ \frac{1}{2}\mu_e(!\mathbf{F}_W)\left[2q^e_{wg}\left(h^e_{wg}-h^d_{wg}\right)+\left(q^e_{wc}-q^d_{wc}\right)\left(h^e_{wc}-h^d_{wc}\right)+\right.\\
&\quad \left.\left(q^e_{wc}-q^d_{wc}\right)\left(h^e_{wc}-h^d_{wg}+h^d_{wc}-h^d_{wg}\right)\right] \qquad \text{(C.69)}\\
&= \mu_e\left(q^e_{wg}c_{wg}+q^e_{wc}c_{wc}\right)\left(T^e-T^d\right)\\
&+ (\mathbf{F}_W)\mu_e\left(q^e_{wg}-q^d_{wg}\right)L^d_W-(!\mathbf{F}_W)\mu_e\left(q^e_{wc}-q^d_{wc}\right)L^d_W \qquad \text{(C.70)}
\end{aligned}
$$

Then, the corresponding terms for ammonia:

$$
\begin{aligned}
&\frac{1}{2}\mu_e\left[\left(q^e_{ac}+q^d_{ac}\right)\left(h^e_{ac}-h^d_{ac}\right)+\left(q^e_{ac}-q^d_{ac}\right)\left(h^e_{ac}+h^d_{ac}\right)\right.\\
&\left.+\left(q^e_{ag}+q^d_{ag}\right)\left(h^e_{ag}-h^d_{ag}\right)+\left(q^e_{ag}-q^d_{ag}\right)\left(h^e_{ag}+h^d_{ag}\right)\right]\\
&= \frac{1}{2}\mu_e(\mathbf{F}_A)\left[\left(q^e_{ag}+q^d_{ag}\right)\left(h^e_{ag}-h^d_{ag}\right)+\left(q^e_{ag}-q^d_{ag}\right)\left(h^e_{ag}-h^d_{ac}+h^d_{ag}-h^d_{ac}\right)\right.\\
&\quad \left.+2q^e_{ac}\left(h^e_{ac}-h^d_{ac}\right)\right]\\
&+ \frac{1}{2}\mu_e(!\mathbf{F}_A)\left[2q^e_{ag}\left(h^e_{ag}-h^d_{ag}\right)+\left(q^e_{ac}-q^d_{ac}\right)\left(h^e_{ac}-h^d_{ac}\right)+\right.\\
&\quad \left.\left(q^e_{ac}-q^d_{ac}\right)\left(h^e_{ac}-h^d_{ag}+h^d_{ac}-h^d_{ag}\right)\right] \qquad \text{(C.71)}\\
&= \mu_e\left(q^e_{ag}c_{ag}+q^e_{ac}c_{ac}\right)\left(T^e-T^d\right)\\
&+ (\mathbf{F}_A)\mu_e\left(q^e_{ag}-q^d_{ag}\right)L^d_A-(!\mathbf{F}_A)\mu_e\left(q^e_{ac}-q^d_{ac}\right)L^d_A \qquad \text{(C.72)}
\end{aligned}
$$

From the above system of ammonia equations, I borrowed a term of $+(\mathbf{F}_S!\mathbf{F}_A)h^d_{ag}\mu_e\left(q^e_{ag}-q^d_{ag}\right)$ and placed it in the block of NH_4SH entrainment terms, which are collectively referenced as X:

$$
\begin{aligned}
X \equiv\ & \frac{1}{2}\mu_e\left[\left(q^e_{ac}+q^d_{ac}\right)\left(h^e_{ac}-h^d_{ac}\right)+\left(q^e_{ac}-q^d_{ac}\right)\left(h^e_{ac}+h^d_{ac}\right)\right.\\
&\left.+\left(q^e_{ag}+q^d_{ag}\right)\left(h^e_{ag}-h^d_{ag}\right)+\left(q^e_{ag}-q^d_{ag}\right)\left(h^e_{ag}+h^d_{ag}\right)\right]\\
&-(\mathbf{F}_S!\mathbf{F}_A)\left(h^d_{sc}-h^d_{ag}\right)\left(q^e_{ag}-q^d_{ag}\right)\\
&-\left[(\mathbf{F}_S\|\mathbf{F}_A)h^d_{sc}+(!\mathbf{F}_S!\mathbf{F}_A)\left(\alpha h^d_{sg}+\beta h^d_{ag}\right)\right]\mu_e\left(q^e_{sc}-q^d_{sc}\right)\\
&-\left[(!\mathbf{F}_S\|\mathbf{F}_A)h^d_{sg}+(\mathbf{F}_S!\mathbf{F}_A)h^d_{sc}\right]\mu_e\left(q^e_{sg}-q^d_{sg}\right) \qquad \text{(C.73)}
\end{aligned}
$$

The combination of the delta functions for NH_3 and NH_4SH can lead to four (2^2) cases, but only three distinct cases exist here, and I analyze them separately:

$$
X(!\mathbf{F}_S!\mathbf{F}_A) = \frac{1}{2}\mu_e\left[\left(q^e_{sc}-q^d_{sc}\right)\left(h^e_{sc}-h^d_{sc}\right)+2q^e_{sg}\left(h^e_{sg}-h^d_{sg}\right)\right.
$$

$$+\left(q_{sc}^{e}-q_{sc}^{d}\right)\left(h_{sc}^{e}-\alpha h_{sg}^{d}-\beta h_{ag}^{d}+h_{sc}^{d}-\alpha h_{sg}^{d}-\beta h_{ag}^{d}\right)\Big] \quad \text{(C.74)}$$

$$= \mu_e\left(q_{sc}^{e}c_{sc}+q_{sg}^{e}c_{sg}\right)\left(T^{e}-T^{d}\right)-\mu_e\left(q_{sc}^{e}-q_{sc}^{d}\right)L_{sc}^{d} \quad \text{(C.75)}$$

$$X(\mathbf{F}_A) = \frac{1}{2}\mu_e\left[2q_{sc}^{e}\left(h_{sc}^{e}-h_{sc}^{d}\right)+2q_{sg}^{e}\left(h_{sg}^{e}-h_{sg}^{d}\right)\right] \quad \text{(C.76)}$$

$$= \mu_e\left(q_{sc}^{e}c_{sc}+q_{sg}^{e}c_{sg}\right)\left(T^{e}-T^{d}\right) \quad \text{(C.77)}$$

$$X(\mathbf{F}_S!\mathbf{F}_A) = \frac{1}{2}\mu_e\Bigg[2q_{sc}^{e}\left(h_{sc}^{e}-h_{sc}^{d}\right)+2\left(q_{ag}^{e}-q_{ag}^{d}\right)\overbrace{\left(h_{ag}^{d}-h_{sc}^{d}\right)}^{\star 2}$$

$$+\left(q_{sg}^{e}-q_{sg}^{d}\right)\overbrace{\left(h_{sg}^{e}+h_{sg}^{d}-2h_{sc}^{d}\right)}^{\star 1}\Bigg] \quad \text{(C.78)}$$

The reduction of $\star 1$ and $\star 2$ requires the development of one final enthalpy identity. According to Equation C.50,

$$h_{sg}-h_{ag} = c_{sg}\left(T+C_S\right)-c_{ag}\left(T+C_A\right) \quad \text{(C.79)}$$

$$\equiv T\left(c_{sg}-c_{ag}\right)+C_\star \quad \text{(C.80)}$$

The constant $C_\star$ combines the ammonia and H_2S constants of integration from Equations C.50. Unfortunately $C_\star$ is unconstrained. The following derivation assumes that this constant can be set to zero. Although this assumption results in slightly less inelegant equations, it is not mathematically justified. Therefore, the final lapse rate equation in this appendix will have $C_\star$ restored, for thoroughness. Thus, with $C_\star = 0$, the following reduction for $\star 1$ can be performed:

$$\star 1 = -\Big(h_{sc}^{d}-\alpha h_{sg}^{e}-\beta h_{ag}^{e}+h_{sc}^{d}-\alpha h_{sg}^{d}$$

$$-\beta h_{ag}^{d}-\beta h_{sg}^{e}-\beta h_{sg}^{d}+\beta h_{ag}^{e}+\beta h_{ag}^{d}\Big) \quad \text{(C.81)}$$

$$= 2L_{sc}^{d}+\alpha\left(h_{sg}^{e}-h_{sg}^{d}\right)+\beta\left(h_{ag}^{e}-h_{ag}^{d}\right)$$

$$+\beta\left(h_{sg}^{e}+h_{sg}^{d}-h_{ag}^{e}-h_{ag}^{d}\right) \quad \text{(C.82)}$$

$$= 2L_{sc}^{d}+\alpha\left(h_{sg}^{d}-h_{ag}^{d}\right)+\left(h_{sg}^{e}-h_{sg}^{d}\right) \quad \text{(C.83)}$$

$$= 2L_{sc}^{d}+\alpha T^{d}\left(c_{sg}-c_{ag}\right)+\left(h_{sg}^{e}-h_{sg}^{d}\right) \quad \text{(C.84)}$$

$$\star 2 = h_{ag}^d - h_{sc}^d = \beta h_{ag}^d + \alpha h_{sg}^d - h_{sc}^d - \alpha h_{sg}^d + \alpha h_{ag}^d \tag{C.85}$$

$$= L_{sc}^d + \alpha \left(h_{ag}^d - h_{sg}^d\right) \tag{C.86}$$

$$= L_{sc}^d - \alpha T^d \left(c_{sg} - c_{ag}\right) \tag{C.87}$$

The application of these identities to Equation C.78 leads to:

$$\begin{aligned} X(\mathbf{F}_S!\mathbf{F}_A) &= \frac{1}{2}\mu_e \Big[2\left(q_{sc}^e c_{sc} + q_{sg}^e c_{sg}\right)\left(T^e - T^d\right) + 2L_{sc}^d\left(q_{sg}^e - q_{sg}^d + q_{ag}^e - q_{ag}^d\right) \\ &\quad + \alpha\left(q_{sg}^e - q_{sg}^d\right)T^d\left(c_{sg} - c_{ag}\right) - 2\alpha\left(q_{ag}^e - q_{ag}^d\right)T^d\left(c_{sg} - c_{ag}\right)\Big] \quad \text{(C.88)} \\ &= \mu_e\left(c_{sc}q_{sc}^e + c_{sg}q_{sg}^e\right)\left(T^e - T^d\right) + \mu_e L_{sc}^d\left(q_{sg}^e - q_{sg}^d + q_{ag}^e - q_{ag}^d\right) \\ &\quad + \mu_e T^d\left(c_{sg} - c_{ag}\right)\left[\beta\left(q_{sg}^e - q_{sg}^d\right) - \alpha\left(q_{ag}^e - q_{ag}^d\right)\right] \quad \text{(C.89)} \end{aligned}$$

I can now write Equation C.67 in its enthalpy-free form:

$$
\begin{aligned}
0 \;=\; & \frac{1}{\rho}\frac{dp}{dz} - c^{d*}\frac{dT}{dz} + \mu_e\left(T^e - T^d\right)\left[c_d\left(1 - \sum_i q_i^e\right) + \sum_i \left(q_i^e c_i\right)\right] \\
& - (\mathbf{F}_W) L_W^d \left(\frac{\partial Q_W}{\partial p}\frac{dp}{dz} + \frac{\partial Q_W}{\partial T}\frac{dT}{dz}\right) - (\mathbf{F}_A) L_A^d \left(\frac{\partial Q_A}{\partial p}\frac{dp}{dz} + \frac{\partial Q_A}{\partial T}\frac{dT}{dz}\right) \\
& - (\mathbf{F}_S!\mathbf{F}_A) L_S^d \left(\frac{4705\ln(10)K}{T^2\left(\beta Q_S + \alpha Q_{A(S)}\right)}\frac{dT}{dz} - \frac{2K}{p\left(\beta Q_S + \alpha Q_{A(S)}\right)}\frac{dp}{dz}\right) \\
& + \mu_e L_W^d \begin{cases} +(\mathbf{F}_W)\left(q_{wg}^e - q_{wg}^d\right) \\ -(!\mathbf{F}_W)\left(q_{wc}^e - q_{wc}^d\right) \end{cases} \\
& + \mu_e L_A^d \begin{cases} +(\mathbf{F}_A)\left(q_{ag}^e - q_{ag}^d\right) \\ -(!\mathbf{F}_A)\left(q_{ac}^e - q_{ac}^d\right) \end{cases} \\
& + \mu_e L_S^d \begin{cases} +(\mathbf{F}_S!\mathbf{F}_A)\left(q_{sg}^e - q_{sg}^d + q_{ag}^e - q_{ag}^d\right) \\ -(!\mathbf{F}_S!\mathbf{F}_A)\left(q_{sc}^e - q_{sc}^d\right) \end{cases} \\
& + (!\mathbf{F}_A!\mathbf{F}_S)\mu_e T^d\left(c_{sg} - c_{ag}\right)\left[\beta\left(q_{sg}^e - q_{sg}^d\right) - \alpha\left(q_{ag}^e - q_{ag}^d\right)\right]
\end{aligned}
\tag{C.90}
$$

Then, with a little rearranging, as well as the understanding that c^{d*} and c^{e*} respectively contain the downdraft and environmental mixing ratios, the pressure and temperature differentials can be isolated:

$$
\begin{aligned}
& \left[c^{d*} + (\mathbf{F}_W) L_W^d \frac{\partial Q_W}{\partial T} + (\mathbf{F}_A) L_A^d \frac{\partial Q_A}{\partial T} + (\mathbf{F}_S!\mathbf{F}_A) L_S^d \frac{4705\ln(10)K}{T^2\left(\beta Q_S + \alpha Q_{A(S)}\right)}\right]\frac{dT}{dz} \\
= \; & \left[\frac{1}{\rho} - (\mathbf{F}_W) L_W^d \frac{\partial Q_W}{\partial p} - (\mathbf{F}_A) L_A^d \frac{\partial Q_A}{\partial p} - (\mathbf{F}_S!\mathbf{F}_A) L_S^d \frac{-2K}{p\left(\beta Q_S + \alpha Q_{A(S)}\right)}\right]\frac{dp}{dz} \\
& + \mu_e c^{e*}\left(T^e - T^d\right) + \mu_e L_W^d \begin{cases} +(\mathbf{F}_W)\left(q_{wg}^e - q_{wg}^d\right) \\ -(!\mathbf{F}_W)\left(q_{wc}^e - q_{wc}^d\right) \end{cases} \\
& + \mu_e L_A^d \begin{cases} +(\mathbf{F}_A)\left(q_{ag}^e - q_{ag}^d\right) \\ -(!\mathbf{F}_A)\left(q_{ac}^e - q_{ac}^d\right) \end{cases} \\
& + \mu_e L_S^d \begin{cases} +(\mathbf{F}_S!\mathbf{F}_A)\left(q_{sg}^e - q_{sg}^d + q_{ag}^e - q_{ag}^d\right) \\ -(!\mathbf{F}_S!\mathbf{F}_A)\left(q_{sc}^e - q_{sc}^d\right) \end{cases} \\
& + (!\mathbf{F}_A!\mathbf{F}_S)\mu_e T^d\left(c_{sg} - c_{ag}\right)\left[\beta\left(q_{sg}^e - q_{sg}^d\right) - \alpha\left(q_{ag}^e - q_{ag}^d\right)\right]
\end{aligned}
\tag{C.91}
$$

Recall that the reduction of Equation C.78 involved setting the undefined constant of integration $C_\star$ to zero. The lapse rate can be represented without this simplifying

assumption as:

$$
\begin{aligned}
\frac{dT}{dz} \;=\; & \left[c^{d*} + (\mathbf{F}_W) L_W^d \frac{\partial Q_W}{\partial T} + (\mathbf{F}_A) L_A^d \frac{\partial Q_A}{\partial T} + (\mathbf{F}_S !\mathbf{F}_A) L_S^d \frac{4705 \ln(10) K}{T^2 \left(\beta Q_S + \alpha Q_{A(S)}\right)}\right]^{-1} \times \\
& \left(\left[\frac{1}{\rho} - (\mathbf{F}_W) L_W^d \frac{\partial Q_W}{\partial p} - (\mathbf{F}_A) L_A^d \frac{\partial Q_A}{\partial p} - (\mathbf{F}_S !\mathbf{F}_A) L_S^d \frac{-2K}{p\left(\beta Q_S + \alpha Q_{A(S)}\right)}\right] \frac{dp}{dz}\right. \\
& + \mu_e c^{e*} \left(T^e - T^d\right) + \mu_e L_W^d \begin{cases} +(\mathbf{F}_W)\left(q_{wg}^e - q_{wg}^d\right) \\ -(!\mathbf{F}_W)\left(q_{wc}^e - q_{wc}^d\right) \end{cases} \\
& + \mu_e L_A^d \begin{cases} +(\mathbf{F}_A)\left(q_{ag}^e - q_{ag}^d\right) \\ -(!\mathbf{F}_A)\left(q_{ac}^e - q_{ac}^d\right) \end{cases} \\
& + \mu_e L_S^d \begin{cases} +(\mathbf{F}_S !\mathbf{F}_A)\left(q_{sg}^e - q_{sg}^d + q_{ag}^e - q_{ag}^d\right) \\ -(!\mathbf{F}_S !\mathbf{F}_A)\left(q_{sc}^e - q_{sc}^d\right) \end{cases} \\
& \left. + (!\mathbf{F}_A !\mathbf{F}_S) \mu_e \left[C_* + T^d \left(c_{sg} - c_{ag}\right)\right] \left[\beta\left(q_{sg}^e - q_{sg}^d\right) - \alpha\left(q_{ag}^e - q_{ag}^d\right)\right]\right) \qquad \text{(C.92)}
\end{aligned}
$$

BIBLIOGRAPHY

BIBLIOGRAPHY

Adachi, H., Basco, N., James, D.G.L. (1979) A quantitative study of alkyl radical reactions by kinetic spectroscopy. III. Absorption spectrum and rate constants of mutual interaction for the ethyl radical. *Int. J. Chem. Kinet.* 11, 995–1005.

Akimoto, H., Obi, K., Tanaka, I. (1965) Primary process in the photolysis of ethane at 1236 Å. *J. Chem. Phys.* 42, 3864–3868.

Allan, M. (1984) The excited states of 1,3–butadiyne determined by electron energy loss spectroscopy. *J. Chem. Phys.* 80n12, 6020–6024.

Allara, D.L., Shaw, R. (1980) A compilation of kinetic parameters for the thermal degradation of *n*-alkane molecules. *J. Phys. Chem. Ref. Data* 9, 523–559.

Allen, M., Yung, Y.L., Gladstone, G.R. (1992) The relative abundance of ethane to acetylene in the jovian stratosphere. *Icarus* 100, 527–533.

Anastasi, C., Arthur, N.L. (1987) Rate constants for the reaction of CH_3 radicals with C_2H_5, *i*-C_3H_7, and *t*-C_4H_9 radicals. *J. Chem. Soc. Faraday Trans.* 2 83, 277–287.

Anders, E., Grevesse, N. (1989) Abundances of the elements—Meteoritic and solar. *Geochim. Cosmochim. Acta* 53, 197–214.

Ashfold, M.N.R., Fullstone, M.A., Hancock, G., Ketley, G.W. (1981) Singlet methylene kinetics: direct measurements of removal rates of a^1A_1 and b^1B_1 CH_2 and CD_2. *Chemical Physics* 55n2, 245–257.

Atkinson, D.B., Hudgens, J.W., (1999) Rate coefficients for the propargyl radical self-reaction and oxygen addition reaction measured using ultraviolet cavity ring-down spectroscopy. *J. Phys. Chem. A* 103, 4242–4252.

Atreya, S.K. (1986) *Atmospheres and Ionospheres of the Outer Planets and Their Satellites.* New York-Berlin: Springer-Verlag.

Atreya, S.K., Romani, P.N. (1985) Photochemistry and clouds of Jupiter, Saturn and Uranus. In *Recent Advances in Planetary Meteorology*, ed. G. E. Hunt, pp. 17–68. New York: Cambridge University Press.

Atreya, S.K., T.M. Donahue, and W.R. Kuhn (1977) The distribution of ammonia and its photochemical products on Jupiter. *Icarus* 31, 348.

Atreya, S.K., Donahue, T.M., Festou, M.C. (1981) Jupiter: Structure and composition of the upper atmosphere. *Astrophys. J.* 247, L43–L47.

Atreya, S.K., Owen, T.C., Wong, M.H., Niemann, H.B., Mahaffy, P.R. (1996) Condensible volatiles, clouds, and implications for meteorology in the Galileo Probe entry region. *Bull. Am. Astron. Soc.* 28, 1133.

Atreya, S.K., Wong, M.H., Owen, T.C., Niemann, H.B., Mahaffy, P.R. (1997) Chemistry and Clouds of the Atmosphere of Jupiter: A Galileo Perspective. In *Three Galileos: The Man, The Spacecraft, The Telescope*, ed. C. Barbieri et al., pp.249–260.

Dordrecht, The Netherlands: Kluwer Academic Publishers.

Atreya, S.K., Edgington, S.G, Encrenaz, Th., and Feuchtgruber, H. (1999a) ISO observations of C_2H_2 on Uranus and CH_3 on Saturn: Implications for atmospheric vertical mixing in the Voyager and ISO epochs, and a call for relevant laboratory data. In *The Universe As Seen by ISO*, ed. P. Cox et al., ESA SP-427.

Atreya, S.K., Wong, M.H., Owen, T.O., Mahaffy, P.R. Niemann, H.B., de Pater, I., Drossart, P., Encrenaz, Th. (1999b) A comparison of the atmospheres of Jupiter and Saturn: Deep atmospheric composition, cloud structure, vertical mixing, and origin. *Planetary and Space Science* 47, 1243–1262.

Au, J.W., Cooper, G., Brion, C.E. (1993) The molecular and dissociative photoionization of ethane, propane, and *n*-butane: absolute oscillator strengths (10–80 eV) and breakdown pathways. *Chemical Physics* 173n2, 241–265.

Baines, K.H., Mickelson, M.E., Larson, L.E., Ferguson, D.W. (1995) The abundances of methane and ortho/para hydrogen on Uranus and Neptune: Implications of new laboratory 4-0 quadrupole line parameters. *Icarus* 114, 328–340.

Baker, R.D., Schubert, G. (1998) Deep convective entrainment by downdrafts in Jupiter's atmosphere. *Icarus* 136, 340–343.

Banfield, D., Gierasch, P.J., Bell, M., Ustinov, E., Ingersoll, A.P., Vasavada, A.R., West, R.A., Belton, M.J.S. (1998) Jupiter's cloud structure from Galileo imaging data. *Icarus* 135, 230–250.

Bar-Nun, A., Kleinfeld, I., Kochavi, E. (1988) Trapping of gas mixtures by amorphous water ice. *Phys. Rev. B.* 38, 7749–7754.

Baron, R., Joseph, R.D., Owen, T.C., Tennyson, J., Miller, S., Ballester, G.E. (1991) Imaging Jupiter's aurorae from H_3^+ emissions in the 3–4 μm band. *Nature* 353, 539–542.

Baulch, D.L. et al. (1992) Evaluated kinetic data for combustion modelling. *J. Phys. Chem. Ref. Data* 21, 411–734.

Becker, K.H., Engelhardt, B., Wiesen, P., Bayes, K.D. (1989) Rate constants for $CH(X^2\Pi)$ reactions at low total pressures. *Chemical Physics Letters* 154n4, 342–348.

Bergmann, K., Demtröder, W. (1968) Mass-spectrometric investigation of the primary processes in the photodissociation of 1,3–butadiene. *J. Chem. Phys.* 48, 18–22.

Berman, M.R., Lin, M.C. (1983) Kinetics and mechanisms of the reactions of CH with CH_4, C_2H_6, and n-C_4H_{10}. *Chem. Phys.* 82, 435–442.

Bevington, P.R., Robinson, D.K. (1992) *Data reduction and error analysis for the physical sciences.* Dubuque IA: WCB/McGraw-Hill.

Bishop, J., Romani, P.N., Atreya, S.K. (1998) Voyager 2 ultraviolet spectrometer solar occultations at Neptune: photochemical modeling of the 125–165 nm lightcurves. *Planet. Space Sci.* 46, 1–20.

Bjoraker, G.L. (1985) *The gas composition and vertical cloud structure of Jupiter's troposphere derived from five micron spectroscopic observations.* Ph.D. Thesis. Tucson AZ: The University of Arizona.

Bjoraker, G.L., Larson, H.P., Kunde, V.G. (1986) The gas composition of Jupiter derived from 5-μm airborne spectroscopic observations. *Icarus* 66, 579–609.

Bjoraker, G.L., Larson, H.P., Kunde, V.G. (1986) The abundance and distribution of water vapor in Jupiter's atmosphere. *Astrophys. J.* 311, 1058–1072.

Bodenheimer, P., Pollack, J. B. (1986) Calculations of the accretion and evolution of giant planets—The effects of solid cores. *Icarus* 67, 391–408.

Bohland, T., Temps, F.,Wagner, H.G. (1985) The contribution of intersystem crossing and reaction in the removal of $CH_2(\tilde{a}\ ^1A_1)$ by hydrocarbons studied with the LMR. *Ber. Bunsen-Ges. Phys. Chem.* 89, 1013–1018.

Bohland, T., Temps, F.,Wagner, H.G. (1986) Kinetics of the reactions of CH_2 $(\tilde{X}\,^3B_1)$ radicals with C_2H_2 and C_4H_2 in the temperature range 296 K $\leq$T $\leq$700 K. In *Twenty-first symposium international on combustion*, pp. 841–850. Pittsburgh PA: Combustion Institute.

Boss, A.P. (1986) Theoretical determination of the minimum protostellar mass. In *Astrophysics of brown dwarfs*, pp. 206-210. Proceedings of the Workshop, Fairfax, VA, Oct. 14–15, 1985. Cambridge, England and New York: Cambridge University Press.

Braude, E.A. (1945) Ultra-violet light absorption and the structure of organic compounds. *Annu. Rep. Prog. Chem.* 42, 105–130.

Braun, W., Bass, A.M., Pilling, M. (1970) Flash photolysis of ketene and diazomethane: The production and reaction kinetics of triplet and singlet methylene. *J. Chem. Phys.* 52, 5131–5143.

Broadfoot, A.L., Belton, M.J.S., Takacs, P.Z., Sandel, B.R., Shemansky, D.E., Holberg, J.B., Ajello, J.M., Atreya, S.K., Donahue, T.M., Moos, H.W., Bertaux, J.L., Blamont, J.E., Strobel, D.F., McConnell, J.C., Dalgarno, A., Goody, R., McElroy, M.B. (1979) Extreme ultraviolet observations from Voyager 1 encounter with Jupiter. *Science* 204, 979–982.

Brouard, M., McPherson, M.T., Pilling, M.J. (1989) Experimental and RRKM modelling study of the CH_3 + H and CH_3 + D reactions. *J. Phys. Chem.* 93, 4047–4059.

Brownsword, R.A., Canosa, A., Rowe, B.R., Sims, I.R., Smith, I.W.M., Stewart, D.W.A., Symonds, A.C., Travers, D. (1997) Kinetics over a wide range of temperature (13–744 K): Rate constants for the reactions of CH (n=0) with H_2 and D_2 and for the removal of CH (n=1) by H_2 and D_2. *J. Chem. Phys.* 106, 7662–7677.

Bézard, B., Feuchtgruber, H., Moses, J.I., Encrenaz, T. (1998) Detection of methyl radicals (CH3) on Saturn. *Astron. Astrophys.* 334, L41–L44.

Bézard, B. (1998) Detection of new hydrocarbons on the giant planets. *Bull. Am. Astron.*

Soc. 30, 1059.

Caldwell, J.J. (1977) Ultraviolet observations of Mars and Saturn by the TD1A and OAO-2 satellites. *Icarus* 32, 190–209.

Callear, A.B., Smith, G.B. (1986) Recurring chains following addition of atomic hydrogen to acetylene. *J. Phys. Chem.* 90, 3229–3237.

Calvert, J.G., Pitts, J.N. Jr. (1966) *Photochemistry*. New York NY: Wiley.

Cameron, A.G.W. (1978) Physics of the primitive solar accretion disk. *Moon and the Planets* 18, 5–40.

Cameron, A.G.W. (1989) Comment following "The formation of the solar system: Consensus, alternatives, and missing factors," by G.W. Wetherill. In *The Formation and Evolution of Planetary Systems*, eds. H.A. Weaver and L. Danly, p. 29. Cambridge: University of Cambridge Press.

Canosa, A., Sims, I.R., Travers, D., Smith, I.W.M., Rowe, B.R. (1997) Reactions of the methylidine radical with CH_4, C_2H_2, C_2H_4, C_2H_6, and but-1-ene studied between 23 and 295 K with a CRESU apparatus. *Astron. Astrophys.* 323, 644–651.

Carlson, B.E., Lacis, A.A., Rossow, W.B. (1993) Tropospheric gas composition and cloud structure of the Jovian North Equatorial Belt. *J. Geophys. Res.* 98, 5251–5290.

Chang, A.H.H., Mebel, A.M., Yang, X.M., Lin, S.H., Lee, Y.T. (1998) Ab initio/RRKM approach toward the understanding of ethylene photodissociation. *J. Chem. Phys.* 109, 2748–2761.

Chastaing, D., James, P.I., Sims, I.R., Smith, I.W.M. (1998) Neutral-neutral reactions at the temperatures of interstellar clouds: Rate coefficients for reactions of C_2H radicals with O_2, C_2H_2, C_2H_4 and C_3H_6 down to 15 K. *Faraday Discuss. Chem. Soc.* 109, 165–181.

Chen, F., Judge, D.L., Wu, C.Y.R. (1999) Temperature dependent photoabsorption cross sections of allene and methylacetylene in the VUV-UV region. Submitted to *J.Quant. Spectrosc. Radiative Transfer*, 16 June 1999.

Chen, F., Judge, D.L., Wu, C.Y.R., Caldwell, J.J., White, H.P., Wagener, R. (1991) High-resolution, low-temperature photoabsorption cross sections of C_2H_2, PH_3, and GeH_4, with application to Saturn's atmosphere. *J. Geophys. Res.* 96(E2), 17519–17527.

Cole, J.A., Bittner, J.D., Longwell, J.P. (1984) Formation mechanisms of aromatic compounds in aliphatic flames. *Combust. Flame* 56, 51–70.

Collin, G.J. (1988) Photochemistry of simple olefins: Chemistry of electronic excited states or hot ground state? *Adv. Photochem.* 14, 135–176.

Collin, G.J., Wieckowski, A. (1978) Photolysis of *n*-butene and isobutene at 174.3–174.5 nm (7.10 eV). *J. Photochem.* 8, 103–116.

Conrath, B.J., Gierasch, P.J. (1984) Global variation of the para hydrogen fraction in Jupiter's atmosphere and implications for dynamics on the outer planets. *Icarus* 57, 184–204.

Cotton, W.R. (1989) *Storm and cloud dynamics.* San Diego CA: Academic Press, Inc.

Courtin, R., Gautier, D., Marten, A., Bézard, B., Hanel, R. (1984) The composition of Saturn's atmosphere at Northern temperate latitudes from Voyager IRIS spectra: NH_3, PH_3, C_2H_2, C_2H_6, CH_3D, CH_4, and the Saturnian D/H ratio. *Astrophys. J.* 287, 899–916.

Darwin, G.H. (1899) *Mon. Not. Roy. Astron. Soc.* 60, 82.

Dean, J.A., ed. (1992) *Lange's Handbook of Chemistry.* New York NY: McGraw-Hill.

de Graauw, Th., Feuchtgruber, H., Bézard, B., Drossart, P., Encrenaz, Th., Beintema, D.A., Griffin, M., Heras, A., Kessler, M., Leech, K., Lellouch, E., Morris, P., Roelfsema, P.R., Roos-Serote, M., Salama, A., Vandenbussche, B., Valentijn, E.A., Davis, G.R., Naylor, D.A. (1997) First results of ISO SWS observations of Saturn: Detection of CO_2, CH_3C_2H, C_4H_2 and tropospheric H_2O. *Astron. Astrophys.* 321, L13-L16.

de Pater, I., Massie, S.T. (1985) Models of the millimeter-centimeter spectra of the giant planets, *Icarus* 62, 143–171.

de Pater, I. (1991) The significance of microwave observations for the planets. *Physics Reports (Review section of Physics Letters)* 200n1, 1–50.

de Pater, I., Dickel, J. R. (1986) Jupiter's zone-belt structure at radio wavelengths. I. Observations. *Astrophysical Journal, Part 1* 308, 459–471.

de Pater, I., Dunn, D., Romani, P.N., Zahnle, K. (2001) Reconciling Galileo Probe Data and Ground-based Radio Observations of Ammonia on Jupiter. *Icarus*, in press.

de Pater, I., Heiles, C., Wong, M.H., Maddalena, R.J., Bird, M.K., Funke, O., Neidhoefer, J., Price, R.M., Kesteven, M., Calabretta, M., Klein, M.J., Gulkis, S., Bolton, S.J., Foster, R.S., Sukumar, S., Strom, R.G., LePoole, R.S., Spoelstra, T., Robison, M., Hunstead, R.W., Campbell-Wilson, D., Ye, T., Dulk, G., LeBlanc, Y., Galopeau, P., Gerard, E., Lecheaux, A. (1995) Outburst of Jupiter's Synchrotron Radiation Following the Impact of Comet P/Shoemaker-Levy 9. *Science* 268n5219, 1879–1883.

Del Genio, A.D., McGrattan, K.B. (1990) Moist convection and the vertical structure and water abundance of Jupiter's atmosphere. *Icarus* 84, 29–53.

Diaz, Z., Doepker, R.D. (1977) Gas-phase photolysis of 1,2–butadiene at 147.0 nm. *J. Phys. Chem.* 81, 1442–1446.

Drossart, P. (1998) Saturn tropospheric water measured with ISO/SWS. *Bull. Am. Astron. Soc.* 30, 1060.

Drossart, P., Encrenaz, Th. (1982) The abundance of water on Jupiter from the Voyager IRIS data at 5 micron. *Icarus* 52, 483–491.

Drossart, P., Maillard, J-P., Caldwell, J., Kim S.J., Watson, J.K.G., Majewsky, W.A., Tennyson, J., Miller, S., Atreya, S.K., Clarke, J.T., Waite, J.H., Wagener, R. (1989) Detection of H_3^+ on Jupiter. *Nature* 340, 539–541.

Edgington, S.G. (1997) *Latitude variations of the abundances of ammonia, acetylene, and phosphine and vertical mixing in the atmospheres of Jupiter and Saturn.* Ph.D. Thesis. Ann Arbor MI: The University of Michigan.

Edgington, S.G., Atreya, S.K., Trafton, L.M., Caldwell, J.J., Beebe, R.F., Simon, A.A., West, R.A., and Barnet, C. (1998) On the latitude variation of ammonia, acetylene, and phosphine altitude profiles on Jupiter from HST Faint Object Spectrograph observations. *Icarus* 133, 192–209.

Edgington, S.G., Atreya, S.K., Trafton, L.M., Caldwell, J.J., Beebe, R.F., Simon, A.A., West, R.A. (1999) Ammonia and eddy mixing variations in the upper troposphere of Jupiter from HST Faint Object Spectrograph observations. *Icarus* 142, 342–356.

Encrenaz, Th., Combes, M., Zeau, Y. (1978) The spectrum of Jupiter between 10 and 13 microns: An estimate of the Jovian $^{14}N/^{15}N$ ratio. *Astron. Astrophys.* 70, 29.

Fahr, A., Nayak, A.K. (1994) Temperature dependent ultraviolet absorption cross sections of 1,3–butadiene and butadiyne. *Chem. Phys.* 189n3, 725–731.

Fahr, A., Nayak, A.K. (1996) Temperature dependent ultraviolet absorption cross sections of propylene, methylacetylene and vinylacetylene. *Chem. Phys.* 203n3, 351–358.

Fahr, A., Hassanzadeh, P., Atkinson, D.B. (1998) Ultraviolet absorption spectrum and cross-sections of vinyl (C_2H_3) radical in the 225–238 nm region. *Chem. Phys.* 236n1-3, 43–51.

Fahr, A., Laufer, A., Klein, R., Braun, W. (1991) Reaction rate of determinations of vinyl radical reactions with vinyl, methyl, and hydrogen atoms. *J. Phys. Chem.* 95, 3218.

Fahr, A., P.S. Monks, L.J. Stief, and H.A. Laufer (1995) Experimental determination of the rate constant for the reaction of C_2H_3 with H_2 and implications for the partitioning of hydrocarbons in atmospheres of the outer planets. *Icarus* 116, 415–422.

Fegley, B. Jr., Lodders, K. (1994) Chemical models of the deep atmospheres of Jupiter and Saturn. *Icarus* 110, 117–154.

Festou, M.C., Atreya, S.K., Donahue, T.M., Sandel, B.R., Shemansky, D.E, and Broadfoot, A.L. (1981) Composition and thermal profile of the Jovian atmosphere determined by the Voyager ultraviolet stellar occultation experiment. *J. Geophys. Res.* 86, 5715.

Feuchtgruber, H., Lellouch, E., de Graauw, Th., Bézard, B., Encrenaz, Th., Griffin, M. (1997) External source of oxygen in the atmospheres of the giant planets. *Nature* 389, 159–162.

Folkner, W.M., Woo, R., Nandi, S. (1998) Ammonia abundance in Jupiter's atmosphere derived from attenuation of the Galileo probe's radio signal. *J. Geophys. Res.* 103, 22847–22856.

Fouchet, T., Lellouch, E., Bézard, B., Encrenaz, Th., Drossart, P., Feuchtgruber, H., de Graauw, T. (2000) ISO-SWS observations of Jupiter: Measurement of the ammonia tropospheric profile and of the 15N/14N isotopic ratio. *Icarus* 143, 223–243.

Frank, P., Just, Th. (1980) High temperature thermal decomposition of acetylene and diacetylene at low relative concentrations. *Combust. Flame* 38, 231–248.

Frommhold, L., Birnbaum, G. (1984) Hydrogen dimer structures in the F.I.R. spectra of Jupiter and Saturn. *Astrophys. J.* 283, L79–L82.

Frost, R.K., Arrington, C.A., Ramos, C., Zwier, T.S. (1996) Ultraviolet photochemistry of diacetylene: The metastable C4H2* reaction with ethane, propene, and propyne. *J. Am. Chem. Soc.* 118, 4451–4461.

Gallant, R.A. (1980) *Our Universe.* Washington DC: National Geographic Society.

Gautier, D., Owen, T. (1989) The composition of outer planet atmospheres. In *Origin and Evolution of Planetary and Satellite Atmospheres*, eds. S.K. Atreya et al., pp. 487–512. Tucson AZ: University of Arizona Press.

Gautier, D., Marten, A., Baluteau, J.P., Bachet, G. (1983) About unidentified features in the Voyager far infrared spectra of Jupiter and Saturn. *Canad. J. Phys.* 61, 1455–1461.

Gautier, D., Bézard, B., Marten, A., Baluteau, J.P., Scott, N., Chedin, A., Kunde, V., Hanel, R. (1982) The C/H ratio in Jupiter from the Voyager infrared investigation. *Astrophys. J.* 257, 901–912.

Gierasch, P.J., Ingersoll, A.P., Banfield, D., Ewald, S.P., Helfenstein, P., Simon-Miller, A., Vasavada, A., Breneman, H.H., Senske, D.A., and the Galileo Imaging Team (2000) Observation of moist convection in Jupiter's atmosphere. *Nature* 403, 628–630.

Gladstone, G.R. (1983) *Radiative transfer and photochemistry in the upper atmosphere of Jupiter.* Ph.D. Thesis. Pasadena CA: California Institute of Technology.

Gladstone, G.R., Allen, M., Yung, Y.L. (1996) Hydrocarbon photochemistry in the upper atmosphere of Jupiter. *Icarus* 119, 1–52.

Glicker, S., Okabe, H. (1987) Photochemistry of diacetylene. *J. Phys. Chem.* 91, 437–440.

Gorden, R., Ausloos, P. (1967) Gas phase photolysis and radiolysis of methane: formation of hydrogen and ethylene. *J. Chem. Phys.* 46, 4823–4834.

Guillot, T. (1995) Condensation of methane, ammonia, and water and the inhibition of convection in giant planets. *Science* 269, 1697–1699.

Haman, K.E. (1973) On the updraft-downdraft interaction in convective clouds. *Acta Geophysica Polonica* 21n3, 215–233.

Haman, K.E., Niewiadomski, M. (1980) Cold downdrafts in cumulonimbus clouds. *Tellus* 32, 525–536.

Hampson, R.F., McNesby, J.R. (1965) Vacuum ultraviolet photolysis of ethane at high

temperature. *J. Chem. Phys.* 42, 2200.

Hanel, R., Conrath, B., Flasar, M., Kunde, V., Lowman, P., Maguire, W., Pearl, J., Perraglia, J., Samuelson, R., Gautier, D., Gierasch, P., Kumar, S., Ponnamperuma, C. (1979) Infrared observations of the Jovian system from Voyager 1. *Science* 204, 972.

Hanning-Lee, M.A., Pilling, M.J. (1992) Kinetics of the reaction between H-atoms and allyl radicals. *Int. J. Chem. Kinet.* 24(3), 271–278.

Hautman, D.J., Santoro, R.J., Dryer, F.L., Glassman, I. (1981) An overall and detailed kinetic study of the pyrolysis of propane. *Int. J. Chem. Kinet.* 13, 149–172.

Hess, S.L. (1959) *Introduction to Theoretical Meteorology.* New York NY: Holt, Rinehart, and Winston.

Hill, K.L., Doepker, R.D. (1972) Vacuum-ultraviolet photolysis of the C_4H_6 isomers. IV. 1-Butyne. *J. Phys. Chem.* 76, 1112–1119.

Hintregger, H.E. (1981) Representations of solar EUV fluxes for aeronomical applications. *Adv. Space Res.* 1, 39–52.

Hoffman, J.P., Steffes, P.G., DeBoer, D.R. (1999) Laboratory measurements of phosphine opacity: Implications for planetary radio science. *Icarus* 140, 235–238.

Hoffman, J.H., Hodges, R.R., Jr., McElroy, M.B., Donahue, T.M., Kolpin, M. (1979) Composition and structure of the Venus atmosphere: results from Pioneer Venus. *Science* 205, 49–52.

Holland, D.M.P., Shaw, D.A., Hayes, M.A., Shpinkova, L.G., Rennie, E.E., Karlsson, L., Baltzer, P., Wannberg, B. (1997) The effect of vibrational and electronic autoionization on the vibrational populations in the wavelength range 618–750 Å. *Chem. Phys.* 219n1, 91–116.

Homann, K.H., Schweinfurth, H. (1981) Kinetics and mechanism of hydrocarbon formation in the system C_2H_2/O/H. *Ber. Bunsenges. Phys. Chem.* 85, 569–577.

Hoobler, R.J., Leone, S.R. (1997) Rate coefficients for reactions of ethynyl radical (C_2H) with HCN and CH_3CN: Implications for the formation of complex nitriles on Titan. *Journal of Geophysical Research* 102, 28717–28724.

Houze, R.A. (1993) *Cloud Dynamics.* San Diego CA: Academic Press.

Hueso, R., Sánchez-Lavega, A. (2001) A three-dimensional model of moist convection for the giant planets: The Jupiter case. *Icarus*, in press.

Hueso, R., Sánchez-Lavega, A., Drossart, P. (1999) A theoretical study of parcel stability and cloud distribution in a Jovian hot spot. *Planetary and Space Science* 47, 1263–1275.

Hunten, D.M. (1975) Vertical transport in atmospheres. In *Atmospheres of Earth and the Planets*, ed. B.M. McCormac, pp. 59–72. Dordrecht, Holland: D.Reidel Publishing

Company.

Hunziker, H.E., Kneppe, H., McLean, A.D., Siegbahn, P., Wendt, H.R. (1983) Visible electronic absorption spectrum of vinyl radical. *Can. J. Chem.* 61, 993–995.

Ibragimov, K.Y., Solodovnik, A.A. (1991) NH_4SH and cloud cover in the atmospheres of the giant planets. *Kinematika i Fizika Nebesnykh Tel* 7, 58–63.

Iribarne, J.V., Godson, W.L. (1981) *Atmospheric thermodynamics.* Boston: Kluwer Academic Publishers.

Irvine, W.M., Knacke, R.F. (1989) The chemistry of interstellar gas and grains. In *Origin and Evolution of Planetary and Satellite Atmospheres*, eds. S.K. Atreya et al. Tucson AZ: University of Arizona Press.

Jackson, J.A., Lias, S.G. (1974) Primary processes in the photolysis of *n*-butane with 8.4 and 10.0 eV photons. *J. Photochem.* 3, 151–162.

Jenkin, M.E., Murrells, T.P., Shalliker, S.J., Hayman, G.D. (1993) Kinetics and product study of the self-reactions of allyl and allyl peroxy radicals at 296 K. *J. Chem. Soc. Faraday Trans.* 89n3, 433–446.

Johnston, G.R., Cuff, D.R.A., Price, D. (1978) Mechanisms for the photochemical production of hydrocarbons in gaseous hydrocarbon systems. *Prog. React. Kinet.* 8, 231–291.

Judge, D.L., Carlson, R.W. (1974) Pioneer 10 observations of the ultraviolet glow in the vicinity of Jupiter. *Science* 183, 317–318.

Karwat, E. (1924) Der Dampfdruck des festen Chlorwasserstoffs, Methans und Ammoniaks. *Z. Phys. Chem. Stöchiomet. Verwandtschaftsr.* 112, 486–490.

Kaye, J.A., Strobel, D.F. (1984) Phosphine photochemistry in the atmosphere of Saturn. *Icarus* 59, 314.

Kiefer, J.H., Vondrasek, W.A. (1990) The mechanism of the homogeneous pyrolysis of acetylene. *Int. J. Chem. Kin.* 22(7), 747–786.

Kim, S.J., Caldwell, J., Rivolo, A.R., Wagener, R., Orton, G.S. (1985) Infrared polar brightness of Jupiter 3. Spectrometry from the Voyager 1 IRIS experiment. *Icarus* 64, 233–248.

Kim, S.J., Drossart, P., Caldwell, J.J., Maillard, J.-P., Herbst, T., Shure, M. (1991) Images of aurorae on Jupiter from H_3^+ emission at 4 μm. *Nature* 353, 536–539.

Kloster-Jensen, E., Haink, H.-J., Christen, H. (1974) The electronic spectra of unsubstituted mono- to penta-acetylene in the gas phase and in solution in the range 1100 to 4000 Å. *Helv. Chim. Acta* 57, 1731–1744.

Koch, E.E., Skibowski, M. (1971) Optical absorption of gaseous methane, ethane, propane and butane and reflection of solid methane and ethane in the vacuum ultraviolet. *Chem. Phys. Letters.* 9n5, 429–432.

Kostiuk, T., Mumma, M.J., Espenak, F., Deming, D., Jennings, D.E., Maguire, E., Zipoy, D. (1983) Measurements of stratospheric ethane in the Jovian south polar region from infrared heterodyne spectroscopy of the n9 band near 12 μm. *Astrophys. J.* 265, 564–569.

Krasnopolsky, V.A. (1995) Uniqueness of a solution of a steady state photochemical problem: Applications to Mars. *J. Geophys. Res.* 100nE2, 3263–3276.

Kunde, V.G., Hanel, R.A., Maguire, W., Gautier, D., Baluteau, J.P., Maarten, A., Chedia, A., Husson, N., Scott, N. (1982) The tropospheric gas composition of Jupiter's north equatorial belt (NH_3, PH_3, CH_3D, GeH_4, H_2O) and the Jovian D/H isotopic ratio. *Astrophys. J.* 263, 443–467.

Langford, A.O., Petek, H., Moore, C.B. (1983) Collisional removal of $CH_2(^1A_1)$: Absolute rate constants for atomic and molecular collisional partners at 295 K. *J. Chem. Phys.* 78, 6650–6659.

Larson, H.P., Davis, D.S., Hoffman, R., Bjoraker, G. (1984) The Jovian atmospheric window at 2.7 μm: A search for H2S. *Icarus* 60, 621–639.

Laufer, A.H., Gardner, E.P., Kwok, T.L., Yung, Y.L. (1983) Computations and estimates of rate coefficients for hydrocarbon reactions of interest to the atmospheres of the outer solar system. *Icarus* 56, 560–567.

Laufer, A.H., McNesby, J.R. (1968) Photolysis of methane at 1236 Å: Quantum yield of hydrogen formation. *J. Chem. Phys.* 49, 2272–2278.

Lee, L.C., Chiang, C.C. (1983) Photodissociation of CH_4. *J. Chem. Phys.* 78, 688–691.

Lellouch, E., Lacome, N., Guelachvili, G., (1987) Ammonia: experimental absolute linestrengths and self-broadening parameters in the 1800– to 2100–cm^{-1} range. *Journal of Molecular Spectroscopy* 124n2, 333–347.

Lellouch, E., Drossart, P., Encrenaz, Th. (1989) A new analysis of the jovian 5-micron Voyager/IRIS spectra. *Icarus* 77, 457–465.

Lias, S.G., Collin, G.J., Rebbert, R.E., Ausloos, P. (1970) Photolysis of ethane at 11.6–11.8 eV. *J. Chem. Phys.* 52, 1841–1851.

Lightfoot, P.D., Pilling, M.J. (1987) Temperature and pressure dependence of the rate constant for the addition of H to C_2H. *J. Phys. Chem.* 91, 3373–3379.

Lindal, G.F., Wood, G.E., Levy, G.S., Anderson, J.D., Sweetnam, D.N., Hotz, H.B., Buckles, B.J., Holmes, D.F., Doms, P.E., Eshleman, V.R., Tyler, G.L., Croft, T.A. (1981) The atmosphere of Jupiter: an analysis of the Voyager radio occultation measurements. *J. Geophys. Res.* 86, 8721–8727.

Lindzen, R.S. (1971) Tides and gravity in the upper atmosphere. In *Mesospheric models and related experiments*, ed. G. Fiocco, pp. 122–130. Dordrecht, Holland: D.Reidel Publishing Company.

Little, B., Anger, Clifford D., Ingersoll, A.P., Vasavada, A.R., Senske, D.A., Breneman,

H.H., Borucki, W.J., the Galileo SSI Team (1999) Galileo Images of Lightning on Jupiter. Icarus 142, 306–323.

Lunine, J.I., Hunten, D.M. (1987) Moist convection and the abundance of water in the troposphere of Jupiter. *Icarus* 69, 566–570.

Mahaffy, P.R., Niemann, H.B., Alpert, A., Atreya, S.K., Donahue, T.M., Owen, T.C. (1998a) Heavy noble gases in the atmosphere of Jupiter. *Bull. Am. Astron. Soc.* 30, 1066.

Mahaffy, P.R., Donahue, T.M., Atreya, S.K., Owen, T.C., Niemann, H.B. (1998b) Galileo Probe measurements of D/H and $^3He/^4He$ in Jupiter's atmosphere. *Space Science Rev.* 84, 251–263.

Mahaffy, P.R. (1996) Personal communication, Greenbelt MD: oral, February.

Mahaffy, P.R. (1997) Personal communication, Internet: email, 28 November.

Mahaffy, P.R., Niemann, H.B., Demick, J. (1999) Measurement of ammonia at Jupiter with the Galileo Probe Mass Spectrometer. *Bull. Am. Astron. Soc.* 31, 1154.

Mahaffy, P.R., Niemann, H.B., Atreya, S.K., Wong, M.H., Owen, T.C. (2000) $^{15}N/^{14}N$ isotope ratio in the Jovian Atmosphere. *Bull. Am. Astron. Soc.* 32, 1015.

McDonald, J.R., Baronavski, A.P., Donnelly, V.M. (1978) Multiphoton-vacuum-ultraviolet laser photodissociation of acetylene: emission from electronically excited fragments. *Chem. Phys.* 33n2, 161–170.

McNesby, J.R., Okabe, H. (1964) Vacuum ultraviolet photochemistry. *Adv. Photochem.* 3, 157–240.

Mizuno, H. (1980) Formation of the giant planets. *Prog. Theor. Phys.* 64, 544–557.

Mizuno, H., Nakazawa, K., Hayashi, C. (1978) Instability of a gaseous envelope surrounding a planetary core and formation of giant planets. *Prog. Theoret. Phys.* 60n3, 699–710.

Monks, P.S., Nesbitt, F.L., Payne, W.A., Scanlon, M., Stief, L.F. (1995) Kinetics and products of the reactions between H and C_2H_2 at T=213K and T=298K. *J. Phys. Chem.* 99, 17151.

Mordaunt, D.H., Lambert, I.R., Morley, G.P., Ashfold, M.N.R., Dixon, R.N., Western, C.M., Schnieder, L., Welge, K.H. (1993) Primary product channels in the photodissociation of methane at 121.6 nm. *J. Chem. Phys.* 98, 2054.

Mount, G.H., Moos, H.W. (1978) Photoabsorption cross sections of methane and ethane 1380–1600 Å, at T = 295 K and T = 200 K. *Astrophys. J.* 224, L35–L38.

Mount, G.H., Warden, E.S., Moos, H.W. (1977) Photoabsorption cross sections of methane from 1400 to 1850 Å, *Astrophys. J.* 214, L47–L49.

Nakajima, K., Takehiro, S., Ishiwatari, M., Hayashi, Y.-Y. (2000) Numerical modeling of

Jupiter's moist convection layer. *Geophys. Res. Lett.* 27n19, 3129–3132.

Nakayama, T., Watanabe, K. (1964) Absorption and photoionization coefficients of acetylene, propyne, and 1-butyne. *J. Chem. Phys.* 40, 558–561.

Nava, D.F., Mitchell, M.B., Stief, L.J. (1986) The reaction H + C_4H_2: Absolute rate constant measurement and implication for atmospheric modeling of Titan. *J. Geophys. Res.* 91, 4585–4589.

Niedzielski, J.P., Geblewicz, P., Gawlowski, J. (1979) Gas phase photolysis of 1-butene at 123.7 nm (10.0 eV). *J. Photochem.* 10, 287–295.

Niedzielski, J.P., Makulski, W., Gawlowski, J. (1978) Gas phase photolysis of 1-butene at 147 nm (8.4 eV). *J. Photochem.* 9, 519–528.

Niemann, H.B., Harpold, D.N., Atreya, S.K., Carignan, G.R., Hunten, D.M., Owen, T.C. (1992) Galileo probe mass spectrometer experiment. *Space Sci. Rev.* 60, 111–142.

Niemann, H.B., Atreya, S.K., Carignan, G.R., Donahue, T.M., Haberman, J.A., Harpold, D.N., Hartle, R.E., Hunten, D.M., Kasprzak, W.T., Mahaffy, P.R., Owen, T.C., Spencer, N.W., Way, S.H. (1996) The Galileo Probe Mass Spectrometer: Composition of Jupiter's atmosphere. *Science* 272, 846–849.

Niemann, H.B., Atreya, S.K., Carignan, G.R., Donahue, T.M., Haberman, J.A., Harpold, D.N., Hartle, R.E., Hunten, D.M., Kasprzak, W.T., Mahaffy, P.R., Owen, T.C., Way, S.H. (1998) The composition of the Jovian atmosphere as determined by the Galileo Probe Mass Spectrometer. *J. Geophys. Res.* 103, 22831–22846.

Niewiadomski, M. (1979) A numerical model of the updraft-downdraft interaction in Cb clouds. *Acta Geophysica Polonica* 27, 277–291.

Noll, K.S., Larson, H.P. (1991) The spectrum of Saturn from 1990–2230 cm^{-1}: Abundances of AsH_3, CH_3D, CO, GeH_4, and PH_3. *Icarus* 89, 168–189.

Noll, K.S, Larson, H.P. (1990) The abundance of AsH_3 in Jupiter. *Icarus* 83, 494–499.

Noll, K.S., Knacke, R.F., Geballe, R.T., Tokunaga, A.T. (1988) The origin and vertical distribution of carbon monoxide on Jupiter. *Astrophys. J.* 324, 1210–1218.

Noll, K.S., Knacke, R.F., Tokunaga, A.T., Lacy, J.H., Beck, S., and Serabyn, E. (1986) The abundances of ethane and acetylene in the atmospheres of Jupiter and Saturn. *Icarus* 65, 257.

Obi, K., Akimoto, H., Ogata, Y., Tanaka, I. (1971) Photolyses of propane, *n*-butane, and cyclobutane at Xe and Kr resonance lines. *J. Chem. Phys.* 55n8, 3822–3828.

Okabe, H. (1978) *Photochemistry of Small Molecules*. New York NY: John Wiley & Sons, Inc.

Okabe, H. (1981) Photochemistry of acetylene at 1470 Å. *J. Chem. Phys.* 75, 2772–2778.

Okabe, H. (1983a) Photochemistry of acetylene at 1849 Å. *J. Chem. Phys.* 78, 1312–1317.

Okabe, H. (1983b) Photochemistry of acetylene. *Can. J. Chem. Phys.* 75, 850–855.

Okabe, H., Becker, D.A. (1963) Vacuum ultraviolet photochemistry. VII. Photolysis of *n*-butane. *J. Chem. Phys.* 39, 2549–2555.

Opansky, B.J., Leone, S.R. (1996) Low-temperature rate coefficients of C_2H with CH_4 and CD_4 from 154 to 359 K. *J. Phys. Chem.* 100, 4888–4892.

Orton, G.S., Fisher, B.M., Baines, K.H., Stewart, A.T., Friedson, A.J., Ortiz, J.L., Marinova, M., Ressler, M., Dayal, A., Hoffmann, W., Hora, J., Hinkley, S., Krishnan, V., Masanovic, M., Tesic, J., Tziolas, A., Parija, K.C. (1998) Characteristics of the Galileo probe entry site from Earth-based remote sensing observations. *J. Geophys. Res.* 103, 22791–22814.

Owen, T.C., Mahaffy, P., Niemann, H.B., Atreya, S.K., Donahue, T.M., Bar-Nun, A., de Pater, I. (1999) A low-temperature origin for the planetesimals that formed Jupiter. *Nature* 402, 269–270.

Owen, T.C., McKellar, A., Encrenaz, Th., Lecacheux, J., deBergh, C., Maillard, J. (1977) A study of the 1.56 micron NH_3 band on Jupiter and Saturn. *Astron. Astrophys.* 54, 291–295.

Owen, T.C., Atreya, S.K., Niemann, H.B., Mahaffy, P. (1996) The composition of Jupiter's atmosphere: Implications for origin. *EOS, Trans. Suppl.* 77(46), F438.

Owen, T.C., Atreya, S.K., Mahaffy, P., Niemann, H.B., Wong, M.H. (1997) On the origin of Jupiter's atmosphere and the volatiles on the Medicean Stars. In *Three Galileos: The Man, The Spacecraft, The Telescope*, ed. C. Barbieri et al., pp.289–297. Dordrecht, The Netherlands: Kluwer Academic Publishers.

Owen, T.C., Mason, H.P. (1969) New studies of Jupiter's atmosphere. *J. Atmos. Sci.* 26, 870–873.

Pawlowska-Mankiewicz, H. (1987) On the mechanisms of downdraft maintenance in cumulonimbus clouds. *Tellus* 39A, 266–270.

Perri, F., Cameron, A.G.W. (1974) Hydrodynamic instability of the solar nebula in the presence of a planetary core. *Icarus* 22, 416–425.

Pitts, W.M., Pasternack, L., McDonald, J.R. (1982) Temperature dependence of the C_2 ($X^1\Sigma_g^+$) reaction with H_2 and CH_4 and C_3 ($X^1\Sigma_g^+$ and $a^3\Pi_4$ equilibrated states) with O2. *Chem. Phys.* 68, 417–422.

Podolak, M., Hubbard, W.B., Pollack, J.B. (1993) Gaseous accretion and the formation of giant planets. In *Protostars and Planets III*, ed. E.H. Levy and J.I. Lunine, pp. 1109–1147. Tucson AZ: University of Arizona Press.

Pollack, J.B., Hollenbach, D., Simonelli, D., Beckwith, S., Roush, T.L., Fong, W. (1990) Optical properties of grains in molecular clouds and accretion disks. In *Reports of Planetary Geology and Geophysics*, p.560 (SEE N92-10728 01-91). Washington DC: NASA.

Pollack, J.B., Lunine, J.I., Tittemore, W.C. (1991) Origin of the Uranian Satellites. In *Uranus*, eds. J.T. Bergstralh et al., pp.469–512. Tucson AZ: University of Arizona Press.

Pratt, G.L., Wood, S.W. (1984) Kinetics of the reaction of methyl radicals with oxygen. *J. Chem. Soc. Faraday Trans. 1* 80, 3419–3427.

Prinn, R.G., Fegely, B. Jr. (1989) Solar nebula chemistry: Origin of planetary, satellite, and cometary volatiles. In *Origin and Evolution of Planetary and Satellite Atmospheres*, eds. S.K. Atreya et al., pp. 78–136. Tucson AZ: University of Arizona Press.

Press, W.H., Teukolsky, S.A., Vetterling, W.H., Flannery, B.P. (1992) *Numerical Recipes in FORTRAN: The Art of Scientific Computing.* Cambridge UK: Cambridge University Press.

Pruppacher, H.R., Klett, J.D. (1978) *Microphysics of Clouds and Precipitation.* Boston MA: D.Reidel Publishing Company.

Rabalais, J.W., McDonald, J.M., Scherr, V., McGlynn, S.P. (1971) Electronic spectroscopy of isoelectronic molecules. II. Linear triatomic groupings containing sixteen valence electrons. *Chem. Rev.* 71, 73.

Ragent, B., Rages, K.A., Knight, T.C.D., Arvin, P., Orton, G.S. (1998) The clouds of Jupiter: Results of the Galileo Jupiter Mission Probe Nephelometer Experiment. *J. Geophys. Res.* 103, 22891–22909.

Rebbert, R.E. Ausloos, P. (1973) Photolysis of methane: Quantum yield of $C(^1D)$ and CH. *J. Photochem.* 1, 171–176.

Richards, P.G., Fennelly, J.A., Torr, D.G. (1994) EUVAC: A solar EUV flux model for aeronomic calculations. *J. Geophys. Res.* 99nA5, 8981–8992.

Romani, P.N. (1986) *Clouds and methane photochemical hazes on the outer planets.* Ph.D. Thesis. Ann Arbor MI: The University of Michigan.

Romani, P.N., Atreya, S.K. (1988) Methane photochemistry and haze production on Neptune. *Icarus* 74, 424.

Romani, P.N., de Pater, I. and Zahnle, K. (1995) Galileo, SL9, and Jupiter's deep atmosphere. *Bull. Am. Astron. Soc.* 27, 81.

Roos-Serote, M., Drossart, P., Encrenaz, Th., Carlson, R.W., Leader F. (1999) Constraints on the Tropospheric Cloud Structure of Jupiter from Spectroscopy in the 5-μm Region: A Comparison between Voyager/IRIS, Galileo-NIMS, and ISO-SWS Spectra. *Icarus* 137, 315–340.

Roos-Serote, M., Drossart, P., Encrenaz, Th., Lellouch, E., Carlson, R., Baines, K., Kamp, L., Orton, G., Muhlman, R., Calcutt, S., Irwin, P., Taylor, F., Weir, A. (1998) Analysis of Jupiter NEB hot spots in the 4–5 mm range from Galileo/NIMS observations: Measurements of cloud opacity, water and ammonia. *J. Geophys. Res.* 103, 23023–23042.

Roulston, M.S., Stevenson, D.J. (1995) Prediction of neon depletion in Jupiter's atmosphere (abstract). EOS 76, F343.

Samson, J.A.R., Marmo, F.F., Watanabe, K. (1962) Absorption and photoionization coefficients of propylene and butene-1 in the vacuum ultraviolet. *J. Chem. Phys.* 36, 1133–1167.

Schmitt, R.G., Brehm, R.K. (1966) Double beam spectroscopy in the far ultraviolet. 1: 1150Å to 3600Å. *Appl. Opt.* 5, 1111.

Scott, D.W., Oliver, G.D., Gross, M.E., Hubbard, W.N., Huffman, H.M. (1949) Hydrazine: Heat capacity, heats of fusion and vaporization, vapor pressure, entropy and thermodynamic functions. *J. Amer. Chem. Soc.* 71, 2293.

Seiff, A., Kirk, D.B., Knight, T.C.D., Mihalov, J.D., Blanchard, R.C., Young, R.E., Schubert, G., von Zahn, U., Lehmacher, G., Milos, F.S., Wang, J. (1996) Structure of the atmosphere of Jupiter: Galileo probe measurements. *Science* 272, 844.

Seiff, A., Kirk, D.B., Knight, T.C.D., Young, R.E., Mihalov, J.D., Young, L.A., Milos, F.S., Schubert, G., Blanchard, R.C., Atkinson, D. (1998) Thermal structure of Jupiter's atmosphere near the edge of a 5-μm hot spot in the north equatorial belt. *J. Geophys. Res.* 103, 22857–22889.

Seiff, A., Kirk, D.B., Mihalov, J., Knight, T.C.D. (1999) Further evaluation of waves and turbulence encountered by the Galileo Probe during descent in Jupiter's atmosphere. *Geophys. Res. Lett.* 26n9, 1199–1202.

Seiff, A., Kirk, D.B., Young, R.E., Schubert, G. (2001) Atmospheric flow within Jupiter's 5-micron hot spots. Submitted to *Planetary and Space Science* in 1998.

Seki, K., Okabe, H. (1993) Photochemistry of acetylene at 193.3 nm. *J. Phys. Chem.* 97, 5284–5290.

Shin, K.S., Michael, J.V. (1991) Rate constants (296–1700 K) for the reactions $C_2H + C_2H_2 \rightarrow C_4H_2 + H$ and $C_2D_2 \rightarrow C_4D_2 + D$. *J. Phys. Chem.* 95, 5864–5869.

Showman, A.P. (2000) Personal communication, Lisboa, Portugal: oral, 3 April.

Showman, A.P., Dowling, T.E. (2000) Nonlinear simulations of Jupiter's 5-micron hot spots. *Science* 289, 1737–1740.

Showman, A.P., Ingersoll, A.P. (1998) Interpretation of Galileo Probe data and implications for Jupiter's dry downdrafts. *Icarus* 132, 205–220.

Simpson, J. (1971) On cumulus entrainment and one-dimensional models. *J. Atmos. Sci.* 28, 449–455.

Slanger, T.G., Black, G. (1982) Photodissociative channels at 1216 Å for H_2O, NH_3, and CH_4. *J. Chem. Phys.* 77, 2432–2437.

Smith, G.R., Shemansky, D.E., Holberg, J.B., Broadfoot, A.L., Sandel, B.R. (1983) Saturn's upper atmosphere from the Voyager 2 EUV solar and stellar occultations. *J.*

Geophys. Res. 88, 8667–8678.

Smith, B.A., Hunt, G.E. (1976) Motions and morphology of clouds in the atmosphere of Jupiter. In *Jupiter*, ed. T. Gehrels, pp. 564–585. Tucson AZ: University of Arizona Press.

Smoluchowski, R. (1976) Origin and Structure of Jupiter and its Satellites. In *Jupiter*, ed. T. Gehrels, pp. 3–21. Tucson AZ: University of Arizona Press.

Sromovsky, L.A., Best, F.A., Collard, A.D., Fry, P.M., Revercomb, H.E., Freedman, R.S., Orton, G.S., Hayden, J.L., Tomasko, M.G., Lemmon, M.T. (1996) Solar and thermal radiation in Jupiter's atmosphere: Initial results of the Galileo probe net flux radiometer. *Science* 272, 851–854.

Sromovsky, L.A., Collard, A.D., Fry, P.M., Orton, G.S., Lemmon, M.T., Tomasko, M.G., Freedman, R.S. (1998) Galileo Probe measurements of thermal and solar radiation fluxes in the Jovian atmosphere. *J. Geophys. Res.* 103, 22929–22978.

Stevenson, D.J. (1982) Interiors of the giant planets. *Ann. Rev. Earth Planet. Sci.* 10, 257–295.

Stoker, C.R. (1986) Moist convection: A mechanism for producing the vertical structure of the Jovian equatorial plumes. *Icarus* 67, 106–125.

Strobel, D.F. (1977) NH_3 and PH_3 photochemistry in the Jovian atmosphere. *Astrophys. J.* 214, L97.

Strom, K.M., Strom, S.E., Edwards, S., Cabrit, S., Skrutskie, M.F. (1989) Circumstellar material associated with solar-type pre-main-sequence stars–A possible constraint on the timescale for planet building. *Astron. J.* 97, 1451–1470.

Suto, M., Lee, L.C. (1984) Quantitative photoexcitation and fluorescence studies of C_2H_2 in vacuum ultraviolet. *J. Chem. Phys.* 80, 4824–4831.

Tanzawa, T., Gardiner, W.C. Jr. (1980) Reaction mechanism of the homogeneous thermal decomposition of acetylene. *J. Phys. Chem.* 84, 236–239.

Tobiska, W.K., Eparvier, F.G. (1998) EUV97: Improvements to EUV irradiance modeling in the soft x-rays and FUV. *Solar Phys.* 177, 147–159.

Toublanc, D., Parisot, J.P., Brillet, J., Gautier, D., Raulin, F., McKay, C.P. (1995) Photochemical modeling of Titan's atmosphere. *Icarus* 113, 2–26.

Trilling, D.E., Benz, W., Guillot, T., Lunine, J.I., Hubbard, W.B., Burrows, A. (1998) Orbital Evolution and Migration of Giant Planets: Modeling Extrasolar Planets. *Astrophysical Journal* 500, 428.

Tsang, W. (1988) Chemical kinetic data-base for combustion chemistry. Part 3. Propane. *J. Phys. Chem. Ref. Data* 17, 887–952.

Tsang, W. (1991) Chemical kinetic data base for combustion chemistry. V. Propene. *J. Phys. Chem. Ref. Data* 20, 221–274.

Tsang, W., Hampson, R.F. (1986) Chemical kinetic data base for combustion chemistry, part 1, Methane and related compounds. *J. Phys. Chem. Ref. Data* 15, 1087–1279.

von Zahn, U., Hunten, D.M., Lehmacher, G. (1998) Helium in Jupiter's atmosphere: Results form the Galileo probe Helium Interferometer Experiment. *J. Geophys. Res.* 103, 22815–22829.

Wagner, Von H. G., Zellnar, R. (1972a) Reaktionen von wassers-toffatoman mit ungesättigten C_3-kohlenwasserstoffen. II. Die reaktion von H-atomen mit methylacetylen. *Ber. Bunsenges. Phys. Chem.* 76, 518–525.

Wagner, Von H. G., Zellnar, R. (1972b) Reaktionen von wassers-toffatoman mit ungesättigten C_3-kohlenwasserstoffen. II. Die reaktion von H-atomen mit allen. *Ber. Bunsenges. Phys. Chem.* 76, 667–672.

Warnatz, J. (1984) Rate coefficients in the C/H/O system. In *Combustion Chemistry.* New York NY: Springer Verlag.

Washburn, E.W. (1924) The vapor pressure of ice and of water below the freezing point. *Monthly Weather Review*, 488–490.

Washburn, E.W., ed. (1928) *International Critical Tables.* New York NY: McGraw-Hill Book Co., Inc.

Weidenschilling, S.J., Lewis, J.S. (1973) Atmospheric and cloud structure of the Jovian planets. *Icarus* 20, 465–476.

Weisstein, E.W., Serabyn, E. (1996) Submillimeter line search in Jupiter and Saturn. *Icarus* 123, 23–36.

Weisstein, E.W., Serabyn, E. (1994) Detection of the 267 GHz J=1–0 rotational transition of PH_3 in Saturn with a new Fourier transform spectrometer. *Icarus* 109, 367.

West, R.A., Strobel, D.F., Tomasko, M.G. (1986) Clouds, aerosols, and photochemistry in the Jovian atmosphere. *Icarus* 65, 161–217.

Whytock, D.A., Payne, W.A., Stief, L.J. (1976) Rate of the reaction of atomic hydrogen with propyne over an extended pressure and temperature range. *J. Chem. Phys.* 65, 191–195.

Wilson, E.H., Atreya, S.K. (2000) Sensitivity studies of methane photolysis and its impact on hydrocarbon chemistry in the atmosphere of Titan. *J. Geophys. Res.* 105nE8, 20263–20273.

Wong, M.H. (1982) *King of the Planets.* Fourth grade science report. San Jose CA: McCollam Elementary School.

Wong, M.H., Atreya, S.K., Romani, P.N. (1998) Downdraft entrainment model. *Bull. Am. Astron. Soc.* 30, 1075.

Wong, M.H., Atreya, S.K., Mahaffy, P.R. (1999) Error analysis of Galileo Probe Mass Spectrometer atmospheric mixing ratio measurements. *Bull. Am. Astron. Soc.* 31,

1154.

Wong, M.H., de Pater, I., Heiles, C., Millan, R., Maddalena, Kesteven, M., Price, R.M., Calabretta, M. (1996) Observations of Jupiter's 20-cm Synchrotron Emission during the Impacts of Comet P/Shoemaker-Levy 9. *Icarus* 121, 457–468.

Wu, C.Y.R., Chen, T.S., Liu, G.S., Judge, D.L., Caldwell, J.J. (1989) Photoabsorption of C_2H_2 in the 1530–1930Å region: a temperature dependence study. *J. Chem. Phys.* 91, 272.

Yair, Y., Levin, Z., Tzivion, S. (1995) Microphysical processes and dynamics of a Jovian thundercloud. *Icarus* 114n2, 278–299.

Ye, C., Suto, M., Lee, L.C. (1988) CH(A,B-X) fluorescence from vacuum ultraviolet excitation of CH_3. *J. Chem. Phys.* 89, 2797–2802.

Young, K.C. (1993) *Microphysical Processes in Clouds.* New York NY: Oxford University Press.

Young, R.E. (1998) The Galileo probe mission to Jupiter: Science overview. *J. Geophys. Res.* 103, 22775–22790.

Young, R.E. (2000) Correction to "The Galileo probe mission to Jupiter: Science overview," by R.E. Young. *J. Geophys. Res.* 105, 12093.

Yung, Y.L., Allen, M., Pinto, J.P. (1984) Photochemistry of the atmosphere of Titan: Comparison between model and observations. *Astrophys. J. Suppl.* 55, 465–506.

Zabarnick, S., Fleming, J.W., Lin, M.C. (1986) Kinetic study of the reaction $CH(X^2\Pi) + H_2 \leftrightarrow CH_2(X^3B_1) + H$ in the temperature range 372 to 675 K. *J. Chem. Phys.* 85, 4373–4376.

Zelikoff, M., Watanabe, K. (1953) Absorption coefficients of ethylene in the vacuum ultraviolet. *J. Opt. Soc. Am.* 43, 756–759.

Ziegler, W.T. (1959) *The vapor pressures of some hydrocarbons in the liquid and solid state at low temperatures.* Technical Note 4. Washington DC: National Bureau of Standards.

Ziegler, W.T., Kirk, B.S., Mullins, J.C., Berquist, A.R. (1964) *Calculation of the vapor pressure and heats of sublimation of liquids and solids below one atmosphere pressure. VII. Ethane.* Technical Report No. 2. Eng. Expt. Station, Georgia Institute of Technology.

EPA/NIH mass spectral data base. Vol.I. Molecular weights 30-186, eds. Heller, S.R., Milne, G.W.A. (1978) Washington DC: National Bureau of Standards.

NIST/EPA/NIH Mass Spectral Database, version 4.5. (1994) Gaithersburg MD: U.S. Department of Commerce.